UNIVERSITY OF BIRMINGHAM

OPTIMISING THE PRODUCTION OF MICROFIBRILLATED CELLULOSE IN A STIRRED MEDIA MILL

by

Lewis R. Taylor

A thesis submitted to the
University of Birmingham
for the degree of
DOCTOR OF ENGINEERING

School of Chemical Engineering
College of Engineering & Physical Sciences
University of Birmingham
October 2020

ABSTRACT

Stirred media mills are used to produce microfibrillated cellulose (MFC) in the *FiberLean* process. This work uses a laboratory-scale mill to investigate the influence of various operating conditions and feed characteristics on product properties. Microscopy and optical image analysis identify fibril breakage and fibrillation as distinct processes, which respond differently to various operating conditions, and must be tailored to optimise MFC quality. Media surface roughness is shown to enhance grinding efficiency, likely by increasing local pressure, and the role of mineral particles in expediting this process is identified. The influence of stress intensity on product particle size and fibrillation is also assessed, along with the interaction of this parameter with media roughness, permitting a general prediction of fibre breakage rate. Large variations in MFC quality between different fibre feedstocks are identified, and analysis of feed fibre properties demonstrates that a high hemicellulose content facilitates liberation of fine fibrils, and a high zero-span tensile strength results in long liberated fibrils. Combining these parameters enables a good prediction of MFC quality from feed measurements. Finally, it was found that optimising grinding conditions for specific feed fibre properties permitted up to a 50 % increase in MFC tensile strength versus standard conditions.

For my family

ACKNOWLEDGEMENTS

Several people were instrumental in helping me complete this work. Firstly, I would like to thank my academic supervisor, Stuart Blackburn, my industrial supervisor, David Skuse, and the head of the EngD programme, Richard Greenwood, for their guidance and help, and the opportunities they made available over the years. They also proof-read this thesis, which as the reader may have the misfortune to notice, is not the smallest in the world. A large fraction of this work also benefitted from the advice of Jon Phipps, *FiberLean*'s lead scientist, whose technical wisdom and tendency to ask difficult questions was invaluable.

The resources and technical support of both *FiberLean* and *Imerys* were vital for this work. Amongst these, I would like to thank Martin Taylor, Gary Sleeman, and Byron Burnhill for the SEM microscopy, Adam Gould for the XRD tests, Chris Grace for powder physical testing, Tony Hiorns for help with the laser profilometer, and Nigel Rowe for supplying some of the grinding media. My thanks also for the work carried out by external organisations, including the media bead cross-section preparations by *Camborne School of Mines* and the fibre chemical characterisations by *Labtium Oy.*

There are many people whomst I should thank for their friendship and maintenance of some level of sanity, particularly when writing this thesis during the 2020 apocalypse. Amongst these are my FiberLean colleagues, including Ben Bulson, Paymaan Tahamtan, Daniel Hewson, Tania Selina, Louise Haley, and Sapphire Wilson-Claridge. Of particular note is Caterina Palange, who by engaging me in several-hour-long 'debates' kept my brain from rusting. Finally, a strong thanks to my family, a reliable source of support throughout my whole life, including my parents Joanne and Phillip, my brothers Chris and Ash, and my dog Luka.

TABLE OF CONTENTS

TABLE OF FIGURES

LIST OF TABLES

1. INTRODUCTION

1.1. Microfibrillated Cellulose

Cellulose is an essential structural polymer in higher plants, and is a fundamental component of paper products and most natural textiles. The mechanical properties which cellulose fibres impart on these applications is a consequence of a fractal-like microstructure that is constituted of smaller *fibril* and *microfibril* sub-units.

In 1982, it was discovered that fibres can be disintegrated to liberate these finer components, greatly increasing specific surface area and hydrogen bonding capability[1-2]. This product was termed *microfibrillated cellulose* (MFC), and has since found numerous applications that exploit its hydrophilicity, high surface area, and high specific strength. These include rheological modifiers in food, paint and drilling fluids, toughening concrete, strengthening paper, in biodegradable packaging (i.e. polystyrene foam replacement), and in barrier coatings, amongst many others[3-4]. MFC will likely have a substantial ecological benefit, since in many applications it displaces petrochemicals, and in strengthening additive applications (such as in paper) permits a decrease in materials used for a given absolute strength specification. The potential market is expected to be enormous, with estimates of around 30 million tonnes per annum given[5].

In only the last decade have technological advancements reduced the production cost sufficiently to make MFC economical in many of these applications. As of 2020, around a dozen commercial MFC producers are active, though market penetration so far has been very limited, with annual sales in the tens of thousands of tonnes.

1.2. FiberLean Technologies

FiberLean Technologies is a joint venture between *Imerys*, the world's largest minerals processing company, and *Omya,* the world's largest calcium carbonate producer. *FiberLean* has adapted stirred media mill technology from the minerals processing industry, to mechanically disintegrate fibres into MFC. A stirred media mill (or *grinder*) is a vessel containing small grinding media beads, which are agitated by an impeller, to break down the feed[6]. In the *FiberLean* process, fibres are typically co-processed with paper filler-grade mineral particles such as calcium carbonate, which improves the energy efficiency[6]. The resultant MFC has a broad distribution of fibril diameters, from micron-scale fibrils, to microfibrils tens of nanometres in diameter, see Figure 1.1.

The very high media surface area enhances fibre breakage rate, and the wearing parts are cheap media beads, rather than expensive precision-engineered components used in alternative methods. Stirred media mills are also much more robust and reliable than the homogenisers typically used for MFC production, having wide tolerances and none of the blockage issues.

Consequently, the *FiberLean* process has a high throughput, with low operating costs, capital costs, and downtime. For this reason, and because of the funding and customer contacts of *Imerys* and *Omya*, *FiberLean* is currently the world's largest MFC producer, with five commercial plants and a total annual capacity of 12,000 dry tonnes. Because shipping low solids content MFC suspensions is uneconomical, and drying and redispersing MFC is difficult, *FiberLean* usually employs *satellite plants*, where a MFC production plant is built at each customer site, typically using the fibre and mineral sources that the customer already has available.

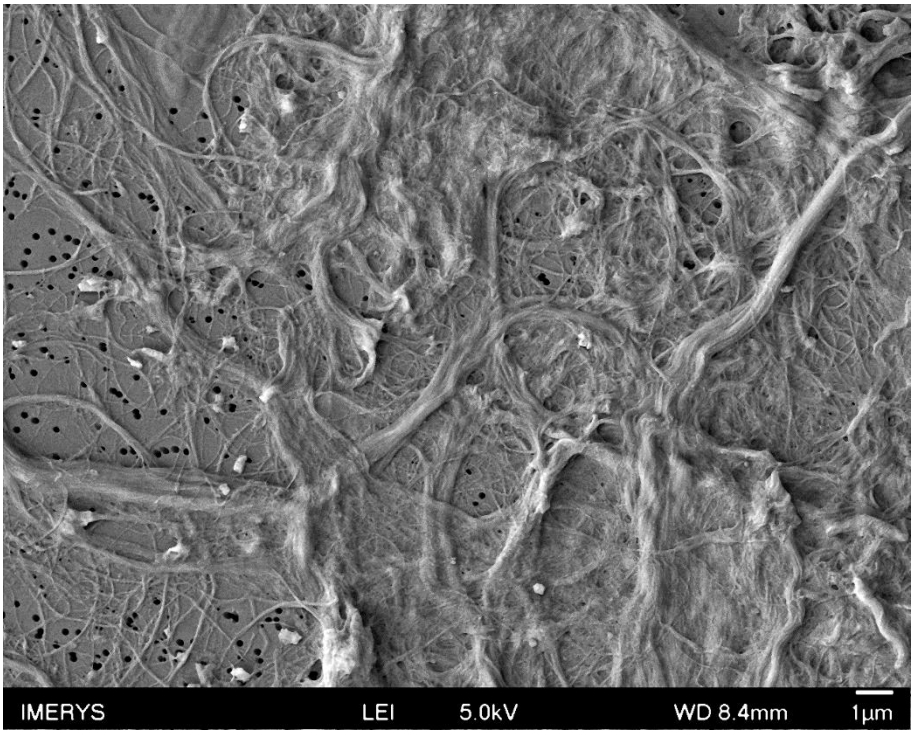

Figure 1.1 *– Scanning electron microscopy image of FiberLean MFC.*

1.3. Commercial Basis for *FiberLean* MFC

Although *FiberLean* is starting to see success in non-paper applications, all satellite plants built so far supply paper mills, where MFC is added to the paper furnish to substantially increase the specific strength. This allows mills to increase the loading of paper filler minerals (i.e. calcium carbonate, talc, or kaolin) which disrupt fibre bonding and decrease strength; MFC strongly associates with the filler mineral, so a 2% dosage of typical *FiberLean* MFC permits a 10 – 15% increase in mineral fraction for a given paper tensile strength[7]. This allows for the maintenance of strength specifications, whilst improving other properties such as opacity and printability, but the primary advantage is reducing cost by replacing fibre with mineral; as Figure 1.2 shows, wood pulp prices are much higher than those of paper filler minerals (kaolin is given as an example).

Considering the steady decline in the printing and writing paper market, such savings may be necessary to maintain mill profitability. In addition to benefitting from MFC sales, *FiberLean's*

parent companies, *Imerys* and *Omya*, sell large quantities of mineral to this industry, so this increased mineral loading enabled by MFC mitigates the decline in demand.

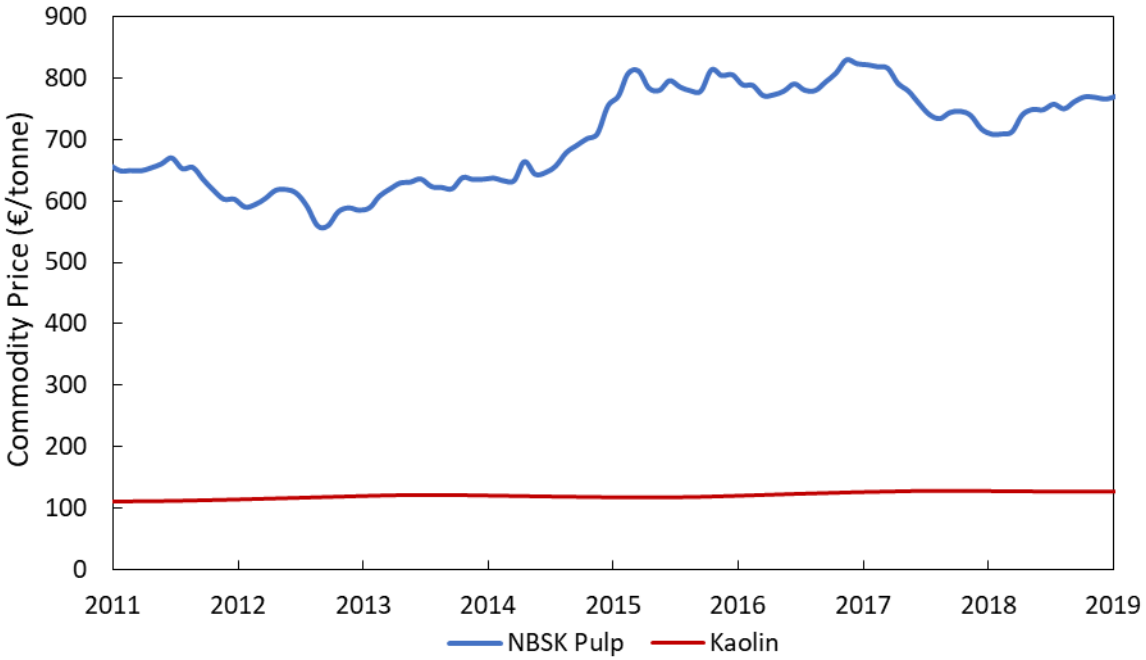

Figure 1.2 *– Market prices of Nordic bleached softwood kraft pulp and kaolin mineral over time. Pulp prices from IndexMundi[8] and kaolin prices from Statista[9].*

The tensile strength of MFC-derived nanopaper is strongly predictive of the filler increase enabled, and also correlates with effectiveness in most non-paper applications, so work in optimising process inputs to maximise this parameter at minimal cost can greatly increase the attractiveness of *FiberLean* MFC to potential customers.

1.4. Project Objectives

This research investigates the production of MFC using a lab-scale stirred media mill under a wide range of conditions. The overarching aim of this project was to improve understanding of the core *FiberLean* process, and maximise MFC strength whilst minimising operating cost. The specific objectives addressed in this work in order to advance this aim were as follows:

- Explore the evolution of product properties and microstructure during grinding, and how this is affected by operating conditions.

- Demonstrate and explain the influence of media surface roughness and mineral content on grinding efficiency and product properties.
- Investigate the extent to which stress intensity theory applies to grinding cellulose fibres.
- Assess the variation in MFC quality between fibre species, and which fibre properties yield good MFC.
- Determine how feed fibre properties influence the choice of optimum operating conditions.

With these objectives met, *FiberLean* would be better suited for optimising the feed composition, grinding media properties, and grinder impeller speed, to maximise the net value gained from this process. Any insights gained in pursuing these objectives that can explain how and why fibres break and fibrillate into MFC under certain conditions would also be welcome since this would aid in the sensible selection of operating conditions for new situations.

1.5. Thesis Layout

The contents of each subsequent chapter are summarised below:

Chapter 2 is the literature review for all work pertinent for this thesis, along with theoretical background explaining stress intensity theory and Hertzian contact mechanics.

Chapter 3 details the materials used and the methods employed in the experimental work.

Chapter 4 addresses the first objective, observing how the microstructure and product quality parameters change as grinding progresses during typical operating conditions, after which the

effects of varying media size, media density, and impeller speed are shown, and a mechanistic model is introduced to suggest why breakage rate differs with operating conditions.

Chapter 5 investigates the influence that media surface roughness and mineral content have on MFC quality and grinding efficiency. A mechanistic reason is suggested, which in the case of media roughness is supported by microscopy and an adaption of the contact mechanics model from Chapter 4.

Chapter 6 investigates the influence of stress intensity on MFC quality, by varying impeller speed and media size, and by combining with data from Chapter 5 amalgamates the effect of both roughness and stress intensity to produce a factor that is largely predictive of MFC grinding.

Chapter 7 assesses the MFC quality using a large number of fibre species as feedstocks, and develops a relationship between feed fibre properties and MFC tensile strength.

Chapter 8 looks into the interactions between fibre properties and operating conditions, to aid in extending the conclusions of Chapters 5 and 6 to other feedstocks.

Chapter 9 gives a summary of the conclusions of each chapter, and details future work suggested from important unanswered questions in this work.

Two publications have been produced based upon this work, attached as Appendix B1 and B2; the first is a literature review on the subject of stirred media milling, some of which is used in Chapter 2, and in the second paper, the results of Chapter 7 are reported.

2. LITERATURE REVIEW AND THEORETICAL BACKGROUND

2.1. Cellulose Structure

Cellulose fibres are extracted from plant matter (typically wood) by pulping and bleaching processes, producing a 'pulp' that is used primarily in paper and cellulose-based packaging to impart mechanical properties. These mechanical properties are a consequence of the fibre microstructure, which is fractal-like with several hierarchies of fibre-like sub-units. A fibre consists of parallel *fibril* chains with micron-scale diameters, similarly constituted of *microfibrils* around 30 nm in diameter. Microfibrils in turn contain *elementary fibrils* around 3.5 nm in diameter, which consist of parallel molecular cellulose chains[10]. A representation of a fibre microstructure is shown as Figure 2.1.

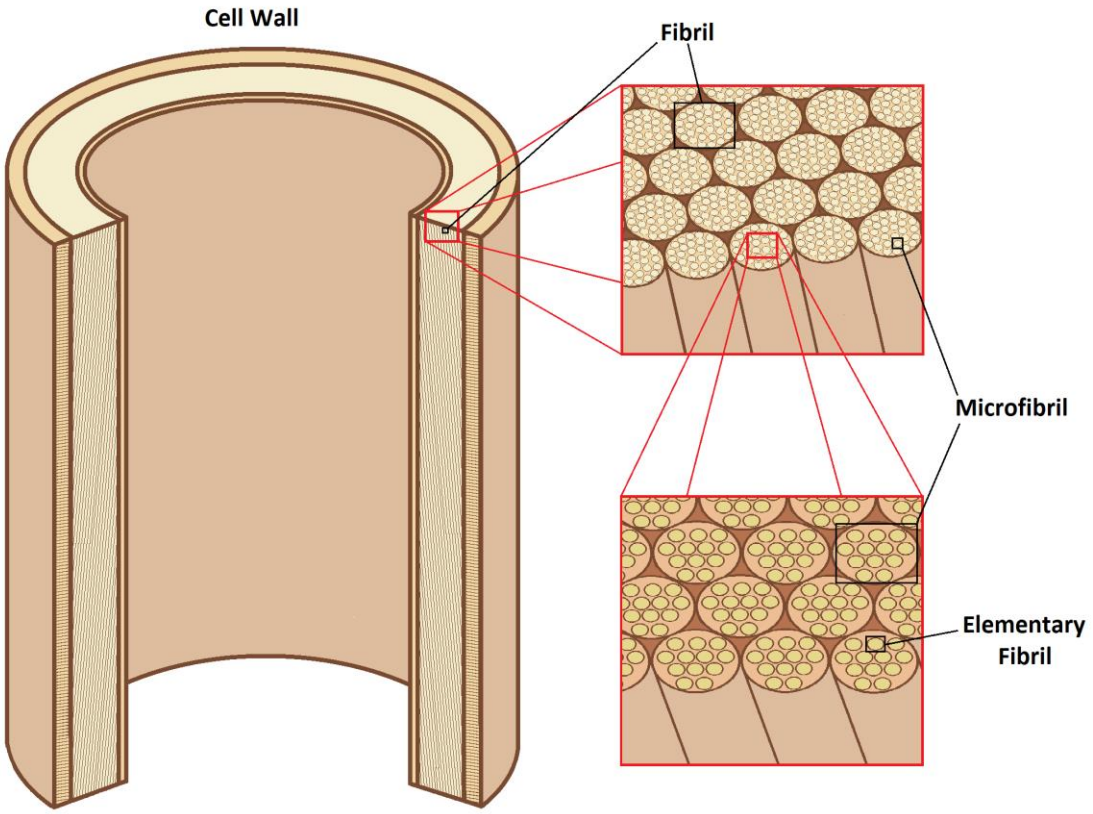

Figure 2.1 *– Hierarchical structures of fibrils, microfibrils, and elementary fibrils within a cellulose fibre cell wall.*

Within the cell wall, cellulose fibrils are assembled in several concentric layers; starting from the outermost layer, these are termed the primary wall, S1 secondary wall, S2 secondary wall, and the tertiary wall, with the latter encapsulating the *lumen,* a hollow space at the fibre centre (see Figure 2.2)[11].

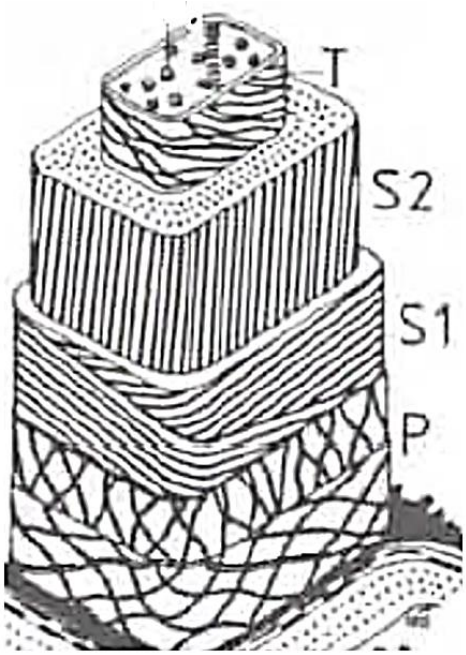

Figure 2.2 *– Wood fibre cell wall structure, P = primary wall, S1 = secondary wall 1, S2 = secondary wall 2, and T = tertiary wall (taken from Fengel and Wegner[11]).*

The fibril arrangements within these layers determine the mechanical properties; in the primary wall, fibrils are randomly arranged in a 0.1 µm[12] thick layer, but in other layers they are wound helically with a different *microfibril angle* in each layer. The S1 and tertiary layers have a gentle slope, with microfibril angles typically above 60%[12], giving ring-like fibril arrangements. The tertiary layer, being merely 0.1 µm thick, maintains lumen integrity, whereas the S1 layer, up to 0.4 µm thick[13], provides most of the transverse compressive strength of the fibre[11]. The S2 layer comprises around 80% of the fibre, and has a steep microfibril angle (5° – 30°)[13] close to the longitudinal axis, and is largely responsible for fibre tensile strength.

Cellulosic fibres in untreated wood contain comparable fractions of cellulose, hemicellulose, and lignin. When producing *chemical pulp*, fibres undergo pulping stages (typically the *kraft* (sulphate) process) to remove almost all the lignin and a large fraction of the hemicellulose, and to individualise the fibres[13]. Subsequently, fibres are typically refined to modify properties, wherein mechanical forces cause *internal fibrillation* and *external fibrillation* (for a review, see Gharehkhani et al.[14]). Internal fibrillation involves 'delaminating' fibrils within the S2 layer, with water infiltrating these newly created gaps, causing fibre swelling; this enhances fibre flexibility and conformability, improving inter-fibre contact[15]. External fibrillation involves damaging the P and S1 layers, to extend some fibrils away from the fibre, increasing the specific surface area available for inter-fibre bonding[15]. By using different refining techniques, Kang and Paulapuro[16] controlled internal and external fibrillation independently and showed that both enhance tensile strength.

2.2. Microfibrillated Cellulose Production

The original process by Turbak et al.[1] and Herrick et al.[2] required up to 20 passes through a homogenizer, necessitating excessive energy input (30,000 kWh/t)[1], although more recent advances have reduced this by an order of magnitude[17]. Fibres are now commonly pre-treated with a disc refiner[17], which damages the P and S1 layers, exposes the S2 layer, and causes internal fibrillation, thereby greatly facilitating homogenization[18]. Other alternative mechanical processes have also been employed, including friction grinders[19] and microfluidization[20]. *FiberLean Technologies* uses stirred media mills for this purpose, which so far has superior cost-effectiveness and scalability than these other methods.

Because of the fractal-like microstructure, and statistical nature of mechanical disintegration, MFC produced entirely mechanically has a broad width distribution of product particles[17],

typically consisting of a mixture of fibres, fibre fragments, fibrils, and microfibrils[10]. These methods can typically disintegrate fibres into fibrils with widths below 100 nm[21] but are largely incapable of liberating the finest microfibril structures. Enzymatic pre-treatment steps cleave some amorphous microfibril regions, reducing energy input[22-24], but still struggles to liberate elementary fibrils.

Microfibrillation at the finest scales requires chemical pre-treatment steps. The most popular method is 2,2,6,6-tetramethylpiperidine-1-oxy radical oxidation (TEMPO)[25], which attaches high concentrations of carboxyl groups to microfibril surfaces; the resultant anionic charges cause mutual repulsion between microfibrils, greatly facilitating disintegration into 3 – 5 nm width particles[26]. Other chemical pre-treatment methods also charge microfibrils, including the carboxymethylation method[27]. Although these methods require minimal mechanical energy, the cost of the chemicals, and the associated equipment to apply this safely with large throughputs has limited this method to low volume, high value applications.

If fibres are sufficiently delignified, MFC can be produced from almost any cellulose source. These include hardwoods, softwoods, and non-wood sources (e.g. cotton, abaca, flax, and sugar beet)[21]. The fibre source has a strong influence on MFC properties; for example, abaca and sisal fibres produce finer MFC than flax and hemp[28]. Other studies also investigate the influence of fibres species[29-30], but each are limited to a small selection of pulps, making obvious links between feed fibre properties and MFC properties elusive.

2.3. Paper Tensile Strength

The most widely used paper tensile strength theory was developed by Page[31]. This postulates that sheet failure occurs by a combination of fibre cross-sections breaking, and inter-fibre

bonds failing, with the weakest mechanism dominating sheet tensile strength. Equation 2.1 states the Page Equation:

$$\frac{1}{T} = \frac{9}{8Z} + \frac{12A\rho}{\tau_B PL(RBA)} \dots [2.1]$$

where *T* is the sheet tensile index (Nm/g), *Z* is the zero-span tensile index (Nm/g), *A* is the fibre cross-sectional area (m^2), *P* is the fibre cross-section perimeter (m), ρ is the fibre density (kg/m^3), *L* is the fibre length (m), τ_B is the shear bond strength per unit area (Pa), and *RBA* is the relative bonded area.

Zero-span tensile index is a measure of individual fibre strength. *RBA* represents the fraction of fibre surface area used for inter-fibre bonding. The first term on the right-hand side represents the weakness of individual fibres, whereas the second term represents the weakness of inter-fibre bonds. Typically, paper fails mainly by inter-fibre bonds breaking, making the second term limiting. Adding MFC to a fibre furnish greatly increases *RBA*[32], improving tensile strength considerably.

2.4. Zero-Span Tensile Index

The zero-span tensile index of a paper sheet is measured when the tensile tester clamps are essentially touching. Because almost all fibres are held by both clamps simultaneously, they fail by cross-sectional breakage, negating inter-fibre bonding effects. Several factors influence zero-span strength, including microfibril angle, which gives a negative correlation[33-34].

Zero-span tensile index is strongly affected by the presence of fibre flaws; greater frequencies of fibril discontinuities and cross-sectional flaws increase breakage probability. Literature supports this notion: Zeng et al.[35] damaged fibres by refining, finding zero-span strength to be inversely proportional to fibre kink frequency. Joutsimo et al.[36] induced cell wall damage

(dislocations) by homogenization, decreasing fibre strength; they attributed this to inducing non-uniform load distributions across the cross-section.

Fibril and microfibril-scale damage is also important; Nevell and Nugawela[37] caused localised damage to microfibrils with acid, and Wathén[38] damaged microfibrils homogeneously by thermal ageing degradation, and in both cases fibre zero-span tensile strength was substantially decreased. Since zero-span strength is indicative of fibril quality, a strong influence on MFC properties is expected.

2.5. Fibre Chemistry

Fibre chemical composition is important in papermaking. Most cellulose sources are rich in hemicellulose before processing, much of which remains in the cell wall after pulping. Hemicellulose encompasses various polysaccharides with differing monomer sugars, functional groups, and branching degrees, and are classified into various families. Hardwood hemicellulose is almost all xylans, whereas in softwoods, glucomannans and xylans are present in comparable amounts[39]. Unlike cellulose, which is partially crystalline, hemicellulose is amorphous, with much lower degrees of polymerisation[11].

Hemicellulose closely associates with cellulose, forming layers between microfibrils (with xylan and glucomannan apparently having comparable functions[40]), and readily swells in water[41]. NMR studies show that removing hemicellulose content during pulping increases fibril aggregate widths, providing evidence for hemicellulose inhibiting microfibril coalescence[42-44]. Hemicellulose also aids fibre refining; chemically removing it before refining decreases the post-refining tensile strength[45].

High hemicellulose pulps are therefore expected to produce stronger MFC. Literature supports this: Iwamoto et al.[46] dried pulp after removing hemicellulose by alkali treatment,

resulting in irreversible microfibril aggregation, inhibiting fibrillation. Numerous authors correlated high hemicellulose content with better microfibril yields and individualisation; this seems true whether comparing fibres from different plant sources[28-30] or different pulping conditions[29, 47-48].

Two mechanisms offer explanations for this benefit. Hemicellulose chains on liberated microfibril surfaces can extend outwards in water, bridging neighbouring microfibrils[45]; higher hemicellulose pulps enhance this effect as more liberated microfibril surface area is coated in hemicellulose. This is supported by Arola et al. who removed hemicellulose from nanocellulose with xylanase enzymes, reducing tensile strength, despite barely affecting microfibril geometry[49].

Additionally, high hemicellulose fibres usually produce finer microfibrils when fibrillated, demonstrated by microscopy in various studies[28-29, 46]. Hemicellulose forms a weak, amorphous layer separating microfibrils, so can be expected to facilitate breakage along the direction of microfibril lengths, reducing microfibril diameter, increasing aspect ratio, and consequently improving tensile strength. Xylan also contributes a surface charge from carboxyl group dissociation, though whether this induces sufficient microfibril repulsion to be significant is not clear.

Cellulosic fibres also contain lignin, which is an amorphous phenolic polymer that holds the other components together in a hard matrix. For thermomechanical and chemithermomechanical pulp, (having no lignin removal steps), this lignin coating inhibits mechanical fibrillation, leading to poor MFC[50-51]. Once surface lignin is removed, the role of residual lignin within the cell wall is not obvious; good quality MFC can still be obtained with high lignin, unbleached chemical pulp[48].

2.6. Stirred Media Mills

FiberLean is the only nanocellulose manufacturer that produces MFC using a stirred media mill. The author has published a review giving a broad background on stirred media mills[52], attached as Appendix B1, though a brief discussion is given here.

Stirred media mills were developed for fine and ultrafine grinding in the minerals processing industry, and provide large efficiency benefits compared to the ball mills traditionally used. The design used in the *FiberLean* process is the *Stirred Media Detritor* (SMD), which at industrial scale consists of an octagonal tank, and a vertical pin impeller. The tank is loaded with grinding media beads of several millimetres in size, and an aqueous feed suspension is added. The impeller fluidises the media with the charge, and by a combination of impact, compression, and attrition forces, break the feed into finer particles. The forces applied can be very high, up to accelerations in the thousands of m/s^2 [53]. A schematic of a SMD is given as Figure 2.3.

The impeller accelerates the closest media beads to up around 40% of the tip speed[54-55]. The media circulates about the pot, colliding with media in neighbouring streamlines, transferring kinetic energy radially outwards. Velocity differences between two colliding media results in a force applied to particles trapped between them. Due to a sharp shear rate gradient near the impeller[55], 90% of the input energy is dissipated in the 10% of the grinder volume around this region, the *high intensity grinding zone*[56].

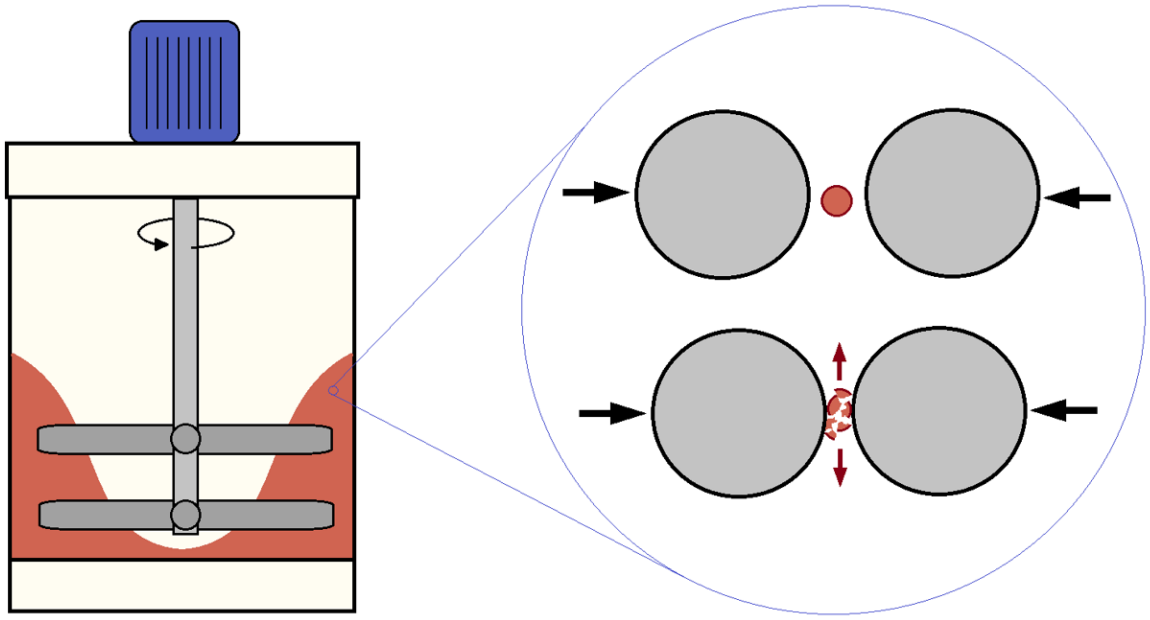

Figure 2.3 – *A schematic of a Stirred Media Detritor, wherein a pin impeller agitates a suspension of grinding media beads to comminute a charge.*

The dominant grinding mechanism has been a subject of debate; some suggest attrition is most important[57] (where very fine particles are broken off from much larger particles), others imply compression[58] (steady application of a pressure force until a particle breaks), while modelling by Kwade[59] implies both take place comparably. Simulations suggest attrition dominates at low collision energies, whereas compression dominates at higher energies[60]; consequently, operating conditions likely influence the major particle breakage mechanism.

Published work on SMD production of MFC is minimal, being exclusive to *FiberLean*, but concepts used in fine mineral grinding and alternative fibrillation processes (e.g. refining) can aid understanding. Of these concepts, *Stress Intensity theory* is essential, relating operating conditions to grinding performance.

2.7. Stress Intensity Theory

Specific energy input is the dominant factor influencing product particle size[61]. However, the kinetic energy of a media collision is also critical; this has been investigated by Kwade et al., who developed *Stress Intensity* theory[62]. The author refers to their own review for a more detailed description[52], though a summary is given here.

Specific energy input is proportional to the product of the *stress number* (*SN*)*,* and the *stress energy* (*SE*). Stress number is a measure of the average number of collisions per particle during a grind, and stress energy is a measure of the energy of each collision. For brittle particles, the stress number is proportional to[63]:

$$SN \propto \frac{\varphi_{GM}(1-\varepsilon)}{\left(1-\varphi_{GM}(1-\varepsilon)\right)c_V}\frac{nt}{{d_{GM}}^2} \quad \ldots [2.2]$$

where φ_{GM} is the mill fill fraction, ε is the media porosity (volume of slurry divided by the total filled volume), n is the impeller revolution speed, t is the grind time, c_V is the solids content (vol%) and d_{GM} is the grinding media diameter. The stress energy of a collision is assumed to be proportional to the maximum possible collision energy, SE_{GM}, which is the energy of a grinding media bead changing its velocity from the impeller tip speed to zero[64]:

$$SE \propto SE_{GM} = d_{GM}^3 v_t^2 \rho_{GM} \quad \ldots [2.3]$$

where ρ_{GM} is the grinding media density and v_t is the impeller tip speed. Stress energy is the energy applied to the media by the mill; *stress intensity* (SI), on the other hand, is defined to represent the stresses imparted upon the product[64]. They are technically different, since various energy transfer factors affect stress intensity, but they are considered proportional when these factors are constant, and are often used interchangeably.

Each material has an optimum stress intensity where product particle size is minimised at a given energy input, with the stress intensity versus particle size curve following a characteristic shape (see Figure 2.4 (a)). Particles break at a critical stress; at stress intensities much lower than this, particles deform elastically, so no grinding takes place. With increasing stress intensity, an increased fraction of the collisions can break particles, rapidly increasing size reduction rate. At much higher stress intensities, more collisions have excessive energy which is mostly wasted, lowering particle size reduction rate (as stress number is also lower). These two effects confluence at a minimum particle size around the optimum stress intensity[65]. Smaller particles have less cross-sectional area to break, so optimum stress intensity decreases with finer feed sizes, and also decreases with energy input as the product particle size declines[65] (see Figure 2.4 (b)).

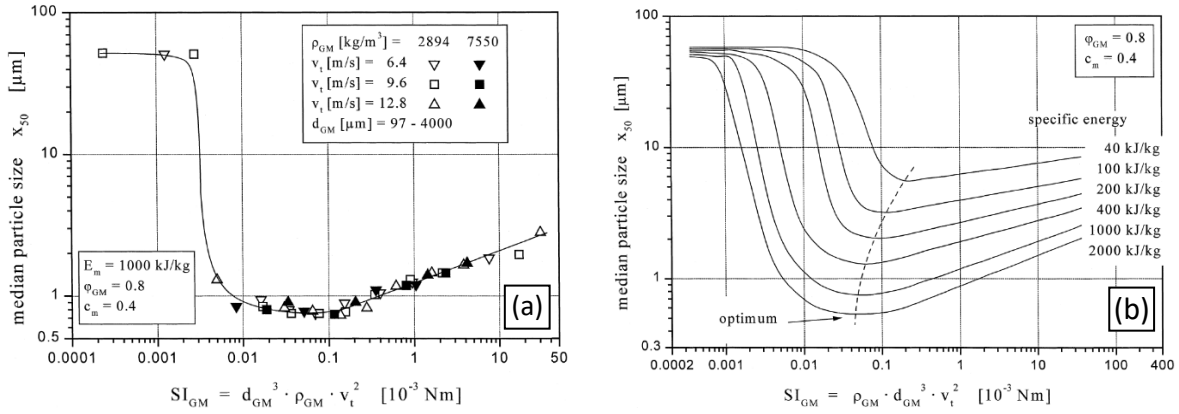

Figure 2.4 *– (a) Median particle size versus maximum stress intensity for the comminution of limestone, (b) how the characteristic curve in (a) varies with energy input (figures taken from Becker et al.[65]).*

Becker et al.[65] found that minerals harder than the grinding media were much more difficult to grind since the media accommodates most of the deformation during a collision. They rewrote Equation 2.3 to define the stress intensity applied to the product, SI_P, which includes the ratio of the Youngs' moduli of the product (Y_P) and grinding media (Y_{GM}):

$$SI_P = d_{GM}^3 \rho_{GM} v_t^2 \left(1 + \frac{Y_P}{Y_{GM}}\right)^{-1} \quad \ldots [2.4]$$

At higher solids contents, viscosity becomes considerable so Breitung-Faes and Kwade included a viscosity factor r_η to account for viscous dampening[66]:

$$SI_P = r_\eta d_{GM}^3 \rho_{GM} v_t^2 \left(1 + \frac{Y_P}{Y_{GM}}\right)^{-1} \quad \ldots [2.5]$$

This viscosity factor can be calculated by considering Stokes' Law[67]:

$$r_\eta = \left[1 + \frac{1}{St_{GM}} ln\left(\frac{x}{d_{GM}}\right)\right]^2 \qquad where\ St_{GM} = \frac{v_{GM} d_{GM} \rho_{GM}}{9\eta} \quad \ldots [2.6]$$

where x is the product particle size (the distance that media must approach within to cause any breakage), St_{GM} is grinding media Stokes' number, and η is the suspension viscosity. At a critical viscosity η_C, media momentum is insufficient to exclude the intervening fluid, preventing contact and making r_η zero (a viscous grinding limit)[67]:

$$\eta_c = \frac{v_{GM,max} d_{GM} \rho_{GM}}{9\big(ln(d_{GM}) - ln(x)\big)} \quad \ldots [2.7]$$

where $v_{GM,max}$ is the maximum grinding media velocity (which is a fraction of the tip speed).

Stress intensity and stress number have been directly measured by microscopy observations of the size and frequency of impact sites on plastically deformable probe particles[58, 68], which supports the proportionalities claimed by stress intensity theory. They also found that stress intensities have a broad frequency distribution, extending to two or three orders of magnitude below the theoretical value, supporting earlier modelling work[69].

According to stress intensity theory, media size, density, and impeller speed are interchangeable in that different permutations should give the same performance if stress intensity is identical. However, as described here, this theory does not consider differing

energy transfer efficiencies and energy distribution differences, nor has it been successfully applied to soft, non-isotropic materials such as cellulose before.

2.8. Energy-Size Relationships and Work Indices

The relationship between energy input and particle size is typically encapsulated by some form of the *Walker Equation*[70]:

$$dE = -K_n \frac{dx}{x^n} \dots [2.8]$$

where E is the energy input, x is the product particle size, K_n is the grinding coefficient, and n is the grinding exponent. When integrated between the feed size x_f and final product size x_p this becomes:

$$E = \frac{K_n}{n-1}\left(\frac{1}{x_p^{n-1}} - \frac{1}{x_f^{n-1}}\right) \dots [2.9]$$

Rittinger's Law[71] and Bond's Law[72] are typically applied to fine grinding, with the former assuming energy input is proportional to surface area generated, and the latter assuming pre-existing cracks are exploited. Equation 2.9 encompasses both laws depending on the value of n, with n = 2 for Rittinger's Law, and n = 1.5 for Bond's Law, though any value of n other than 1 may be used. From analysis of fine and ultrafine mineral grinding data in literature, the author has shown that the typical best fit n exponent matches Rittinger's Law, though this depends greatly on feed characteristics and grinding conditions[52] (see Appendix B1). Work by Riley on the *FiberLean* process over a variety of conditions[73] has shown that the best fit n exponent varies between 1.4 and 2.3 for cellulose grinding.

In previous work with the *FiberLean* process, the ratio of the particle size change to the energy input was used to measure efficiency[73] but this is generally inappropriate, because finer sizes

take progressively more energy to grind. A more useful efficiency definition is found by rearranging Equation 2.9 to find an effective K_n, with an appropriate grinding law (*n* value) chosen as common between series. The *Operating Bond Work Index* W_{iO}[74] common in minerals grinding is such a definition, where *n* is 1.5:

$$Wi_O = \frac{E}{\frac{10}{\sqrt{x_p}} - \frac{10}{\sqrt{x_f}}} \dots [2.10]$$

An *Operating Rittinger Index*, $K_{R,Op}$ has also been defined for ultrafine grinding, where $n = 2$[75]:

$$K_{R,Op} = \frac{E}{\left(\frac{1}{x_p} - \frac{1}{x_f}\right)} \dots [2.11]$$

Many energy-size relationships in this work fit Rittinger's Law well, so $K_{R,Op}$ is frequently used to measure grinding efficiency. Rittinger's Law does not need to be followed closely for $K_{R,Op}$ to be useful, but the closer the fit, the wider the range of product and feed sizes over which an efficiency comparison can reliably be made[52].

2.9. Media Surface Roughness

Previous comparisons by *FiberLean* between different media species have yielded results incongruous with stress intensity theory, such as by Riley[73], who suggested that surface roughness could be a cause. Subsequently, *FiberLean* trialled a rough zirconia-alumina composite media, finding that MFC strength was improved at lower energy inputs compared to smooth zirconia[76]. This apparent sensitivity to surface roughness is surprising, as in mineral grinding literature it is rarely mentioned. The limited work on this subject is summarised here.

Durant et al. found that media with a higher friction coefficient (and visibly higher surface roughnesses) increase power draw[77], though in other work the effect on grinding efficiency

is inconclusive as other important parameters were changed simultaneously[78]. Becker et al.[79] compared alumina media of different primary grain sizes (which is related to surface roughness), finding a higher wear rate with larger grain sizes, but differences in grinding performance were not obvious.

In stirred media milling of calcium carbonate, Tamblyn suspected an influence of media surface roughness[80], but did not provide direct evidence. To the author's knowledge, the only explicit investigation of media surface roughness was by Skuse on calcium carbonate grinding[81]; Rougher media increased power draw, but no difference in energy efficiency was seen.

Despite the null results for minerals grinding, there evidence of surface roughness improving cellulose microfibrillation using other production methods; Björkqvist et al.[82-83] produced MFC using a cone refiner with roughened surfaces. Microfibrillation efficiency was improved with increasing roughness up to a point, before it declined again. The paucity of data regarding the influence of roughness for both stirred media milling and for MFC production suggests that this warrants a detailed study.

2.10. Previous Work

The *University of Birmingham* and *Imerys* have carried out Positron Emission Particle Tracking (PEPT) on the mill geometry used in the present work, in the context of calcium carbonate milling. This involved tracking the location of a radioactive grinding media bead from gamma ray emissions, allowing the computing of velocity and kinetic energy distributions throughout the mill. The first work was by Tamblyn[80], who found that the *normalised velocity*, (mean velocity divided by the tip speed), decreases at higher speeds, undermining the assumption

inherent in stress intensity theory that collision velocity is proportional to maximum velocity. Additionally, a higher mean velocity enhances particle size reduction.

Later work by Skuse[81] showed that the collision force follows a Maxwell-Boltzmann distribution, with a long tail at higher forces. They identified how media accelerations vary with operating conditions, with typical values in the high intensity grinding zone being around 10-1000 m/s^2. They also showed how forces are highest around the impellers but media collisions occur more frequently immediately above and below the impeller zones, between the impeller and the wall (see Figure 2.5). Wall slip was significant around the impeller height, and the impeller tip only transferred around half its velocity to the neighbouring media, so the real velocity gradient is much lower than theoretically expected.

Two authors have previously produced theses investigating the *FiberLean* process; Pinkney[84] and Riley[73]. Between them, they investigated the influence of various operating conditions (media density and size, impeller speed, mineral content, and mill geometry) on MFC quality. Unfortunately, quality measurements at that time were limited to the inherently noisy burst strength test, which obscures all but the largest influences. For example, Riley showed a rapid increase in MFC burst strength with energy input, followed by a peak and gradual decline, but investigations of other factors such as media size on MFC quality were inconclusive.

Much of their research investigated the change in MFC particle size, which alone is a poor measure of product quality, but both were able to show a steady decay in size with energy input, and Riley was able to identify an optimum impeller speed at which size reduction is maximised, as expected from stress intensity theory. Pinkney demonstrated that increasing the mineral fraction within the grind enhances MFC size reduction, though the effect on MFC strength was unclear. Riley modelled energy-size relationships with the Walker equation

(Equation 2.8), but the necessity of screening caused a sampling bias for coarser samples, and prevented including low energy MFC in this analysis.

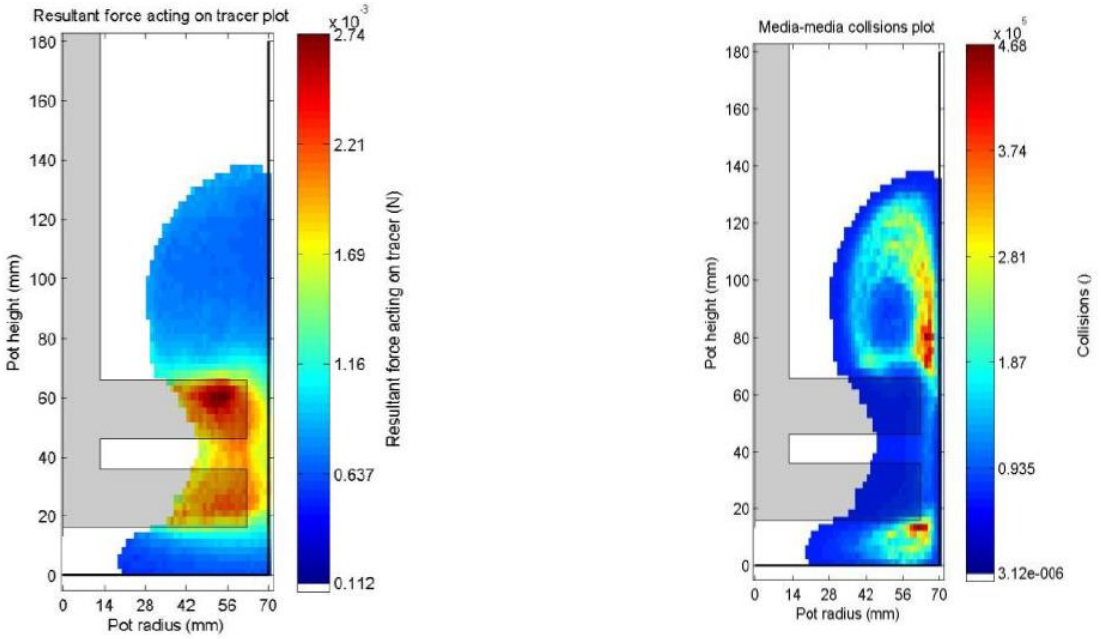

Figure 2.5 *– Force distribution (left) and collision distribution (right) within the grinder (taken from Skuse[81]).*

Both Pinkney and Riley used PEPT to investigate various factors in MFC grinding. An interesting result from Pinkney's work was that a shear-thickening (starch) suspension with media absent gave flow patterns similar to typical MFC grinds, implying that the media experiences a dilatancy effect in high acceleration regions, causing greater frictional dissipation and apparent 'shear-thickening' behaviour.

From PEPT, Riley found that the mean kinetic energy *increased* with energy input; this is unexpected, though a sensible explanation is decreasing high shear viscosity with decreasing product sizes. Mean kinetic energy was also proportional to the impeller tip speed, not the *square* of the tip speed as expected from stress intensity theory; this adds to the evidence that energy transfer efficiency between the impeller and media declines at higher tip speeds. The kinetic energy frequency distribution is broadest at the optimum impeller speed, with more

collisions having sufficient energy to break fibres than above the optimum impeller speed; this could be due to media increasingly centrifuging away from the impeller. Similar analysis was not carried out with other conditions e.g. media size, so this correlation could be a coincidence.

PEPT work from these four authors highlights the importance of flow patterns and energy distribution, factors that are not considered in basic stress intensity theory. However, more fundamental work regarding how the fibres break up, the effect of operating conditions, media properties, and the effect of fibre species were either not investigated, or proper characterisation was hampered by inadequacies of the measurement techniques. The present work aims to fill that gap.

2.11. Contact Mechanics

Later in this thesis, an alternative framework is developed to explain fibre deformation and breakup, which is based on Hertzian contact mechanics, introduced below.

As first described by Hertz, when a curved surface impacts another body, the surfaces deform to ensure a region of intimate contact between them[85]. Hertz theory describes the interface shape and pressure distributions given mathematically smooth, elastic surfaces. A diagram of a Hertzian contact is shown as Figure 2.6 (taken from Johnson[85]) showing the contact area dimensions and the *z*-axis displacement depth of each surface under the applied load. Pressures and contact areas are influenced by the body shape and material properties, and to perform these calculations, an equivalent Young's modulus *Y** (*Contact Modulus*) and radius of curvature *R*, are defined.

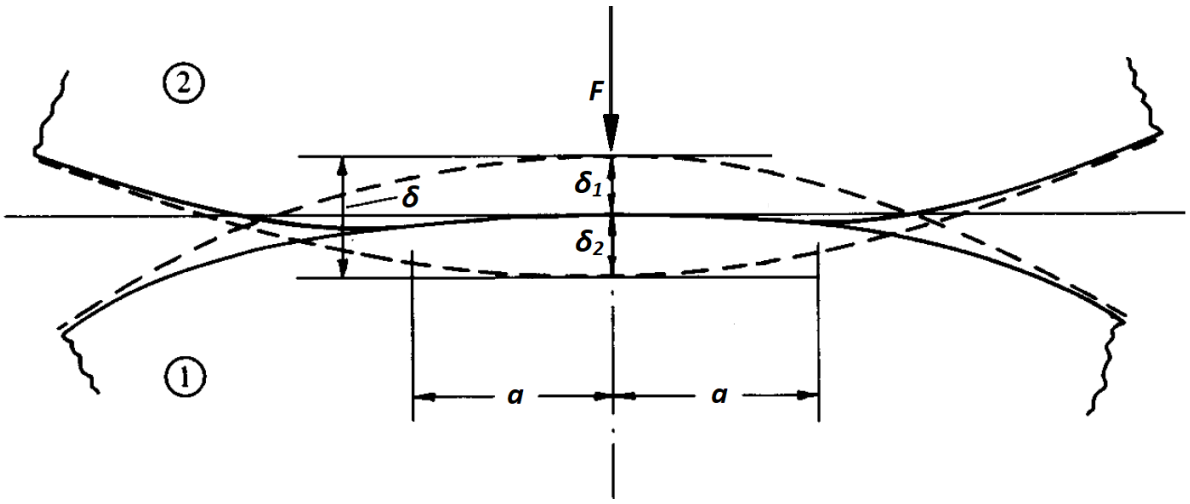

Figure 2.6 *– Diagram showing the collision of two curved surfaces under an applied load F. The solid curves show the surface of the bodies during collision, and the dashed curve shows the surface of the bodies with no load applied. Maximum z-axis displacement δ is the sum of the displacements of each surface δ_1 and δ_2 due to elastic deformation, and a is the radius of curvature of the contact area (figure adapted from Johnson (1985)[85]).*

Y^* is calculated from the Young's moduli (Y_1 and Y_2) and the Poisson ratios (v_1 and v_2) of the two bodies:

$$\frac{1}{Y^*} = \frac{1 - v_1^2}{Y_1} + \frac{1 - v_2^2}{Y_2} \quad \ldots [2.12]$$

which, for identical materials, simplifies to:

$$Y^* = \frac{Y}{2 - 2v^2} \ldots [2.13]$$

The relative curvature ($1/R$) is the sum of the curvatures of both colliding bodies ($1/R_1$ and $1/R_2$, where R_1 and R_2 are their respective radii):

$$\frac{1}{R} = \frac{1}{R_1} + \frac{1}{R_2} \ldots [2.14]$$

For spheres of equal curvature, R is therefore half the sphere radius. If the normal force applied, F, is known, these values can be used to calculate the total displacement depth of the colliding bodies, δ, the contact area radius a, and the maximum collision pressure p_0:

$$a = \left(\frac{3FR}{4Y^*}\right)^{1/3} \quad \ldots [2.15]$$

$$p_0 = \frac{3F}{2\pi a^2} = \left(\frac{6FY^{*2}}{\pi^3 R^2}\right)^{\frac{1}{3}} \ldots [2.16]$$

$$\delta = \frac{\pi a p_0}{2Y^*} \ldots [2.17]$$

The derivations of Equations [2.15] – [2.17] are shown by Johnson[85]. The maximum pressure p_0 is 50% greater than the mean pressure across the whole collision surface, $\bar{p}$.

A comparison of the three media species most widely used in the present work is given in Table 2.1, showing the relevant media properties, and the calculated values of *Y** and *R* using Equations [2.13] and [2.14] for a media-media collision. Note that the Poisson ratios and Young's moduli are taken from literature for bulk materials, and may not be accurate to the specific formulation of the material used in this media.

Table 2.1 *– Model parameters of each media species used in the Hertzian contact mechanics calculations.*

Material	Diameter (mm)	Density (kg/m³)	Young's Modulus *Y* (GPa)	Poisson Ratio *v* (-)	Media Bead Mass (kg)	Radius of Curvature *R* (m)	Contact Modulus *Y** (GPa)
Glass	3	2500	70[86]	0.22[87]	3.5×10^{-5}	7.5×10^{-4}	36.9
Zirconia	3	6000	210[88]	0.3[88]	8.5×10^{-5}	7.5×10^{-4}	115.4
Mullite	3	2700	150[89]	0.25[89]	3.8×10^{-5}	7.5×10^{-4}	80.0

To evaluate contact pressures, areas, and displacements, the collision force is needed, which can be determined from acceleration measurements since media mass is known. PEPT data from Skuse[81] shows that at an impeller speed of 800 rpm (the standard in the present work) the mean acceleration between the impellers was found to be around 100 m/s^2, although due to the broad frequency distribution, some collisions approached 1000 m/s^2. 100 m/s^2 is used

as a rough estimate at 800 rpm, and is assumed constant with media density and size, though this acceleration is assumed to be proportional to the square of the impeller speed (as Skuse's data shows[81]) for other impeller speeds.

Considering a range of possible accelerations between 1 – 1000 m/s^2, the data in Table 2.1, and Equations [2.15] and [2.17], the contact area diameter and the maximum pressure applied were calculated for each media type and plotted as Figure 2.7 (a) and (b) respectively. This shows that naked media-media collisions are expected to have contact area diameters of several microns with pressures of hundreds of MPa under standard grinding conditions.

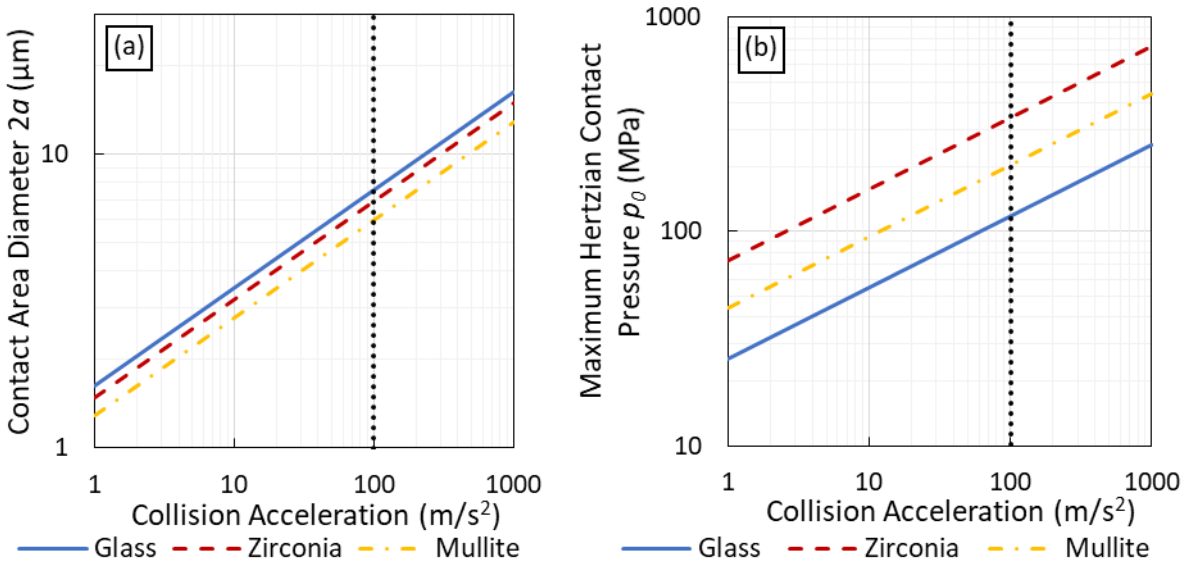

Figure 2.7 *– (a) Contact area diameter versus collision acceleration for three media types, (b) maximum Hertzian contact pressure versus collision acceleration for three media types. The vertical line at 100 m/s^2 represents the acceleration believed to be typical of the grinder impeller region at 800 rpm.*

This foundation is used as a basis for adapting the theory to include the deformation of a fibre under compression by colliding media in Chapter 4, and to accommodate the media surface roughness in Chapter 5.

3. MATERIALS AND METHODS

3.1. Fibre Sources

To investigate relationships between feed properties and MFC quality, numerous fibre sources were obtained, see Table 3.1. All chapters other than Chapter 7 and Chapter 8 exclusively use *Nordic Pine* fibres.

Table 3.1 *– The fibre sources used in this work.*

Softwood		Hardwood		Non-wood	
Pulp	**Identity**	**Pulp**	**Identity**	**Pulp**	**Identity**
Nordic Pine	*Metsä* 'Botnia Pine RMA'	Birch #1	*Södra* 'Gold Birch Z'	Cotton	Cotton linters pulp†
Black Spruce	*Resolute Forest Products* 'Resolute SFK-90'	Birch #2	Confidential*	Jeans	Recycled jeans cotton†
Radiata Pine	*Arauco* 'Arauco BKP'	Eucalyptus	*UPM* 'Bleached Eucalyptus Kraft Pulp'	Abaca	Confidential*
Southern Pine	Confidential*	Acacia	Confidential*	Sisal	Unbleached kraft pulp†
Enzyme-treated Nordic Pine	*Metsä* 'Botnia Pine RMA', enzyme-treated by *Omya*	European HW	Confidential*	Kenaf	Unbleached kraft pulp†
Douglas Fir	Confidential*	South Asian HW	Confidential*	Miscanthus	Confidential*
Dissolving Pulp	*Domsjö Fabriker AB* – 'Domsjö Cellulose Plus'	Tissue Dust	Confidential*	Sorghum	Confidential*
				Giant Reed	Confidential*
				Flax	Bleached flax fibres‡

** Supplied by FiberLean, origin cannot be disclosed for commercial sensitivity reasons.*
† Purchased from a pulp wholesaler Carriage House Paper (carriagehousepaper.com).
‡ Purchased from a textile fibre wholesaler, World of Wool (worldofwool.co.uk).

Almost all fibres used are bleached kraft pulps. Exceptions include *dissolving pulp*, produced from the sulphite process, and some non-woods (*kenaf*, *sisal*, and *Giant Reed*) which underwent the kraft process without bleaching. *Tissue dust* fibres were obtained from the dust extraction system at a tissue mill.

Miscanthus, *sorghum*, *bagasse*, *enzyme-treated Nordic pine*, and *Giant Reed* were supplied as a cake (roughly 30% solids), *tissue dust* was supplied as dry cylindrical pucks, and *flax* was supplied as bundles of long fibres. All other fibre species were supplied as dry pulp board. *Flax* was cut into shorter (< 3 mm) fibres with a paper guillotine to avoid choking the grinder. Dry pulps were soaked in water overnight, broken down in a pulp disintegrator and dewatered with a vacuum filter into a high solids cake.

3.2. Mineral

The mineral that was added during grinding, and added to the product for nanopaper formulation, was *Intracarb^{TM} 60 L* (IC60) marble-derived ground calcium carbonate supplied by *Imerys*. This had a solids content of roughly 70 wt%, with a size specification of 60 wt% < 2 μm[90].

3.3. Grinding Media

This work used numerous grinding media sources, of varying sizes, densities, and surface roughnesses. The properties of media as supplied are listed in Table 3.2, although some batches had their surface roughness modified, discussed in Section 3.14. Densities were measured by water displacement with glass pycnometers (four tests per sample). Mean media sizes were determined by measuring the diameters of 300 beads with digital calipers.

Table 3.2 *– Properties of the grinding media used in this study.*

Name	Material	Supplier	Density (g/cm^3)	Size (mm)
Mullite A (2.9 mm)	Mullite-derived	*Kings*	2.69	2.91
Mullite A (2 mm)	Mullite A, worn in industrial grinder	*Kings*	2.64	2.01
Mullite A (1.7 mm)	Mullite A, worn in industrial grinder	*Kings*	2.64	1.66
Mullite B (2.9 mm)	Mullite-derived	*Kings*	2.80	2.96
Mullite B (1 mm)	Mullite-derived	*Kings*	2.80	0.99
Mullite C	Mullite-derived	*Keramax*	2.71	3.03
Mullite D	Mullite-derived	*Imerys*	2.74	3.45
Glass A (3.1 mm)	Soda lime glass	*Glen Mills*	2.48	3.11
Glass A (1.8 mm)	Soda lime glass	*Glen Mills*	2.51	1.81
Glass A (0.9 mm)	Soda lime glass	*Glen Mills*	2.49	0.90
Zirconia A (2.8 mm)	Yttria-stabilised zirconia	*ChemCo*	6.05	2.77
Zirconia A (2.2 mm)	Yttria-stabilised zirconia	*ChemCo*	6.04	2.23
Zirconia D (2.9 mm)	Ceria-stabilised zirconia	*FOX*	6.04	2.89
Zirconia D (2.5 mm)	Ceria-stabilised zirconia	*FOX*	6.02	2.49
Zirconia D (2.1 mm)	Ceria-stabilised zirconia	*FOX*	6.04	2.11
Zirconia D (1.5 mm)	Ceria-stabilised zirconia	*FOX*	6.04	1.51
Zirconia D (1 mm)	Ceria-stabilised zirconia	*FOX*	5.99	0.97
Zirconia E	(Zirconia A, worn in grinder)	*ChemCo*	6.04	2.79
Zirconia F	Ceria-stabilised zirconia	*St. Gobain*	6.20	2.93
Ultrafine Carbolite	Mullite-derived	*Carbolite*	2.67	0.77
Alumina	Alumina	*Imerys*	3.63	3.31
Zirconium Silicate A	Zirconium silicate	*Kings*	4.05	2.89
Zirconium Silicate B	Zirconium silicate	*St. Gobain*	4.17	3.23
Zirconium Silicate C	Zirconium silicate	*Cenotec*	4.06	2.87

3.4. Lab Grinder

MFC was produced using a lab-scale 500 W *Cheetah* sand grinder, consisting of a 4-arm pin impeller, and a cylindrical grinder pot. To minimise wear and product contamination, the impellers and pot are polyurethane-lined. Figure 3.1 shows a photograph of the impeller and pot, along with a to-scale schematic.

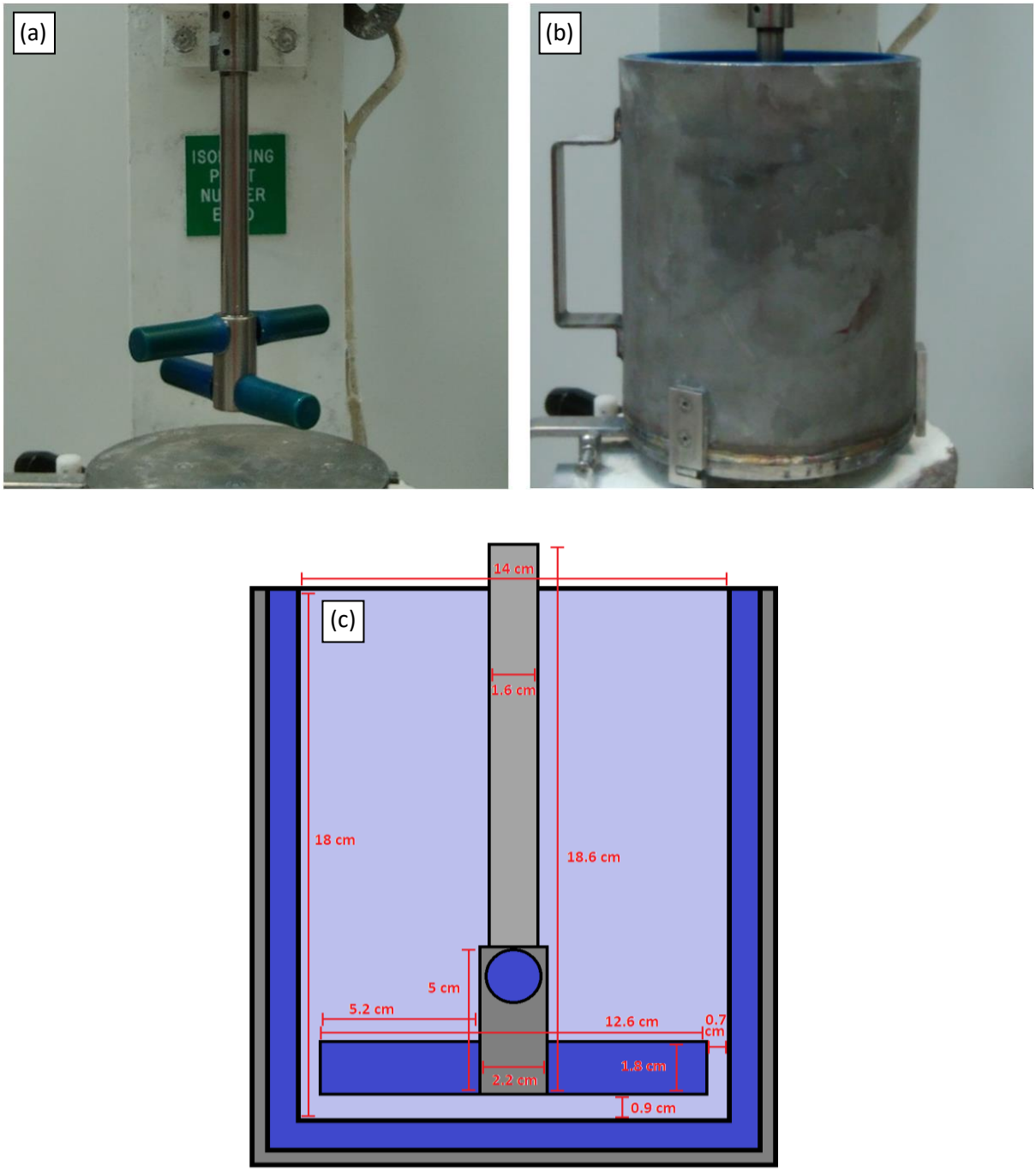

Figure 3.1 *– Photographs of (a) the lab grinder impeller and (b) pot, and (c) a schematic of the grinder.*

Power draw was measured using a load cell attached to the grinder mount; grinding media transfers torque from the impeller to the pot wall, with the torque arm rotating to apply a force to the load cell, which is converted to a power draw (energy input is the time-integral of power draw).

3.5. MFC Production

The grinder requires a charge slurry volume of 578 cm^3, with 523 cm^3 of grinding media, to achieve the target media volume concentration (MVC) of 47.5%. Based upon the measured solids contents of the fibre and mineral, the amounts required to achieve this slurry volume with the target solids and fibre contents were calculated. The mineral was added to the pot first, followed by the fibre, then the additional water. The pot was attached to the grinder mount, and grinding media was added whilst the impeller slowly rotated. The impeller speed was increased to the target value (usually 800 rpm, or 5.45 m/s tip speed), and the grind continued until the target energy input (measured by kWh/t of fibre) is achieved.

Subsequently, the grinder was stopped, and the pot contents were mixed with additional water and poured into a 1.7 mm vibrating screen, where the product was collected as the underflow whilst the media was retained. When the media was too fine for the screen, or when the product was too coarse, an alternative method was used where the charge was mixed with 1 litre of water in a bucket, which forced the media to quickly settle, allowing the supernatant to be collected as the product.

3.6. Product Composition Measurement

The slurry solids content was measured by weighing a sample on a balance before and after oven-drying. The fibre dry mass fraction (the % Pulp On Product, or 'POP') was determined by weighing the dried sample in a crucible before and after placing it in a furnace at 450°C for 2 hours (where the fibre content burns away).

The presence of worn grinding media in the product (% Media On Product, or 'MOP') was calculated for 100% POP (mineral-free) samples by the measured POP subtracted from 100%. For samples containing calcium carbonate mineral, following the POP measurement the

samples were placed back into the furnace at 950°C for 30 minutes, where the calcium carbonate decomposed into calcium oxide and CO_2. IC60 has a loss of ignition of 43.5%, and the difference between this value and the loss of ignition of the sample was used to infer the fraction of mineral present that is not calcium carbonate.

3.7. MFC Nanopaper Production

Mineral content disrupts fibre-fibre interactions, lowering paper strength, so the same mineral content for all samples was required. IC60 mineral was added to the MFC slurry to produce a sample composition of 20% POP. Sufficient sample was added to a beaker to account for 4.4 g dry mass (220 gsm), after which around 400 mL of water was added, followed by 1 mL of a 0.2% polyDADMAC flocculant solution. A filter paper was secured in a vacuum sheet former, before the sample was poured in and the vacuum engaged. Following drainage, the filter paper was removed with the MFC web attached, and dried in a *Rapid Köthen* dryer under compression at 90°C for 7 minutes. After drying and being removed from the filter paper, the MFC sheets were left overnight in a conditioned lab at 23°C and 50% relative humidity. For each sample tested, three sheets were produced.

3.8. MFC Tensile Testing

After conditioning, the sheets were weighed, before each were cut into five 15 mm wide strips with a twin-bladed paper strip cutter. The strips were clamped in a *Testometric M350* tensile tester (see Figure 3.2) and strained at a constant rate until failure. The tensile index is calculated using[91]:

$$T = \frac{1000 * F}{m * w * a^{-1}} \quad \ldots [3.1]$$

where T is the tensile index (Nm/g), F is the force at breakage (N), m is the sheet weight (g), w is the strip width (mm), and a^{-1} is the reciprocal of the sheet area (m^{-2}). The value of w is 15 mm, and the value of a^{-1} is 50 m^{-2} (as the sheet area is 0.02 m^2). Averages were taken of the five strips for each sheet, and a standard deviation was calculated from the averages of all three sheets.

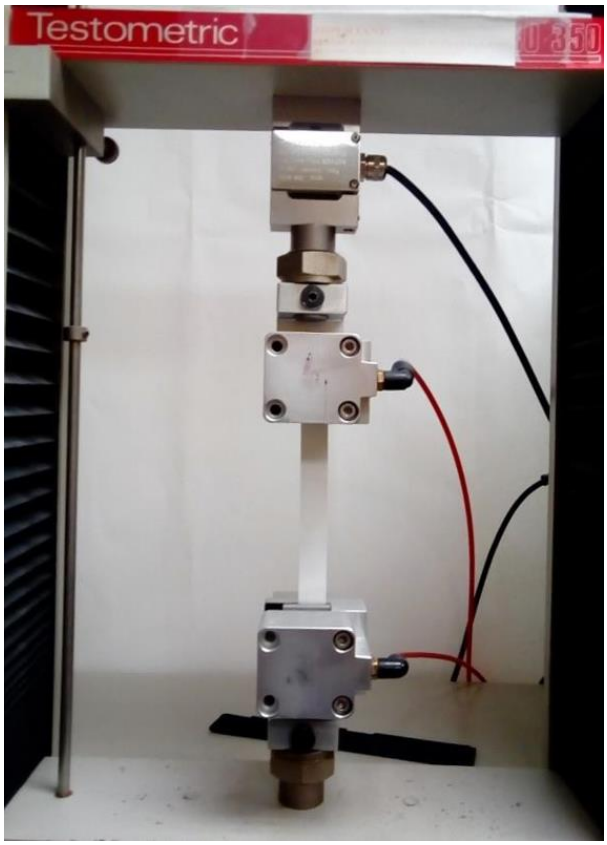

Figure 3.2 *– The tensile tester with a nanopaper strip.*

Mineral retention usually approached 100%, but some poorly fibrillated samples had poor retention, apparent from deficiencies of sheet weight. The strips from such samples were burned in the furnace at 450°C to measure fibre content. For well-fibrillated samples, the strip POP value was always between 20 – 21%, though for poorly processed MFC, this could reach up to 25%. All samples with POP values above 21% had their strength values divided by the ratio of their fibre content with that of a 4.4 g 21% POP sheet, to normalise to the upper end

of the acceptable region. This normalisation ignores differences in the disruptive effects of the mineral, but as shown in Figure A5.20 in Appendix A5, such differences between 21% and 25% POP are minor. Samples with strip POP values between 20 – 21% POP were not normalised to avoid introduction of further noise (as strip POP measurements are particularly noisy).

3.9. Fibre Zero-Span Tensile Testing

The zero-span tensile strength of all feed pulps in Table 3.1 was measured according to the TAPPI standard *T 231 cm-07*[92]. This necessitated creating 60 gsm mineral-free handsheets following the TAPPI standard *T 205 sp-12*[93]. Each sheet was cut into five 20 mm wide strips with a twin-bladed cutter, placed in a *Pulmac* zero-span tensile tester (see Figure 3.3), and strained until broken. These tests were carried out both wet and dry (four sheets for each); when wet, the strips were first immersed in distilled water for one minute, with a paper towel absorbing excess water. The zero-span tensile index is calculated using Equation 3.1, with w = 20 mm.

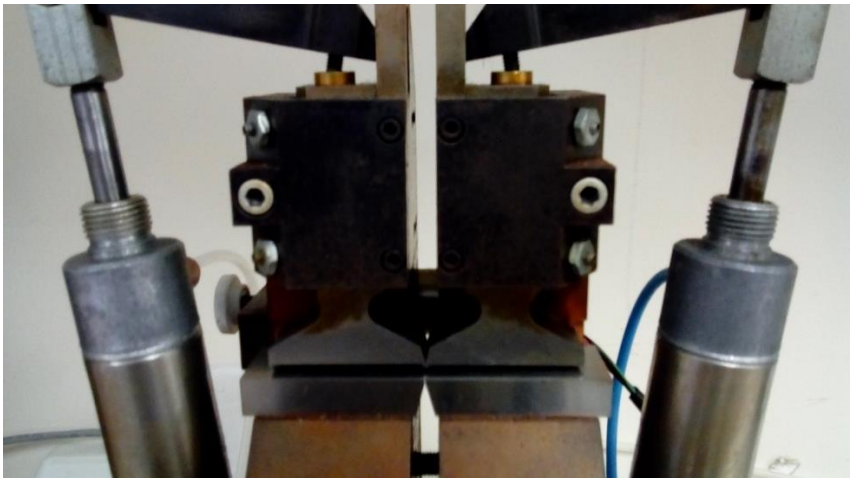

Figure 3.3 *– The zero-span tensile tester.*

3.10. Fibre Chemistry Measurements

The cellulose, hemicellulose, and lignin contents of the fibres listed in Table 3.1 were measured externally by *Labtium Oy*. The cellulose and hemicellulose values were derived from carbohydrate content measurements, via the SCAN-CM 71:09 method[94], wherein polysaccharides are dissolved into monomer sugar residues, which are measured by anion exchange chromatography to obtain mass fractions of glucose, xylose, mannose, arabinose, and galactose.

The xylan hemicellulose content was assumed to consist of all the xylose and arabinose, and the glucomannan hemicellulose content was assumed to consist of all the galactose, mannose, and one unit of glucose for every four units of mannose (which is a typical ratio[39]). The cellulose content consists of the remaining glucose. The (negligible) hemicellulose content of cotton was also used for the jeans cotton because the presence of the dye was expected to interfere with the measurement. This assumption is reasonable as textile-grade cotton contains negligible hemicellulose[95].

Acid-soluble and insoluble lignin contents were determined by *Labtium Oy* with a modified TAPPI standard *T 222 om-88 test*[96]; the polysaccharides were dissolved and extracted, and the residual acid-insoluble lignin was collected and weighed. The acid-soluble lignin values were determined from UV spectrophotometry of the extracted filtrate at a wavelength of 280 nm, where interference from other dissolved compounds is minimal[97].

3.11. Fibre Analyser Measurements

A *Valmet FS5 Fibre Image Analyser* characterised the geometry of feed fibres and MFC products. A 0.002% fibre solids suspension is added to the sample beaker, which upon

initiation of the test is agitated and pumped past a camera. The camera takes several hundred greyscale pictures (e.g. Figure 3.4).

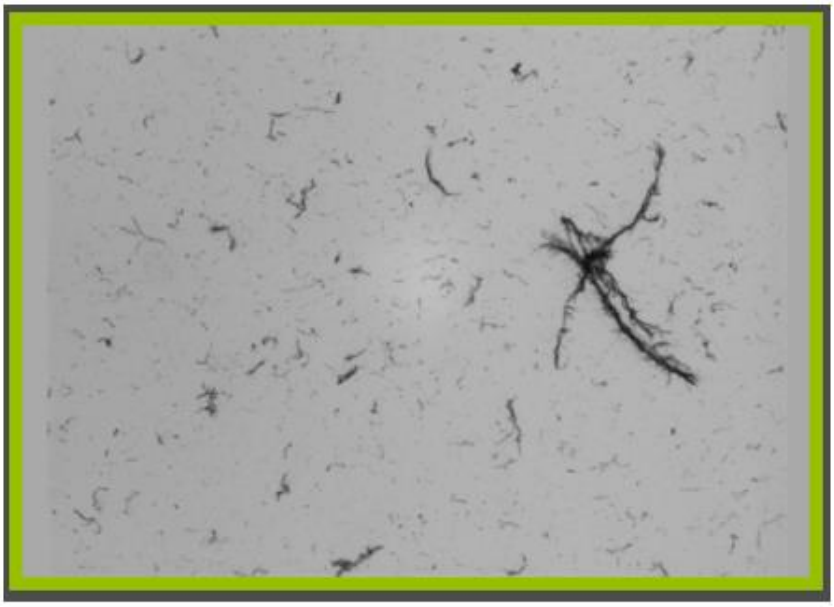

Figure 3.4 *– An image of a MFC suspension taken by the fibre analyser camera.*

A computer algorithm determines numerous geometric parameters for the identified particles, including:

- ***Lc(n)*** – **number-weighted mean fibre length (mm):** This includes all particles with widths greater than 10 μm.
- ***Lc(l)*** – **length-weighted mean fibre length (mm):** Measured in the same way as *Lc(n)*, but weighted by the fibre length. This is more commonly used in the paper industry than *Lc(n)* as the latter is very sensitive to fine particles (which may constitute only a small mass fraction).
- **Fibre width (μm)** – The mean length-weighted fibre width for particles with widths greater than 10 μm.

- **Coarseness (mg/m)** – The weight per unit length of fibre (a measure of fibre thickness), measured optically from the total length of all fibres divided by the estimated mass (inferred from image contrast).

- **Curl (%):** The mean deviation of the fibre length from a straight axis.

- **Kink (m^{-1})**: The number of sharp bends per unit fibre length, indicating fibre damage.

- ***Fines A* (%)**: Low aspect ratio fines, with lengths below 0.2 mm and widths above 10 μm, as a percentage of the total projected area of all measured objects, and are included in fibre length calculations.

- ***Fines B* (%)**: High aspect ratio particles, with widths below 10 μm and lengths greater than 0.2 mm, as a percentage of the total lengths of all particles above 0.2 mm. These particles are *not* included in the fibre length calculations.

- ***Fibrillation %*:** A measure of the fibre 'external fibrillation', determined by the inferred fibril area divided by the total fibre area. Fibril area is inferred from the sharpness of the interface between the fibre and surrounding medium.

In recent years, optical fibre analysers have become sensitive enough to characterise relatively coarse MFC particles. This is currently a rare method in literature, with only a few examples found[98-99]. One problem with this technique is MFC particles are much finer than fibres, so finer scales of fibrillation are below the resolution limit. Consequently the coarser particles being measured must be assumed to be representative of the invisible finer scales. Secondly, *FiberLean* MFC is predominantly not fully individualised fibrils, as instead fibrils are physically connected in aggregate networks (e.g. see Figure 3.7 in Section 3.12). In this case, what some parameters physically correspond to is not obvious. The author is not privy to *Valmet*'s

proprietary algorithms, but from correspondence with them, it was learned that 'fibre length' of a highly branched MFC particle is the longest contiguous end-to-end distance, with fibre widths, kink and curl determined solely for this branch.

Using a wealth of data from both this thesis and from *FiberLean*, a good general correlation between fibre analyser parameters and tensile strength has proved elusive. However, some influences are obvious; a high *Fines B* or *Fibrillation %* value (referred to as *fibrillation parameters*) indicates good fibrillation and high tensile strength. MFC fibre length should also be as high as possible, given that the fibre cell wall is effectively disintegrated (indicated by high fibrillation parameters), since as the Page Equation suggests, longer particles lead to higher strength. *Lc(l)*, *Fines B*, and *Fibrillation %* are therefore focused on in this work. In the context of MFC, *Fibrillation %* represents external fibrils which are still attached to large particles (fibres, fibre fractions, and coarse MFC aggregates), and *Fines B* particles are long, thin liberated fibrils or fibril bundles. This becomes increasingly clear throughout this thesis from microscopy images of various MFC samples.

To investigate the sensitivity of the results to variations in fibre and mineral content, a 100 POP MFC sample was produced, mixed with IC60 to various compositions before testing. Fibre solids content very weakly affects the results, and mineral content exclusively affects *Fines A* content (large mineral particles could be being detected), see Figure 3.5, and the *Fibrillation %* value, see Figure 3.6, (the mineral increases background opacity, decreasing contrast and therefore exaggerating the fibrillation measurement). Therefore, to fairly compare these parameters, all samples must be tested at the same mineral content.

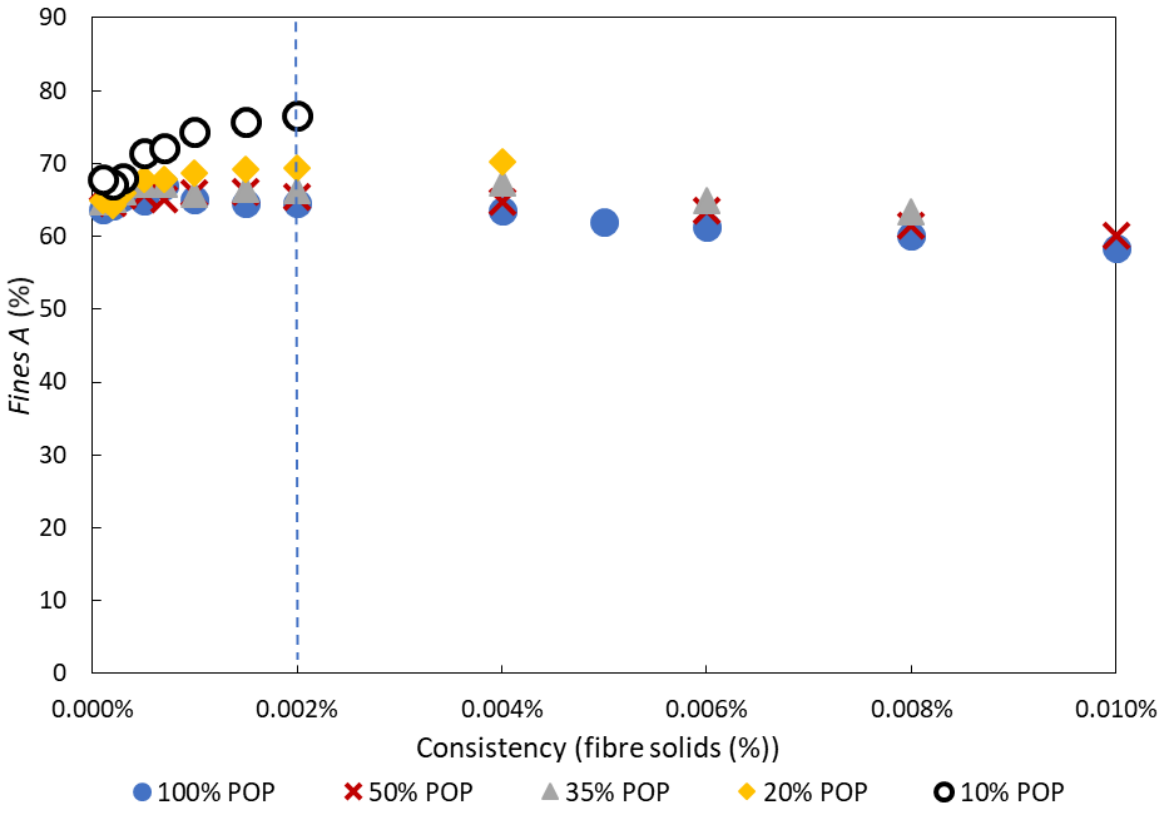

Figure 3.5 *– Fines A % versus fibre solids content for a 100 POP MFC diluted to various mineral contents. The blue dashed line represents the standard consistency.*

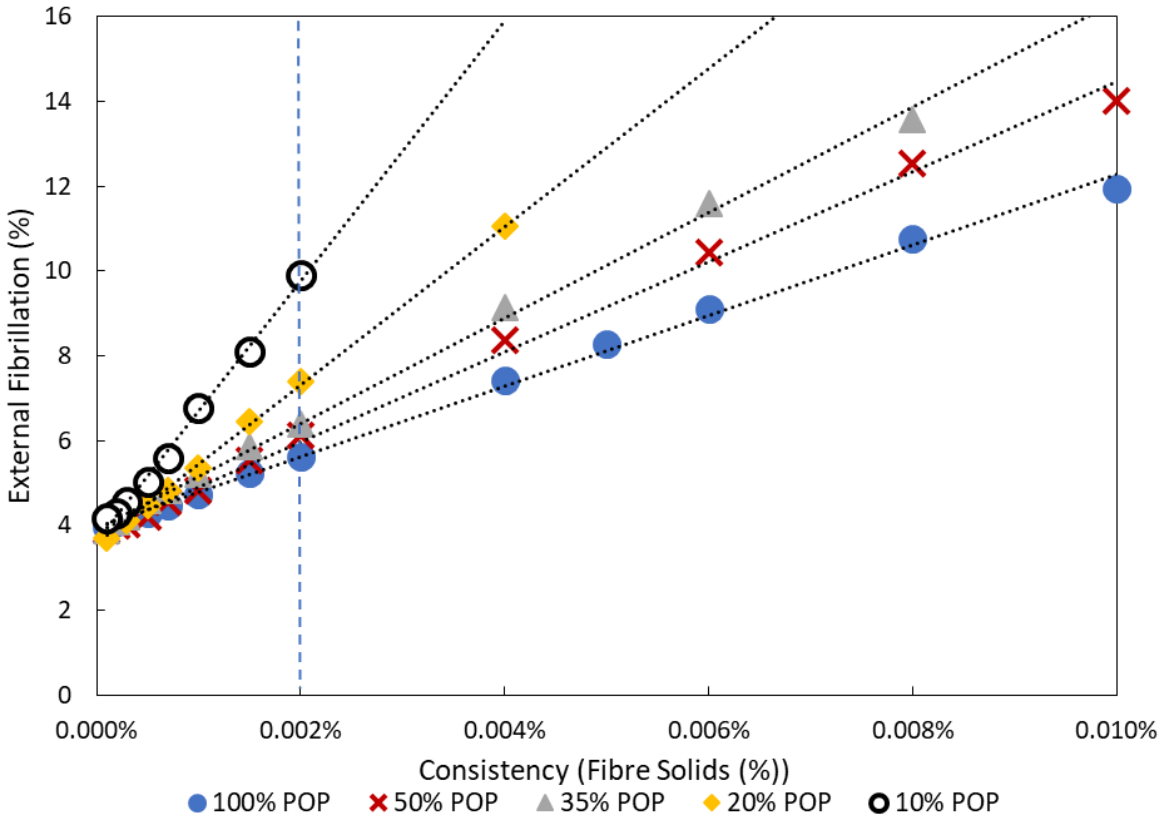

Figure 3.6 *– Fibrillation % versus fibre solids content for a 100 POP MFC diluted to various mineral contents. The blue dashed line represents the standard consistency.*

3.12. Differential Interference Contrast Microscopy

A *Reichert Polyvar Met* microscope was used in Differential Interference Contrast (DIC) mode, wherein polarised light is separated at the sample plane, and recombined before viewing. The resultant interference emphasises object edges, making it ideal for observing fibril-scale features. These images were taken with a *wet* sample, partially dried into a thin film. Figure 3.7 shows a DIC microscopy image of a typical MFC, easily distinguishing both fibrils and mineral particles (the latter being the small low aspect ratio specks).

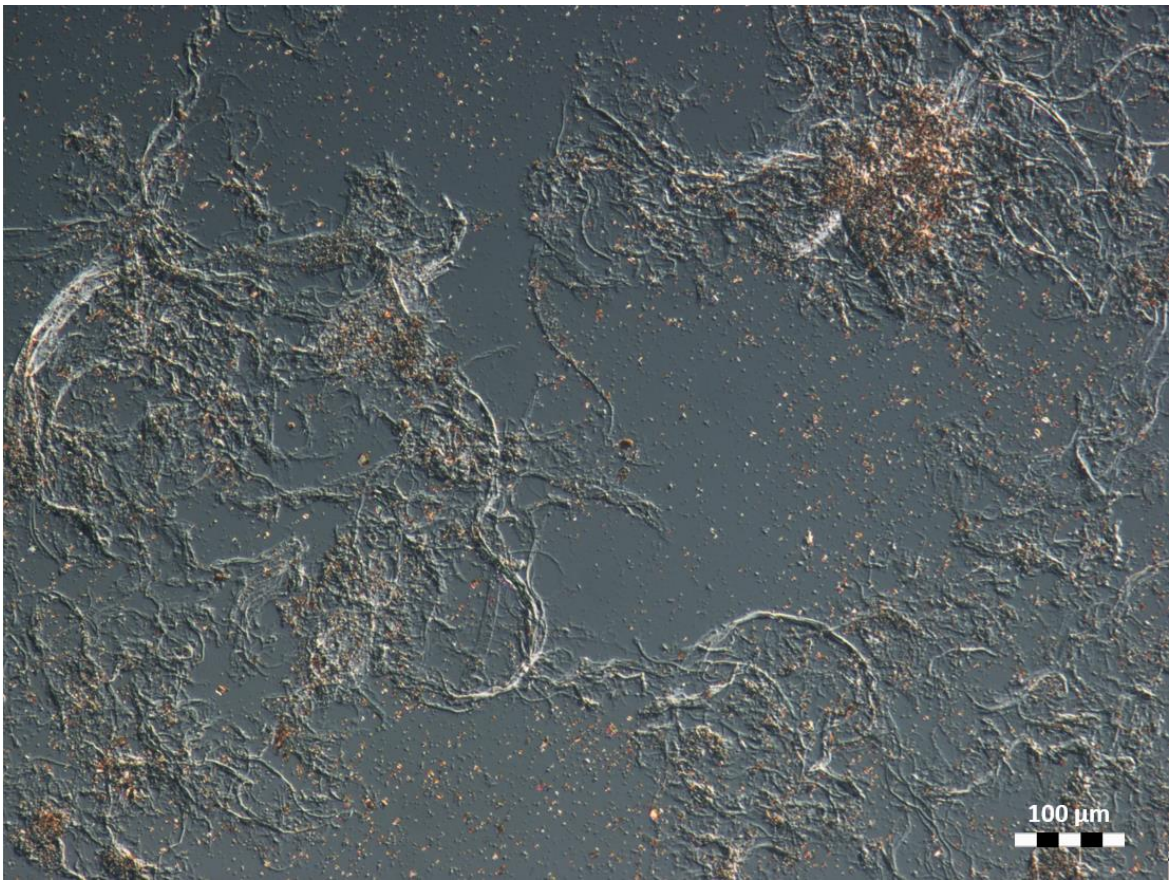

Figure 3.7 *– Differential interference contrast microscopy image of a typical MFC sample.*

3.13. Scanning Electron Microscopy

A *Jeol 6700* scanning electron microscope was used by *Imerys* to characterise nanoscopic features of some MFC samples. A dilute MFC sample was filtered through a 0.2 µm nucleopore membrane, before being sputter coated to form a conductive platinum monolayer. Images

were formed with secondary electron emissions. Several grinding media bead cross-sections were also imaged with SEM; this required first encasing the bead in resin, and slicing a cross-section with a diamond saw (these preparation steps were carried out by *Camborne School of Mines*).

3.14. Media Roughening

Part of the media roughness investigation involved obtaining a large batch of smooth media, and roughening the surface to different degrees. The media was roughened by operating the lab grinder with the media added, in the presence of an abrasive mineral (silicon carbide, supplied by *Minerals-Water Ltd.*), using a sacrificial pot and impeller. Most roughened batches were produced from glass media, though there was also limited success at roughening zirconia. Table 3.3 lists the smooth feed media and the methods employed to produce each roughened media batch.

Table 3.3 *– Identity of all batches of media roughened in the grinder.*

Batch	Production Method
Glass A	Smooth glass media (feed)
Glass B	Glass A, 80-grit silicon carbide with guar gum viscosity modifier
Glass C	Glass A, 80-grit silicon carbide
Glass D	Glass A, 220-grit silicon carbide
Glass E	Glass D, worn in water grind for 150 Wh
Glass F	Glass A, 1200-grit silicon carbide
Glass G	Glass F, worn in water grind for 150 Wh
Glass H	Glass A, 400-grit silicon carbide
Glass I	Glass A, recycled 400-grit silicon carbide (now passes a 38 µm screen)
Glass J	Glass A, *Molochite Superfine* abrasive (40 wt% < 2 µm)
Glass K	Glass A, 1200-grit silicon carbide, ran for only 30 seconds
Glass L	Glass G, worn in water grind for 150 Wh
Zirconia A	Smooth yttria-stabilised zirconia (feed)
Zirconia B	Zirconia A, 220-grit silicon carbide
Zirconia C	Zirconia B, after a single 3000 kWh/t grind

Unless stated otherwise, these grinds used 1500 g glass media or 4368 g zirconia media, with 584 g of water and 50 g of abrasive added, and the grinder was operated at 600 rpm for 5

minutes. Abrasive particle sizes were varied between batches, which had a limited effect on roughness, but to target finer roughnesses, some roughened media batches were subsequently smoothened by grinding with a water charge.

For the *Glass B* batch, abrasive was added to a 1% guar gum suspension, which had a dampening viscous effect that inhibited fine scales of roughness whilst allowing larger-scale craters. For *Glass J*, the less-hard *Molochite Superfine* abrasive (40 wt% < 2 µm size specification) (obtained from *Imerys*) was used. Grinding silicon carbide with *Zirconia A* did cause some roughening (*Zirconia B*), but this was very transient, with the media becoming markedly smoother after a single grind (*Zirconia C*). This roughening technique was very effective for glass media, however.

3.15. Laser Profilometry

An interferometric laser profilometer (see Figure 3.8 (a)), custom-built by *Imerys*, was used to produce a height map of the media surface, from which surface roughness parameters were derived. This technique has an *x*-*y* plane resolution of 2 µm and a *z*-axis resolution of 10 nm. A 1024 µm-long profile is taken in the *y*-direction, with the height values recorded once the machine determines that the measurement is stable. The laser then moves 2 µm in the *x*-direction, scanning another profile, and continuing in this manner until a 1024 – 1024 µm surface has been imaged. One-dimensional roughness parameters (see Section 3.16) are computed for each profile, and corresponding mean, median, and standard deviations are calculated from all 512 profiles. However, excessive noise when analysed in the perpendicular direction prevented two-dimensional roughness parameters from being calculated.

To ensure reflectivity of the transparent glass media, all samples were sputter coated with a thin (approximately 10 nm) layer of platinum before measurement, after being secured on a

tape pad (see Figure 3.8 (b)). Usually, three media beads for each media batch were measured, although more were measured if a large roughness variation was evident within a batch. It was also found that this technique was incapable of measuring surface roughness of media beads significantly smaller than 3 mm because this resulted in the angle towards the edges of the scan becoming too steep to return a signal. Consequently, it was assumed that the roughness measured for coarse media also applied to the equivalent finer media.

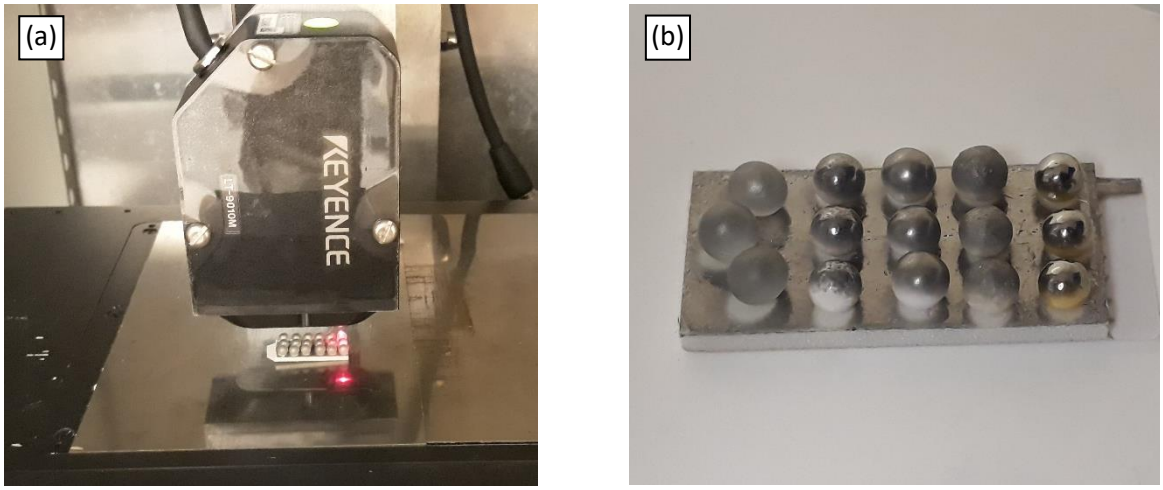

Figure 3.8 *– (a) Imerys 'Laserscape' interferometric laser profilometer, (b) media samples, attached to a tape pad and coated in platinum.*

3.16. Roughness Parameter Definitions

Whitehouse[100] defines various surface roughness parameters:

Arithmetic surface roughness R_a

The most commonly used parameter, and is the arithmetic mean absolute displacement between a point and the surface mean line:

$$R_a = \frac{1}{l_r}\int_0^{l_r} |z(x)|\, dx \ldots [3.2]$$

where l_r is the sampling length, and $z(x)$ is the height deviation from the mean line.

RMS surface roughness R_q

Root Mean Square surface roughness R_q is calculated using:

$$R_q = \sqrt{\frac{1}{l_r}\int_0^{l_r} z(x)^2\,dx} \ldots [3.3]$$

Skewness R_{sk}

Skewness is a measurement of surface height asymmetry about the mean line.

$$R_{sk} = \frac{1}{R_q^3}\left[\frac{1}{l_r}\int_0^{l_r} z^3(x)\,dx\right] \ldots [3.4]$$

A positive skewness means that the peak tail of the distribution is longer than the valley tail, and negative skewness is the vice versa (see Figure 3.9 (a)).

Kurtosis, R_{ku}

The kurtosis value R_{ku} represents the sharpness of the height distribution. For a Gaussian distribution, R_{ku} = 3, for a sharper distribution R_{ku} > 3, and for a blunter distribution, R_{ku} < 3 (see Figure 3.9 (b)). Kurtosis is calculated by:

$$R_{ku} = \frac{1}{R_q^4}\left[\frac{1}{l_r}\int_0^{l_r} z^4(x)\,dx\right] \ldots [3.5]$$

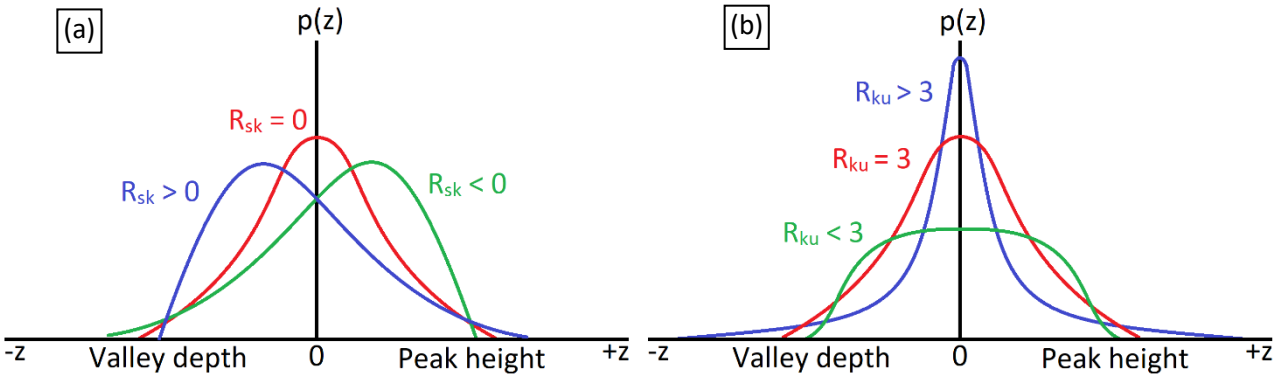

Figure 3.9 *– Peak and valley distributions (a) with different skewness values, and (b) with different kurtosis values.*

Maximum peak height R_p and valley depth R_v

R_p and R_v are the maximum deviation of a profile above and below the mean line respectively.

Japanese Industrial Standard roughness, $R_{z,JIS}$

$R_{z,JIS}$ is the average height difference between the five highest peaks and the five deepest valleys within the sampling length:

$$R_{z,JIS} = \frac{1}{5}\left(\sum_{i=1}^{i=5} z_{pi} - \sum_{i=1}^{i=5} z_{vi}\right) \ldots [3.6]$$

where z_{pi} and z_{vi} are the i^{th} highest peak and i^{th} deepest valley within the sampling length.

RMS profile slope, $R_{\Delta q}$

The slope $\theta(x)$ is calculated by subtracting the height at point (x-1) from the height of point x.

The RMS profile slope $R_{\Delta q}$ is calculated by:

$$R_{\Delta q} = \sqrt{\frac{1}{l_r}\int_0^{l_r} (\theta(x) - \bar{\theta})^2 dx} \ldots [3.7]$$

where $\bar{\theta}$ is the mean slope of the entire surface.

Mean spacing between profile peaks RS_m

RS_m is calculated using:

$$RS_m = \frac{1}{n_p}\sum_{i=1}^{i=n_p} S_i \ldots [3.8]$$

where n_p is the number of peaks in the sampling length, and S_i is the width of peak *i*.

Mean asperity curvature k_s

Mean asperity curvature k_s is defined by Johnson[85], and is a function of both peak frequency and peak height:

$$k = (z_{i+1} - 2z_i + z_{i-1})/h^2 \ldots [3.9]$$

$$k_s = \sqrt{\frac{1}{n}\sum_{i=1}^{i=n} k^2} \quad \ldots [3.10]$$

where *k* is the local curvature calculated from the heights z_{i+1}, z_i, and z_{i-1} at points *i+1*, *i*, and *i-1* respectively, *n* is the number of data points, and *h* is the distance between consecutive measurement points.

3.17. Calculating Roughness Parameters

A *Matlab* script was created to calculate all roughness parameters (shown as Appendix A1), except for k_s, which used an *Excel* worksheet. Before determination, macroscopic media curvature needs accounting for, and 'peak', 'valley', and 'mean line' need appropriate definitions.

Accounting for media curvature

A 6th order 'best fit' polynomial curve was applied to each profile to match the arc of the macroscopic media curvature. This polynomial was subtracted from the raw data for each profile to isolate the roughness profile, resulting in a surface roughness map (see Figure 3.10).

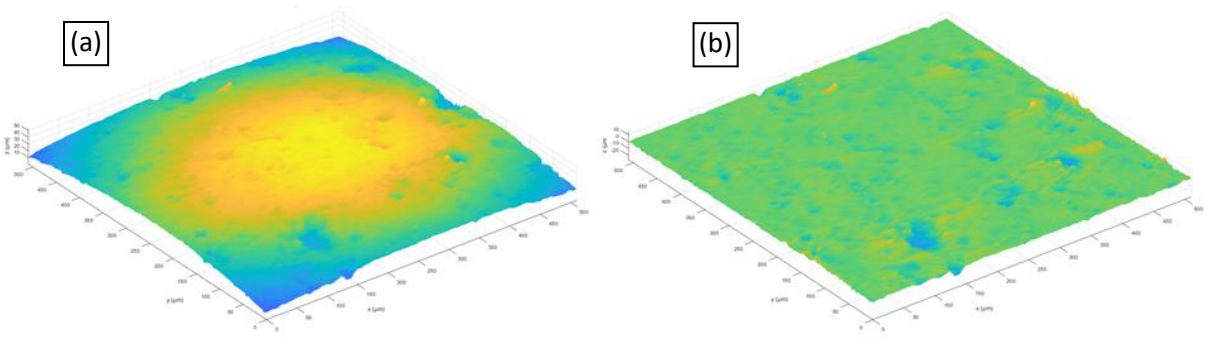

Figure 3.10 *– (a) Raw height map of a media surface, and (b) roughness map, created by subtracting a 6th order polynomial best fit curve (with 1 standard deviation outlier removal) from each profile.*

Definition of 'peak', 'valley', and 'mean line'

For some parameters ($R_{z,JIS}$ and RS_m), 'peak' and 'valley' needed defining. A peak is the highest point within a positive region of a profile between two centre-line crossings, with smaller local maxima within the same region between the crossing points discounted. A valley is defined identically as the vice versa, the lowest point within a negative region. This is clarified visually in Figure 3.11.

The mean line is conventionally defined as the average profile height after macroscopic curvature is subtracted. However, most media had considerable negative skew, resulting in disproportionately deep valleys which drag the mean line down below most of the surface (see the red dashed line in Figure 3.12). To counter this, the initial polynomial fit used to accommodate media curvature was used as a *preliminary* mean line to isolate the roughness. The standard deviation of the absolute difference between this line and the data points was calculated, and then a new polynomial was fitted to the original profile with all points greater

than one standard deviation from the mean excluded. This greatly reduced the influence of deep valleys on the mean line, shifting it closer to the true datum (see the black dashed line in Figure 3.12). This method led to a mean line that better tracked the media curvature, as Figure 3.13 shows, and was used in the roughness parameter calculations.

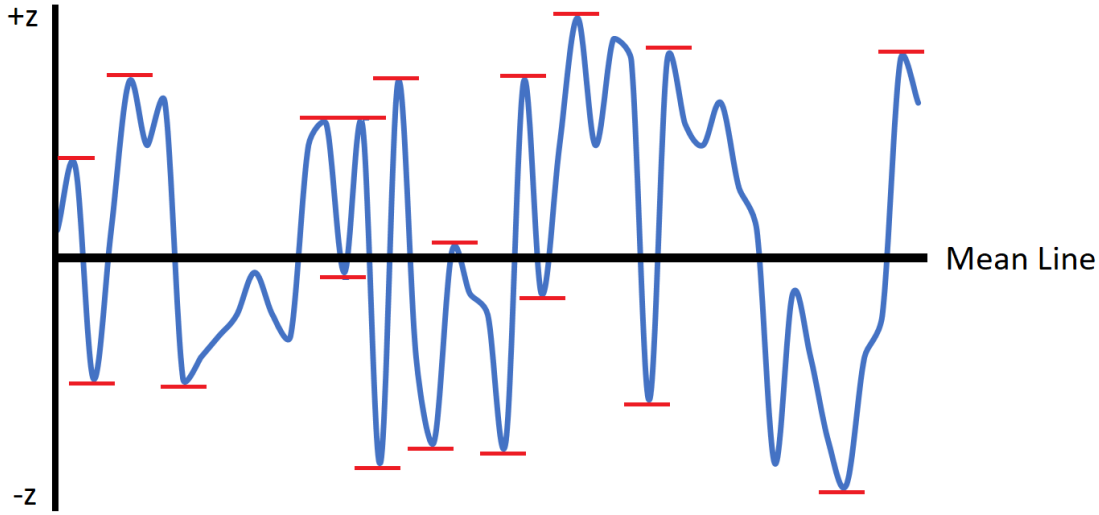

Figure 3.11 *– A roughness profile example to demonstrate the definition of a peak and valley. Peaks and valleys are represented by the red bars.*

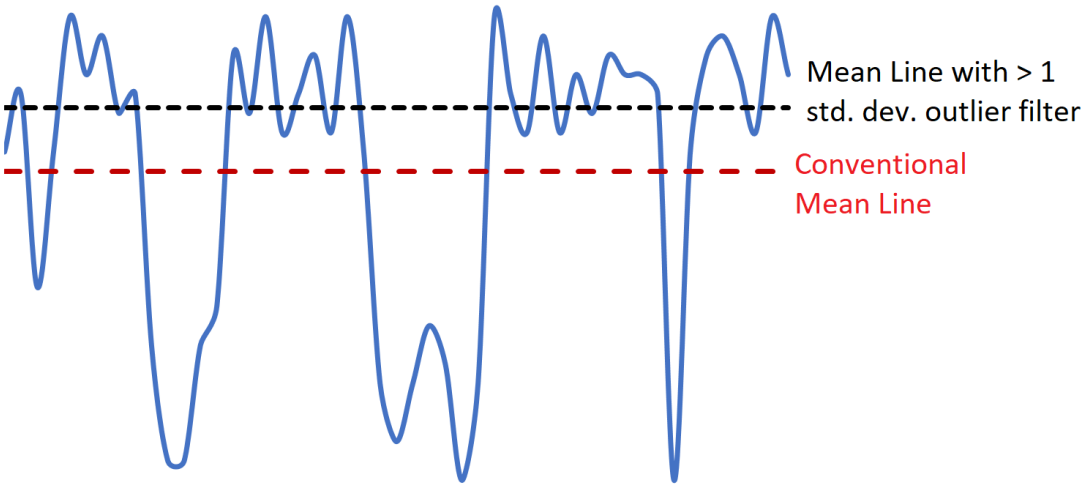

Figure 3.12 *– A mean line of a roughness profile (red dashes), and a mean line calculated after points more than 1 standard deviation away from the original mean line have been removed (black dashes).*

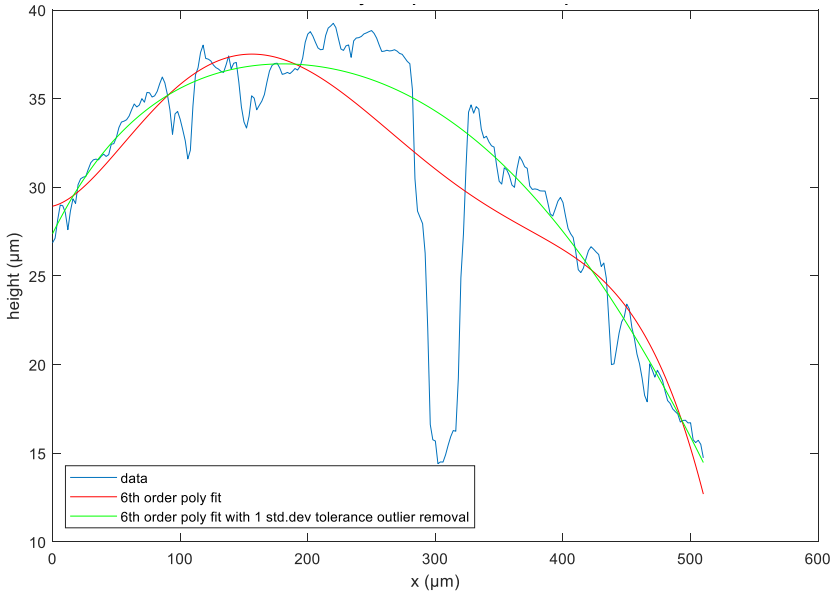

Figure 3.13 *– High negative skew surface profile, plotted using the Matlab script, with the preliminary best fit curve (red) and the best fit curve after excluding data points more than 1 standard deviation away from the preliminary fit (green).*

3.18. Error Analysis

Internal uncertainty

Tensile strength measurements were carried out on three separate sheets for each sample. Analysing data from 155 MFC samples produced in this work, the mean standard deviation was found to be 2.99% of the mean tensile index. Consequently, this test is considered to be fairly reliable and repeatable. Figure 3.14 shows that the samples with high standard deviations tended to have low strengths; low strength MFC tended to be under-developed and coarse, and so more subject to inhomogeneities in the sheets.

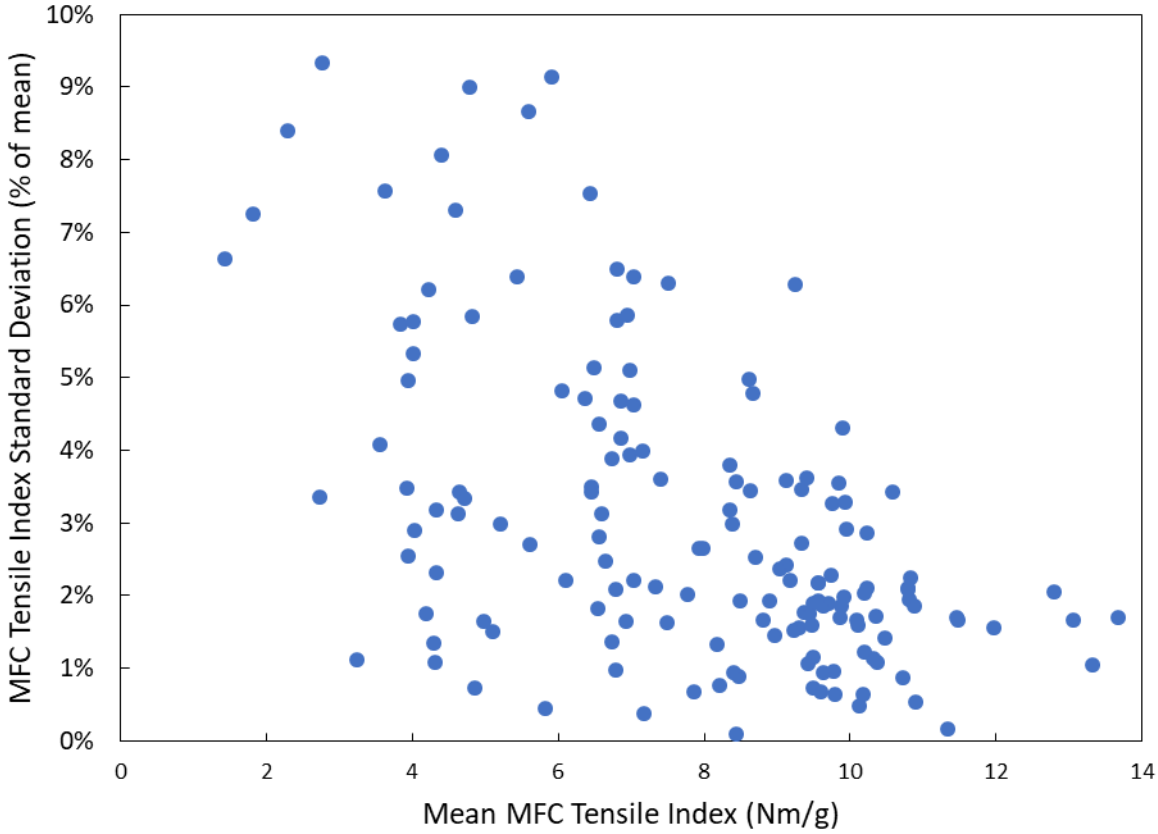

Figure 3.14 *– Standard deviation of the MFC tensile index versus the mean MFC tensile index for 155 MFC samples tested as part of this work.*

Most samples underwent fibre analyser testing three times, allowing a standard deviation to be calculated. The average standard deviations for 113 samples (as a percentage of the mean) is given for key fibre analyser parameters in Table 3.4, along with the uncertainty for the MFC tensile test; these values are very low, so one data point per sample is sufficient to be confident in the measured value.

Table 3.4 *– Determination of internal uncertainty of the fibre analyser and MFC tensile index data. The standard deviations were calculated from three tests for each samples, with the average standard deviation across all samples shown here (from 113 samples for fibre analyser data and 155 samples for tensile index data).*

	Lc(n) **(mm)**	***Lc(l)*** **(mm)**	***Fines B*** **(%)**	***Fibrillation %***	**MFC Tensile Index (Nm/g)**
Average standard deviation (% of mean)	1.20%	1.50%	3.14%	2.72%	2.99%

External uncertainty

There are numerous steps in producing and analysing an MFC sample, with many opportunities for the introduction of error. Although internal repeats identify apparatus error, external repeats (i.e. multiple samples with the same inputs produced from the grinder) in general were impractical due to the multiplication of time and resources required. Instead, external uncertainty was assessed using a 'standard' MFC sample produced and characterised numerous times over several years, under identical input conditions. These results are shown in Table 3.5.

Table 3.5 *– Properties of a 'standard' sample produced multiple times over several years (Nordic pine fibres, IC60 mineral, 2.9 mm 'Mullite A' media, 2.5% total solids content, 50% POP, 800 rpm impeller speed, 3000 kWh/t energy input).*

Date	Laser Diffraction d_{50} (µm)*	*Lc(n)* (mm)	*Lc(l)* (mm)	*Fines B* (%)	*Fibrillation %*	Tensile Index (Nm/g)	Media Wear (%MOP)
Dec-2016	110					9.44	8.00
Feb-2017	113					9.19	8.55
Feb-2017	109					9.68	9.14
Feb-2017	115					9.22	7.87
Mar-2017	105					9.04	7.60
Sep-2017	113	0.141	0.222	27.33	5.33	8.90	6.79
Nov-2017	118	0.147	0.237	29.39	4.98	9.64	6.62
Jun-2018		0.138	0.209	27.33	5.26	8.59	6.29
Dec-2019		0.146	0.231	28.95	5.24	10.18	
Feb-2020		0.143	0.227	27.95	5.28	9.96	7.02
Apr-2020		0.139	0.218	28.60	4.99	9.75	
May-2020		0.139	0.214	25.96	5.36	9.60	7.72
Mean	**111.9**	**0.142**	**0.223**	**27.93**	**5.21**	**9.43**	**7.56**
Standard deviation (% of mean)	**3.81%**	**2.47%**	**4.43%**	**4.19%**	**3.00%**	**4.87%**	**11.81%**

****** The laser diffraction method employs a Malvern Insitec Wet laser diffraction particle size analyser, which was the particle size characterisation technique in earlier work by Riley[73] and Pinkney[84]. This was used in the present work until it was later superseded by the fibre analyser in late 2017.*

The external uncertainties are shown as the bottom row in Table 3.5; for the fibre analyser and tensile index data, these are around double the internal uncertainties in Table 3.4,

showing that around half of the error is due to the characterisation tests, and half due to true variations in the product attributes as produced in the grinder under specific conditions, or else longer-term variations which are not encapsulated by internal repeats carried out in immediate succession.

Possible sources of this external error are listed below:

- Drift in the grinder load cell – a sharp application of forces can cause a drifting away from the calibration set point, so consequently the load cells are calibrated at least monthly.
- Grinding media variations – Including media sampling differences between grinds, changes in particle size distribution over continued use, and the possibility of replacement grinding media having different properties (especially roughness).
- Changes in IC60 mineral properties – if the IC60 particle size distribution changed significantly, this would affect the tensile test. *Imerys* maintains a tight product specification, but errors in sampling from *FiberLean*'s industrial stockpile cannot be ruled out (e.g. differences in segregation between collected samples).
- Differences in nanopaper sheet formation – either due to the polyDADMAC being diluted incorrectly or decaying over time, or the vacuum pressure being inconsistent.
- Differences in tensile testing – errors in temperature and humidity control (although this was always monitored) or a drift of the tensile tester away from calibration.

The first two sources of error can be expected to affect all property measurements, whereas the last three are exclusive to the tensile strength measurements.

Towards the end of this work, it became increasingly clear that the grinder load cell drift was a dominant source of external uncertainty, and was later checked for daily, by recording power draw using a reserved batch of ‘calibration’ grinding media.

Despite the external uncertainties being around twice as large as the internal uncertainties, for fibre analyser and tensile strength data it is still relatively minor, allowing for comparison of data series generated at different time periods with good confidence. The media wear test was the only parameter with considerable error, with an average uncertainty of 12%. This is because the media content in the sample is typically very small, which results in high sensitivity to errors in the POP and MOP measurements. Therefore, low MOP values cannot be considered reliable due to particularly low sample mass, so where possible a gradient of an energy input versus MOP curve is used to assess media wear rate.

4. INTRODUCTION TO STIRRED MEDIA MILLING OF CELLULOSE

4.1. Analysis of a Typical Energy Sweep

4.1.1 Introduction

To introduce key concepts for this work, and to identify the processes involved in disintegrating fibres into MFC, a typical 'energy sweep' was carried out, and the resultant samples extensively characterised. In an energy sweep, samples are produced over a range of energy inputs to observe the evolution of MFC properties. *Nordic pine* fibres were chosen as the feed, since this is the most commonly used species by *FiberLean* (and is applicable to a large number of potential customers).

Grinds were carried out with *Mullite A* media, at 5% total solids content, and 50% POP (50 dry wt% *IC60 mineral*), with an impeller speed of 800 rpm and a media volume concentration (MVC) of 47.5%. Samples were produced with specific energy inputs between 500 – 5000 kWh/t at 500 kWh/t intervals, with an additional sample at 250 kWh/t. All samples underwent fibre analysis and tensile strength testing, and some samples underwent DIC microscopy to observe product geometry. These results are discussed in the following sections.

4.1.2. DIC Microscopy

During a stress event in grinding (i.e. a media collision compressing a fibre), two parallel processes occur; hydrogen bonds between parallel fibrils and microfibrils are broken, causing radial *delamination* (analogous to internal fibrillation) and secondly, fibril and microfibril cross-sections are broken. The relative prevalence of each controls fibre disintegration and MFC attributes. The following microscopy images demonstrate both processes.

Figure 4.1 shows a DIC microscopy image of the feed fibres, where both earlywood (ribbon-like with thin walls and collapsed lumens) and latewood (cylindrical, thick-walled) fibres are apparent. A very small amount of external fibrillation is apparent here.

Figure 4.2 shows these fibres after 500 kWh/t of processing. Impact sites where two media have collided and compressed the fibre cell wall are obvious, causing extensive fibril delamination. Damage severity varies greatly between impact events, primarily due to the broad stress intensity distribution, so consequently some impacts completely break fibres whilst others only slightly disrupt the cell wall. Figure 4.2 shows two broken fibre ends; these are poorly fibrillated, having so far had insufficient time to fray exposed fibrils. External fibrillation has also been generated outside obvious impact sites, so there are stress events that disrupt the S1 layer to extend fibrils, with insufficient momentum for cell wall collapse. Low collision intensities can thus generate fibrillation without fibre cross-sectional breakage.

Figure 4.3 shows the MFC at 1000 kWh/t, where the fibre structure is mostly intact, though further stress events have frayed fibrils at breakage sites, and exploited S1 cell wall damage, peeling the fibre apart into long fibrils. This continues at 1500 kWh/t (Figure 4.4), where most of the fibre cell wall has fragmented into smaller fibril bundles.

Figure 4.5 shows the MFC at 3000 kWh/t, which is later shown to exhibit the maximum tensile strength. The cell wall has fully disintegrated into fibrils, with further delamination reducing their diameters compared to lower energy inputs; however, cross-sectional fibril breakage is extensive, making fibril lengths much shorter. Most fibrils are not independent, being physically rooted into larger aggregate particles; these aggregates are what the fibre analyser interprets as a ‘fibre’.

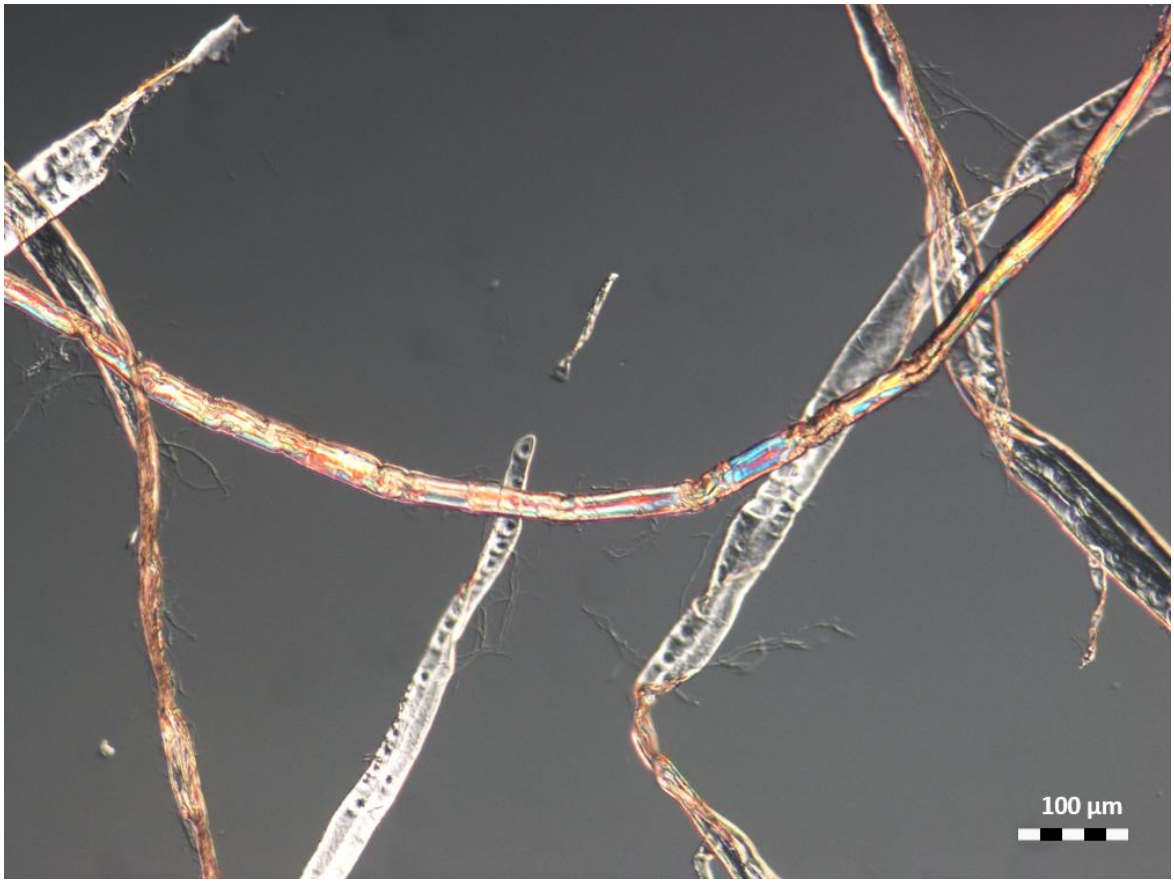

Figure 4.1 *– DIC microscopy image of Nordic pine feed fibres at an energy input of 0 kWh/t.*

Figure 4.2 *– DIC microscopy image of MFC at an energy input of 500 kWh/t.*

Figure 4.3 *– DIC microscopy image of MFC at an energy input of 1000 kWh/t.*

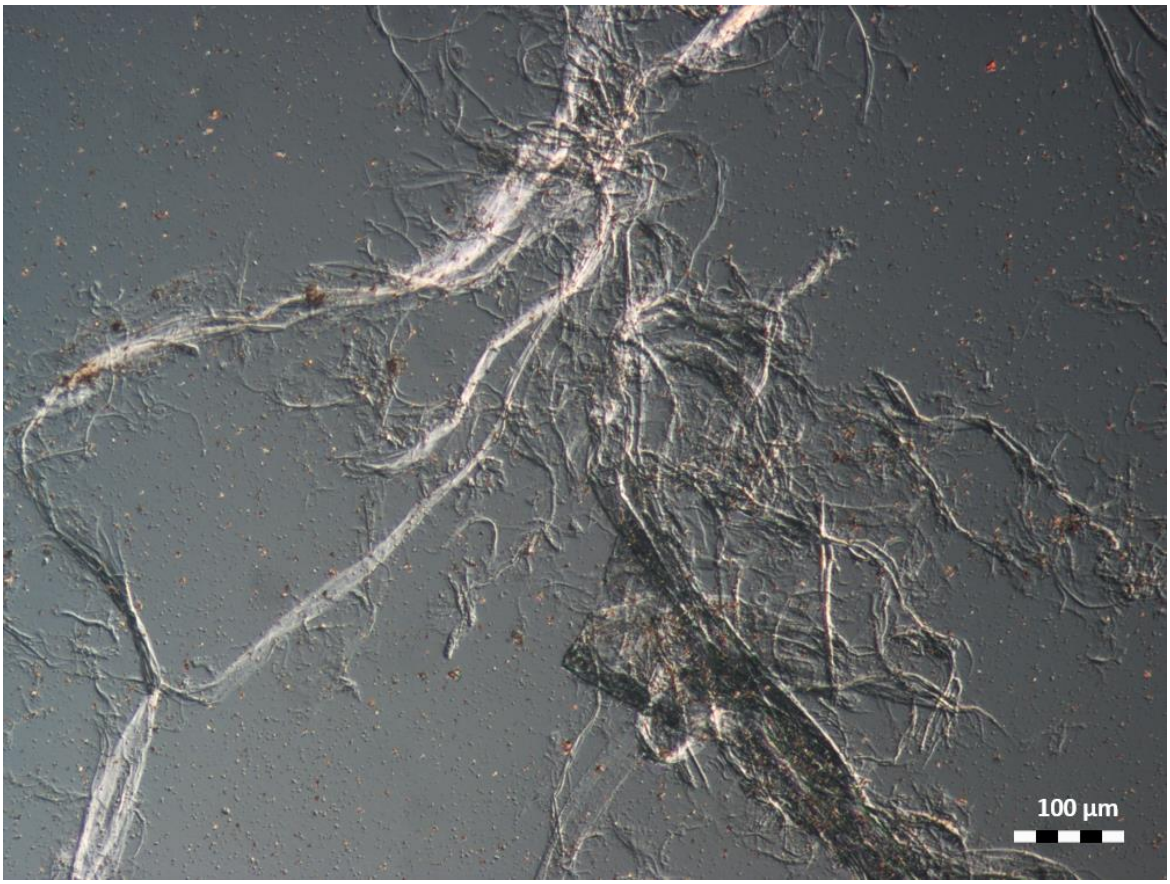

Figure 4.4 *– DIC microscopy image of MFC at an energy input of 1500 kWh/t.*

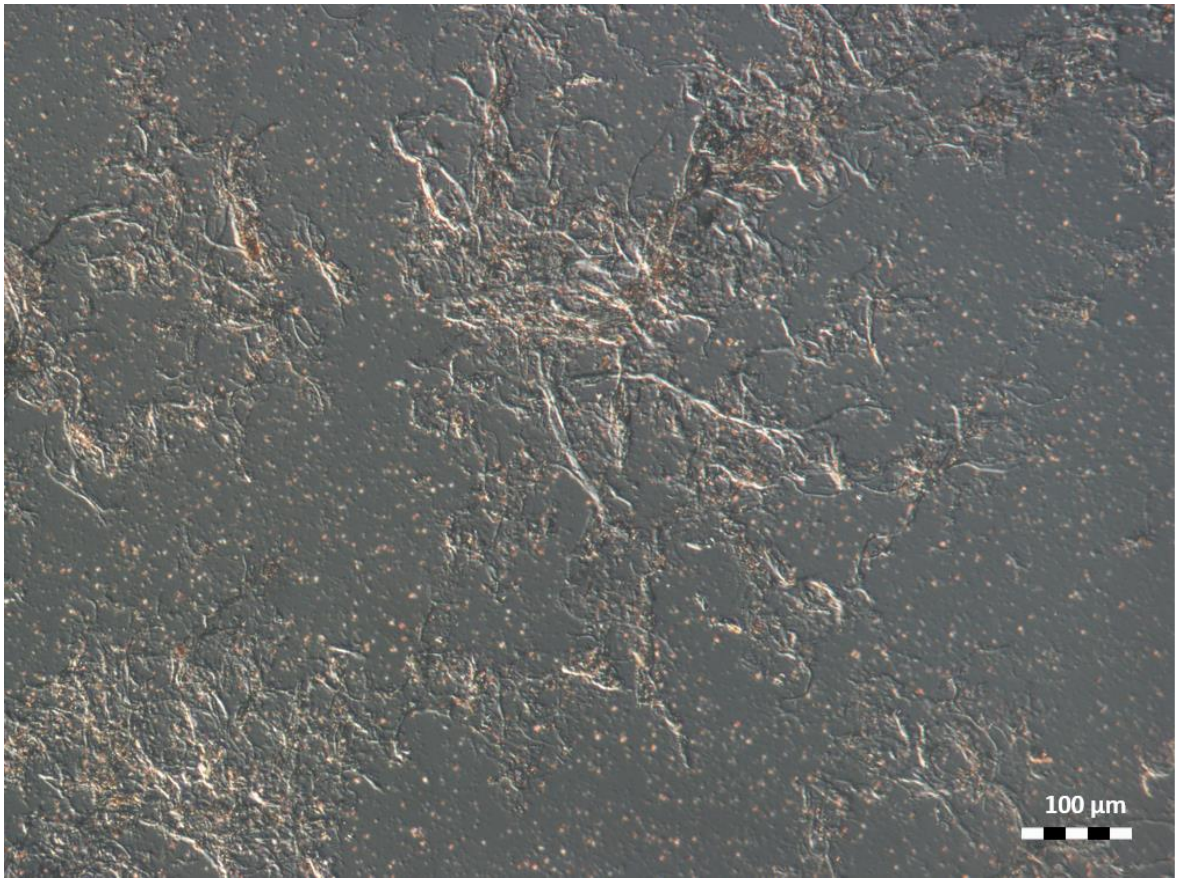

Figure 4.5 *– DIC microscopy image of MFC at an energy input of 3000 kWh/t.*

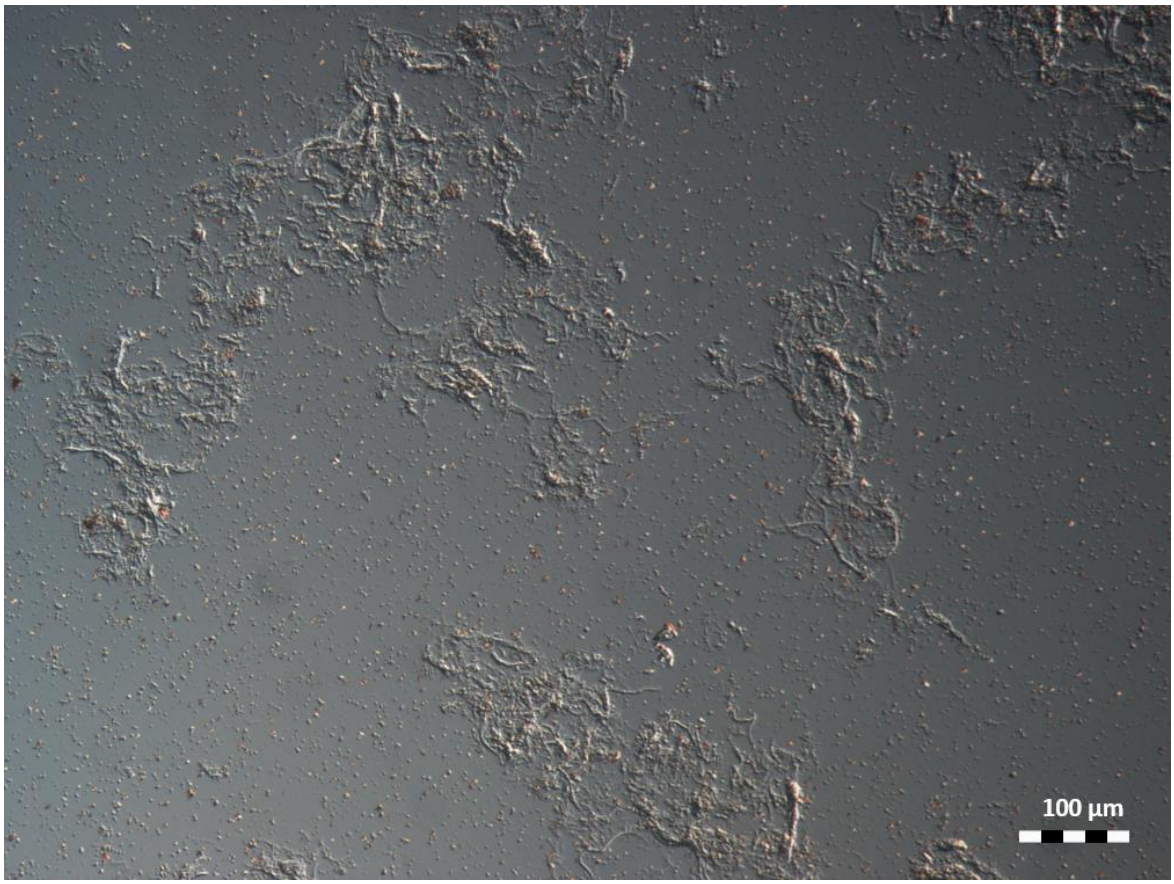

Figure 4.6 *– DIC microscopy image of MFC at an energy input of 5000 kWh/t.*

Figure 4.6 shows the MFC at 5000 kWh/t, where fibrils are finer than at 3000 kWh/t, but are much shorter, forming smaller aggregates; this is 'over-ground' MFC, beyond the optimum energy input, with a lower strength.

These images show that fibril delamination dominates at low energy input, creating long fibrils as the fibre disintegrates. With increasing energy input, there is less cell wall remaining to disintegrate, so fibril liberation slows; however, cross-sectional breakages of liberated fibrils continues unhindered, leading to a decline in MFC quality.

Since the covalent bonds of fibril cross-sections are much stronger than hydrogen bonds between fibrils, fibrillation likely has a lower optimum stress intensity than fibril breakage. As particles become finer, the area to break in a collision decreases, so given constant media momentum, the force per unit area increases. This likely acts to accelerate fibril cross-sectional breakage as grinding progresses.

The effects of these fibrillation and breakage processes on quantitative measurements of MFC properties are given in the next section.

4.1.3. MFC Property Measurements

MFC Length and Width

Figure 4.7 shows the effect of energy input on number-weighted (*Lc(n)*) and length-weighted (*Lc(l)*) fibre lengths, and average fibre width, as measured by the fibre analyser. Both *Lc(n)* and *Lc(l)* initially decay rapidly, with the rate diminishing with energy input. As the previous section implies, at higher energy inputs, fibre length measurements are increasingly dominated by fibril aggregate networks rather than intact fibres. There is a peak in fibre width at around 1000 kWh/t, which is expected to be due to internal fibrillation swelling the fibre, prior to disintegration into liberated fibrils.

Rittinger's Law, introduced in Section 2.8, postulates that energy input should be proportional to the surface area generated (more accurately, surface energy created). An Operating Rittinger Index $K_{R,Op}$ was defined as a measure of grindability under given operating conditions, which can be calculated using Equation 2.11, on an *Lc(n)* or *Lc(l)* basis. A plot of $K_{R,Op}$ versus energy input for both length definitions is given as Figure 4.8.

The *Lc(n)*-based $K_{R,Op}$ value is roughly constant with energy input, therefore following Rittinger's Law well. However, *Lc(n)* is sometimes a poor measure of MFC particle size since its reduction can be driven by disproportionate breakage of fine particles, being only weakly affected by intact large particles where most of the cellulose mass may be. *Lc(l)* is therefore a better measure of particle size, but Figure 4.8 shows that *Lc(l)*-based $K_{R,Op}$ decreases with energy input; it does not follow Rittinger's Law except at higher energy inputs. Though partly due to the length-weighting transformation, this can vary greatly with operating conditions even at similar *Lc(n)* values, so some of this effect is real. This is expected; below the optimum stress intensity, larger particles would be harder to break due to the collision energy being dissipated across a larger cross-section.

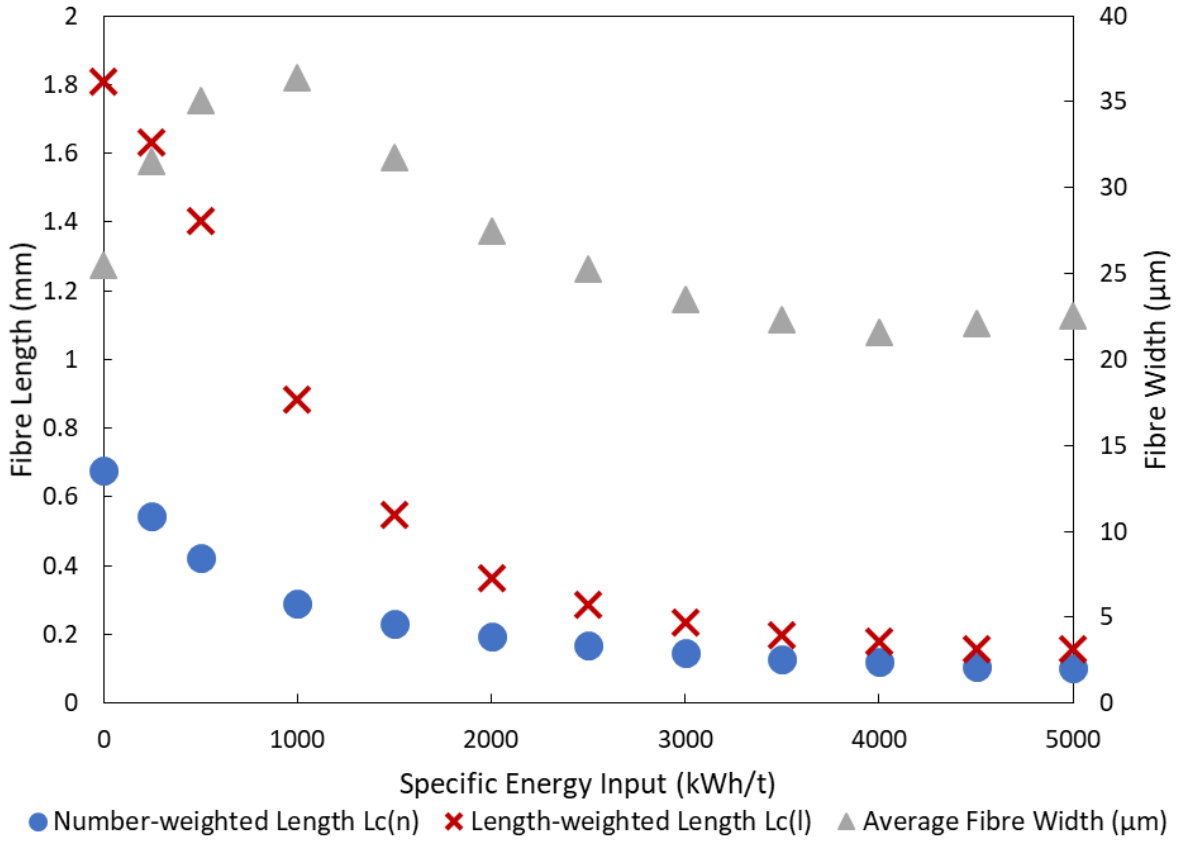

Figure 4.7 *– MFC number-weighted and length-weighted average fibre lengths, and length-weighted fibre widths, versus energy input.*

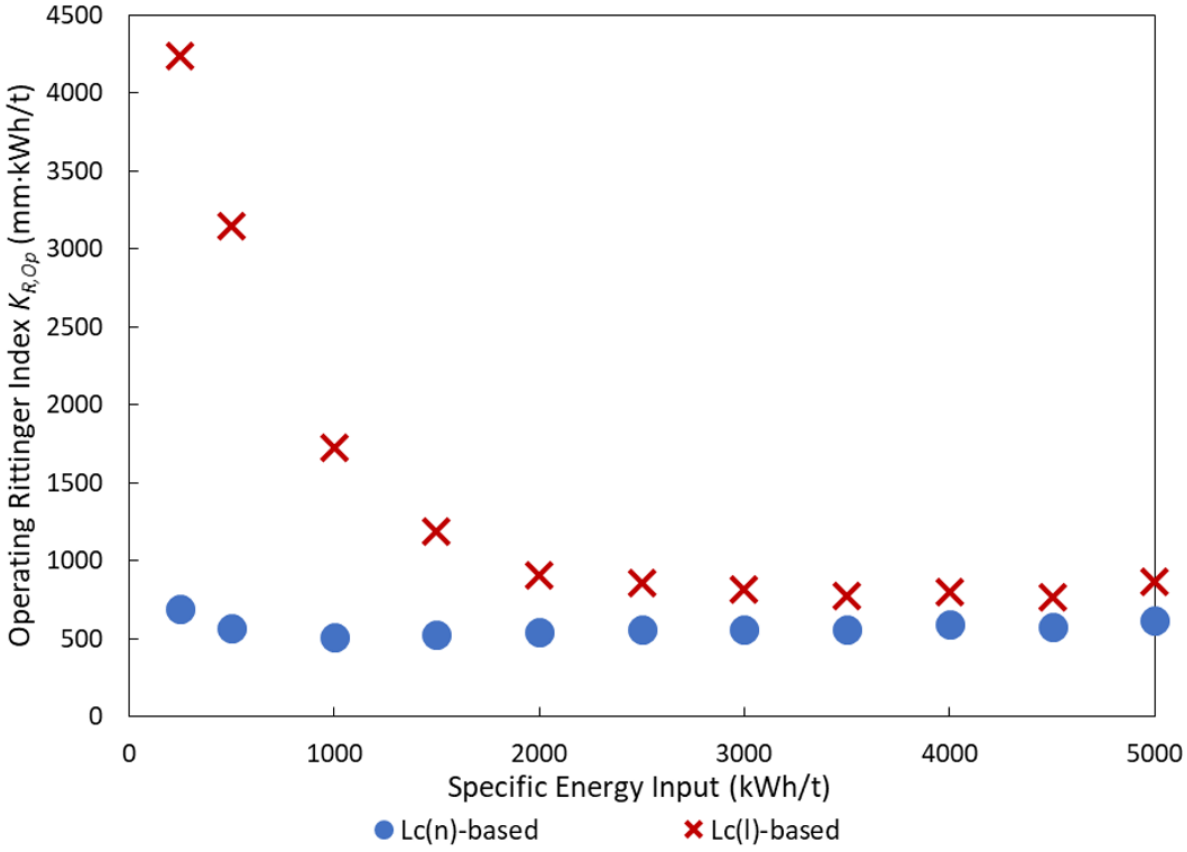

Figure 4.8 *– Lc(n)-based and Lc(l)-based $K_{R,Op}$ versus energy input.*

Fines B and Fibrillation %

Both *Fines B* and *Fibrillation %* parameters give indications of the fibrillation quality and tend to correlate with tensile strength. *Fibrillation %* represents external fibrils extending from the fibre or MFC particle, and *Fines B* particles are *high aspect ratio fines*, either individualised fibrils or long, thin MFC particles. Figure 4.9 shows how these vary with energy input in this example. The *Fibrillation %* value initially increases linearly, before slowing to a peak, then declining. *Fines B*, on the other hand, follows an S-shaped curve, with a lag time before a rapid acceleration, followed by slowing towards a plateau.

External fibrillation is likely caused both from fibrils fraying at impact points, and from the disruption of the S1 cell wall layer (Figure 4.2 shows examples of both). The peak and decline is believed to be because further grinding breaks off external fibrils into *Fines B* particles. This has a similar rationalisation as the fibril generation and breakage concept behind the peak tensile strength (see the subsequent section), with these two peaks consistently occurring at similar energy inputs, making *Fibrillation %* a useful quality control parameter (it is far quicker to test than tensile strength). These external fibrils, being intermediates between unbroken fibres and *Fines B* particles, are usually less sensitive to changes in operating conditions, so when differences are small, they are often not discussed for brevity.

The S-shaped *Fines B* versus energy input curve is consistently seen throughout this work, regardless of operating conditions, so *Fines B* generation appears to be a *second-order effect*. This makes sense mechanistically; an impacted fibre is unlikely to instantly disintegrate into liberated fibrils; instead, subsequent stress events must exploit breakages to separate fibrils first into external fibrils, then break them loose into *Fines B* particles. This is not the MFC-

particle end-state, however; excessive grinding can break lengths to below 0.2 mm (the defined minimum for *Fines B*), eventually decreasing *Fines B* content.

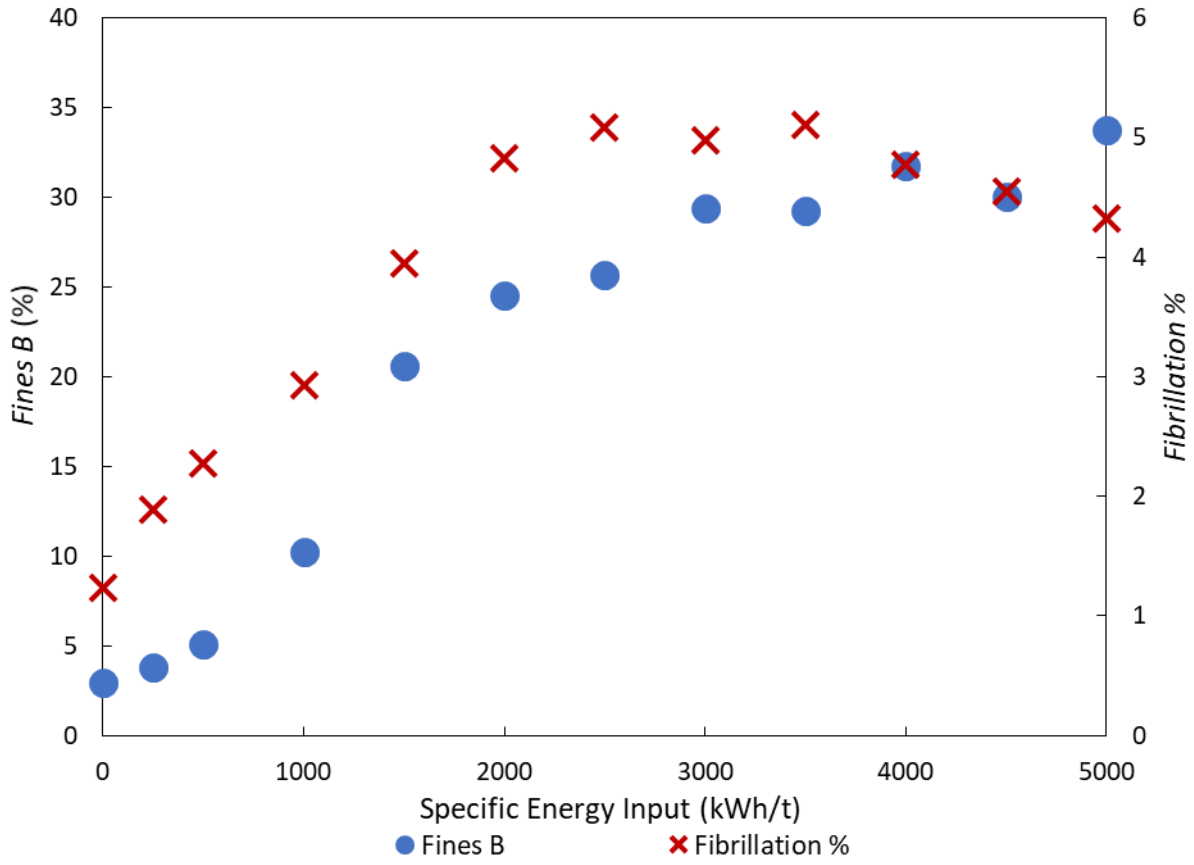

Figure 4.9 *– MFC high aspect ratio fines and external fibrillation versus energy input.*

Tensile Index

Figure 4.10 shows the variation in tensile index with energy input. Feed fibres have very low tensile strength, but this rapidly increases at low energy inputs. The marginal benefit decreases until a peak is reached at the optimum energy input, above which strength gradually declines.

The explanation is obvious from the microscopy images in Section 4.1.2; there is a balance between the strengthening effect of fibril liberation from the fibre cell wall, and the degrading effect of breaking liberated fibril cross-sections that determines tensile strength; one expects from the Page Equation (Equation 2.1) that long, thin fibrils lead to high strength. At low

energy inputs, there is a lot of cell wall to disintegrate into fibrils, so long liberated fibrils are rapidly generated, greatly increasing strength. As the cell wall fraction from which to liberate fibrils declines with energy input, this strengthening process slows. Concurrently, the greater concentration of liberated fibrils increases fibril breakage rate, so the decline does not slow with energy input. The optimum energy input occurs at the point where the degradation process exceeds the strengthening process.

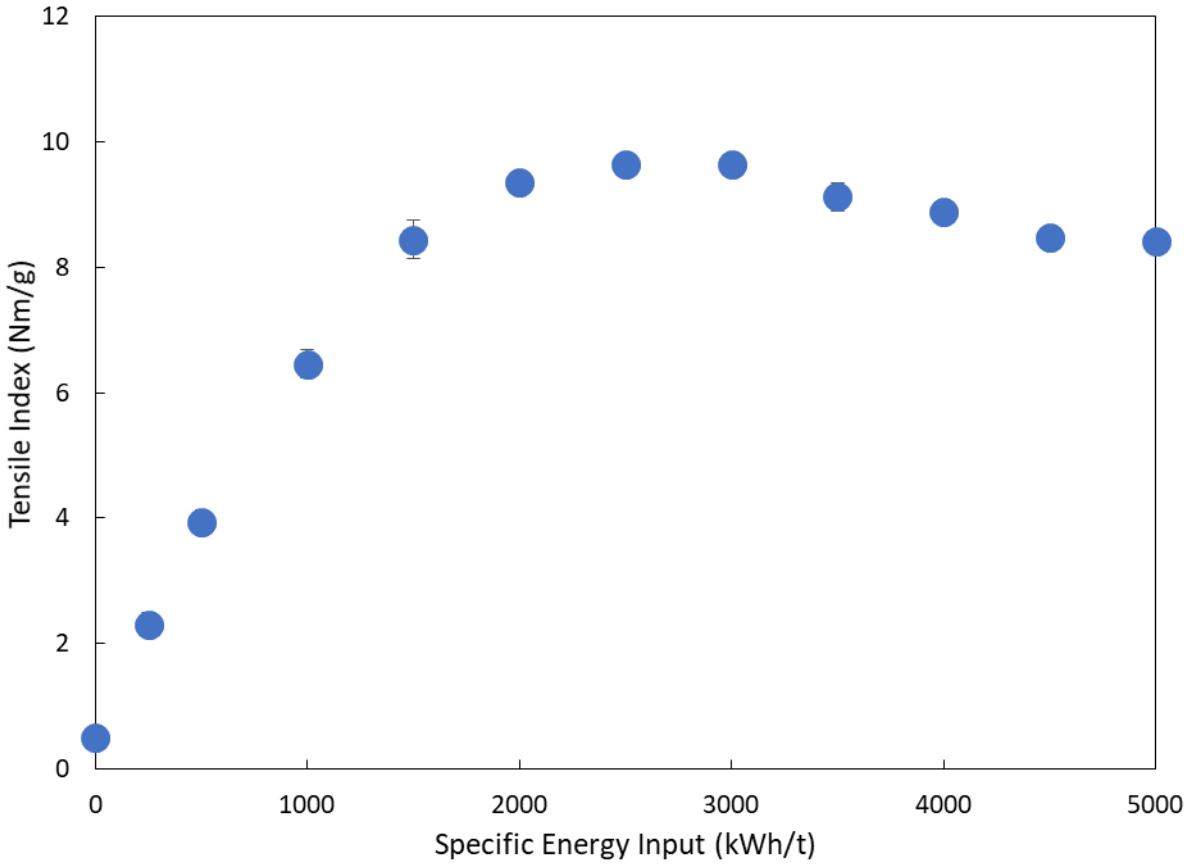

Figure 4.10 *– MFC tensile index versus energy input.*

Normalised MFC Properties Curves

MFC length, *Fines B* content, *Fibrillation %*, and tensile strength were normalised based upon their maximum values, and plotted against energy input as Figure 4.11, for ease of comparison. This makes it obvious that *Fibrillation %* and tensile index peak at similar energy inputs, as previously mentioned. Also, the decay in *Lc(l)*, the increase and eventual decline of

Fibrillation %, and the second-order increase of *Fines B*, follow the patterns one would expect for chemical reactions in series, supporting the assertion that *Fibrillation %* is an intermediate between fibres and *Fines B* particles. These characteristic curves are representative of most energy sweeps carried out in this research.

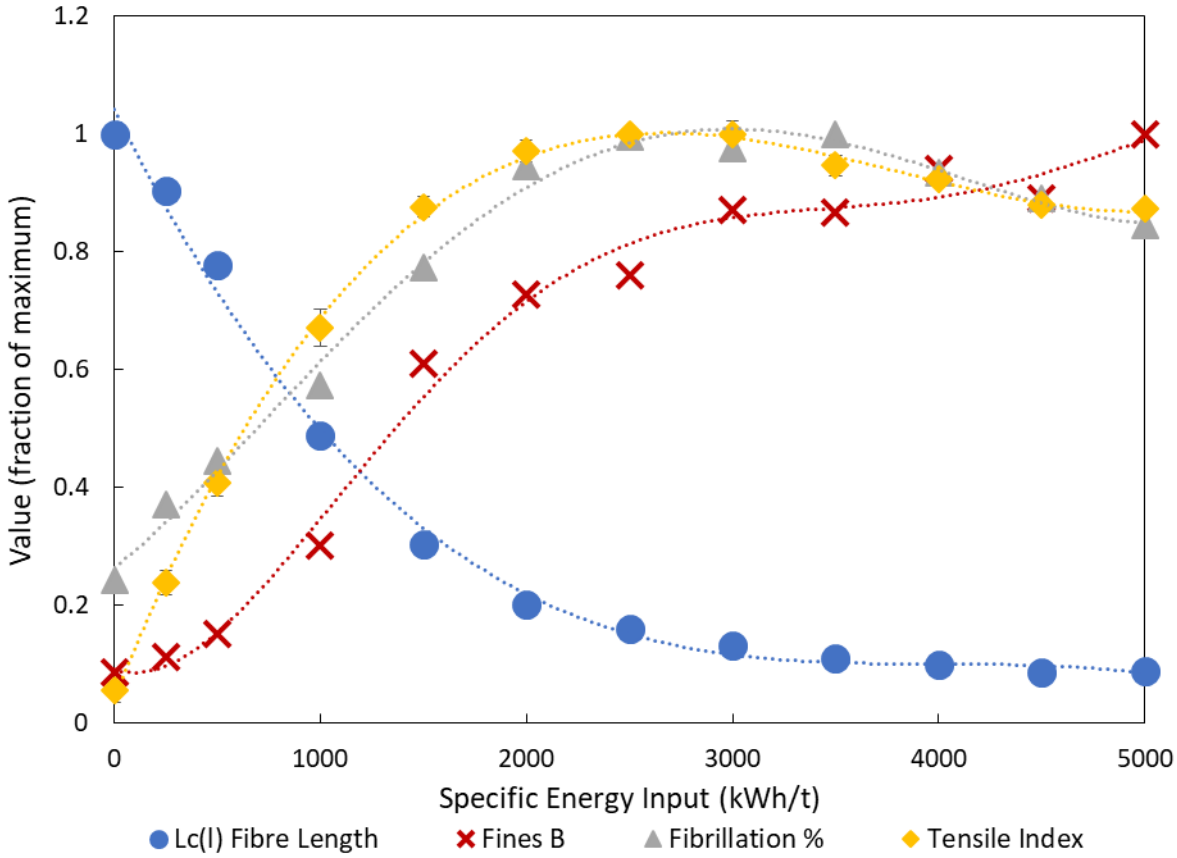

Figure 4.11 *– Plots of MFC fibre length, Fines B, Fibrillation % and tensile index versus energy, normalised to the maximum value of each parameter.*

4.1.4. Conclusions

Microscopy images in this section demonstrate the evolution of product microstructure under typical grinding conditions. Media impacts cause complete or partial breakage of the fibre cross-sections, and longitudinal separation of neighbouring fibrils. Other processes (perhaps lower intensity collisions or shear forces) exploit the exposed fibrils at these breakage sites, causing local disintegration of the cell wall into long, thin fibrils. This consequently leads to a

rapid increase in tensile strength with energy input, though with diminishing returns as there is increasingly less under-ground fibre to delaminate. Eventually, breakage of liberated fibrils outpaces this delamination, decreasing fibril aspect ratio and so lowering strength. MFC quality is clearly determined by a balance of fibrillation and fibril degradation.

Fibre analyser results plotted against energy input show how fibre length, external fibrillation (*Fibrillation %*), and high aspect ratio fines (*Fines B*) change with energy input. It is suggested that upon a media impact with a fibre, external fibrillation is generated at the breakage site, which is slowly extended until it is broken off to generate *Fines B* particles.

By controlling collision forces, and controlling the fibril cross-sectional strengths and inter-fibril forces, it is expected that MFC quality can be maximised, and energy input minimised, which is the overarching aim of this thesis. To aid understanding, Section 4.3 demonstrates extreme cases where either the fibril breakage or the fibrillation mechanisms have been greatly suppressed.

However, the microscopy images make clear that fibre breakage is primarily caused by normal media-media collisions, and fibrillation takes place subsequently from these breakage sites. The next section describes an adaption of Hertzian contact mechanics theory to consider a media bead colliding with a fibre, giving suggestions for what conditions are required for effective grinding, and the impact site deformation dimensions expected.

4.2. Contact Mechanics – Compression of a Fibre in a Media Collision

Hertzian contact theory was introduced for a naked media-media collision in Section 2.11, which predicted very high contact pressures and very small contact areas. Collision with an intervening fibre is now considered.

A soft fibre caught between two media would expand the deformation area and dissipate pressure over a wider area. Therefore, a collision between a media bead and a flat semi-infinite cellulose surface is considered. Since only one surface is curved, the radius of curvature *1/R* is now that of a single bead. The contact modulus *Y** must be recalculated using Equation 4.1, restated here using the Young's moduli and Poisson ratios of the media (Y_m and v_m) and the cellulose (Y_C and v_C):

$$\frac{1}{Y^*} = \frac{1 - v_m^2}{Y_m} + \frac{1 - v_c^2}{Y_c} \dots [4.1]$$

The evaluation of Y_C is complicated because cellulose has a hierarchical structure that can be deformed over many length-scales, from micron-scale fibre lumens to Angstrom-scale molecular chains, and mechanical properties differ with scale. On the larger scale, the Young's modulus of a fibre cell wall (with a collapsed lumen) under instantaneous tangential compression in an aqueous environment has been calculated as approximately 0.03 GPa[101]. A wet fibre is readily deformable since fibrils can move within the ultrastructure without necessitating finer-scale microfibril deformation (see Figure 4.12 (a)). This cell wall Young's modulus is termed $Y_{C,W}$.

At closer approaches, the media excludes cell wall mass between them, causing plastic deformation and delaminating fibrils and microfibrils. At very short separation distances, the media would stress a layer of individual microfibrils (see Figure 4.12 (b)), which can cause breakage. When modelling microfibril breakage, rather than $Y_{C,W}$, the compressive Young's modulus of the individual microfibrils $Y_{C,mi}$ should be used. Cabrera et al.[102] determined this value to be 15 GPa.

All ceramic media have Young's moduli far greater than either $Y_{C,W}$ and $Y_{C,mi}$, so Y^* is determined almost entirely by cellulose elasticity. However, whether $Y_{C,W}$ or $Y_{C,mi}$ is used greatly affects the contact pressure and area calculations. The Poisson ratio of Cellulose 1β was found by Nakamura et al.[103] to be 0.377; the Poisson ratio of the cell wall is unknown, but is assumed to be the same.

Note that due to the absence of cellulose plastic deformation data, this model must assume that once the fibre cell wall yields, the deformation dimensions are the same as if entirely elastic deformation were taking place.

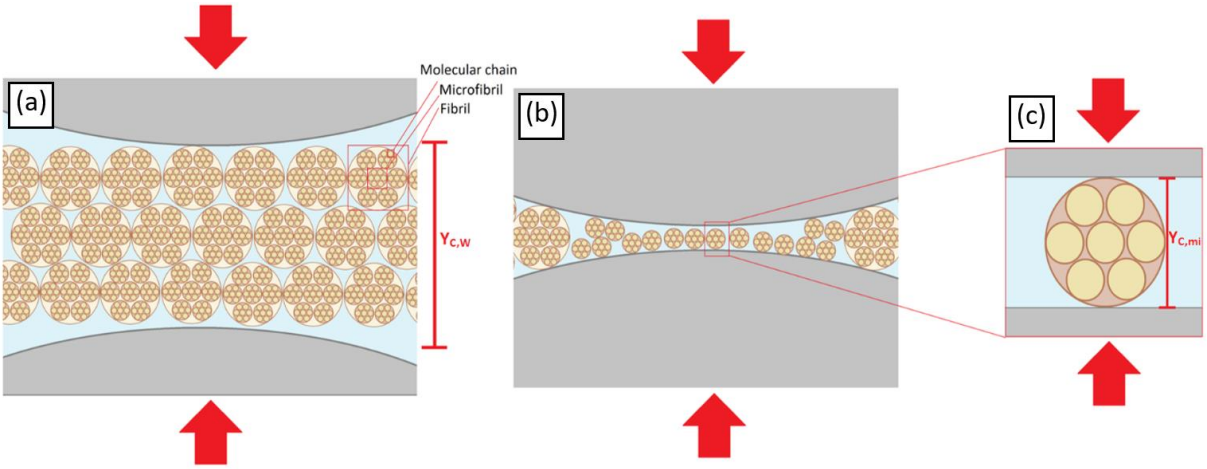

Figure 4.12 *– Schematic of a media collision causing compressive deformation of cellulose (radial cross-section) at different length-scales; (a) initially, the media deforms the macroscopic fibre cell wall; here, the Young's modulus $Y_{C,W}$ is assumed to be relatively low, 0.03 GPa. (b) A collision of sufficient momentum would cause plastic deformation, delaminating fibrils and microfibrils and excluding material from the gap until individual microfibrils are stressed. (c) in such a case, the microfibril Young's modulus, $Y_{C,mi}$, better describes the response; this is assumed to be relatively high, 15 GPa.*

Figure 4.13 shows the expected maximum Hertzian pressures experienced for each media species for both definitions of Y_C, with the average acceleration at an impeller speed of 800 rpm highlighted (100 m/s^2, see Section 2.11). Unlike in naked media-media collisions, this is insensitive to media elasticity as the cellulose accommodates essentially all the deformation. The pressures expected for macroscopic cell wall deformation ($Y_C = Y_{C,W}$) are relatively low, around 1 MPa, but if the media approaches close enough to stress individual microfibrils (Y_C =

$Y_{C,mi}$), pressures are much higher, at around 40-50 MPa. *Fibrils*, the intermediate structure between the cell wall and microfibrils, are expected to experience an intermediate pressure, but no data on fibril elasticity were found.

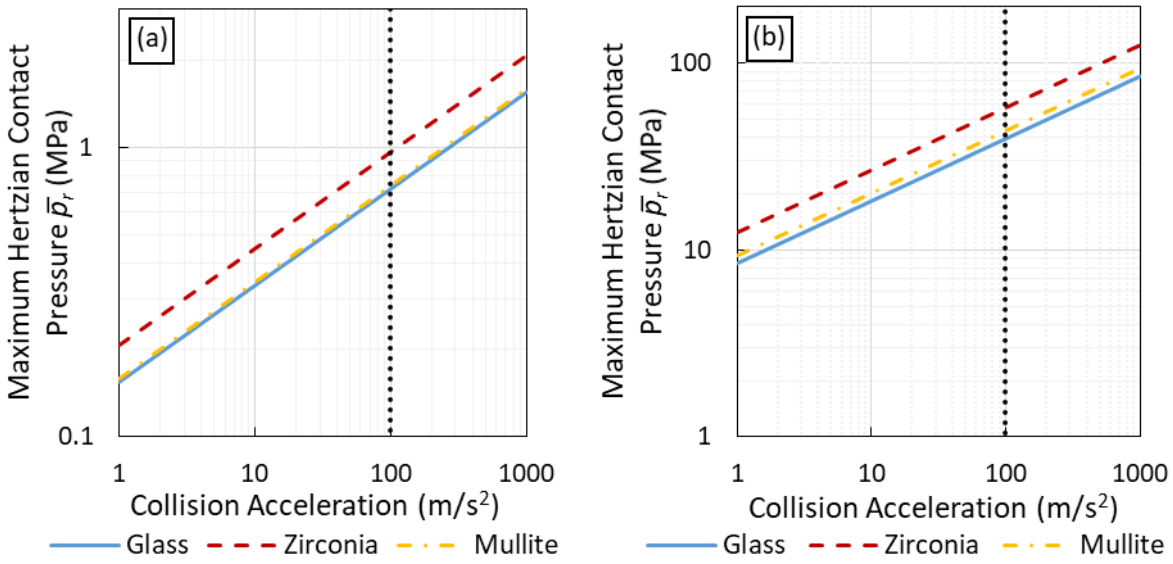

Figure 4.13 *– (a) Maximum Hertzian contact pressures for three media species (a) for $Y_C = Y_{C,W} = 0.03$ GPa, and (b) $Y_C = Y_{C,mi} = 15$ GPa. The vertical line represents the expected typical acceleration in the impeller region at an impeller speed of 800 rpm.*

Under the model shown in Figure 4.12, media must approach sufficiently close to exclude a large part of the highly deformable cell wall to stress individual microfibrils (and so Y_C increases from $Y_{C,W}$ to $Y_{C,mi}$, greatly increasing local pressure). One can assess this likelihood by comparing the fibre cell wall thickness to the expected cell wall indentation depth caused by the media collision, δ_C, which is the *z*-axis displacement depth of the cellulose, found using Equation 4.2 (from the displacement of one body, derived by Johnson[85]):

$$\delta_c = \frac{1 - v_c^2}{Y_c}\left(\frac{\pi a p_0}{2}\right) \ldots [4.2]$$

For cell wall deformation, $Y_C = Y_{C,W}$. Cellulose fibres have cell wall thicknesses around 1 – 5 µm, so for collisions where δ_C is similar to or greater than this, there is a high probability of stressing individual microfibrils, so breakage is more likely. From this, one can predict that

cellulose grinding should be most effective under conditions that give expected indentation depths of the same magnitude as the cell wall thickness.

Figure 4.14 (a) and (b) shows the expected contact area diameters and indentation depths for cell wall deformation respectively. The green box on Figure 4.14 (b) shows the range of typical cell wall thicknesses, with the dotted vertical line representing the typical accelerations expected under standard grinding conditions. The curves for each media type intersect with the typical acceleration within the green box, indicating that collisions should be around the intensity expected to delaminate the cell wall and stress microfibrils, and that zirconia media should be superior to glass and mullite.

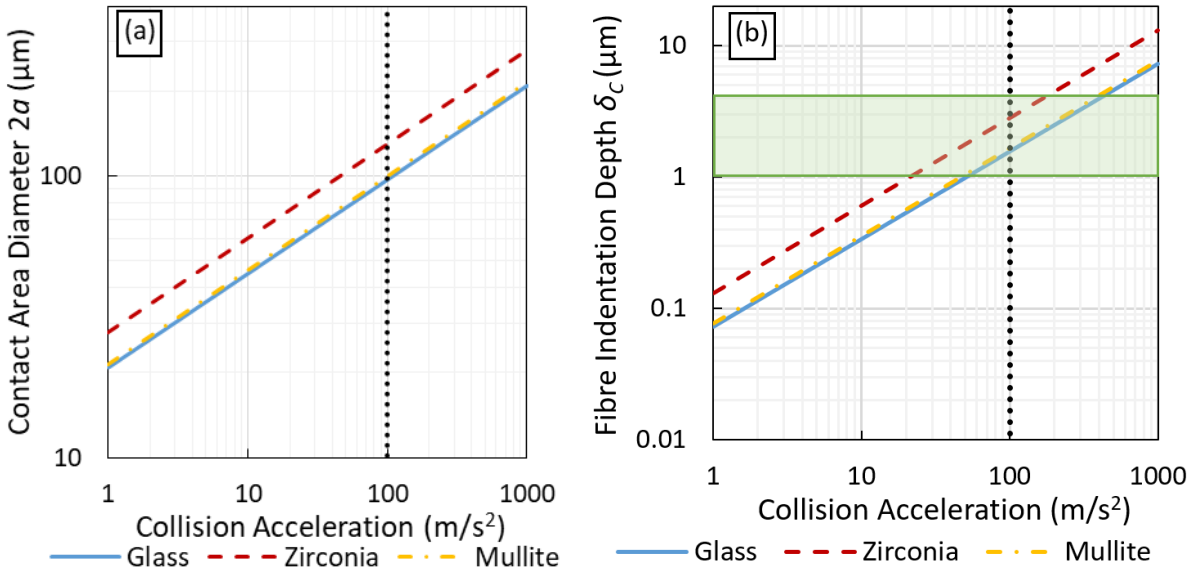

Figure 4.14 *– For a cellulose Young's modulus of $Y_{C,W}$ = 0.03 GPa, (a) predicted contact area diameter, and (b) predicted fibre indentation depth. The vertical line represents the expected typical acceleration in the impeller region at an impeller speed of 800 rpm. The green box shows typical fibre cell wall thicknesses.*

Figure 4.14 suggests that under the grinding conditions in Section 4.1, the impact site diameters visible in microscopy should be around 100 µm (along the longitudinal axis, since fibre diameter limits the radial direction), and indentation depths should be comparable to cell wall thicknesses. However, this assumes a characteristic collision acceleration of 100 m/s^2;

the PEPT data by Skuse[81] shows a broad distribution of accelerations around this average, with some up to 1000 m/s^2, so a wide spread is expected. However, lower accelerations give lower indentation depths so are less likely to leave noticeable damage (especially because the fibre can elastically deform at small indentations), and impact site diameters are expected to expand somewhat after the collision as further stresses fray the internal fibrils, so one expects a bias towards impact site diameters above 100 µm to be observed.

In Chapter 5, a sample from a *Mullite A* grind at 500 kWh/t under otherwise similar conditions to those in Section 4.1 was extensively imaged with DIC microscopy. Examples of impact sites observed are shown as Figure 4.15. The obvious impact site diameters range between 125 – 235 µm, which is above what one would expect from this theory, but is reasonable when the expected bias is considered. From this, it is predicted that grinding conditions that give calculated δ_C values of appreciably less than the fibre cell wall thickness should leave barely any visible impact sites.

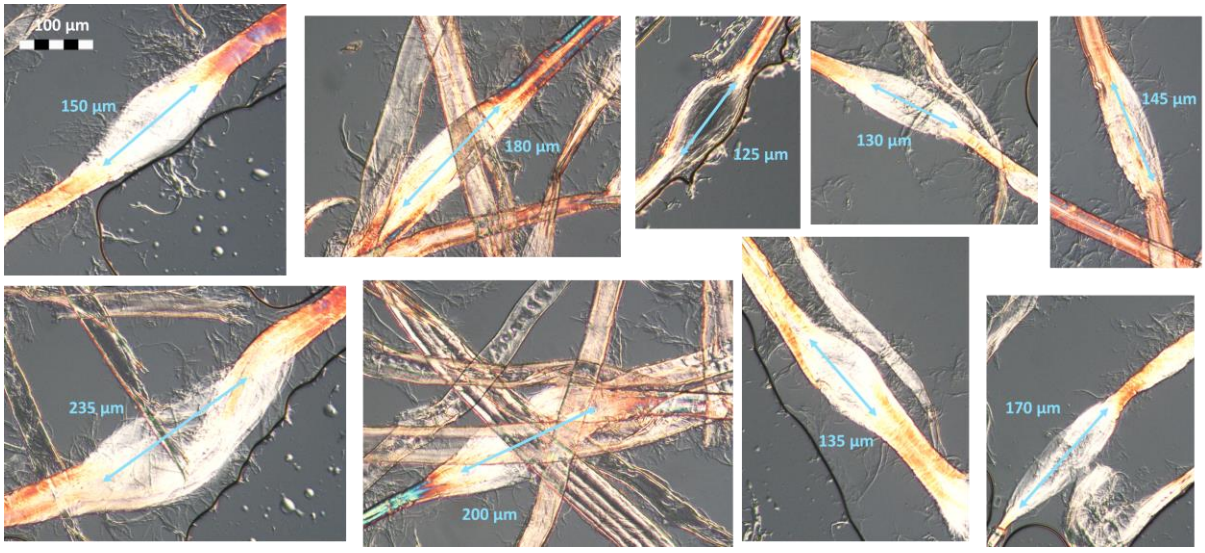

Figure 4.15 *– DIC microscopy images of delaminated cell walls at media impact sites for a 100 POP Mullite A grind at 500 kWh/t (detailed in Section 5.3), showing impact site diameters around what one would expect from the applied Hertzian contact mechanics theory.*

4.3. Suppressing Fibrillation and Suppressing Breakage

4.3.1. Introduction

Section 4.1 showed that there are two parallel processes occurring during cellulose grinding; fibril liberation (fibrillation) and fibril damage (cross-sectional breakage). By changing various operational parameters and feed composition, their influence can be altered. In this section, two extreme cases, where conditions are selected to strongly suppress either fibrillation or fibril breakage, show the influence that this can have on product morphology.

Both grinds were carried out mineral-free (100 POP) at 2.5% fibre solids, 47.5% MVC, 800 rpm impeller speed, and an energy input of 3000 kWh/t. A control was also made with these conditions using *Mullite B* media, and otherwise standard conditions.

Background – Suppressed Fibrillation: LiCl Salt Addition

The tendency for fibrillation can be suppressed by increasing the forces between neighbouring fibrils. In preliminary work, this was attempted by adding NaCl or $CaCl_2$ salts, or lowering the pH, to neutralise or mask microfibril charge, negating mutual microfibril repulsion. However, the resultant MFC strength decrease was small, implying that surface charge is relatively unimportant. Using a hygroscopic suspension was pursued as an alternative.

During fibrillation, water disrupts hydrogen bonding between neighbouring fibrils and microfibrils, facilitating separation. Therefore, adding an extremely hygroscopic salt would reduce water availability for hydrogen bond disruption, suppressing fibrillation. 18 mol/L of LiCl was added to the charge a day before grinding, lowering the water activity to around 0.165[104] (i.e. only a sixth of the water present was available for fibril wetting. Feed composition was calculated by a volume basis to account for the density increase.

Background – Suppressed Breakage: Nylon Media Grinds

Increasing inter-fibril forces is achievable, but increasing fibril cross-section strength is not. However, there is a way to delaminate fibrils whilst largely preserving fibril cross-sections. As mentioned in Section 2.7, Becker et al.[65] noticed that media with lower Young's moduli are poorer at grinding harder minerals, and defined an effective stress intensity accommodating this, see Equation 2.4.

In the previous section, it was suggested that media must approach close enough to exclude most of the cell wall and stress individual microfibrils to cause breakage. Consequently, the microfibril Young's modulus, $Y_{C,mi}$ = 15 GPa, is used as Y_P in Equation 2.4. This is far lower than the Young's moduli of all ceramic media, with even the lowest (glass) having a Y_{GM} of 69 GPa[86]. However, nylon media was acquired from *Imerys*; the Y_{GM} of nylon is around 3 GPa[86], so in a collision it should competently deform the fibre cell wall and cause fibrillation (as Y_{GM} is much greater than the $Y_{C,W}$ of 0.03 GPa), but would struggle to break microfibril cross-sections since the effective stress intensity according to Equation 2.4 is greatly reduced (and so will also struggle to break larger fibril-scale cross-sections).

The nylon media is not exactly comparable to the mullite media; it has an ellipsoidal prism shape, has a smaller equivalent spherical diameter (2.6 mm), and a lower density (1.15 g/cm^3). It therefore cannot be claimed to suppress fibril breakage *whilst keeping fibrillation tendency the same*. However, the striking effect on MFC geometry is unrivalled by any other permutation of operating parameters, so the author is confident that the low media elasticity is the dominant cause.

4.3.2. Fibre Analyser Results and Tensile Index

Figure 4.16 shows the *Lc(l)* value (a), *Fines B* content (b), *Fibrillation %* (c), and tensile index (d) of the control, the suppressed fibrillation (LiCl salt) sample, and the suppressed breakage (nylon media) sample.

Figure 4.16 (a) shows that the *Lc(l)* value of the suppressed breakage sample is much higher than the control, showing that breakage suppression is successful (this is far coarser than with later grinds of even lower stress intensity, e.g. with 1.67 mm media, see Figure 4.28). The suppressed fibrillation sample is significantly finer than the control, despite similar cross-sectional strengths. As will be shown, this is primarily because the liberated fines are shorter.

Despite the nylon media severely reducing fibril breakage, Figure 4.16 (b) shows a similarly high *Fines B* value as the control. Because fibril breakage is suppressed, many more of the liberated fibrils are sufficiently long to be classed as *Fines B*. This high *Fines B* value for such extremely coarse MFC is unique compared to any other case investigated in this work.

The suppressed fibrillation sample, however, has an extremely low *Fines B* content, showing that despite rapid fibre breakage, the constituent fibrils struggle to separate into liberated fibrils. The liberated fibrils are also shorter, as later microscopy images show; this is believed to be because strong inter-fibril forces would make it more energetically favourable for the crack to propagate across fibril cross-sections, rather than around the fibrils and exploiting pre-existing defects, leading to shorter fibrils once liberated.

External fibrillation for both the suppressed breakage and suppressed fibrillation grinds are lower than the control, as Figure 4.16 (c) shows. For the former, this is because fewer fibril cross-sections are broken, leading to fewer external fibrils. For the latter, there are many more breakage sites, but the fibrils produced are shorter, leading to a lower *Fibrillation %* value.

Figure 4.16 (d) shows that the suppressed fibrillation sample has a very low tensile index, which is due to an extreme deficiency in liberated high aspect ratio fibrils. The suppressed breakage sample has an intermediate strength, as although large fractions of the fibre are intact, liberated fibrils are of excellent quality.

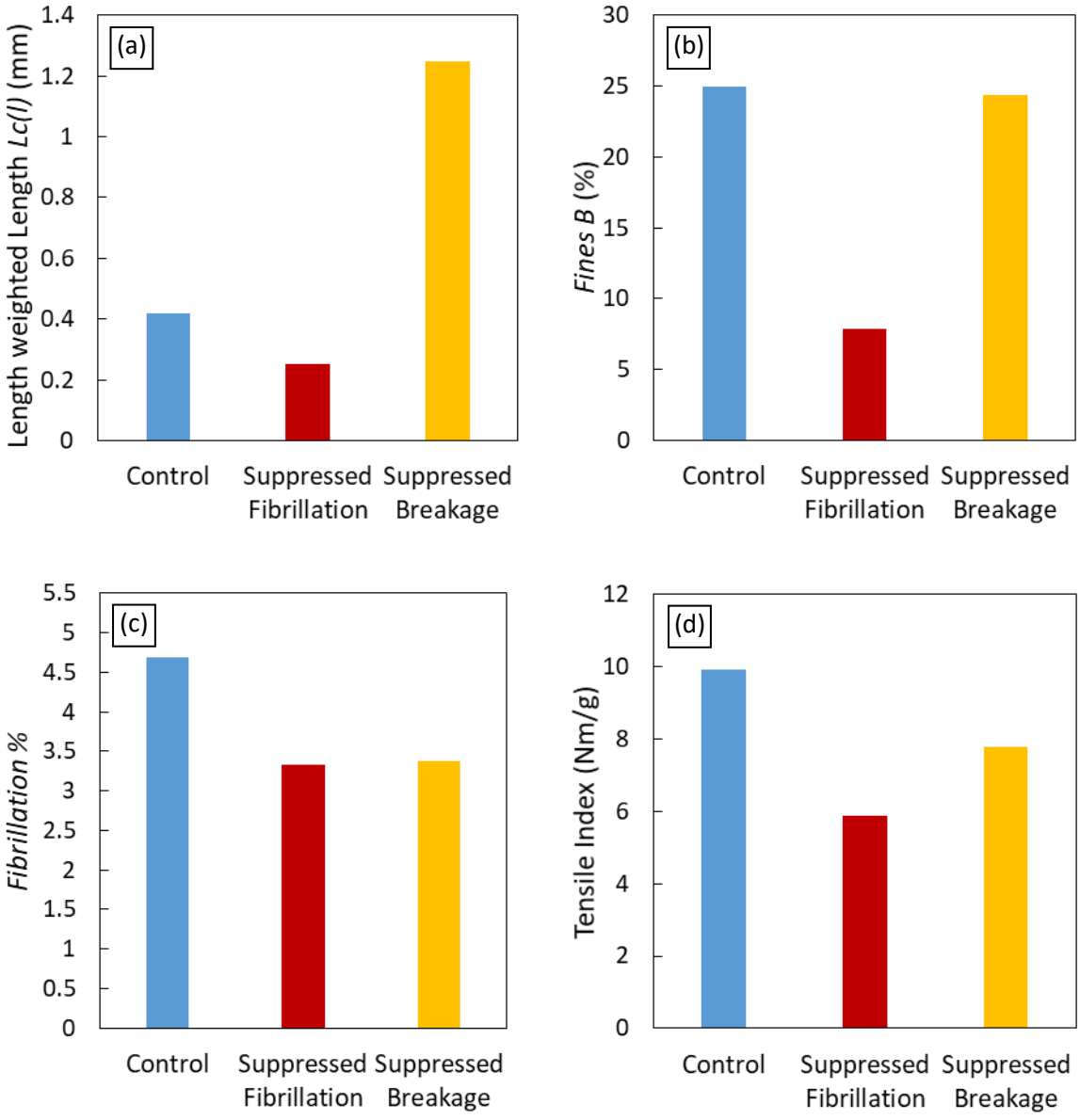

Figure 4.16 *– (a) MFC fibre length, (b) Fines B, (c) Fibrillation %, and (d) tensile index at 3000 kWh/t, of a sample where fibrillation has been suppressed (hygroscopic salt addition), and where fibril breakage has been suppressed (nylon media), versus a control.*

4.3.3. DIC Images

Figure 4.17 shows the control sample MFC at 3000 kWh/t. It is well-fibrillated, with most of the fibre structure broken up into long, fine fibrils, indicative of a strong MFC.

Figure 4.18 shows the suppressed fibrillation MFC at 3000 kWh/t. Large fragments of fibre cell wall remain, since separation into independent fibrils is clearly difficult. The liberated fibrils are very short, likely because of strong inter-fibril forces increasing the tendency of breakages to pass through fibril cross-sections rather than pass round them to exploit pre-existing flaws. The lower *Fines B*, *Fibrillation %*, and tensile index are obvious from this image. To compare with Figure 4.2, the grinder was briefly stopped at 500 kWh/t, to extract a small sample for microscopy; this is shown as Figure 4.19; here, the brittle fracture of these fibres is very obvious, with fibrillation at breakage sites greatly suppressed.

The suppressed breakage sample showed high inhomogeneity, so two images are displayed here; one showing relatively intact fibre structures (Figure 4.20) and the other showing many liberated fibrils (Figure 4.21). Figure 4.20 shows extreme internal fibrillation within relatively intact fibres, whereas Figure 4.21 shows extremely long liberated fibrils, providing strong evidence that low media elasticity inhibits fibril breakage. These long fibrils explain the high *Fines B* value despite most of the original fibre remaining intact. However, because the liberated fibrils are difficult to damage, Figure 4.20 and 4.21 appear deficient at the finest scales of fibrillation seen in Figure 4.17.

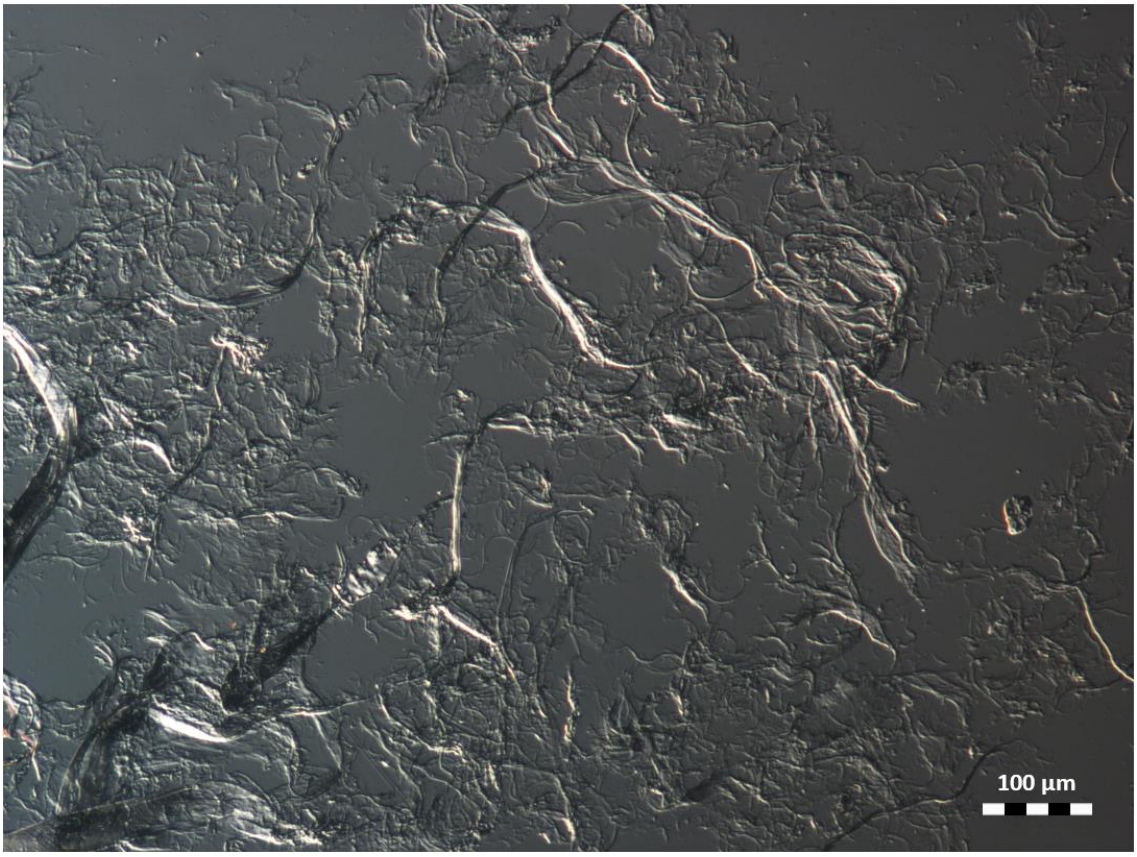

Figure 4.17 *– DIC microscopy image of the MFC control ground to 3000 kWh/t with Mullite B media.*

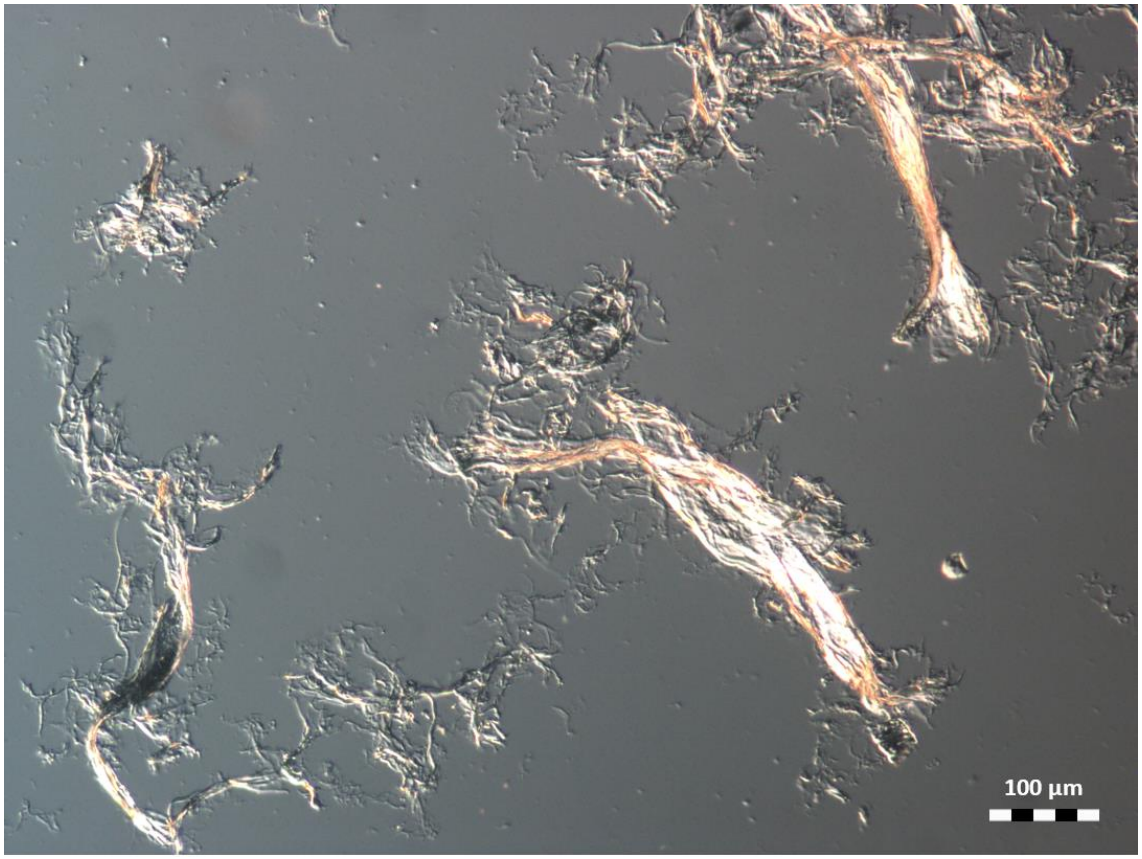

Figure 4.18 *– DIC microscopy image of MFC ground to 3000 kWh/t in a hygroscopic LiCl solution.*

Figure 4.19 *– DIC microscopy image of MFC ground to 500 kWh/t in a hygroscopic LiCl solution.*

Figure 4.20 *– DIC microscopy image of MFC ground to 3000 kWh/t with nylon media, with partially intact fibres.*

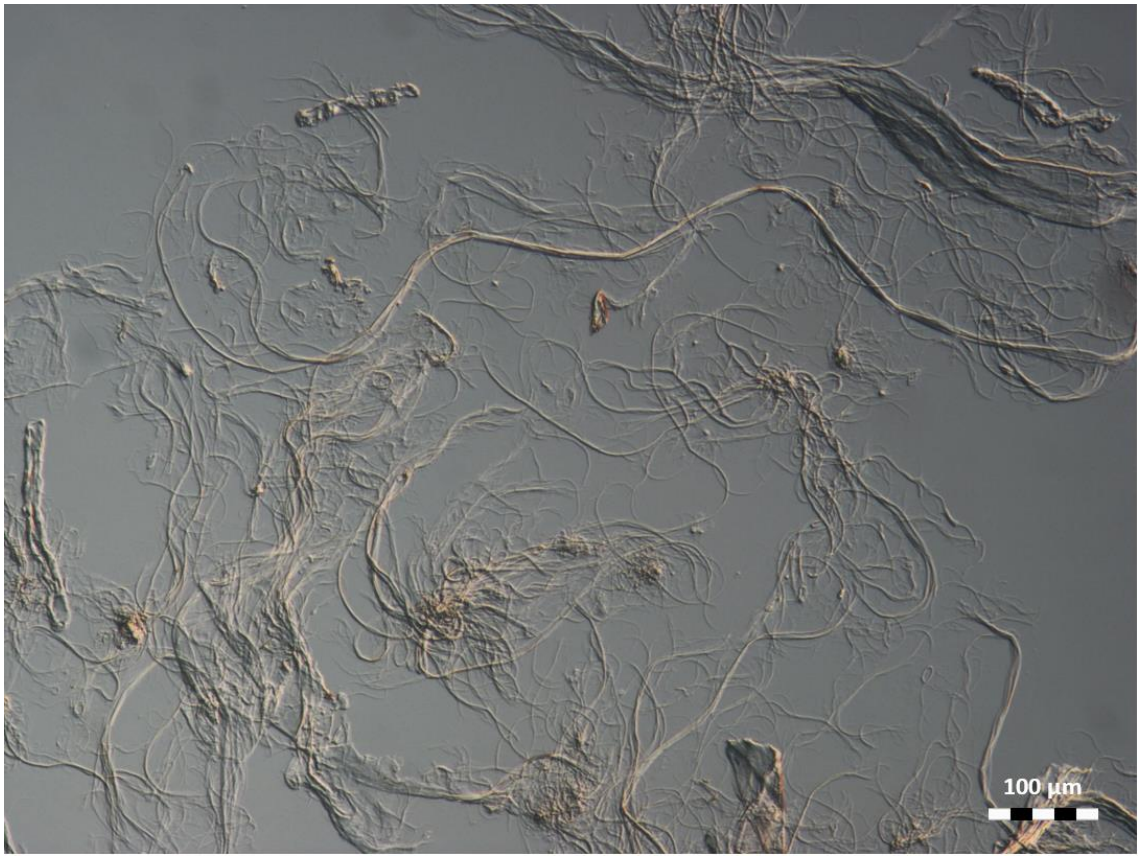

Figure 4.21 *– DIC microscopy image of MFC ground to 3000 kWh/t with nylon media, showing free fibrils.*

4.3.4. Conclusions

The fibre analyser results and microscopy images show that adding hygroscopic salts to suppress fibrillation, and using low elasticity media to suppress fibril breakage, was successful. The striking differences in MFC geometry observed with microscopy is quantified with fibre analyser parameters, and their influence on tensile strength is not surprising. The MFC produced with nylon grinding media is expected to give a high tensile strength at very high energy input once the fibres are fully disintegrated, since liberated fibrils remain relatively undamaged, but this is impractical industrially due to extreme difficulty in separating the product from the media. There is no reason why one would add lithium chloride or else suppress fibrillation industrially.

These examples, however, highlight the influence that the fibril breakage and fibrillation mechanisms have on product properties, and shows that they are controllable by tailoring feed properties and the stresses applied. These results also demonstrate that particle size alone is a poor measure of product quality, since some processes affect MFC length and fibrillation separately. More practical routes to tailor operating conditions, and their effect on fibrillation and breakage processes, are discussed in the following sections.

4.4. Influence of Impeller Speed on MFC Properties

4.4.1. Introduction

Equation 2.3 in Section 2.7 shows that stress energy (and stress intensity) is proportional to the impeller tip speed squared, and so impeller speed should strongly influence grinding performance. It is also the simplest parameter to vary industrially. The energy sweep in Section 4.1 was carried out at an impeller speed of 800 rpm (5.45 m/s tip speed). In this section, it is compared with energy sweeps where impeller speed was 400 rpm (2.72 m/s tip speed) and 1200 rpm (8.17 m/s tip speed), at otherwise identical grinding conditions.

4.4.2. Fibre Analyser Results

Fibre Length

Figure 4.22 shows the effect of energy input on *Lc(l)* for each series. The initial length reduction rate is much slower for the 400 rpm series than the 800 rpm series, whereas the 1200 rpm series is substantially quicker, though at higher energy inputs, these curves converge. Figure 4.23 plots the *Lc(l)*-based Operating Rittinger Index ($K_{R,Op}$) versus fibre length, demonstrating that at coarser sizes, a higher impeller speed is more effective, with the trend reversing at finer sizes.

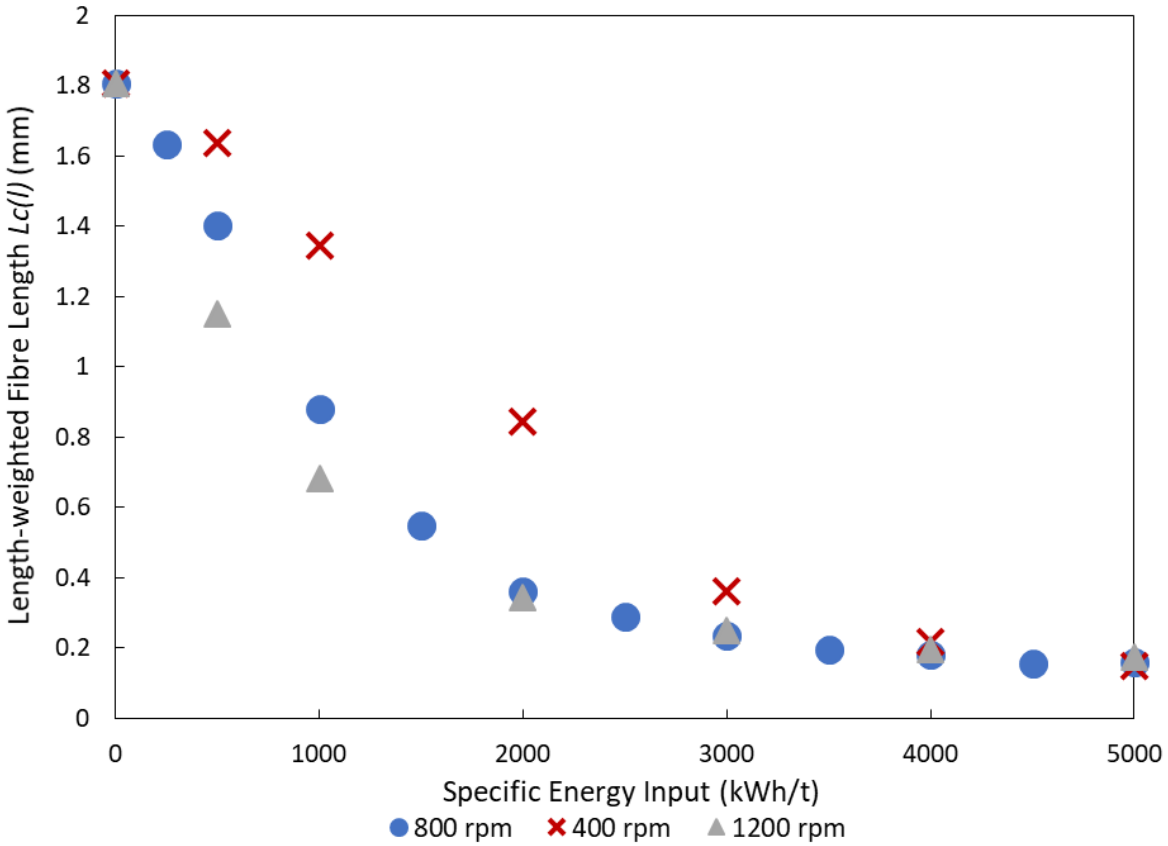

Figure 4.22 – MFC Lc(l) versus energy input for three impeller speeds.

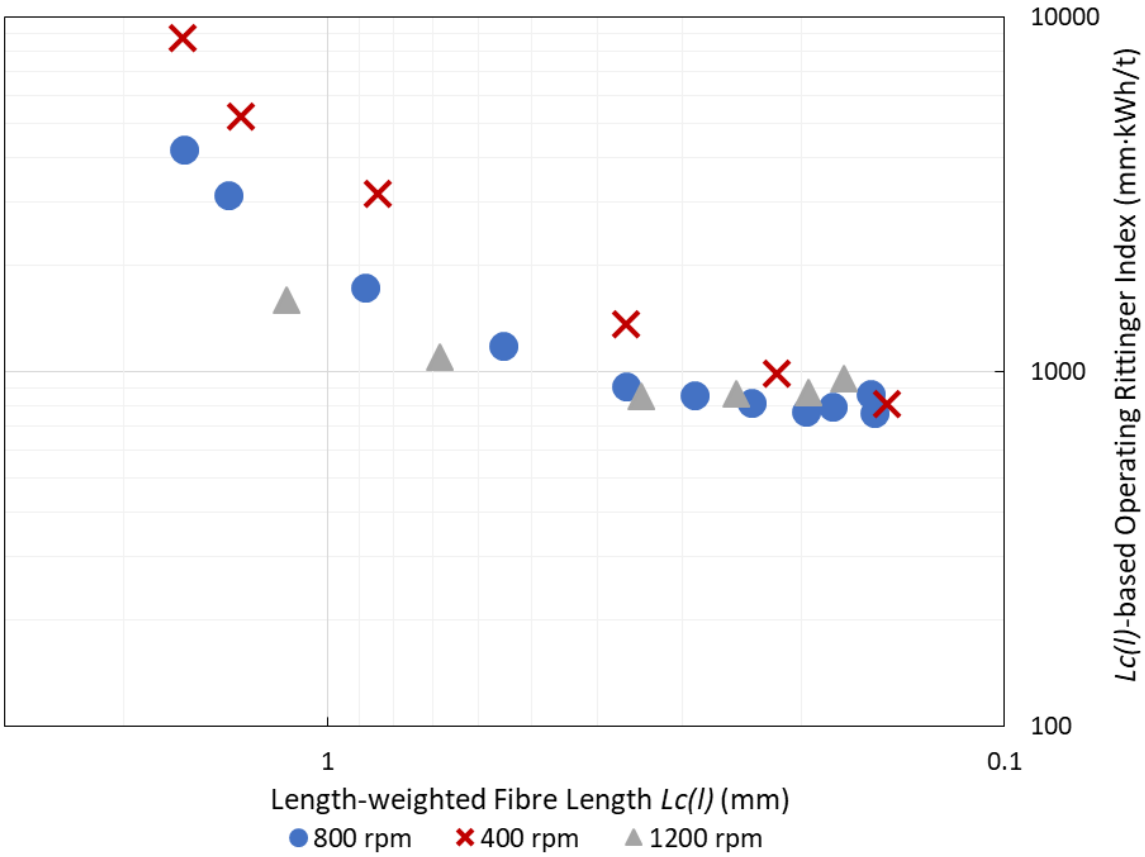

Figure 4.23 – *Lc(l)-based $K_{R,Op}$ versus MFC Lc(l) for three impeller speeds.*

Since larger particles have more cross-sectional area to break, a higher stress intensity is required; consequently, for larger particles, the 1200 rpm series is the most efficient at breakage, whereas the 400 rpm series is much slower, with around double the $K_{R,Op}$ values. Despite this, all media have similar $K_{R,Op}$ values at fine sizes, so lower impeller speeds must be markedly better at fine particle size reduction to compensate. To minimise particle size, a form of 'cascade grinding' where high impeller speeds break large fibres, before impeller speed is decreased for effective fine particle disintegration, would maximise fibre breakage efficiency.

Fines B

Figure 4.24 shows how *Fines B* content varies with energy input and Figure 4.25 plots *Fines B* against MFC length to accommodate differences in breakage rate. The 800 rpm series gives the highest *Fines B* generation at all energy inputs, whereas the 1200 rpm series is consistently lower, and the 400 rpm series initially matches the 800 rpm series, but plateaus much earlier.

As Section 4.1 showed, *Fines B* generation is a second-order effect, which does not require high intensities like cross-sectional breakage does. At 1200 rpm, the high impeller speed efficiently breaks fibres, but the high stress intensity results in a low stress number (see Section 2.7), meaning fewer low intensity stress events to exploit these breakages, peel apart fibrils, and liberate them, resulting in low *Fines B* generation at a given MFC length.

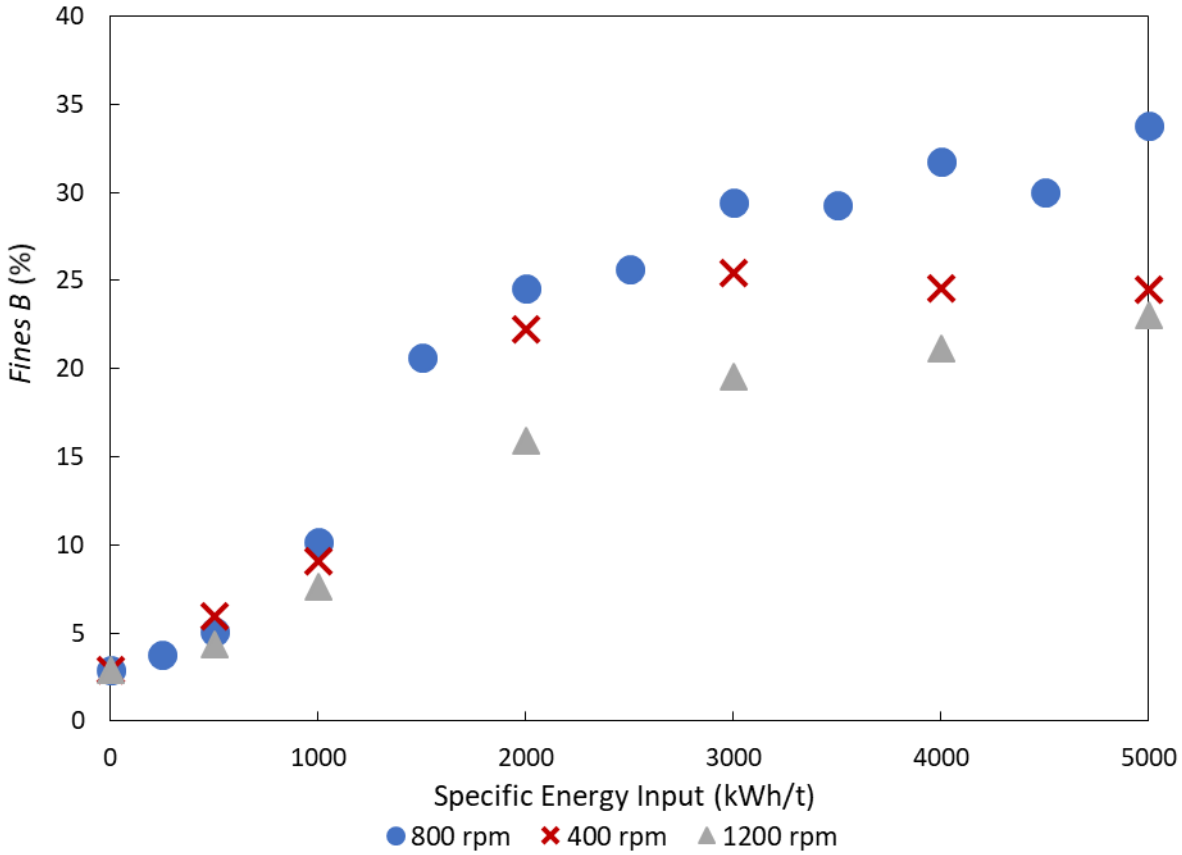

Figure 4.24 *– Fines B content versus energy input for three impeller speeds.*

Figure 4.25 shows that at 400 rpm, *Fines B* generation is markedly superior at coarse particle sizes; since a lower impeller speed leads to a high number of low intensity stress events, any given fibre break is exploited effectively. This does not correspond to a higher total *Fines B* content than the 800 rpm series due to the lower fibre breakage rate. Above 3000 kWh/t, *Fines B* content stops increasing for the 400 rpm series, so *Fines B* particle degradation balances their generation. One might think that the high number of low intensity stress events would degrade liberated fibrils better, but fine media grinds in Section 4.5 show the opposite effect; this may instead be due to poor media suspension damaging liberated fibrils.

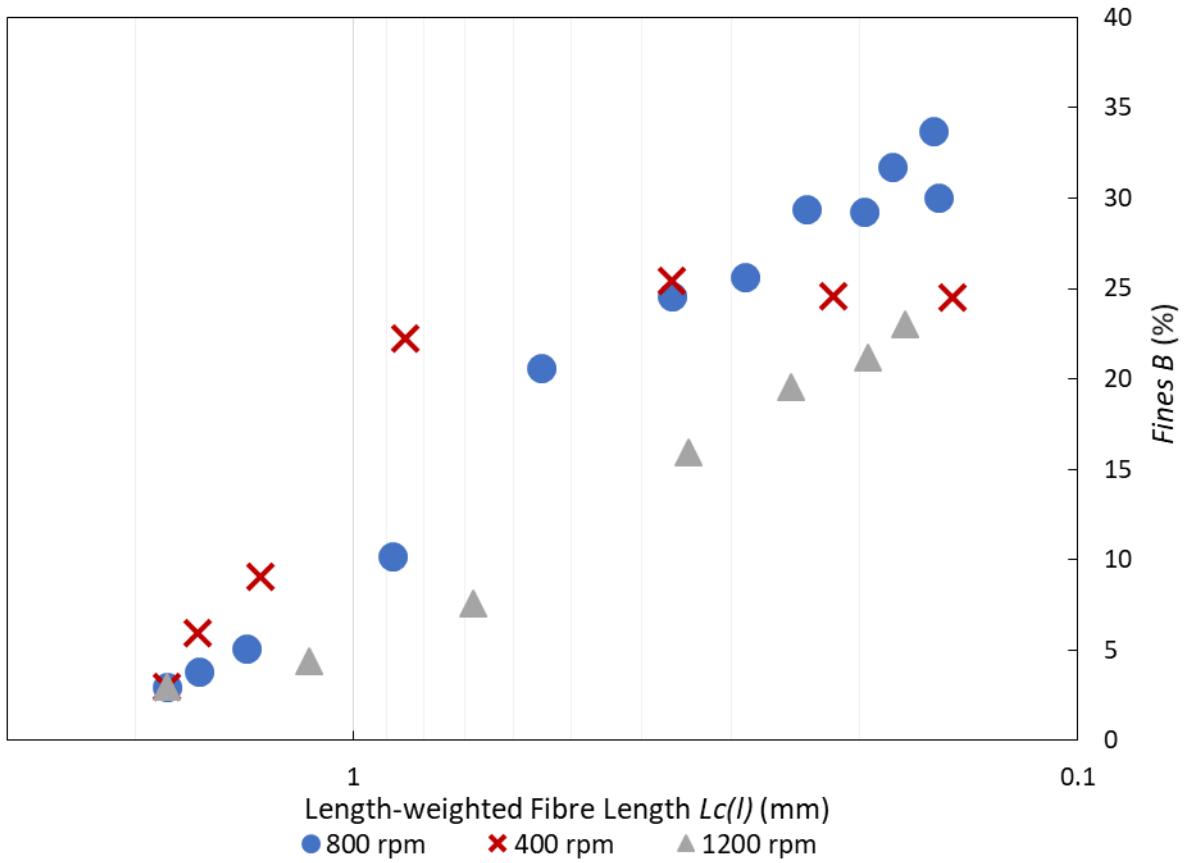

Figure 4.25 *– Fines B content versus Lc(l) for three impeller speeds.*

Fibrillation %

Figure 4.26 shows how external fibrillation changes with energy input for each impeller speed. All reach similar peak values, though the 800 rpm series reaches it sooner, so is expected to have a lower optimum energy input for tensile strength. Whereas the 400 rpm series matched the 800 rpm series with *Fines B* generation, it gives much lower values of *Fibrillation %*; this is probably because of the high number of low energy stress events, breaking off external fibrils into free *Fines B* particles, and the poor generation of external fibrils due to slow fibre breakage. Conversely, the 1200 rpm series has a high *Fibrillation %* value despite low *Fines B* value, since the high fibre breakage rate rapidly generates external fibrils, but there is less time to break them off into free fibrils.

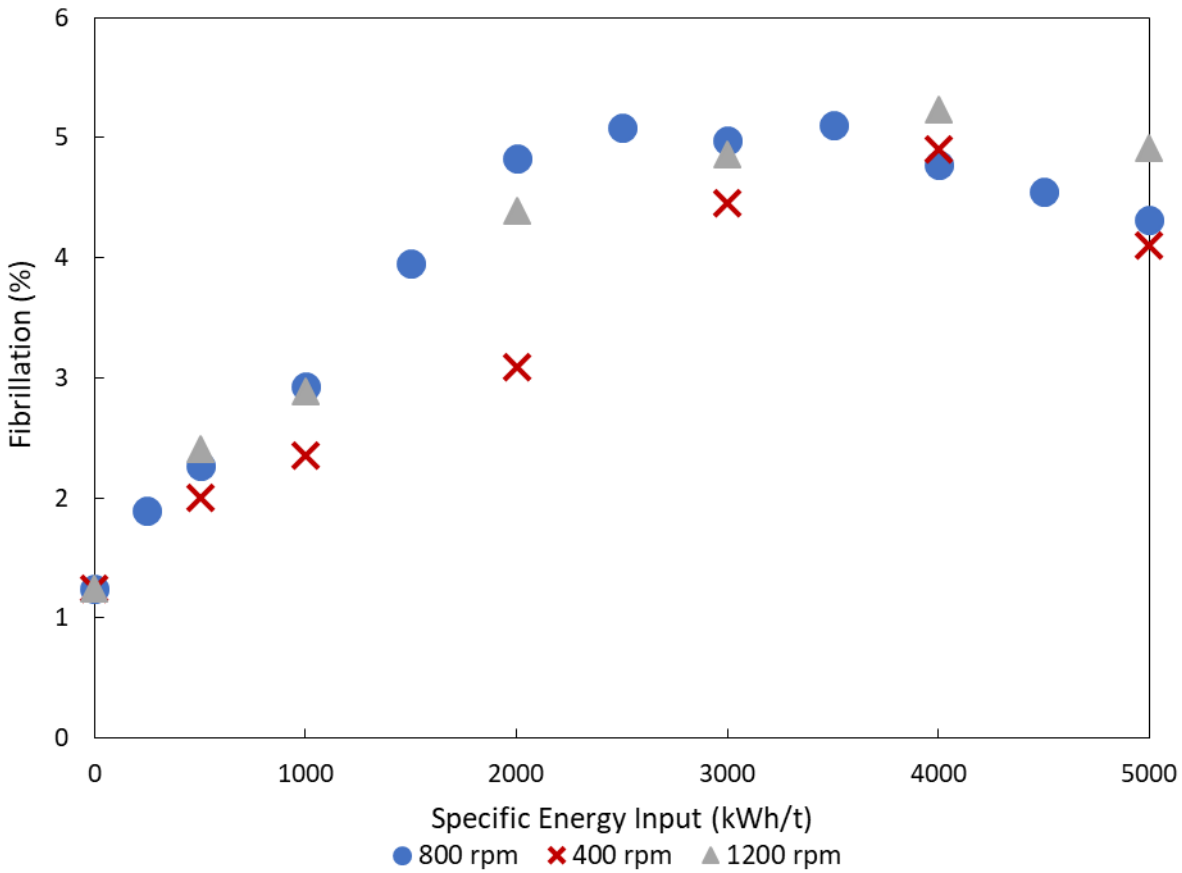

Figure 4.26 *– Fibrillation % versus energy input for three impeller speeds.*

4.4.3. Tensile Index

Figure 4.27 shows the tensile index versus energy input for each impeller speed. As could be expected from the consistently higher *Fines B* and *Fibrillation %* values, the 800 rpm series is the strongest across all energy inputs, especially between 1500 – 3000 kWh/t. The rationale is exactly the same as for *Fines B* generation, with the 800 rpm series having the optimum balance between breaking fibres, generating free fibrils from those breakages, and minimising liberated fibril damage.

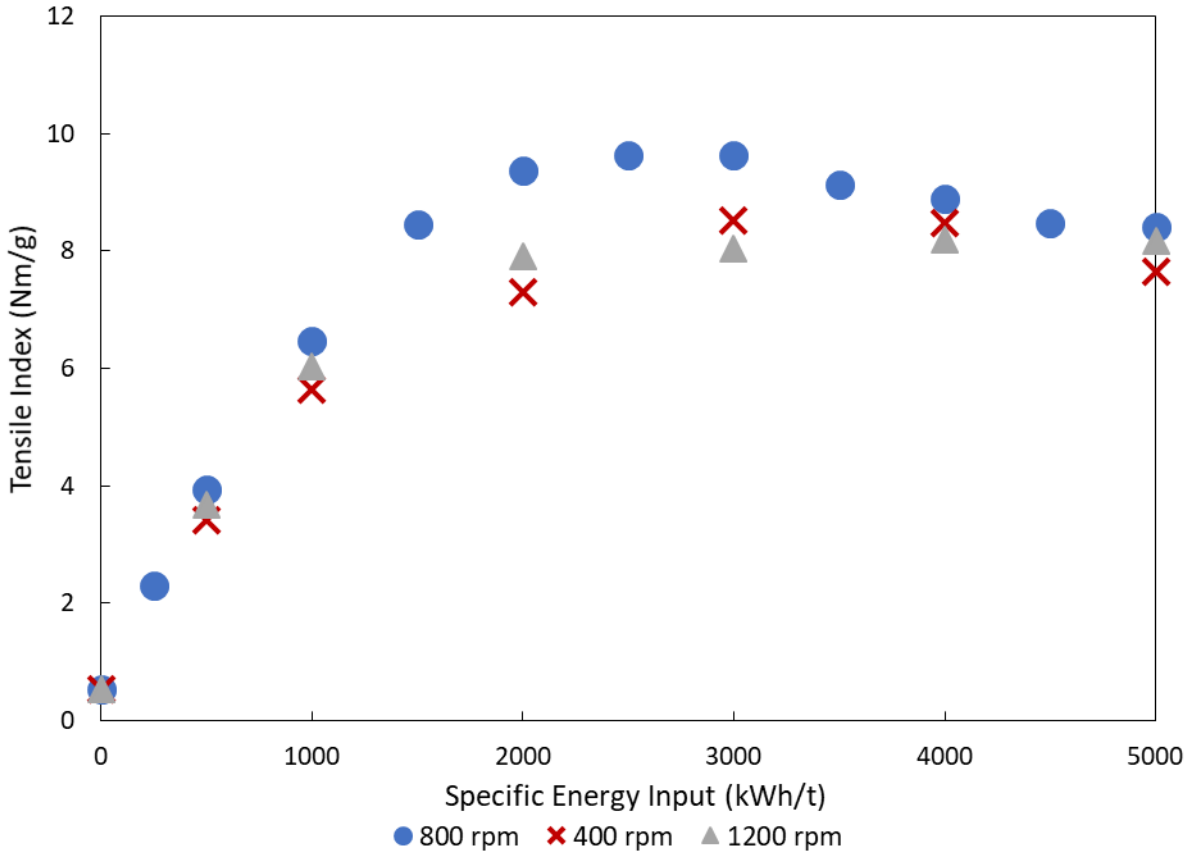

Figure 4.27 *– Tensile index versus energy input for three impeller speeds.*

4.4.4. Conclusions

As expected from stress intensity theory, the optimum impeller speed for size reduction decreases with decreasing particle size. However, length reduction and fibrillation are somewhat independent; although the higher impeller speed easily breaks large fibres, there are too few stress events to exploit these breakages for effective fibrillation, leading to low *Fines B* values and low strength. Conversely, the lower impeller speed effectively fibrillates breakages due to a high stress number, but breakages are much less frequent, so the *total* fibrillation is deficient (for both *Fines B* and *Fibrillation %*), leading to lower strengths. The 800 rpm series gives the optimum balance, maximising the high aspect ratio fines present and

developing more external fibrils earlier, giving the highest strength at the lowest energy input. The next section investigates an alternative method of altering stress intensity; media size.

4.5. Influence of Media Size on MFC Properties

4.5.1. Introduction

During an internal project, *FiberLean* collected worn mullite media (*Mullite A*) from downstream screening processes, and provided two media batches with mean sizes of 2 mm and 1.67 mm (since wear is almost exclusively attrition, this media is still highly spherical). By comparing this with the original 2.9 mm *Mullite A* media, one can assess the influence of media size on product properties. Additionally, a very fine (0.88 mm) *Carbolite* (mullite-based) media was obtained, and was expected to cause severe under-grinding. Larger media than 2.9 mm was avoided because of concerns regarding choking the narrow gap between the impeller and grinder wall. Grinds were carried out with each media under the same conditions as Section 4.1, at energy inputs of 1500, 3000, and 4500 kWh/t.

4.5.2. Fibre Analyser Results

Fibre Length

Figure 4.28 shows the variation in fibre length with energy input. As expected, finer media results in a slower length decay rate as fewer collisions have sufficient momentum to break fibre cross-sections. This is extreme for the 0.88 mm Carbolite series. Stress intensity theory implies that finer media would be more effective at grinding finer particles, so with sufficiently fine media one would expect a bimodal product distribution to develop, with the finer feed particles being ground preferentially. This is obvious from a plot of *Lc(l)* versus *Lc(n)* (Figure 4.29), showing that at long lengths, finer media disproportionately decreases the *Lc(n)* value compared to *Lc(l)* (indicating finer particles are being disproportionately broken).

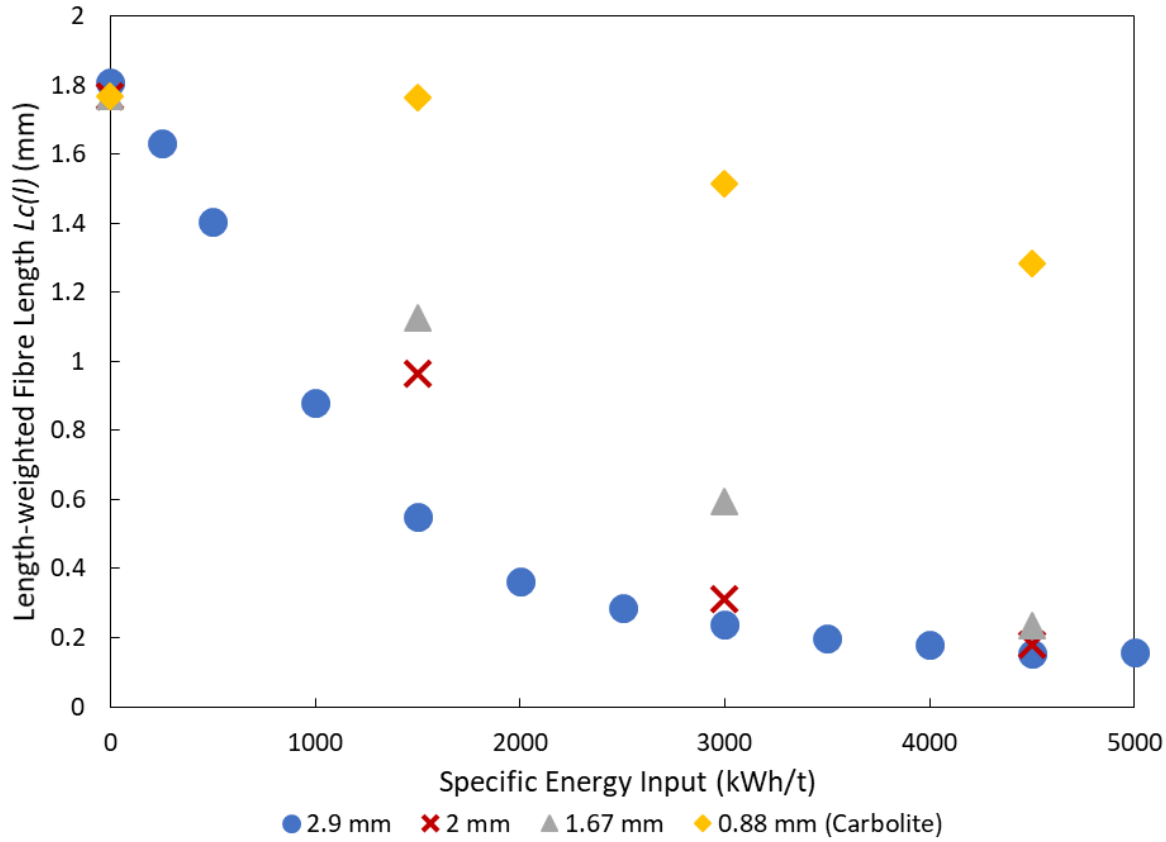

Figure 4.28 *– MFC Lc(l) versus energy input for each media size.*

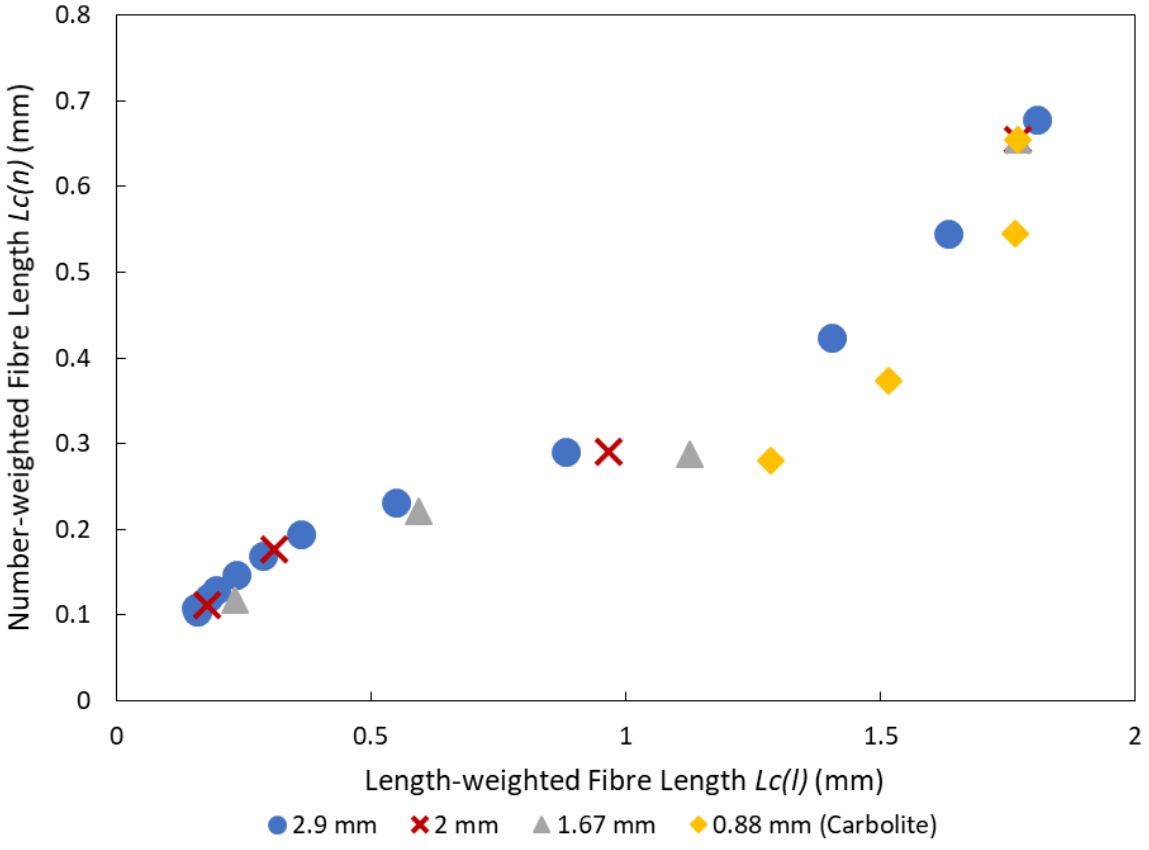

Figure 4.29 *– Lc(n) versus Lc(l) for each media size.*

Fines B

Figure 4.30 shows the *Fines B* content versus energy input for each series. At 1500 kWh/t, the coarser media has a better *Fines B* generation, because of the higher fibre breakage rate, but at higher energy inputs, the 1.67 mm and 2 mm media have higher values. The *Fines B* generation of the 0.88 mm media is poor regardless of energy, since it is incompetent at breaking fibre cross-sections. Figure 4.31 shows that finer media gives higher *Fines B* values at given fibre lengths, likely because of the higher number of lower intensity stress events to exploit any breakages (as with low impeller speed).

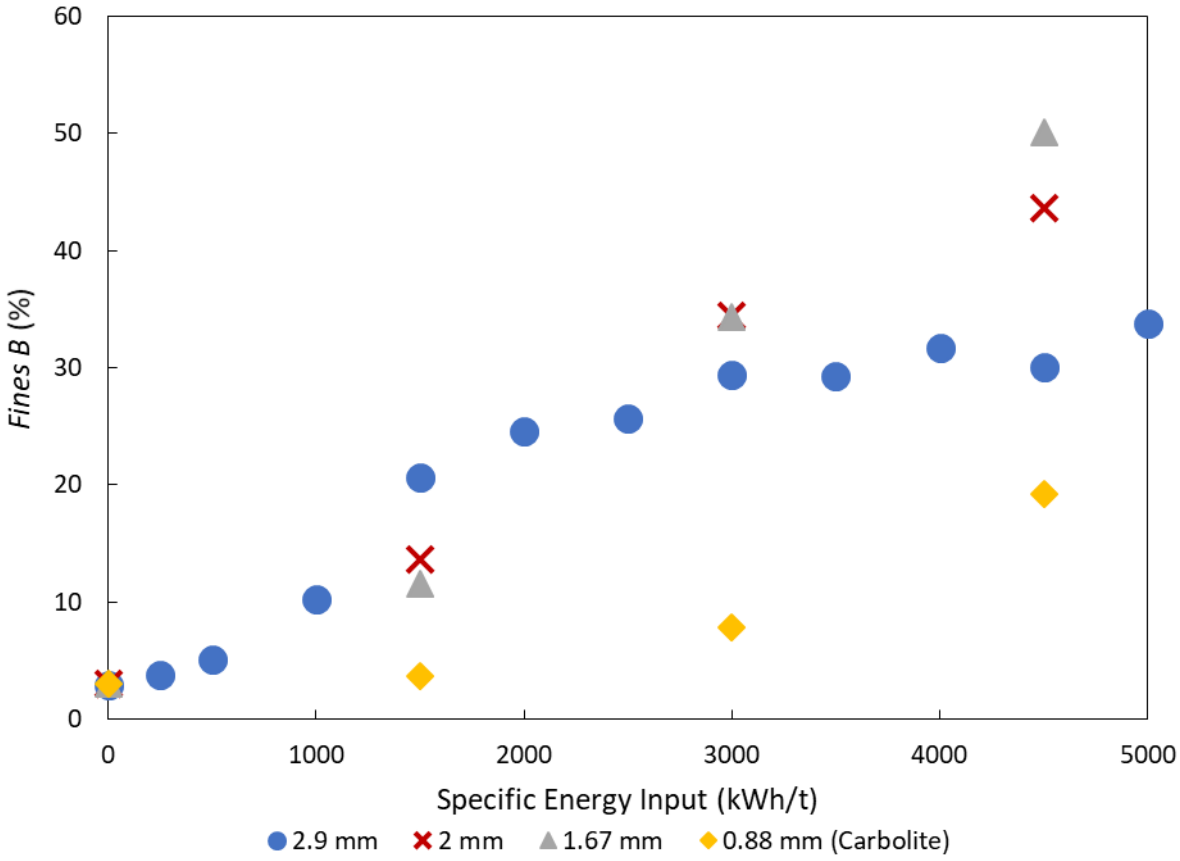

Figure 4.30 *– Fines B content versus energy input for each media size.*

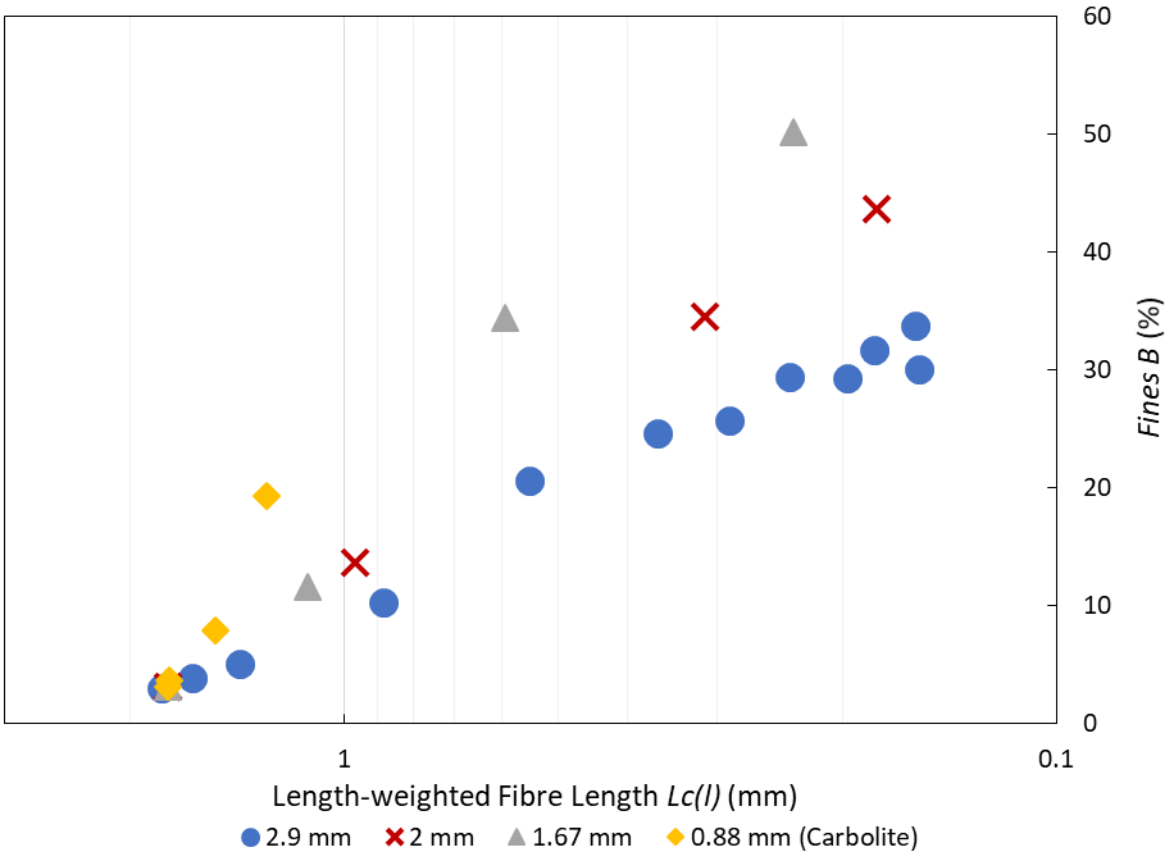

Figure 4.31 *– Fines B content versus MFC length for each media size.*

Fibrillation %

Figure 4.32 shows that, as expected, the finer media peaks in fibrillation at higher energy inputs than the larger media, and the 1.67 mm and 2 mm series apparently having a higher peak value. Fibrillation remains poor for the 0.88 mm series regardless of energy input.

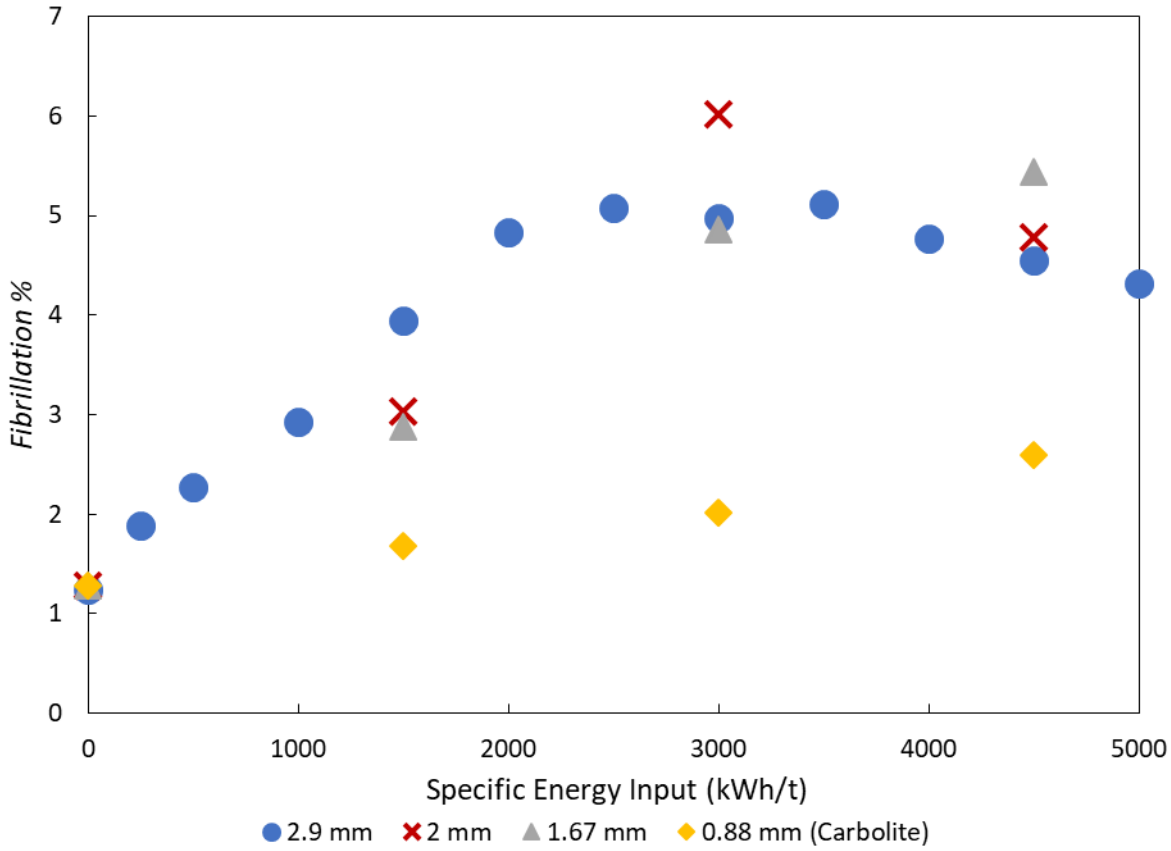

Figure 4.32 *– External fibrillation versus energy input for each media size.*

4.5.3. Tensile Index

Figure 4.33 shows how the tensile index is affected by energy input for each media size. All series reach similar peak strength values (9 – 10 Nm/g), although the strength for the 0.88 mm series is clearly still increasing. Although the resolution is not sufficient to be certain, the 1.67 mm and 2 mm series appear to have a higher optimum energy input than the 2.9 mm series. The 1.67 and 2 mm series having a similar peak strength to the 2.9 mm series is unexpected, considering that *Fibrillation %*, *Fines B*, and MFC length are all higher for the fine media; although the fine media is excellent at fibrillation where breakages have occurred, in this case the high MFC length indicates that a large fraction of the fibre is not fully disintegrated. By the time these fibres are fully disintegrated (i.e. at 4500 kWh/t), the fibrils already liberated have been sufficiently damaged to cancel out any further strength improvement from this. It is

interesting that finer media performs better than lower impeller speeds with coarse media here, and this is discussed later in Section 6.2.

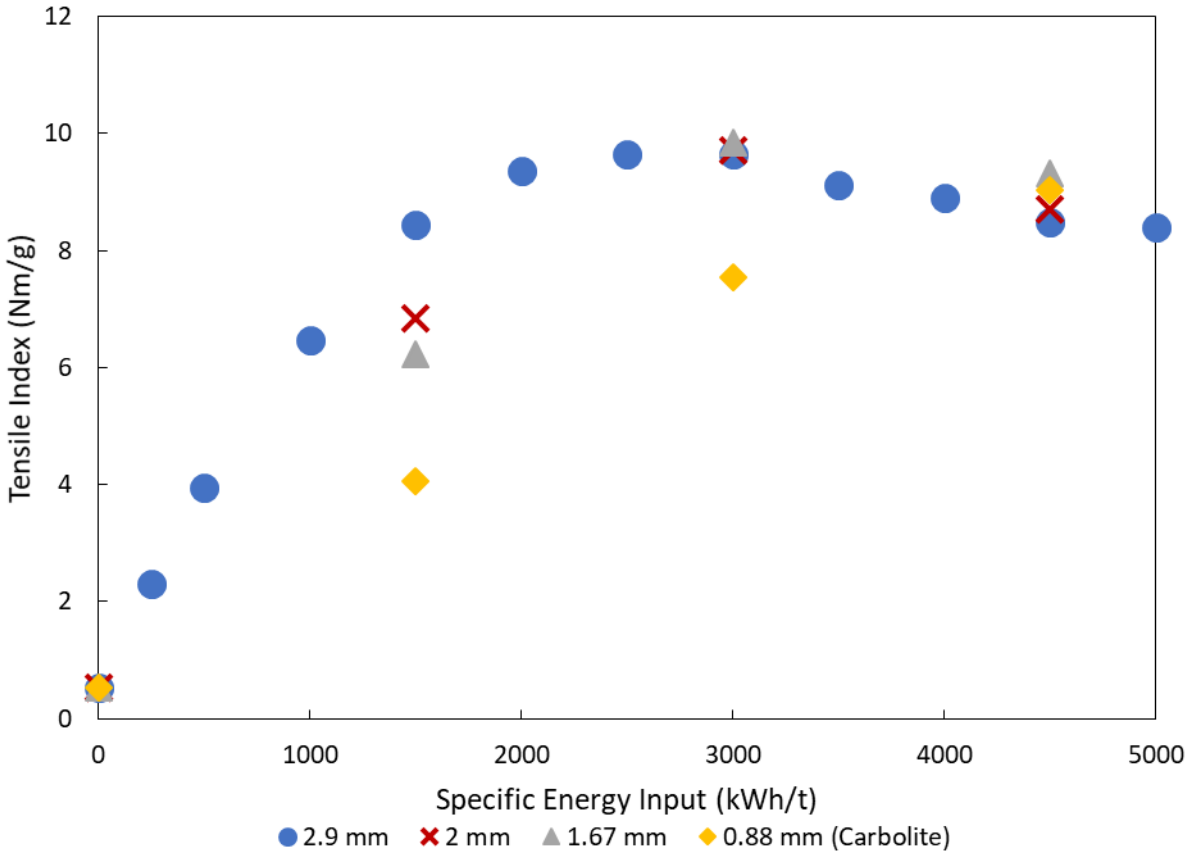

Figure 4.33 *– Tensile index versus energy input for each media size.*

4.5.4. Conclusions

Moderately reducing the media size slows fibre breakage, although fibrillation is more effective when normalised by length. This leads to similar peak tensile strengths as when coarse media is used, but at higher energy inputs. Very fine media has poor fibre breakage and fibrillation, but can eventually give a high tensile strength regardless, because these long, fibrillated fibres can form extensive networks. As with the previous section, the general principle is that more intense collisions aid fibre break-up, but provide fewer opportunities for fibrillation and strength development; cascade grinding would make sense here, using a large

media to break fibres, and later discharge into a second grinder with fine media to effectively fibrillate at the breakages.

4.6. Influence of Media Density on MFC Properties

Media density is the other parameter which determines stress intensity, and is only controllable by changing media composition. The series from Section 4.1 is compared with an energy sweep with the higher density *Zirconia D* media of the same media size, with a density of 6 g/cm^3 compared to the 2.7 g/cm^3 for mullite. More series were planned, but these experiments uncovered a serious complication, showing that the media density factor cannot be isolated here. The full results from these experiments are shown later in Section 5.3 once this is properly clarified.

Figure 4.34 is a plot of fibre length versus energy input, showing a much slower fibre breakage rate for the denser media, which is contrary to expectations since the other high stress intensity series (1200 rpm impeller speed) was much more efficient at low energy inputs. Clearly, unseen factors are involved.

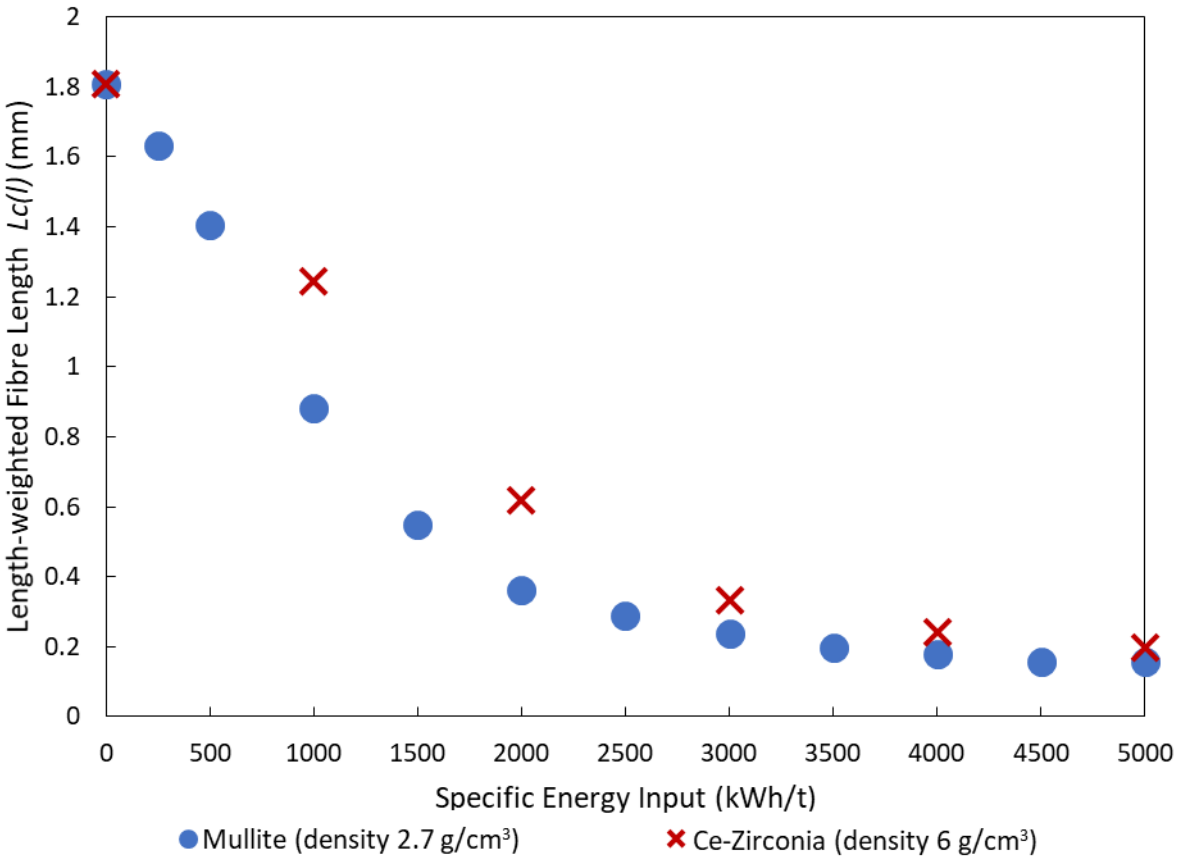

Figure 4.34 *– MFC fibre length versus energy input for two media densities.*

Fines B, *Fibrillation %*, and tensile strength results also showed much stronger differences than one expects from the modest difference in stress intensity (these data are shown later in Figure 5.24, Figure 5.26, and Figure 5.28). Another hint at additional factors is that the *Zirconia D* used had a substantially higher efficiency than the *Zirconia A* media that FiberLean uses industrially, despite similar stress intensities; the only noticeable difference was that *Zirconia D* had a lower surface gloss, and the mullite media had a far lower gloss. A lower gloss indicates a higher surface roughness, so this was identified as the hidden parameter causing the unexpected results; here, the lower gloss media gave more efficient grinding, as is also implied by previously published work detailed in Section 2.9. Surface roughness is therefore thoroughly investigated in Chapter 5.

4.7. Summary

Section 4.1 shows the evolution of fibre length, external fibrillation, high aspect ratio fines generation, and tensile strength under typical grinding conditions. From microscopy images, the mechanisms taking place can be identified; media collisions locally compress the fibre, which can completely or partially break, also often delaminating fibrils at the impact sites. Other lower-intensity processes cause increased separation of the exposed fibrils at these breakage points, forming first external fibrillation, and then free high aspect ratio fine particles.

Applying Hertzian contact mechanics to a semi-infinite cellulose surface in Section 4.2 predicts Hertzian contact pressures experienced by the cell wall and microfibrils, and predicts impact site diameters close to those observed in microscopy. It is predicted that efficient grinding occurs at operating conditions that give calculated indentation depths similar to cell wall thicknesses.

The peak tensile strength and associated optimum energy input is a function of the relative propensities of the fibrillation and fibril breakage processes. Section 4.3 demonstrates extreme cases where fibrillation is suppressed with hygroscopic salt addition, and fibril breakage is suppressed by using low elasticity nylon media. These examples demonstrate that weak inter-fibril forces facilitate fibrillation, and imply that fibril cross-sectional strengths should be sufficiently weak to permit fibre breakage, but strong enough to resist degradation once liberated.

Three methods of controlling grinding intensity are then demonstrated; changing impeller speed, media size, and media density. Lowering the stress intensity by decreasing media size or impeller speed reduces fibre breakage rate, but fibrillation is higher per breakage site due

to the higher number of stress events; however, this leads to poorer efficiency overall. Conversely, higher impeller speeds are very effective at breaking fibres, but with excessive stress intensity, the stress number is too low for effective fibrillation, so strength is relatively poor. Improving the relative propensity of fibrillation compared to fibre breakage at lower stress intensities is similar to what is observed with platy mineral particles; in stirred media milling of kaolin[105], graphite[106], and boron nitride[107], it has been found that a lower stress intensity enhances platelet delamination whilst reducing platelet breakage.

The effect of media density is inconclusive due to interference from roughness differences between media species. Clearly, the influence of surface roughness must be characterised for a complete understanding of the relationship between grinding conditions and product attributes; this is investigated in the following chapter.

5. THE INFLUENCE OF MEDIA SURFACE ROUGHNESS AND MINERAL CONTENT ON MFC PRODUCTION

5.1. Introduction

5.1.1. Scope of Work

This chapter focuses on understanding what are later termed *pressure-concentrating factors*, namely the influence that media surface roughness and mineral content have on grinding performance and MFC properties. As discussed in Chapter 2, media surface roughness was suspected to affect cellulose grinding, and the unusual results in Section 4.6 also implies this. Additionally, *FiberLean* has long asserted that the mineral content increases MFC grinding efficiency, which is supported by work by both Riley[73] and Pinkney[84]. However, the author considered its influence worth investigating again, using the novel characterisation techniques in this work, and to compare its influence with that of media roughness.

This chapter is divided as follows: the rest of this section comments on the media surface roughness measurements and SEM images of media cross-sections. Section 5.2 investigates media with a very broad range of roughness values, most of which were artificially roughened with an abrasive, and compares the MFC produced at two energy inputs. Section 5.3 details energy sweeps with four media species with different surface roughnesses to identify efficiency changes, and also compares the grinds with and without mineral addition to see if the effect of mineral particles is analogous to roughness. Section 5.4 focuses on the mineral particles, showing a trial using a coarser mineral, and another experiment where POP is varied across a wide range. Section 5.5 explores the results of a microscopy assay of low energy MFC produced by media of two different roughnesses, visually demonstrating the asserted

mechanism for the influence of roughness. Finally, Section 5.6 adapts the fibre-based Hertzian contact mechanics theory from Section 4.2 to include media roughness, which can rationalise the experimental results observed.

5.1.2. Media Surface Roughness Measurement Results

The roughness parameters defined in Section 3.16 were determined for each media species using the laser profilometry method described in Section 3.15 and 3.16, and are shown as Table A3.1 in Appendix A3. The abrasive-roughened media usually becomes smoother when used, so the values before and after grinding were measured and the average value used. Laser profilometry intensity maps are provided as Figure A3.1 in Appendix A3 to aid visualisation.

The median arithmetic roughness R_a correlates well with all other roughness parameters investigated (see Figure A3.2 – A3.9 in Appendix A3), except for skewness R_{sk} and kurtosis R_{ku} (see Figure A3.10 – A3.11 in Appendix A3). However, no correlation was noticed between these exceptions and MFC properties, suggesting that they are inconsequential. Therefore, R_a is the characteristic surface roughness parameter to which MFC properties are later correlated.

Peak height distributions follow a Gaussian-like distribution with negative skew and positive excess kurtosis, and peak spacing distributions show a Poisson-like distribution. These plots are shown for *Mullite A* in Figure 5.1 and 5.2, with these distributions representing the cratered surface observed (see Figure A3.1 in Appendix A3).

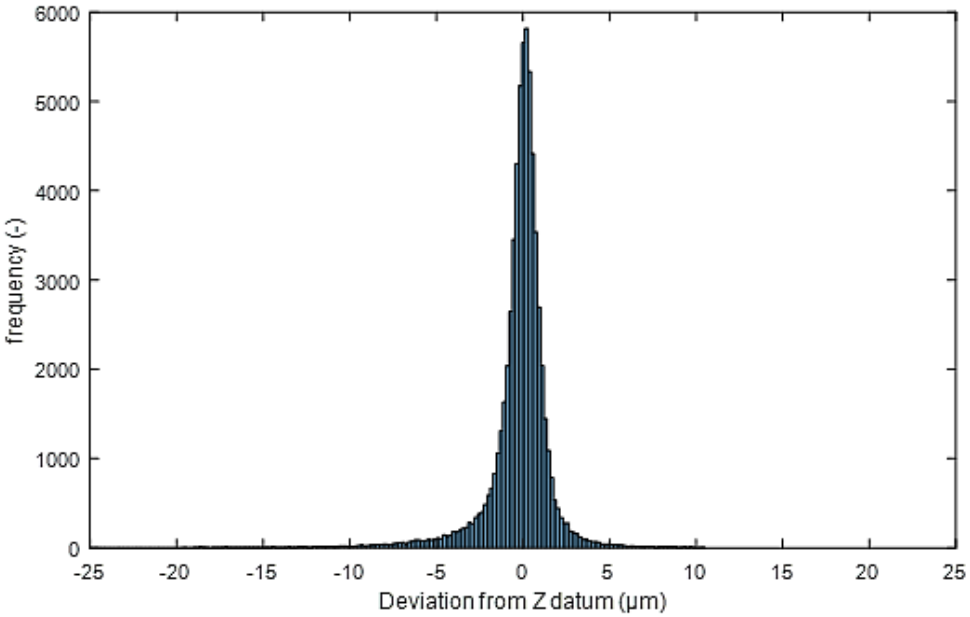

Figure 5.1 *– Peak height and valley depth distribution for a Mullite A sample.*

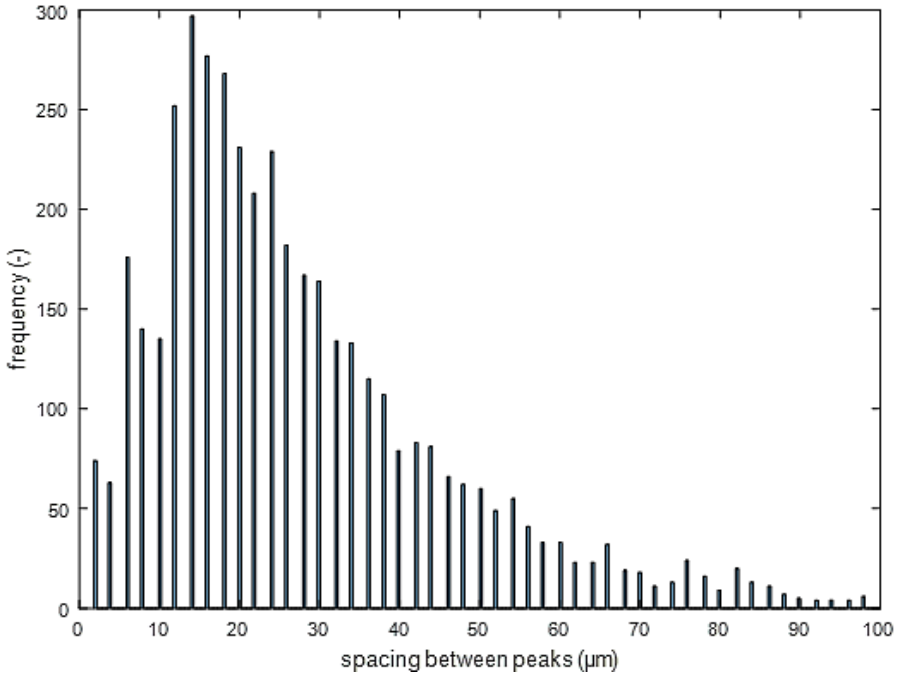

Figure 5.2 *– Peak spacing distribution for a Mullite A sample.*

5.1.3. SEM of Media Cross-Sections

To verify laser profilometry results, selected media were encased in resin and sliced into cross-sections (by *Camborne School of Mines*), then imaged with SEM. Cross-sections are shown as

Figure 5.3 (a) and (b) for *Mullite A* and *Zirconia A,* and Figure 5.4 (a) and (b) for smooth *Glass A* and rough *Glass D*.

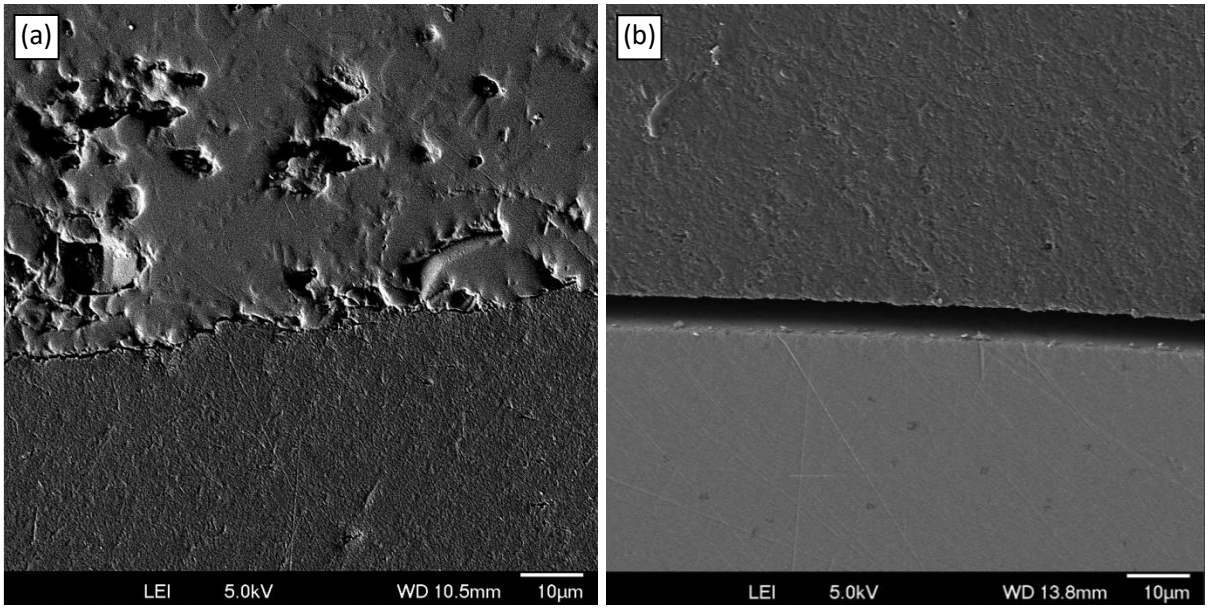

Figure 5.3 *– SEM images of cross-sections of (a) mullite (Mullite A) and (b) zirconia (Zirconia A) grinding media.*

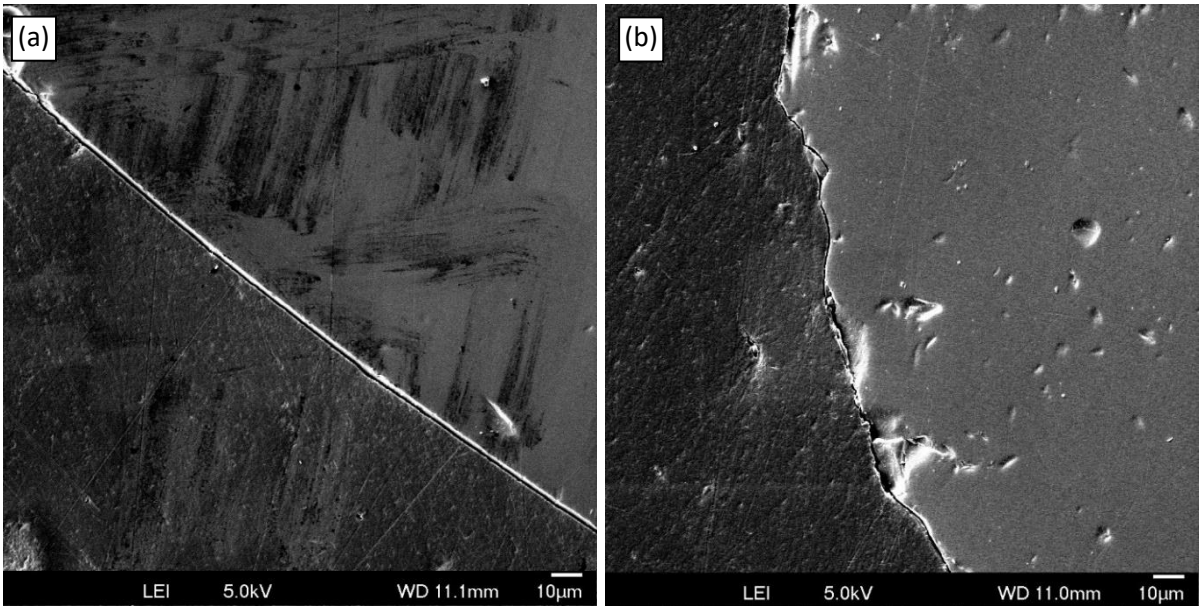

Figure 5.4 *– SEM images of cross-sections of (a) smooth (R_a = 0.12 µm) glass media (Glass A) and (b) rough (R_a = 2.34 µm) glass media (Glass D).*

Grinding media surface roughness is largely a consequence of the media formulation and production process. Most media is made by sintering powder ('granulation'), giving an intrinsic surface roughness related to the powder particle size. Comparing Figure 5.3 (a) and (b) shows

that zirconia media is much smoother than mullite media, which is due to the much finer powder size used to produce the former. Internal X-ray diffraction tests show that 'mullite' media is not pure, instead consisting of crystalline mullite phases embedded within amorphous silica; this is apparent in Figure 5.3 (a), where discrete grains are visible. Differential wear is expected between the two phases, which is suspected to be another reason why mullite media maintains a high 'equilibrium' surface roughness with continual use. In contrast, though zirconia is smooth as produced, extensive use slightly increases roughness from the accumulation of small chips and surface defects (as has happened with *Zirconia E*).

Figure 5.4 (a) and (b) show that abrasive roughening can lead to a very high surface roughness in the case of glass. Both mullite and rough glass cross-sections show peak heights comparable to laser profilometry measurements (R_a = 0.97 µm for *Mullite A* and R_a = 2.34 µm for *Glass D*), verifying that the technique yields realistic measurements.

5.2. Influence of Media Roughness on MFC Properties

5.2.1. Experimental

This investigation characterises the influence on MFC properties of a wide range of media roughnesses for several media densities. This involved all abrasive-roughened media introduced in Section 3.14 (Table 3.3), along with *Mullite A, B*, and *C*, alumina media, *Zirconium Silicate A*, *B,* and *C*, and *Zirconia D*, and *E*, (see Table 3.2 in Section 3.3).

The grinder impeller speed was 800 rpm, and all media were roughly 3 mm in diameter, but when plotting the data, the media are divided into four series based upon density and composition: glass (2.5 g/cm^3), mullite (2.7 g/cm^3), alumina/zirconium silicate (around 4.0 g/cm^3), and zirconia (6.0 g/cm^3).

Target energy inputs were 3000 kWh/t (the optimum for *Mullite A*) and 1000 kWh/t (where MFC properties are more sensitive to efficiency differences), and charge composition was 2.5% fibre solids and 100% POP (the mineral was excluded in case it had a similar effect to roughness). MFC tensile strengths and fibre analyser data were obtained, with some samples imaged with DIC microscopy.

5.2.2. Power Draw

The grinder power draw is shown for the 3000 kWh/t series after 1 minute (Figure 5.5 (a)) and as an average across the grind (Figure 5.5 (b)). As expected, at constant surface roughness, denser media has a higher power draw. Roughness also increases power draw, though eventually with diminishing influence. Industrially, power draw can therefore be used as a proxy to identify differences in surface roughness (given otherwise identical conditions).

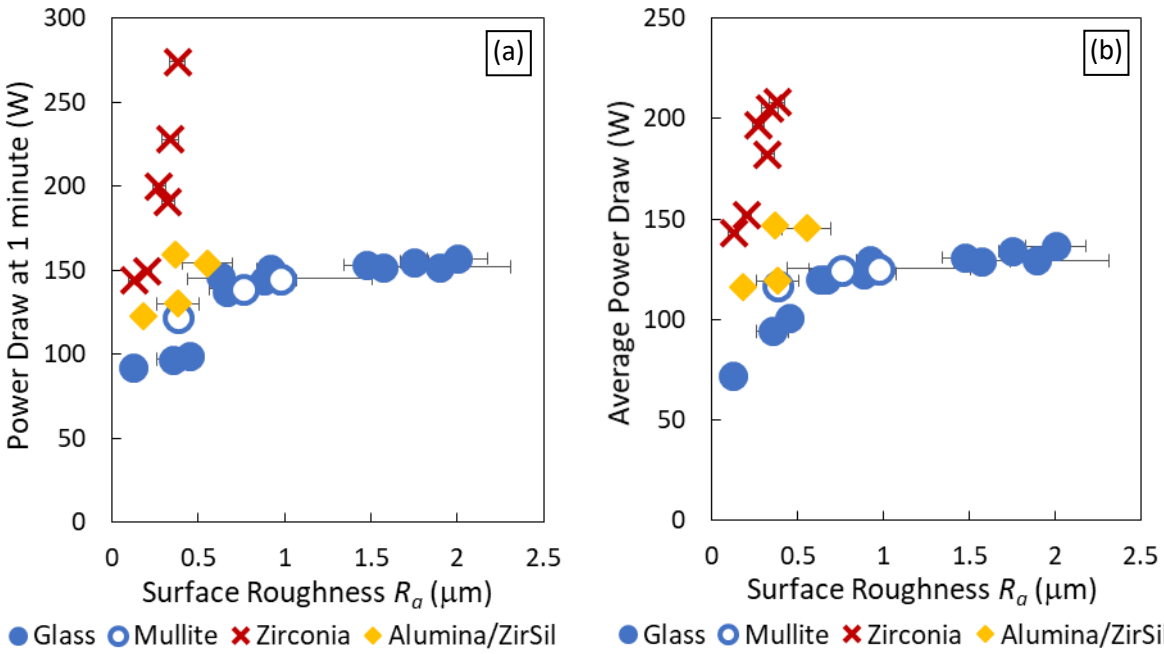

Figure 5.5 *– Power draw for the 3000 kWh/t grind, (a) after 1 minute, (b) average over the entire grind.*

A higher roughness probably increases power draw due to higher friction between beads resisting impeller motion. The work by Skuse[81] also found that rougher media increased

power draw; PEPT data showed higher forces throughout the grinder, *despite similar average velocity distributions*, indicating that roughness imparts additional acceleration out-of-plane from the streamlines.

5.2.3. Media Wear

Figure 5.6 plots media wear at 3000 kWh/t against surface roughness. For glass media, with a broad roughness range, surface roughness clearly correlates with media wear. For higher density media, MOP values are too low for reliable comparison, though zirconia consistently gives lower wear. *Zirconia* E is the exception, with disproportionately high wear (9.5% MOP), likely because of embrittlement from the accumulation of microcracks over extensive use.

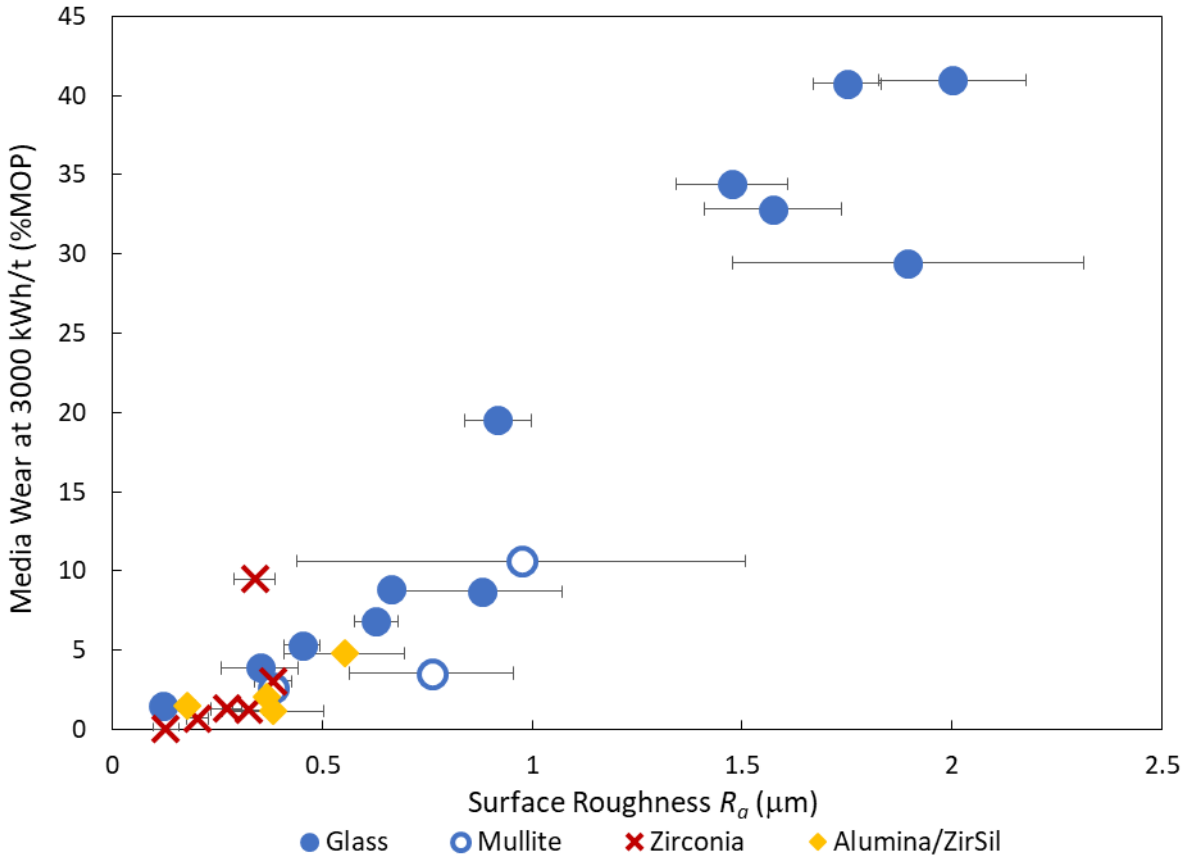

Figure 5.6 – Media wear at 3000 kWh/t (% MOP) versus media roughness for each media composition.

Critically, at very low roughness, media wear approaches zero, implying that wear is dominated by attrition of asperities rather than compressive failure. A small number of broken

beads are seen with glass media, so some compressive failure is possible. This investigation also cannot account for microcrack accumulation over extensive industrial usage which would eventually increase compressive failure probability. However, considering that the smoothest mullite wears similarly to zirconia of a similar roughness, the low wear characteristic of zirconia is probably more because of its smoothness rather than its relative strength.

5.2.4. MFC Fibre Length

Figure 5.7 (a) and (b) shows the MFC length-weighted length for each media species on a linear and a logarithmic scale. Fibre length decays with increasing roughness, fitting a power law relationship (linear on a log-log scale). Controlling for roughness, zirconia media gives finer MFC, probably because the higher stress intensity enhances breakage; this is the result that Section 4.6 was expected to show. Density differences between glass and alumina/zirconium silicate appear insufficient to cause deviations.

The difference between zirconia and glass is extreme at low roughness values. Roughness enhances fibre breakage at any density, so perhaps acts to multiply stress intensity to produce an *effective stress intensity* that better determines breakage. At high surface roughnesses, this effective stress intensity would be around the optimum, where the characteristic stress intensity versus particle size curve (see Figure 2.4) is almost flat, with minor stress intensity variations from density differences having little influence. When effective stress intensities are too low for efficient breakage (low roughness), the system would be located on a steep section of Figure 2.4, so changing density would have a strong effect on particle size. This may explain the divergence between glass and zirconia at low roughnesses.

Regardless of the validity of this *effective stress intensity*, surface roughness strongly influencing particle breakage is a profound conclusion, since this is not observed in minerals

grinding. This likely is due to fibre microstructure; a fibrous particle cross-section can *partially break* under impacts that would merely cause elastic deformation in hard, isotropic mineral particles. These partial breakages leave the region more susceptible to breakage and fibrillation in further stress events. Consequently, roughness asperities concentrating collision pressure into smaller areas may greatly enhance these localised breakages. This hypothesis is supported by microscopy assays in Section 5.4.

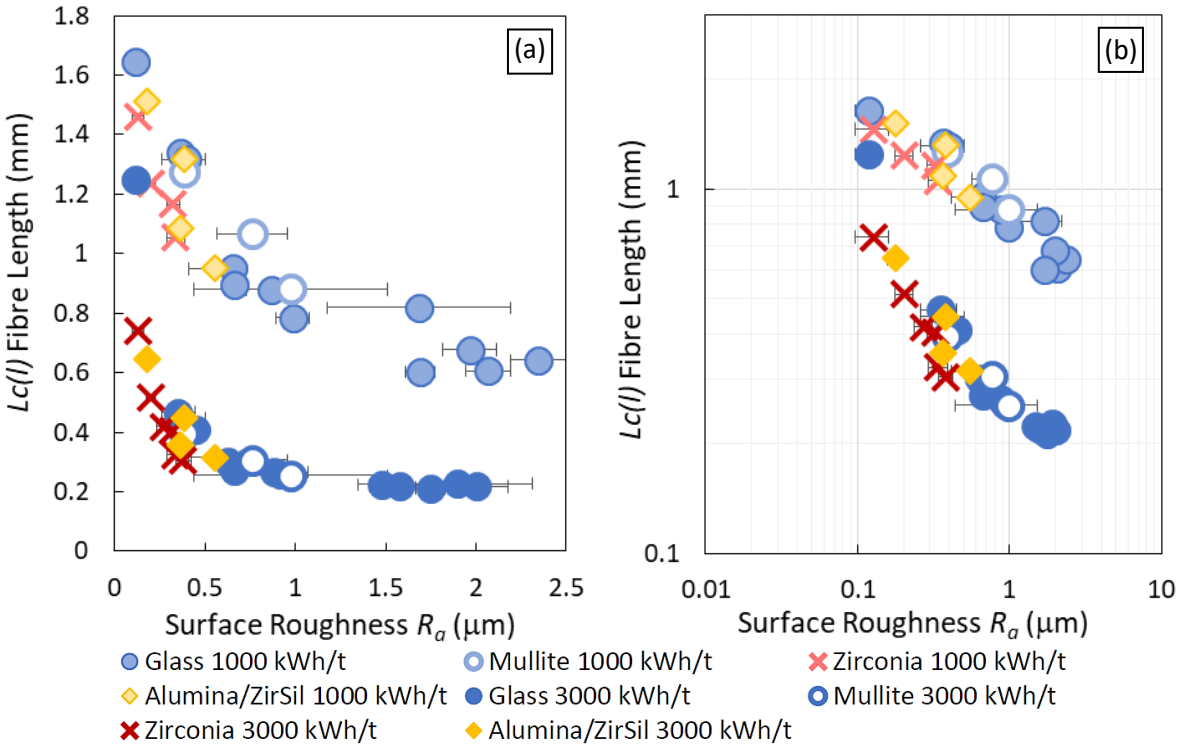

Figure 5.7 *– Lc(l) versus media roughness at 1000 kWh/t and 3000 kWh/t for each media composition (a) on a linear scale, and (b) on a log-log scale.*

5.2.5. Fines B and Fibrillation %

Figure 5.8 shows how media roughness influences *Fines B* generation. At 1000 kWh/t, the relationship is roughly linear, but at 3000 kWh/t, *Fines B* increases rapidly with roughness, before plateauing at around 0.7 µm, and perhaps decreasing at high roughnesses. This looks similar to the typical energy input versus *Fines B* curve (see Figure 4.9), which is intuitive if roughness primarily affects breakage efficiency. At low roughnesses (and lower grinding

efficiency), the effective energy input would be on the steep upcoming part of Figure 4.9; consequently, changes in roughness strongly influence *Fines B* generation. At higher roughnesses, fibre disintegration is much more extensive, corresponding to a relatively low gradient region of Figure 4.9, so sensitivity to roughness differences is lower.

The plateau and possible decline at high roughnesses cannot entirely be explained by efficiency differences; energy sweeps in Section 5.3 show higher *Fines B* values than the plateau in Figure 5.8. Instead, the excessive wear particles generated at high roughnesses could act like IC60 mineral particles, degrading liberated fibrils (as Sections 5.3 and 5.4 later show the mineral to do).

Figure 5.8 shows no obvious differences in *Fines B* generation between media densities when roughness is accounted for; this contrasts with the effect of impeller speed (Figure 4.24), which strongly influences *Fines B* generation. However, when *Fines B* is plotted against *Lc(l)* (see Figure 5.9) the expected differences are seen; at shorter fibre lengths, denser media results in lower *Fines B* values at a given *Lc(l)* value; the explanation is probably the same as for impeller speed in Chapter 4; higher intensities mean fewer stress events to fibrillate at fibre breakages.

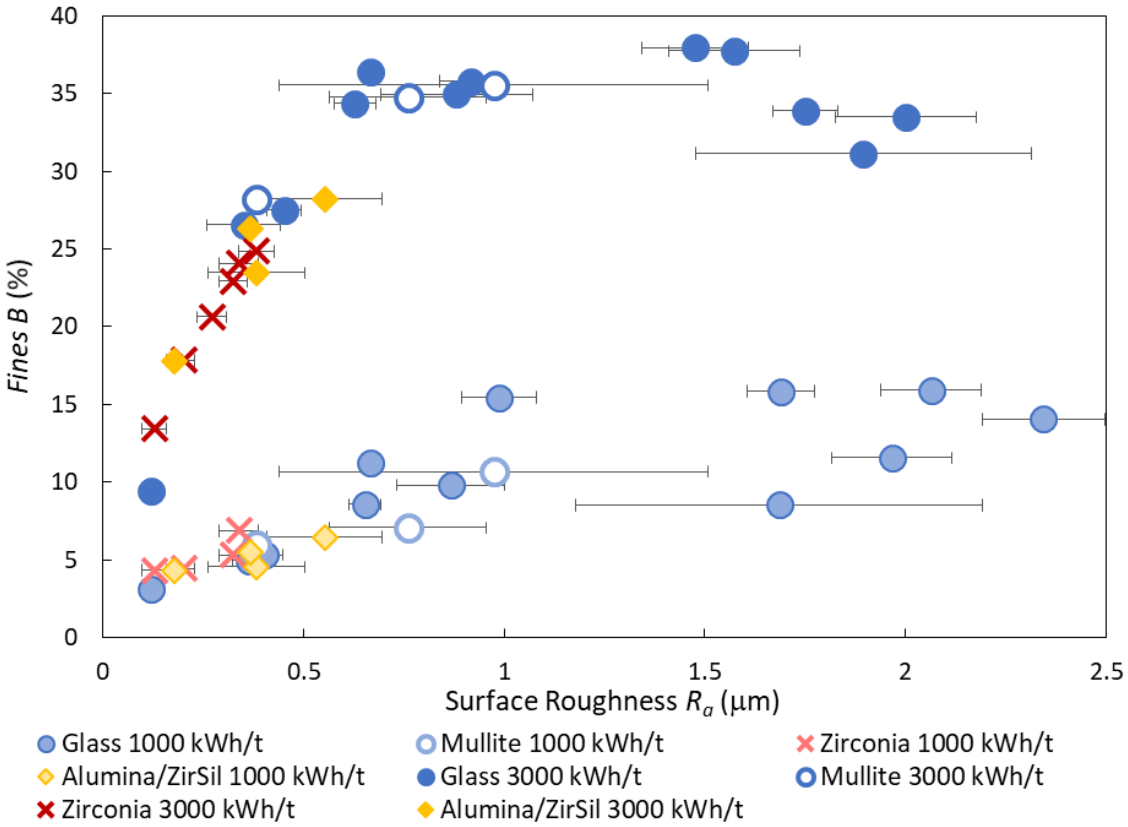

Figure 5.8 *– Fines B versus media roughness for each media composition at 1000 kWh/t and 3000 kWh/t.*

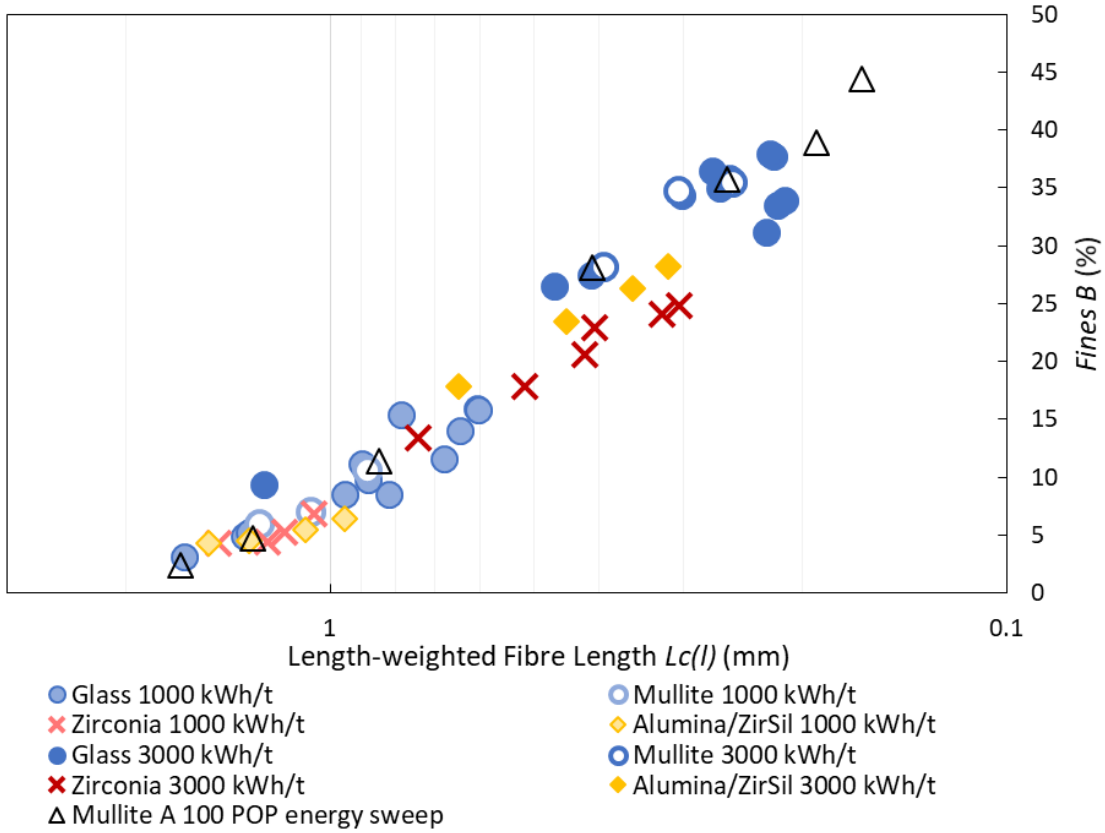

Figure 5.9 *– Fines B versus Lc(l) for each media composition at 1000 kWh/t and 3000 kWh/t, with data included from a Mullite A energy sweep in Section 5.3.*

The 100 POP energy sweep data for *Mullite A* shown later in Section 5.3 is also plotted on Figure 5.9, which matches well with glass and mullite media of differing roughnesses up until very fine *Lc(l)* values. This implies that roughness does not significantly influence fibrillation at a given breakage event, with the improvement in *Fines B* driven entirely by increases in breakage rate. The deviation at very fine sizes is thought to be due to the aforementioned wear issue.

Figure 5.10 shows the effect of media roughness on *Fibrillation %*, which exhibits very similar patterns as seen with *Fines B*. Figure 5.11 shows a plot of *Fibrillation %* versus fibre length, also giving a similar inverse correlation as the *Fines B* equivalent. Denser media gives lower external fibrillation for a given MFC length, but the effect is much weaker than for *Fines B*.

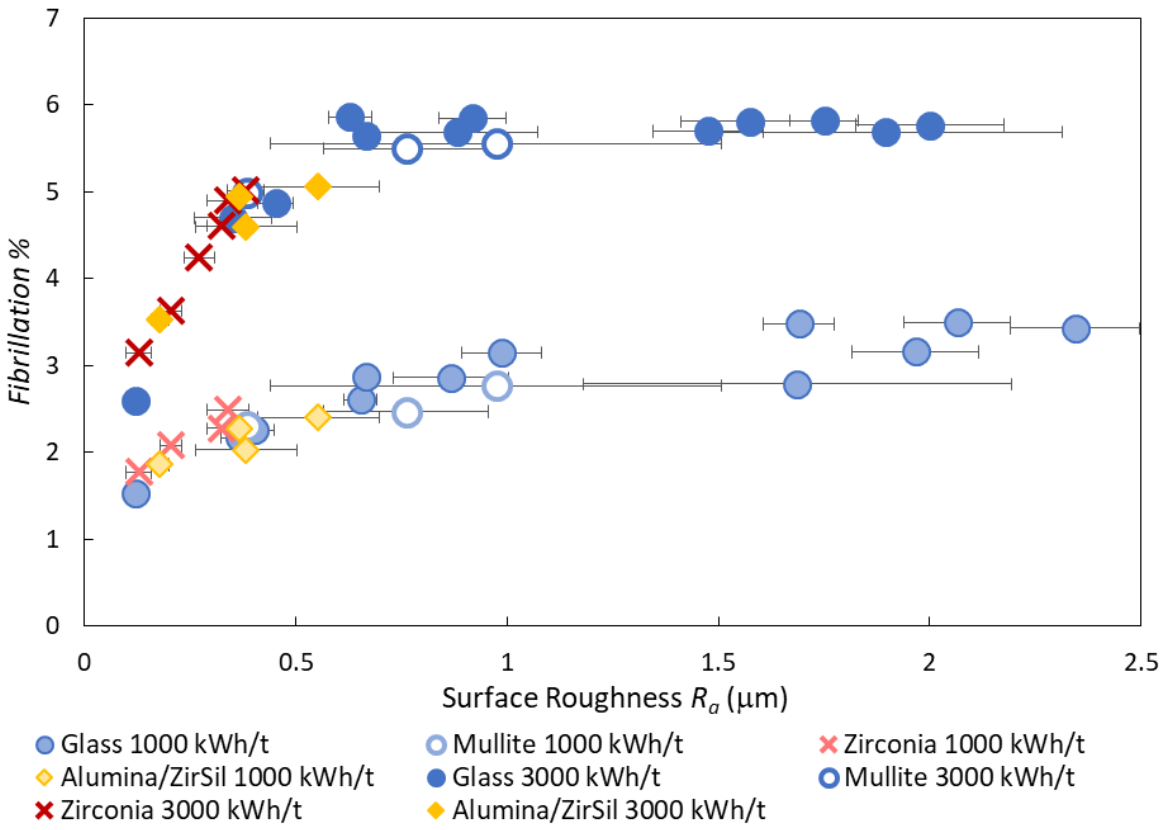

Figure 5.10 *– Fibrillation % versus media roughness for each media composition at 1000 kWh/t and 3000 kWh/t.*

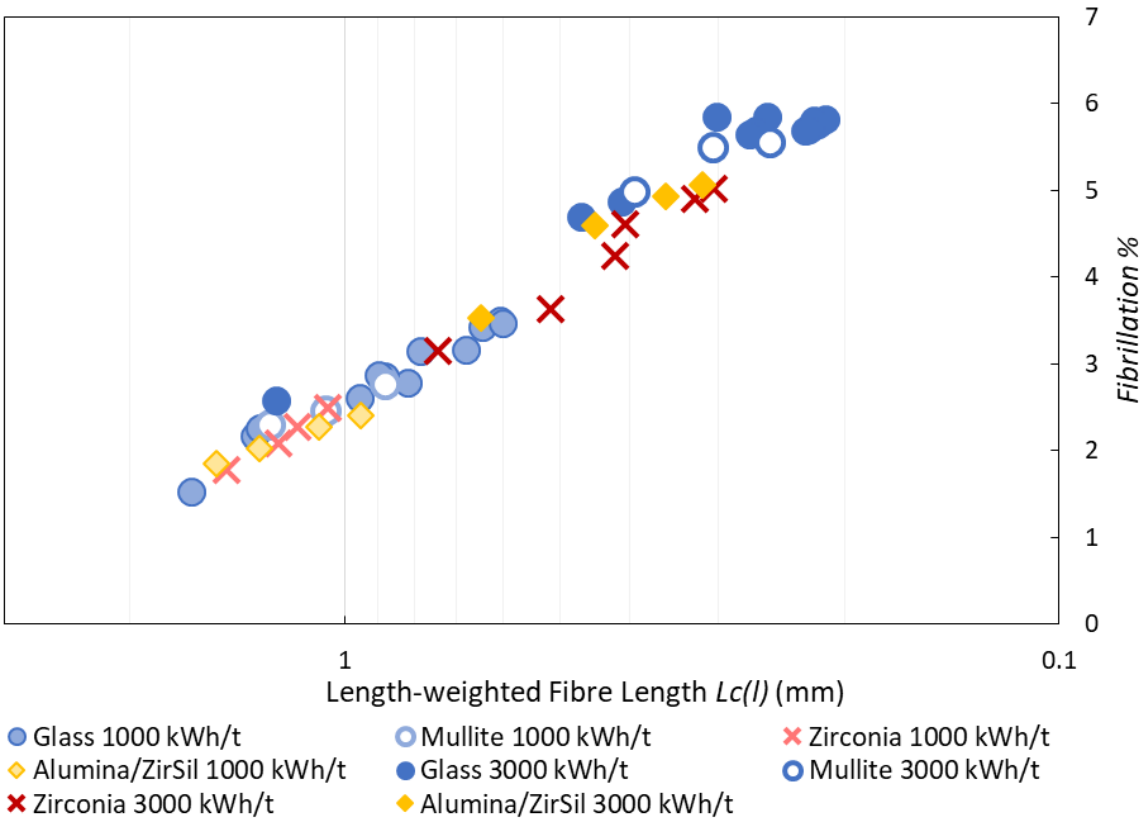

Figure 5.11 *– Fibrillation % versus MFC fibre length for each media composition at 1000 kWh/t and 3000 kWh/t.*

5.2.6. Tensile Strength

Figure 5.12 plots the MFC tensile index versus media roughness. At 1000 kWh/t, increasing roughness gradually increases strength up to a plateau at around 1 µm. For 3000 kWh/t, the increase is much more rapid, peaking at around 0.7 µm, before declining slightly at high roughnesses.

The lower optimum roughness at higher energy input can be understood from considering a typical energy – tensile index curve (e.g. Figure 4.10 for *Mullite A,* R_a = 0.97 µm). At low energy input, the gradient is steep and therefore highly sensitive to efficiency changes from roughness differences. Since MFC is very under-processed at 1000 kWh/t regardless of roughness, all media are on the steep upcoming part of their respective energy – tensile index curves, and the rougher media (1 µm and above) is more advanced along this curve.

At 100 POP, *Mullite A* reaches its optimum energy input at 3000 kWh/t (see the later energy sweep in Section 5.3.5). Since the energy – tensile index curve is very flat here, modest roughness changes about R_a = 1 µm barely affect tensile strength in Figure 5.12, and roughness must be substantially lowered (below 0.7 µm) for a sufficient efficiency drop to for the MFC to be sufficiently under-ground to be sensitive to roughness changes.

At 3000 kWh/t, tensile strength decreases at very high roughnesses, to 1 – 1.5 Nm/g below the peak value; this may partly be due to over-grinding, but a contribution is expected from the extreme levels of media wear degrading liberated fibrils, since Sections 5.3 and 5.4 later demonstrate that mineral content lowers peak tensile strength. It was initially suspected that this worn media interferes with the tensile test, but washing high wear samples through a 25 µm screen to remove the wear before retesting tensile strength made no significant difference (see Table A3.2 in Appendix A3).

Interestingly, media density barely influences tensile index once roughness is accounted for, likely because of similar *Fines B* and *Fibrillation %* generation regardless of media density at a given roughness value; the more efficient breakage rate with denser media is cancelled out by the lower fibrillation per breakage, leading to similar totals, and similar tensile strengths.

It was initially considered that the effects of roughness could be due to the higher power draw. To investigate, another 3000 kWh/t grind was carried out with smooth *Glass A* media, with the impeller speed increased to match the power draw of a rough glass media (*Glass F*). Table A3.3 in Appendix A3 shows these results; efficiency is improved slightly, indicating a higher optimum stress intensity for smoother media, but grinding performance is still far poorer than *Glass F*, demonstrating that the benefit of roughness is mostly not due to power draw.

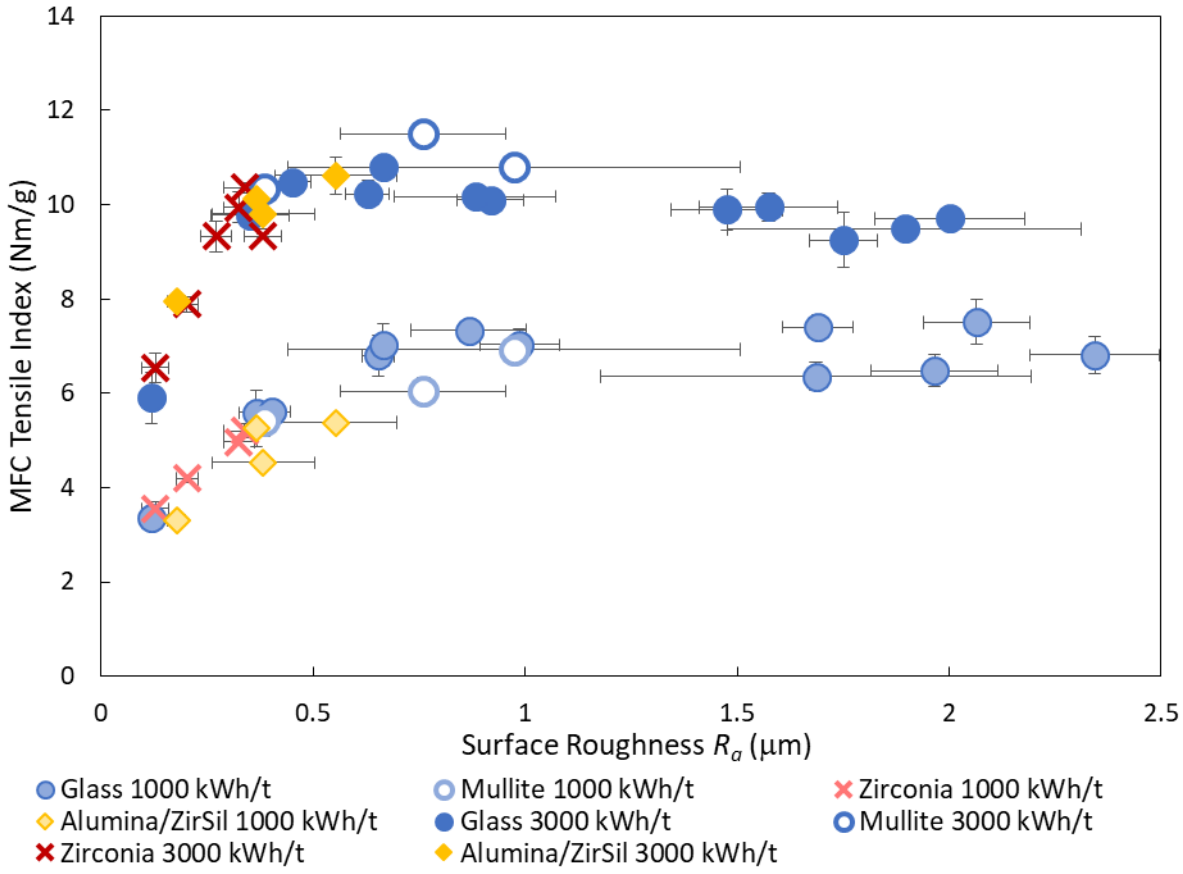

Figure 5.12 *– MFC tensile index versus media roughness for each media composition at 1000 kWh/t and 3000 kWh/t.*

5.2.7. DIC Microscopy

The influence of roughness on product microstructure is striking. Figures 5.13 – 5.17 show microscopy images of MFC at 3000 kWh/t for *Glass A* (R_a = 0.12 µm), *Glass E* (R_a = 0.88 µm), *Mullite A* (R_a = 0.97 µm), *Glass B* (R_a = 1.90 µm), and *Glass D* (R_a = 2.34 µm). Figure 5.13 demonstrates that very low roughness media is largely incompetent at fibre breakage. Disintegration becomes increasingly effective with higher roughnesses (Figures 5.14 and 5.15), though marginal benefits diminish at high roughnesses (Figures 5.16 and 5.17) where MFC geometry appears similar as for moderate roughnesses. The high media wear in Figures 5.16 and 5.17 is obvious, and probably increases fibril degradation.

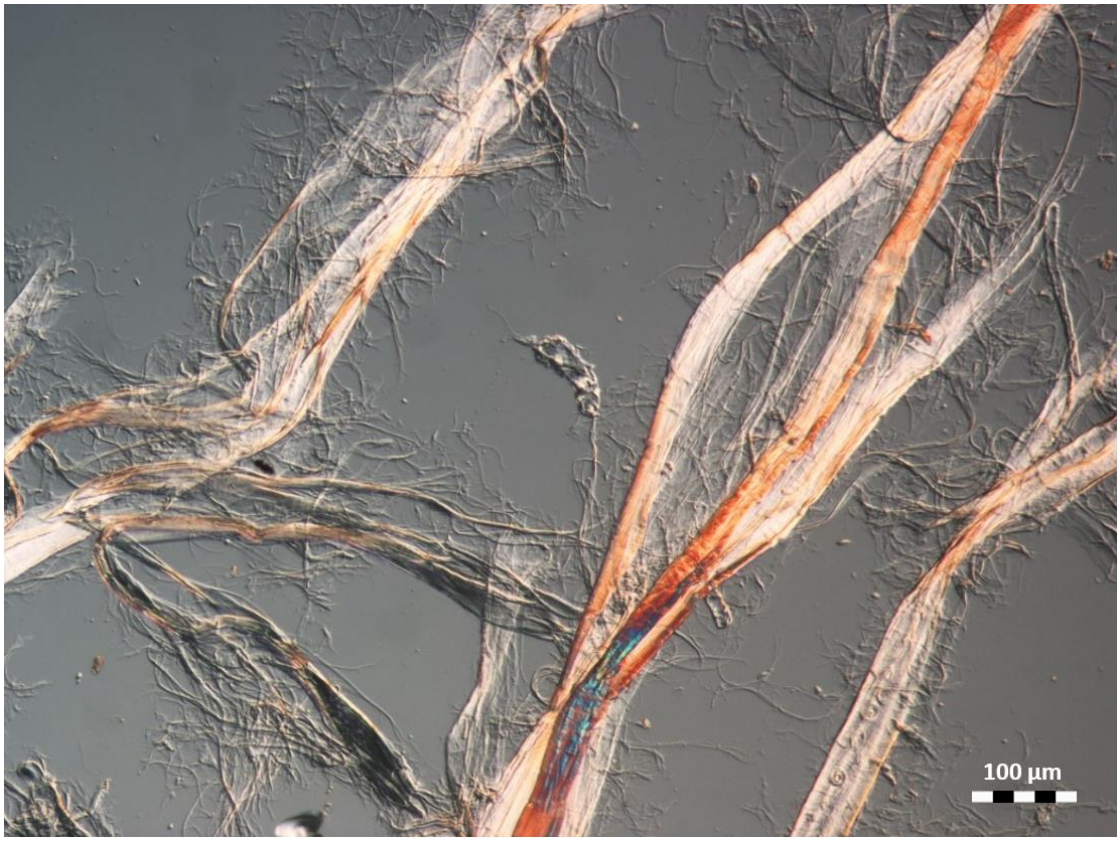

Figure 5.13 *– DIC microscopy image of MFC produced at 3000 kWh/t using smooth glass (Glass A), R_a = 0.12 µm.*

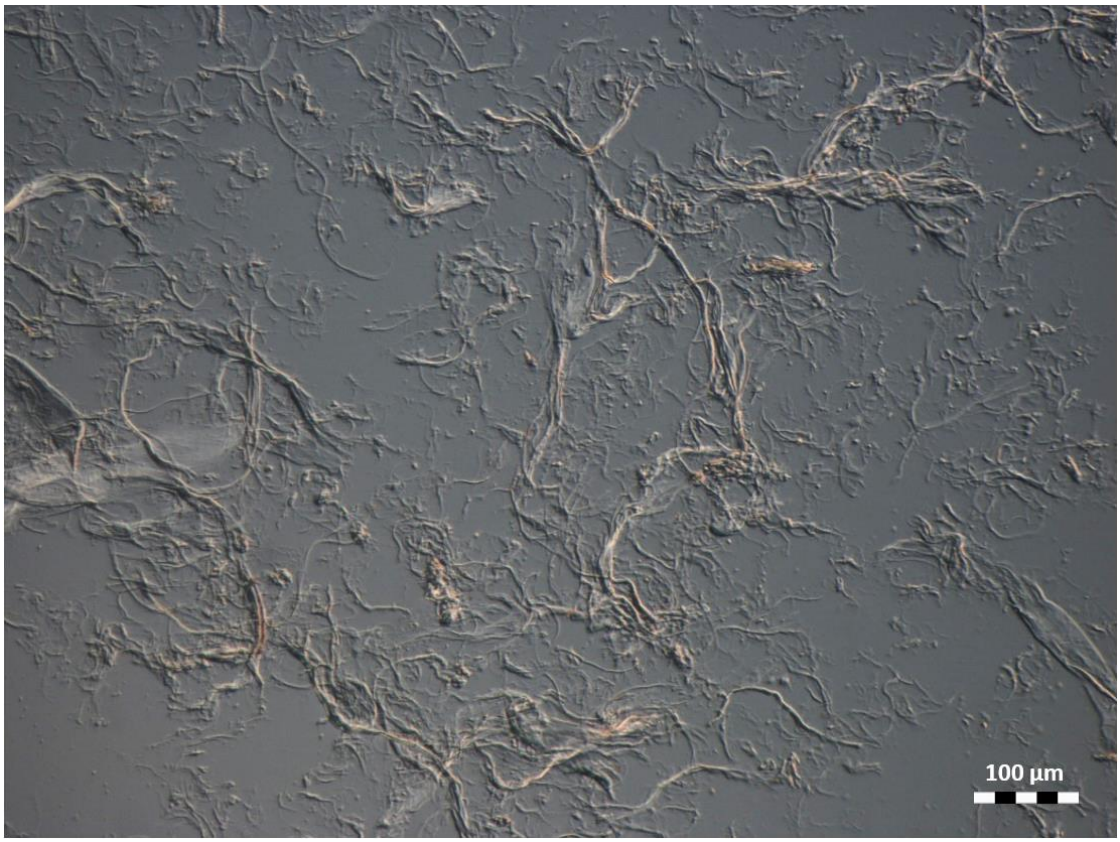

Figure 5.14 *– DIC microscopy image of MFC produced at 3000 kWh/t using rough glass (Glass E), R_a = 0.88 µm.*

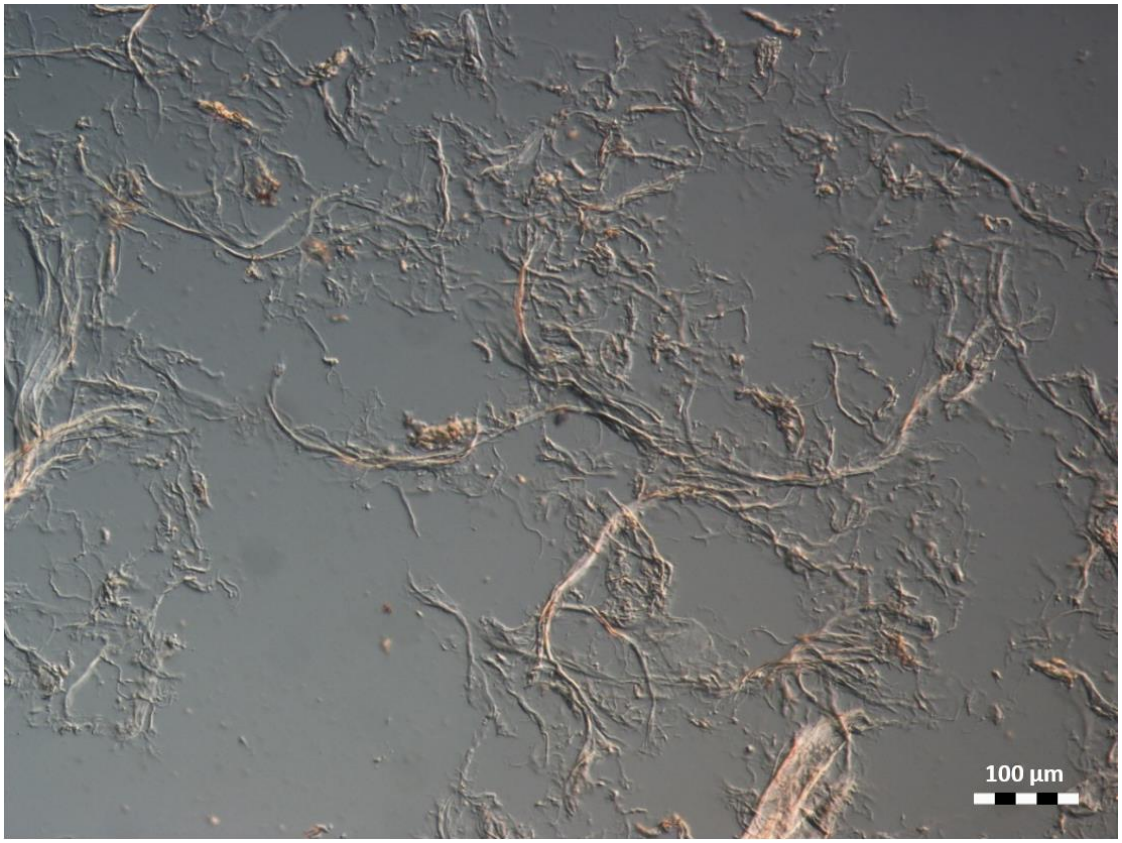

Figure 5.15 *– DIC microscopy image of MFC produced at 3000 kWh/t using rough mullite (Mullite A),* R_a *= 0.97 µm.*

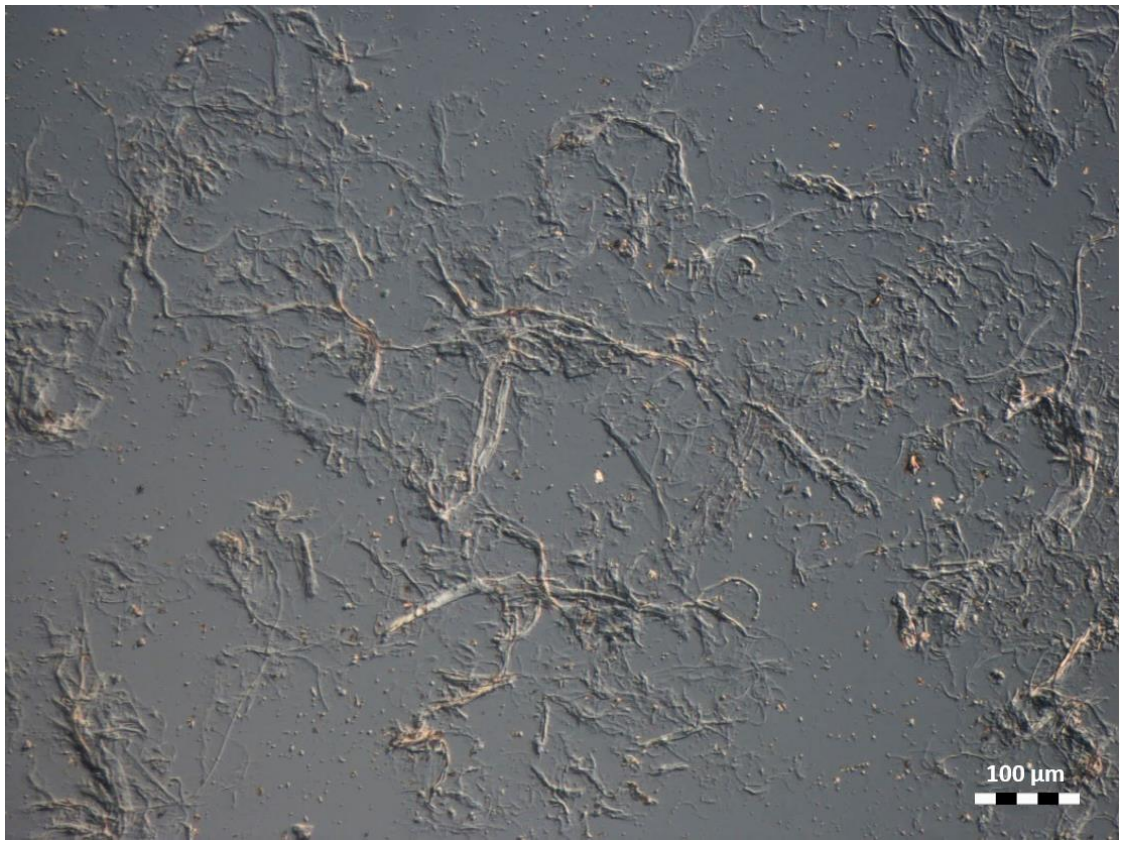

Figure 5.16 *– DIC microscopy image of MFC produced at 3000 kWh/t using rough glass (Glass B),* R_a *= 1.90 µm.*

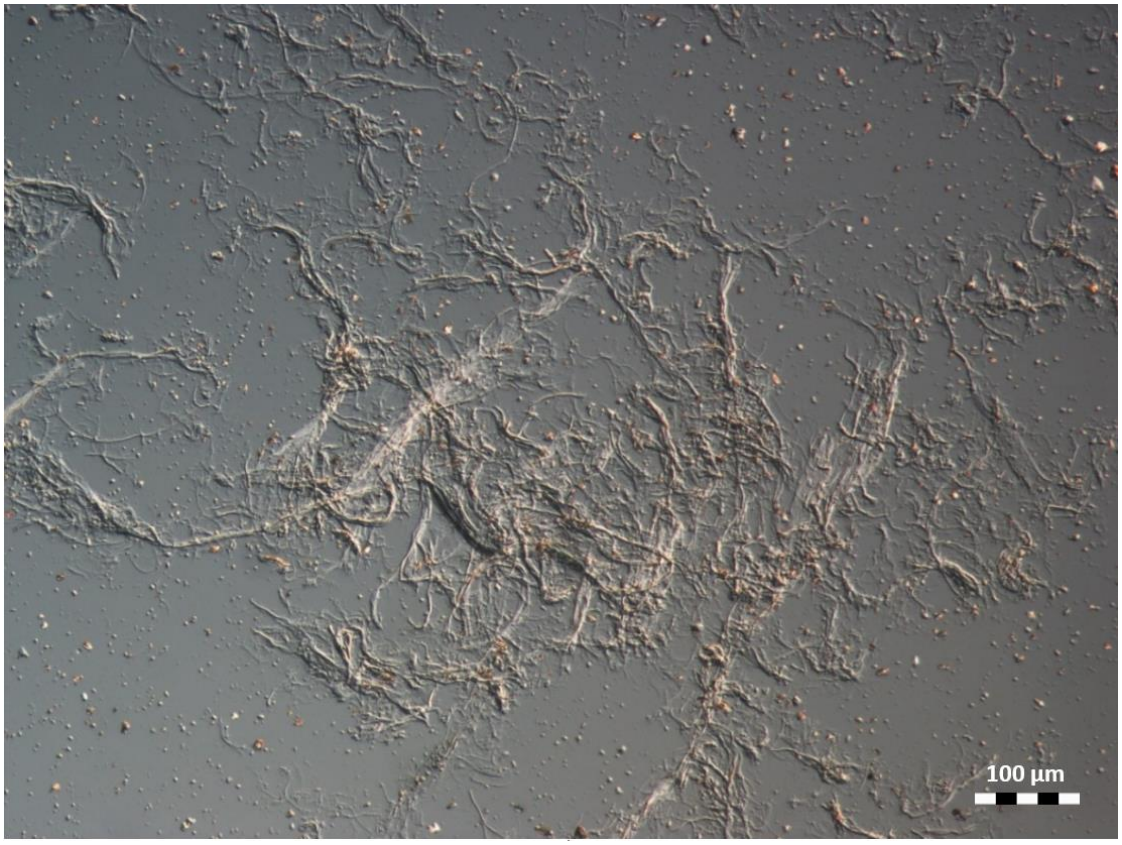

Figure 5.17 *– DIC Microscopy image of MFC produced at 3000 kWh/t using rough glass (Glass D),* R_a *= 2.34 µm.*

5.2.8. Roughness-Adjusted Stress Intensity

Stress intensity theory assumes no role of media roughness, which these results contradict. Media roughness clearly increases fibre breakage rate, which work later in this chapter suggests is because of roughness asperities concentrating pressure. One could change breakage rate by changing either the stress intensity or this pressure-concentrating effect. Considering roughness as an 'efficiency factor', these two parameters were multiplied to form a *roughness-adjusted stress intensity* $SI \cdot R_a$.

This was plotted as the *x*-axis against all MFC quality parameters, with the graphs for *Lc(l)* and tensile index shown as Figure 5.18 and 5.19 respectively. Compared to R_a alone, the denser media data are shifted to the right, apparently solving the discrepancy between media densities for MFC length. However, the media densities consequently no longer coincide for

Fines B, *Fibrillation %*, and tensile index. (e.g. Figure 5.19), suggesting that $SI{\cdot}R_a$ may account for fibre and fibril breakage well, but does not directly predict fibrillation. Fibre breakage requires a higher stress intensity than any subsequent fibrillation process. Consequently, the high stress intensity from the higher density increases fibre breakage rate, but is superfluous for fibrillation, and the consequent lower stress numbers lower fibrillation rate per breakage event, lowering strength for a given $SI{\cdot}R_a$ value.

The stress intensity variations in this study are insufficient to unequivocally demonstrate that this $SI{\cdot}R_a$, parameter controls MFC length, so this is revisited in Chapter 6 where variations in impeller speed and media size are also investigated. An alternative route for accommodating roughness is given in Section 5.6 where the contact mechanics model from Section 4.2 is further developed.

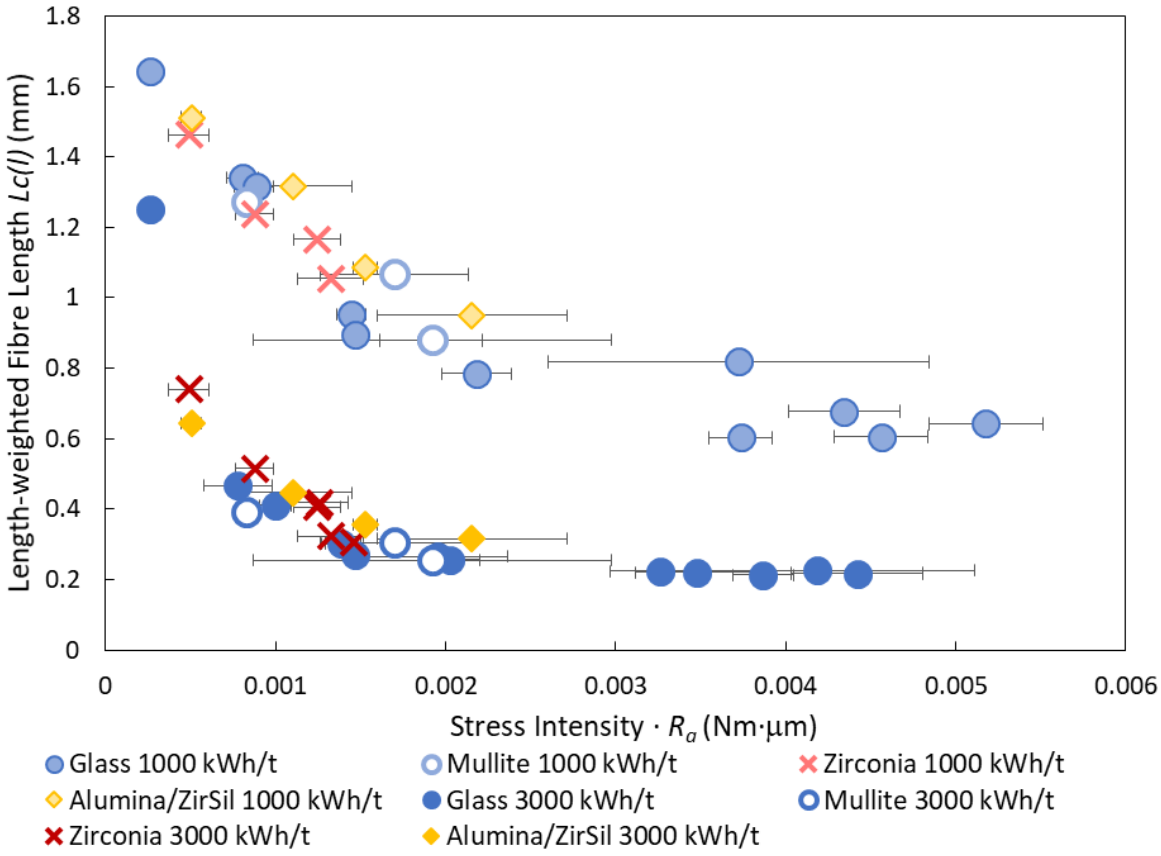

Figure 5.18 *– MFC fibre length versus $SI{\cdot}R_a$ for each media species.*

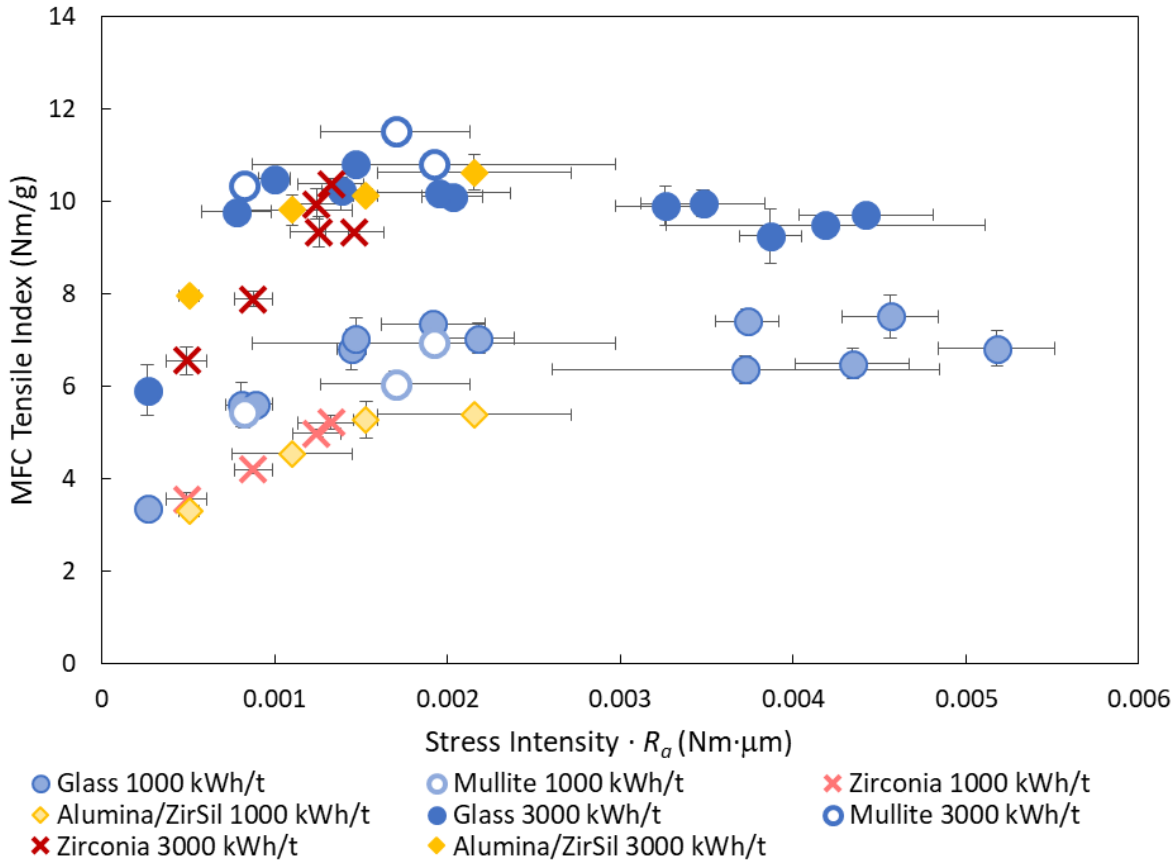

Figure 5.19 *– MFC tensile index versus SI·R_a for each media species.*

5.2.9. Conclusions

This work investigated a very wide range of media surface roughnesses, both as acquired naturally, and artificially roughened with an abrasive. Power draw increases with roughness, and by controlling for roughness, it is obvious that media density increases power draw. Media wear also increases with surface roughness, and wear rate approaches zero for smooth media, indicating that most media wear is due to asperity attrition rather than compressive failure.

Media roughness strongly influences fibre breakage. At very low roughness, size reduction efficiency is greatly reduced, largely maintaining the fibre ultrastructure at 3000 kWh/t. Higher roughnesses increase breakage efficiency, though with decreasing marginal benefit. When

roughness is controlled for, higher density media produces finer MFC, especially at low roughnesses.

Both fibrillation parameters (*Fines B* and *Fibrillation %*) increase linearly with roughness at 1000 kWh/t, but at 3000 kWh/t, they sharply increase before reaching a plateau, with no apparent influence of media density. Plotting these parameters against MFC length suggests that roughness does not directly influence fibrillation for a given breakage event, and increases these parameters solely by increasing fibre breakage rate.

Consequently, at low roughnesses, MFC tensile strength at 3000 kWh/t increases rapidly with roughness, up until an optimum around 0.7 µm, beyond which strength slowly declines. The 1000 kWh/t series shows a more gradual increase, plateauing at a higher roughness value (1 µm), so clearly the optimum roughness decreases with increasing energy input.

The enhancement of breakage rate suggests that asperities concentrate collision pressure to aid localised fibril breakage within a cross-section. This is investigated later with microscopy (Section 5.5), and is later supported by theoretical considerations (Section 5.6), but in this section, the roughness and stress intensity were multiplied into a product that gave a more universal correlation with MFC length between media densities. This is revisited in Chapter 6.

The key conclusion from this study is that *a higher surface roughness increases grinding efficiency*, so tensile strength is expected to peak at lower energy inputs with rougher media. This comes at the cost of increased media wear rate, so there is an economically optimum surface roughness which provides the best balance of media cost, energy cost, and feed fibre cost. To demonstrate the influence on optimum energy input, the next section compares energy sweeps for media with different roughnesses.

5.3. Effect of Media Roughness and Mineral Content on Energy Sweeps

5.3.1. Experimental

The previous section demonstrated clear correlations between media roughness and MFC properties, and attributed this to improved grinding efficiency. To verify this, energy sweeps were undertaken with four media species: *Mullite A* (R_a = 0.97 µm), *Mullite B* (R_a = 0.38 µm), *Glass A* (R_a = 0.12 µm) and *Zirconia D* (R_a = 0.2 µm). The first three have similar densities (2.5 – 2.8 g/cm^3) so essentially differ solely by roughness, whereas the higher density zirconia media is implicative of the influence of higher stress intensities.

Mineral content was suspected to act analogously to surface roughness, locally concentrating media collision pressures. To investigate, energy sweeps were carried out both at 100 POP (mineral-free) and 50 POP. Energy inputs chosen varied between series due to clearly different grinding efficiencies; these ranged from 500 – 5000 kWh/t for *Mullite A* and *B*, 1000 – 10000 kWh/t for *Zirconia D*, and 1500 – 12000 kWh/t for *Glass A*. Data for the 50 POP *Mullite A* and *Zirconia D* series were taken from Section 4.1 and 4.6. Fibre analyser results were taken (with 100% POP samples diluted with IC60 mineral to 50% POP for comparable *Fibrillation %* values) and tensile strengths measured.

5.3.2. Media Wear

Figure 5.20 shows how energy input affects media wear, as *% of fibre mass MOF*, (MOP / POP), (MOF accommodates for mass differences between 100 % POP and 50% POP). All media show significant wear except *Zirconia D,* where no obvious increase with energy input is seen. To compensate for noise, the *gradients* of the MOF – energy input curves were compared rather than individual data points (see Table 5.1). For *Mullite A* and *B,* the gradient at 50 POP is slightly lower, whereas the opposite is true for *Glass A*. The drastic media wear reduction with

mineral addition claimed by Riley[73] is not apparent, but he compared MOP rather than MOF, so those observations are primarily an artefact of low POP samples having more total mass to dilute the wear percentage.

Table 5.1 *– Gradient of the media wear versus energy input curve for each series.*

	Mullite A (R_a = 0.97 µm)		***Mullite B*** (R_a = 0.38 µm)		***Glass A*** (R_a = 0.12 µm)		***Zirconia D*** (R_a = 0.20 µm)	
	100 POP	**50 POP**	**100 POP**	**50 POP**	**100 POP**	**50 POP**	**100 POP**	**50 POP**
Gradient (%/1000 kWh/t)	5.96	5.22	0.717	0.647	1.26	1.54	-	-

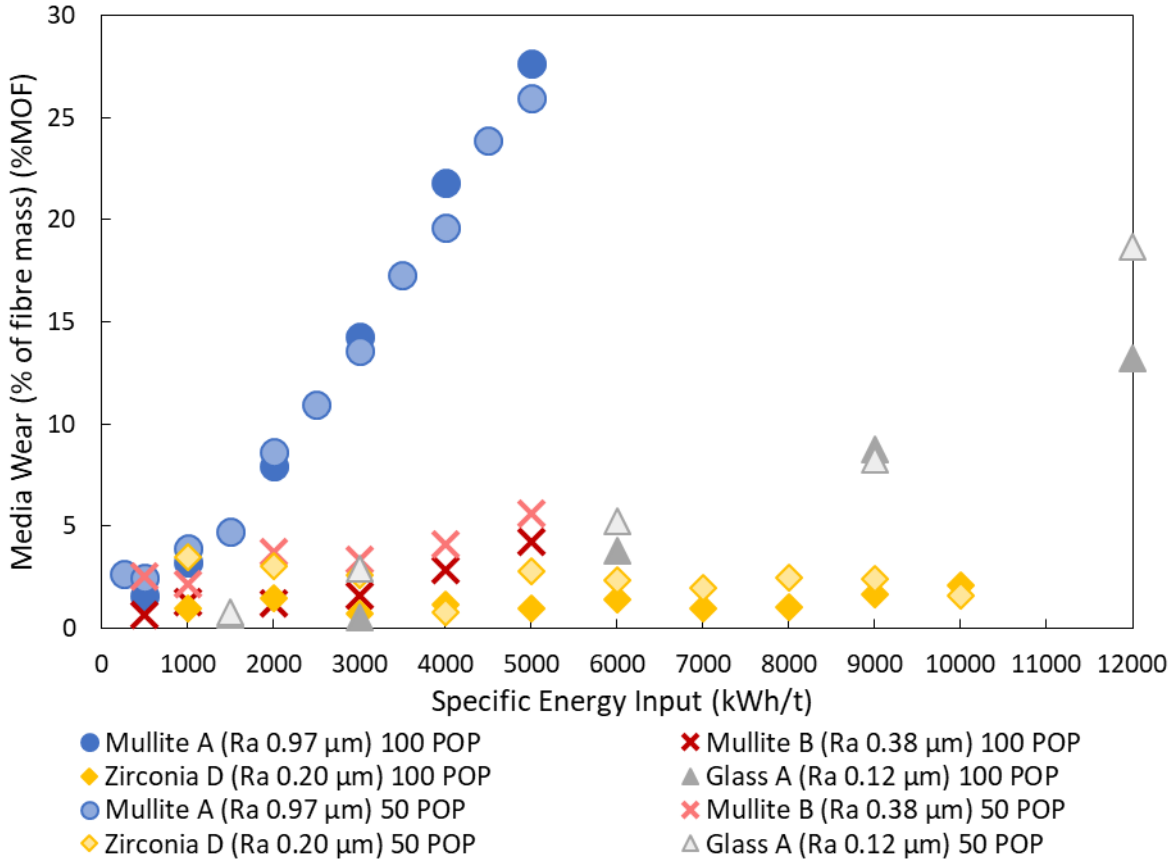

Figure 5.20 *– Media wear (%MOF) versus energy input for four media species with and without mineral addition.*

Figure 5.6, suggests that media wear is proportional to surface roughness. However, though the rougher mullite has eight times the wear of the smoother mullite, the smoothest media, *Glass A*, has a higher wear rate than *Mullite B*. Additionally, Zirconia D, though rougher than *Glass A*, has no measurable wear. After using *Glass A*, some broken beads were found,

suggesting that compressive failure generates wear particles, contaminating the product. For weaker media, at low roughnesses, compressive failure may dominate wear, though Figure 5.6 remains compelling in showing the dominance of attrition wear at higher roughnesses.

5.3.3. MFC Fibre Length

For each series, a plot of length-weighted fibre length and energy input is shown as Figure 5.21, divided into the 100 POP and 50 POP series in Figure 5.22 (a) and (b) for clarity.

For media of similar densities, at both 100 POP and 50 POP, increasing roughness greatly increases length degradation rate, though convergence is approached at high energy inputs. These differences are lesser for the 50 POP curves. The zirconia and *Mullite B* curves largely coincide; *Zirconia D* has around half the roughness and twice the density, therefore having a similar $SI \cdot R_a$ value, suggesting that this parameter controls fibre breakage.

For the roughest media, mineral addition has little effect, though for smoother media, it greatly decreases MFC length at moderate energy inputs. Additionally, with mineral addition, a lag time is seen before the effect accelerates, whereas the curves for differing roughnesses immediately have different gradients, suggesting different mechanisms (this is discussed in Section 5.3.7).

Considering $K_{R,Op}$ values (Figure 5.23), smoother media is much less effective at particle breakage at lower energy input, though this discrepancy is greatly lessened at higher energy input. This implies that roughness is instrumental in breaking fibres, but less important for disintegrating finer particles. Therefore, using rough media to break fibres, before discharging into a second grinder with smoother media to finish grinding could maintaining high efficiency whilst allowing for media wear reduction.

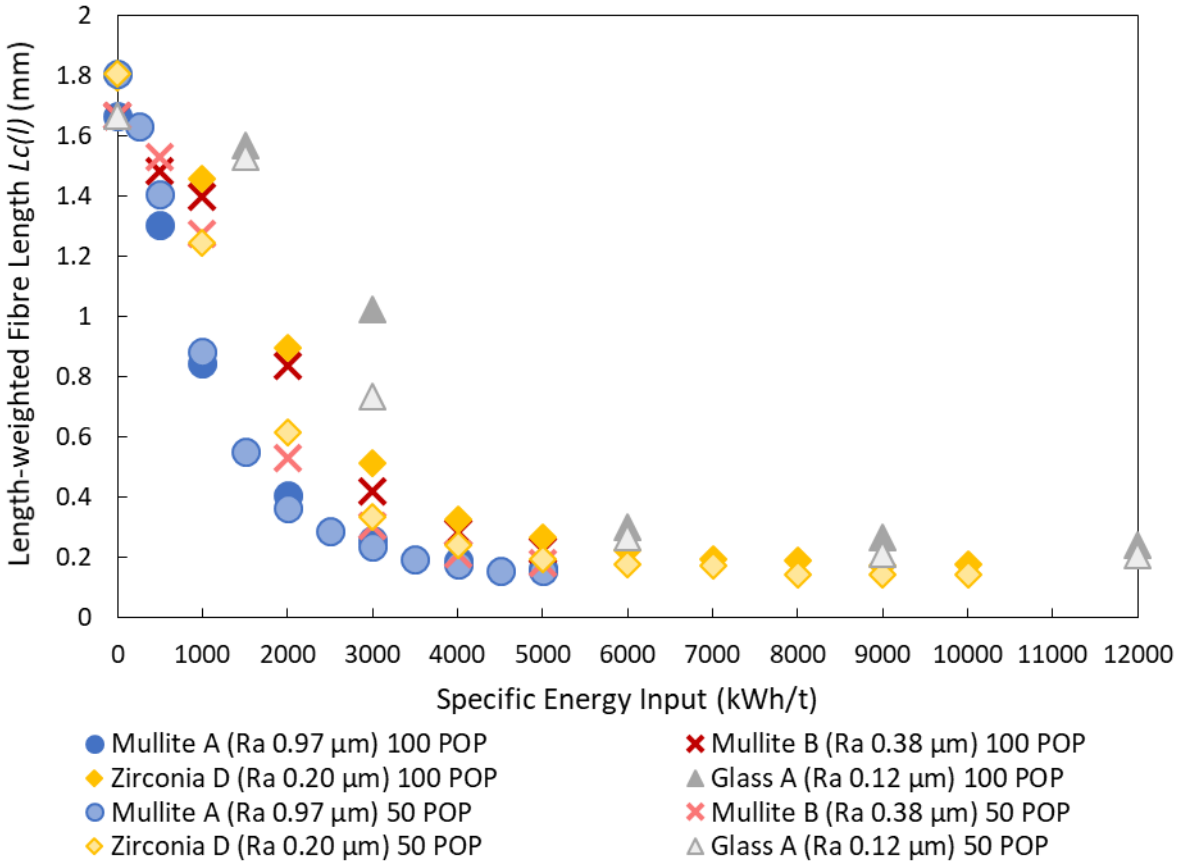

Figure 5.21 *– MFC fibre length versus energy input for four media species with and without mineral addition.*

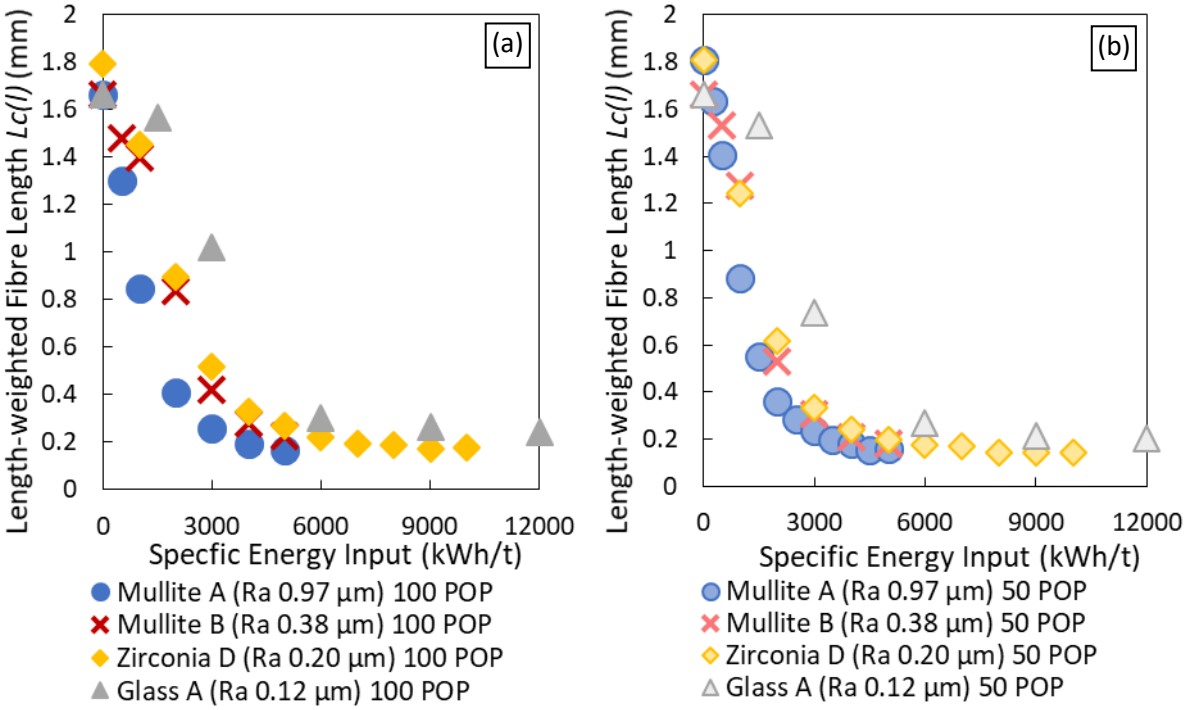

Figure 5.22 *– MFC fibre length versus energy input for four media species at (a) 100 POP and (b) 50 POP.*

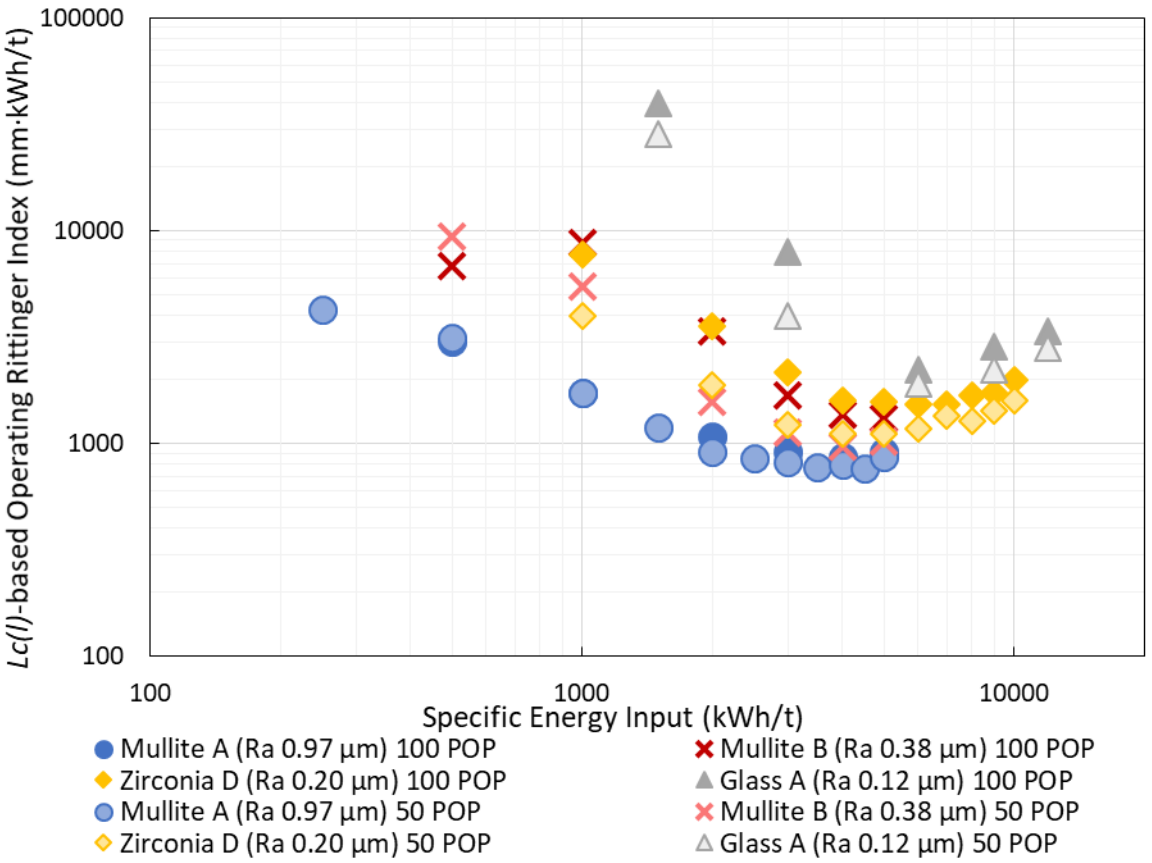

Figure 5.23 *– Lc(l)-based $K_{R,Op}$ versus energy input for four media species, with and without mineral addition.*

5.3.4. Fines B and Fibrillation %

Figure 5.24 shows the variation in *Fines B* for each series. The rougher media greatly enhances *Fines B* generation compared to smoother media. Unexpectedly, despite having a similar effect as roughness on fibre breakup, mineral addition has the *opposite* effect on *Fines B* generation, causing degradation once MFC is moderately well-processed. This effect appears stronger with smoother media, and is extreme for *Zirconia D*, indicating that higher stress intensities enhance this. The effect of roughness on *Fines B* generation is obvious immediately at low energy input, whereas the influence of mineral is only apparent at higher energy input, implying that the effect of mineral is degrading liberated fibrils rather than suppressing their generation.

Figure 5.25 plots the *Fines B* content versus *Lc(l)*; at 100 POP, *Mullite A* and *Mullite B* coincide, indicating that roughness in this range increases *Fines B only* by increasing fibre breakage rate. *Glass A* media, with extremely low roughness, gives higher *Fines B* values at finer product sizes; this is believed to be because a small fraction of feed fibres remain intact at high energy inputs, increasing *Lc(l)* (plotting *Lc(l)* versus *Lc(n)*, Figure A3.12 in Appendix A3, indicates this, as does microscopy (Figure A3.13)). Additionally, *Fines B* degradation from mineral addition is greater for smoother media than rougher media at given MFC sizes, and greater for higher density media.

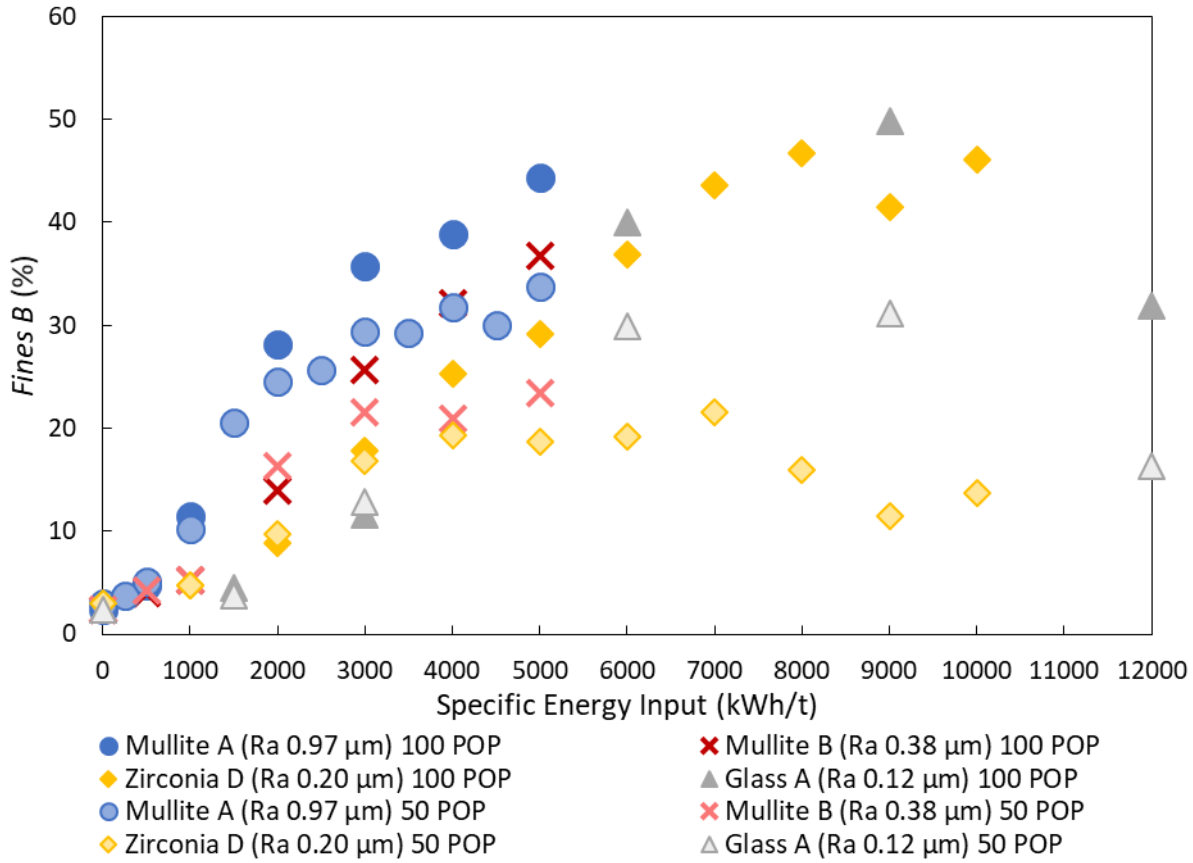

Figure 5.24 *– Fines B versus energy input for four media species, with and without mineral addition.*

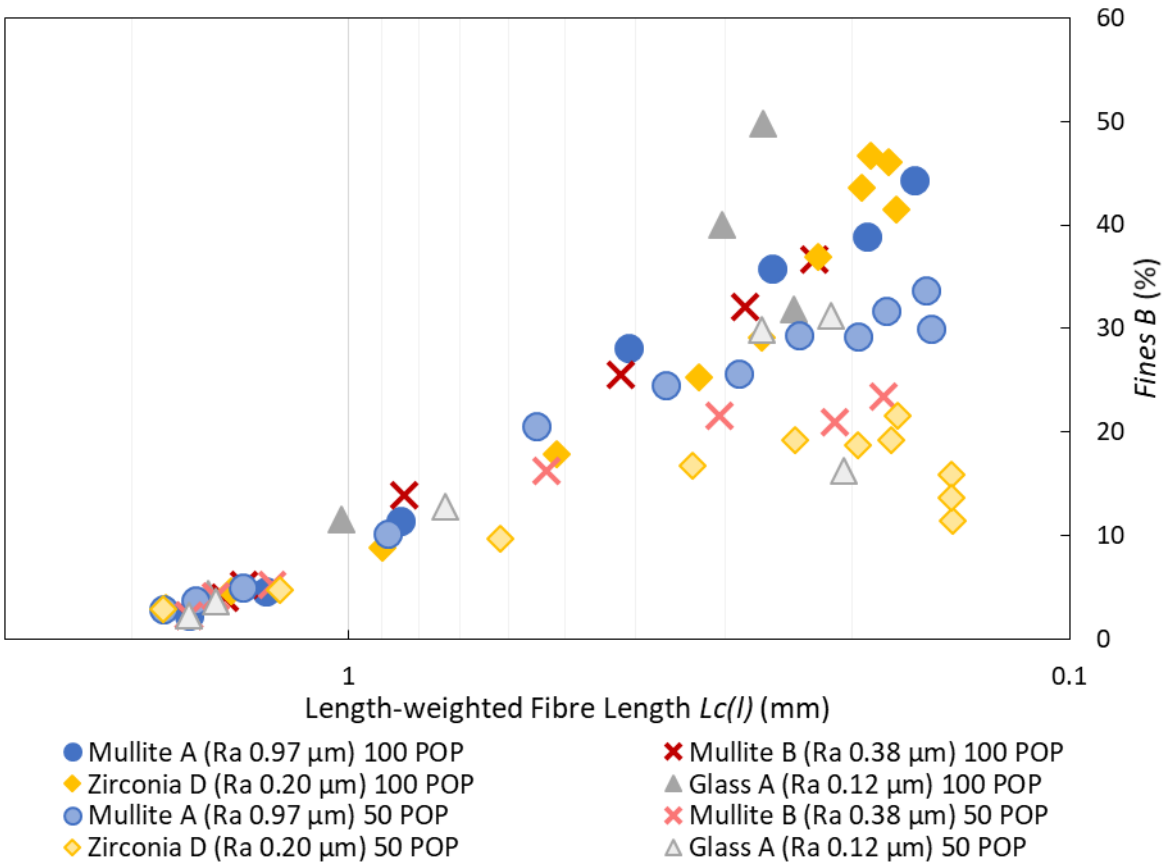

Figure 5.25 *– Fines B versus Lc(l) for four media species, with and without mineral addition.*

Figure 5.26 shows how *Fibrillation %* changes with energy input; the rougher media develops external fibrillation more rapidly with energy input, reaching peak values earlier. Degradation from mineral addition is only apparent at higher energy inputs; this is expected if the mineral breaks external fibrils, since these must be first generated before they are degraded.

Plotting *Fibrillation %* against *Lc(l)* (Figure 5.27) shows similar effects to *Fines B*, with the two mullite media at 100 POP coinciding, and the mineral content lowering *Fibrillation %* at finer sizes. However, *Glass A* shows a *deficiency* of external fibrillation unlike the surplus seen with *Fines B*; the lower power draw and the consequent longer grind times probably liberates more external fibrils into free fibrils.

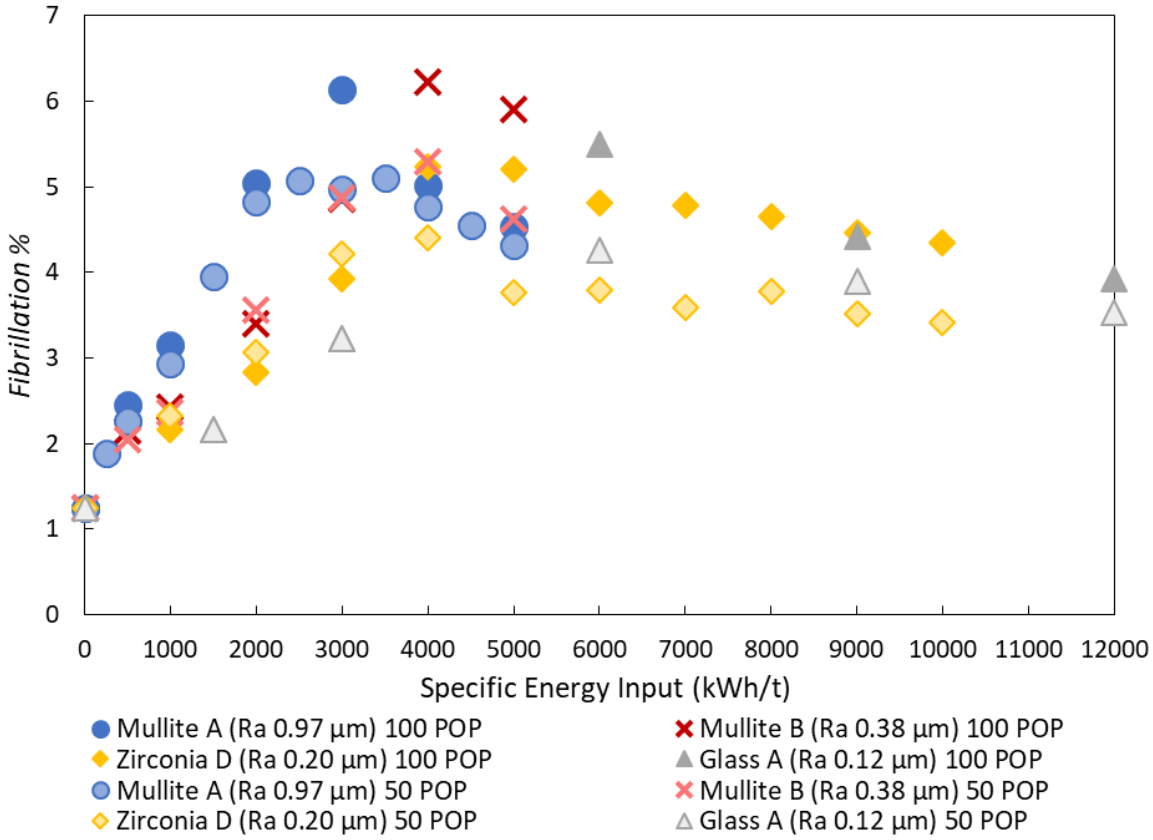

Figure 5.26 *– Fibrillation % versus energy input for four media species, with and without mineral addition.*

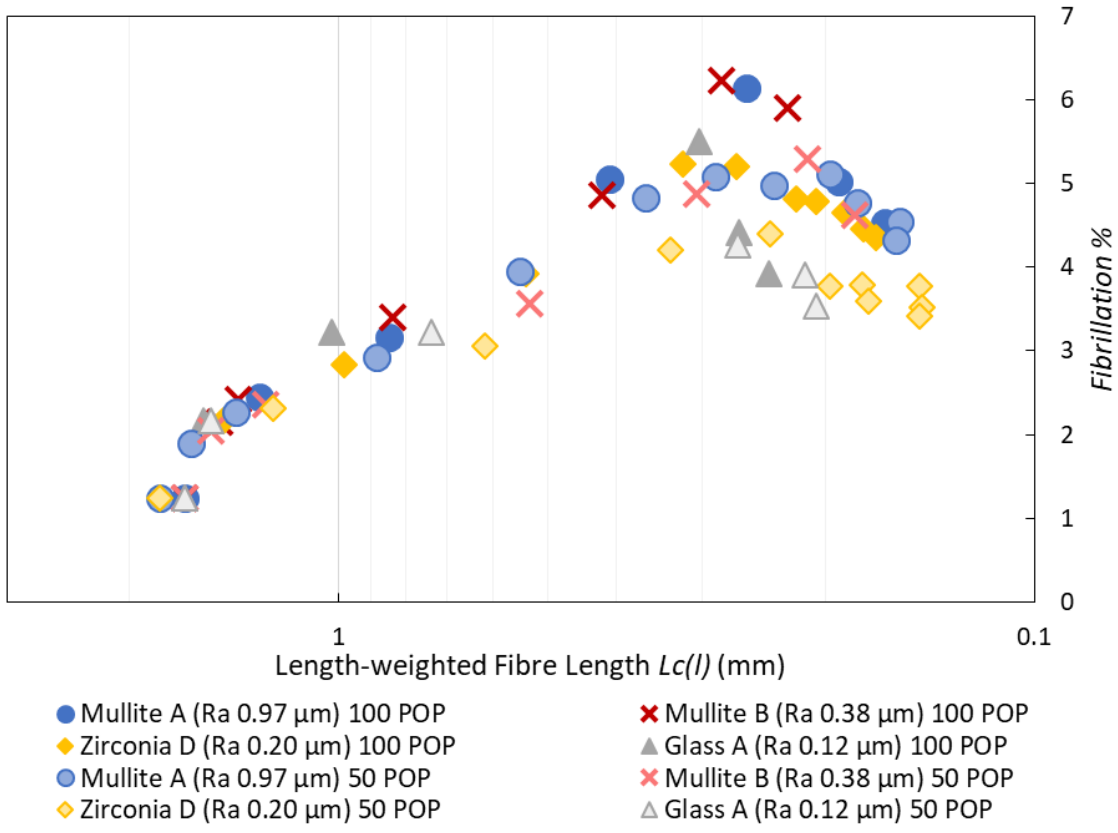

Figure 5.27 *– Fibrillation % versus Lc(l) for four media species, with and without mineral addition.*

5.3.5. Tensile Strength

Figure 5.28 shows the MFC tensile index versus energy input for each series, which are split into the 100 POP and 50 POP series in Figure 5.29 (a) and (b). At 100 POP, Figure 5.29 (a) shows that the rougher media rapidly develops tensile strength, exceeding 10 Nm/g by 2000 kWh/t, with smoother media having lower effectiveness and higher peak energy inputs.

Figure 5.28 shows that for *Mullite B*, *Zirconia D*, and *Glass A*, at low energy inputs the tensile index at 50 POP is higher than at 100 POP, and mineral addition lowers the optimum energy input, though beyond this optimum, strength decline is more rapid. Mineral addition does not benefit the roughest media (*Mullite A*), instead degrading strength as the optimum energy input is approached.

At lower energy inputs, mineral addition provides a relative benefit to smoother media, making differences between media species lesser at 50 POP than at 100 POP (compare Figure 5.29 (a) and (b)). Rougher media therefore has the strongest relative advantage for mineral-free grinds, but many of these applications would be intolerant of the high media wear rate. Therefore, mineral addition can compensate for insufficient surface roughness to improve low energy strength development, though lowering peak strength and causing rapid decay beyond the peak due to liberated fibril degradation. For sufficiently rough media, the mineral effect is superfluous, giving no benefit, and instead merely degrading peak strength.

Figure 5.30 plots the MFC tensile index against *Lc(l)*; at finer sizes, all media other than *Glass A* coincide at 50 POP, despite *Fines B* and *Fibrillation %* values differing drastically. This is expected to be because when mineral particles degrade liberated fibrils, their length decreases below the *Fines B* specification, yet they still contribute to strength. These differences complicate the comparison of fibrillation parameters upon mineral addition under

different grinding conditions; however, because this discrepancy is thought to be caused by unmeasured sub-*Fines B* particles, such differences are minimal at lower energy inputs (Figures 5.25, 5.27 and 5.30 show that all series coincide at coarser sizes). *In* general, higher *Fines B* and *Fibrillation %* values correlate with stronger MFC, but this effect suggests general correlations between fibre analyser data and tensile strength are fundamentally limited, particularly at high energy inputs.

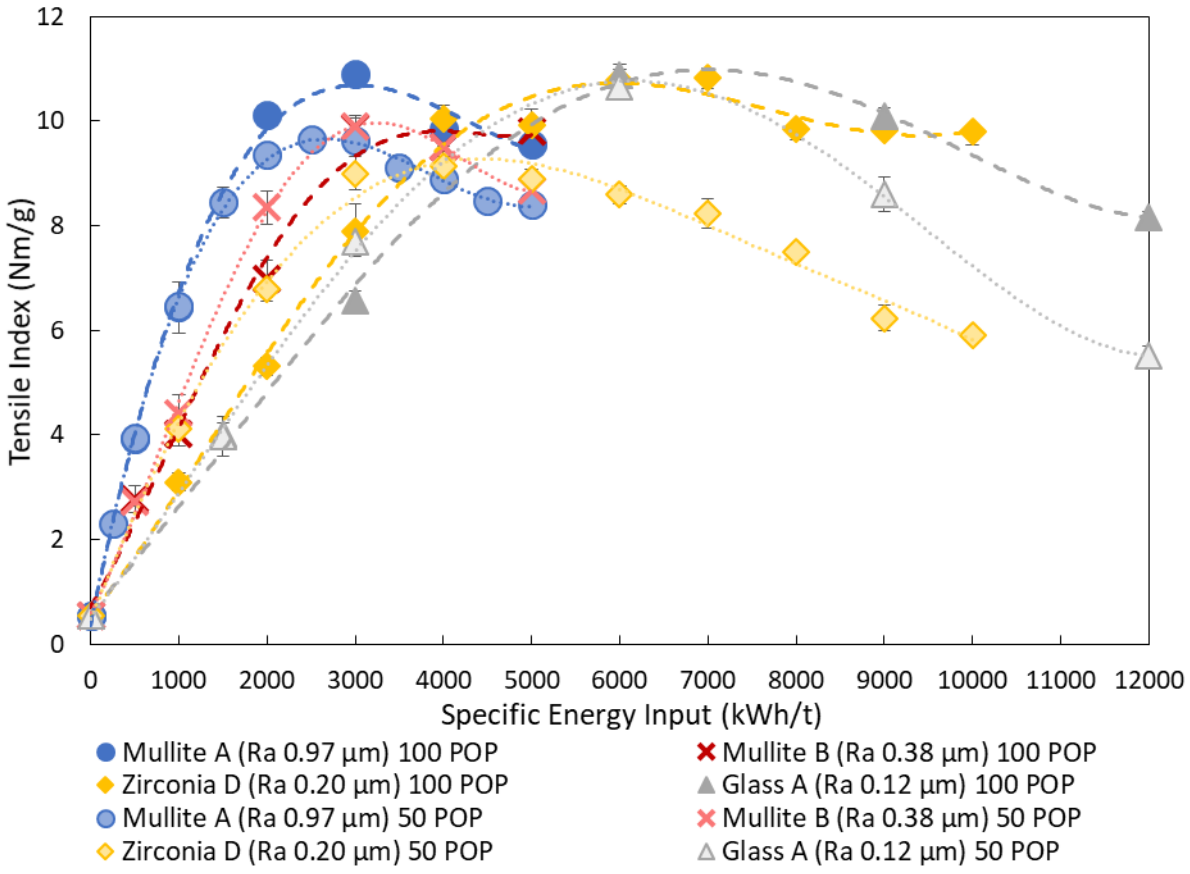

Figure 5.28 *– Tensile index versus energy input for four media species, with and without mineral addition. Lines are added to guide the eye.*

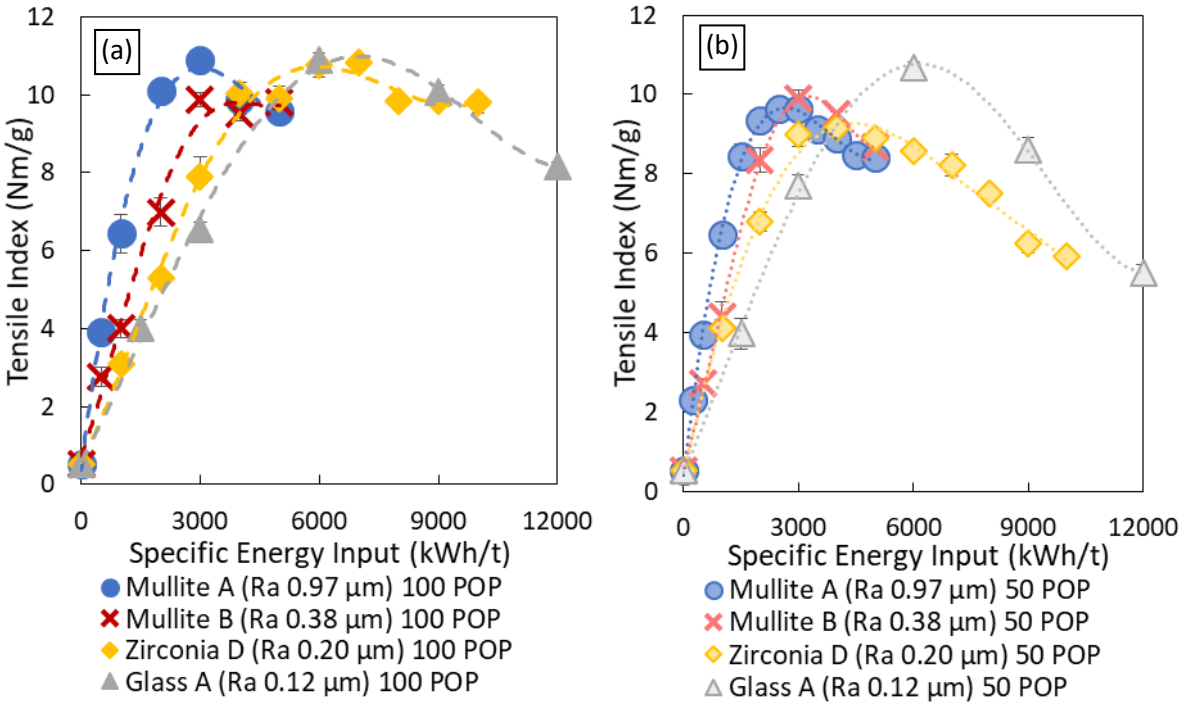

Figure 5.29 *– Tensile index versus energy input for four media species at (a) 100 POP and (b) 50 POP. Lines are added to guide the eye.*

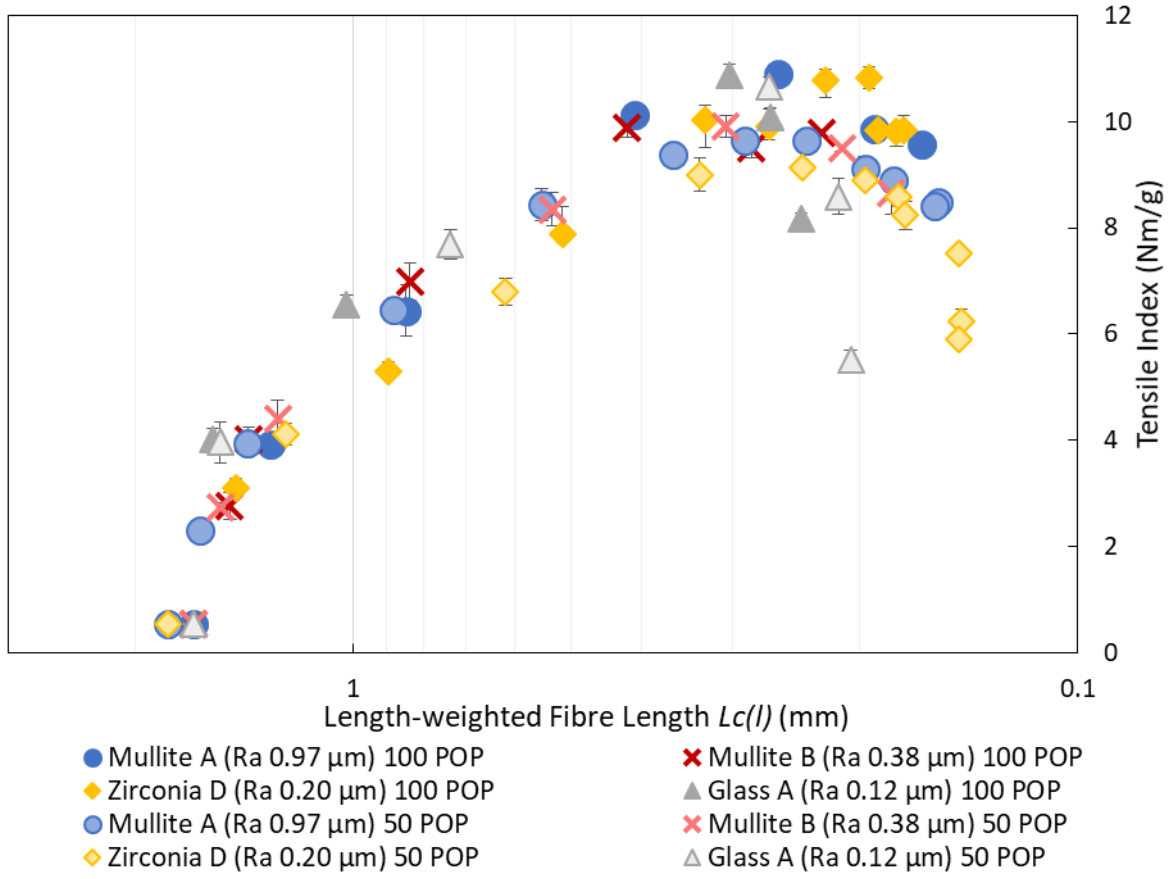

Figure 5.30 *– Tensile index versus Lc(l) for four media species, with and without mineral addition.*

5.3.6. DIC Microscopy

Microscopy showed no obvious morphological differences between MFC near the optimum energy input of each series. However, the sometimes extreme degradation effect of mineral particles on liberated fibrils was obvious; for example, MFC produced at 9000 kWh/t by *Zirconia D* media at 100 POP and 50 POP are shown as Figures 5.31 and 5.32. The 100 POP sample shows an abundance of fine, relatively long liberated fibrils, whereas the 50 POP sample shows much shorter fibrils. The former has a *Fines B* content of 42% compared to 11% for the latter, which is not surprising from these images. This morphology difference results in a 40% lower strength for the 50 POP sample.

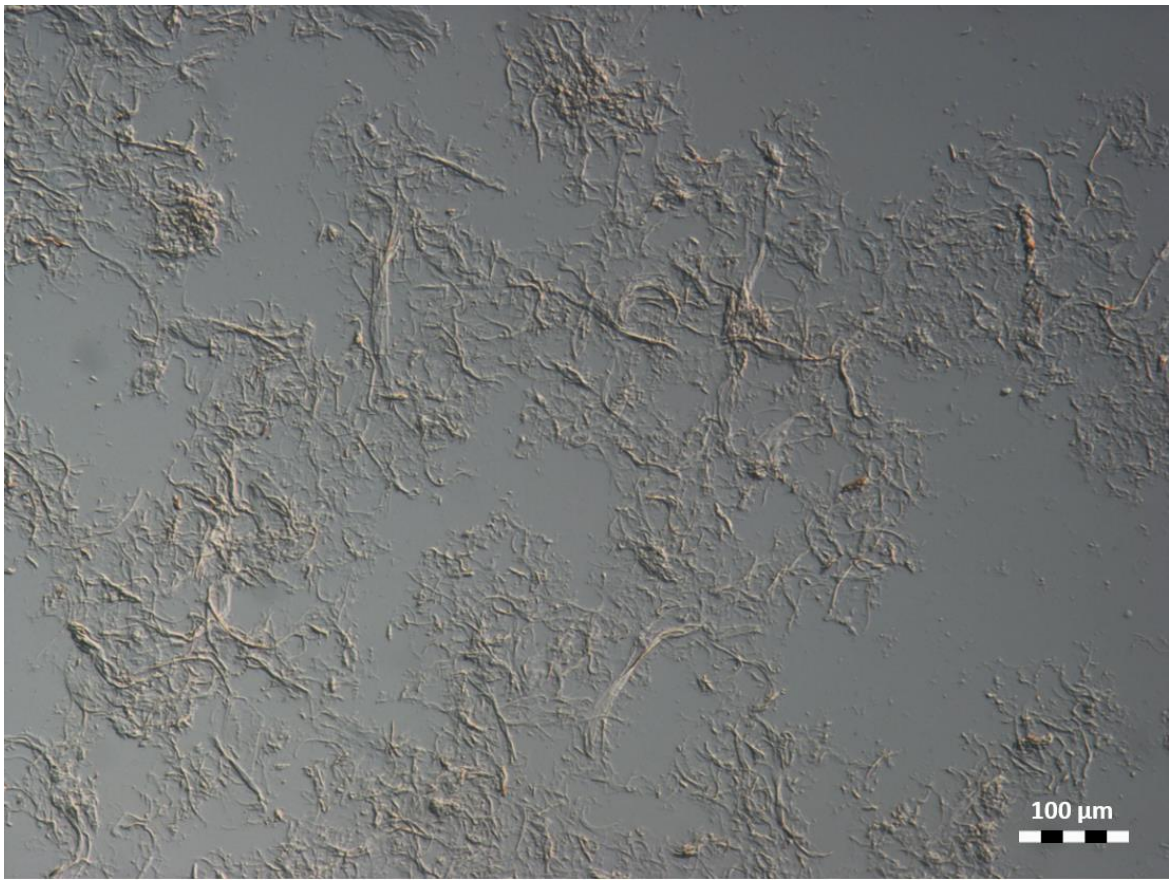

Figure 5.31 *– DIC microscopy image of 100 POP MFC produced at 9000 kWh/t with Zirconia D media.*

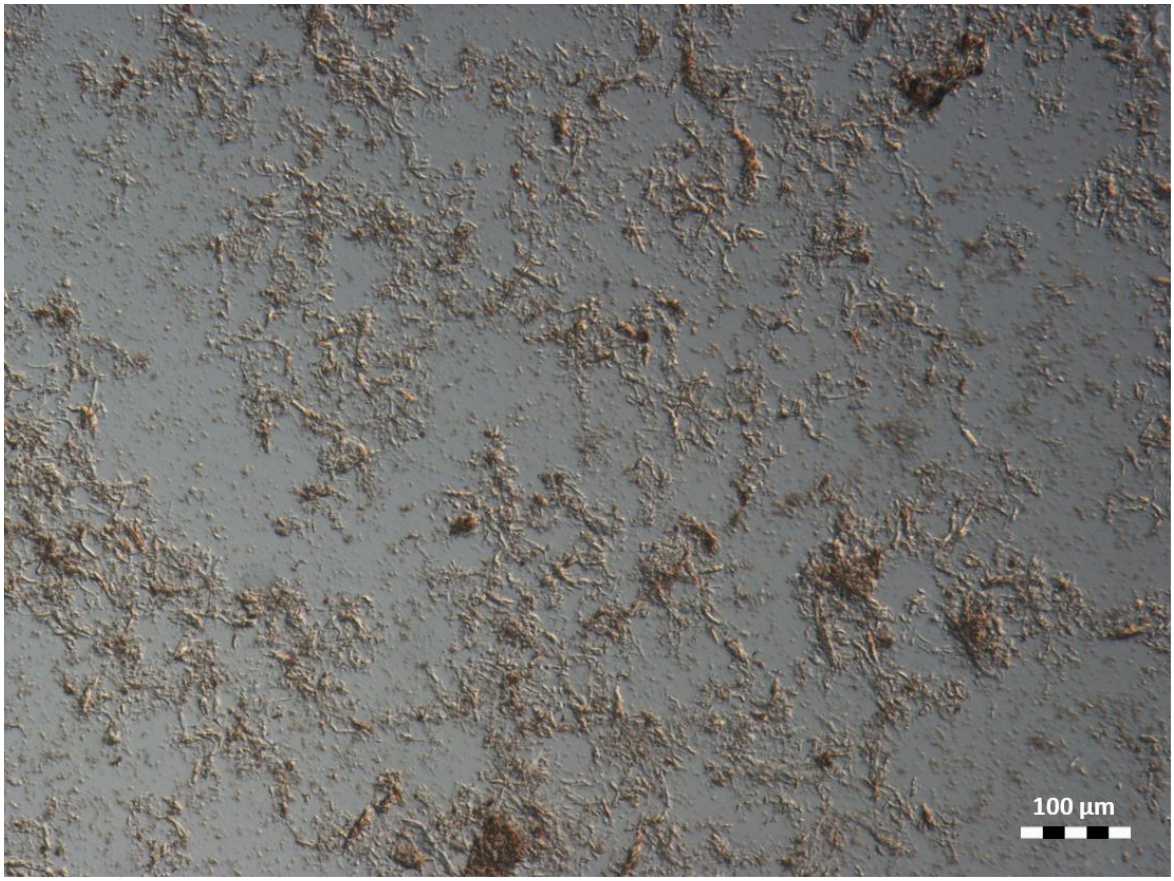

Figure 5.32 *– DIC microscopy image of 50 POP MFC produced at 9000 kWh/t with Zirconia D media.*

5.3.7. Discussion

These results demonstrate unambiguously that media surface roughness improves grinding efficiency, for any MFC quality parameter, which was expected from Section 5.2. Roughness does not significantly influence the peak tensile strength, nor appears to influence MFC quality parameters at given MFC lengths in the absence of mineral addition, indicating that its contribution to fibrillation is solely due to increasing fibre breakage rate. The mechanisms involved here are later investigated with microscopy in Section 5.5.

Mineral particles, as with roughness asperities, also aid in fibre length degradation, particularly for smoother media, which is expected to be for the same reason; during a media collision, mineral particles are compressed into a fibre or fibril, concentrating pressure.

Henceforth, when discussing this mechanism, both roughness asperities and mineral particles are referred to as *pressure-concentrating factors*.

For further insight, the number of mineral particles and media asperities in a 50 POP grind were estimated in Section A3.2 in Appendix A3, the results of which suggest that there are 500 – 1000 times as many mineral particles present as roughness asperities, though much of the mineral, being loose in suspension, may be excluded from the gap between colliding media.

Laser profilometry suggests that roughness asperities are typically between 20 – 30 μm in width (see Table A3.1 in Appendix A3), comparable to fibre widths and far larger than mineral particles (1 – 2 μm). This may explain the greater effectiveness of roughness at fibre breakage, despite mineral particles being more numerous; a media asperity can compress and break a larger contiguous area in a single impact event, whereas each mineral particle is limited to causing up to 2 μm of damage to the fibre cross-section. The pressure-concentrating events from mineral particles are therefore more homogeneously distributed about the impact site, so are less capable of breaking the fibre.

Though mineral particles may be too small for efficient fibre breakage, they are comparable to liberated fibril diameters, so the contact area under compression is likely ideal for fibril breakage. This, coupled with the much higher number of these pressure-concentrating events compared to those from roughness asperities, can explain the disproportionately strong effect the mineral has on liberated fibril degradation compared to fibre length degradation, thereby explaining why it has the opposite effect to roughness on *Fibrillation %* and *Fines B*.

In contrast to the immediate effect of roughness on length degradation, there is a clear lag time before the effect of the mineral is seen. This could be due to the lower effectiveness of

finer pressure-concentrating factors requiring damage accumulation from several collisions before fibre breakage accelerates. Alternatively, this could be caused by the low internal and external fibrillation early in the grind being is less capable of retaining mineral particles with the cellulose and preventing their exclusion as the media approach. In an attempt to decouple these influences, Section 5.4 tests a coarser mineral. The reason for the delay before the mineral degrades *Fines B* and *Fibrillation %* is obvious; such fibrils must first be generated before they are degraded.

The mineral content has a weaker influence for rougher media grinds. Three explanations are suggested; firstly, rougher media have less contact area in a collision, compressing fewer mineral particles into the fibre, with the remainder being unutilised between asperities. The second is that a certain 'penetration depth' may be required for efficient fibril breakage; *Mullite A* (R_a = 0.97 µm) has asperities comparable to mineral sizes, compared to substantially finer asperities on the smoother media. Consequently, for rougher media, the mineral is superfluous, though it enhances penetration depth for smoother media. Finally, the hypothesised pressure-concentrating effect may eventually be saturated; the rougher media would be closer to this limit at 100 POP, meaning that mineral addition would have a lesser influence; this possibility is investigated in Section 5.4, where differing mineral contents are added to *Mullite A* and *Mullite B* grinds.

5.3.8. Conclusions

This section supports Section 5.2 by demonstrating that the primary influence of media roughness is in improving fibre breakage efficiency, which improves fibrillation by increasing the breakage site frequency from which fibrils can fray. The influence of mineral content is more complicated; it enhances fibre breakage rate and improves tensile strength at lower

energy inputs for smoother media, but no clear benefit is seen with rougher media. Mineral particles readily degrade liberated fibrils, causing substantial drops in *Fines B* and *Fibrillation %*, somewhat lower peak tensile strengths, and rapidly degrading strengths beyond the optimum. Additionally, the grind must progress somewhat before the mineral content significantly influences any of these parameters. Various mechanisms to explain these observations were outlined in the previous subsection.

No influence of the mineral content on wear rate is clear, although the results from the glass and zirconia media imply that at low roughnesses, compressive failure and media composition may dominate wear rate. Despite smoother mullite media lowering energy efficiency, it is likely more sensible to use industrially than the rougher mullite due to the much lower wear rate.

The subsequent section investigates some of the suggested mechanisms regarding the role of the mineral content, by using a coarser mineral to test the hypothesis that fine mineral sizes inhibit fibre breakage, and varying grind POP for rough and smooth media to investigate whether the pressure-concentration effect can be saturated.

5.4. Influence of Mineral Content and Mineral Size

Two sets of experiments to supplement Sections 5.2 and 5.3 are briefly detailed here; firstly, an energy sweep was carried out with coarse mineral added, aiming to increase the area damaged by each particle, and secondly, varying quantities of IC60 mineral were added to *Mullite A* and *Mullite B* grinds to see if the results converge at low POP.

5.4.1. Coarse Mineral Grinds

A 50 POP energy sweep between 500 – 5000 kWh/t was carried out using *Mullite B,* with *Marmara flour* (from *Imerys*) as the mineral, a coarse GCC with 60 wt% of particles below 20 µm. Consequently, particle widths are similar to roughness asperity widths, so the coarser mineral should enhance fibre breakage if this factor is important.

DIC microscopy images taken at 0, 1000, and 3000 kWh/t (Figure 5.33 (a), (b), and (c)) show initially coarse mineral sizes, but by 1000 kWh/t they are much smaller, and by 3000 kWh/t are comparable to IC60. Therefore, unfortunately, only at low energy inputs can a coarse mineral size be assumed.

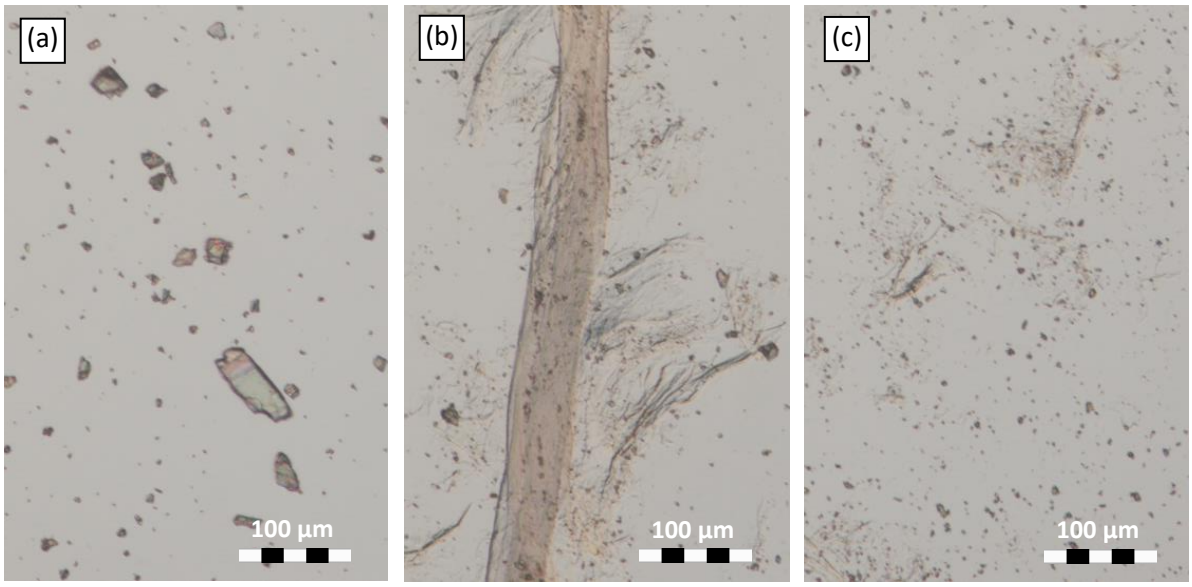

Figure 5.33 *– DIC microscopy images focusing on the mineral particles for the Marmara flour grinds at (a) 0 kWh/t, (b) 1000 kWh/t, and (c) 3000 kWh/t.*

Figure 5.34 shows that there is a similar delay before MFC length decay accelerates with the Marmara flour grind as the IC60 *Mullite B* series; the much coarser mineral is inconsequential here. Consequently, this delay instead believed to be due to the poor mineral capturing efficiency when the fibre is poorly fibrillated. However, after considerable fibrillation (1000 – 2000 kWh/t), the coarser mineral somewhat enhances fibre breakage compared to the

equivalent IC60 series, (despite the mineral itself already been greatly reduced in size), suggesting that coarse mineral particles enhance breakage rate in the manner hypothesised, but must be first captured effectively.

Figure 5.35 and 5.36 show *Fines B* and *Fibrillation %* content for each series. Both Marmara flour and IC60 cause similar degradation to liberated fibrils at high energy inputs; this is probably because at this stage, the Marmara flour has been ground to a size similar to IC60.

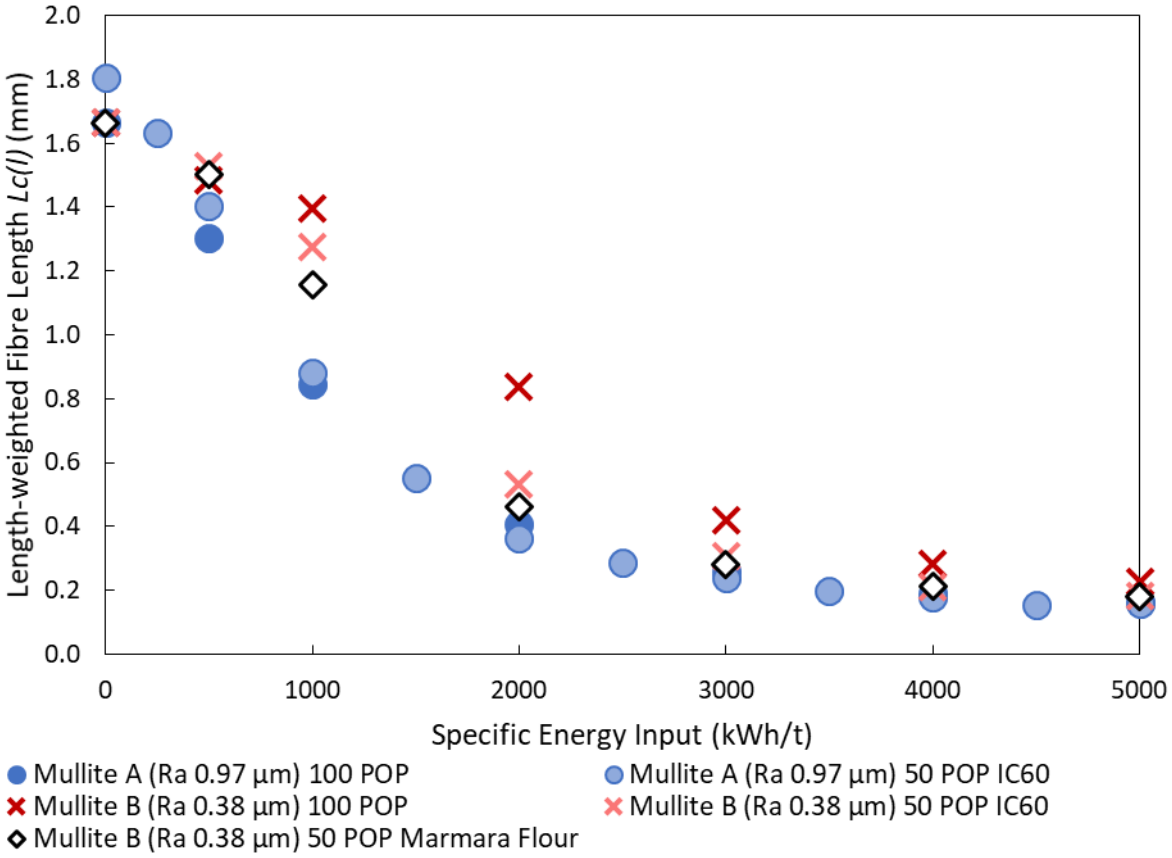

Figure 5.34 *– MFC Lc(l) of the Marmara flour series, compared with previous mullite energy sweeps.*

In summary, these results indicate that the effectiveness of mineral content at low energy input is limited by poor mineral retention between the colliding media rather than mineral size. The faster length reduction observed at moderate energy inputs suggests that future work investigating the influence of mineral size would be fruitful, if the minerals used are much more resistant to grinding.

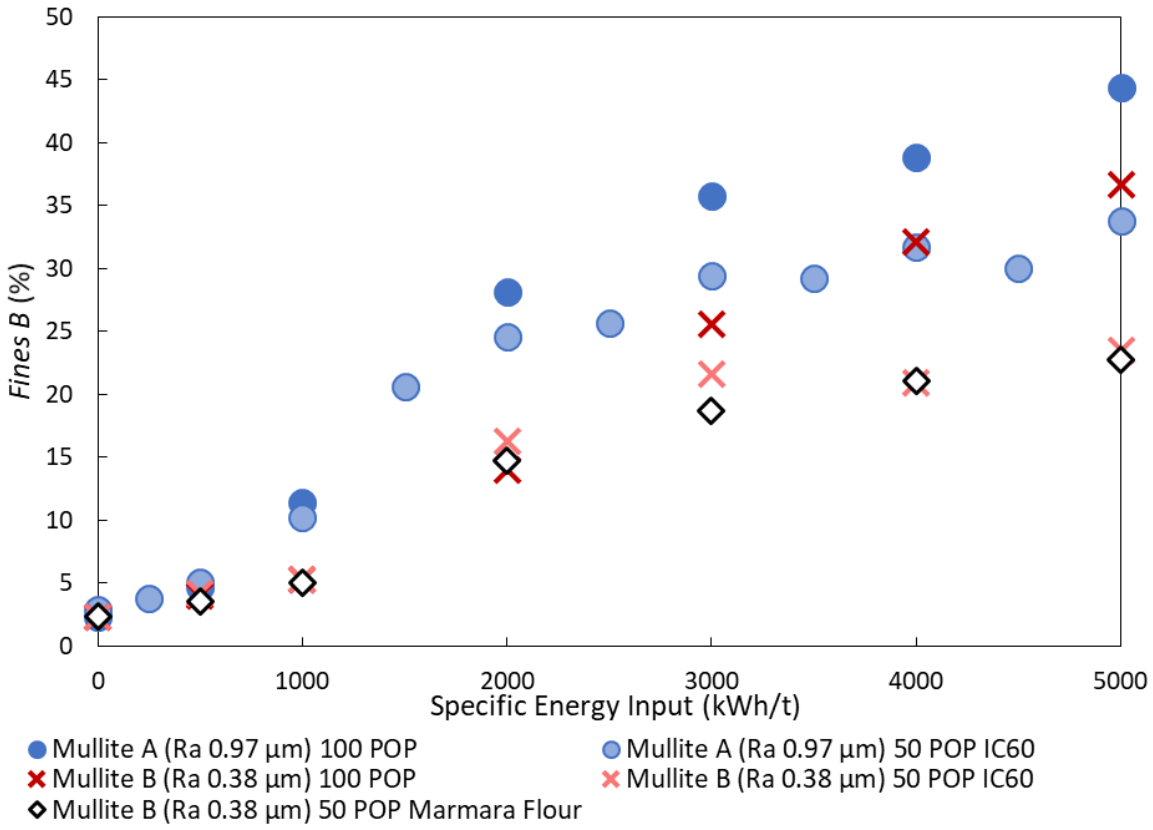

Figure 5.35 *– Fines B content of the Marmara flour series, compared with previous mullite energy sweeps.*

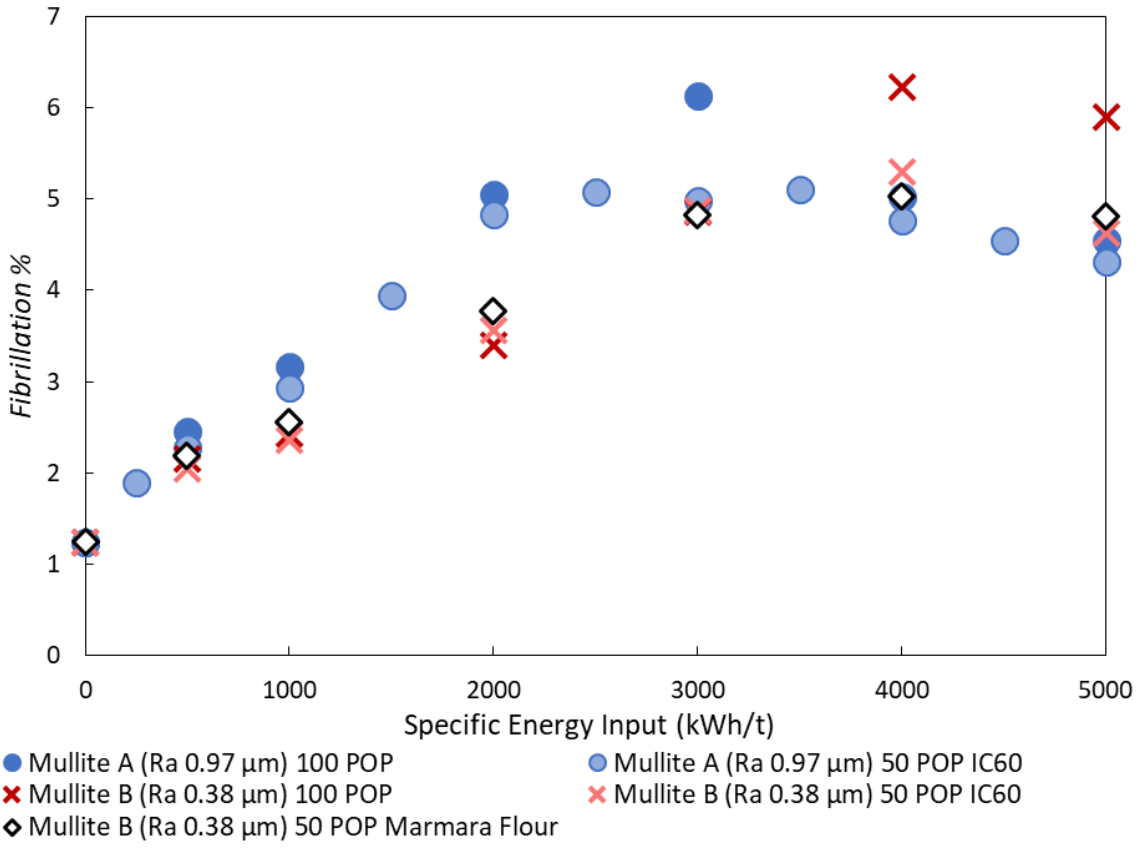

Figure 5.36 *– Fibrillation % of the Marmara flour series, compared with previous mullite energy sweeps.*

5.4.2. Mineral Content Investigation

Though only 50 POP and 100 POP grinds have been investigated so far, industrially, 20 POP grinds are common, and typically *Mullite A* wears sufficiently to decrease a 100 POP grind to around 90 POP; the sensitivity of MFC properties to mineral content, and how this interacts with roughness, must be understood. Consequently, grinds with *Mullite A* and *Mullite B* media were undertaken at 3000 kWh/t, at 100, 90, 50, 20, and 10 POP (with mineral contents of 0, 0.11, 1, 4, and 9 g/g fibre respectively).

Figure 5.37 shows how mineral content influences *Lc(l)*; the breakage rate increase with mineral content is much greater for the smoother media, with this media producing much coarser MFC than the rougher media at 100 POP, but comparable particle sizes at 10 POP. MFC length also decays with mineral content for the rougher media, albeit much more slowly. Both curves converge at very high mineral contents, indicating that the pressure-concentrating effect can be saturated. Since this asymptotic limit appears common to both roughness and mineral content, at 100 POP, *Mullite A* is already much closer to this limit than *Mullite B*, so the addition of mineral to the former has a much lesser effect.

Figure 5.38 shows the influence of mineral content on *Fines B* content. A similar pattern is seen as with *Lc(l)*, with both media experiencing a rapid decay which slows and converges at high mineral contents, implying that a similar limiting effect is applicable to damaging liberated fibrils.

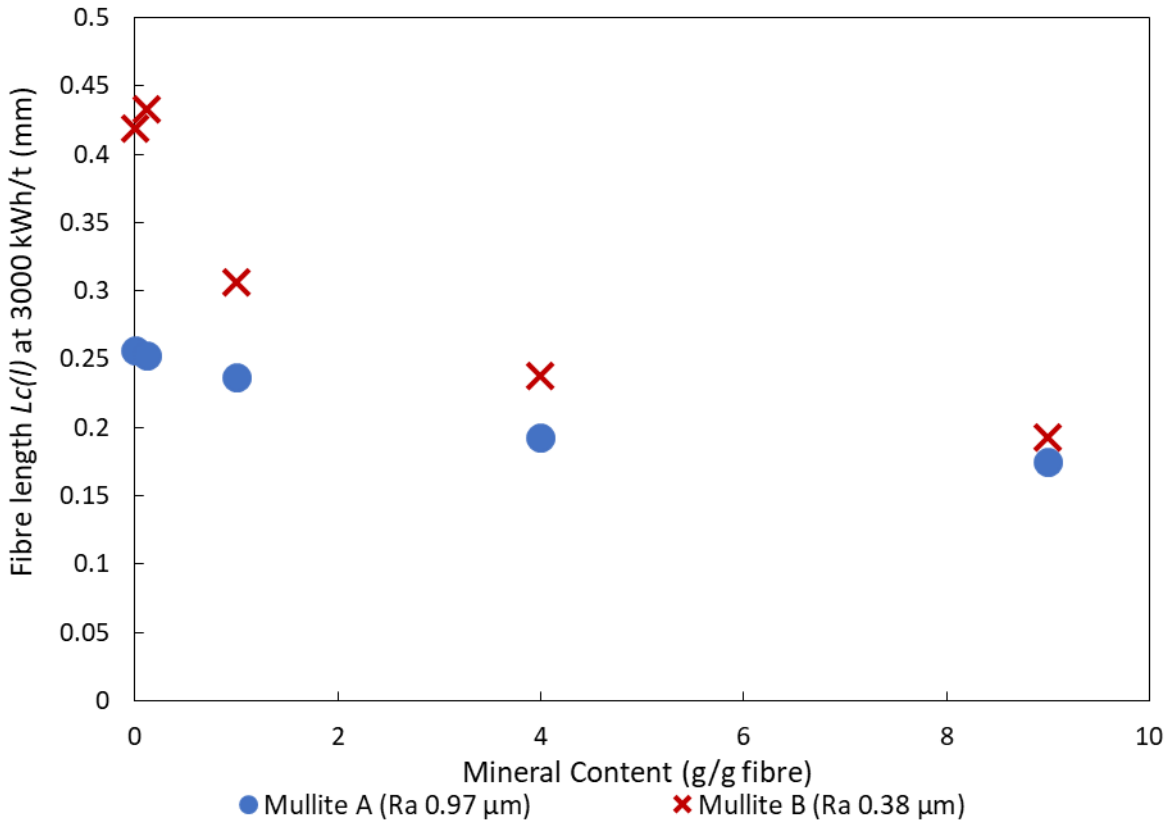

Figure 5.37 *– MFC fibre length at 3000 kWh/t versus mineral content for Mullite A and Mullite B media.*

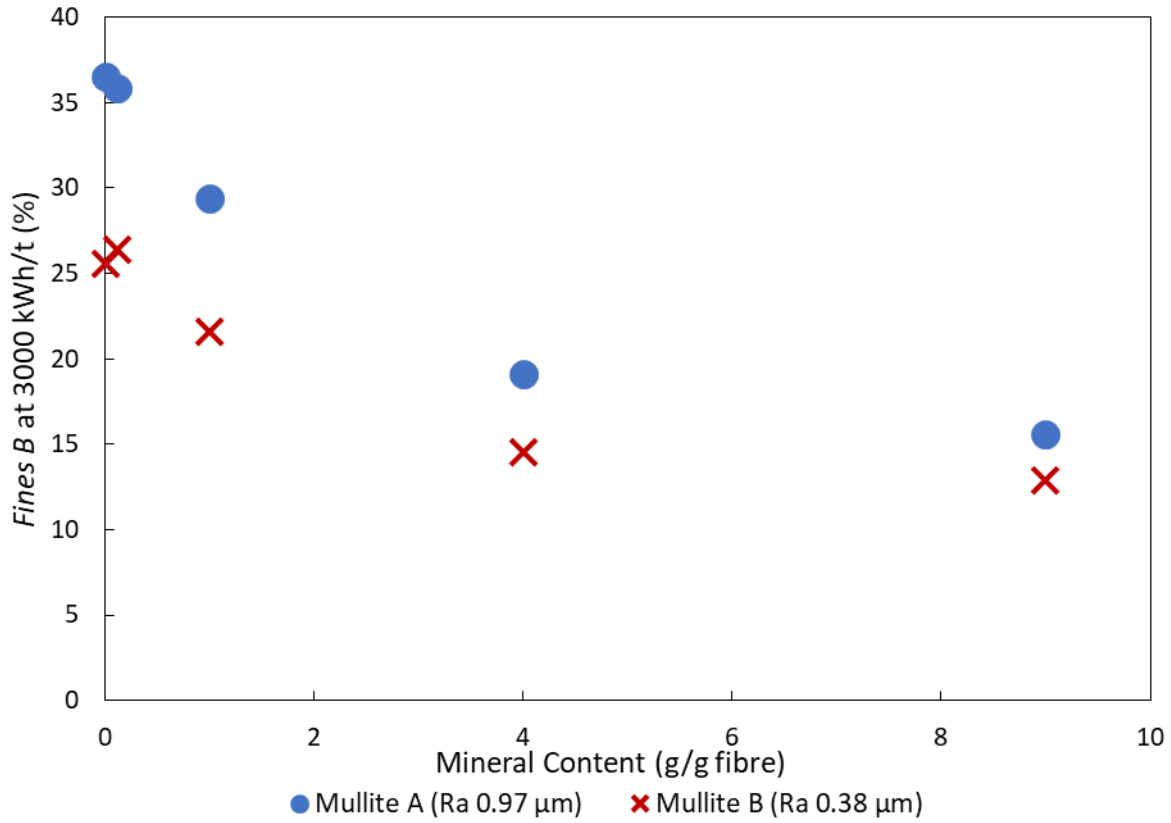

Figure 5.38 *– Fines B content at 3000 kWh/t versus mineral content for Mullite A and Mullite B media.*

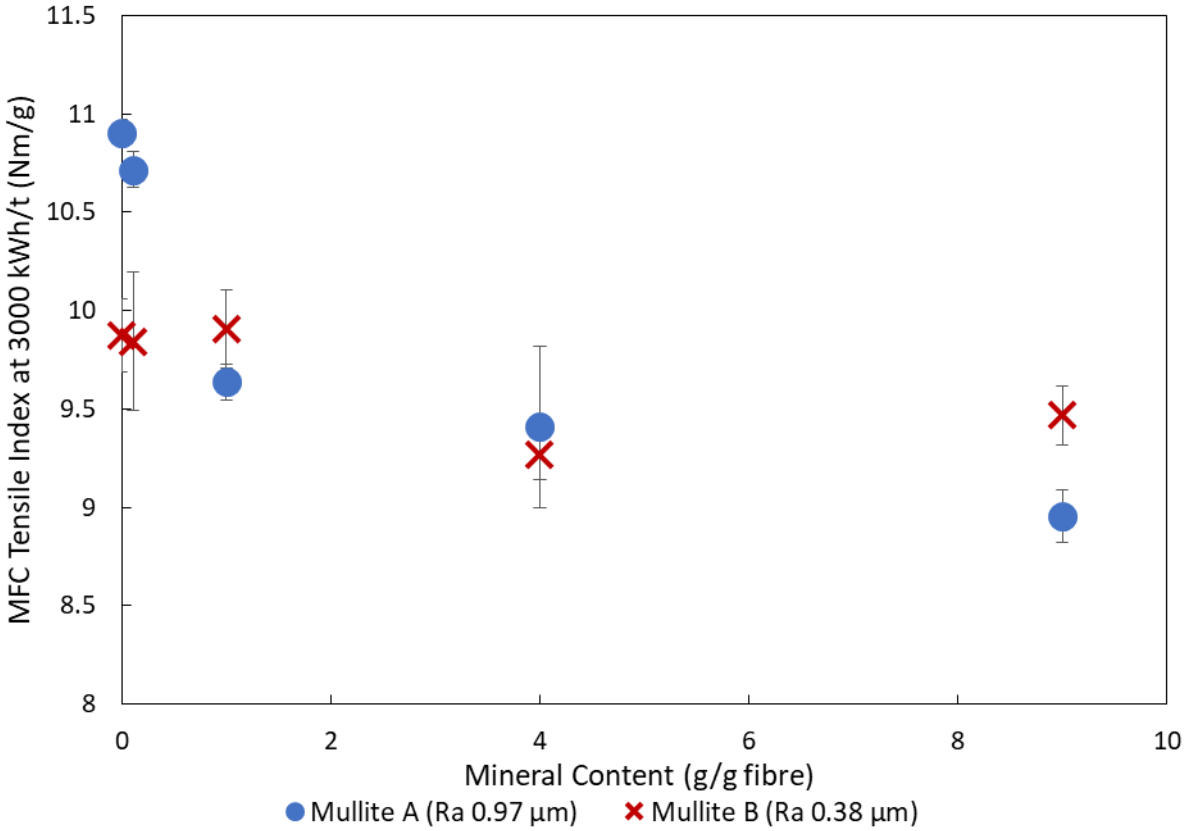

Figure 5.39 *– Tensile index at 3000 kWh/t versus mineral content for Mullite A and Mullite B media.*

As Figure 5.39 demonstrates, mineral content barely affects tensile strength for *Mullite B*, likely because of under-grinding at 100 POP and 3000 kWh/t; efficiency improvements from mineral addition are cancelled out by increased fibril degradation. In contrast, at 100 POP, *Mullite A* is at peak tensile strength, so experiences no efficiency benefit, instead exhibiting a small exponential-like decrease in strength with increasing mineral content.

At 3000 kWh/t, there is negligible difference in strength between the 100 POP and 90 POP grinds, suggesting typical media wear with *Mullite A* does not influence MFC properties. However, between 100 POP and 50 POP the *Mullite A* series loses around 1 Nm/g of strength, so the weaker strengths observed for very rough glass media in Figure 5.12 are likely due to extreme media wear (measured POP approaches 50%, see Figure 5.6).

To summarise, there is a limit to the effect of increasing mineral content on MFC length and Fines B degradation that is common with media roughness, so consequently mineral addition is more influential for smoother media.

5.5. Microscopy Analysis of Fibre Breakage

5.5.1. Introduction

As Section 4.1 demonstrates, intact fibres can plastically deform under compression at impact points, so microscopy observations can infer the mechanisms involved in grinding. The abundance of localised impact sites at low energy input (e.g. Figure 4.2) indicate that fibre breakage is dominated by normal collisions between media. Previous results in this chapter demonstrate that rougher media greatly enhance fibre breakage, but it is unclear whether other mechanisms, such as frictional shear forces, are present. By imaging a large number of deformations, judgements can be made on what mechanisms dominate.

Products from 100 POP grinds produced with *Mullite A* (R_a = 0.97 µm) and *Mullite B* (R_a = 0.38 µm) with energy inputs of 500 kWh/t were imaged with DIC microscopy. The low energy was necessary to minimise second-order fibrillation effects obscuring media impact events. All fibres on the slide were imaged, yielding over 100 fibres for both cases, and deformation and breakage features were categorised. Independent liberated fibrils were not included in this analysis.

For this classification, a *breakage* is an event where the fibre cross-section has completely broken, inferred from damage at *fibre endpoints*. A *deformation* is where a collision has caused damage but failed to break the fibre in two. These features are classified as follows:

5.5.2. Feature Categorisation – Fibre Deformations

Fibre Delamination

Fibre delamination deformations occur where the cell wall has been crushed by a media collision, radially separating the constituent fibrils from their neighbours (this does not necessitate fibril cross-sectional breakage). These are sub-categorised as 'large' or 'small' based upon how much of the cell wall remains intact. Examples are shown as Figure 5.40.

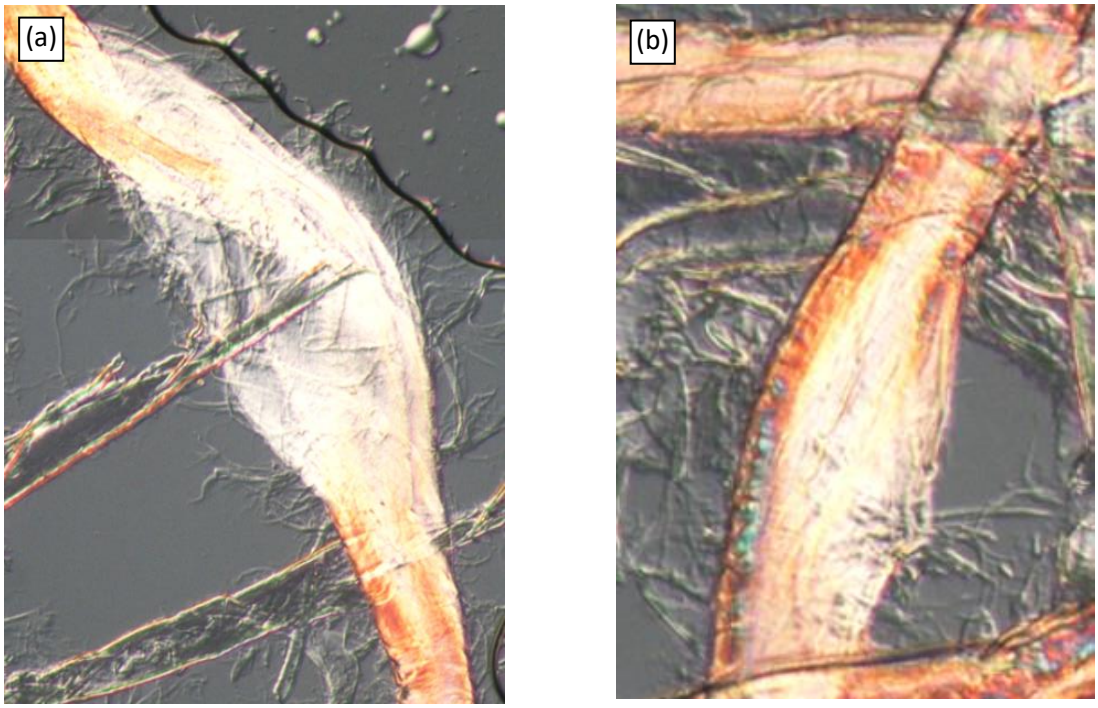

Figure 5.40 *– Examples of (a) a large delamination and (b) a small delamination.*

Partial Fracture

Partial fractures occur where an impact has not clearly delaminated fibrils, but instead has caused a brittle breakage across a fraction of the fibre cross-section. *Large* partial fractures are defined as at least half of the cross-section broken, with others being *small* partial fractures. An example of each is shown as Figure 5.41.

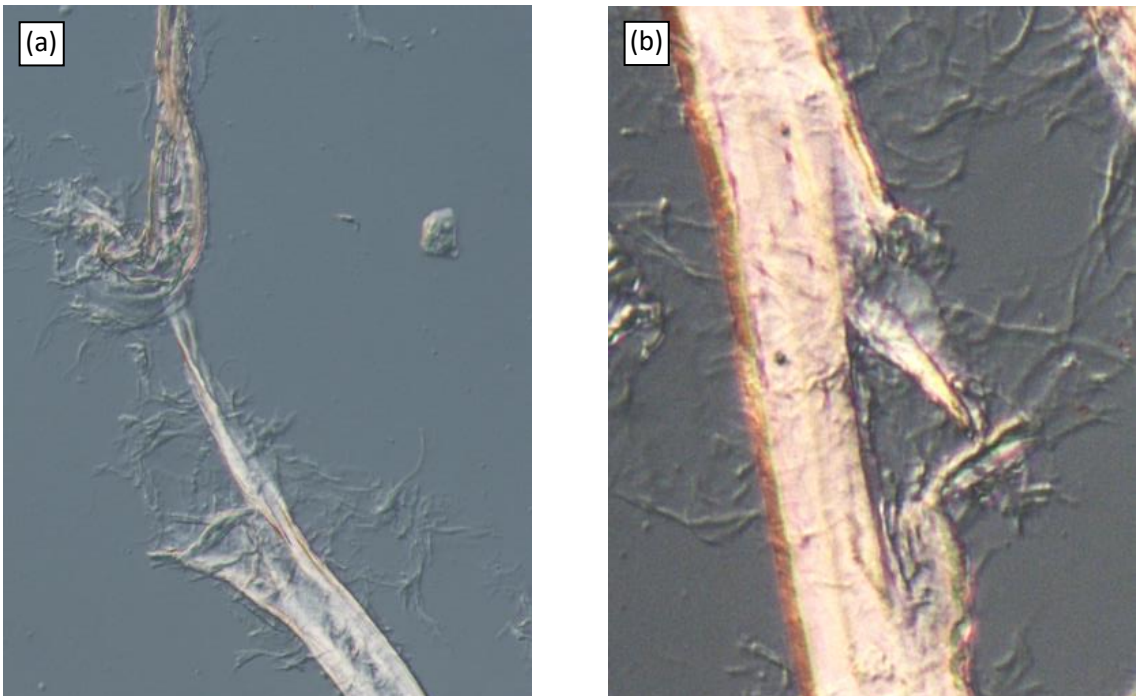

Figure 5.41 *– Examples of (a) a large partial fracture and (b) a small partial fracture.*

5.5.3. Feature Categorisation – Fibre Breakage

The fibre endpoints were classified as follows:

1. End intact – the original fibre endpoint is still present (see Figure 5.42 (a)).

2. Brittle break – the fibre has completely broken in a brittle manner (see Figure 5.42 (b)).

3. Break at delamination – an impact that caused a delamination event also broke the entire cross-section (see Figure 5.43 (a)).

4. Unclear category – the manner in which the fibre broke is unclear, usually because second-order fibrillation effects following breakage have obscured those features (e.g. see Figure 5.43 (b)).

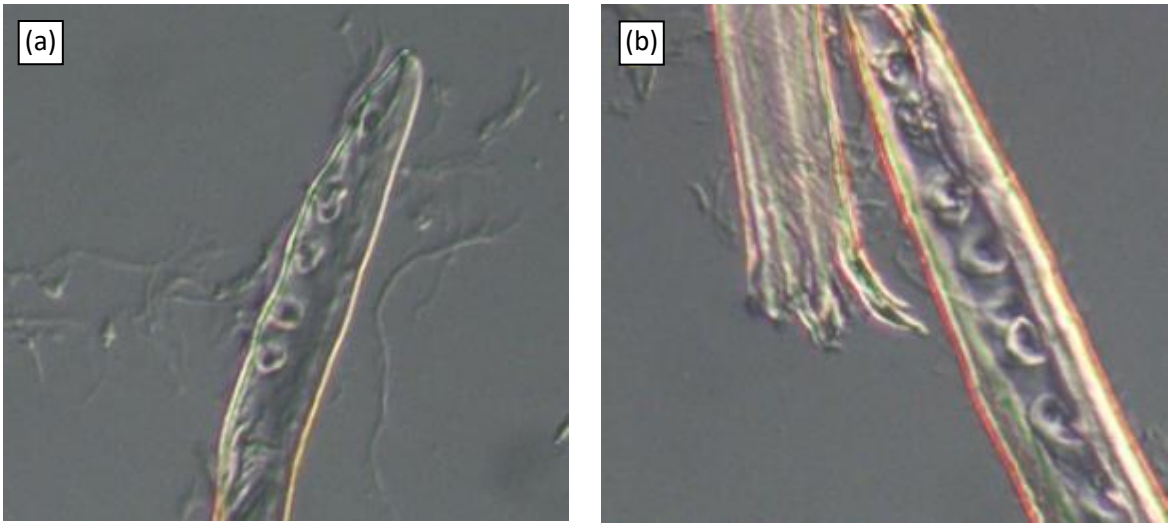

Figure 5.42 *– Examples of (a) an intact fibre end, and (b) a brittle fracture fibre end.*

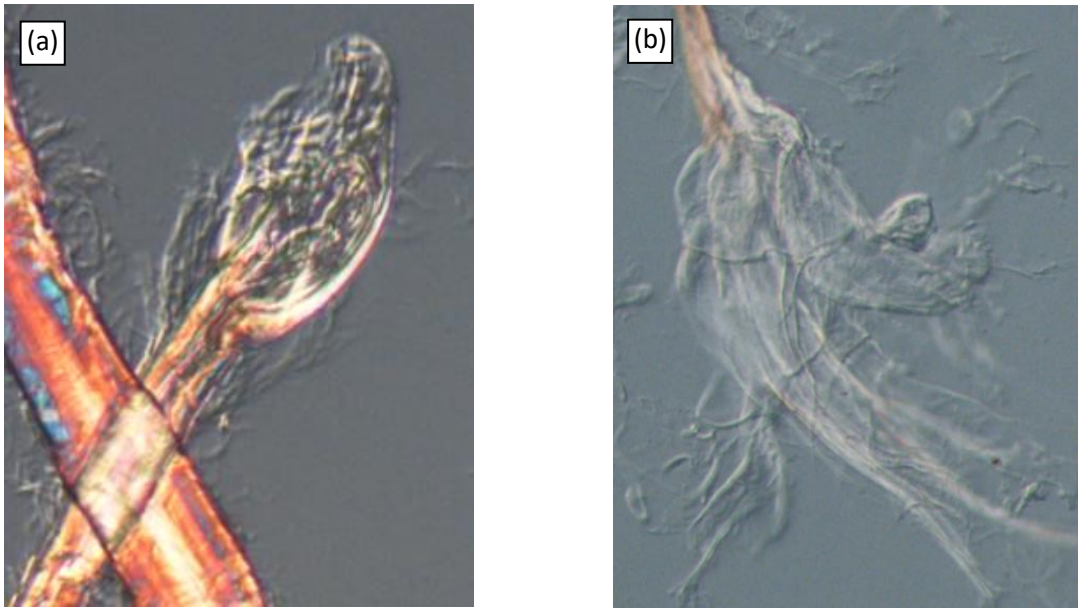

Figure 5.43 *– Examples of (a) a delamination at a broken end, and (b) a broken end where the breakage type is obscured by extensive fibrillation.*

5.5.4. Microscopy Assay Results

The results of these categorisations are shown in Table 5.2. In addition to assessing the deformations and breakages, fibre lengths were measured manually, giving *Lc(n)* values of 1.64 mm and 1.94 mm for *Mullite A* and *Mullite B* respectively; these are much higher than the fibre analyser *Lc(n)* as the fines present are excluded from the analysis. This allows for the frequencies of each feature per unit length to be calculated.

It is unclear why some fibres delaminate during impacts whereas others undergo brittle fractures; this is likely influenced by the different fibre types present (i.e. latewood and earlywood fibres), and whether the cell wall has sufficiently swollen with water.

Table 5.2 *– The results of the microscopy assay, showing total amounts of deformations and breakages, and values per unit fibre length.*

		Total		**Frequency per unit fibre length (m^{-1})**	
		Mullite A	***Mullite B***	***Mullite A***	***Mullite B***
Fibre Deformations	Large delamination	36	29	196	80
	Small delamination	32	49	174	151
	Large partial fracture	25	7	136	22
	Small partial fracture	22	19	120	58
Fibre Breakages	End intact	143	254	779	780
	End brittle break	27	23	147	71
	Break at delamination	21	20	114	60
	End broken, unclear category*	19	9	103	29
	End obscured†	14	30	76	92
	Fibres analysed	112	168		
	Total analysed length (mm)	183.6	325.5		
	Average fibre length *Lc(n)* (mm)	1.64	1.94		
	Total breakages per fibre	0.299	0.155		
	Total breakage frequency (m^{-1})‡	182	80		
	Total deformation frequency (m^{-1})	626	310		
	Fraction of deformations leading to breakage	22.6%	20.5%		

**'Unclear category' is where the fibre end has experienced extensive fibrillation or fraying, making it impossible to determine the manner in which it originally broke.*

† Some ends were overlapped by other fibres and were invisible.

‡ The sum of all broken fibre ends is divided by two to avoid double counting.

Because delamination deformations do not necessitate fibril breakage, they are *not* expected to be enhanced by roughness asperities concentrating pressure. It is surprising therefore that the rougher mullite greatly increases delamination deformation frequency (which implies a higher *stress number*), and increases the typical deformation size. A potential explanation is suggested in Section 5.2.2; rough media may increase random motion out-of-plane from the media streamline, increasing collision frequency. Additionally, the increased friction may

reduce the tendency of fibres to slip from the gap when compressed in a media collision, increasing deformation frequency and severity.

The rougher media gives a three-fold increase in brittle-like partial fracture frequency, whilst also increasing the proportion of larger fractures. This increase is far greater than for the delamination deformations, indicating that this is not due to better capturing efficiency or a higher stress number. Rather, this is what one would expect if media asperities were to concentrate forces to cause localised cross-sectional breakage.

Both brittle-like and delamination-like breakage frequencies are roughly doubled when the rougher media is used, though these are underestimates as the *Mullite A* MFC has many uncategorised breakages (a faster breakage rate means more second-order fibrillation effects to obscure breakages). This two-fold breakage rate increase is consistent with Figure 5.23, which shows that at 500 kWh/t, *Mullite A* has roughly half the $K_{R,Op}$ value as *Mullite B*.

Despite the breakage rate difference, the fraction of deformations that have caused complete fibre breakage is roughly 20% for both *Mullite A* and *Mullite B.* Therefore, although higher roughnesses enhance fibre breakage, it also permits some impacts to cause partial fractures that would have otherwise had insufficient local pressure to do so, and there is a possible improvement in capturing efficiency and stress number also, maintaining the 'success rate' of each collision.

Essentially all deformations could be classified with the listed criteria, and are consistent with normal media-media impacts (i.e. highly localised damage). The presence of other mechanisms, such as a shredding action induced by shearing motion, were not obvious, indicating that they have little influence on fibre breakage. This does not rule out these

alternative mechanisms improving fibrillation subsequent to breakage, but plots of *Fines B* and *Fibrillation %* against *Lc(l)* (Figures 5.9, 5.11, 5.25, and 5.27) show no clear differences between roughnesses at 100 POP, which seems to preclude this.

5.5.5. Summary

The features observed from microscopy of low energy MFC indicates that fibre breakage is dominated by normal media-media collisions, and that rougher media enhances both deformation rate and breakage rate. The rougher media greatly increases the frequency of brittle-like breakages and partial fractures, supporting the hypothesis that media asperities concentrate forces and enhance local cross-sectional breakage. Rougher media also increase delamination deformations, though to a much lesser extent; this indicates that roughness may improve fibre capturing efficiency (possibly by reducing slippage under compression), though there may also be a more chaotic media motion that increases impact frequency.

5.6. Contact Mechanics – Incorporating Media Roughness

The previous section is evidence that the beneficial effect of roughness on fibre disintegration is due to the increased probability of fibre breakage in a normal media-media collision. The fibre would make contact with the media at the roughness asperities, so collision pressure is concentrated in those regions. The Hertzian contact mechanics model, previously applied in Section 4.2 to cellulose fibre deformation, can be further modified to incorporate roughness and estimate the pressures experienced at these asperity 'microcontacts'.

Two rough surfaces in contact will only meet at their asperities, so the *real* contact area is a fraction of the *nominal* contact area calculated from Hertzian theory[85]. A rougher surface has a lower real contact area, though higher contact pressures will elastically deform and flatten the asperities, increasing contact area (when colliding with a fibre, the cellulose would deform

to accommodate the asperities). The shape of the asperities influences contact pressure; if they are hemispherical, with a Gaussian height distribution, real contact area grows proportionally with increasing load applied, *maintaining the same pressure at a microcontact*[85]. With these assumptions, microcontact pressure $\bar{p}_r$ can be estimated[85]:

$$\bar{p}_r = \frac{F}{A} = 0.35Y^*(\sigma_s k_s)^{0.5} \ldots [5.1]$$

where σ_s is the Gaussian standard deviation of summit heights, A is the real contact area, and k_s is the asperity curvature. For a Gaussian-like summit height distribution, the Gaussian standard deviation σ_s is approximately equal to the RMS surface roughness R_q[85] (defined in Section 3.16). For a media-media collision, R_q must be doubled to accommodate roughnesses of both beads, but for media colliding with cellulose, R_q of a single bead is sufficient (cellulose 'asperities' are too soft to be of consequence).

The mean curvature of all surface asperities is used as the k_s value. According to Johnson[85], this is approximately the root-mean-square curvature of the surface, σ_k. This is calculated using the curvature k at each point on the surface, found by comparing the height z at point i with the neighbouring heights at *i-1* and *i+1*:

$$k = (z_{i+1} - 2z_i + z_{i-1})/h^2 \ldots [5.2]$$

$$k_s \approx \sigma_k = \sqrt{(1/n)\sum_{i=1}^{i=n} k^2} \ldots [5.3]$$

where z_{i-1}, z_i, and z_{i+1} are heights at points *i-1*, *i*, and *i+1* respectively, h is the distance between points (the sampling interval), and n is the number of data points.

It is shown later in Figure 5.45 that mean asperity curvature is approximately proportional to RMS surface roughness:

$$k_s \propto R_q \ldots [5.4]$$

Substituting into Equation 5.1:

$$\bar{p_r} \propto Y^* \left({R_q}^2\right)^{0.5}$$

$$\bar{p_r} \propto Y^* R_q \ldots [5.5]$$

It can be expected therefore that *microcontact pressure is directly proportional to surface roughness*. According to this theory, increasing media momentum does not increase microcontact pressure, but instead increases the microcontact area that experiences this pressure. Both of these are expected to increase breakage rate. In a media-fibre collision, *Y** is defined by Equation 4.1 and can apply to either cell wall deformation ($Y_{C,W}$) or microfibril deformation ($Y_{C,mi}$).

The roughness parameters for each media used in Section 5.2 were used to calculate the microcontact pressure according to Equation 5.1. Figure 5.44 plots these pressures (on a $Y_{C,mi}$ basis, i.e. what the *microfibrils* experience) against arithmetic roughness R_a, showing (a) absolute pressure, and (b) the microcontact pressure relative to the Hertzian pressure for mathematically smooth media, assuming an acceleration of 100 m/s^2. From this, microcontact pressure is expected to increase linearly with roughness, which can explain the effect on fibre breakage rate observed throughout this chapter.

Figure 5.44 (b) suggests that the roughness can cause a pressure concentration effect between 20 and 200 times that of mathematically smooth media, and Figure 5.44 (a) shows extremely high microcontact pressures, up to around 5000 MPa. Microcontact pressure estimates for

Mullite A and *Mullite B* are 2930 MPa and 1640 MPa respectively, differing by a factor of two, which is interesting considering that Section 5.4 shows differences in fibre breakage rate are of that magnitude.

Even the smoothest media gives a microcontact pressure of 690 MPa, which is still able to break fibres, albeit much more slowly than rough media. Homogenisers, with typical maximum pressures of around 100 MPa, may require up to 20 passes to disintegrate untreated fibres into MFC[1-2], so the author suggests that this poor performance is because of the lower localised pressures involved compared to stirred media milling.

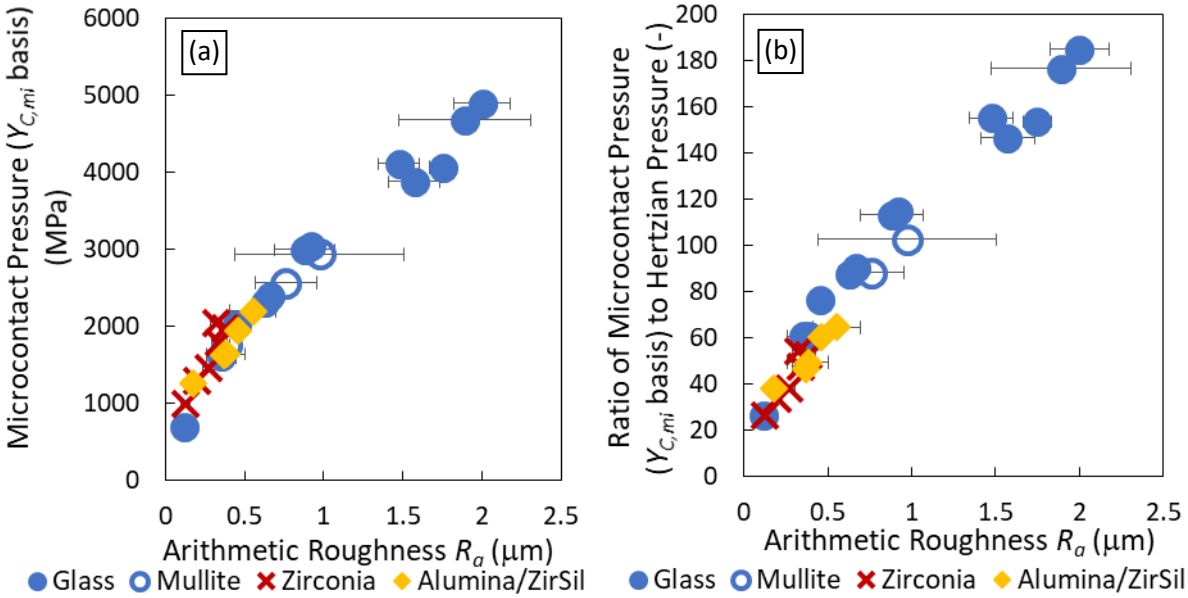

Figure 5.44 *– (a) Theoretical microcontact pressure and (b) ratio of microcontact pressure to Hertzian pressure, versus media roughness, at an acceleration of 100 m/s² for $Y_C = Y_{C,mi}$.*

The data spread in Figure 5.44 is due to errors in the assumption that R_a is proportional to the parameters on the right hand side of Equation 5.1; the vast majority of this is because the correlation between R_a and k_s is far from perfect, see Figure 5.45.

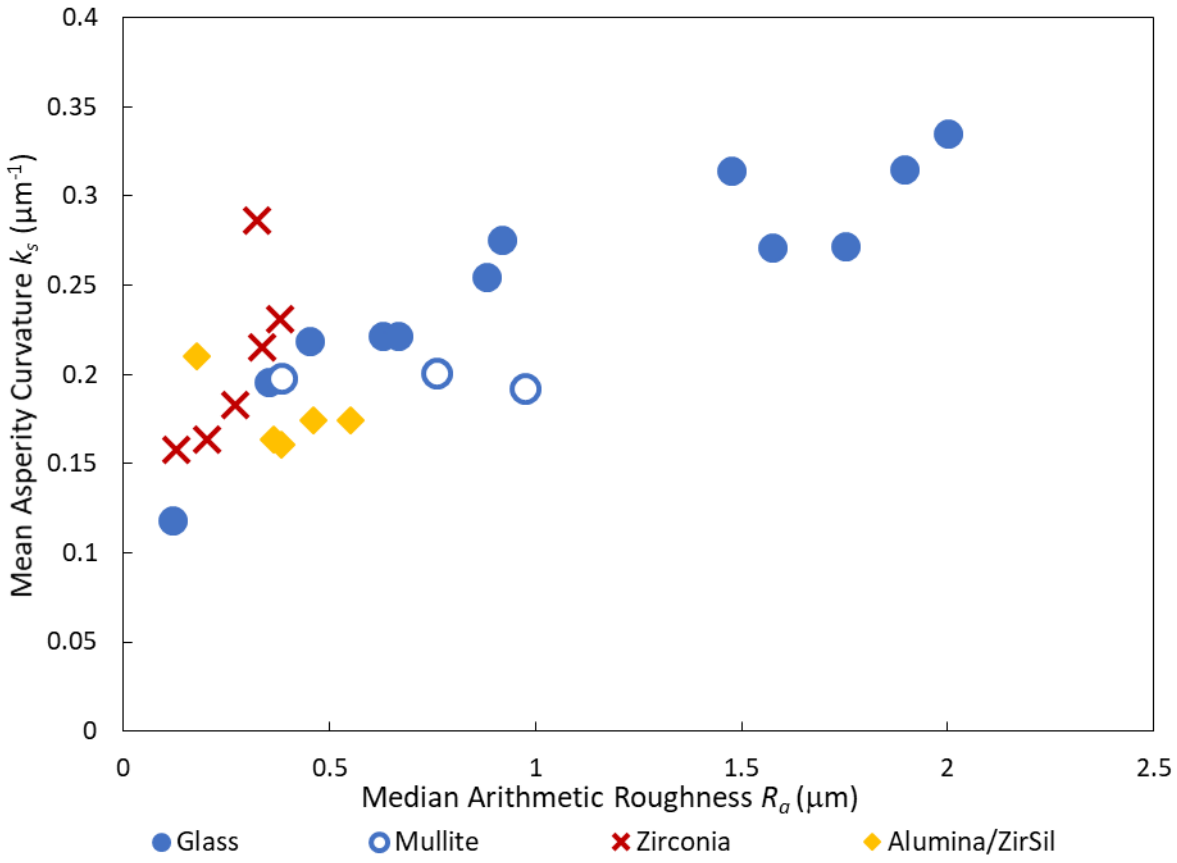

Figure 5.45 *– Mean asperity curvature versus median arithmetic roughness for each media species.*

With microcontact pressures calculated, and found to be roughly proportional to media roughness, the figures in Section 5.2 can be replotted against microcontact pressure rather than R_a. Two examples are shown here, with Figure 5.46 and 5.47 showing plots of microcontact pressure with *Lc(l)* and tensile index respectively. The *y*-intercept in Figure 5.45 indicates that media with minimal peak heights have a correspondingly higher peak frequency to maintain a significant minimum k_s value. Consequently, the calculated microcontact pressure, proportional to a geometric average of R_q and k_s, stretches the plot in the *x*-direction at low roughnesses compared to the plot against R_a. Comparing Figures 5.46 and 5.47 with their R_a-based equivalents (Figures 5.7 and 5.12), this transformation is obvious. The general pattern, however, is very similar.

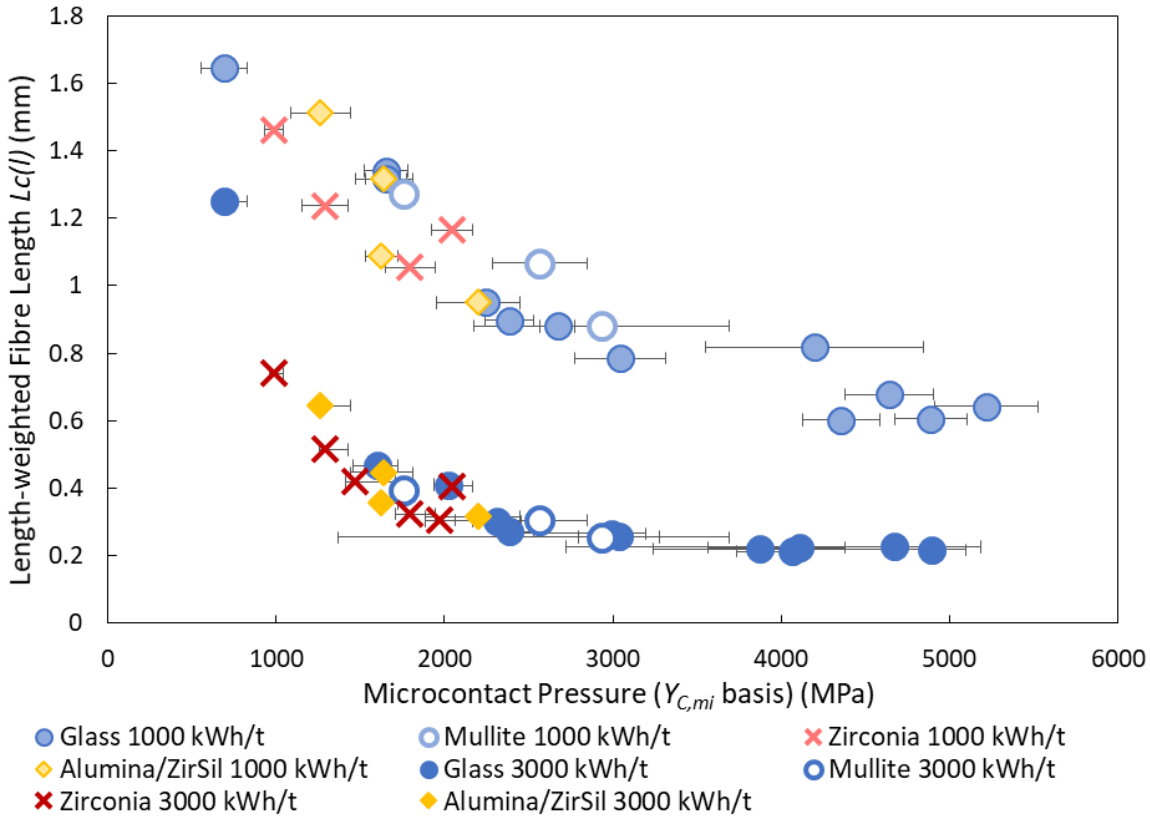

Figure 5.46 *– MFC fibre length at 1000 kWh/t and 3000 kWh/t versus microcontact pressure, calculated on the basis of microfibril compression assuming 100 m/s^2 acceleration.*

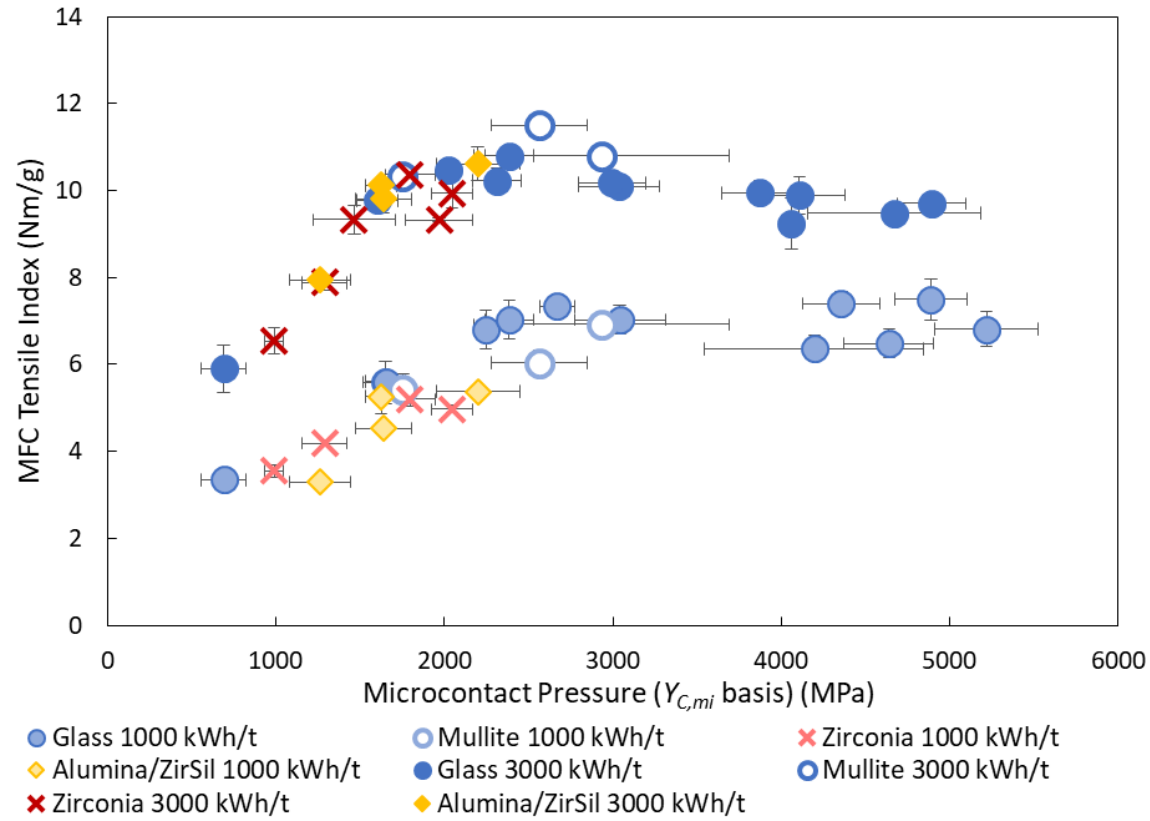

Figure 5.47 *– MFC tensile index at 1000 kWh/t and 3000 kWh/t versus microcontact pressure, calculated on the basis of microfibril compression assuming 100 m/s^2 acceleration.*

To summarise, the Hertzian contact mechanics theory previously modified for cellulose compression has again been modified to incorporate media surface roughness, to estimate the microcontact pressure experienced by the fibre at the asperities. Roughness can be expected to enhance microcontact pressure in a linear manner, with the media used in this study amplifying the pressure between 20 to 200 times the Hertzian pressure. Replotting the results from Section 5.2 against this calculated microcontact pressure gives similar results, so provides no new insights. However, the theory predicting a large increase in normal pressure experienced by the cellulose with roughness can explain the enhanced fibre breakage rate, and supports the hypothesis that this improvement is due to concentrating pressure in localised regions during normal media-media collisions.

5.7. Summary

Section 5.2 shows that media roughness strongly enhances grinding efficiency, and follows a good enough correlation with MFC parameters for it to be predictive. Evidence from this study suggests that roughness does not improve fibrillation directly, but increases the rate of fibre cross-sectional breakage, with the broken regions fibrillating independently. These results implied, but did not prove, that the optimum energy input is lower for rougher media, suggesting the potential for energy cost savings; however, these results also show a good correlation between media roughness and media wear rate, so there is an economically optimum roughness that balances energy cost with media cost. Controlling for roughness also allowed for a fair comparison of media with different densities; as expected from the higher stress intensity, higher density media gave higher power draws, and increased fibre breakage rate, though at a cost of poorer fibrillation at each breakage site.

In Section 5.3, energy sweeps were completed for four media species with different roughnesses. This confirmed that rougher media primarily influences energy efficiency, showing that higher tensile strengths are obtainable at lower energy inputs with rougher media. 100 POP and 50 POP energy sweeps were also compared; mineral addition was found to improve tensile strength at lower energy inputs for smoother media, although this slightly reduces peak tensile strength and increases degradation at high energy inputs. Rougher media grinds showed no benefit from mineral addition, and was instead degraded. The mineral content aids fibre breakage, but disproportionately enhances breakage of liberated fibrils, which likely explains the lower peak tensile strengths.

Section 5.4 further clarified the influence of mineral content. A coarser mineral was used in an attempt to enhance breakage rate, but the delay before the mineral was seen to affect MFC length was similar to the finer mineral, so it was concluded that this delay was due to mineral exclusion from a collision, the propensity for which is decreased as fibres fibrillate and capture mineral particles. The variation in MFC properties at 3000 kWh/t with mineral content was also investigated, finding that with the addition of mineral beyond 50 POP, the same trends seen between 100 POP and 50 POP continue, with MFC length being decreased and *Fines B* being degraded at higher mineral contents, though diminishing with scale. The results for rougher and smoother mullite also converge at higher mineral loadings, showing that roughness and mineral particles share the same limit of the pressure-concentrating effect.

The microscopy images in Section 5.5 show a great increase in brittle fracture rate when rougher media is used, implicative of the pressure-concentrating effect that the roughness asperities are asserted to have. Additionally, ‘delamination’ impacts also increase, indicating

either an increase in stress number, or an increase in capturing efficiency due to media friction reducing fibre slippage.

Finally, Section 5.6 has further developed the Hertzian contact theory model to consider a rough media colliding with a cellulose surface. Microcontact pressures on the microfibrils are estimated to be between 500 – 5000 MPa, an increase in pressure 20 – 200 times greater than expected from mathematically smooth media. Microcontact pressure was found correlate linearly with surface roughness, and appears to rationalise the enhancement in breakage rate seen in normal media-media collisions.

In addition to identifying the existence of an economically optimum media roughness, the interplay between media roughness and mineral content is another important industrial implication; if a smooth media is used, lower POP grinds should be undertaken, since the mineral particles can compensate somewhat for the poorer fibre breakage and lower energy efficiency. Conversely, if a sufficiently rough media is acquired, the media alone is highly capable of efficient grinding, and no mineral should be added since it lowers peak tensile strength without giving further efficiency improvements.

A limited attempt to consider the influence of stress intensity was attempted, by considering media of different densities in Section 5.2 and 5.3, and in the former, the product of stress intensity and media roughness appeared to correlate with MFC length. However, the stress intensity range was insufficient to properly validate this correlation, and the influence of stress intensity itself, though invoked in Chapter 4, has not yet been unambiguously demonstrated for cellulose grinding. This is addressed in the next chapter.

6. THE EFFECT OF STRESS INTENSITY ON CELLULOSE GRINDING

6.1. Introduction

This chapter investigates the effect of stress intensity on fibre breakage and fibrillation parameters, and the interaction between this and media roughness. As a preliminary investigation, this chapter starts by revisiting data from 50 POP *Mullite A* energy sweeps from Chapter 4. The second section considers a series of mineral-free grinds with zirconia media at a single energy input, with many permutations of media size and impeller speed; this investigates the extent to which stress intensity theory is adhered to, once surface roughness is kept constant. Finally, data from the current chapter and Chapter 5 are combined, along with additional grinds carried out under a range of conditions to investigate the interaction between stress intensity and surface roughness, for a more complete description of the influence of operating conditions on MFC length and fibrillation.

6.2. Comparison of 50 POP Mullite Energy Sweeps

Previous energy sweeps in Chapter 4 varied impeller speed and media size for 50 POP *Mullite A* grinds. Considering these results together, a preliminary assessment of the importance of stress intensity can be made. Table 6.1 shows the stress intensities (calculated using Equation 2.3) and constituent variables for each series.

Table 6.1 *– Stress intensities, impeller speeds, and media sizes of each Mullite A series in Chapter 4.*

Stress Intensity ($x10^{-3}$) (Nm)	Impeller Speed (rpm)	Media Size (mm)
0.36	800	1.7
0.48	400	2.9
0.63	800	2.0
1.92	800	2.9
4.32	1200	2.9

The corresponding energy-size relationships are shown as Figure 6.1. At low energy inputs, higher stress intensities cause a faster decay, with lower stress intensities following in the expected order. These curves converge high energy inputs, which is expected the as optimum stress intensity decreases with decreasing size.

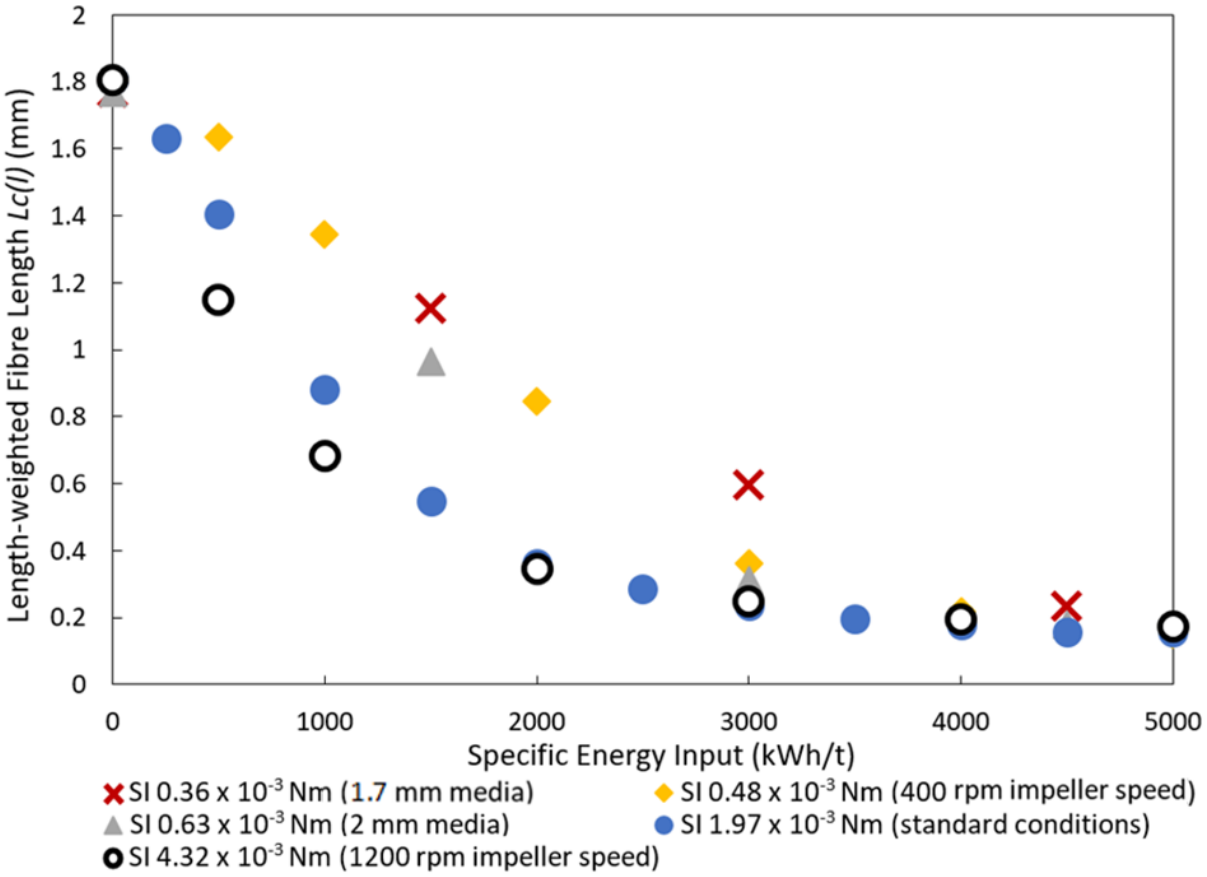

Figure 6.1 *– MFC fibre length versus energy input for the five Mullite A series investigated in Chapter 4.*

Figure 6.2 plots *Lc(l)*-based $K_{R,Op}$ against stress intensity at 1500, 3000, and 4500 kWh/t (the 400 rpm and 1200 rpm impeller speed series required interpolation to obtain $K_{R,Op}$ values at 1500 and 4500 kWh/t). Here, the archetypical shape of the stress intensity – particle size curve (e.g. Figure 2.4) is apparent, with a rapid decay at lower stress intensities, followed by a flatter region approaching the optimum. Additionally, with increasing energy input, a rapid increase in grinding effectiveness occurs at lower stress intensities, decreasing optimum stress

intensity, consistent with Figure 2.4 (b). These results imply that the general trend expected from stress intensity theory is followed, in terms of particle size reduction.

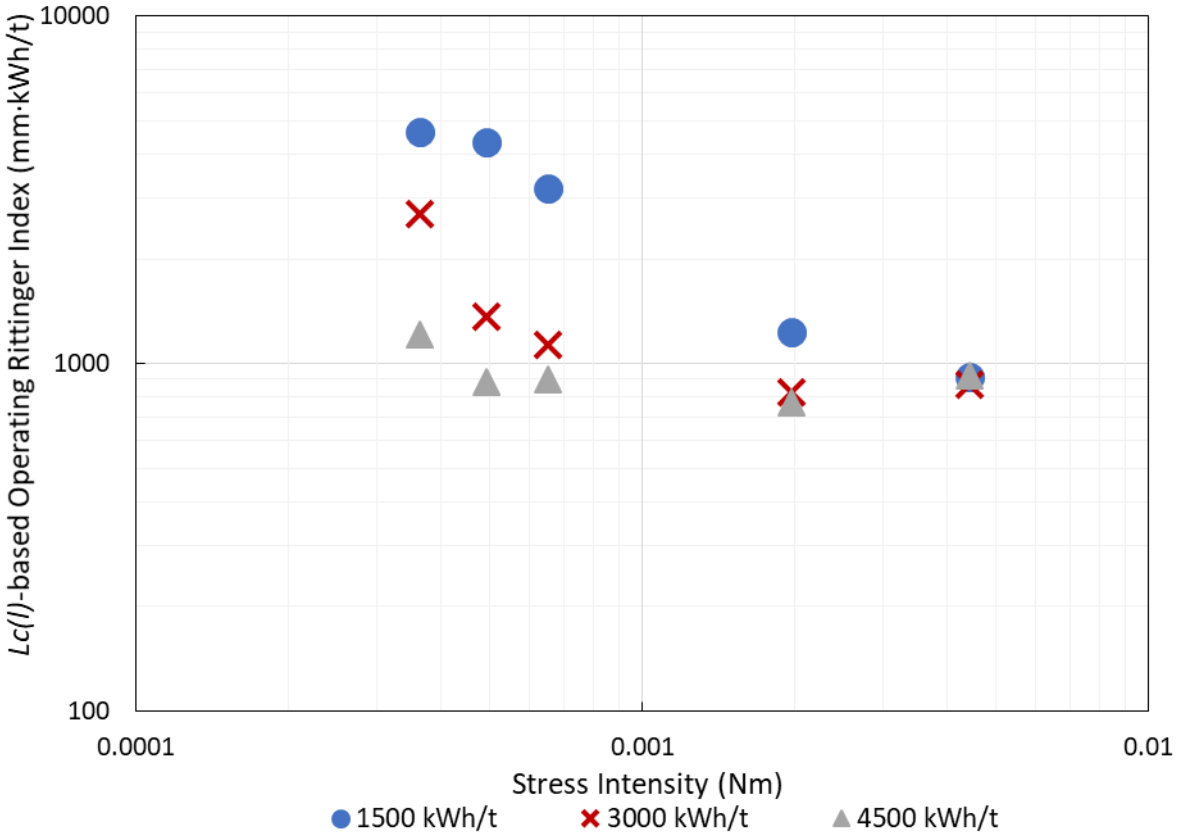

Figure 6.2 *– Lc(l)-based $K_{R,Op}$ versus stress intensity at several energy inputs for the five Mullite A series investigated in Chapter 4.*

A plot of *Fines B* content versus energy input (Figure 6.3) shows no such clear pattern with stress intensity, notably with the 800 rpm and 1200 rpm impeller speed series having drastically different values despite similar $K_{R,Op}$ values. Plotting *Fines B* content against *Lc(l)* (Figure 6.4) demonstrates that high stress intensities leads to poorer fibrillation when fibre breakage rate is controlled for, probably due to the lower stress number. Additionally, despite the lower impeller speed series having a stress intensity intermediate of the two fine media series, the *Fines B* generation is much lower, although Figure 6.4 shows this discrepancy only occurs at finer sizes. The reason for this is unknown, but difficulty in suspending the coarser media at lower impeller speeds is suspected, which would lead to a settled high-MVC zone

that may enhance fibril degradation. Apart from this exception, however, for a given breakage rate, lower stress intensities enhance *Fines B* generation. Whether this leads to greater net *Fines B* content depends on whether this compensates for the poorer breakage rate. Similar, but less extreme, effects are also noticed with *Fibrillation %*, and both have the expected consequences on tensile strength (see Figure A4.1 and A4.2 in Appendix A4 respectively).

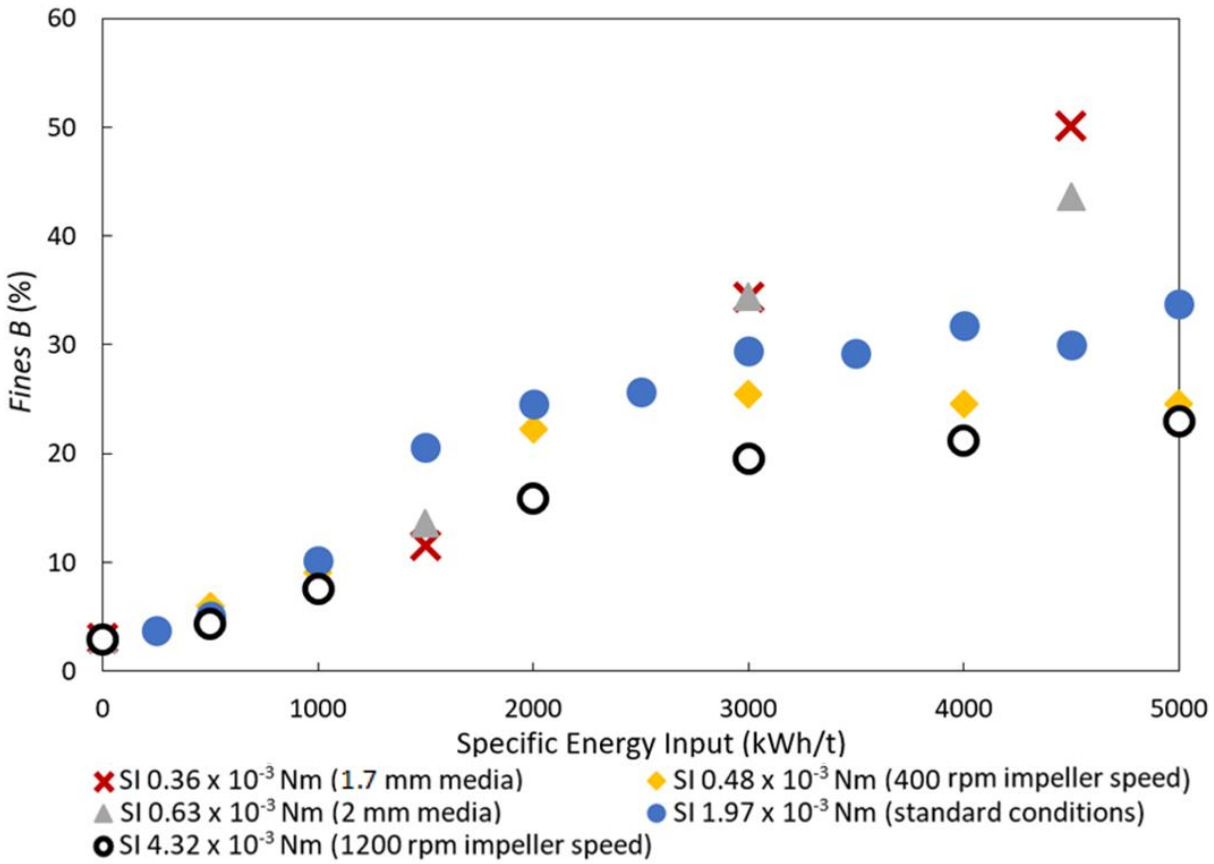

Figure 6.3 *– Fines B versus energy input for the five Mullite A series investigated in Chapter 4.*

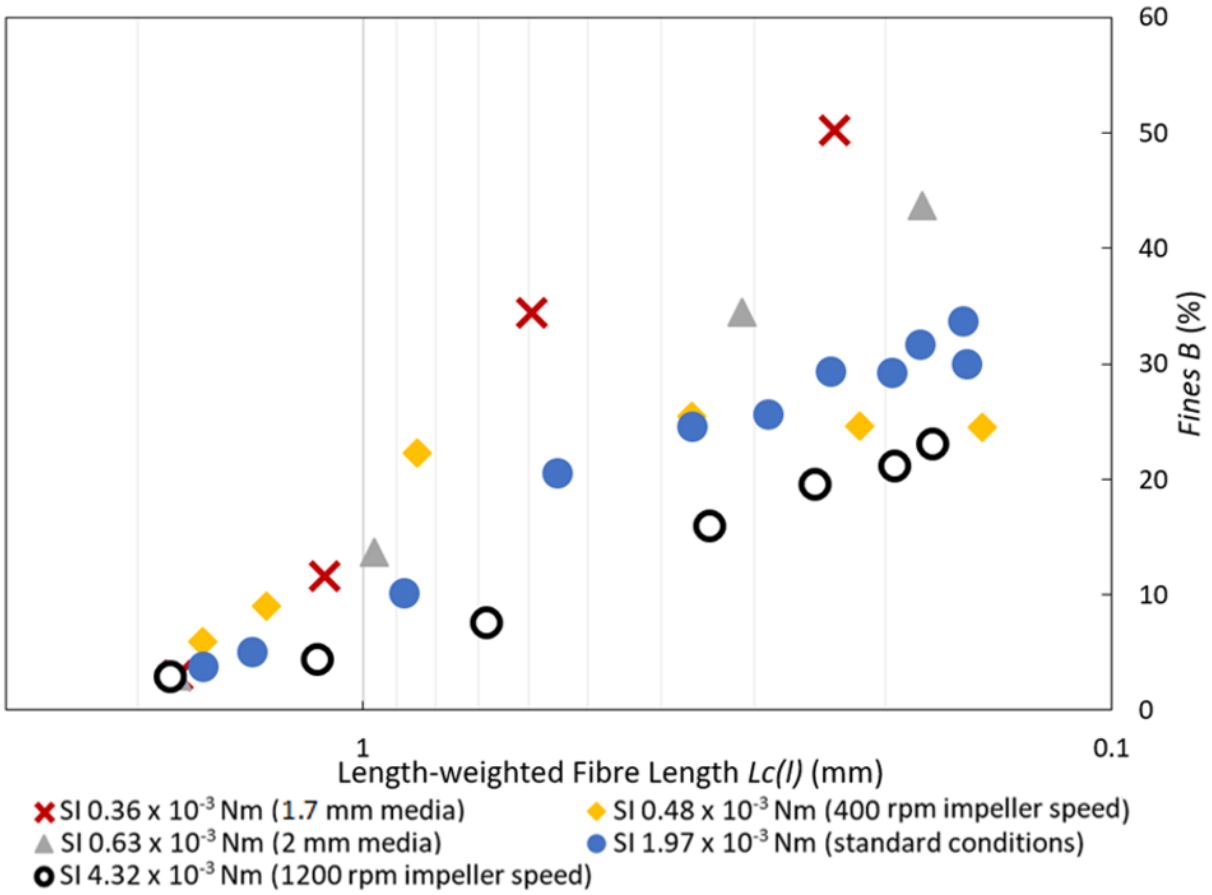

Figure 6.4 *– Fines B versus Lc(l) for the five Mullite A series investigated in Chapter 4.*

These energy sweeps imply that stress intensity may control length reduction, but the results on fibrillation parameters and the consequent tensile strength are more complicated. The next section gives a much more detailed characterisation of the effect of stress intensity.

6.3. Mineral-free Zirconia Stress Intensity Study

6.3.1. Experimental

To investigate the influence of stress intensity on MFC properties, ceria-zirconia media (*Zirconia D*) of five size bands (mean sizes of 2.9, 2.5, 2.1, 1.5, and 1.0 mm) were used to carry out 3000 kWh/t grinds at impeller speeds of 300, 500, 800, 1100, and 1500 rpm. These grinds were at 100 POP, with the mineral being excluded since the observed interaction shown in Sections 5.3 and 5.4 between mineral content and roughness with MFC length and *Fines B* degradation would be a complicating factor.

Ceria-zirconia media (*Zirconia D*) was selected partly because the high density (6 g/cm^3) enabled higher stress intensities, since operational issues limited the increase in impeller speed and media size. Also, technical issues prevented the roughnesses of media sizes significantly below 2.9 mm from being measured; this media had a R_a value of 0.2 µm, providing a surface gloss that is visually very sensitive to roughness changes. Therefore, the consistency of media roughness between sizes could be verified by eye.

Fibre analyser parameters were measured for all samples, but tensile strength was not, due to time limitations. *Fines B* and *Fibrillation %* are used as proxies; the low roughness would cause under-grinding at 3000 kWh/t (as Section 5.3 shows), so the degradation of liberated fibrils that complicates the relationship with tensile strength is minimised.

6.3.2. Power Draw

Figure 6.5 shows the influence of impeller speed on average power draw for the five media sizes. A strong correlation is seen, with the power draw at 1500 rpm being tenfold that at 300 rpm. Power draw increases with coarser media, but the influence is much weaker. Therefore, assuming stress intensity controls product performance, applying it with a high impeller speed and fine media gives an enormous throughput advantage compared to the coarse media at low impeller speed, greatly decreasing grinder volume and capital cost, given that the grinder motor is not limiting.

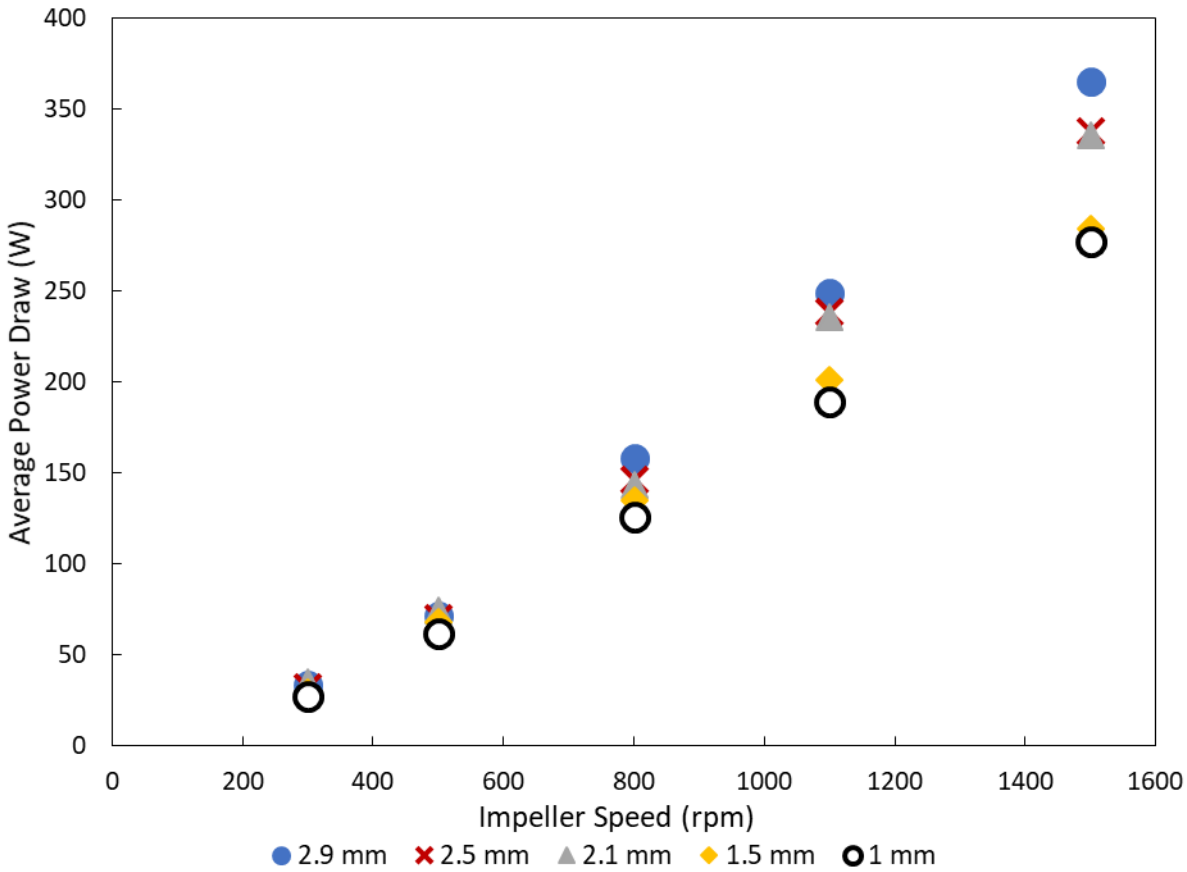

Figure 6.5 *– Average grinder power draw versus impeller speed for five media sizes.*

6.3.3. Fibre Length

The influence of stress intensity on *Lc(l)* is given by Figure 6.6. At very low stress intensities, the curve is very flat, but decreases rapidly at moderate stress intensities. For the three larger media, a minimum is reached, beyond which the product size gradually increases at higher stress intensities. This is expected from stress intensity theory, although the curves for each media largely do not coincide, with finer media generally being more efficient at a given stress intensity.

Since at low stress intensities, product size is similar to feed size, breakage rate differences are understated in Figure 6.6, so in Figure 6.7 the *Lc(l)*-based $K_{R,Op}$ is plotted, which makes the differences more obvious; for example, the 1 mm media 1500 rpm series has a similar stress

intensity to the 2.9 mm media 300 rpm series, but has around four times the breakage rate. Reasons for this size-specific effect are suggested later.

At the lowest stress intensities, *Lc(l) increases* slightly compared to the feed (up to 1.87 mm compared to 1.66 mm); this is probably because fibres are straightened, reducing the kink (suggesting that the kink is not perfectly accommodated in length measurements, underrepresenting the true feed size). Consequently, the $K_{R,Op}$ calculations require an arbitrary 'true' feed size value (1.9 mm is chosen) to avoid negative values at the lowest stress intensities.

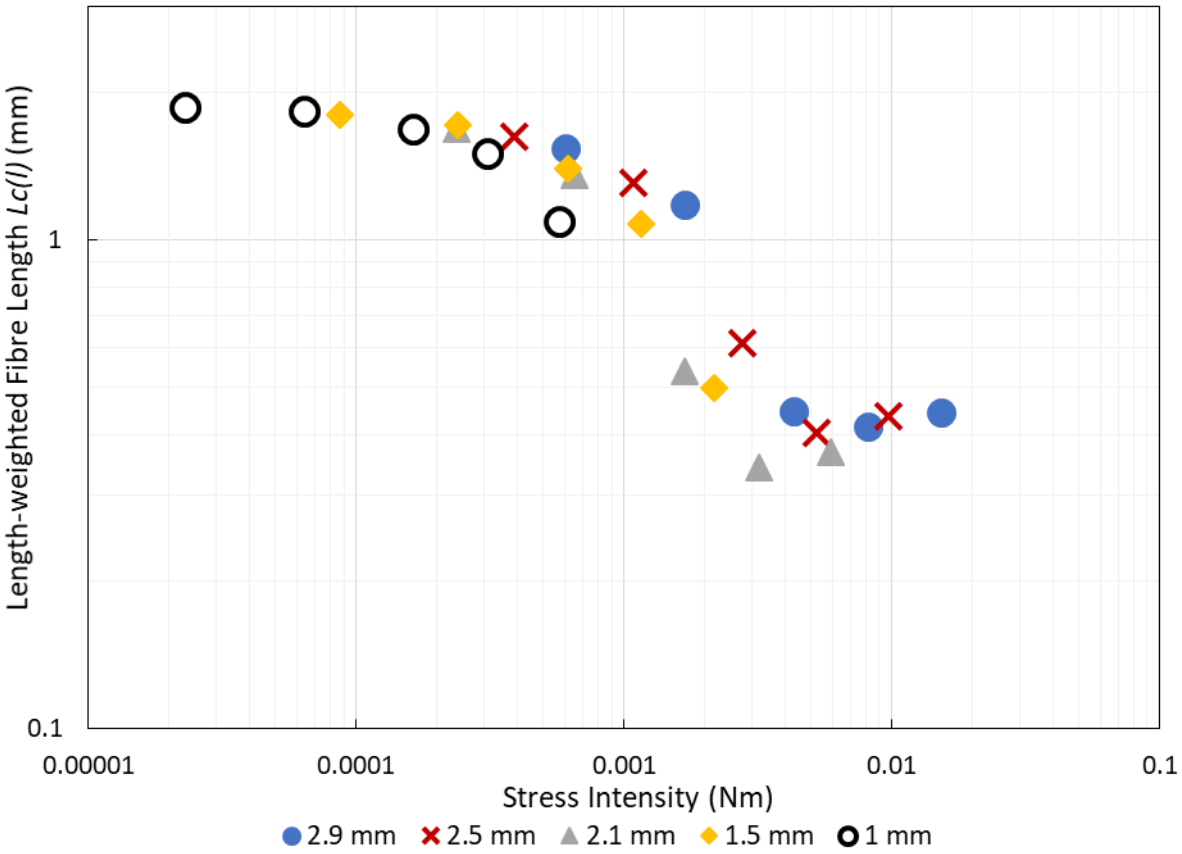

Figure 6.6 *– MFC fibre length versus stress intensity for five media sizes.*

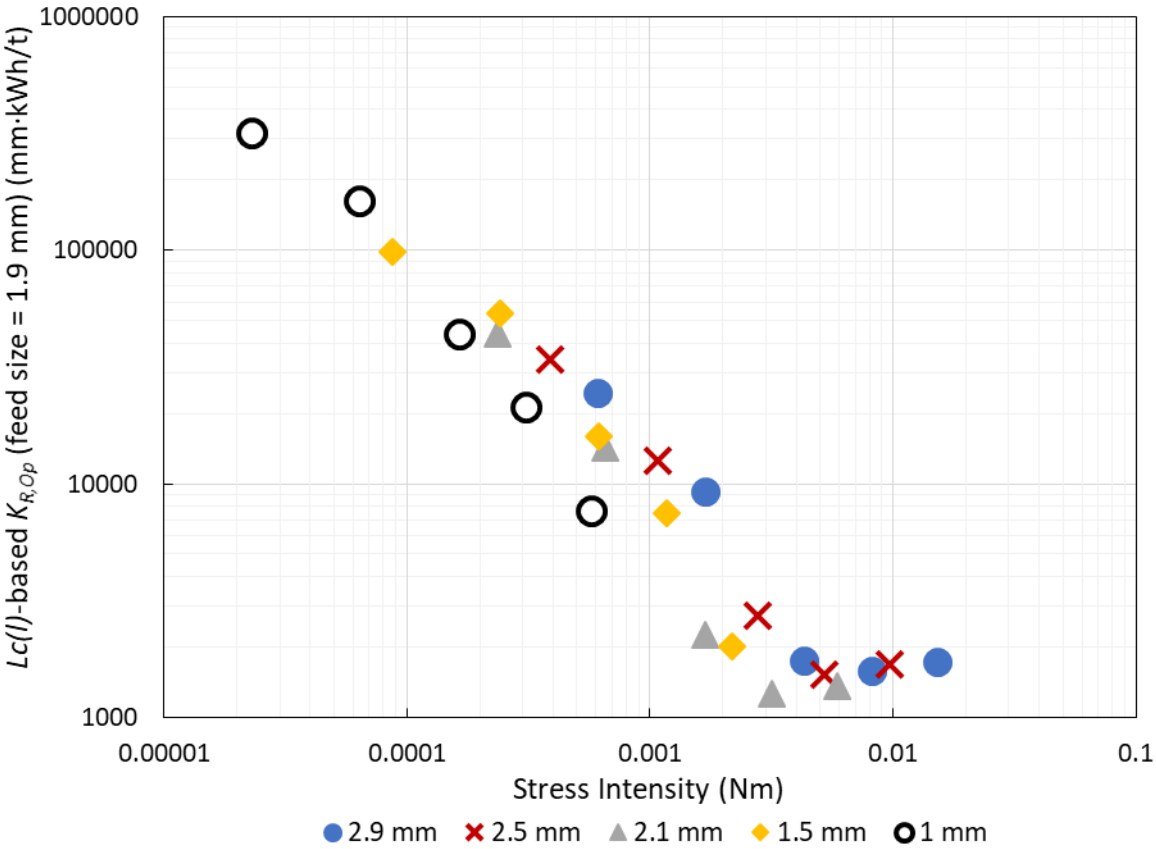

Figure 6.7 *– Lc(l)-based $K_{R,Op}$ versus stress intensity for five media sizes.*

6.3.4. Fines B and Fibrillation %

Figure 6.8 and 6.9 show the *Fines B* and *Fibrillation %* values versus stress intensity. They both exhibit similar patterns, although the effects on *Fines B* content are stronger. The inverse effect to *Lc(l)* is apparent; an increase in *Fines B* and *Fibrillation %* content with stress intensity, followed by a peak, and a decline beyond the optimum stress intensity. In this case, the optimum stress intensity appears similar to that for *Lc(l)*, although considering the gradients about these peaks, the true optimum is likely slightly lower. The fall in *Fines B* beyond the optimum is much harsher than the corresponding coarsening effect with *Lc(l)*, since the fewer opportunities to fibrillate per breakage is coupled with fewer breakages. Note that these values do not represent *peak Fines B* and *Fibrillation %*, as all samples are at least somewhat

under-ground; it is fully expected that at the optimum energy input, finer media will give substantially higher fibrillation parameters, as is seen in Figure 6.3.

The curves for each media coincide poorly; at constant stress intensity, finer media have higher *Fines B* and *Fibrillation %* values. The curves are much closer together in a plot of *Fines B* and *Fibrillation %* against *Lc(l)* (Figures 6.10 and 6.11), showing that differences in fibrillation parameters are primarily due to breakage rate differences.

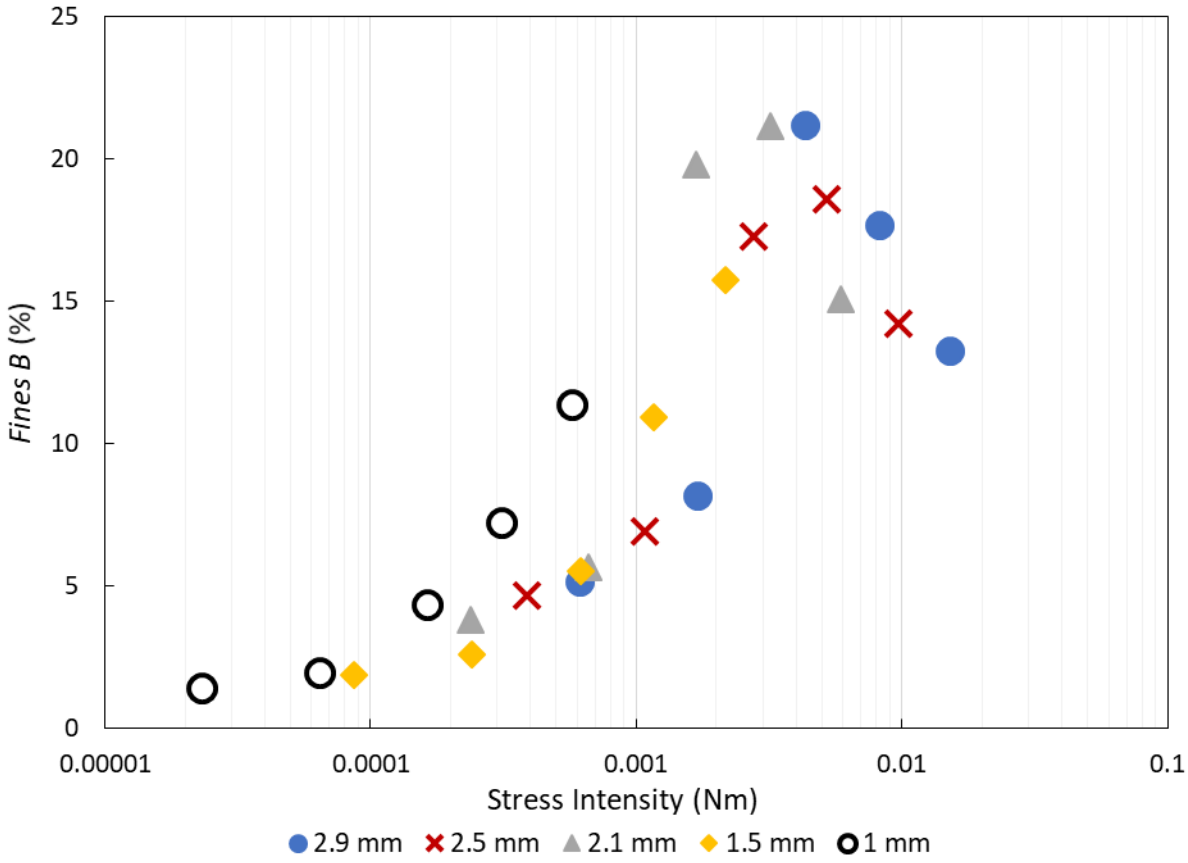

Figure 6.8 *– Fines B versus stress intensity for five media sizes.*

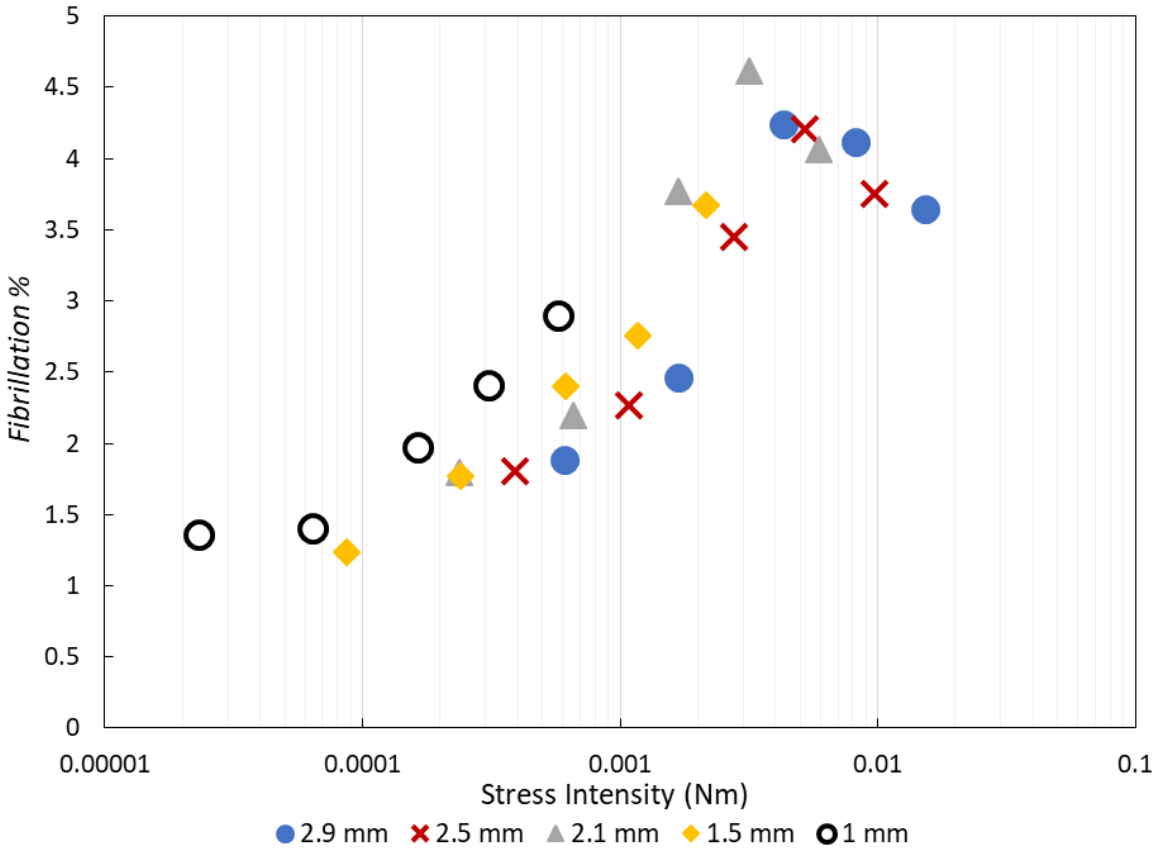

Figure 6.9 *– Fibrillation % versus stress intensity for five media sizes.*

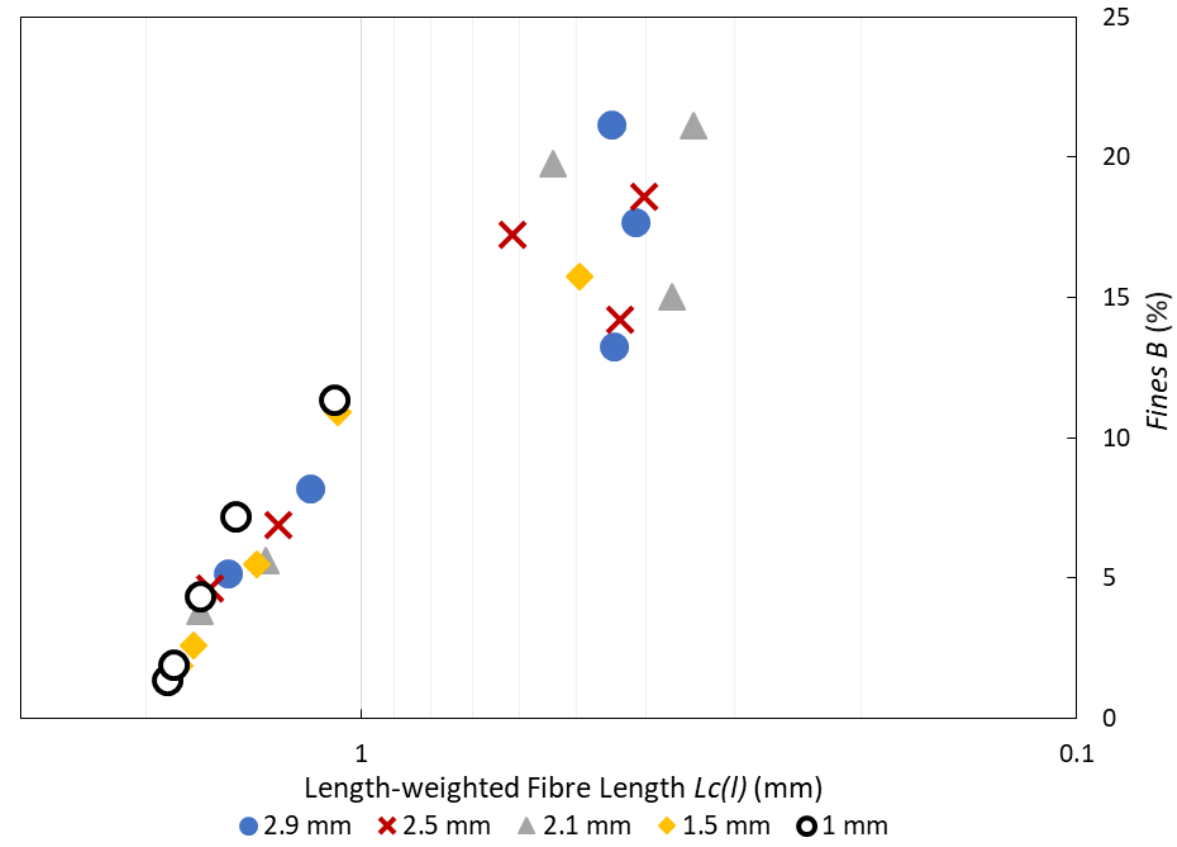

Figure 6.10 *– Fines B versus Lc(l) for five media sizes.*

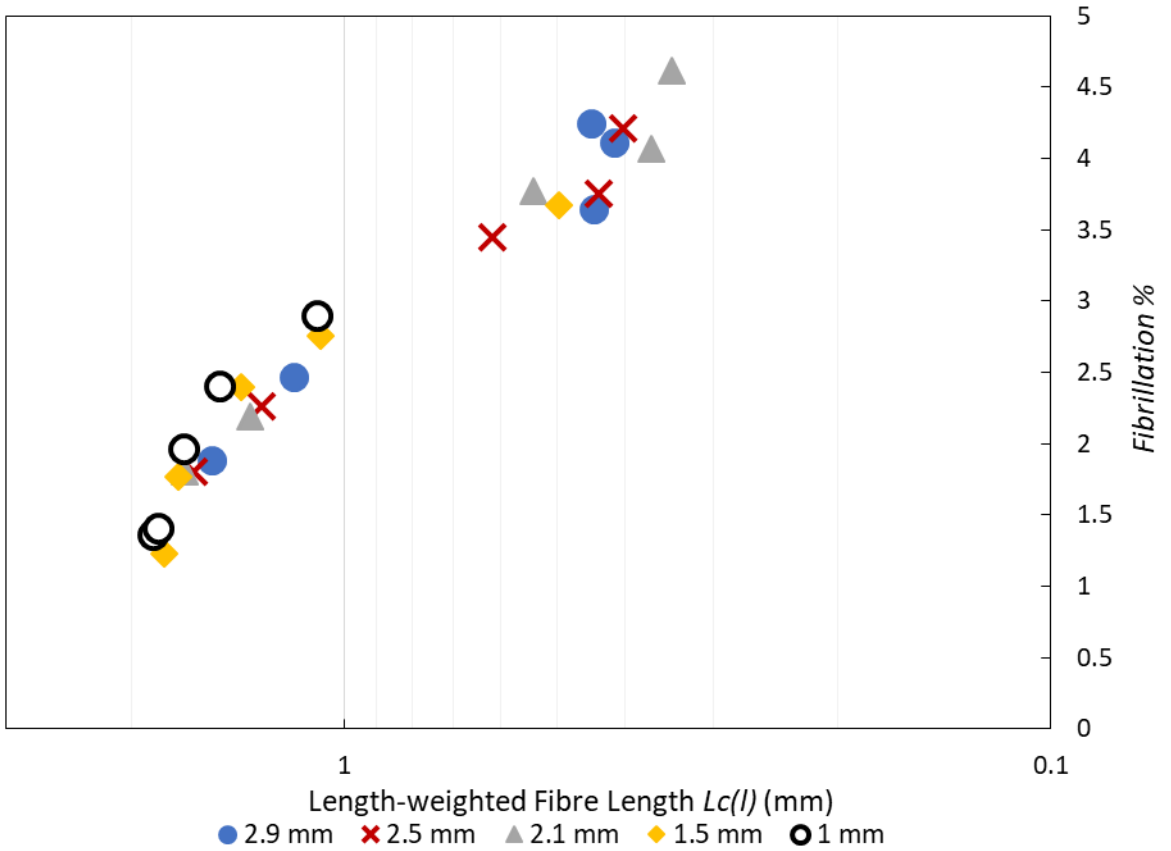

Figure 6.11 *– Fibrillation % versus Lc(l) for five media sizes.*

6.3.5. DIC Microscopy Images

Figures 6.12 and 6.13 show microscopy images of MFC produced with 2.9 mm media at impeller speeds of 800 rpm and 1500 rpm respectively. Figures 6.6, 6.8, and 6.9 show that, though MFC fibre lengths are similar, the *Fibrillation %* and *Fines B* content of the 800 rpm series are much higher. The extensive external fibrillation is obvious in Figure 6.12, and there are numerous loose high aspect ratio particles, but in Figure 6.13, fibre breaks are much cleaner, with little fibrillation taking place at the ends; this supports the assertion that, because of the much higher power draw at higher impeller speeds, there is insufficient time in the grinder for lower intensity stress events to exploit these breakages.

Both the 1 mm media 1500 rpm series and the 2.9 mm media 300 rpm series have stress intensities of around 6 x 10^{-4} Nm, and differ greatly in fibre analyser results; representative

microscopy images are shown as Figure 6.14 and 6.15 respectively. These verify the fibre analyser results, as cross-sectional breakages are more common, external fibrillation more extensive, and liberated fibrils more numerous in the 1 mm media 1500 rpm series. Despite the higher breakage rate of that series, when comparing many images, the 2.9 mm media 300 rpm series tended to exhibit flatter fibres with wider cross-sections. Fibre width measurements between the series (Figure 6.16) confirm that at a given stress intensity, coarser media indeed results in higher fibre width peaks. This is unexpected as fibre flattening suggests more intense collisions, yet breakage rate is lower. In the next section, the modified Hertzian contact mechanics model offers a potential explanation.

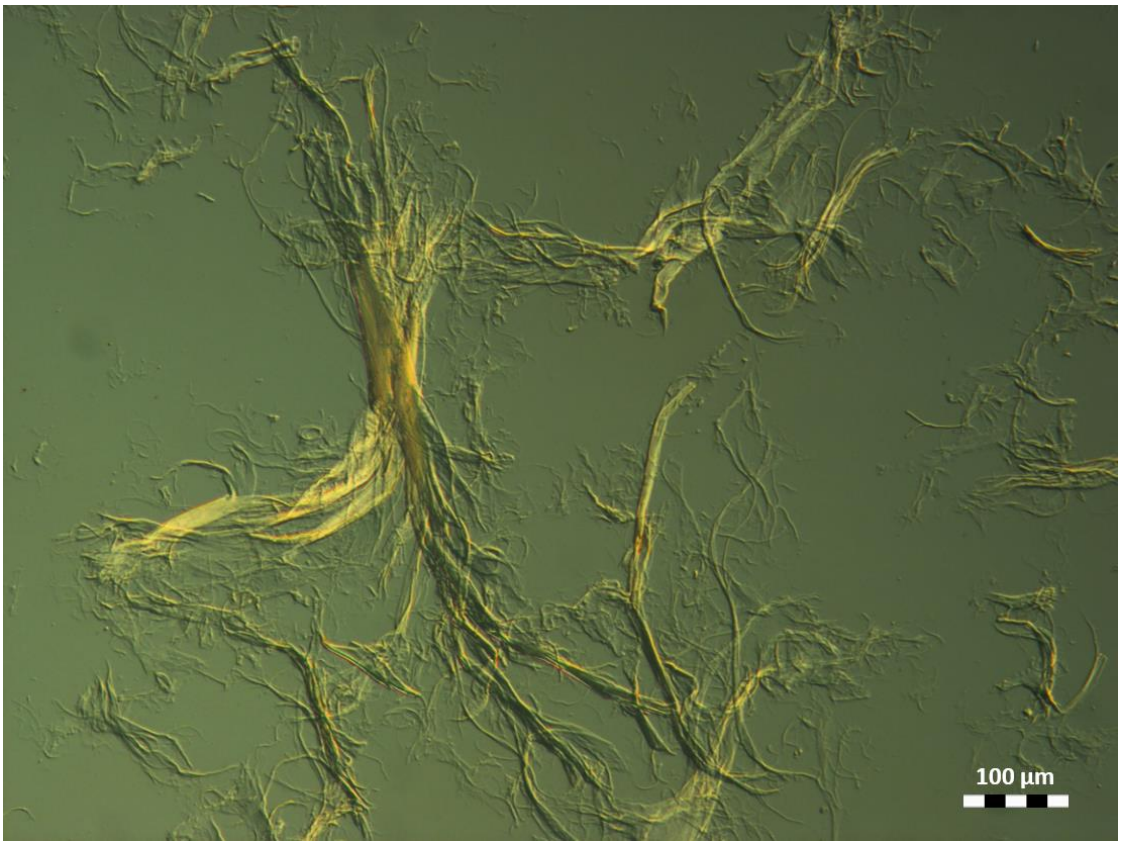

Figure 6.12 *– DIC microscopy image of MFC produced at 3000 kWh/t with 2.9 mm media and 800 rpm impeller speed.*

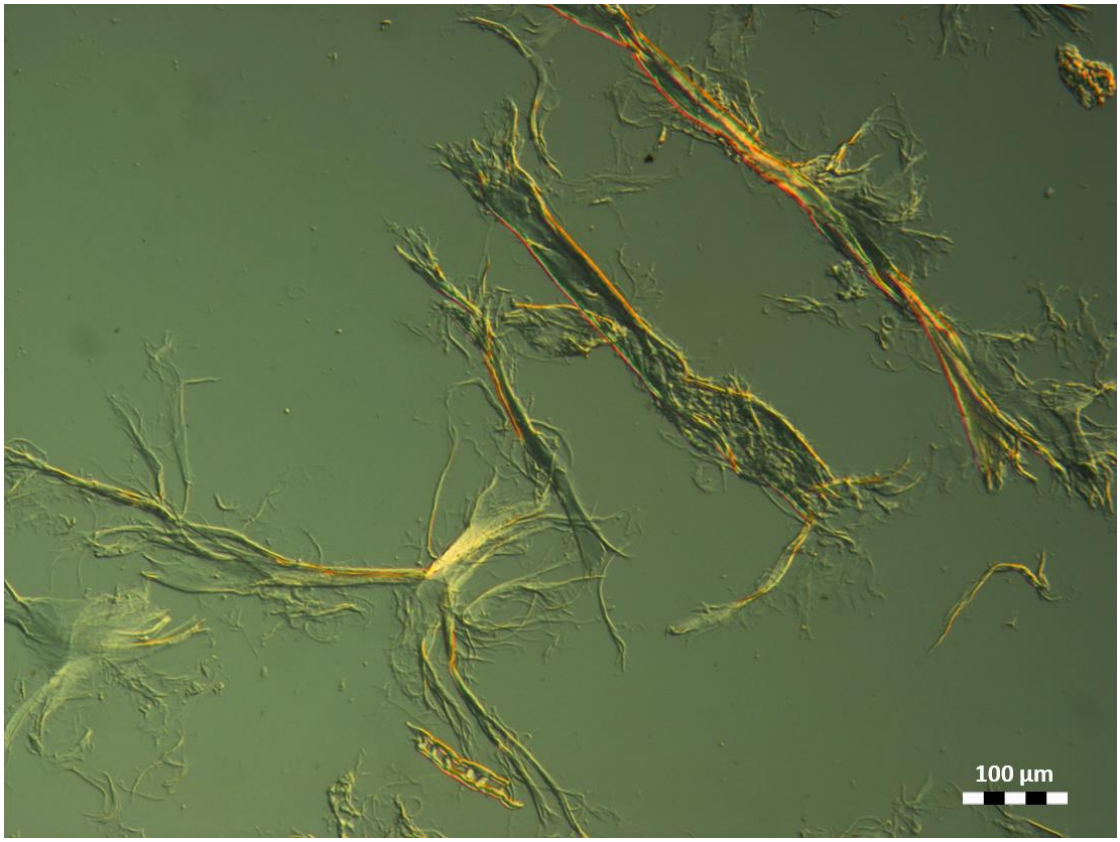

Figure 6.13 *– DIC microscopy image of MFC produced at 3000 kWh/t with 2.9 mm media and 1500 rpm impeller speed.*

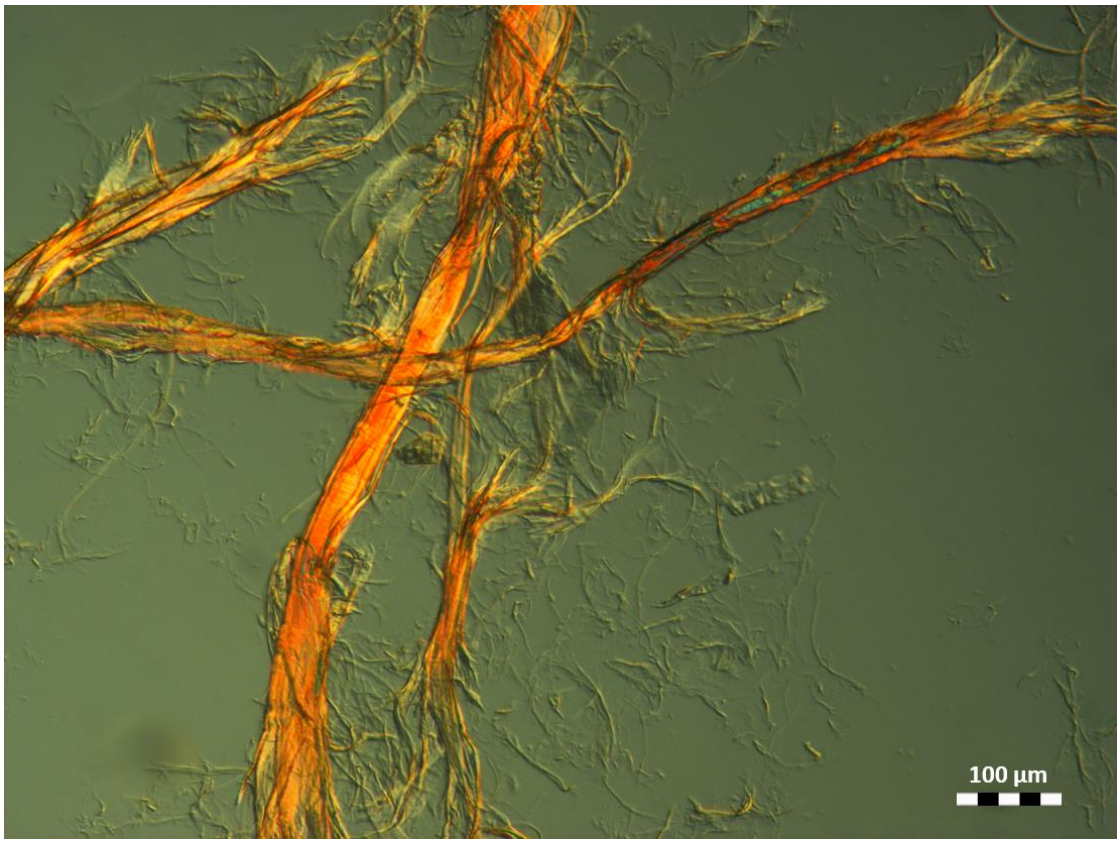

Figure 6.14 *– DIC microscopy image of MFC produced at 3000 kWh/t with 1 mm media and 1500 rpm impeller speed.*

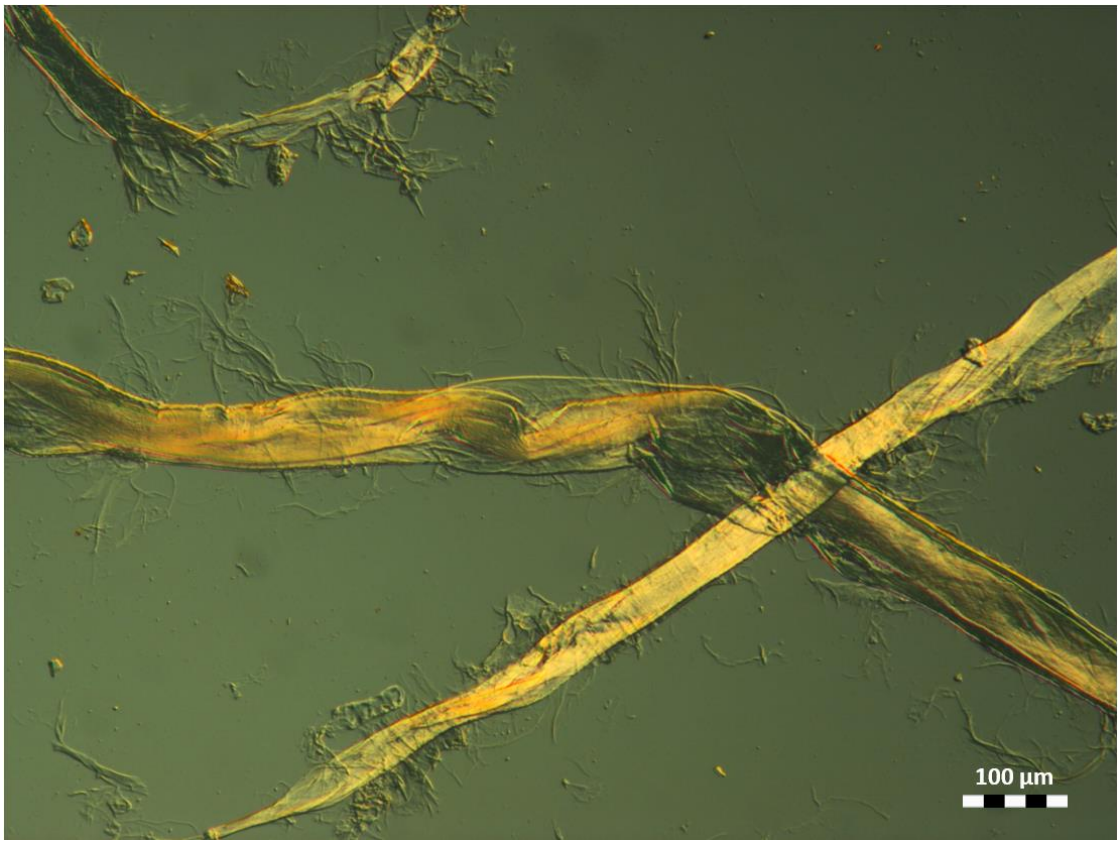

Figure 6.15 *– DIC microscopy image of MFC produced at 3000 kWh/t with 2.9 mm media and 300 rpm impeller speed.*

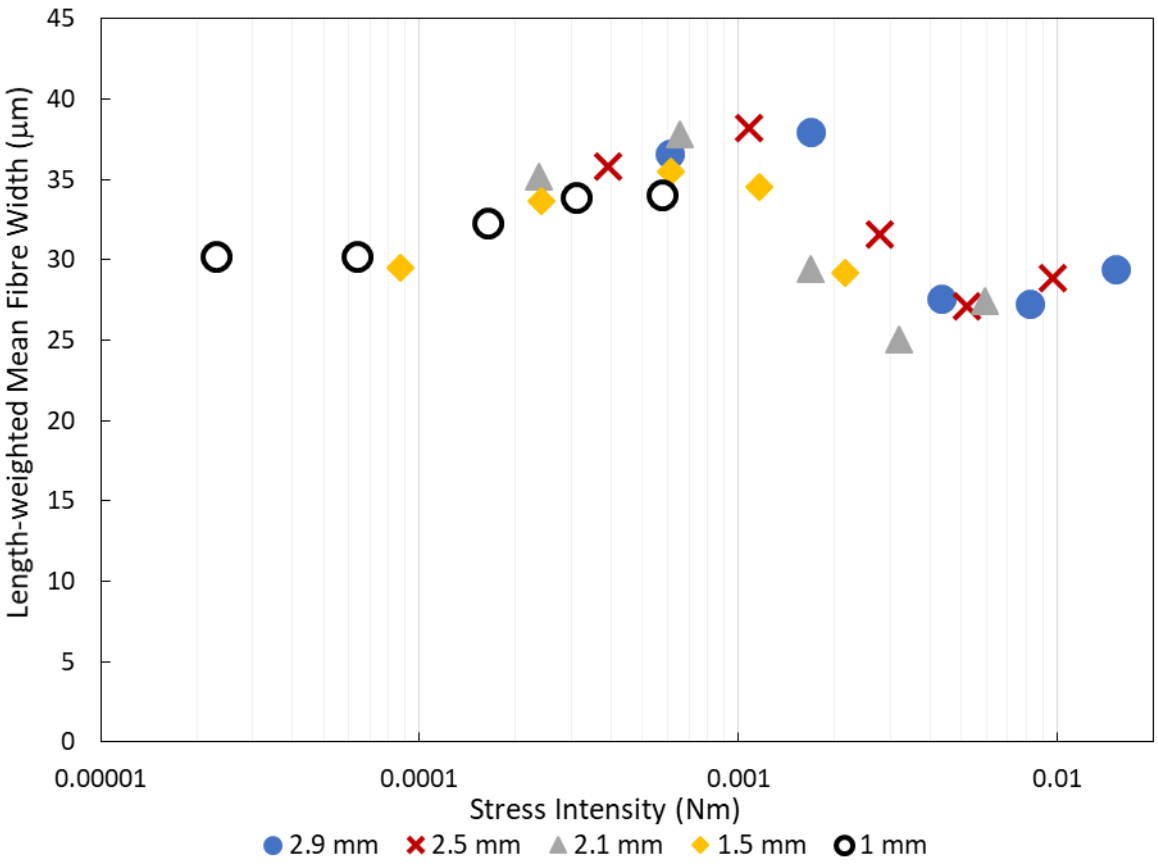

Figure 6.16 *– Mean fibre width versus stress intensity for five media sizes.*

6.3.6. Hertzian Contact Mechanics Model

Although finer media improves grinding efficiency at a given stress intensity, the 2.1 mm media appears to be disproportionately effective. A closer examination reveals that this media has slightly lower gloss than the others, indicating that a slightly higher roughness is improving breakage rate. However, this does not explain the discrepancy between the other media sizes.

Four candidate explanations were investigated, including differences in stress number, viscous dampening, media suspension, and media curvature. The first three are detailed in Section A4.2 in Appendix A4, and were found to be insufficient. Stress number differences between series at certain stress intensities are not believed to be accurate, instead suggesting errors in the assumptions of stress intensity theory. Viscous dampening shifts the curves slightly closer together when generous estimates of charge viscosity are used, and likely plays a limited role. Media suspension differences may sometimes be important, but since systems are sharply divided between suspended and unsuspended, this cannot explain continuous differences apparent over such a wide range.

The Hertzian contact mechanics model developed in Section 4.2 suggests an influence of media curvature (and therefore an additional media size effect). Due to similar roughnesses, the modification in Chapter 5 is not used, instead Hertzian deformation dimensions under given stressing conditions are considered. It is believed that fibres must be compressed to an appreciable fraction of the cell wall thickness to break, so the *indentation depth* should have similar values to this. Substituting Equations [2.15] and [2.16] into the equation for cellulose indentation δ_C (Equation 4.2) and simplifying, one obtains the following proportionality:

$$\delta_C \propto \frac{F^{\frac{2}{3}}}{R^{\frac{1}{3}}} \dots [6.1]$$

where *F* is the normal force, and *R* is the media radius of curvature. Force is calculated by Newton's Second Law, equal to the media bead mass multiplied by the acceleration. PEPT data from Skuse[81] shows that acceleration around the impellers is roughly proportional to the square of the media velocity, so force in this model has exactly the same proportionalities to grinding parameters as stress intensity. However, the Hertzian model includes media curvature; smaller media has greater curvature (lower *R* values), concentrating collision force over a smaller area, thereby causing deeper indentations with smaller diameters than larger media with identical stress intensities.

The relationship between both indentation depth and indentation diameter with stress intensity is shown as Figure 6.17 (a) and (b) respectively. The green box in Figure 6.17 (a) shows the range of cell wall thicknesses typical for *Nordic pine* fibres. A strong increase in δ_C for the 1 mm media at a given stress intensity is seen, which at 6 x 10^{-4} Nm approaches cell wall thicknesses, whereas at this stress intensity, the 300 rpm 2.9 mm media gives a substantially lower indentation depth, so the former is expected to have a higher breakage rate. Additionally, Figure 6.17 (b) predicts a wider impact area for larger media. Both predictions are supported by the aforementioned fibre analyser and microscopy observations, suggesting that media curvature is indeed important.

Plotting *Lc(l)* against δ_C (Figure 6.18), shows that accommodating media curvature significantly improves the general fit between media sizes compared to Figure 6.6. Additionally, the expected rapid length decrease across indentation depths comparable to cell wall thicknesses is observed. Both findings support the accuracy of the theory, though it does not remove all discrepancies, notably the 2.1 mm series, which as mentioned earlier is believed to be due to a slightly higher roughness.

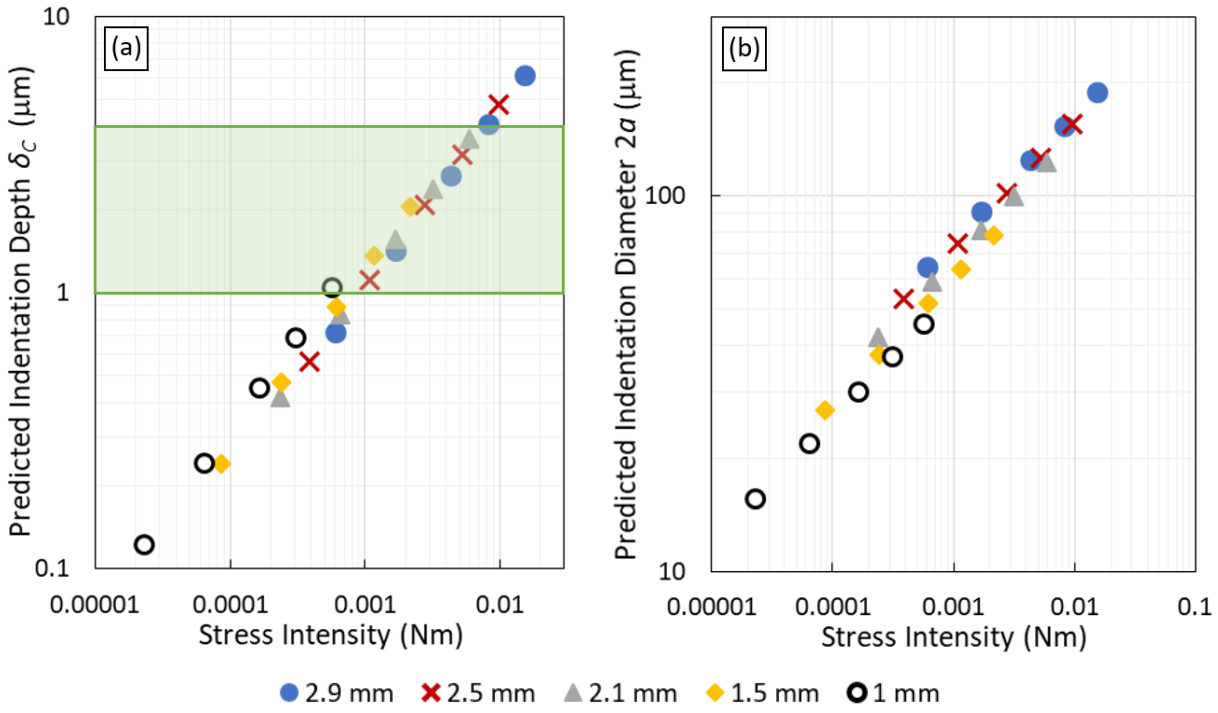

Figure 6.17 *– The influence of stress intensity on (a) predicted indentation depth, and (b) predicted indentation diameter using the modified Hertzian contact mechanics model, for five media sizes. The green region represents typical cell wall thicknesses for Nordic pine fibres.*

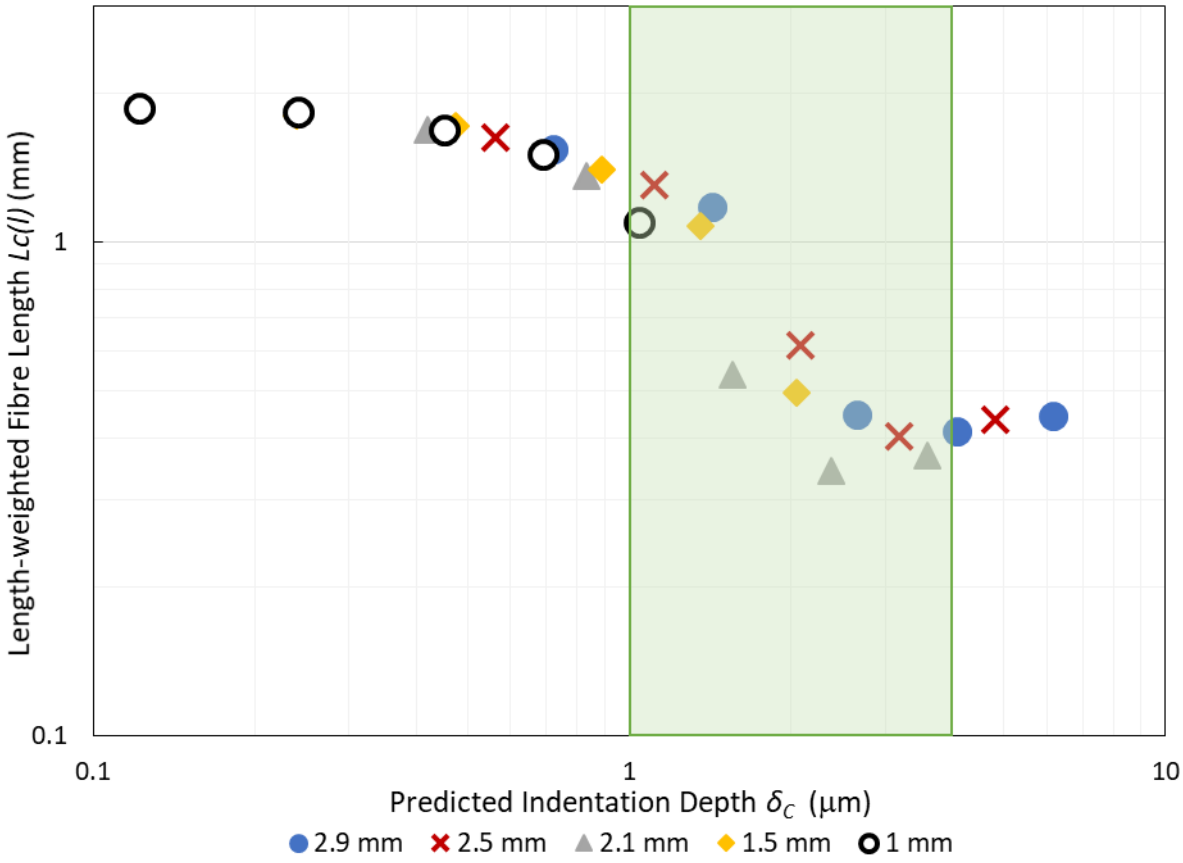

Figure 6.18 *– MFC fibre length versus predicted cellulose indentation depth from the modified Hertzian contact mechanics model, for five media sizes.*

6.3.7. Conclusions

Plotting MFC length against stress intensity shows the expected characteristic pattern; a flat gradient at low stress intensities, followed by a rapid decay, a minimum at the optimum stress intensity, and then a gradual increase in size. The *Fines B* and *Fibrillation %* contents largely follow an equivalent pattern, increasing in proportion with length decay, and reaching peak values at similar stress intensities. Beyond the optimum stress intensity, *Fines B* and *Fibrillation %* decline very sharply, because despite the high fibre breakage efficiency there are insufficient opportunities to effectively fibrillate at these breakages; microscopy images appear to confirm this.

Although stress intensity theory is generally followed, clearly other factors are involved as curves for each media size do not coincide; at a given stress intensity, finer media (with higher impeller speeds) give higher breakage rates and proportionally higher fibrillation parameters than coarser media (with lower impeller speeds). The modified Hertzian contact mechanics theory considers the effect of media curvature, and plotting the predicted indentation depths from this theory against MFC length reconciles most of the discrepancies between media sizes, and this theory also explains microscopy observations regarding fibre width differences.

Power draw is much more sensitive to impeller speed than media size, so to obtain a target stress intensity, choosing a finer media with a higher impeller speed greatly improves throughput, decreasing grinder volume and capital cost. However, screening issues and the expected higher wear rate limits this strategy, so it is not obvious which permutation of media size and impeller speed gives the economically optimum balance.

The next section expands the consideration of stress intensity to different media compositions, also changing density and media roughness, and investigates the combination of stress intensity and roughness into a single parameter to predict MFC properties.

6.4. Expanded Study of Stress Intensity and Roughness

6.4.1. Experimental

To combine and expand the investigations of stress intensity and surface roughness, the data from Section 6.3 and Section 5.2 were combined, and supplemented with additional grinds with various media densities, roughnesses, sizes, and impeller speeds. Grinds were carried out at 100 POP, and most targeted an energy input of 3000 kWh/t, though some grinds were repeated at 1000 kWh/t for a limited assessment of the influence of energy input. The full list of samples, and their input conditions, are displayed in Tables A4.1, A4.2, and A4.3 in Appendix A4. As with Section 6.2, fibre analyser results were taken for the additional grinds listed in Table A4.3 and supplemented with the results from Section 5.2 and 6.3, but tensile strengths were not measured, due to time constraints.

6.4.2. Effect of Stress Intensity and Effect of Roughness

MFC fibre analyser parameters were first plotted against stress intensity and media roughness independently. *Lc(l)* and *Fines B* were plotted against stress intensity as Figure 6.19 and Figure 6.20. To aid understanding, the data were separated into bands based on their roughness values. Where sufficient data is present, Figure 6.19 shows that other roughness values follow a similar pattern to that observed in Figure 6.6, but at a given stress intensity, the curves for higher roughness are shifted downwards (i.e. are more efficient), and seem to have lower optimum stress intensities (although data for some roughnesses is too sparse to judge). The

effect of roughness is particularly striking at stress intensities of around 2 x 10^{-3} Nm, where *Lc(l)* values can vary between 0.21 – 1.25 mm.

The *Fines B* content shows an equivalent pattern; at given stress intensities, higher roughness values result in higher *Fines B* contents; the optimum stress intensity for maximising *Fines B* appears lower at higher roughnesses, and for stress intensities beyond the optimum, the decline in *Fines B* content appears harsher for rougher media. Concomitant with Section 6.3.4, the peak in *Fines B* content occurs at, or slightly below, the optimum stress intensity for *Lc(l)* reduction for each roughness value. It is important to clarify, however, that Figure 6.20 does not show *peak Fines B* values, 3000 kWh/t is clearly closer to the optimum energy input for rougher media, and if energy input was increased sufficiently, peak values are expected to be greater for lower stress intensity grinds (at least with finer media) as Figure 6.3 suggests.

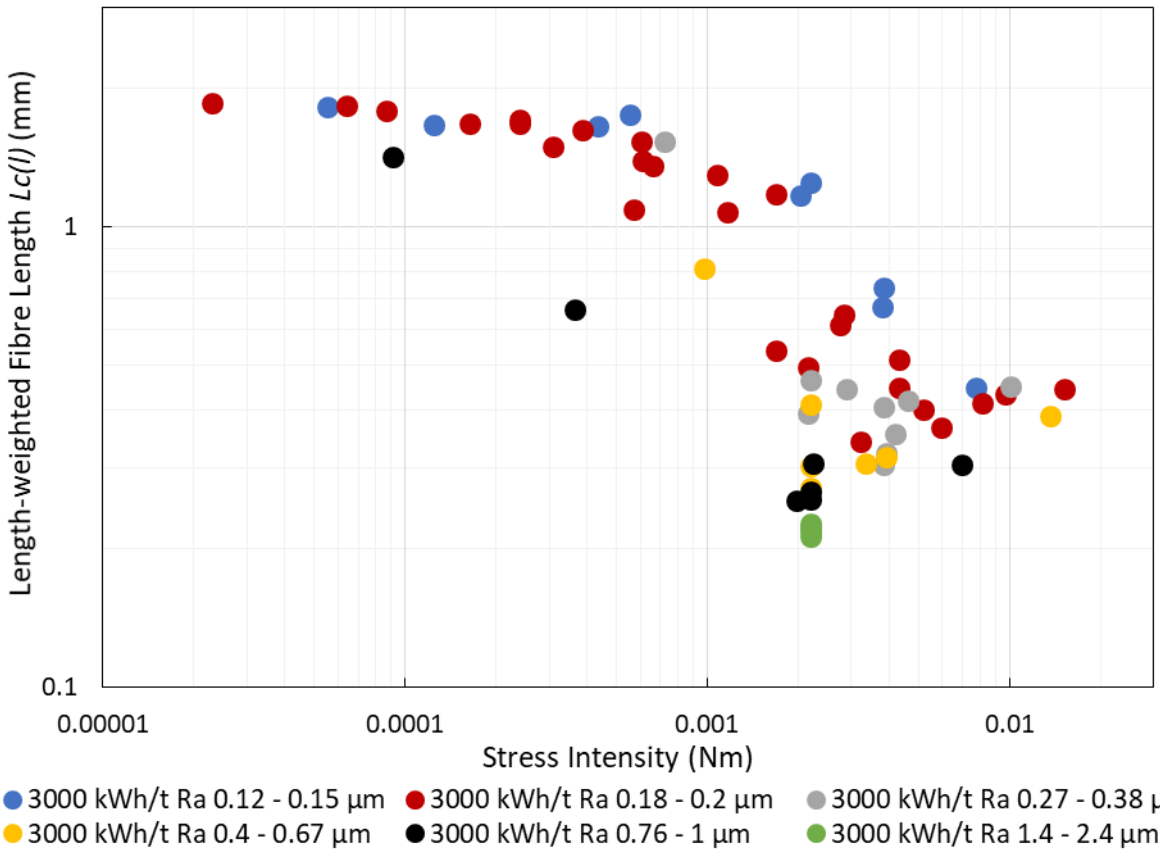

Figure 6.19 *– MFC fibre length at 3000 kWh/t versus stress intensity for various media roughness values.*

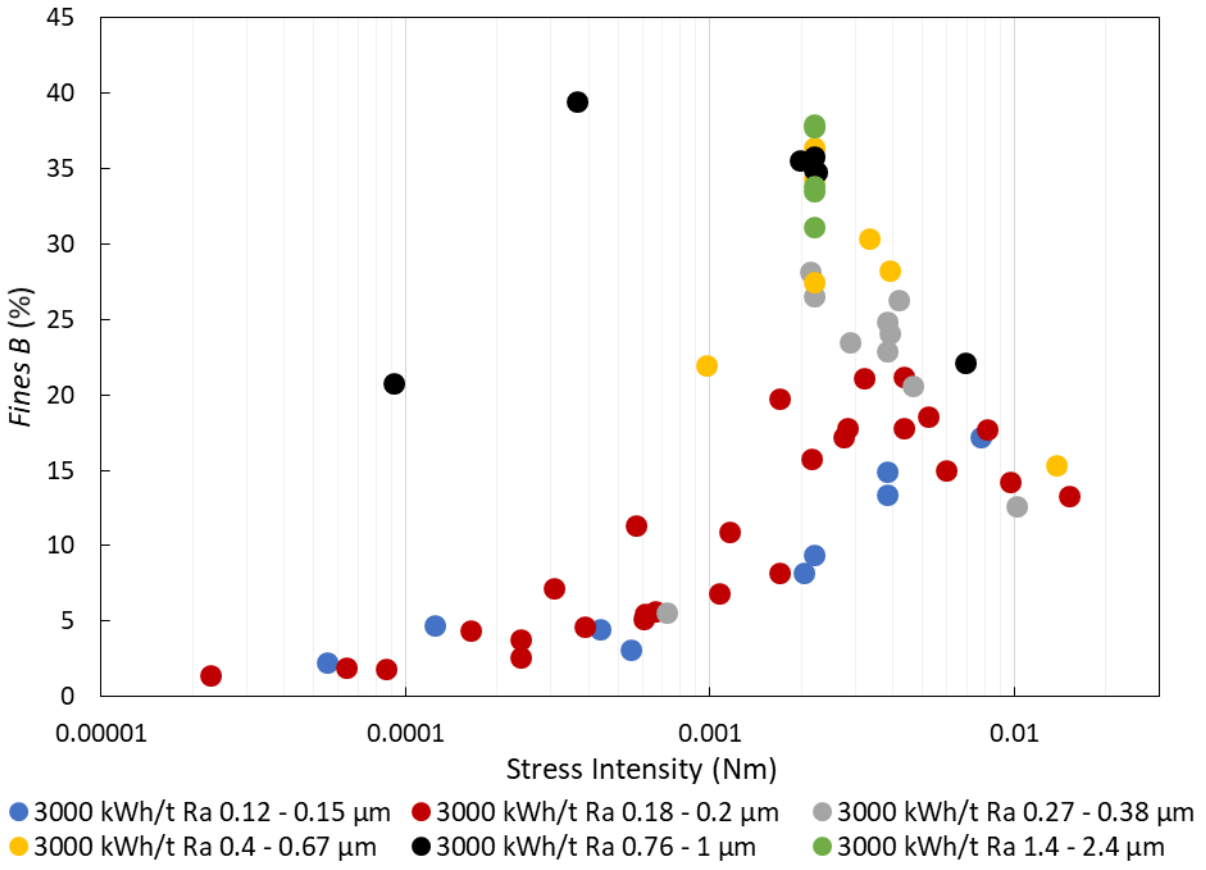

Figure 6.20 *– Fines B content at 3000 kWh/t versus stress intensity for various media roughness values.*

Figure 6.21 shows the influence of media roughness on (a) *Lc(l)* and (b) *Fines B* content for various stress intensity ranges. In general, higher roughnesses give lower *Lc(l)* values at a given stress intensity, though this plateaus at around 0.00038 – 0.0004 Nm, and reverses for the highest stress intensity band (representing the reversal seen in Figure 6.19). The importance of stress intensity is obvious at R_a = 0.2 µm (where the data is mostly from Section 6.3), where depending on stress intensity, *Lc(l)* varies between 0.34 – 1.87 mm. *Fines B* content shows a similar relationship, although the maximum in *Fines B* at a given roughness is obtained at a lower stress intensity of around 0.0021 Nm/g. Unlike with stress intensity, the relationship between roughness and *Lc(l)* has no inflection point, with increasing roughnesses continually increasing breakage rate, for all stress intensities.

Stress intensity and surface roughness therefore appear to have similar and complementary effects on length reduction and fibrillation, with the exception that stress intensity has an optimum value beyond which it excessively wastes energy. Both parameters are expected to increase the pressure experienced in localised regions of the fibre cross-section, with stress intensity increasing the total collision force, and the roughness concentrating these forces into smaller regions. The simplest model is considering roughness as an efficiency factor to stress intensity, to produce a *roughness-modified stress intensity*; this is discussed below.

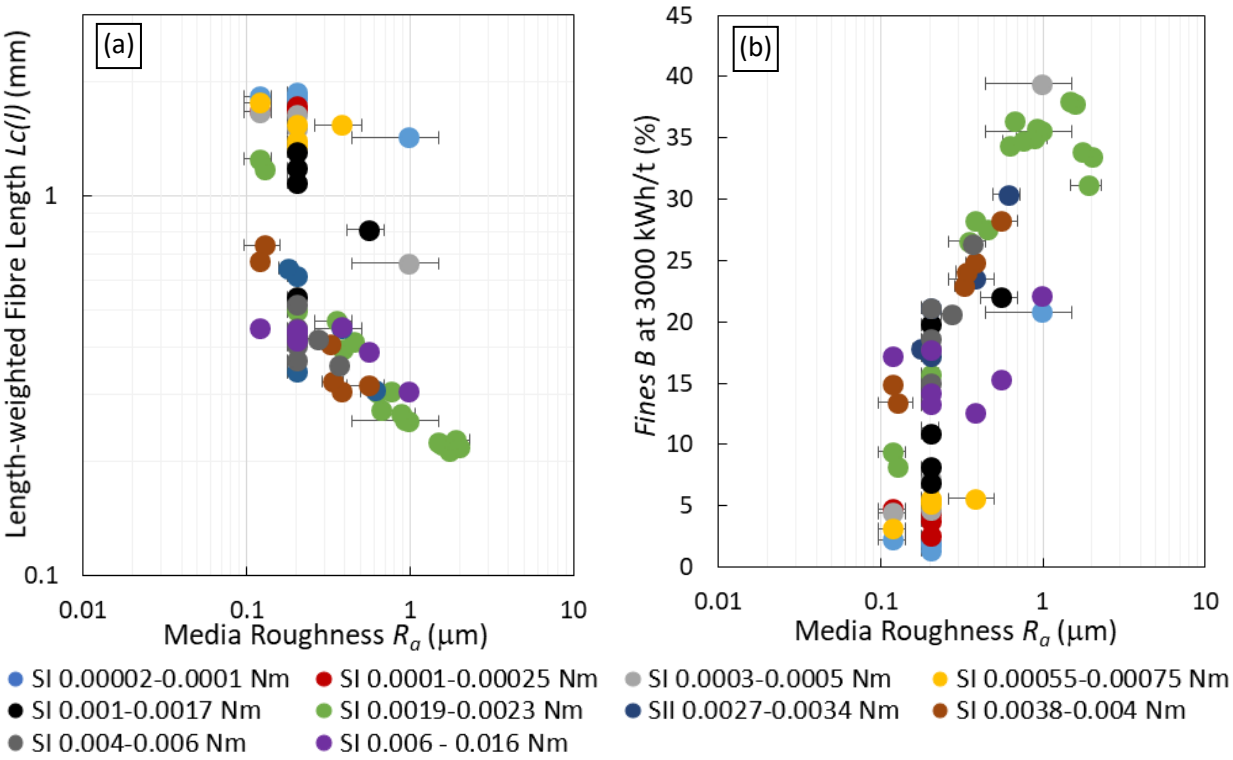

Figure 6.21 *– The influence of surface roughness on (a) Lc(l) and (b) Fines B content at 3000 kWh/t for media of different stress intensities.*

6.4.3. Roughness-Modified Stress Intensity

Lc(l) is plotted against the product of stress intensity and surface roughness ($SI \cdot R_a$) as Figure 6.22 (for both the 3000 kWh/t and 1000 kWh/t data). Compared to a plot against stress intensity alone (Figure 6.19) data points have shifted rightwards proportionally to media roughness, and now the curves for all roughnesses coincide below the optimum stress

intensity. The optimum $SI{\cdot}R_a$ value is also higher for rougher media, so these series consequently peel away from the general fit at higher $SI{\cdot}R_a$ values, thereby reaching lower minimum *Lc(l)* values. Hence, a general inverse relationship is apparent between roughness-modified stress intensity and MFC length, given that stress intensity is below the optimum.

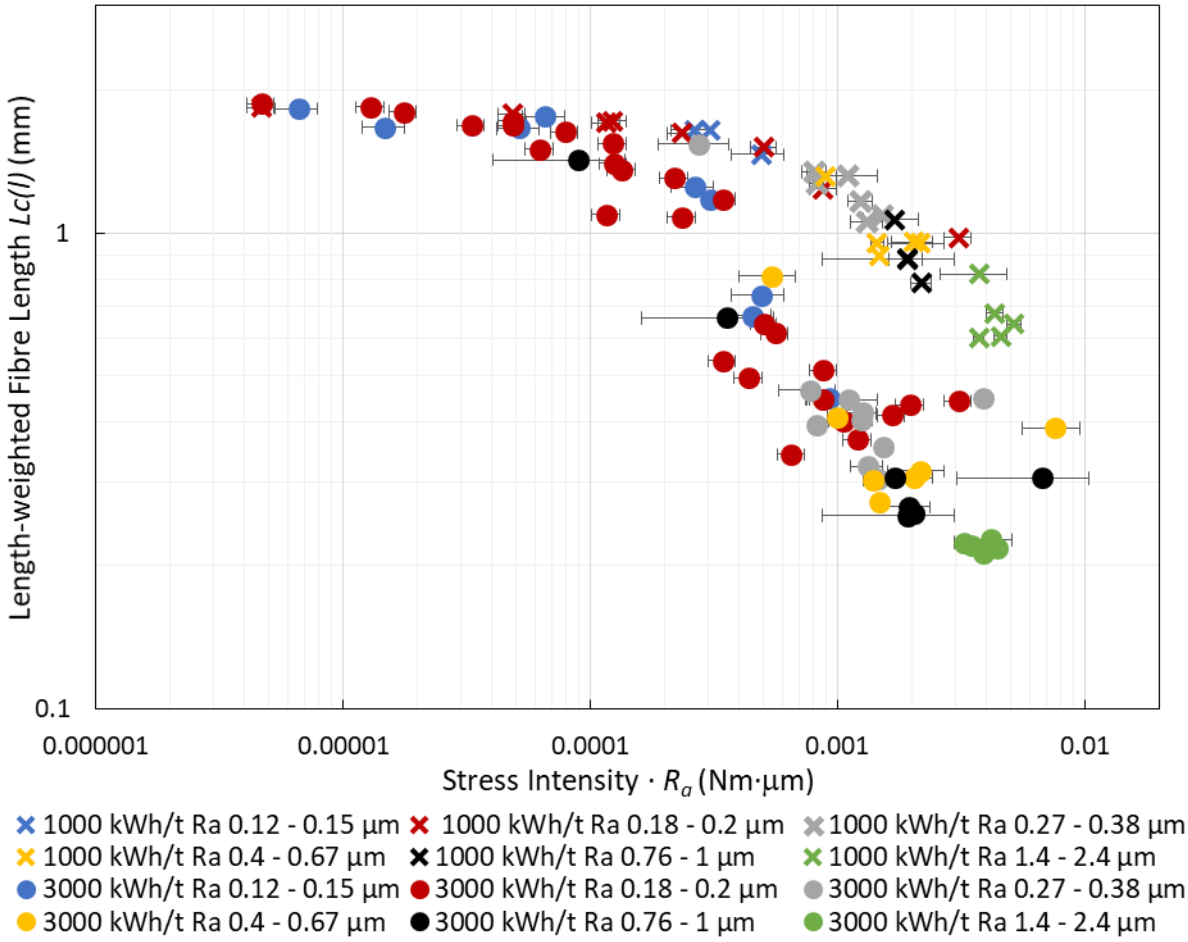

Figure 6.22 *– Lc(l) versus $SI{\cdot}R_a$ at 1000 kWh/t and 3000 kWh/t for various media roughness values.*

Perhaps more telling is the plot of *Lc(l)*-based $K_{R,Op}$ versus $SI{\cdot}R_a$ at 3000 kWh/t (Figure 6.23); this shows a linear relationship on the log-log plot (representing a *power-law* relationship), until the optimum value is approached for each roughness. A similar relationship is seen at 1000 kWh/t (Figure 6.24), giving $K_{R,Op}$ values somewhat greater than at 3000 kWh/t, which is expected as *Lc(l)*-based $K_{R,Op}$ decreases with energy input (when plotting *Lc(n)*-based $K_{R,Op}$, however, both energy inputs collapse onto one curve, see Figure A4.7 in Appendix A4).

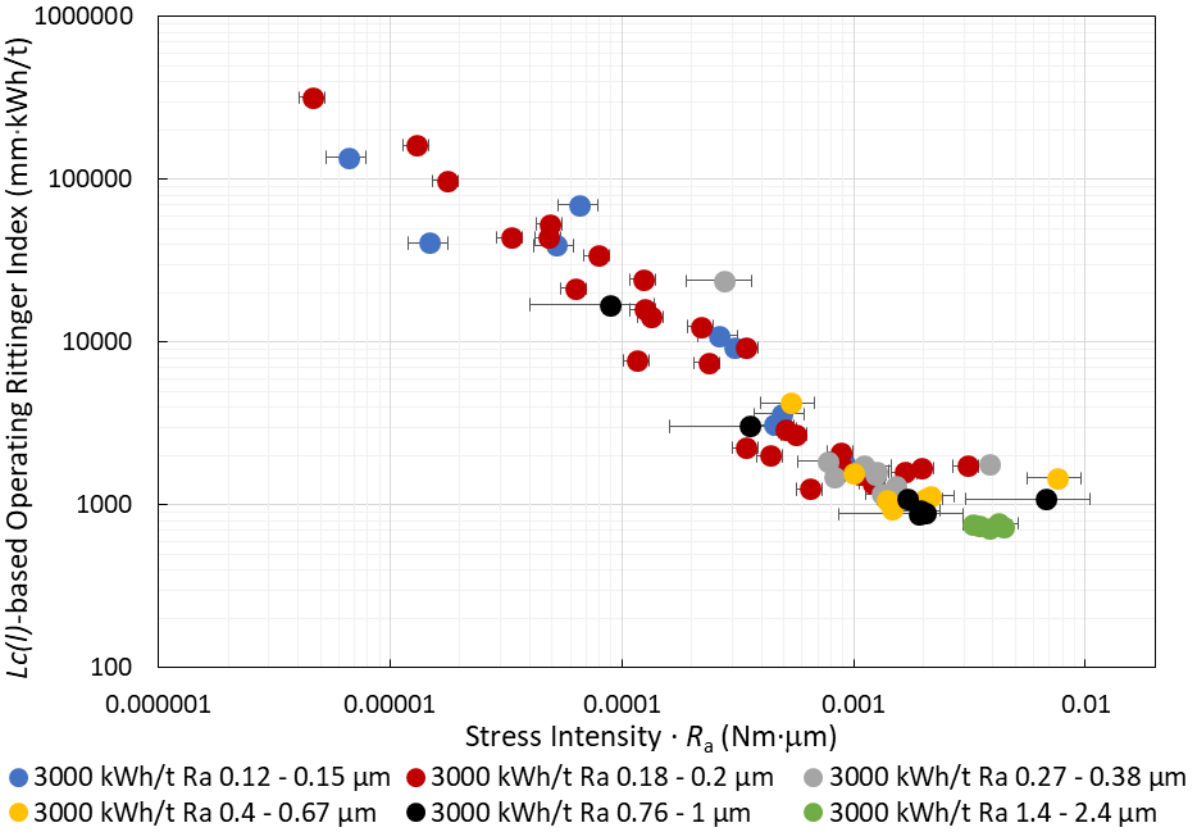

Figure 6.23 *– Lc(l)-based $K_{R,Op}$ versus SI·R_a at 3000 kWh/t for various media roughness values.*

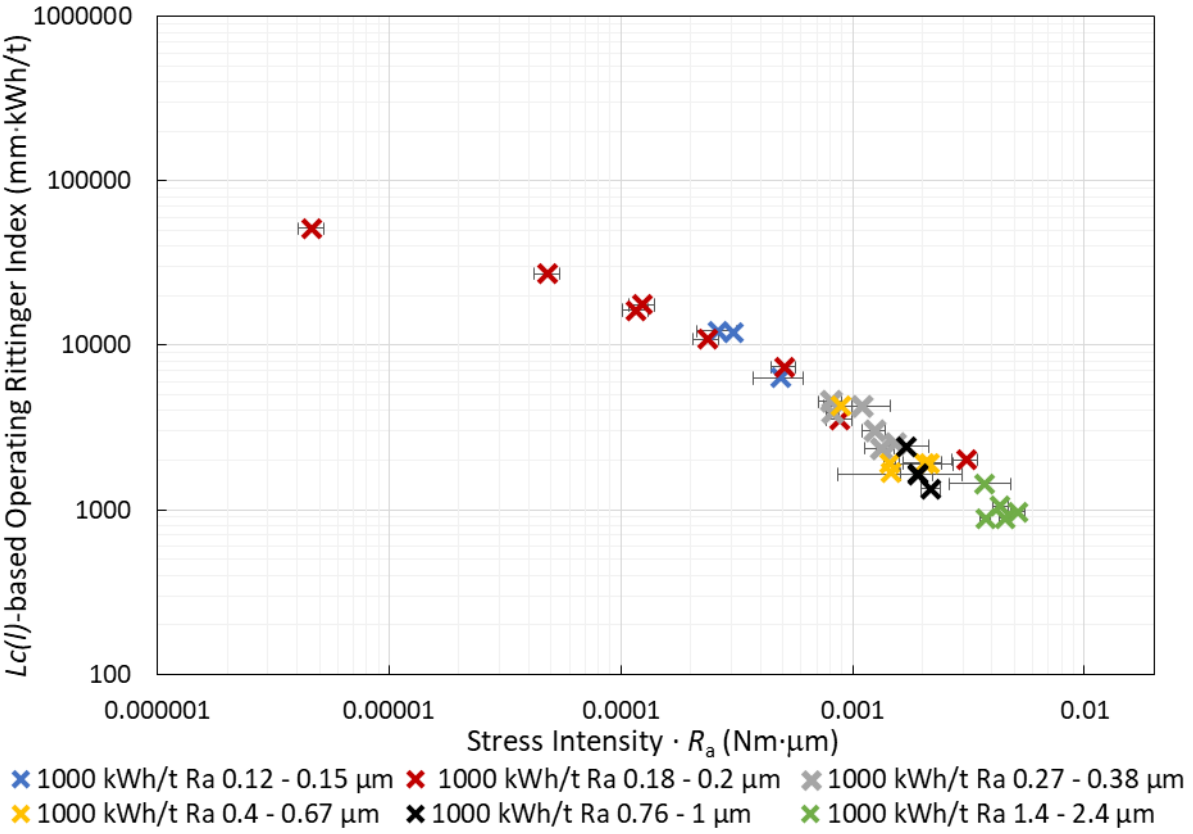

Figure 6.24 *– Lc(l)-based $K_{R,Op}$ versus SI·R_a at 1000 kWh/t for various media roughness values.*

The *Fines B* and *Fibrillation %* values are plotted against $SI \cdot R_a$ in Figure 6.25 and 6.26 respectively. In general, an equivalent relationship as with *Lc(l)* is seen; below the optimum $SI \cdot R_a$ value, curves for all roughness values appear to fit a single power-law relationship, with optimum $SI \cdot R_a$ values increasing with roughness. This increase in peak values for high roughnesses is probably because the higher local pressures experienced do not come at a cost of a greatly reduced stress number, as they do when using a higher impeller speed, for example, i.e. there is no value of roughness investigated that is 'excessive'.

Two notable outliers exist in Figure 6.25, in the 0.76 – 1 μm R_a series; at low $SI \cdot R_a$ values, despite fitting in the *Lc(l)* plot, these give higher than expected *Fines B* contents. Plots of *Fines B* against *Lc(l)* in Figure A4.8 in Appendix A4 show disproportionately high values for these points. Therefore, there may be a beneficial effect on fibrillation for low stress intensity grinds with rough media, additional to the influence of fibre breakage rate. In many of these collisions, stress intensity is expected to be largely insufficient to break the fibre cross-section, but these roughness asperities could cause localised cutting of cell wall fibrils even when the fibre is not compressed much by the media impact, which over time could fray and generate external fibrils and liberated fibrils whilst minimising fibre cross-sectional breakage. This effect requires further investigation.

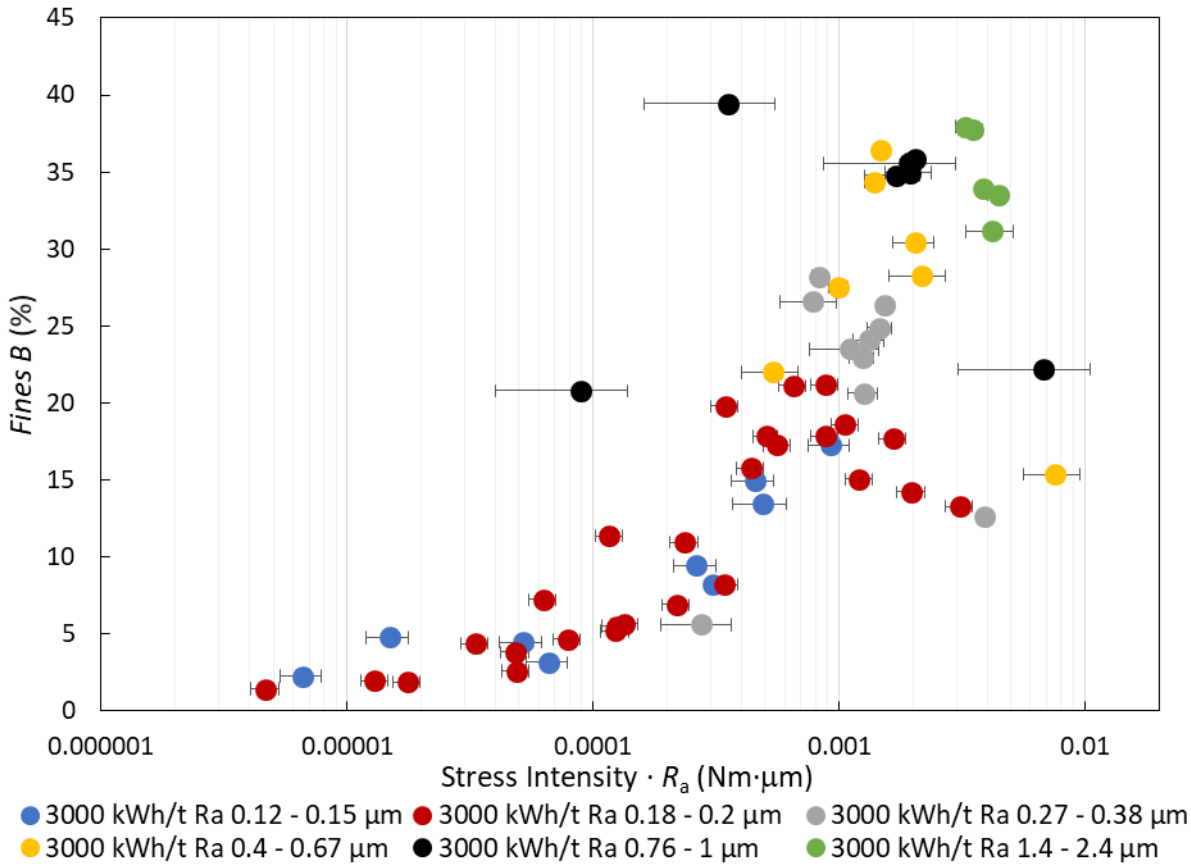

Figure 6.25 *– Fines B content versus SI·R_a at 3000 kWh/t for various media roughness values.*

Media roughness lowers the optimum stress intensity, and improves fibre breakage and fibrillation efficiency at a given stress intensity, leading to deeper minima in the stress intensity versus *Lc(l)* curve. One can transform the curves in Figure 6.19 by plotting data against the product of stress intensity and media roughness, which causes results for all roughnesses to coincide at stress intensities below the optimum. However, this cannot account for the efficiency loss at very high stress intensities, causing a divergence between curves of different roughnesses beyond the optimum *SI·R_a* values.

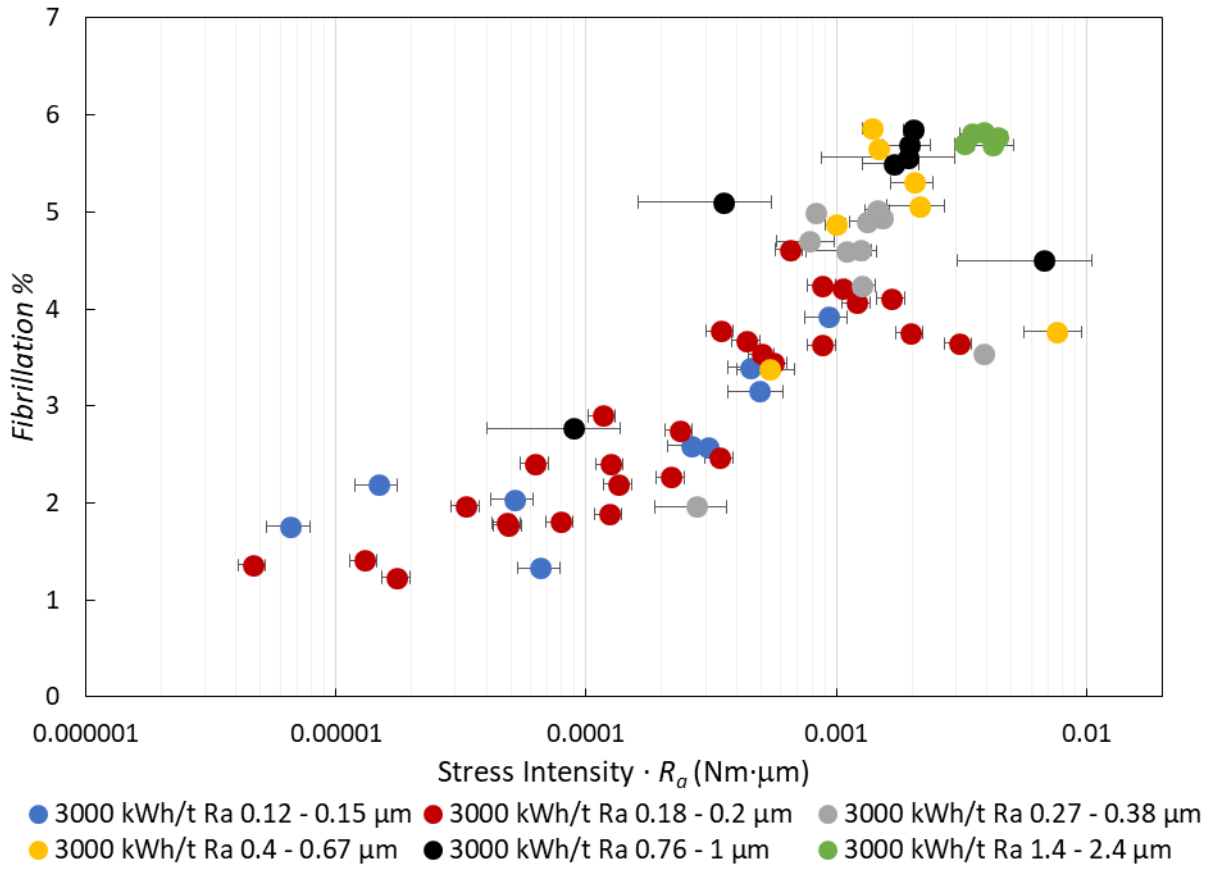

Figure 6.26 *– Fibrillation % versus SI·R_a at 3000 kWh/t for various media roughness values.*

6.4.4. Roughness-Modified Hertzian Contact Mechanics Model

Section 6.3.6 showed that plotting *Lc(l)* against fibre indentation depth as predicted by the Hertzian contact mechanics model accommodates curvature differences between media sizes (smaller media with higher curvature penetrate deeper for a given force, increasing the likelihood of stressing and breaking microfibrils), decreasing spread between data points. The Hertzian contact mechanics model is applied here also, but to accommodate media roughness, the development from Section 5.6 is needed; media roughness and asperity curvature determines *microcontact pressure*.

Theoretically, given a Gaussian height distribution of spherical-shaped asperities, stress intensity does not influence microcontact pressure, instead increasing the contact area that experiences this pressure. The author is not convinced that this holds when considering a

highly compliant cellulose surface; stress intensity affects cellulose indentation depth δ_C, and at higher δ_C values, a greater fraction of collisions would cause sufficient compression to stress individual microfibrils to cause breakage (so apply the $Y_{C,mi}$-based microcontact pressure). The product of δ_C and microcontact pressure is therefore analogous to $SI \cdot R_a$, except the former also considers media curvature and asperity curvature.

Figure 6.27 shows a plot of *Lc(l)* at 3000 kWh/t versus δ_C. The fit is very similar to when stress intensity is used (Figure 6.19), though particularly the 0.18 – 0.20 µm roughness band has less spread. It is interesting that the rapid change in *Lc(l)* occurs at indentation depths comparable to fibre cell wall thicknesses, and rougher media appear to reach an optimum at lower δ_C. Two ways to conceptualise this are suggested; to compensate for smoother media having lower microcontact pressure, stronger collisions are needed to increase microfibril stressing probability. Also, the pressure experienced is realistically not expected to sharply transition between the cell wall microcontact pressure and microfibril microcontact pressure at a certain indentation depth; instead, a continuous transition is expected, for which rougher media with higher microcontact pressures would apply the pressure required for breakage at greater separation distances (i.e. at lower collision forces).

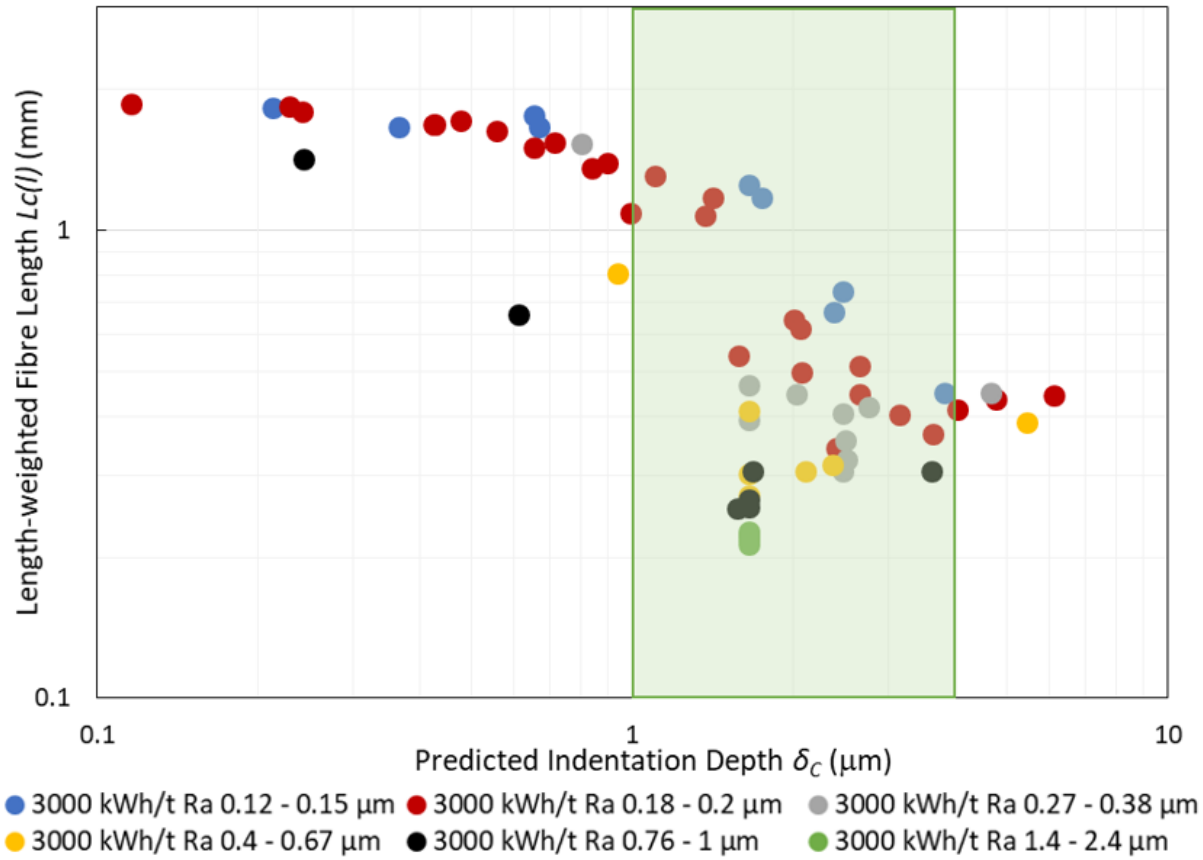

Figure 6.27 *– MFC fibre length versus predicted indentation depth at 3000 kWh/t for various media roughness values. The green box shows the range of cell wall thicknesses typical for Nordic pine fibres.*

The product of microcontact pressure and predicted indentation depth are plotted against *Lc(l)* as Figure 6.28 and *Lc(l)*-based $K_{R,Op}$ as Figure 6.29. As expected, the relationships formed are very similar to that in Figures 6.22 and 6.23 when roughness-modified stress intensity was considered, although the spread is slightly lower in the Hertzian model, primarily since media curvature is accounted for.

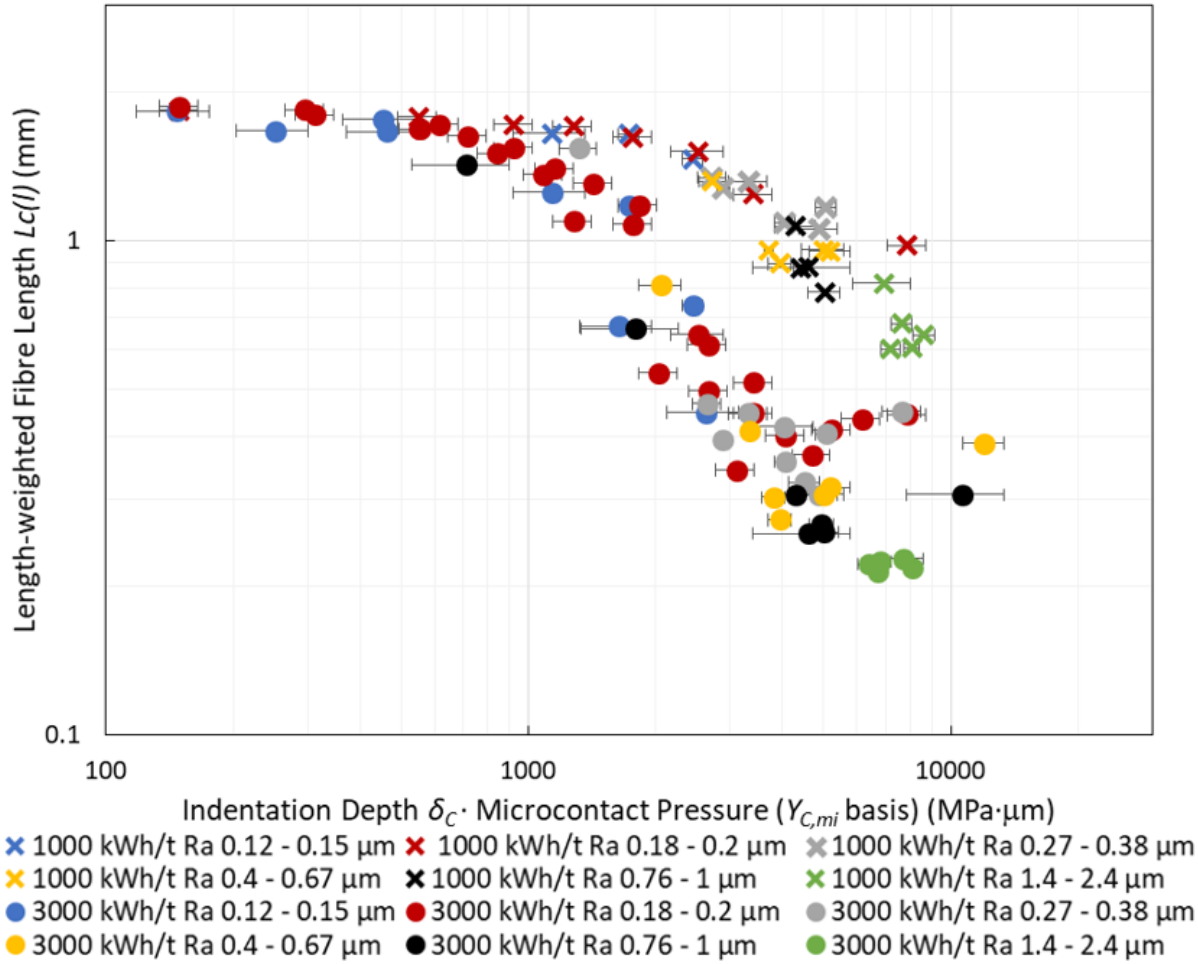

Figure 6.28 *– MFC fibre length at 1000 kWh/t and 3000 kWh/t versus the product of indentation depth and microcontact pressure for various media roughness values.*

The roughness-modified Hertzian model and the roughness-modified stress intensity model give little difference in output, so experimentally determining which is more accurate is difficult. The Hertzian model however can partially explain the unexpected effectiveness of fine media at high impeller speeds, and why coarser media at lower impeller speeds leads to greater fibre flattening but less effective breakage. These effects are relatively weak, however. Other predictions made can be tested in future work; for example, for a given fibre coarseness (i.e. cross-sectional area to break), stress intensity theory predicts no difference in breakage between small diameter, thick-walled fibres, and large diameter, thin-walled fibres, whereas the Hertzian model suggests the latter should break more easily since less indentation depth

is required. Unfortunately finding two fibre species with very similar properties except for this factor is difficult and has not been attempted, and any effects apparent in the study investigating the effect of fibre species in the subsequent chapter are obscured by numerous other important differences between fibres.

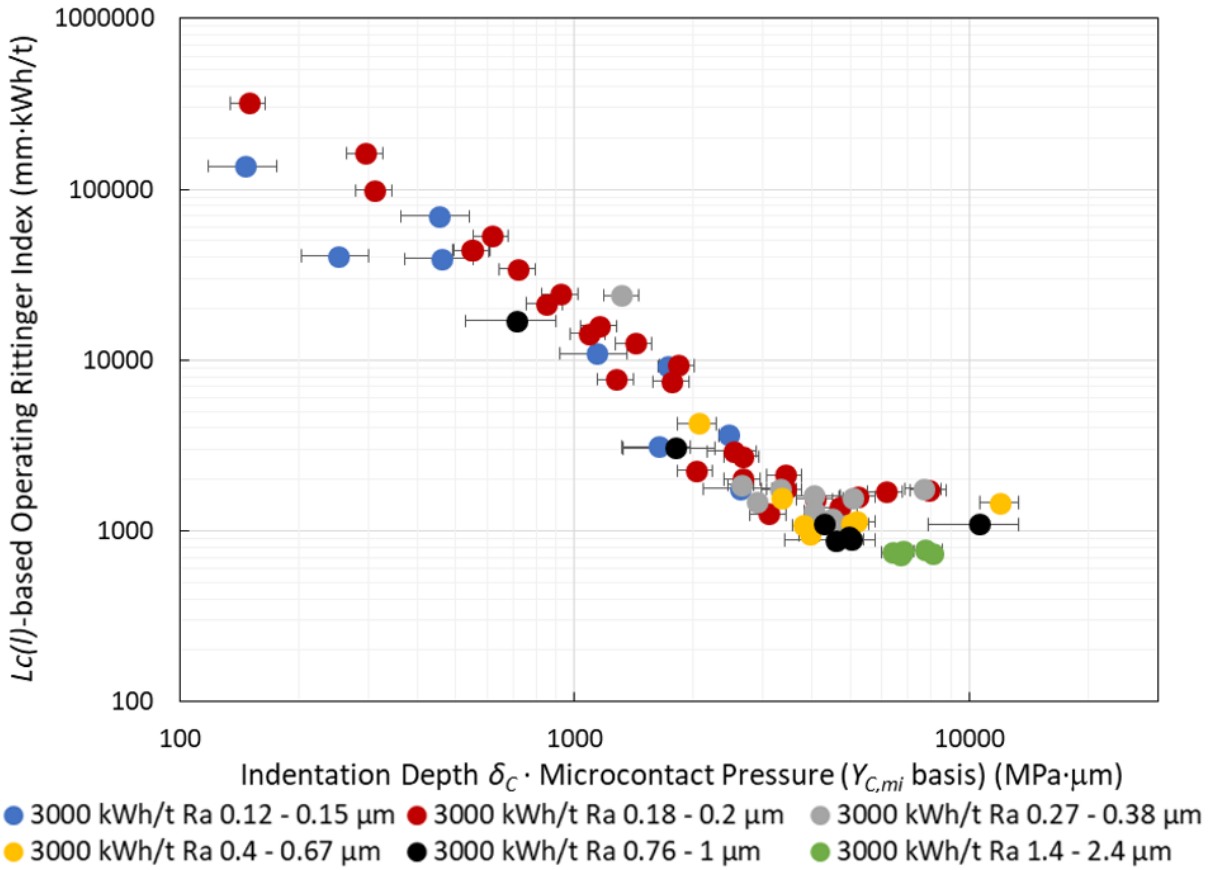

Figure 6.29 *– Lc(l)-based $K_{R,Op}$ at 3000 kWh/t versus the product of indentation depth and microcontact pressure for various media roughness values.*

6.4.5. Conclusions

The archetypical pattern of stress intensity versus particle size is followed for all roughnesses, with higher roughnesses reducing the optimum stress intensity and the MFC length achieved at a given energy input. Fibrillation parameters show a similar effect, so tensile strength likely does also. Multiplying stress intensity and roughness produces a composite parameter that collapses all data on a single curve, given that the stress intensity is below the optimum.

Within this region, the lack of roughness can be compensated for with a higher stress intensity and vice versa, which is understood as stress intensity increasing collision force, and roughness concentrating this force to improve breakage efficiency. Because stress intensity has a limiting optimum value, whereas roughness apparently does not (over the range considered), the correlation with $SI \cdot R_a$ breaks down near the optimum stress intensity for a particular roughness, causing divergence in the post-optimum region between different roughnesses.

Although the relationship with $SI \cdot R_a$ works across broad ranges, when narrowed towards industrially common values, data spread from other unconsidered factors is too great for this to be useful in selecting operating conditions. However, this still demonstrates that below the optimum intensity, increasing stress intensity and surface roughness are interchangeable and equivalent, and if rougher media is used, stress intensity should be decreased to maintain efficiency and vice versa.

An alternative model to describe these results is the roughness-modified Hertzian contact mechanics model. This gives a similar, but slightly better, fit with the data, and suggests that for rougher media, less compression is required to break microfibrils.

6.5. Summary

Section 6.3 demonstrates that stress intensity theory generally applies to fibre breakage, and consequently to subsequent fibrillation processes; although the general principle can be applied industrially, there are considerable discrepancies between media sizes; at a given stress intensity, finer media is superior than coarser media at fibre breakage. The Hertzian contact mechanics-based model can account for a large part of this by considering the higher media curvature to improve penetration into the fibre cell wall.

Section 6.4 showed that higher roughnesses decrease the optimum stress intensity, in addition to improving efficiency; multiplying stress intensity and surface roughness together allowed all media roughnesses to share the same curve for MFC length when below the optimum stress intensity. Above the optimum stress intensity, such a relationship breaks down and the curves diverge. However, these results do demonstrate that to a limited degree, surface roughness and stress intensity have interchangeable effects, and the lack of one can be counteracted by an improvement in the other.

With a given media roughness, one can identify the optimum $SI \cdot R_a$ value, so permutations of media size, density, and impeller speeds can be identified that will give efficient breakage, thereby reducing the parameter space under consideration for optimisation. Industrially, it is important to maximise power draw to increase throughput, so the economically optimum $SI \cdot R_a$ values are likely higher than the size reduction optimum, and likely favour obtaining this value with high impeller speed and low media size, though increased media wear and screening issues complicate this assessment.

This chapter and the previous two chapter together characterise the influence of media properties and operating conditions on MFC properties. However, this has all used exclusively a single fibre species; *Nordic pine.* The fibre source is known to strongly influence MFC quality, so must be investigated to allow for a more universal optimisation. This is the subject of the next chapter.

7. THE INFLUENCE OF FIBRE SPECIES ON MFC PROPERTIES

7.1. Introduction

All work in this thesis so far has solely focused on *Nordic pine* fibres. However, large variations in MFC tensile strength between fibre species are noticed industrially. Since mills are often limited in the available feedstocks available (especially for *integrated* paper mills), this dependency limits which customers can be targeted with a satellite plant model. Prior to this work, the main reasons for these differences were not understood, though some rules of thumb were made, such as birch species being excellent, and acacia species being poor.

As discussed in Section 2.2, almost any cellulose feedstock can be used to produce MFC, and some studies have noted large differences in MFC quality between feed pulps. Typically, these studies compare a small number of feedstocks, and attribute differences in MFC quality to various chemical or physical differences between fibre sources. However, fibres differ in many parameters, and the author believes that these studies typically compare too few fibre sources to demonstrate that the effect is due to one parameter rather than another. The clear exception is fibre hemicellulose content, which many studies show enhances fibrillation.

To remedy this deficiency in the literature, a diverse selection of twenty-four fibre species was used as feedstock for MFC production. The feed fibres underwent various physical and chemical characterisation techniques, with correlations between those parameters and MFC quality investigated. The bulk of this chapter details this, but first, energy sweeps for several feed fibre species are given to show the scale of difference in MFC quality.

7.2. Energy Sweeps with Various Fibre Species

Energy sweeps were completed to investigate the influence of fibre species on MFC quality and optimum energy input. Six fibre species were selected (*birch*, *eucalyptus*, *acacia*, *abaca*, *cotton linters*, and *enzyme-treated Nordic pine* fibres) to complement the *Nordic pine* data from Section 4.1. All grinds were carried out with 2.9 mm *Mullite A* media, at 50% POP and 2.5% fibre solids, at an impeller speed of 800 rpm, with energy inputs up to 5000 kWh/t. Most series were completed prior to acquiring the fibre analyser and DIC microscope, so only the tensile index data is shown here.

Figure 7.1 shows the tensile index versus energy input curves for each fibre species. All fibre sources exhibited a similar pattern, though translated to different magnitudes. The region beyond the optimum energy input where fibril degradation dominates has a similar gradient for all series, though the upcoming fibrillation-dominant region varies greatly, leading to large peak tensile strength variations, from 4 Nm/g for *cotton* to almost 12 Nm/g for *birch*. However, optimum energy input varies little, being between 2500 – 3000 kWh/t for all species except *enzyme-treated Nordic pine*.

The rationalisation given for the archetypical tensile index – energy input curve given in Section 4.1 therefore appears universal for all fibre species, with the optimum energy input representing the point where almost all of the cell wall is disintegrated into fibrils, and above which any benefits to fibrillation of further processing are more-than cancelled out by fibril degradation.

The next section compares MFC produced from twenty-four fibre species. The similar optimum energy inputs between fibre species means that, rather than necessitating a very time-consuming energy sweep for every fibre species, a single energy input at which all fibre

species will likely yield near-optimum MFC quality can be used. From Figure 7.1, this common energy input was chosen as 3000 kWh/t; this is slightly higher than optimum for most species, but was chosen because the degradation-dominant region of the curve beyond the optimum is much less steep than the fibrillation-dominant region. Therefore, considering a new fibre species, less deviation from the peak tensile strength can be expected from overshooting the true optimum energy input than from undershooting.

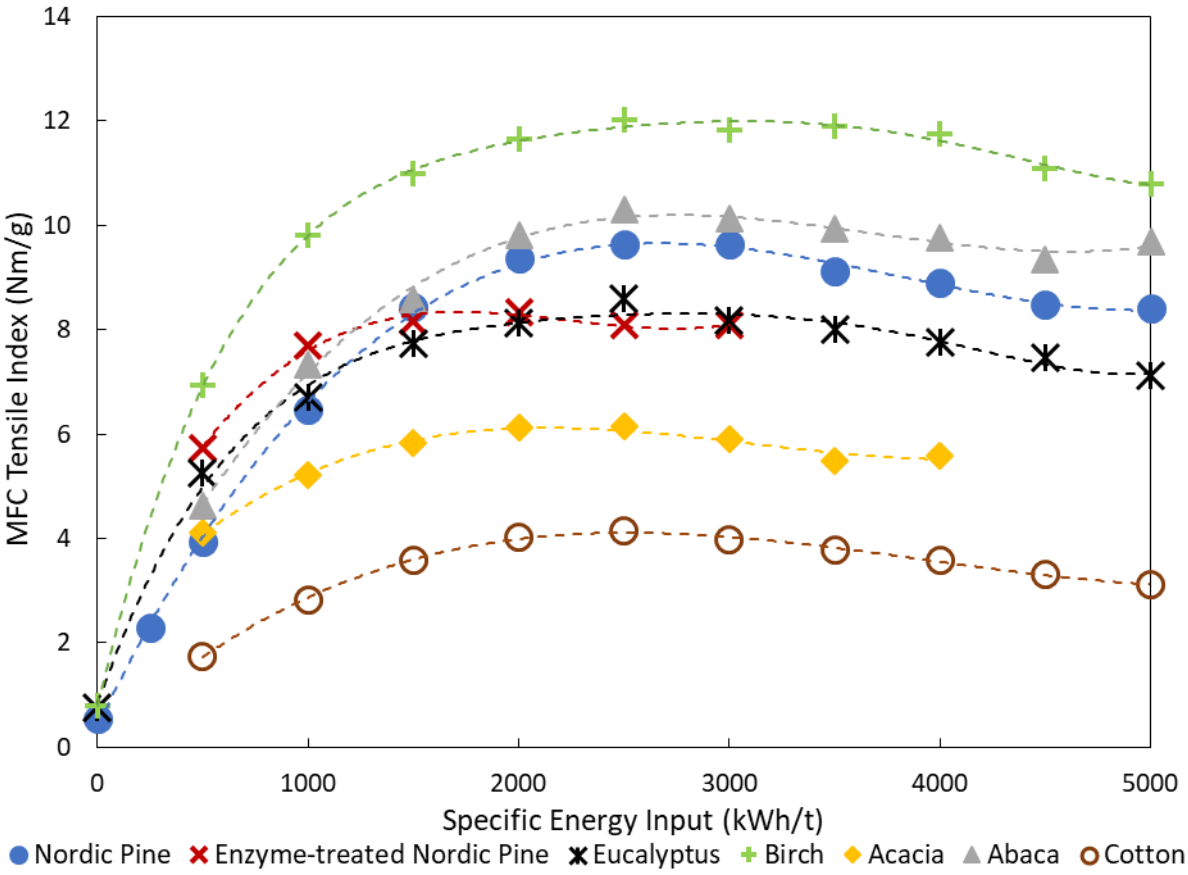

Figure 7.1 *– MFC tensile index versus energy input for seven fibre species.*

7.3. Effect of Fibre Properties on MFC Quality

7.3.1. Experimental

This investigation was undertaken to evaluate many feed fibres from a broad range of sources, to establish the general differences between them, and whether any feed fibre properties

correlate with MFC quality. The results described in this section were published in a journal[108], the article for which is attached as Appendix B2. As previously mentioned, a *common energy input* for all fibre species of 3000 kWh/t was chosen based upon Figure 7.1, for which most fibre species are expected to give tensile strengths close to their peak values.

All twenty-four feed fibres listed in Table 3.1 in Chapter 3 were chemically characterised externally by *Labtium Oy* to determine hemicellulose and lignin contents according to the methods detailed in Section 3.10. Fibre zero-span tensile strength was measured according to Section 3.9. Fibre crystallinity measurements were made using X-ray diffraction, though since the results are inconsequential, they are discussed in Section A5.2 in Appendix A5. Additionally, feed fibre geometry was characterised using the fibre analyser.

Grinds were carried out using 2.9 mm *Mullite A* media at 50% POP, 2.5% fibre solids and an impeller speed of 800 rpm, at an energy input of 3000 kWh/t for all feedstocks listed in Table 3.1. Fibre analyser and tensile strength measurements were undertaken for each sample, and several samples were selected for SEM and DIC microscopy.

7.3.2. Influence of Fibre Geometry

Fibre geometry strongly influences tensile strength in conventional papermaking; as the Page Equation describes, longer and thinner fibres improve tensile strength by increasing the contacts that each fibre makes. Experimentally, this has been seen for both softwoods and hardwoods[109-110]. Despite this, since very little of the initial fibre structure remains after complete disintegration into MFC, a correlation between feed fibre dimensions and MFC properties was not expected. However, higher aspect ratio fibres would increase charge viscosity, lowering effective stress intensity (see Equations [2.5] – [2.7]) and the Hertzian

contact mechanics model developed in Section 4.2 suggests that fibres with thinner cell walls should be easier to disintegrate.

Fibre analyser results for each feedstock are displayed in Table A5.1 in Appendix A5. Graphs of each geometric parameter versus MFC tensile index are displayed as Figures A5.2 – A5.9, though no significant correlation is seen; therefore, under these grinding conditions, fibre geometry does not noticeably influence MFC properties, or at least any influence is concealed by the other differences between fibres discussed later. However, Chapter 8 later shows that feed fibre length influences the optimum operating conditions, and also that for many fibres the conditions used in the present chapter apply an above-optimum stress intensity, likely obscuring any subtle effects of fibre geometry.

7.3.3. Influence of Fibre Chemistry

Hemicellulose content, lignin content, and cellulose crystallinity were investigated, and are each discussed separately below.

Cellulose Crystallinity

Cellulose crystallinity results are shown in Section A5.2 in Appendix A5, and did not correlate significantly with any quality parameter, or even show the expected correlation with fibre zero-span tensile strength; this implies that molecular-scale weaknesses from amorphous regions do not influence fibrillation, and instead larger-scale flaws are important.

Lignin Content

The lignin contents of each fibre species are shown as Table A5.2 in Appendix A5. Only *Giant Reed* fibres contained substantial lignin (12.7%), which does not perform unusually compared to other fibres, so the influence of lignin is inconclusive here, though it can be safely assumed inconsequential in this study.

Hemicellulose Content

The residual hemicellulose in bleached chemical pulp resides within the fibre cell wall, forming layers separating neighbouring microfibrils, which is expected to facilitate their separation under mechanical forces. From this consideration, and the literature introduced in Section 2.5, a positive correlation with MFC quality was expected.

The raw residual sugar data for xylose, mannose, arabinose, and galactose are displayed as Figure A5.1 in Appendix A5 for each fibre species. These are converted to xylan, glucomannan, and total hemicellulose contents (see Table A5.2) according to the assumptions stated in Section 3.10. Giving different weightages to xylan or glucomannan did not improve the correlations, with the best fit found using the *total* hemicellulose content, so this is what is used henceforth. Figure 7.2 shows the MFC tensile index at 3000 kWh/t versus the total hemicellulose content. A reasonable linear correlation exists (with an R^2 value of 0.63), which is far better than any other individual fibre parameter investigated.

As discussed in Section 2.5, two mechanisms are suggested for why hemicellulose improves MFC quality; firstly, a hemicellulose-rich fibre, when disintegrated into MFC, has more hemicellulose chains upon its liberated surface area, forming more bridges between particles upon drying, improving relative bonded area and specific bonding strength. Also, hemicellulose, being a weak amorphous layer, is believed to provide a preferred plane of breakage along the microfibril longitudinal direction, facilitating disintegration into finer microfibrils, therefore increasing aspect ratio.

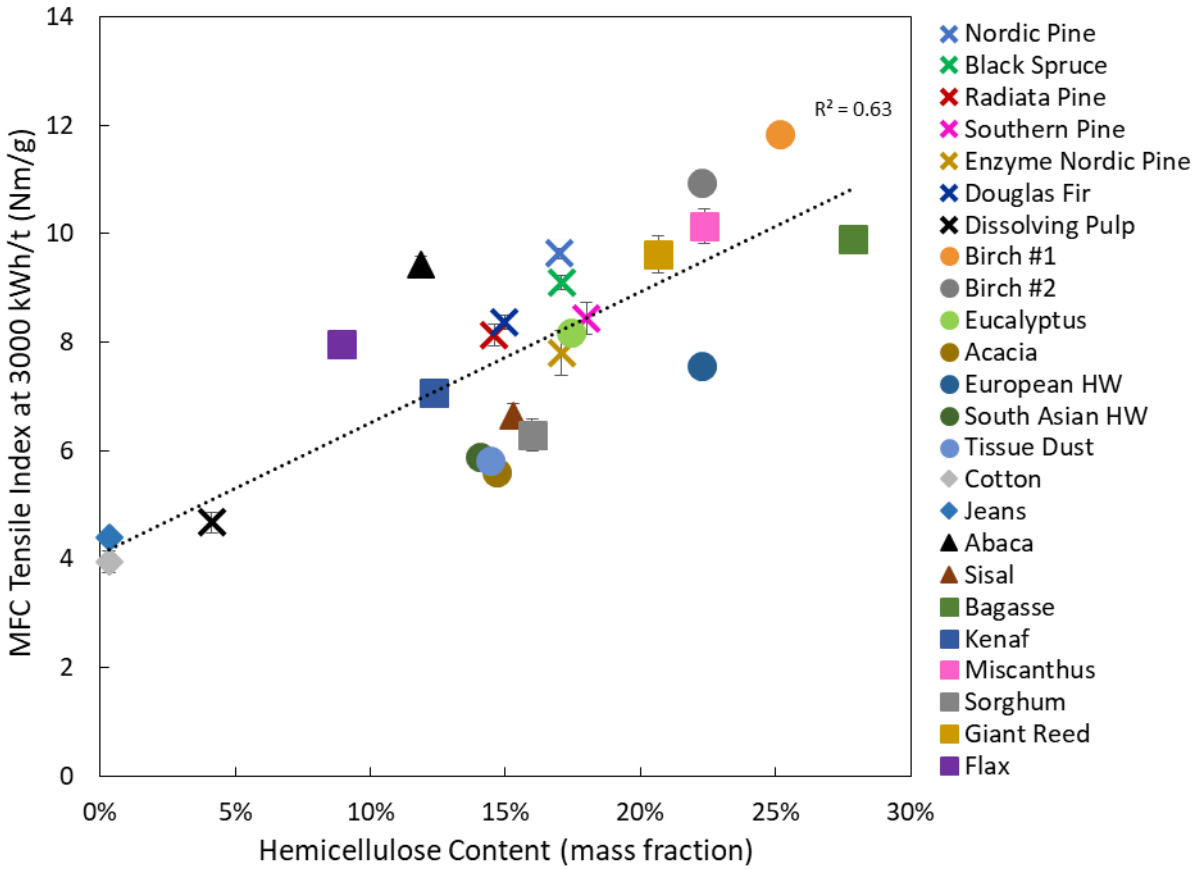

Figure 7.2 *– Fibre hemicellulose content versus MFC tensile index at 3000 kWh/t. Here and in all subsequent plots in this chapter, crosses represent softwoods, circles represent hardwoods, diamonds represent cotton fibres, triangles represent leaf fibres, and squares represent other miscellaneous non-wood sources.*

To verify the existence of the latter mechanism, SEM images were taken of MFC samples with a range of hemicellulose contents. Six of such images are displayed as Figure 7.3. Figures 7.3 (a) and (b) respectively show high hemicellulose *bagasse* and *miscanthus* MFC which exhibit very fine microfibrils. *Nordic pine* and *acacia* MFC (Figures 7.3 (c) and (d)) have moderate hemicellulose content, and consequently have somewhat coarser microfibrils. Finally, Figures 7.3 (e) and (f) show low hemicellulose MFC, *dissolving pulp* and *cotton*, which have by far the coarsest microfibrils. Therefore, clearly, a high hemicellulose content promotes delamination into finer microfibrils. This does not rule out the alternative mechanism regarding the influence of surface hemicellulose also playing a role, however.

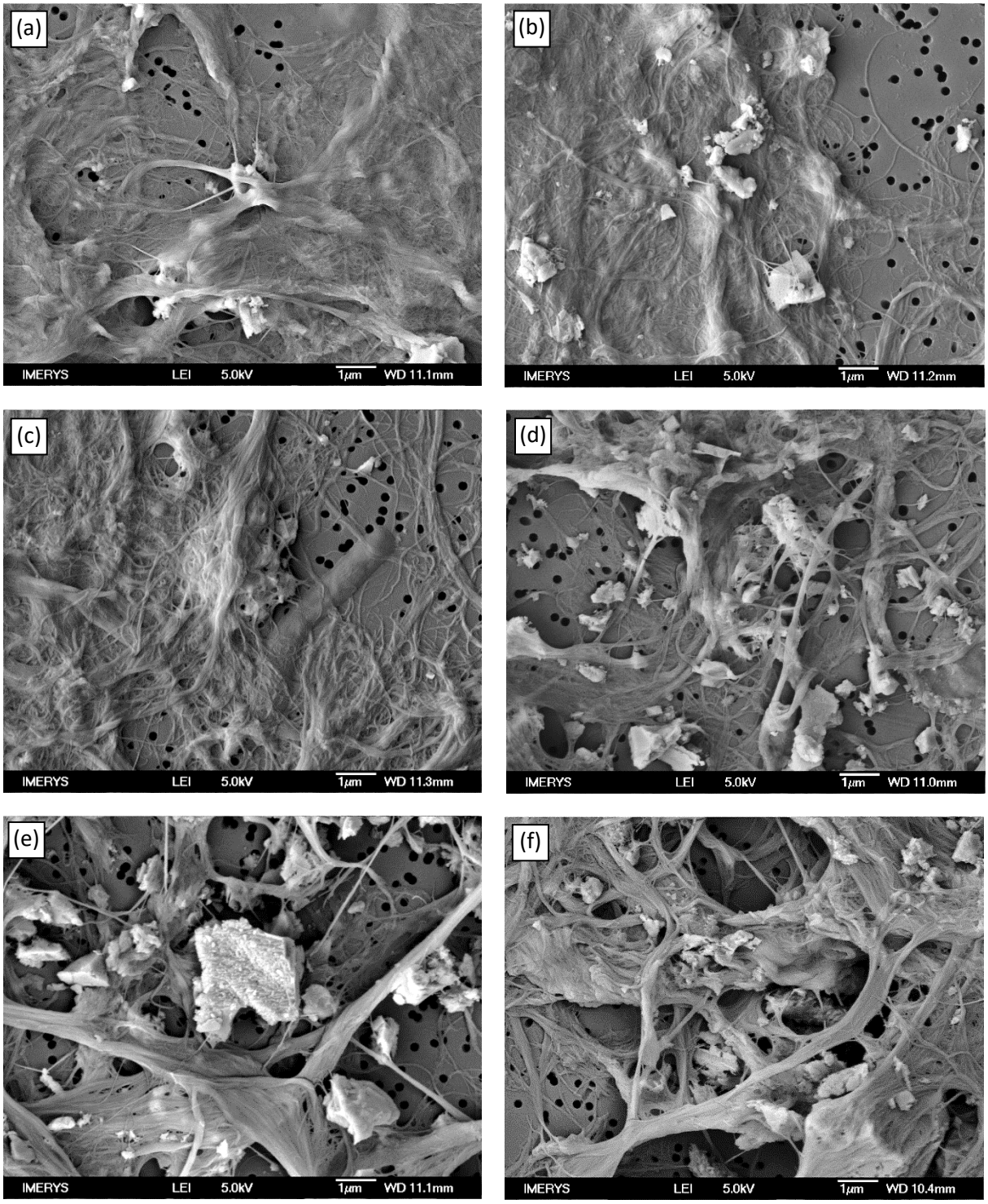

Figure 7.3 *– Secondary electron SEM images of MFC made from (a) bagasse (28% hemicellulose), (b) miscanthus (22% hemicellulose), (c) Nordic pine (17% hemicellulose), (d) acacia (15% hemicellulose), (e) dissolving pulp (4% hemicellulose) and (f) cotton (0% hemicellulose).*

A comparison of Figure 7.3 (c) and (e) is telling; the latter is *dissolving pulp* MFC, which uses a Scandinavian pine/spruce blend feedstock similar to the *Nordic pine* in the former, but with different pulping stages. *Nordic pine* undergoes the kraft pulping process, largely preserving

cell wall hemicellulose, but for *dissolving pulp*, the sulphite process is used, greatly lowering hemicellulose content. Consequently, the fact that these fibres lead to greatly different microfibril widths demonstrates that the correlation between hemicellulose content and finer microfibrils is causal, and not due to high hemicellulose plants coincidentally consisting of intrinsically fine microfibrils.

Plots of hemicellulose content versus fibre analyser quality parameters are shown in Appendix A5 as Figures A5.10 – A5.12. No correlation was seen between hemicellulose and MFC length, or *Fibrillation %*, and the correlation with *Fines B* content was weak, implying that hemicellulose has little influence on the macroscopic fibre disintegration, but instead mainly affects the constituent fibril and microfibril widths within the MFC aggregate particles.

7.3.4. Correlation between Fibre Analyser Parameters and Tensile strength

Although beyond the scope of investigating which *feed fibre* properties influence MFC quality, considering the *product* fibre analyser parameters may also be insightful. MFC tensile index is plotted against MFC *Lc(l)*, *Fines B*, and *Fibrillation %* as Figures A5.13 to A5.15 in Appendix A5; each gives rather weak correlations individually, but an empirical function of *Lc(l)* and *Fines B* gives a good correlation with MFC tensile strength for all fibres except for *abaca* and *flax* (see Figure A5.16). The improvement from including *Lc(l)* is because when fibres are fully disintegrated, a high *Lc(l)* indicates long liberated fibrils which have suffered minimal degradation.

Figure 7.4 shows the correlation between MFC length and tensile strength. Although the general correlation is very weak, the data points form clusters depending on hemicellulose content. Considering the moderate hemicellulose content fraction, a correlation between

MFC length and tensile index is much clearer. Combining fibre length and hemicellulose content is therefore considered in the next section.

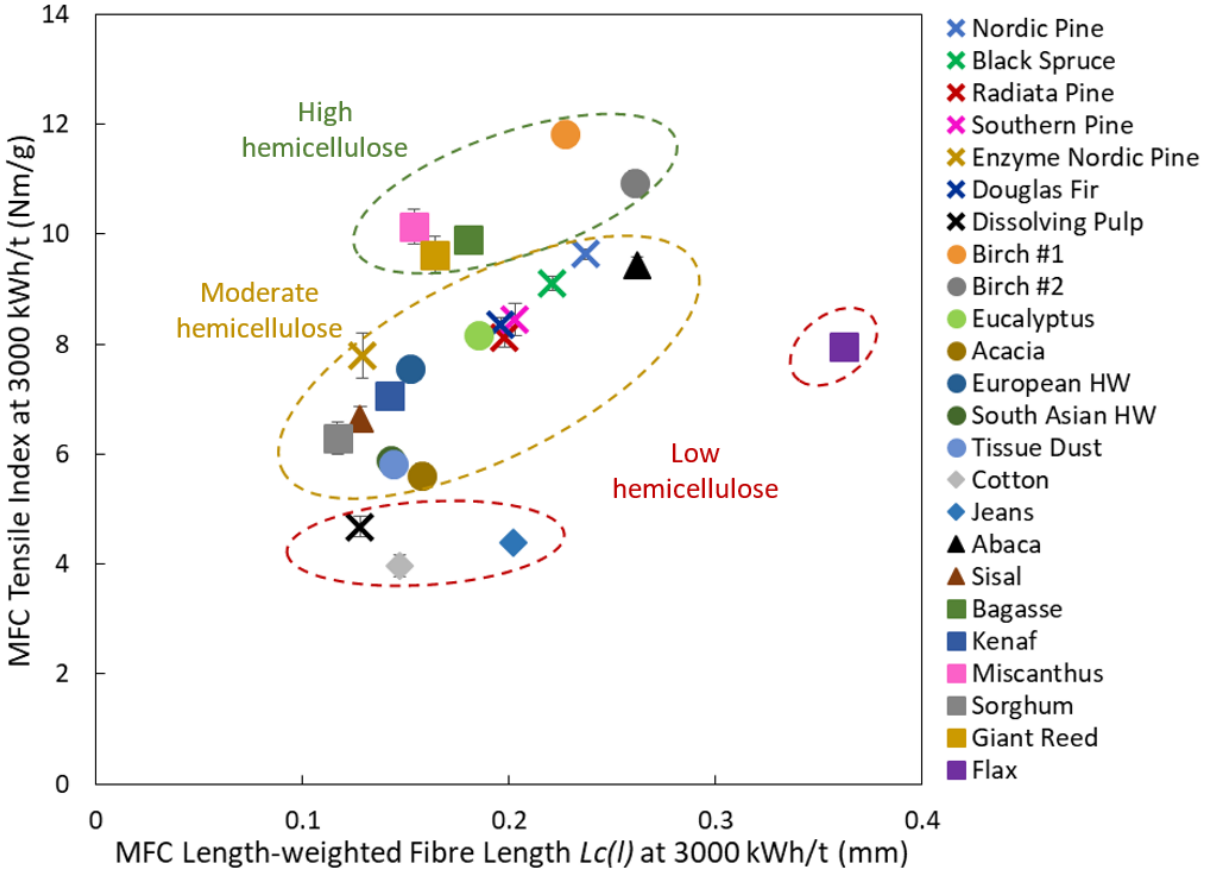

Figure 7.4 *– MFC tensile index versus MFC length, showing clusters with similar hemicellulose contents.*

7.3.5. Product of Hemicellulose Content and MFC Length

The product of feed fibre hemicellulose content and MFC length correlates very well with MFC tensile strength, as Figure 7.5 shows. It appears that MFC length is the primary missing parameter in improving the correlation between hemicellulose content and tensile strength; including it greatly improves the R^2 value from 0.63 to 0.87.

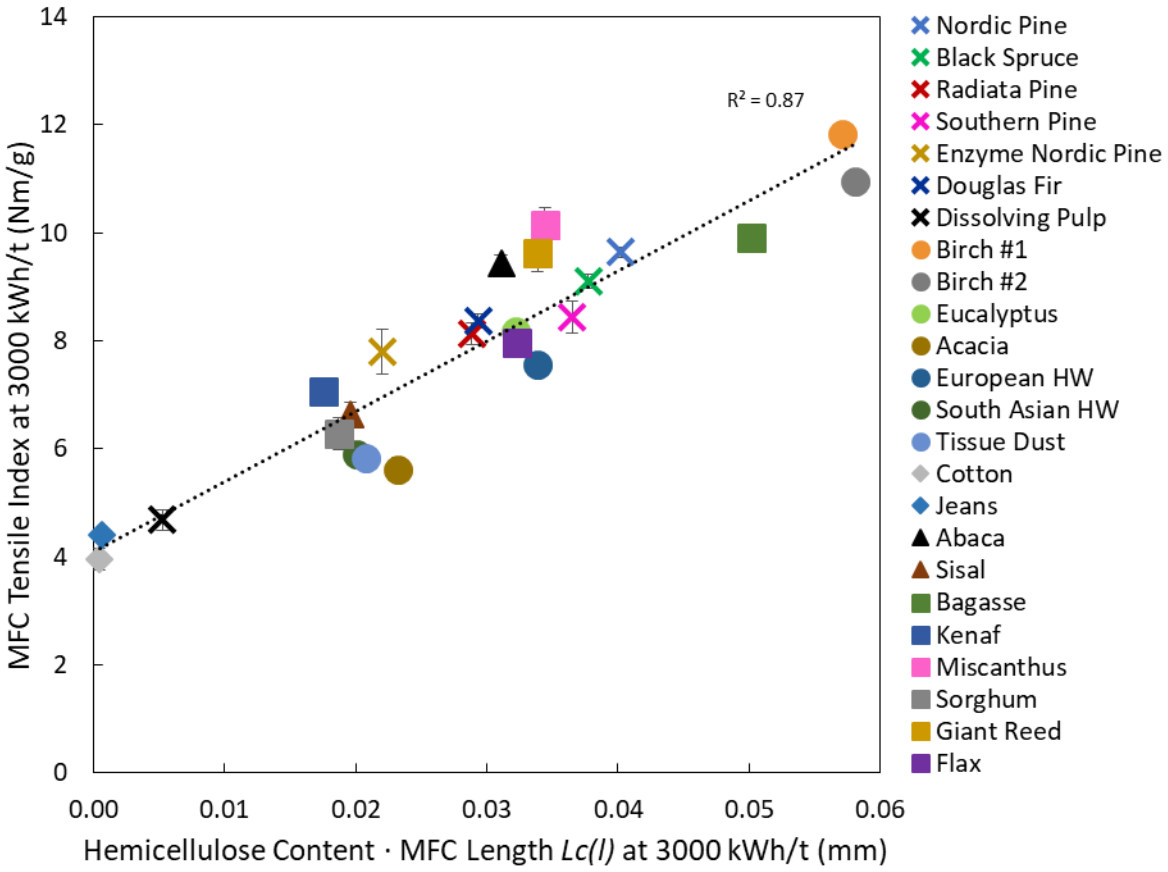

Figure 7.5 *– MFC tensile index versus the product of MFC length and hemicellulose content.*

A consideration of the Page Equation (Equation 2.1) was undertaken to give theoretical grounding on why such a strong correlation exists. Equation 2.1 was derived for straight, individualised fibres in a mineral-free sheet, so may not entirely be applicable to MFC nanopaper with 80 wt% mineral content, and highly entangled, conformable MFC particles. However, the general concepts are expected to hold, i.e. fibre length and relative bonded area improves bonding.

Since disintegrating a fibre into MFC greatly increases relative bonded area, the bonding term of the Page Equation would become less limiting, so with sufficiently extensive fibrillation, sheet failure would eventually be dominated by the zero-span strength term (fibre and fibril cross-sectional breakage). To assess whether this is true for *FiberLean* MFC, an investigation was conducted (shown in Appendix A5.3) where MFC long-span and zero-span tensile

strengths were compared at different mineral loadings. This study estimates that around 25 – 30% of the strip failure is due to fibril cross-sectional breakage in the case of *Nordic pine*, so it is concluded that bonding failure is expected to be dominant, though differences in the relative propensity of fibril breakage failure between fibre species would lead to data spread. However, assuming fibril breakage is negligible is still a reasonable approximation.

Therefore, it is assumed that the fibre weakness term is zero, reducing the Page Equation to:

$$\frac{1}{T} = \frac{12A\rho}{\tau_B PL(RBA)} \dots [7.1]$$

Hemicellulose chains on microfibril surfaces are expected to extend between microfibrils, allowing for more intimate contact. Additionally, high hemicellulose contents facilitate the production of finer microfibrils, which are expected to be more flexible and compliant, enhancing contact between microfibrils, and are more susceptible to capillary forces during drying. These effects are expected to increase relative bonded area, although these same factors likely also increase the specific bond strength, τ_B, by increasing the fraction of bonded area in *molecular* contact. Additionally, hemicellulose content decreasing the fibril diameter would increase the perimeter to cross-sectional area ratio, *P/A*.

Though *P/A*, *RBA*, and τ_B are all expected to positively correlate with hemicellulose content, their relative influences cannot be decoupled. The correlation in Figure 7.2 shows a linear fit, so rather than distinguishing between the three, all these terms are replaced with the hemicellulose content *H* in Equation 7.1. Additionally, it is expected that the MFC length, L_{MFC}, is analogous to the fibre length term *L* in the Page Equation, so this replacement is also made:

$$\frac{1}{T} = k\frac{12\rho}{L_{MFC}H} \dots [7.2]$$

where *k* is a proportionality constant. Density ρ is constant for all MFC, so can be combined with *k* under a single coefficient B_1:

$$\frac{1}{T} = \frac{1}{B_1 L_{MFC} H} \dots [7.3]$$

which can be inverted to obtain the MFC tensile index:

$$T = B_1 L_{MFC} H \dots [7.4]$$

This suggests a linear relationship between the product of hemicellulose content and MFC length, which is what is observed in Figure 7.5. However, there is an intercept at zero hemicellulose content at 4.1 Nm/g; this is expected, as fibrillation cannot *only* be due to hemicellulose content, since for example *cotton* can still produce MFC in its absence. An intercept σ_0 is therefore added to Equation 7.4 to account for the fibrillation that can take place in the absence of hemicellulose.

$$T = B_1 L_{MFC} H + \sigma_0 \dots [7.5]$$

The value of σ_0 no doubt will vary with operating conditions.

Despite the excellent fit in Figure 7.5, this is not a particularly useful relationship, since MFC must first be produced to obtain this MFC fibre length, meaning that it is useless for identifying high quality feedstocks prior to MFC production. It was necessary, therefore, to determine what feed fibre properties influence MFC fibre length to make this model useful.

7.3.6. Influence of Fibre Zero-Span Tensile Index

It is expected that if the cell wall is constituted of long fibrils, after disintegration, the liberated fibrils will also be long. Also, more cross-sectional flaws would facilitate breakage of fibril and

fibre cross-sections. Therefore, fibres with few cross-sectional flaws (less damage, and fewer discontinuities at fibril end-points) are expected to produce longer MFC particles when fully disintegrated. As discussed in Section 2.4, the zero-span tensile index of the fibre is an indirect measure of this, with a high value indicating few flaws. Therefore, the feed fibre zero-span tensile strength is expected to correlate with the MFC fibre length when the fibres are fully disintegrated.

Figure 7.6 plots the feed fibre zero-span tensile strength against the MFC length at 3000 kWh/t. In general, the correlation for most fibre species is good, considering the large error bars for the zero-span strength, although there are several clear exceptions, including *flax*, *sisal*, and *kenaf*. As Section 2.4, mentions, zero-span tensile strength also depends on microfibril angle, so this likely causes these outliers, since microfibril angle is independent of fibril flaws so is not expected to influence MFC length. Microfibril angle can be measured with XRD in wood, but it is much more complicated for individualised fibres, so this was not attempted.

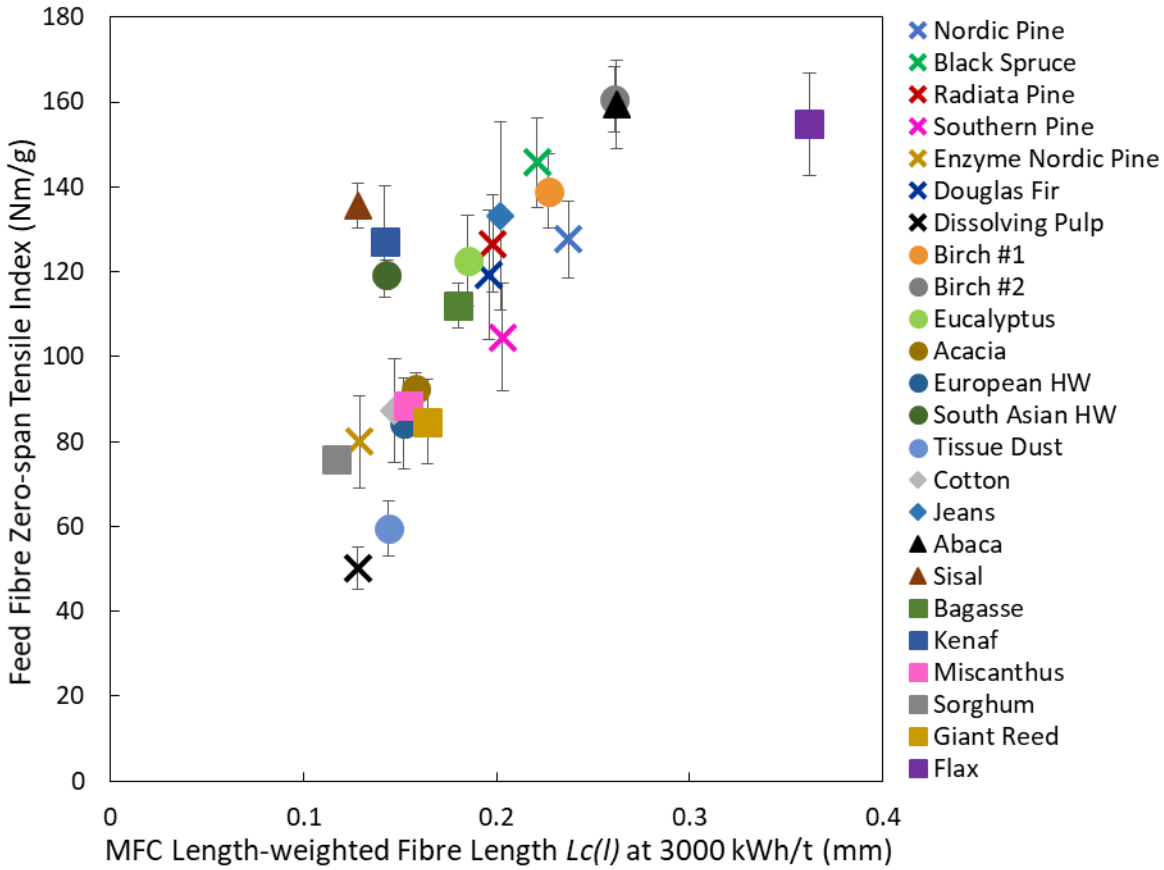

Figure 7.6 *– Feed fibre zero-span tensile index versus MFC fibre length at 3000 kWh/t for all fibre species.*

Despite this complication, the fit is sufficient for most other fibre species, so L_{MFC} in Equation 7.5 can be replaced with the fibre zero-span tensile index Z:

$$T = B_2 Z H + \sigma_0 \ldots [7.6]$$

where B_2 is a proportionality coefficient. Figure 7.7 shows that the product of hemicellulose content and fibre zero-span tensile index correlates fairly well with MFC tensile index. Since the correlation between zero-span tensile index and MFC length is far from perfect, it is not surprising that the fit in Figure 7.7 is significantly poorer than in Figure 7.5. Figure 7.7 fits well at the extremes, but towards the centre of the graph, certain fibre species deviate significantly from the best fit curve.

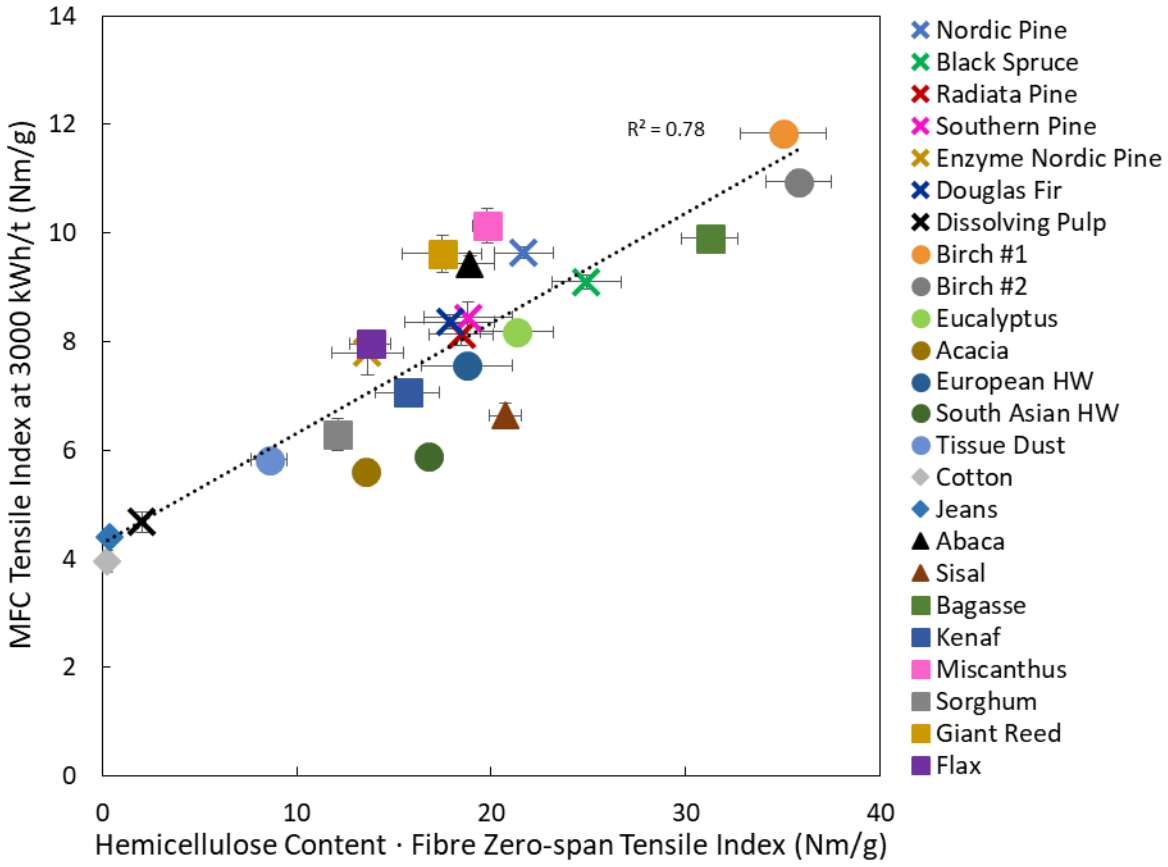

Figure 7.7 *– MFC tensile index at 3000 kWh/t versus the product of feed fibre zero-span tensile index and hemicellulose content for all fibre species.*

A notable comparison is made between *Nordic pine* and *enzyme-treated Nordic pine* fibres, which are physically and chemically similar in every measured way *except* the zero-span tensile index, which is much weaker in the latter. The enzyme-treated variant consequently has a much lower MFC fibre length and a lower tensile strength, implying that the observed relationship with zero-span tensile strength is causal.

Despite the increase in the data spread compared to when MFC length is used, Figure 7.7 still shows a fairly good fit for most fibre species, and this relationship has the key advantage that both input parameters are fibre properties that can be measured without needing to produce the MFC first. This relationship therefore can be useful in shortlisting which fibre species are worth considering as a feed for MFC production.

7.3.7. Differential Interference Contrast Microscopy

MFC of various fibre species at 3000 kWh/t

Supporting evidence for the aforementioned influences of hemicellulose and zero-span tensile strength was obtained with microscopy. SEM images in Section 7.3.3 demonstrate that hemicellulose facilitates finer microfibril generation (Figure 7.3), but due to the small field of view give no indication of fibril lengths, or sizes of the larger MFC aggregates. DIC microscopy, with lower magnification, enables this assessment, whilst still capturing differences in diameters of the larger fibrils present.

Figure 7.8 shows images of six MFC samples produced with fibres of varying hemicellulose contents and zero-span strengths. Figures 7.8 (a) and (b) show *Nordic pine* and *eucalyptus* MFC, both having similar hemicellulose contents and zero-span strengths, but the tensile strength of the former is significantly better; the fibrils in the *Nordic pine* sample appear longer than in the *eucalyptus* sample, so these two feed fibre properties alone clearly do not capture all factors responsible for influencing MFC geometries. However, *tissue dust* MFC (Figure 7.8 (c)), which has only slightly lower hemicellulose content but much lower zero-span strength, consists of much shorter fibrils, resulting in low tensile strength.

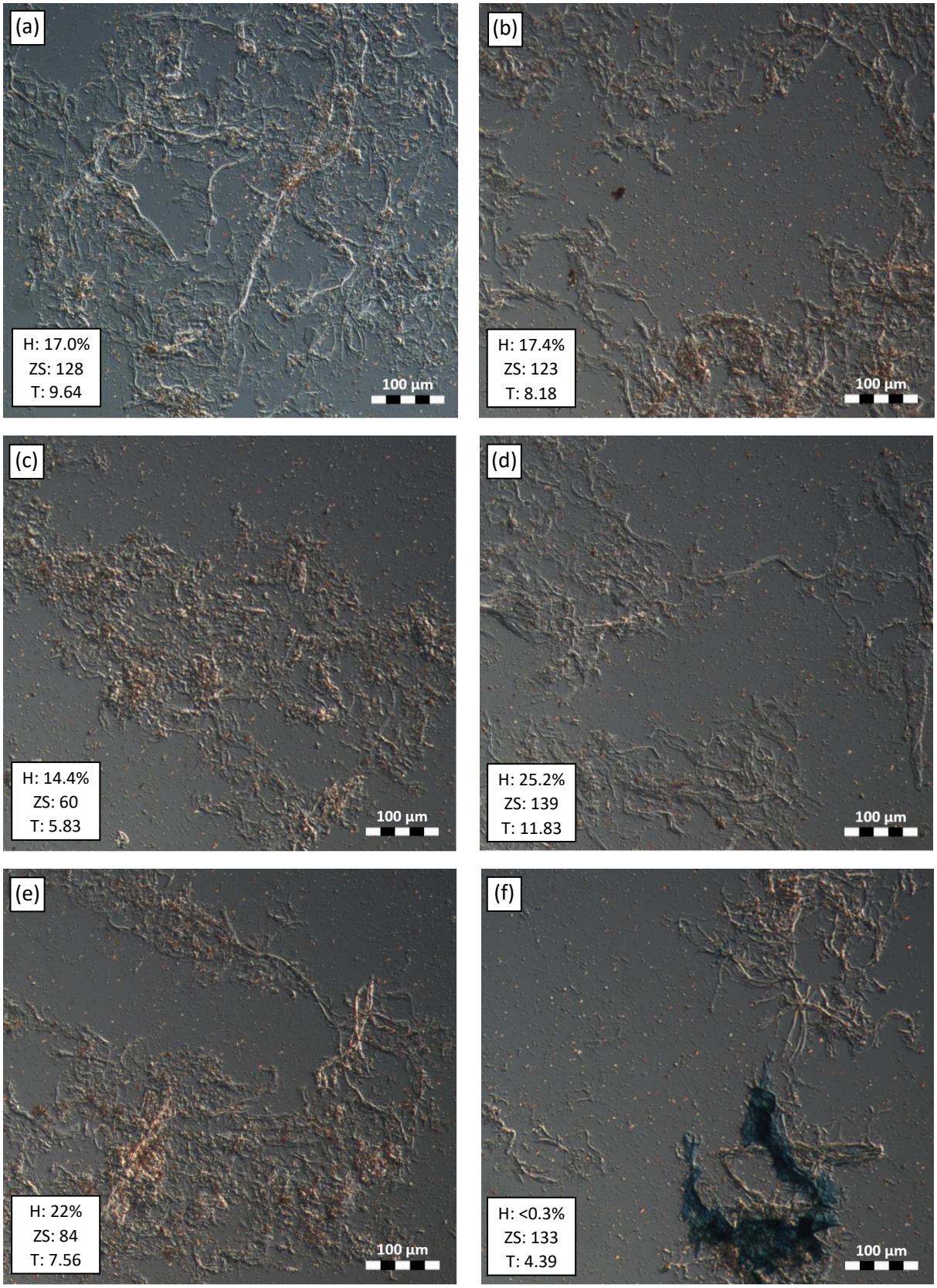

Figure 7.8 *– DIC Microscopy images of (a) Nordic pine, (b) eucalyptus, (c) tissue dust, (d) birch, (e) mixed European hardwood, and (f) jeans cotton MFC produced at 3000 kWh/t. Annotations give the hemicellulose content 'H', the feed zero-span tensile index 'ZS' (Nm/g) and MFC tensile index 'T' (Nm/g).*

Figure 7.8 (d) shows *birch* MFC, with both a high zero-span strength and high hemicellulose content; similarly to Figure 7.8 (a) and (b), fibrils tend to be long, but they also appear thinner, and 'fuzzier', being less well-defined, implying finer-scale fibrillation than visible at this scale (which is supported by SEM images in Figure 7.3). Figure 7.8 (e) shows *mixed European hardwood* MFC, with a hemicellulose content similar to *birch*, but lower zero-span tensile strength; one can see shorter fibrils in this case. Because of the higher hemicellulose content, finer fibrils than for *tissue dust* MFC are expected, which appears true, albeit judgement is difficult due to the already short fibril sizes. Finally, Figure 7.8 (f) shows *jeans* MFC, with a high zero-span strength but negligible hemicellulose content. As expected, liberated fibrils are long, but are much coarser and more sharply defined than in the other examples.

To summarise, the expected influences on fibril length and width of feed fibre hemicellulose content and zero-span strength are observed with microscopy, and are supportive of the suggested mechanisms that hemicellulose facilitates liberation of finer fibrils and a high zero-span tensile strength results in longer liberated fibrils and larger MFC aggregate particles.

Effect of pulping and pre-treatment of Nordic pine fibres on MFC properties

This study has focused mostly on fibres from a wide range of plant species, largely undergoing similar pulping processes. However, these fibres also differ in other attributes, including the precise arrangement of fibrils and microfibrils and hemicelluloses in the ultrastructure (including microfibril angle), and in intrinsic fibril and microfibril dimensions, which are expected to influence MFC properties. Therefore, to better support the findings of this chapter, a single fibre source undergoing different pre-treatments to change the hemicellulose content and zero-span tensile strength is preferable, since these other factors are kept constant.

Three fibres used in this study are suitable for this purpose, all being Nordic pine/spruce blends that underwent different pulping and treatment processes. These fibres are listed below:

1. *Nordic pine*
2. *Enzyme-treated Nordic pine*
3. *Dissolving pulp*

The *enzyme-treated Nordic pine* used the *Nordic pine* fibres as a feed, undergoing an in-house enzymatic degradation process which greatly decreased the zero-span tensile strength whilst maintaining fibre geometry and chemistry. To produce *dissolving pulp*, fibres very similar to *Nordic pine* underwent a sulphite pulping process, removing the majority of cell wall hemicellulose and greatly degrading zero-span tensile strength. Key properties of each of these fibre species and resultant MFC are displayed in Table 7.1.

Table 7.1 *– Fibre properties and MFC properties from three Nordic pine-based fibre sources.*

Fibre Source	Hemicellulose Content	Fibre Zero-Span Tensile Index (Nm/g)	MFC Fibre Length at 3000 kWh/t (*Lc(l)*) (mm)	MFC Tensile Index at 3000 kWh/t (Nm/g)
Nordic pine	17.0%	128	0.237	9.6
Enzyme-treated Nordic pine	17.1%	80	0.129	7.8
Dissolving pulp	4.1%	50	0.128	4.7

Enzymatic degradation, which greatly reduced zero-span tensile strength, also greatly reduces the MFC length, consequently decreasing the MFC tensile index (as Figure 7.1 shows, this is still close to the peak strength, so is mostly not due to overgrinding).

Dissolving pulp shows both a great decrease in zero-span strength and hemicellulose content compared to *Nordic pine*, giving a similar MFC *Lc(l)* value to *enzyme-treated Nordic pine* (perhaps the low hemicellulose content reduces fines generation, causing less reduction in

Lc(l) which cancels out the effect of the even lower zero-span tensile strength). Despite similar *Lc(l)* values, the *dissolving pulp* MFC is much weaker in tensile strength, because the low hemicellulose content inhibits fibrillation.

Microscopy images of MFC taken at low energy inputs tend to be more insightful since the manner of fibre disintegration is observed. Grinds with *Nordic pine*, *enzyme-treated Nordic pine* and *dissolving pulp* fibres were carried out at 1000 kWh/t and DIC microscopy images taken; these are shown as Figure 7.9 (a), (b), and (c) respectively.

Fibre cross-sectional breakage rate is much higher for *enzyme-treated Nordic pine* and *dissolving pulp* fibres than untreated *Nordic pine* fibres, giving much shorter fibre fragments. Additionally, the external fibrils generated in Figure 7.9 (a) are much longer than for the other two fibres, suggesting that a high zero-span strength indeed results in the *generation* of long fibrils, rather than just reducing the degradation of liberated fibrils. However, microscopy images of MFC produced with nylon media and *Nordic pine* fibres (Figure 4.21) show much longer fibrils than in Figure 7.9 (a); consequently, there is still considerable degradation of fibril lengths even at just 1000 kWh/t, and zero-span strength plays a role in resisting this.

The differences between Figures 7.9 (a) and (b), the feed to which differs only in zero-span tensile strength, is strong evidence that high values of this factor slow both fibre breakage and liberated fibril breakage. One could therefore expect a lower optimum energy input for *enzyme-treated Nordic pine*, which Figure 7.1 indeed shows to be the case. The peak tensile strength is believed to be lower because at this lower energy input, there has been less opportunity for fibrillation, and further increases in energy input excessively degrades the weak fibrils.

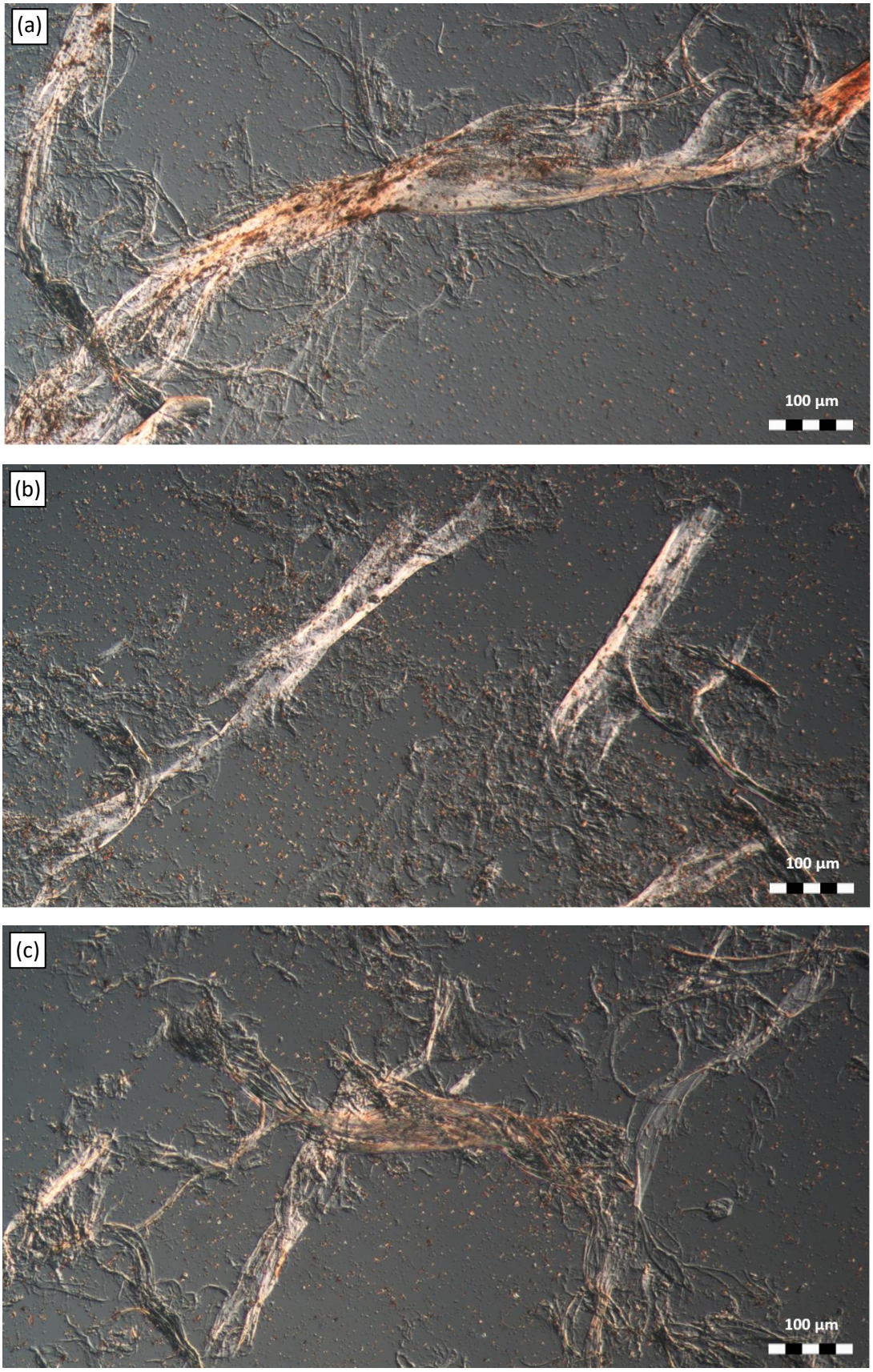

Figure 7.9 *– DIC images of MFC ground to 1000 kWh/t using (a) Nordic pine fibres, (b) enzyme-treated Nordic pine fibres, and (c) dissolving pulp fibres.*

Comparing Figure 7.9 (b) and (c) one can see that the liberated fibrils in the former are much finer, and 'fuzzier', whereas they are coarser for *dissolving pulp* MFC, indicating much less fine-scale fibrillation. This highlights the suppression of fibrillation caused by removing hemicellulose from the cell wall, which was also observed in SEM comparisons of *Nordic pine* and *dissolving pulp* MFC in Figure 7.3.

7.4. Conclusions

Energy sweeps with several fibre species in Section 7.2 show only minor variations in optimum energy input between fibre species, but peak tensile strength values vary greatly. In Section 7.3, MFC was produced from twenty-four fibre species at 3000 kWh/t, which was expected to produce MFC close to the optimum strength for each sample. The hemicellulose content of the feed fibres correlates positively with the MFC tensile index. SEM images in Figure 7.3 clearly demonstrates that higher hemicellulose fibres produce finer MFC, which is believed to be the main reason for the correlation with tensile strength. These findings are consistent with others reported in literature using alternative MFC production methods.

Lignin content was also studied, but was inconclusive as all but one sample contained very small lignin fractions. Cellulose crystallinity was found to have no noticeable influence on any MFC property, nor was any influence of feed fibre geometry noticed, although incorporating the fibre length of the *MFC* as a factor in the hemicellulose correlation improves the fit greatly; this can be rationalised using modifications of the Page Equation.

However, despite the excellent fit, it is not a useful model as it requires producing the MFC first to obtain the inputs. It was surmised that long MFC particles would be produced if the fibres and fibrils have few flaws in their cross-section, in which case the feedstock should have a high zero-span tensile strength. This correlation indeed exists, as Figure 7.6 shows, and so

the product of the hemicellulose content and fibre zero-span tensile strength also correlates well with MFC tensile index, albeit less so than when MFC fibre length is used. The influences of hemicellulose on facilitating liberation of fine fibrils, and the influence of fibre zero-span tensile strength on maintaining long liberated fibrils are validated by microscopy images in Section 7.3.7. This derived relationship uses easily measurable feed fibre properties to predict the resultant MFC strength, providing an effective method to shortlist which feedstocks are worth considering for MFC production.

There is a serious complication, however; Chapters 5 and 6 demonstrate that grinding performance is dependent both on the stress intensity and 'pressure-concentrating factors' (media roughness and mineral particles). There is an associated optimum stress intensity at a given media roughness for maximising fibre breakage and consequent fibrillation, and the grinding conditions used in these experiments are close to the optimum identified for *Nordic pine*. It can be expected that a lower zero-span strength fibre, being easier to break (as Section 7.3.7 demonstrates), would have a lower optimum stress intensity. *Nordic pine* has a relatively high zero-span tensile strength, so the conditions used in this study are expected to be superfluous for many of the weaker fibre species investigated.

Lower zero-span strengths are also thought to lead to lower optimum energy inputs, so it can safely be assumed that almost all fibre species (with the exception of *flax*) are well-disintegrated by 3000 kWh/t, in which case a high zero-span strength leads to longer liberated MFC particles. However, if the stress intensity or energy input was lowered, becoming less effective at grinding high zero-span strength fibres, then the derived relationship is expected to break down since in those cases a large MFC fibre length would instead be indicative of under-grinding.

Therefore, the relationship between the product of hemicellulose content and fibre zero-span tensile strength, and the MFC tensile strength is claimed only for when the fibre is completely disintegrated into MFC, i.e. at or above the optimum energy input, close to the optimum stress intensity. Consequently, there is scope in tuning the grinding conditions to improve the performance of low zero-span strength fibre species, since stress intensity could be lowered to be less damaging to liberated fibrils (and give more time for second-order fibrillation processes to occur) whilst still being effective at fibre breakage. This is the purpose of the next chapter, which repeats some of these grinds with a selection of fibre species, both using a lower stress intensity, and a similar stress intensity to this chapter but with pressure-concentrating factors reduced.

8. THE EFFECT OF FIBRE SPECIES ON OPTIMUM OPERATING CONDITIONS

8.1. Introduction

So far in this work, the influence of stress intensity, media roughness, and mineral content has been investigated for *Nordic pine* fibres only. This pulp consists of intrinsically strong fibrils, as inferred from the high zero-span strength and the long fibrils observed in microscopy of MFC. Since the previous section showed that the standard operating conditions also disintegrates almost all other fibre species effectively, it is expected that weaker fibres can break efficiently at lower roughness-adjusted stress intensities, leading to lower optimum $SI \cdot R_a$ values, with the resulting stress number increase enhancing fibrillation. Experimental work by *FiberLean* supports this; weak *acacia* fibres that produce poor MFC with 3 mm media, were found to produce stronger MFC with fine media. The effective intensity of a media-fibre-media collision can be lowered by two routes; lowering stress intensity by decreasing impeller speed, media size or media density, or otherwise by decreasing the pressure-concentrating factors (media roughness and mineral content). This chapter details experiments exploring both options.

The first study uses fine 1 mm media on numerous fibre species. This is expected to be industrially impractical, but since striking benefits are seen with *acacia* fibres, contrasting with the poor response of *Nordic pine* fibres known from previous experience (such as in Section 4.5), using very fine media is a good proof of concept and highlights the maximum differences that can be expected between different fibre species.

The second set of experiments reduces the pressure-concentrating factors whilst maintaining stress intensity, in mineral-free grinding of various fibres using smoother mullite media. The

$SI \cdot R_a$ change is much less severe, so smaller differences are expected. However, this route is more practical industrially since finer media is more susceptible to screening problems. Both studies are contrasted with the data of the relevant fibre species ground with rough 2.9 mm mullite media in the presence of mineral from Chapter 7.

Finally, work is detailed that investigates the influence of grinding fibre solids content for several fibre species. Fibre solids content has not been explored in the rest of this thesis, and is not explicitly considered in stress intensity theory, but it is an easy parameter to change that produces a strong effect for many fibre species, and is an important factor for grinder optimisation.

8.2. Influence of Fibre Species in Fine Media Grinding

8.2.1. Experimental

This study selects twelve fibre species used in Chapter 7, grinds them with 1 mm media under otherwise identical conditions, and compares the results with the equivalent coarse media grinds. Prior to this work, *FiberLean*'s industrial media supplier discontinued *Mullite A*, so the finer media was composed of *Mullite B* with a lower surface roughness. A comparison of media properties and the grind stress intensities between the two studies is given in Table 8.1:

Table 8.1 *– Properties and stress intensities of both media species. Stress number is calculated with the measured grind time, so differs with fibre species.*

Media	Mean Size (mm)	Media Density (g/cm^3)	Roughness R_a (μm)	Stress Intensity *SI* ($x10^{-3}$ Nm)	Roughness-Adjusted Stress Intensity $SI \cdot R_a$ ($x10^{-3}$ Nm·μm)	Relative Stress Number ($x10^{11}$)
Coarse Mullite	2.91	2.69	0.97	1.97	1.92	0.97 - 1.12
Fine Mullite	1.00	2.80	0.38	0.0832	0.0316	11.4 – 16.5

The coarse mullite has a stress intensity 24 times that of the finer mullite, and a roughness-adjusted stress intensity 60 times higher. Consequently, any differences in optimum stress intensity between fibre species should be obvious.

Chapter 7 demonstrated that 2.9 mm media can disintegrate almost all fibre species into particles much finer than the feed size, allowing for direct comparison of product MFC lengths without issue. However, some fibre species were very resistant to grinding with 1 mm media, so differences in feed size between species become important and complicate the comparison. Consequently, rather than considering raw MFC length, the *Lc(l)*-based Operating Rittinger Index $K_{R,Op}$ is used instead to accommodate differences in feed fibre lengths.

8.2.2. Operating Rittinger Index

Effect of Zero-Span Tensile Index

For coarse media grinds, the fibre zero-span tensile index correlates with the product MFC length (see Figure 8.1). However, Figure 8.2 shows that this is not obvious for the 1 mm grinds; long and short feed fibres clearly follow separate best fit curves (which are exponential rather than linear as in Figure 8.1). Given similar feed fibre lengths, the zero-span tensile index correlates with $K_{R,Op}$, but feed fibre length itself is clearly a dominant factor for low stress intensity grinds.

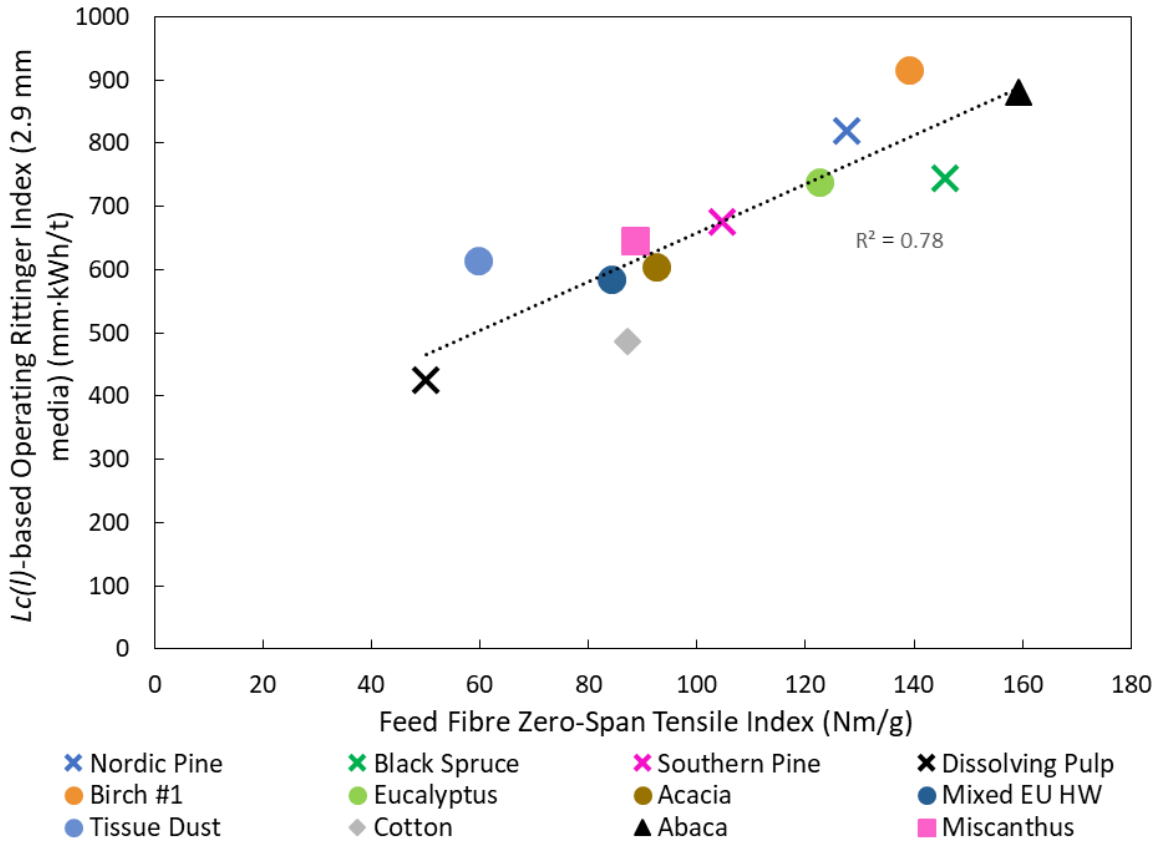

Figure 8.1 *– $K_{R,Op}$ versus fibre zero-span tensile index for the 2.9 mm media grinds.*

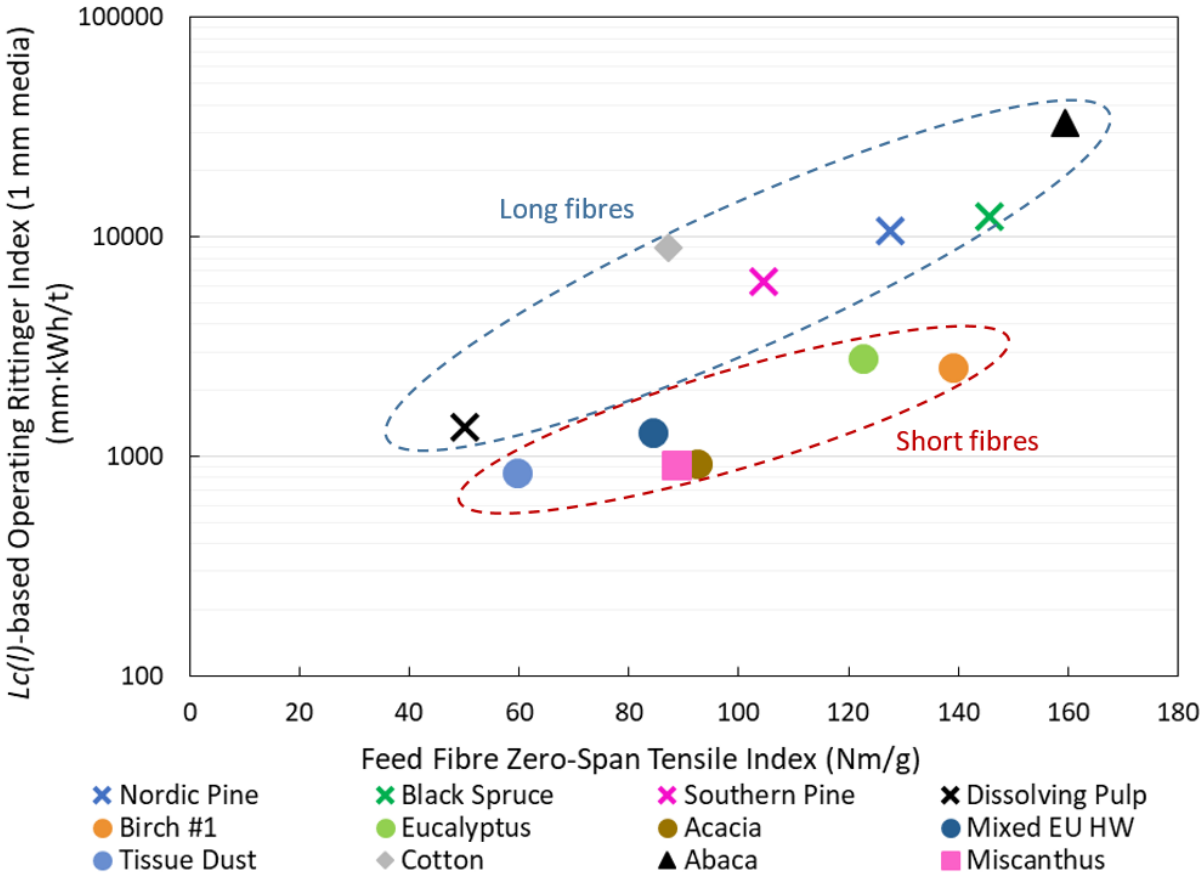

Figure 8.2 *– $K_{R,Op}$ versus fibre zero-span tensile index for the 1 mm media grinds.*

Effect of Feed Fibre Length

Figure 8.3 plots the *Lc(l)*-based $K_{R,Op}$ values against feed fibre length for both media sizes; the coarser media shows no correlation, but the finer media shows a positive exponential trend, thereby feed fibre length retards fibre breakage in the latter case. Longer fibres can make more inter-fibre contacts, thereby increasing viscosity, which could plausibly cause considerable dampening to the collision intensity when fine media is used. Equations [2.5] – [2.7] in Section 2.7 describe how this can be incorporated into stress intensity theory.

The only unknown parameters in these equations are the maximum separation distance required for breakage, *x*, and the charge viscosity, η. The value of *x* was chosen as 4 µm, roughly double the typical cell wall thickness for many fibre species, since the media must compress the cell wall to cause breakage. Since the logarithm of *x* is used, differences between fibres have little influence on r_η. With *x* estimated, the critical viscosity η_C above which all fibre breakage should cease is calculated using Equation 2.7 to be 0.305 Pas and 0.720 Pas for the 1 mm and 2.9 mm media respectively.

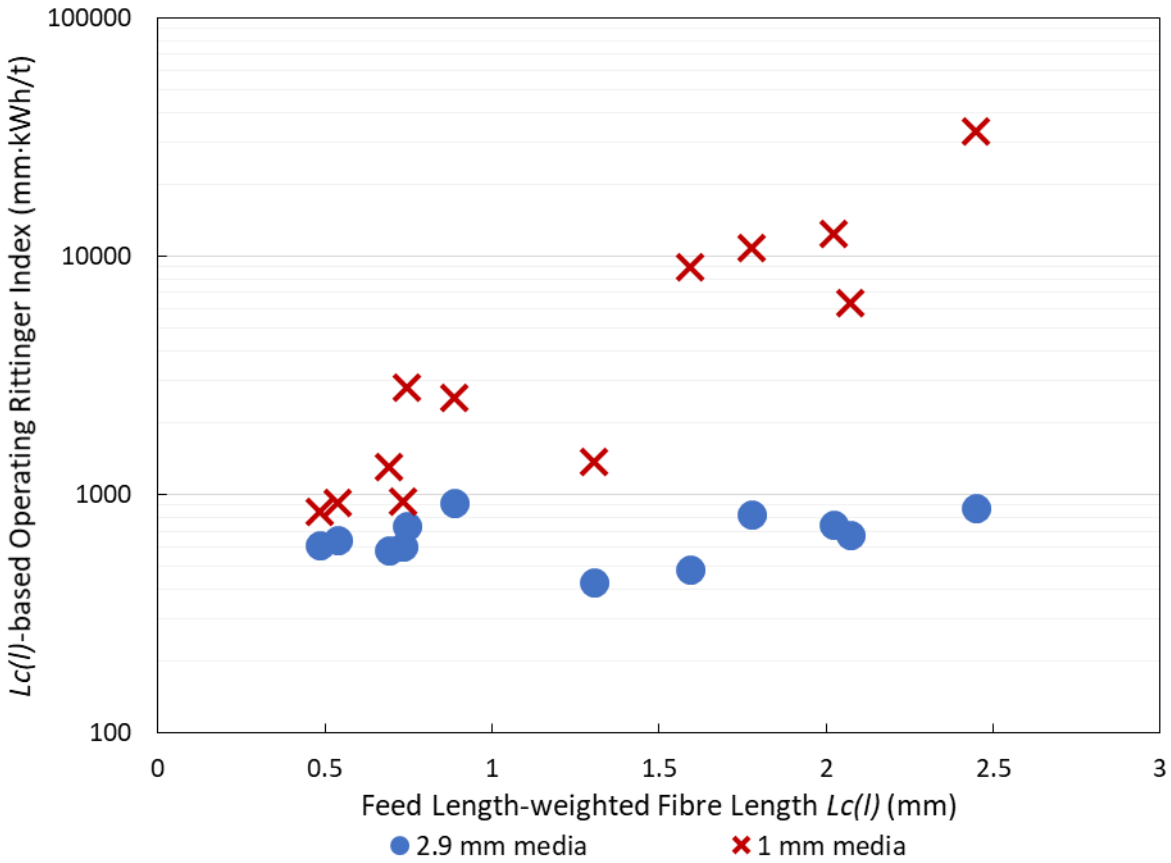

Figure 8.3 *– $K_{R,Op}$ versus feed fibre length for both 2.9 mm and 1 mm media grinds.*

Charge viscosity η is unknown since MFC and pulp rheology was not measured, and the appropriate shear rate to use in its measurement is also unknown. Figure 8.4 (a) plots r_η versus η to identify the values for which obvious differences in dampening exist between the series, with Figure 8.4 (b) showing the inverse of r_η to demonstrate the asymptote at $\eta = \eta_C$. Since the fibres resistant to grinding with fine media are largely intact after grinding, literature data on pulp fibre rheology are used to estimate η in lieu of a measurement.

Fibres and MFC are to some extent shear-thinning, but above around 100 s^{-1}, fibre suspensions enter a turbulent (fluidised) state with a constant apparent viscosity[111]. The shear rate in the high intensity zone of the grinder is unknown, but an estimate of around 7,000 s^{-1} is given in Appendix A2, so fibres are likely fluidised with the constant viscosity during a high intensity impact. Derakhshandeh et al.[111] provides fluidised state viscosities at 2.5% fibre solids of 0.1

Pas and 0.2 Pas for hardwood and softwood kraft pulp respectively. Because power draw tends to decrease with successful grinding, and as PEPT data by Riley shows that media velocity increases with grinding progress[73], the high shear viscosity of effectively disintegrated MFC is probably much lower.

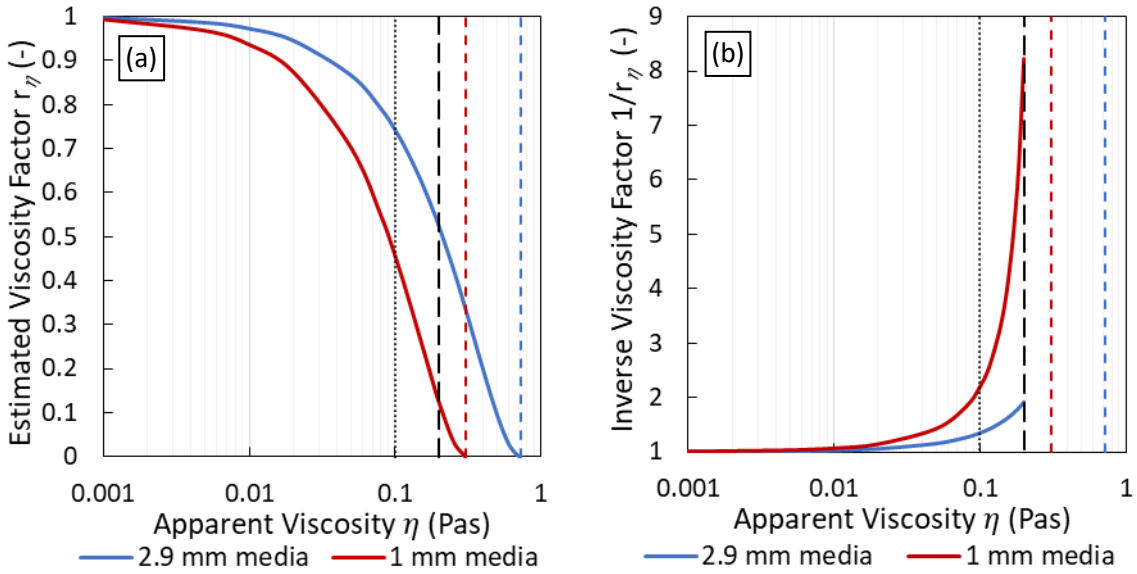

Figure 8.4 *– Influence of apparent viscosity on (a) the viscosity factor and (b) the inverse viscosity factor. Viscous grinding limits for each media are shown with the coloured dotted lines, with estimated softwood (long fibre) and hardwood (short fibre) viscosities from Derakhshandeh et al.[111] shown as the black dashed and dotted lines respectively.*

Figure 8.4 (a) and (b) show that for 1 mm media, a viscosity of 0.2 Pas (with long fibres) can be expected to have around four times the dampening effect than a viscosity of 0.1 Pas (with short fibres), explaining the critical importance of fibre length, whereas for 2.9 mm media, the difference is relatively minor.

Earlier, Figure 6.23 shows that *Lc(l)*-based $K_{R,Op}$ is roughly inversely proportional to $SI \cdot R_a$, when below the optimum $SI \cdot R_a$ value. The high values of $K_{R,Op}$ for the fine media grinds in the present chapter suggests that this assumption holds, so removing the effect of viscosity (effectively multiplying the apparent stress intensity by $1/r_\eta$) should decrease $K_{R,Op}$ by a factor of r_η. Limiting analysis to kraft softwoods and hardwoods of typical sizes, Figure 8.5 plots this

viscosity-corrected $K_{R,Op}$ value against fibre zero-span tensile index, using these estimated viscosity values in the r_η calculation, and shows that discrepancies between the two fibre size classes appear to have been reconciled into a good general correlation.

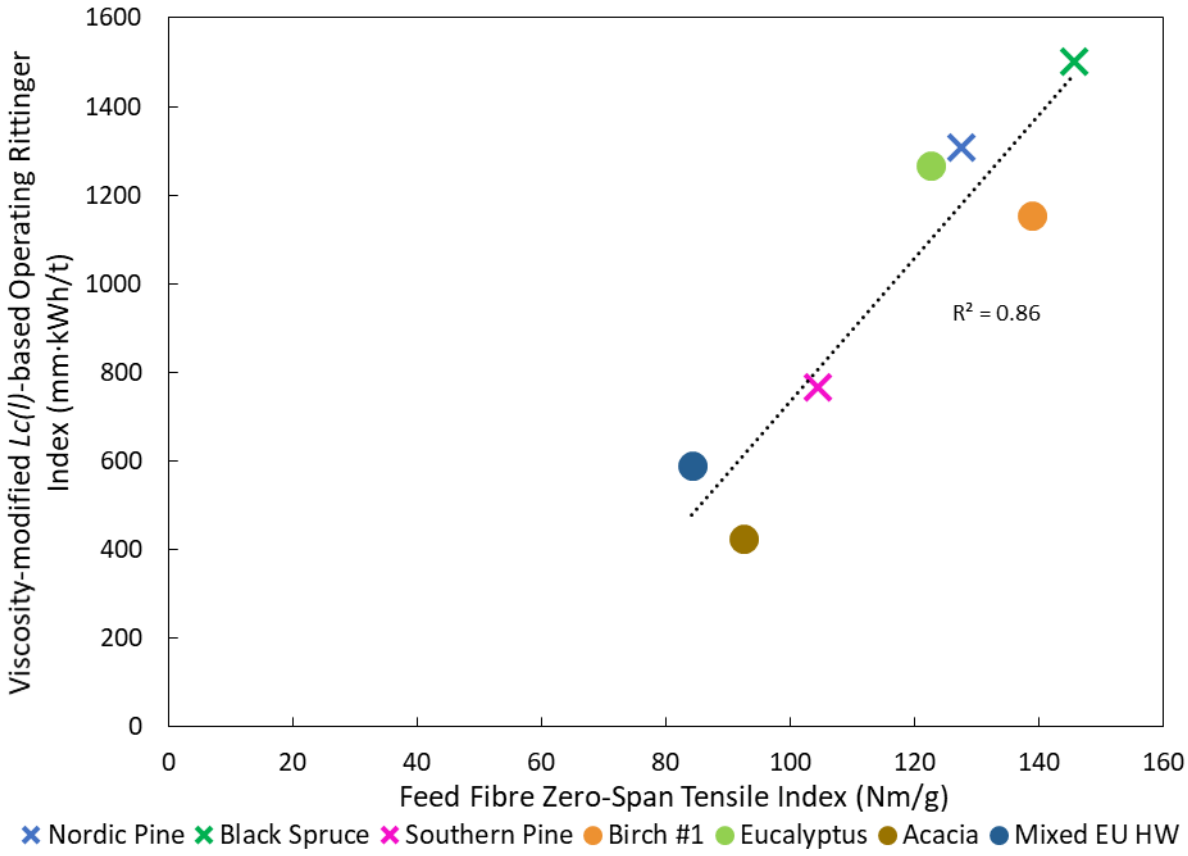

Figure 8.5 *– Zero-span tensile index versus the viscosity modified Lc(l)-based $K_{R,Op}$.*

The assumptions made in these calculations are quite tenuous, requiring that the viscosities used are representative of the selected fibre species at the true grinder shear rates, ignoring the evolution of viscosity as the grind progresses, and assuming that stress intensity is inversely proportional to $K_{R,Op}$. These values therefore cannot be considered accurate, but show that the expected effect is of the right magnitude to explain the apparent influence of fibre length for 1 mm media grinds.

This analysis suggests that lowering the solids contents of fine media grinds should lower the influence of feed fibre length by lowering charge viscosity. To test this, grinds were undertaken with four fibre species, using 1 mm media at 1% fibre solids. Table 8.2 compares the resultant $K_{R,Op}$ values with those at standard grinding solids; for all fibre species which could disintegrate effectively with fine media, lowering the solids content increased $K_{R,Op}$ considerably. However, for *Nordic pine*, which is believed to be strongly viscous-limited, the 1% fibre solids grind *decreased* $K_{R,Op}$ values (so improved grindability). This therefore supports the viscous dampening hypothesis.

Table 8.2 *– $K_{R,Op}$ values for four fibre species after 1 mm media grinds at 2.5% and 1% fibre solids.*

Fibre Species	**Feed *Lc(l)* (mm)**	**$K_{R,Op}$ for 1 mm media grind (mm·kWh/t)**	
		2.5% fibre solids	**1% fibre solids**
Nordic Pine	1.78	10746	7834
Eucalyptus	0.746	2786	3923
Mixed European Hardwood	0.693	1295	1919
Dissolving Pulp	1.306	1364	1925

Feed fibre length is clearly a dominant factor for 1 mm media. There is a small effect expected from Figure 8.4 for the 2.9 mm media, but this is not apparent at all in the experimental results (Figure 8.3); this is believed to be because fibres are ground down very quickly, so differences in feed fibre lengths are quickly neutralised, with charge viscosity eventually being dominated by MFC characteristics.

Note that considering the importance of fibre length, the *crowding factor, N,* is expected to be an appropriate value for comparison between pulps, since this also takes cell wall thickness into account[112]:

$$N \approx \frac{5C_m L^2}{\omega} \ldots [8.1]$$

where C_m is the fibre mass concentration (%), L is the fibre length (m) and ω is the fibre coarseness (kg/m). This was calculated for all fibre species, and follows a similar plot with $K_{R,Op}$ as Figure 8.3 (see Figure 8.6), though requires a log-log scale due to the exponent of L; coarseness differences between fibre species are not sufficient to significantly affect the conclusion drawn. Consequently, for the rest of this chapter, feed fibre length differences are discussed rather than crowding factor, though these parameters are effectively analogous.

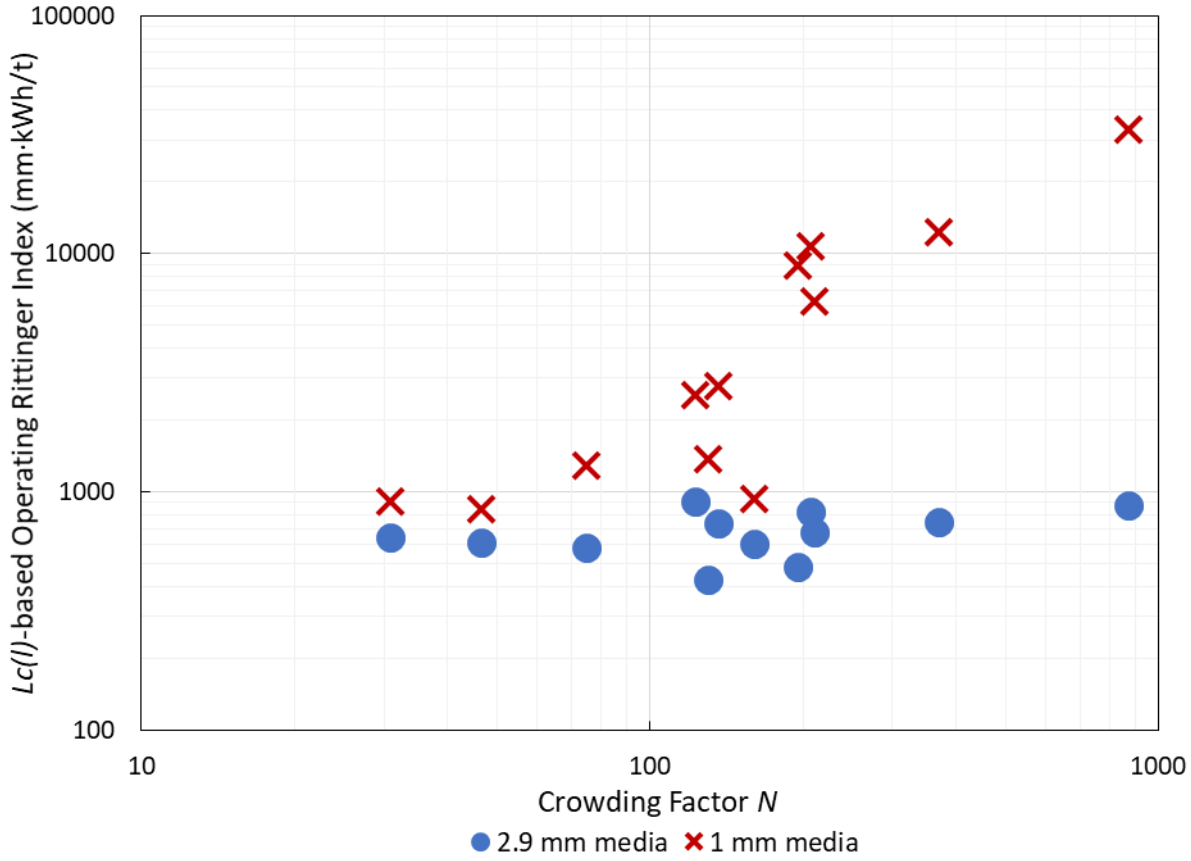

Figure 8.6 *– $K_{R,Op}$ versus crowding factor for both 2.9 mm and 1 mm media grinds.*

8.2.3. Fibre Analyser Results and Tensile Index

Table 8.3 shows the MFC fibre analyser results and tensile index for each fibre species, comparing the 1 mm media and 2.9 mm media data, along with relevant feed fibre properties. A comparison for each parameter is given in the following sections.

Table 8.3 *– Feed fibre properties (Lc(l), hemicellulose content and zero-span tensile index (ZSTI)), and MFC fibre analyser parameters and tensile index, for grinds with 1 mm media and 2.9 mm media.*

	Feed Fibre Properties			***Lc(l)* (mm)**		***Fines B* (%)**		***Fibrillation* %**		**MFC Tensile Index (Nm/g)**	
	***Lc(l)* (mm)**	**Hemi-cell. (%)**	***ZSTI* (Nm/g)**	**1 mm**	**2.9 mm**	**1 mm**	**2.9 mm**	**1 mm**	**2.9 mm**	**1 mm**	**2.9 mm**
Nordic Pine	1.778	17.0	128	1.188	0.237	12.3	29.4	2.80	4.98	7.10	9.64
Black Spruce	2.021	17.1	146	1.356	0.221	8.6	23.4	3.01	5.03	6.80	9.10
Southern Pine	2.071	18.0	105	1.043	0.203	18.2	34.4	2.77	5.50	6.09	8.45
Dissolving Pulp	1.306	4.1	50	0.337	0.128	21.4	21.5	4.20	4.56	7.59	4.68
Birch	0.887	25.2	139	0.433	0.227	28.5	37.3	6.26	5.64	12.94	11.83
Eucalyptus	0.746	17.4	123	0.414	0.185	9.4	30.9	4.40	4.22	10.12	8.18
Acacia	0.735	14.7	93	0.218	0.158	12.4	17.2	4.84	4.64	9.09	5.61
Mixed EU Hardwood	0.693	22.3	84	0.266	0.152	30.6	33.2	6.09	4.87	10.54	7.56
Tissue Dust	0.485	14.4	60	0.179	0.144	24.5	15.9	5.77	4.71	9.26	5.83
Cotton	1.594	0.3	87	1.037	0.147	7.0	9.6	2.34	4.00	2.91	3.96
Abaca	2.450	11.9	159	2.006	0.262	8.6	39.7	2.70	6.07	7.09	9.44
Miscanthus	0.540	22.4	89	0.195	0.154	62.4	51.2	7.78	5.61	12.89	10.14

8.2.4. MFC Length

Figure 8.7 exemplifies the differences in $K_{R,Op}$ between fibre species. All fibre species ground with coarse media produce fine MFC; for 1 mm media, some short fibres are also greatly reduced in size, whereas most long fibre MFC is close to their feed size. Given similar feed lengths, high zero-span strength fibres give longer MFC lengths with 1 mm media (compare *dissolving pulp* to the other softwoods, and *birch* and *eucalyptus* with *acacia* and *mixed European hardwood*). The *Lc(l)* value of the 1 mm series is never lower than the 2.9 mm series, so fibre breakage rate is lower for finer media. An intermediate stress intensity likely maximises breakage rate for the shorter, weaker fibres; comparing the *Lc(l)* values using 2.9

mm and 1 mm media gives an indication of the location of the optimum stress intensity for fibre breakage.

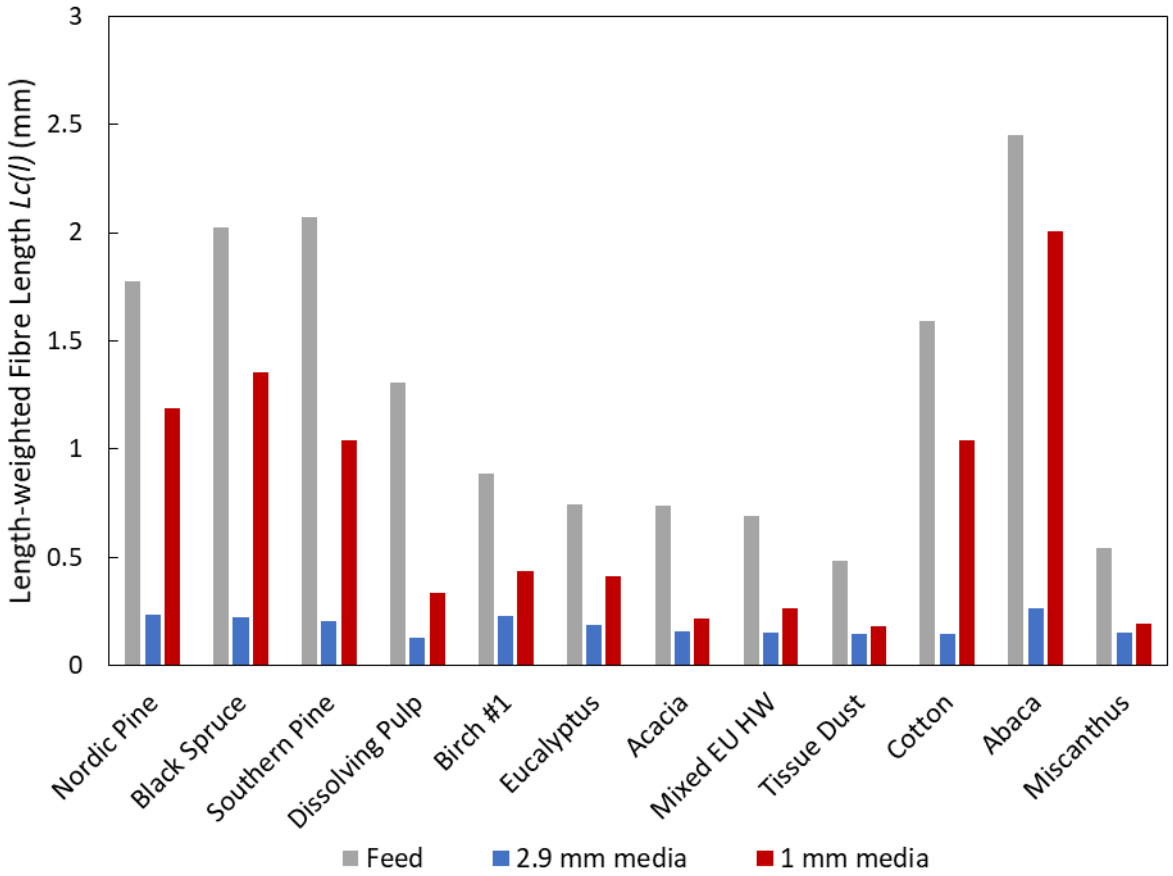

Figure 8.7 *– MFC Lc(l) values for various fibre species ground with 1 mm and 2.9 mm media.*

8.2.5. Fines B

Figure 8.8 shows the differences in *Fines B* generation between the 1 mm and 2.9 mm series. This figure, and Table 8.3, show that long fibre pulps have drastically lower *Fines B* generation with fine media, because fibre breakage rate is far too low. *Dissolving pulp* is the exception, where the very low zero-span strength counteracts the viscous effect and allows similar generation as with coarse media.

Given similar feed lengths, weaker fibres generally permit higher *Fines B* generation with finer media as fibre breakage is easier. The only significant difference between the three kraft

softwoods appears to be zero-span strength, and lower values of this enhances *Fines B* generation for both media sizes.

Miscanthus and *tissue dust*, in fact, give higher *Fines B* values with fine media than with coarse media, despite a lower fibre breakage rate (longer *Lc(l)*); this is likely due to the much higher number of low intensity stress events delaminating very delicate fibrils whilst minimising cross-sectional damage (Table 8.1 indicates that fine media has a much higher stress number, though as explained in Appendix A4.2.1, the calculated values are suspected to be unreliable).

Eucalyptus has minimal *Fines B* generation with fine media, unlike the other hardwoods; this is probably because the high zero-span strength coincides with only a moderate hemicellulose content, so it cannot delaminate as effectively as the higher hemicellulose *birch* and *mixed European hardwood*, whilst also being more resistant to breakage than weaker pulps.

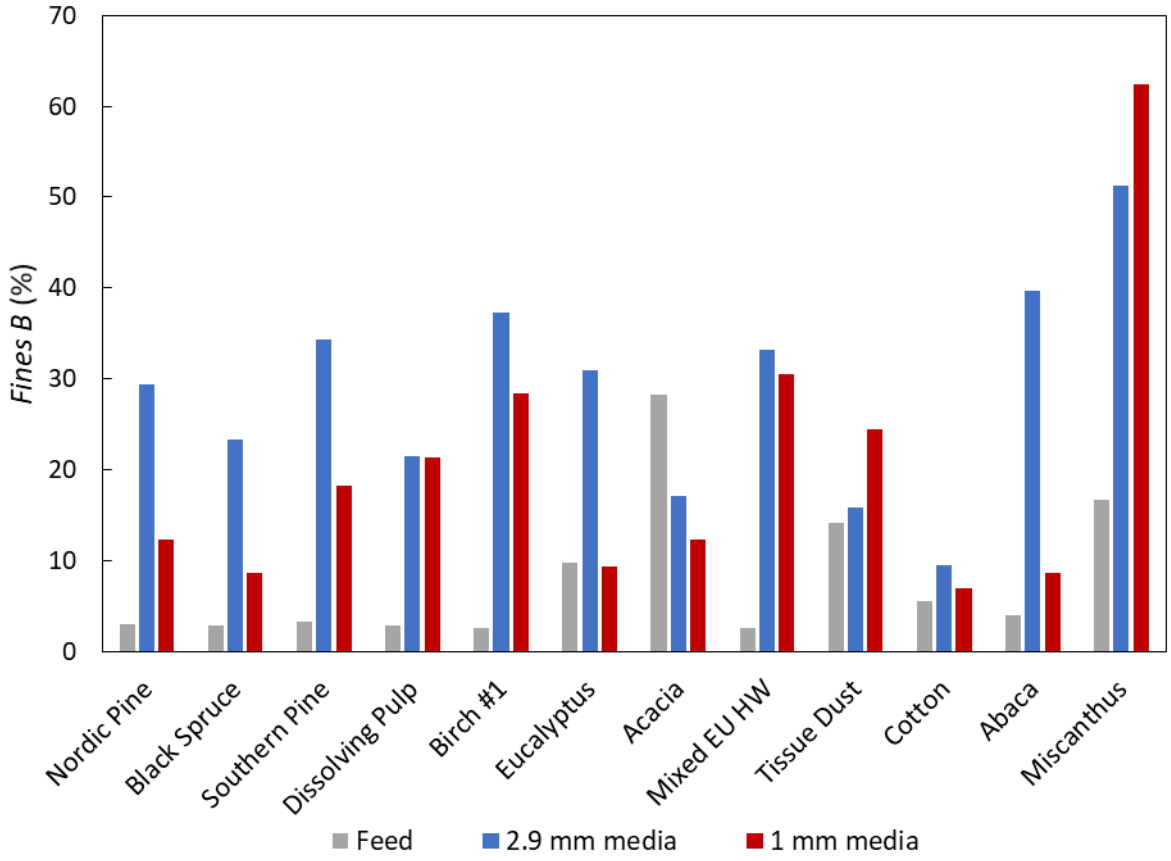

Figure 8.8 *– MFC Fines B values for various fibre species ground with 1 mm and 2.9 mm media.*

8.2.6. Fibrillation %

Figure 8.9 shows a comparison of *Fibrillation %* values. The same general pattern is followed as with *Fines B*, with the strong and long fibres having low values with 1 mm media, though this deficiency is less severe as for *Fines B*, and all hardwoods show some improvement versus coarse media. This implies that fine media can generate external fibrils effectively given low viscous dampening, and unless the fibre is very weak or has a very high hemicellulose content, struggles to break off external fibrils to generate free fibrils. This is particularly striking for *eucalyptus*, where fine media produces a moderate *Fibrillation %* value and a very low *Fines B* value.

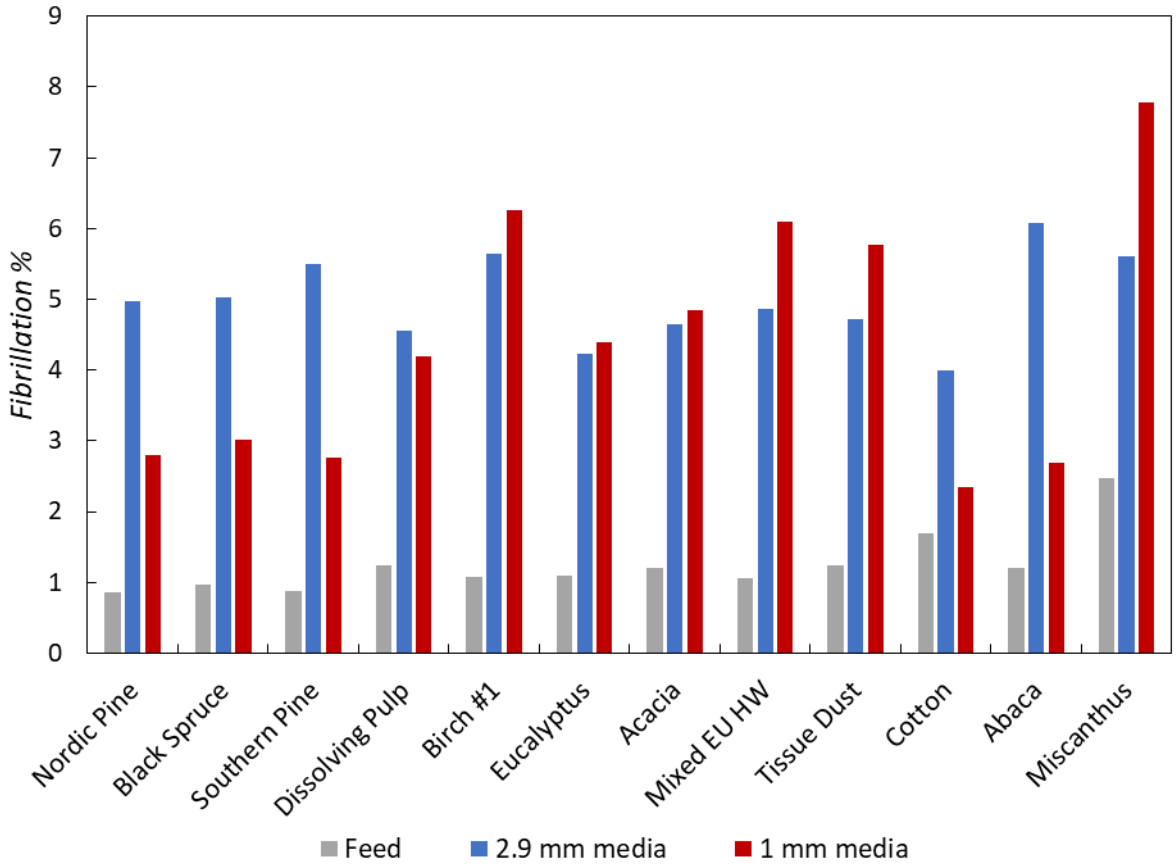

Figure 8.9 *– MFC Fibrillation % values for various fibre species ground with 1 mm and 2.9 mm media.*

8.2.7. MFC Tensile Index

Figure 8.10 compares the MFC tensile index of each fibre species for both series. The strong, long fibre pulps see a 20 – 25% drop in strength with finer media; this is less severe than expected from the low fibrillation parameters, because the very long MFC lengths partially compensates for this. All other fibres benefit at least somewhat with finer media, even in cases where fibrillation parameters do not significantly improve, which is believed to be due to the longer MFC length.

Fibres with low zero-span strength (*dissolving pulp*, *acacia*, *tissue dust*, *miscanthus*, and *mixed European hardwood*) show the largest tensile strength increases with fine media. This is because they are sufficiently weak that low stress intensities easily break down fibre superstructure, whilst the balance of low stress intensity and high stress number increases opportunities for fibrillation whilst minimising liberated fibril damage. *Birch* and *eucalyptus* show a lesser improvement due to their higher zero-span strengths, so fibres are only partially disintegrated with 1 mm media, and liberated fibrils are better able to resist the higher stress intensities experienced with 2.9 mm media.

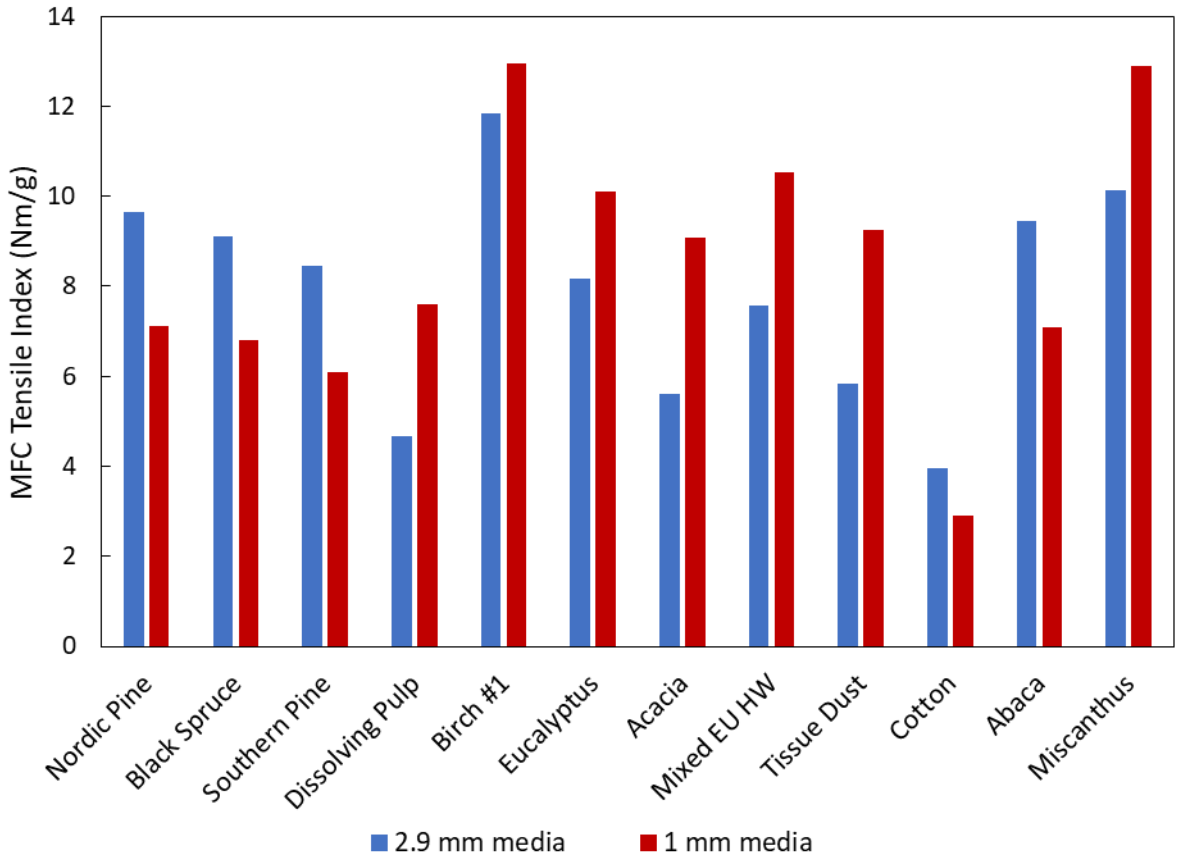

Figure 8.10 *– MFC tensile index for various fibre species ground with 1 mm and 2.9 mm media.*

To better demonstrate the hypothesised mechanisms for the different responses of fibre species, Figure 8.11 plots feed zero-span tensile index against the MFC tensile strength ratio between the fine media and the coarse media. It shows that for short fibres (hardwoods and *miscanthus*), a lower zero-span strength tends to benefit from finer media grinding, whereas for long fibres, there is no such correlation, since viscous dampening with fine media greatly inhibits fibre breakage and the consequent fibrillation, leading to relatively poor strength. *Dissolving pulp* is the exception, where its very low zero-span strength permits effective disintegration.

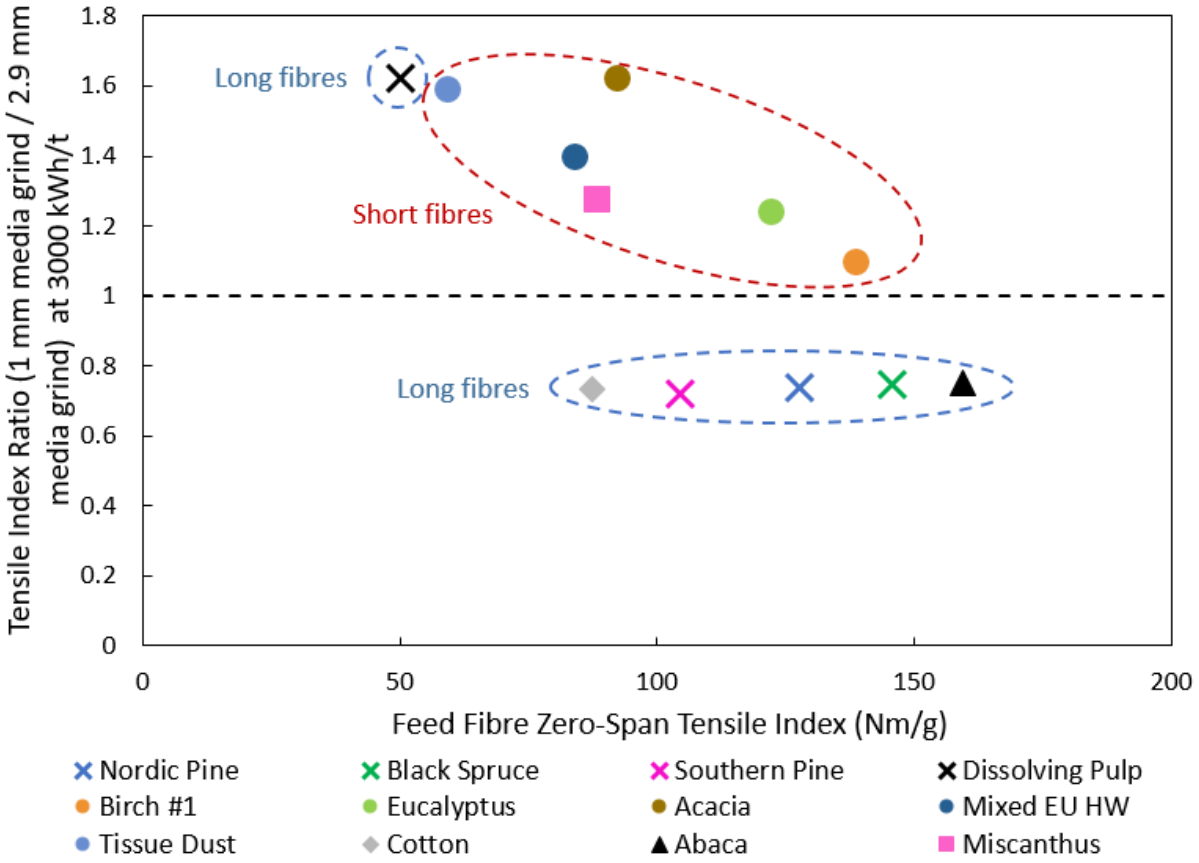

Figure 8.11 *– Ratio of the MFC tensile index between the fine and coarse media series versus the fibre zero-span tensile index.*

8.2.8. Differential Interference Contrast Microscopy

Figure 8.12 shows *Nordic pine*, *eucalyptus*, *mixed European hardwood*, and *tissue dust* MFC ground with both media sizes. A comparison of Figure 8.12 (a) and (e) shows that fine media leaves *Nordic pine* fibres largely intact, though coarse media disintegrates it easily into long, thin fibrils. Figure 8.12 (b) and (f) shows *eucalyptus* MFC ground with fine and coarse media respectively; this has a similar hemicellulose content and zero-span strength as *Nordic pine*, but around half the feed fibre length. The feed fibres are still obvious in the fine media grind, though with fairly extensive external fibrillation (as Figure 8.9 shows), so tensile strength remains high. The coarser media effectively disintegrates *eucalyptus* into fine fibrils, which are longer than those from weaker fibres.

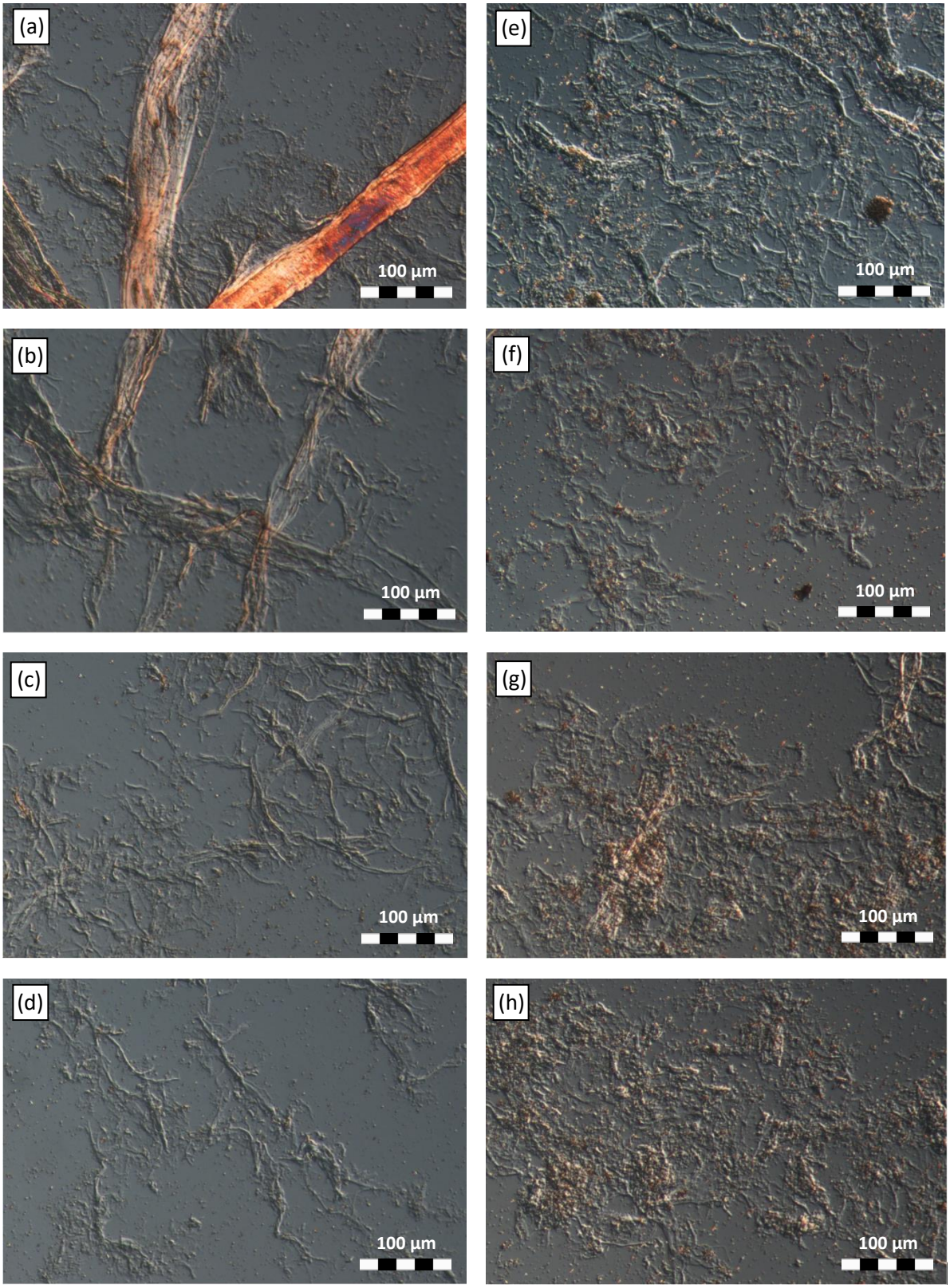

Figure 8.12 *– MFC from 1 mm media grinds for (a) Nordic pine, (b) eucalyptus, (c) mixed European hardwood, and (d) tissue dust, and MFC from 2.9 mm media grinds for (e) Nordic pine, (f) eucalyptus, (g) mixed European hardwood, and (h) tissue dust.*

The *mixed European hardwood* fibres (Figure 8.12 (c) and (g)) have feed sizes similar to *eucalyptus*, but have more hemicellulose (likely aiding fibril delamination), and lower zero-span strength (therefore weaker fibre cross-sections). Consequently, this fibre readily disintegrates into well-processed MFC with 1 mm media, producing a network of long, thin fibrils and consequently a high tensile strength of 10.5 Nm/g. Since the fibrils are weak, they are easily damaged by the larger media, with Figure 8.12 (g) showing very short fibrils (and a lower tensile strength of 7.6 Nm/g).

Tissue dust, being the weakest of the four pulps shown, contains fibrils very susceptible to damage with coarse media, leading to very short liberated fibrils (see Figure 8.12 (h)) and very low strengths (5.8 Nm/g). However, the fibre weakness permits full disintegration with 1 mm media, whilst the lower stress intensities preserve long fibrils (see Figure 8.12 (d)), leading to a much higher tensile strength of 9.3 Nm/g.

8.3. Influence of Fibre Species on Low Pressure-Concentrating Factor Grinds

8.3.1. Experimental

A series of grinds were carried out on twelve fibres species using the same conditions as in Chapter 7, but using the smoother *Mullite B* media, and with no mineral added (100% POP). The fibres trialled were largely the same as in Section 8.2, but some substitutions were necessary due to insufficient supply of some sources. Table 8.4 shows the stress intensity-related media properties for the high and low pressure-concentrating factor series, showing that stress intensity and stress number are similar, but the rougher media has a $SI \cdot R_a$ value 2.5 times that of the smoother media. Fibre and fibril breakage with the rougher media is also aided by mineral addition, but this is not encapsulated by $SI \cdot R_a$.

Table 8.4 *– Media-related properties and stress intensities between the high and low pressure-concentrating factor series. Stress number is calculated with the measured grind time, so differs with fibre species.*

	Mean Size (mm)	**Media Density (g/cm^3)**	**Media Roughness R_a (μm)**	**Stress Intensity *SI* ($x10^{-3}$ Nm)**	**Roughness-Adjusted Stress Intensity $SI \cdot R_a$ ($x10^{-3}$ Nm·μm)**	**Relative Stress Number ($x10^{11}$)**
Rough Mullite	2.91	2.69	0.97	1.97	1.92	0.97 - 1.21
Smooth Mullite	2.96	2.80	0.38	2.14	0.83	0.97 - 1.12

8.3.2. MFC Length

Figure 8.13 shows that the 100 POP smoother media grinds give higher MFC *Lc(l)* values than the 50 POP rougher media grinds, but the difference is dependent on fibre species. Viscous dampening is expected to be similar because of identical stress intensities, so feed fibre length is expected to be unimportant; this is confirmed by Figure 8.14 which shows no obvious correlation between $K_{R,Op}$ and feed *Lc(l)*. Consequently, longer fibres still break fairly easily with smoother media compared to when finer media is used. With viscous effects largely absent, fibre zero-span strength controls $K_{R,Op}$ for the smoother media grinds, as it does with the rougher media (albeit with a poorer fit), see Figure 8.15. For strong fibres, the reduction in pressure-concentrating factors considerably decreases breakage rate, leading to very high $K_{R,Op}$ values. These factors are largely superfluous for weak fibres, which readily disintegrate in the smoother media mineral-free grinds, giving a lesser difference in $K_{R,Op}$ compared to the control series.

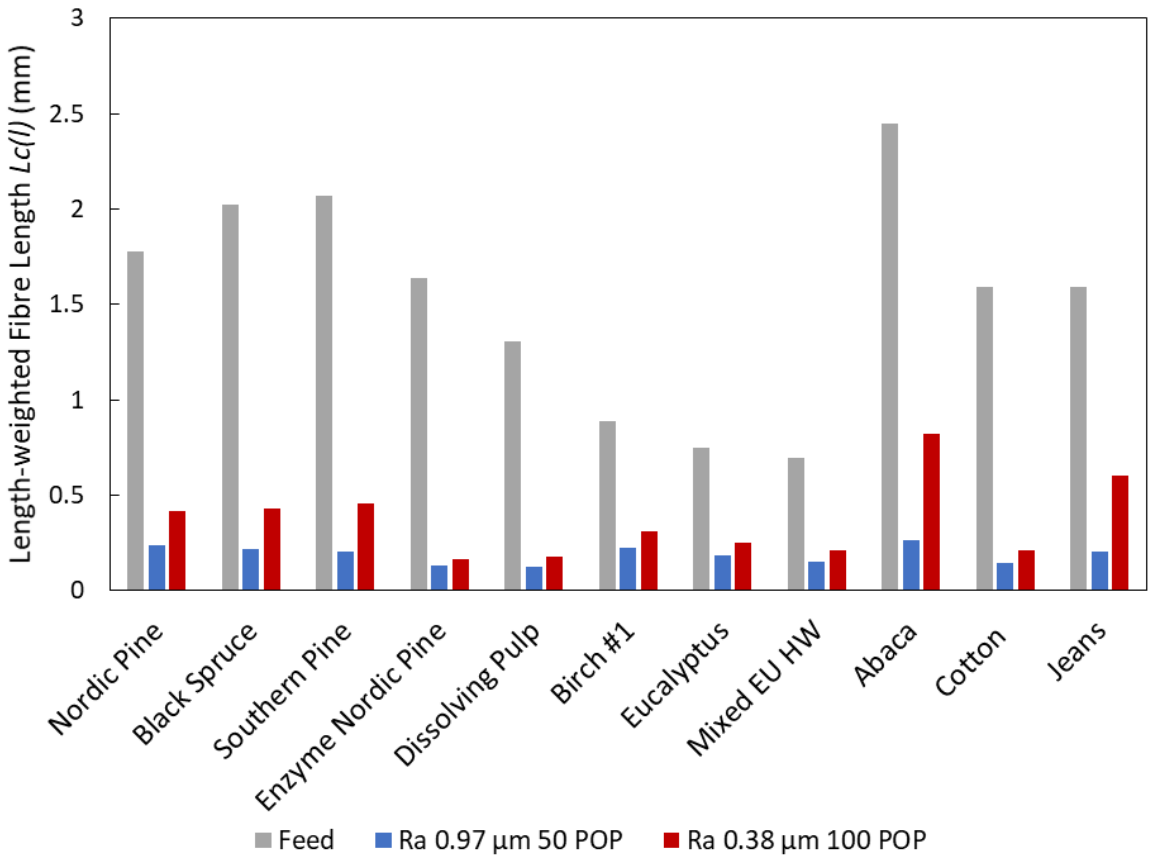

Figure 8.13 *– MFC Lc(l) values for various fibre species for the high and low pressure-concentrating factor series.*

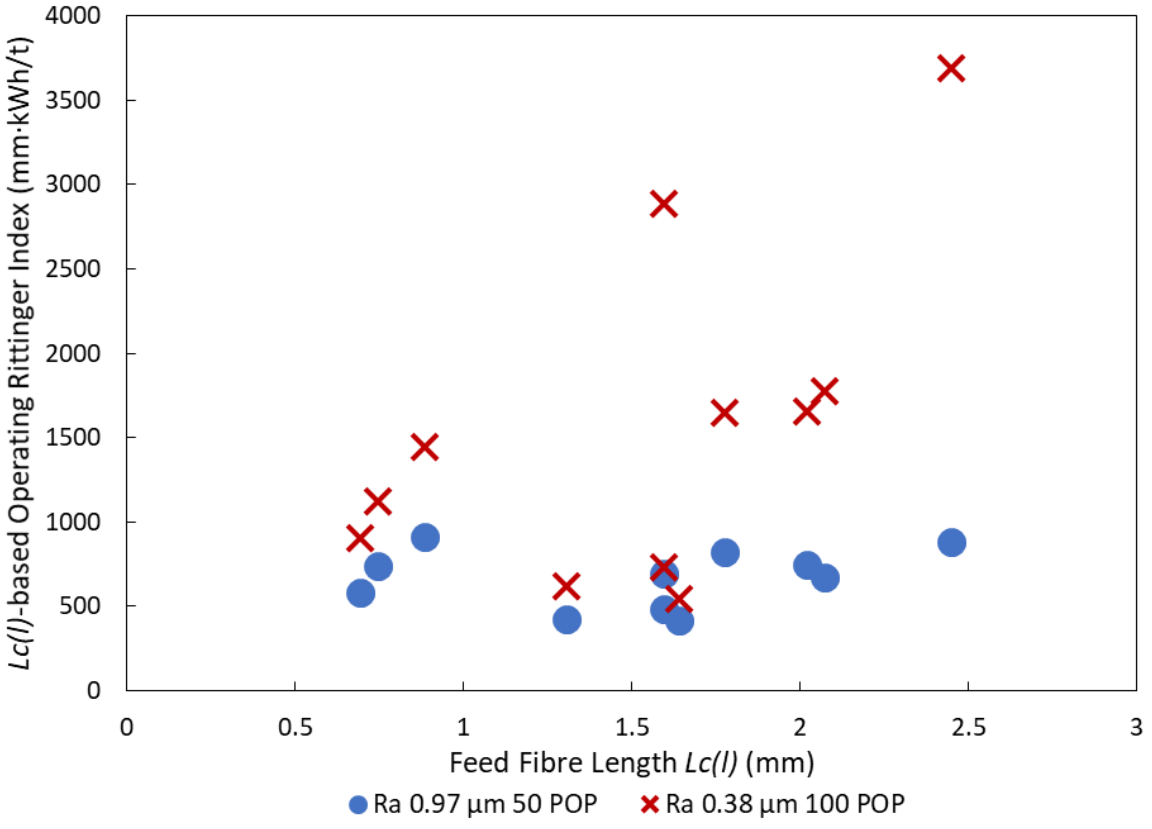

Figure 8.14 *– $K_{R,Op}$ versus feed fibre length for the high and low pressure-concentrating factor series.*

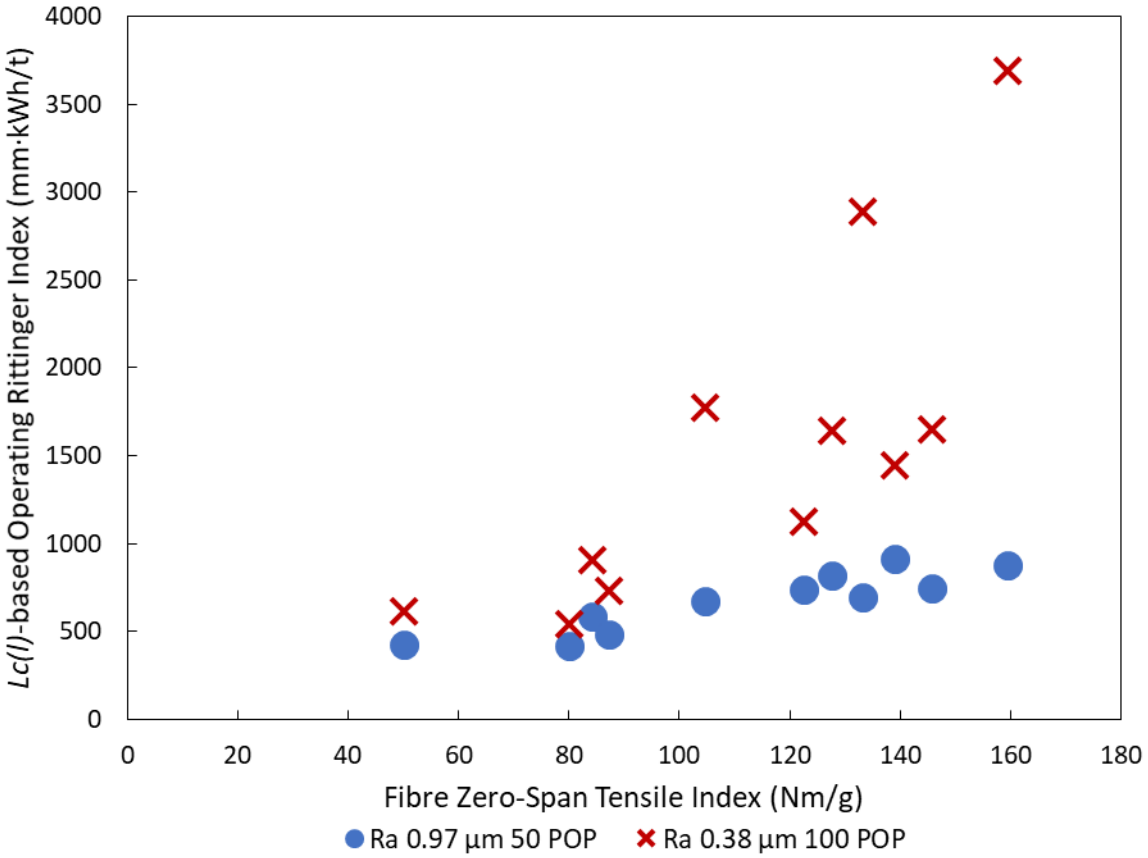

Figure 8.15 *– $K_{R,Op}$ versus feed fibre zero-span tensile index for the high and low pressure-concentrating factor series.*

8.3.3. Fines B

Figure 8.16 shows the *Fines B* content results, which in almost all cases are lower for the smoother media, despite the rougher grinds containing mineral which Chapter 5 shows degrades liberated fibrils. This is probably due to the lower grinding efficiency of smoother media causing significant under-grinding (indicated by *Lc(l)* differences). There is no clear pattern why the differences in *Fines B* are much greater in some fibres than others.

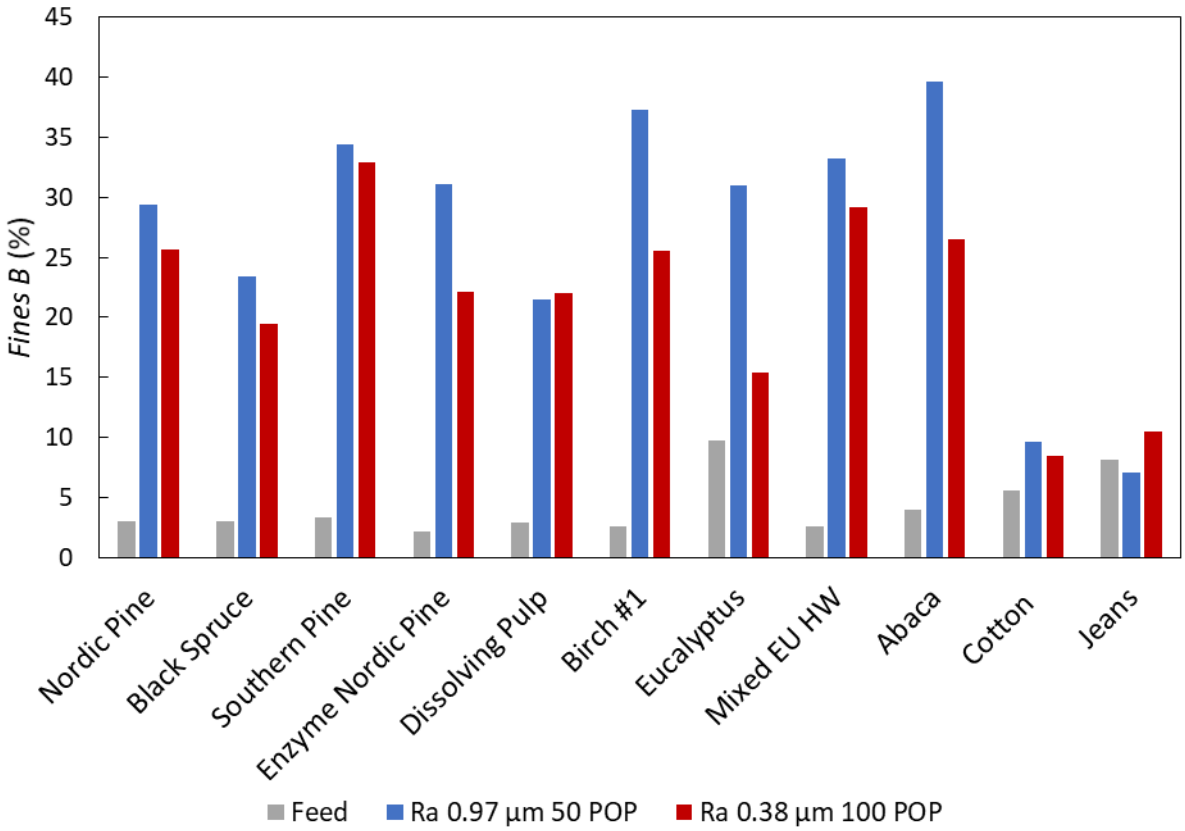

Figure 8.16 *– MFC Fines B values for various fibre species for the high and low pressure-concentrating factor series.*

8.3.4. Fibrillation %

Figure 8.17 shows that external fibrillation is generally improved when pressure-concentrating factors are reduced, and species that generate low *Fines B* values with smoother media tend to have high *Fibrillation %* values. This implies that whilst smoother media readily generates external fibrillation, the reduced degree of pressure concentration (probably from the absence of mineral content, see Chapter 5) reduces the tendency to break off external fibrils into free fibrils.

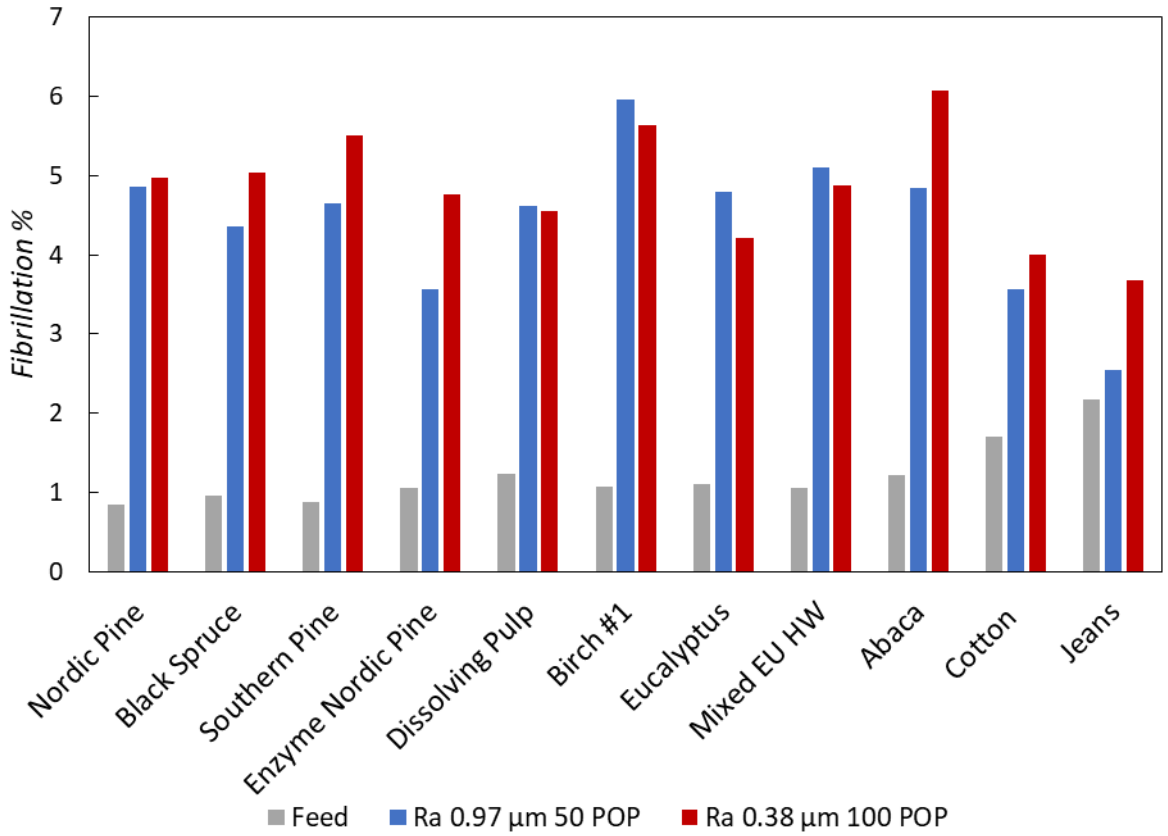

Figure 8.17 *– MFC Fibrillation % values for various fibre species for the high and low pressure-concentrating factor series.*

8.3.5. Tensile Index

Figure 8.18 shows that almost all fibre species gain a significant strength increase for the smoother media 100 POP series, despite the expected under-grinding in many cases. The low zero-span strength fibres show the greatest benefit, including *enzyme treated Nordic pine* (zero-span strength = 80 Nm/g), *dissolving pulp* (zero-span strength = 50 Nm/g) and *mixed European hardwood* (zero-span strength = 84 Nm/g). The weakness of these pulps mean that the fibre structure disintegrates more readily, and so 3000 kWh/t is probably closer to the optimum energy input in these cases than it is in stronger fibres (like *Nordic pine*, which under these conditions reaches peak strength at 4000 kWh/t (see Figure 5.28)). For fibres ground close to their optimum energy inputs, Section 5.3 implies that most of this benefit is due to the absence of mineral reducing free fibril degradation rather than the lower roughness. The

larger increase seen with low zero-span strength fibres may therefore also be due to the relatively weak fibrils being more vulnerable to damage by the mineral particles.

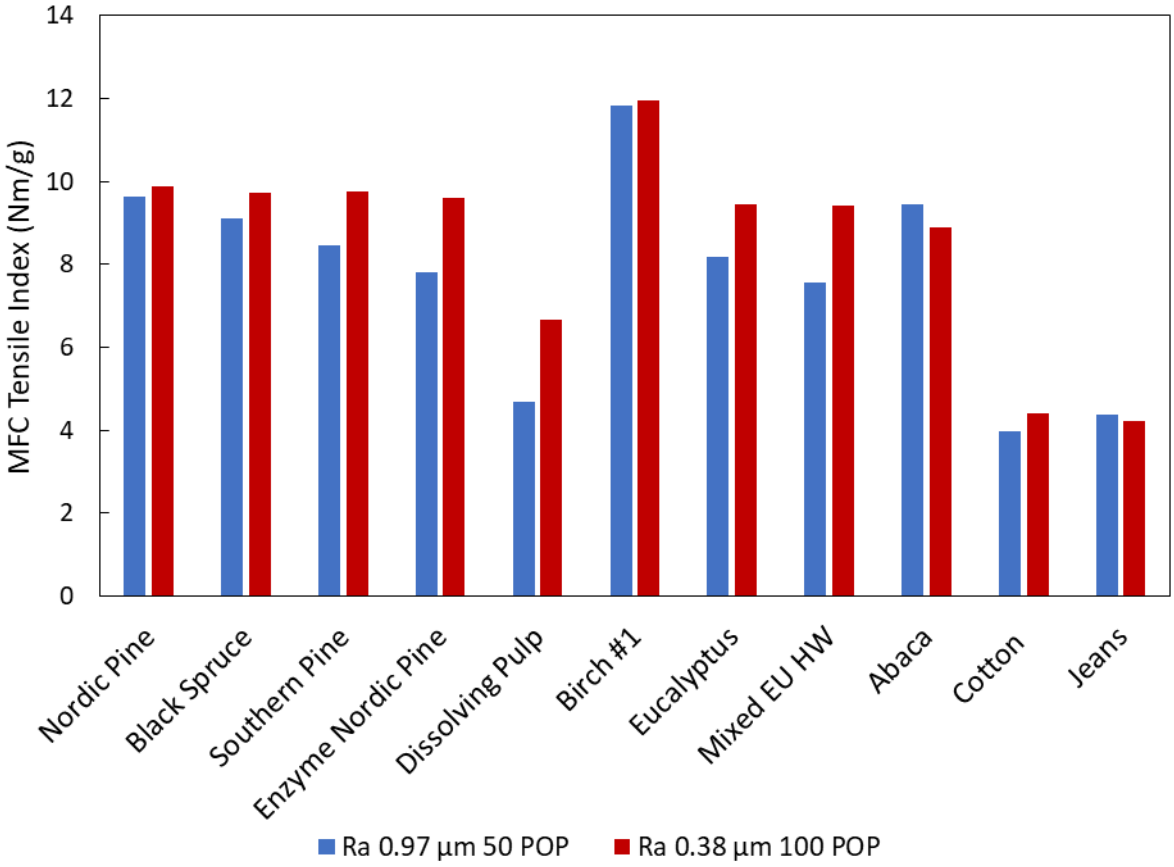

Figure 8.18 *– MFC tensile index for various fibre species for the high and low pressure-concentrating factor series.*

The ratio of the tensile strength between the low and high pressure-concentrating factor grinds is plotted against fibre zero-span tensile index as Figure 8.19, showing a good negative correlation. The explanation for this correlation is believed to be similar as with the fine media grinds; weaker pulps can break apart at lower effective stress intensities, where the weak fibrils that would otherwise be damaged with more pressure-concentrating factors, are better preserved. The correlation is much better and universal than when comparing the 1 mm grinds (see Figure 8.11), probably because viscous dissipation is small for both series in Figure 8.19, better exposing the underlying influence of fibre strength.

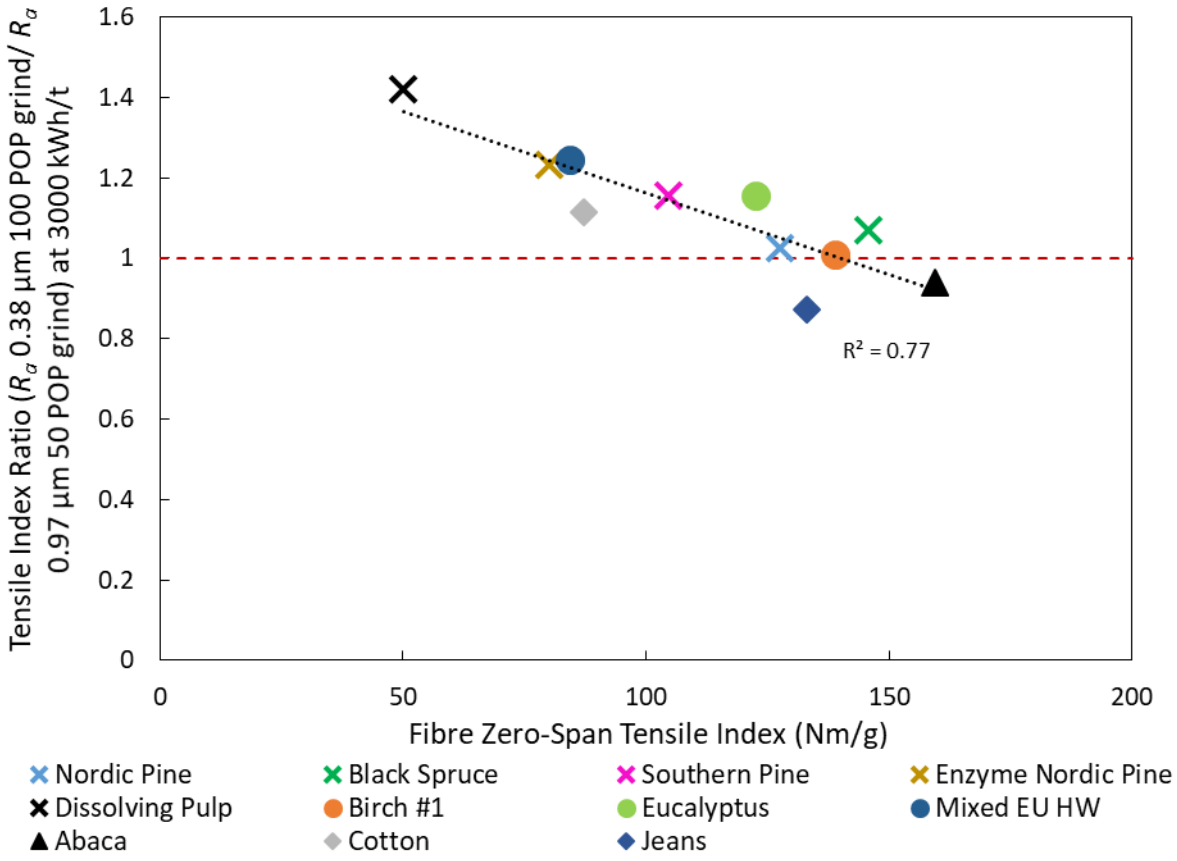

Figure 8.19 *– Ratio of the MFC tensile index between the low and high pressure-concentrating factor series versus fibre zero-span tensile index.*

8.4. Effect on the Hemicellulose – Zero-Span Strength Relationship

For the rough 2.9 mm media series used to derive the relationship between feed properties and tensile strength in Chapter 7, all fibres are readily disintegrated under the chosen conditions, so the fact that strong fibrils (i.e. high zero-span strength) slow fibre disintegration is inconsequential; however, strong fibrils better resist degradation after liberation, which leads to the good positive correlation with tensile strength.

In contrast, for fine media under the chosen conditions, a high zero-span strength leads to under-grinding, giving weak fibres a relative benefit, with this difference magnified by the higher stress number enhancing fibrillation after breakage. Additionally, increased viscous dampening effects with long fibres introduces another complicating parameter not

considered in the model developed in Chapter 7. This causes the collapse in the relationship between fibre zero-span strength and hemicellulose content with MFC strength (see Figure 8.20).

Figure 8.21 compares this relationship for both the high and low pressure-concentrating factor grinds. Here, the relationship still mostly holds for the smoother media as the relative improvement for low zero-span strength fibres is less severe, and viscous dampening is much less significant, than for the 1 mm media series. However, fibres with low zero-span strengths are given a disproportionate boost.

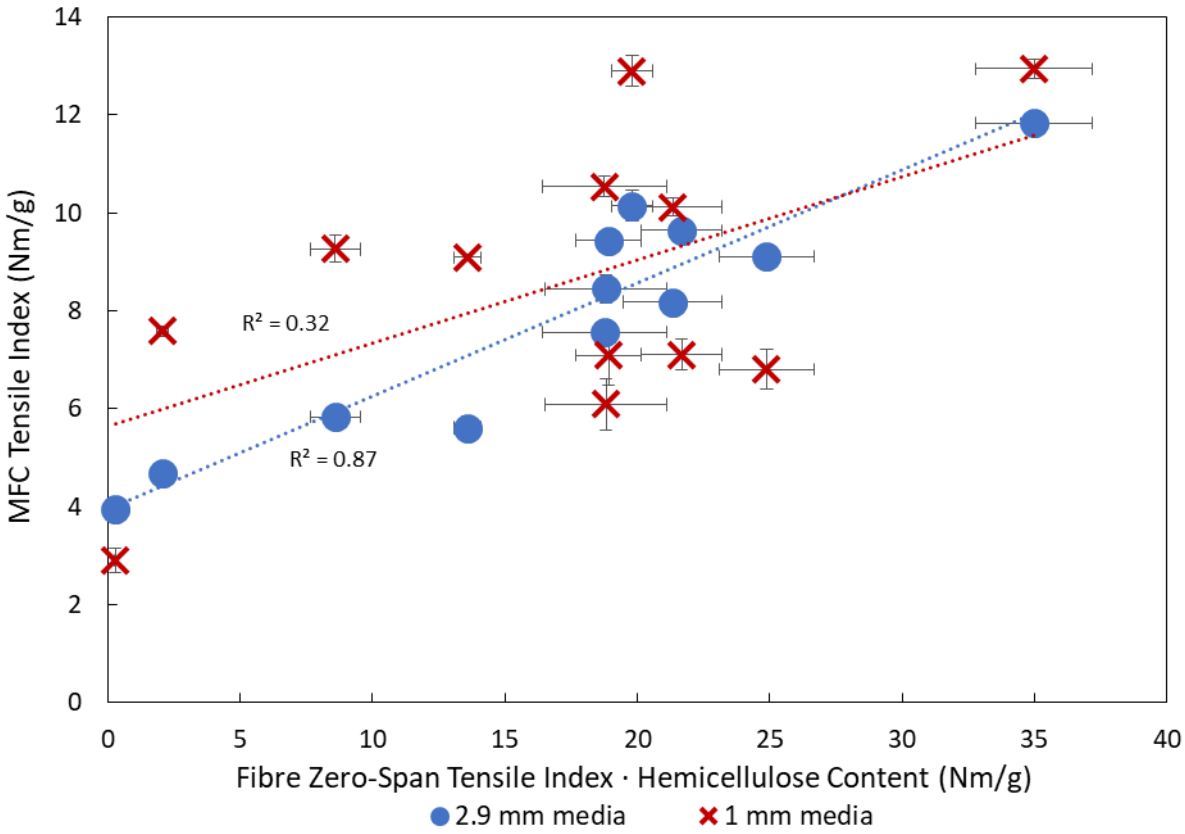

Figure 8.20 *– MFC tensile index at 3000 kWh/t versus the product of fibre zero-span tensile index and hemicellulose content versus, for the coarse and fine media grinds.*

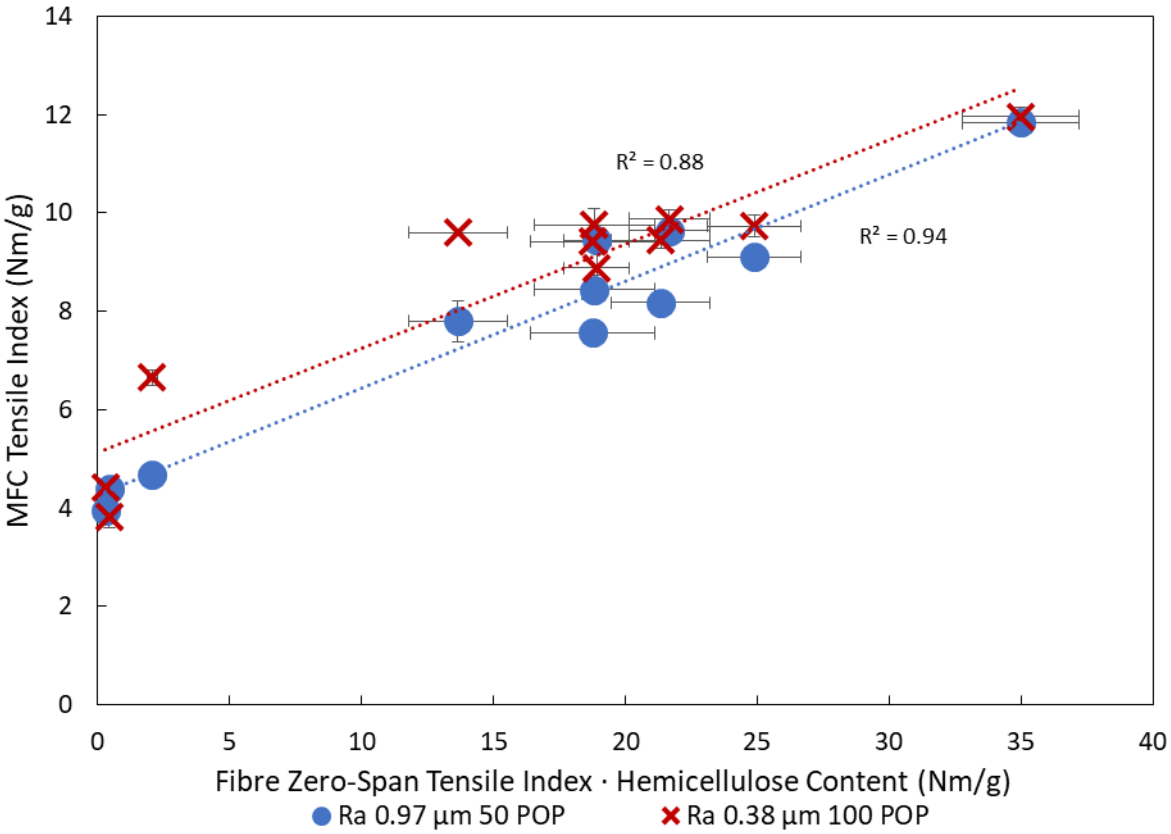

Figure 8.21 *– MFC tensile index at 3000 kWh/t versus the product of fibre zero-span tensile index and hemicellulose content, for the 2.9 mm rougher media 50 POP grinds and smoother media 100 POP grinds.*

Therefore, the hemicellulose – zero-span relationship derived in Chapter 7 is only expected to hold at relatively high roughness-adjusted stress intensities and energy inputs where all fibres are fully disintegrated, so a high zero-span strength solely reduces liberated fibril damage rather than retards fibre breakup. This relationship will cease to fit when MFC strength is no longer a factor of liberated fibrils resisting breakup, and are instead due to some fibres being too strong to be effectively broken up under the selected grinding conditions. The breakdown of this relationship for lower intensity grinding is not a problem however, since it is a result of low zero-span strength fibres that perform poorly under standard conditions, performing much better under these new conditions.

One could argue that the positive correlation observed in Figure 7.7 is entirely due to over-grinding weaker pulps. To demonstrate that this is largely false, Figure 8.22 plots the *acacia* data point with 1 mm media from the present chapter with the 2.9 mm media *acacia* energy sweep from Figure 7.1. The 1 mm media grind gives around a 3 Nm/g strength improvement above the peak tensile strength of the 2.9 mm media series, demonstrating that the observed benefit of finer media is mostly not due to changes in energy efficiency, and is instead because of differences in the balance of fibrillation and fibre breakage.

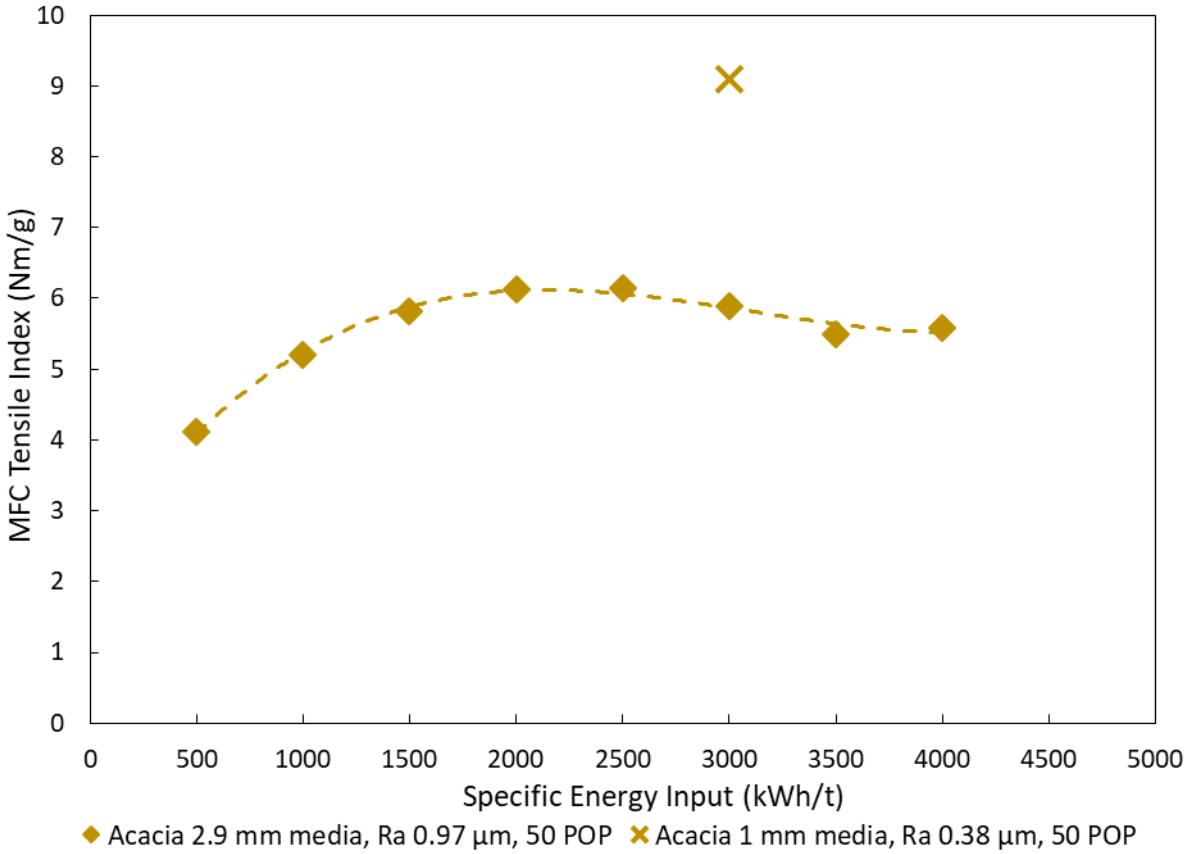

Figure 8.22 *– Energy sweep with acacia fibres under conventional grinding conditions, with the fine media data point shown for comparison.*

If coarse media is used on weak fibres at a lower energy input, this indeed causes less damage to fibrils, but fibrillation is also reduced due to a proportionally lower stress number (so fewer low intensity interactions). By contrast, using the fine media decreases $SI \cdot R_a$ by a factor of 60,

so each interaction is much less likely to damage fibrils, whilst also greatly increases stress number to promote fibrillation. Similarly, the presence of pressure-concentrating factors increases fibril breakage, whilst having a minor influence on fibrillation, so consequently the fibre species that are most vulnerable to fibril damage benefit more from reducing these factors.

8.5. Implications for Industrial Operation

These experiments demonstrate the effects that the two methods of reducing grind intensity have on various fibre species. These are just two cases in a wide parameter space, but still considerable improvements in MFC quality are obtained for some fibre species, so there is enormous potential for further tailoring operating conditions based upon feed fibre properties.

Figure 8.23 compares the MFC tensile index of grinds using conventional 50 POP 2.9 mm rougher media, the 100 POP 2.9 mm smoother media, and the 50 POP 1 mm media, for all fibre species that are common between these series. Long fibres perform uniquely poorly with the fine media, with severe under-grinding probably caused by viscous dampening, but all except abaca show some benefit of reducing the pressure-concentrating factors whilst using coarse media. For shorter fibres, where viscous dissipation with fine media is less significant, greatly reducing the media size leads to a greater strength improvement than reducing the pressure-concentrating factors.

However, there are other important differences between these operating conditions. Critically, finer media requires finer screens, which makes discharging the product much more difficult. Additionally, decreasing media size to 1 mm halves the power draw, thereby halving throughput. Therefore, 1 mm media is not expected to be industrially practical, though a more

moderate size decrease (e.g. 2 mm) is expected to yield benefits for many fibre species whilst being much easier to implement.

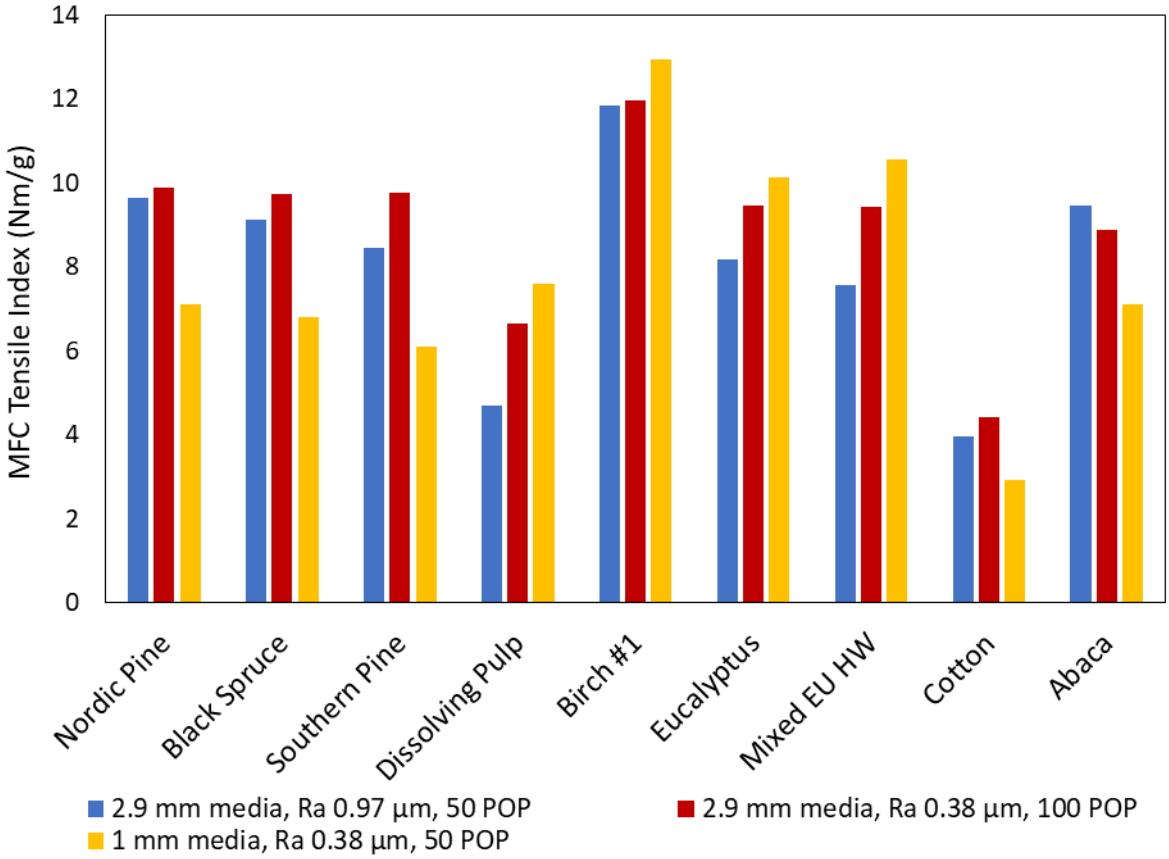

Figure 8.23 *– Comparison of the MFC tensile index of all three series considered in this section for the fibre species that are common between them.*

Using smoother media in the absence of mineral, however, does not inhibit screening (except due to a coarser product), and only slightly reduces power draw. For most fibre species that benefit from finer media grinding, maintaining a large media size and decreasing the pressure-concentrating factors instead provides a strength improvement that is almost as high. For weak fibres, doing so can increase the tensile index by around 2 Nm/g with no significant disadvantages. Additionally, smoother media results in lower media wear rates.

Note that different energy inputs have not been investigated; it is expected that lowering energy input (e.g. to 2000 kWh/t), would decrease the relative efficiency of the smoother

media 100 POP grinds compared to the control grinds (as is seen in Section 5.3). Microscopy images suggest most fibres processed with 1 mm media are under-ground, so lowering energy input would probably be detrimental here also. Clearly, more work is needed before energy input and operating conditions can be properly tailored to optimise the strength / cost relationship of fibres with specific properties.

8.6. Effect of Fibre Species on Optimum Solids Content

8.6.1. Introduction

The influence of the fibre solids content during grinding on MFC properties for various fibre species was also investigated. Although this does not directly influence stress intensity or pressure-concentrating factors as discussed in previous chapters, this parameter was worthwhile investigating since industrially it is a very easy operating condition to change. Changing the fibre solids content is expected to both affect viscous dissipation and the *capturing efficiency* (the number of particles per stress event), so was expected to be important despite having theoretically no influence on stress intensity or microcontact pressure.

Three studies were carried out in this area; the first was a set of preliminary 'solids sweeps', varying grinding solids content at a given specific energy input for several fibre species. This is followed by an expanded solids sweep study, where more fibre species were investigated, and MFC fibre analyser data collected. Finally, pilot-scale energy sweeps using birch fibres at several solids contents were carried out to observe how optimum energy input and peak tensile strength changes.

8.6.2. Preliminary Solids Sweep Investigation

Grinds were carried out with *Nordic pine*, *enzyme-treated Nordic pine*, *birch*, *eucalyptus* and *acacia* fibres, where the fibre solids content was varied, and specific energy input was maintained at the optimum energy input (i.e. *absolute* energy input scaled proportionally with fibre content). The other operating conditions were kept as standard; *Mullite A* media, 47.5% MVC, 800 rpm impeller speed, and 50% POP. These grinds were carried out prior to the acquisition of the fibre analyser, so only tensile index data were collected.

Figure 8.24 shows the influence of fibre solids content on MFC tensile index for each fibre species. For all fibres, increasing the fibre solids content beyond the 2.5% standard decreases tensile strength. However, lowering the solids content improves tensile strength, until a peak is reached, below which further reductions rapidly decrease tensile strength. The improvement from lowering solids content is strongest for *Nordic pine* and *birch* fibres, which peak at around 1% fibre solids; these peak values are substantially higher than their peak strengths in 2.5% fibre solids energy sweeps (see Figure 7.1), showing that solids content has influences beyond differences in energy utilisation.

Though the reasons for the improvement in MFC quality at lower solids content is not apparent from these data alone, the reason behind the rapid decline at extremely low solids contents is obvious; lowering solids content increases the probability that a media-media collision will not capture a fibre between them, therefore wasting energy, and eventually this inefficiency will overcome any benefit of lowering solids content.

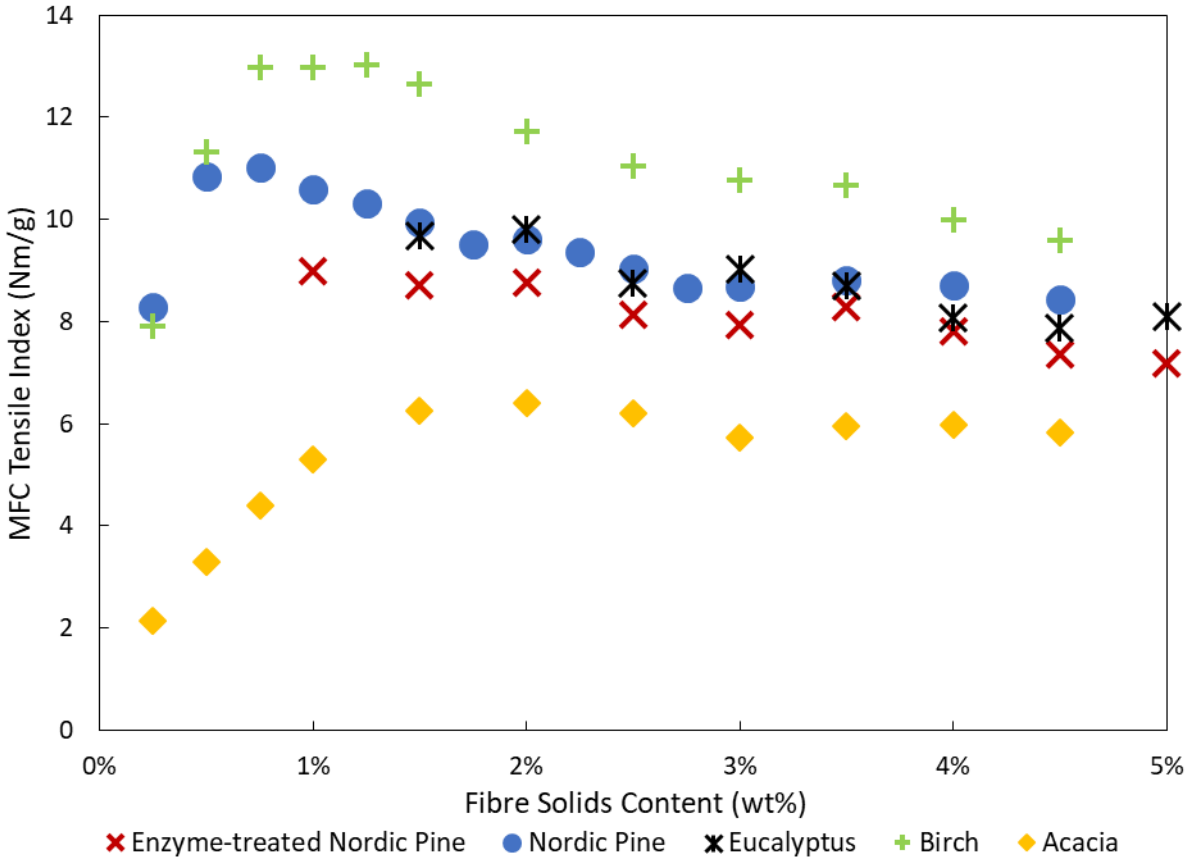

Figure 8.24 *– MFC tensile index versus fibre solids content at the optimum energy input for five fibre species.*

8.6.3. Expanded Solids Sweep Investigation

Upon acquisition of the fibre analyser, and completion of the work in Chapter 7, the solids sweep study was expanded to include seven more fibre species (*abaca*, *cotton*, *jeans*, *kenaf*, *bagasse*, *tissue dust*, and *mixed European hardwood*). Here, grinds were carried out as in Section 8.6.2, with 1%, 2%, 3% and 4% fibre solids contents being targeted. Additionally, *Mullite B* media was used since these grinds were carried out before differences between the performance of *Mullite A* and *Mullite B* were noticed; consequently, grinding efficiency in these series was somewhat lower than in Section 8.6.2.

The variation in MFC tensile index versus solids content is shown as Figure 8.25. For *abaca*, *bagasse*, and *kenaf*, there is a steady strength increase as solids content is lowered, being

highest at 1% fibre solids. *Tissue dust*, *mixed European hardwood*, and *jeans* peak at 2% fibre solids, whereas *cotton* peaks at 3% fibre solids. In general, it appears that fibres that produce higher quality MFC benefit more from decreasing the solids content. For this comparison, the overall gradient of the curve was used as a measure of 'solids sensitivity', defined as the tensile strength at 1% fibre solids minus the tensile strength at 4% fibre solids. Figure 8.26 plots this parameter for the data in both this section and in Section 8.6.2 against the tensile strength data from Chapter 7 for each fibre under standard conditions (i.e. at 2.5% fibre solids). Here, it is obvious that fibres that produce higher quality MFC under standard conditions benefit more from decreasing the fibre solids, though identifying the reasons for this requires a consideration of fibre analyser data.

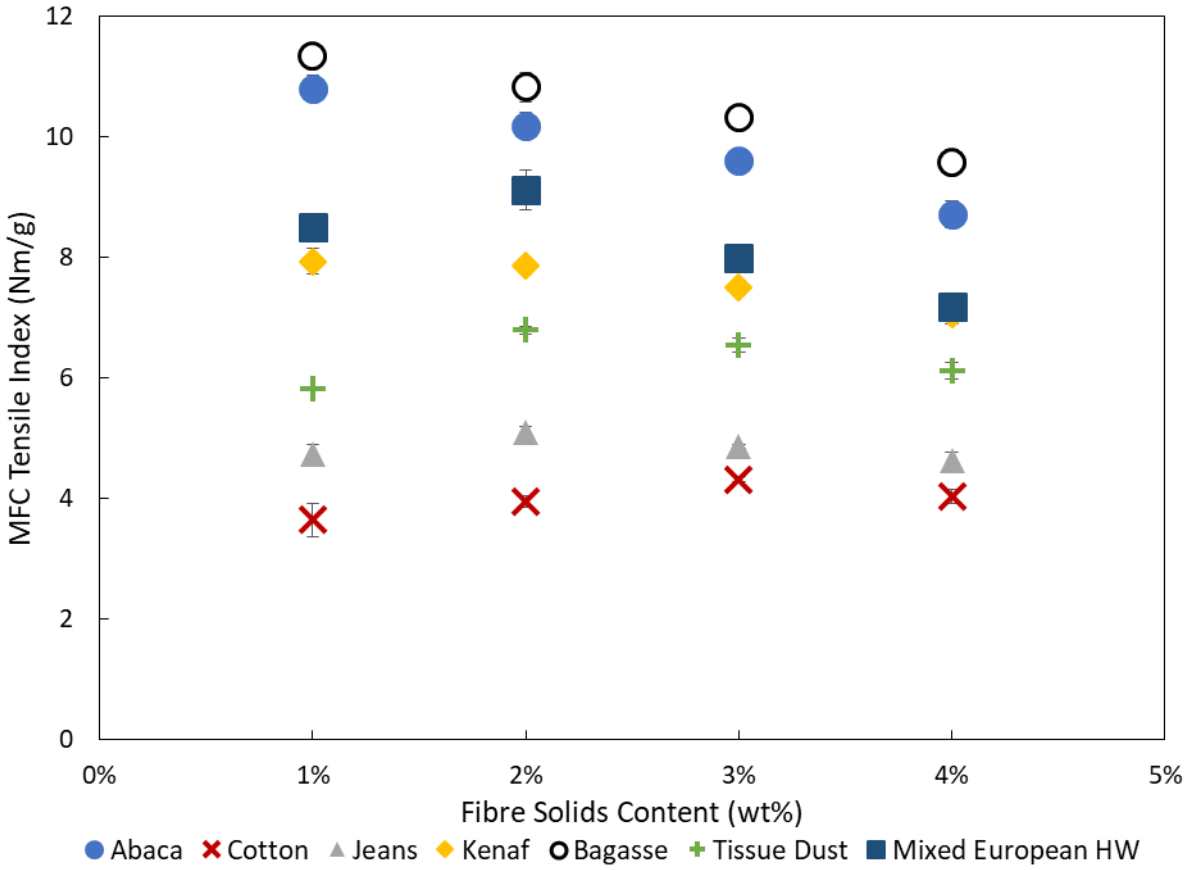

Figure 8.25 *– MFC tensile index at 3000 kWh/t versus fibre solids content for seven fibre species.*

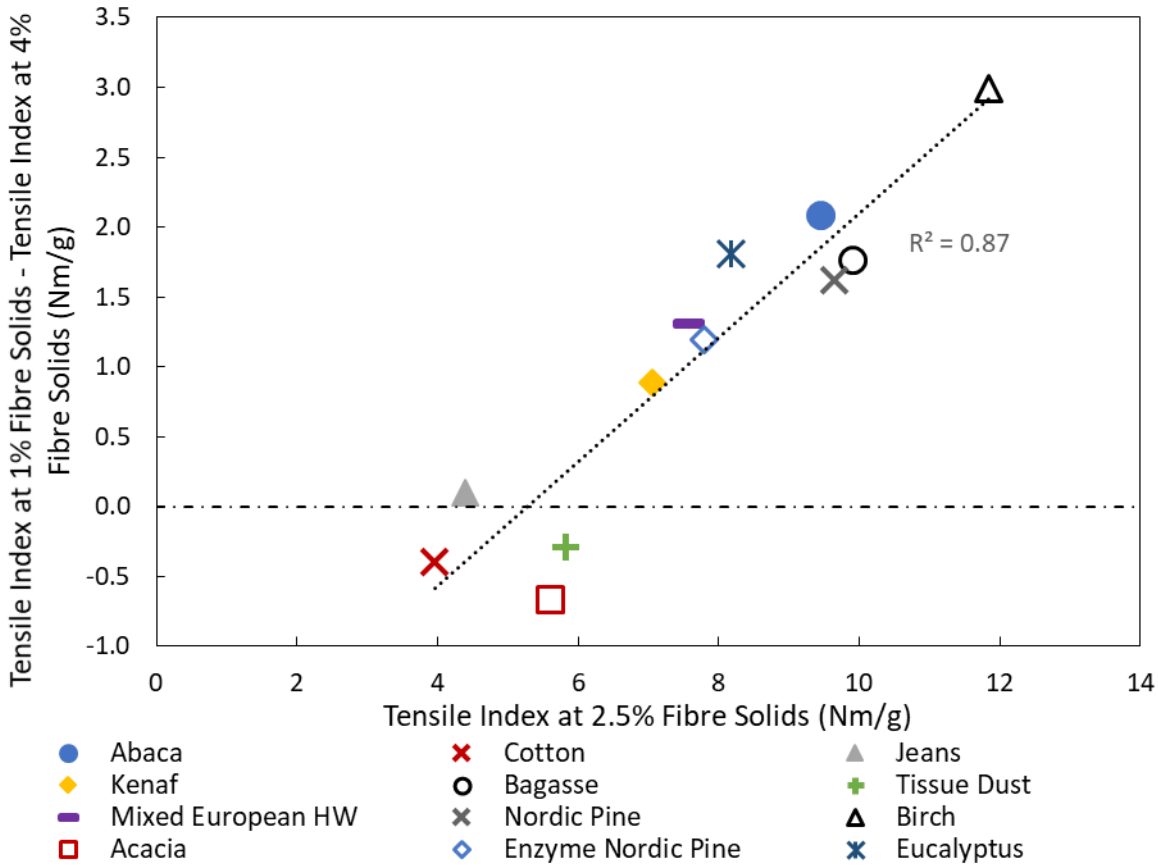

Figure 8.26 *– The sensitivity to solids content (the tensile index at 1% fibre solids minus the tensile index at 4% fibre solids) versus the MFC tensile index under standard conditions for twelve fibre species.*

Fibre analyser results were measured for each sample, with Figures 8.27, 8.28, and 8.29 showing how *Lc(l)*, *Fibrillation %*, and *Fines B* vary with energy input. Surprisingly, for most fibres, Figure 8.27 shows that the *Lc(l)* versus solids content curve is relatively flat. Most fibres, however, reach a minimum *Lc(l)* at moderate solids contents, with the coarser MFC at 1% fibre solids being due to increased inefficiency from media-media contact energy losses, and the coarser MFC at 4% solids probably being due to energy wastage from excessive viscous dampening. Due to the low sensitivity of MFC length to solids content, this cannot explain the tensile strength differences, though as discussed later, this suggests a higher breakage probability per stress event.

The external fibrillation measurements shown by Figure 8.28 are more striking, with all fibre species which yield higher tensile strengths at 1% fibre solids also showing a large improvement in *Fibrillation %* values. In fact, the solids content that gives the maximum *Fibrillation %* value corresponds to the solids content that gives the maximum tensile strength value for all fibre species except *mixed European hardwood*. This implies that differences in the generation of external fibrils is the primary reason why grinding solids content influences tensile strength.

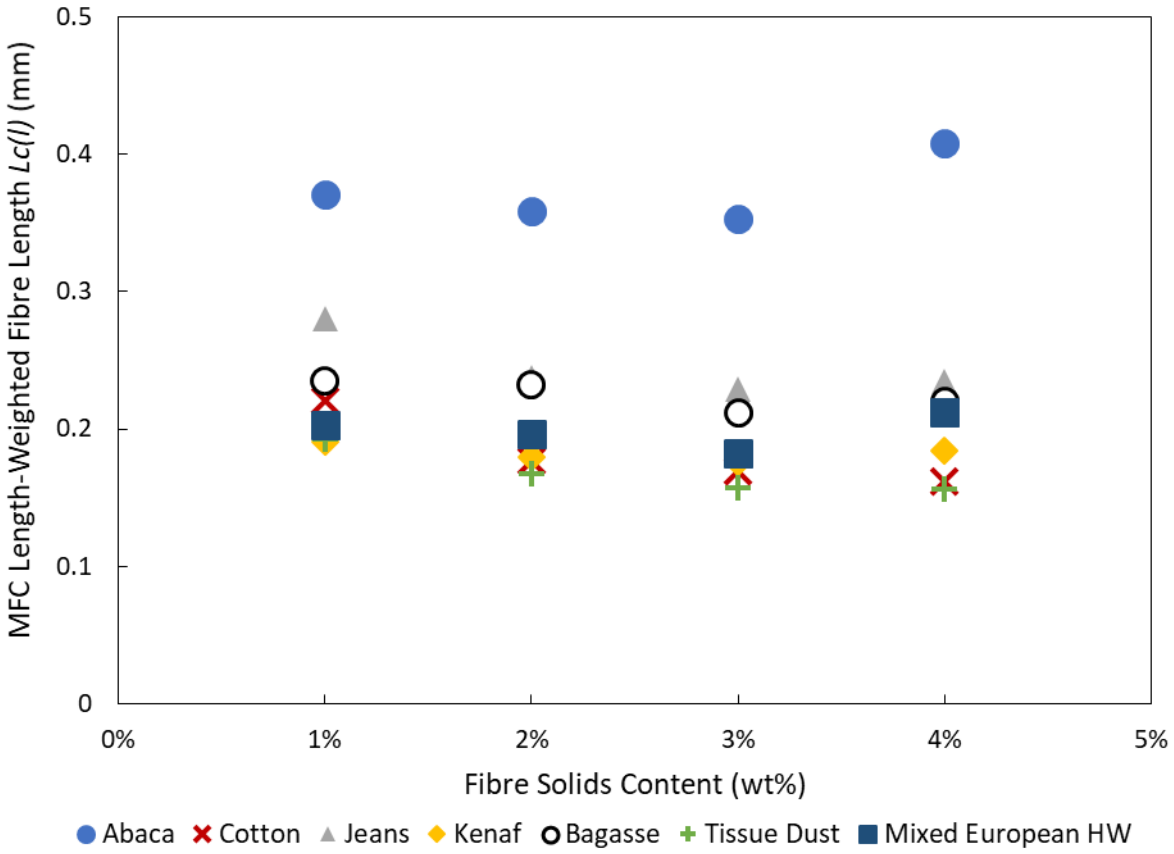

Figure 8.27 *– MFC fibre length at 3000 kWh/t versus fibre solids content for seven fibre species.*

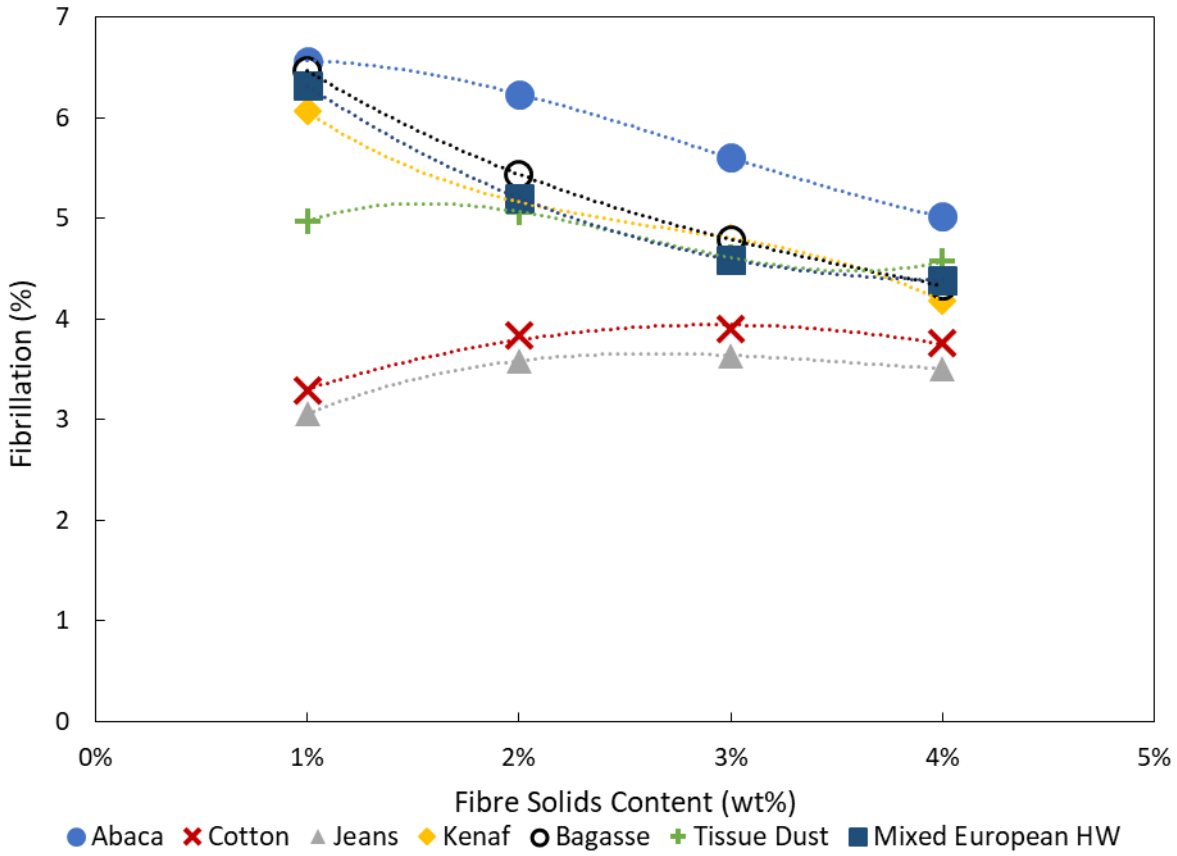

Figure 8.28 *– Fibrillation % at 3000 kWh/t versus fibre solids content for seven fibre species. Due to overlap of data points, lines are added to guide the eye.*

High aspect ratio fines, shown by Figure 8.29, do not follow this pattern, instead peaking at 2% – 3% fibre solids for most fibre species. This leads to the unexpected observation that at 1% fibre solids, *Fibrillation %* is high and *Fines B* is low. However, at 1% fibre solids, *absolute* energy input is very low (since *specific* energy input is normalised by fibre solids content); although fibre breakage is much more effective, leading to rapid external fibril generation, the much shorter time in the grinder provides fewer opportunities for these fibrils to break off to form *Fines B* particles, and less time for these free fibrils to degrade. At 4% fibre solids, both *Fines B* and *Fibrillation %* are low, despite fibre breakage being only slightly worse than at lower solids content; this is believed to be both be because of the converse effect to that at 1% fibre solids regarding absolute energy input, and because the much higher viscous dampening would have a disproportionate effect on the low intensity events that generate

fibrillation at breakages, whilst having a lesser effect on the high intensity collisions where fibres are broken (due to the shear-thinning nature of MFC).

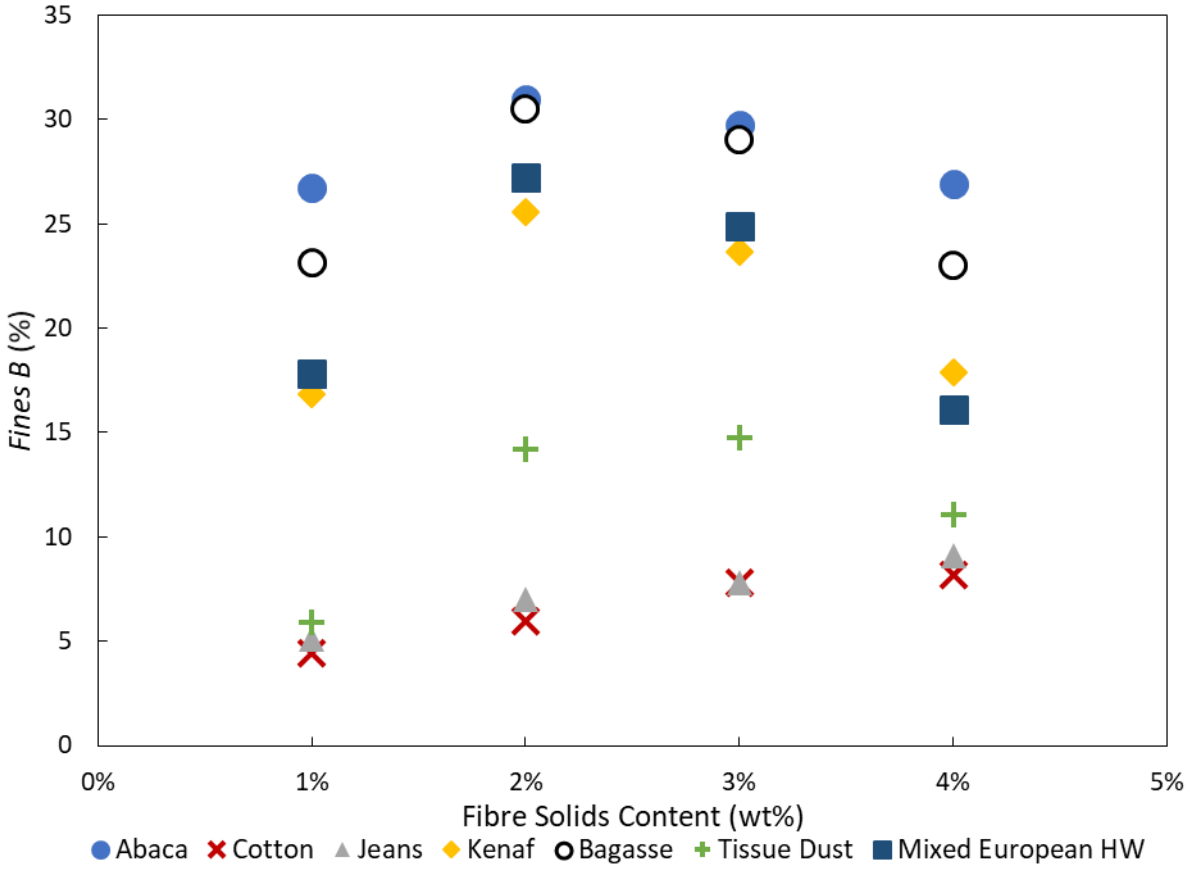

Figure 8.29 *– Fines B content at 3000 kWh/t versus fibre solids content for seven fibre species.*

To summarise, for many fibre species, lowering the grinding fibre solids content improves MFC quality by preserving external fibrillation. For fibres that typically produce good fibrils under standard conditions, it is worth lowering the solids content, but for fibres that yield poor fibrils, one should not, since the increased inefficiency counteracts the benefit.

8.6.4. Pilot-Scale Energy Sweeps

With the rule of thumb identified that fibres which produce good MFC produce even better MFC at lower solids content, *FiberLean* was eager to apply this industrially, especially since solids content is an easy input parameter to change. Consequently, the author carried out

energy sweeps with *birch* fibres at 0.75%, 1.5%, and 2.5% fibre solids using *FiberLean's 'Supermill'* pilot-scale grinder, under grinding conditions believed to be equivalent to those used in the lab-scale grinder. The pilot-scale grinder has outlet screens that are periodically opened to collect a sample, so a single grind provides data for an entire energy sweep.

Figure 8.30 shows the tensile index results; a lower solids content clearly increases strength, with a remarkably high peak value at 0.75% fibre solids of 13.7 Nm/g. Interestingly, optimum energy input varies little, with both 0.75% and 1.5% fibre solids peaking around 3000 kWh/t and 2.5% fibre solids peaking around 2500 kWh/t. Therefore, the efficiency loss from media-media contact is almost cancelled out by improvements in specific fibre breakage and fibrillation over these ranges. Figure 8.31 shows the external fibrillation measurements, which follow essentially the same pattern as MFC tensile index, peaking in similar places, and with higher external fibrillation corresponding to higher MFC strength. This further supports the conclusion that low solids grinding promotes high MFC quality by maximising external fibrillation.

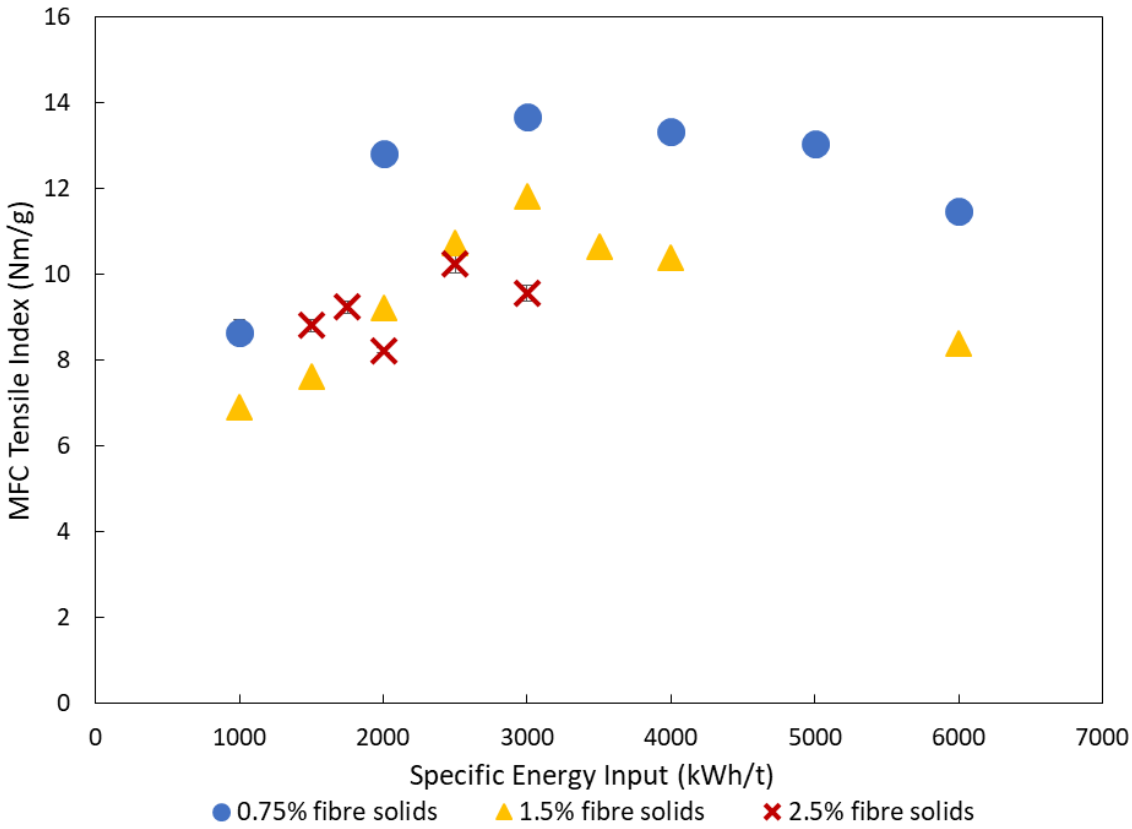

Figure 8.30 *– MFC tensile index versus specific energy input at three fibre solids contents, for pilot scale grinds of birch fibres.*

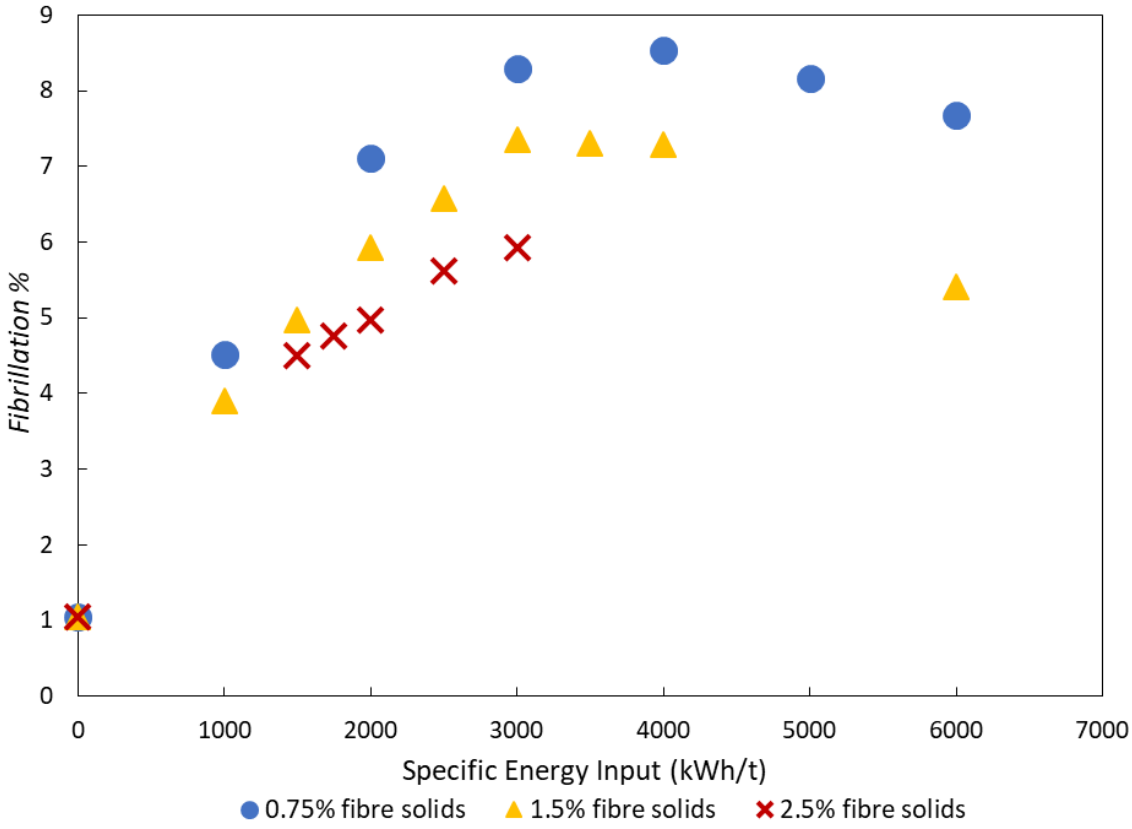

Figure 8.31 *– External fibrillation versus specific energy input at three fibre solids contents, for pilot scale grinds of birch fibres.*

8.6.5. Discussion

Figure 8.27 shows a fairly flat relationship in MFC length with solids content, which is actually quite a profound conclusion that is key to understanding the effect of fibre solids; despite the four-fold difference in fibre concentration between 1% and 4% fibre solids, and the consequent four-fold difference in absolute energy inputs, total breakage rates are similar. Therefore, though lowering the solids content decreases the number of fibres captured per collision, the breakage probability for each fibre in a collision must increase almost proportionally to compensate.

Differences in viscous dampening likely play a role in this, but this difference in capturing efficiency is expected to be the most important, since viscous dampening effects particularly for short fibres with 2.9 mm media are weak at 2.5% fibre solids, see Figure 8.4 (the concept of optimum capturing efficiency was discussed by the author in their stirred media mill review publication, see Appendix B1). At too low solids content, capturing efficiency is so poor that excessive energy is wasted in naked media-media contacts. At too high solids content, many fibres are stressed in a single impact, distributing the energy over more cross-sectional area, thereby decreasing breakage probability for any particular fibre.

At low solids contents, the lower absolute energy input means fewer opportunities to break off external fibrils and damage liberated fibrils (which require less stress than breaking fibres, so is not similarly inhibited at higher solids content when many particles are stressed simultaneously). At the optimum solids content, this improvement in specific fibre breakage probability in a collision is coupled with the maintenance of long external fibrils on these particles, which leads to large, highly fibrillated MFC particles with excellent tensile strength.

With the differing roles of fibre solids content on fibre breakage and fibrillation identified, the shape of Figure 8.26 can now be explained. Fibre species that produce weak MFC under standard grinding conditions struggle to produce long, thin fibrils during fibre breakup, thereby, lowering grinding solids content to preserve these fibrils provides little benefit, which is overcome by energy losses from reduced capturing efficiency and increased naked media-media contact, lowering tensile strength. For fibres that produce long, thin fibrils, especially high hemicellulose pulps with high zero-span tensile strengths (e.g. birch and bagasse), it is worthwhile to lower the solids content since minimising the degradation of these fibrils more-than compensates for the increased energy losses from the lower capturing efficiency, and thereby improves tensile strength.

FiberLean have used the results in this section to optimise the solids content of different fibre species in industrial grinding, which has typically yielded tensile strength improvements between 1 – 2 Nm/g compared to standard conditions, without significantly increasing optimum energy input. However, there are other operational advantages and disadvantages of low solids grinding beyond the influence on MFC properties; lower solids MFC is much easier to discharge from the screens, so coarser MFC at lower energy inputs can be produced industrially. The lower solids content also means higher total volume passing through the grinder, which keeps the polyurethane lining cool and reduces degradation, though this higher water content does reduce functional capacity of storage tanks and make dewatering and drying more difficult.

8.7. Conclusions

Two sets of experiments were undertaken to investigate the effect on MFC quality of reducing grind intensity by (i) reducing macroscopic stress intensity with finer media, and (ii) reducing microcontact pressure by removing pressure-concentrating factors (decreasing surface roughness and removing mineral particles). Further experiments investigated the influence of changing the fibre solids content, which affected the balance of fibre breakage and fibrillation mainly by changing the number of particles stressed in each collision.

Low zero-span strength pulps benefit greatly when fine media is used, because the fibre can still readily disintegrate, but the high stress number and low stress intensity of fine media is ideal for delaminating these relatively delicate fibrils without excessive damage. Some of these improvements are striking, sometimes increasing strength by more than 3 Nm/g compared to coarser media. Unlike with coarse media, fibre length is clearly a very important factor for fine media grinding, which is expected to be due to increased viscous dampening. Consequently, long fibre pulps are very resistant to breakage with fine media, so tensile strength is relatively poor. Longer MFC fibre lengths, higher *Fibrillation %* values, and (usually) lower *Fines B* values when using shorter feed fibres indicate that these lower stress intensities favour fibril delamination, but are below the optimum for fibril cross-sectional breakage, which is the presumed reason behind the strength improvements for many fibres.

For shorter fibres, maintaining the high macroscopic stress intensity but reducing pressure-concentrating factors (100 POP, smoother 2.9 mm media grinds) results in a similar, though lesser, benefit, which is also stronger for weaker fibres. However, because viscous dampening is weak, MFC produced using long feed fibres is usually similarly improved, in contrast with the fine media grinds. Despite typically having a lesser benefit, this route is more sensible

industrially than using fine media, since finer screens are not required, and power draw remains high.

A similar effect on the balance of fibrillation and fibre breakage as with fine media is seen when lowering the grinding solids content; for many fibres, this increases external fibrillation considerably whilst decreasing *Fines B* content. The reason for this is different, however, as stress intensity does not change; instead, decreasing the fibre solids lowers the cross-sectional area over which collision stresses are distributed, thereby increasing breakage efficiency of a fibre caught by the media, which largely cancels out the effect of the lower fibre capturing efficiency, and this also appears to rapidly generate external fibrillation. The proportionally lower absolute energy input results in fewer external fibrils breaking off into free fibrils, and reduces fibril degradation, leading to higher tensile strengths. Preserving fibrillation by lowering solids content has substantial industrial advantages over doing so by reducing media size, since power draw is not substantially reduced, and grinder discharge becomes easier rather than harder.

Fibres that produce long, thin fibrils (i.e. strong MFC under standard conditions) largely benefit more from reducing the solids content, and have a lower optimum solids content before inefficiencies from increased naked media-media contact dominate. This proportionality is different from the fine media grinds and the low pressure-concentrating factor grinds, where in the former both fibre length and fibre strength control the effect, and the latter appears dependent only on fibre strength.

The observed interactions between fibre properties and grind intensities demonstrate that the characteristic stress intensity versus MFC property curves observed in Chapter 6, and the correlation between the product of zero-span strength and hemicellulose content with MFC

strength in Chapter 7, are not universal or independent. Given operating conditions are fixed around standard conditions, the relationship in Chapter 7 is useful as a shortlisting tool. However, if effective stress intensity can be lowered, for example by lowering media size or using smoother media, the relationship is different; hemicellulose content is believed to be beneficial for all cases, but now a low zero-span strength does not discount the fibre as a good feedstock, and instead merely advises which operating conditions are appropriate.

The work in this chapter leads to the following recommendations:

- Fine media should be avoided for long fibres as viscous dissipation causes severe under-grinding. For weaker long fibre pulps, media surface roughness and mineral content should be reduced to lower microcontact pressure instead, as this does not increase viscous dampening, whilst still improving fibrillation and enhancing tensile strength.

- Fibres with lower zero-span tensile strength benefit more from either method of reducing grind intensity. One should use the smallest possible intensity needed to effectively break the fibre down, since this leads to more low energy stress events to enhance fibrillation whilst minimising liberated fibril breakage.

- Reducing grind intensity by reducing pressure-concentrating factors causes fewer industrial operational problems compared to decreasing media size, primarily due to screening issues; for most fibres, the increase in strength from doing the former is only slightly below the latter.

- For fibres that under standard conditions produce long, thin fibrils (high hemicellulose content, high zero-span strength), one should lower the grinding solids content. This

better preserves liberated and external fibrils, but unlike the other two strategies discussed for doing this, does not lower roughness-adjusted stress intensity, so fibre breakage is not substantially inhibited.

- For fibres that produce short fibrils under standard conditions (e.g. tissue dust), lowering the solids content gives no benefit because these weaker fibrils are still broken extensively by the high stress intensity during fibre breakage.

- There is a great potential for combining these effects, for example, lowering media size for very weak fibres (e.g. tissue dust) would produce longer liberated fibrils, which would be better preserved by lowering grinding solids content.

- Given fibre hemicellulose content, zero-span strength, and length measurements are taken, informed choices regarding appropriate grinding conditions to trial can be made. If these feed fibre measurements are not acquired, carrying out a lab grind under standard conditions, measuring tensile strength, and observing fibrillation characteristics with the fibre analyser and microscopy could indicate whether, for example, solids content should be lowered, or stress intensity decreased.

9. CONCLUSIONS AND FUTURE WORK

This work has investigated MFC production via lab-scale stirred media milling of cellulose. Numerous operational parameters have been explored, including impeller speed, media size, density, and surface roughness, mineral content, fibre solids content, and feed fibre properties, with the influence on MFC properties assessed. This chapter summarises the conclusions of each results and discussion chapter, and suggests promising future work, followed by an overarching summary of this thesis.

9.1. Introduction to MFC Grinding

In Chapter 4, an energy sweep under conventional grinding conditions was carried out, with the evolution of MFC characteristics assessed. Upon a media collision, intervening fibres can be completely or partially broken across their cross-sections, exposing the fibril sub-components. Over time, these fibrils increasingly fray from these breakage sites, generating external fibrillation, eventually breaking loose to form free fibrils; once liberated, these fibrils are continuously degraded with further processing. The tensile strength peaks when this degradation effect cancels out any further benefit from increasing fibrillation.

The Hertzian contact mechanics model was applied to predict cell wall deformation dimensions, which largely matched microscopy observations, and it was suggested that media collisions must have sufficient momentum to compress the fibre cell wall to cause breakage.

Fibre cross-sectional breakage and the second-order fibrillation effects are affected differently by changing operating conditions, which was exemplified by two extreme examples given, where fibrillation was suppressed by grinding in a hygroscopic medium, and breakage was suppressed by grinding with low elasticity nylon media.

Energy sweeps were also completed using different media sizes and impeller speeds. In general, lowering the stress intensity by decreasing either factor decreases fibre breakage rate, but increases fibrillation after breakage. Tensile strength is maximised when collision intensity is sufficient to lead to high fibre breakage rates to expose fibrils, but low enough to provide a high stress number that maximises opportunities for fibrillation per breakage site.

9.2. Media Roughness and Mineral Content

Chapter 5 investigated the effect of media roughness on MFC properties, demonstrating that a high roughness greatly improves grinding efficiency. Energy sweeps show that optimum energy input is lowered for rougher media, though no effect on peak tensile strength is obvious. However, rougher media also substantially increases wear rate, so there is an economically optimum roughness which balances energy cost and media cost. Accounting for media roughness allows for the expected effect of media density to be observed; enhancing fibre breakage whilst decreasing fibrillation.

Energy sweeps with different media roughnesses were compared with and without mineral addition, which demonstrates an interaction between these two factors. Mineral addition improves fibre breakage rate, whilst disproportionately degrading liberated fibrils. For rougher media, fibre breakage rate is sufficiently high without mineral particles present, so its addition provides no benefit, instead damaging liberated fibrils and degrading peak tensile strength. For smoother media, which struggles to break fibres, mineral addition improves energy efficiency at low energy inputs. Therefore, whether mineral particles should be added is dependent on media surface roughness.

A microscopy investigation gave evidence that roughness enhances fibre breakage by concentrating collision stresses at localised points on fibre cross-sections. This is supported by

theoretical calculations based upon Hertzian contact mechanics which predicts that microcontact pressure should be directly proportional to surface roughness.

Suggested areas of future work include:

- Investigating the influence of different mineral sizes and shapes, since this will influence the area of damage induced on fibre cross-sections. A coarser mineral was investigated in this work, but it quickly degraded during grinding, so stronger mineral species are needed for a meaningful study.
- A form of roughness 'cascade grinding' could be attempted, where rough media breaks fibre cross-sections and exposes fibrils, before the partially processed product is discharged into a second grinder with smoother media to finish fibrillation; this is expected to substantially reduce media wear.
- Long-term industrial observations of media wear for numerous well-characterised media species are necessary to identify whether microcrack accumulation enhances compressive failure. Once understood, the relationship between roughness and wear rate would be isolated, allowing a more accurate assessment of the economically optimum media roughness.

9.3. Stress Intensity

The results from Chapter 4 demonstrate the importance of stress intensity for controlling fibre breakage and fibrillation. Chapter 6 investigated this by undertaking grinds with different combinations of media size and impeller speed. Stress intensity theory was largely followed, with the characteristic stress intensity – particle size plot exhibited, with an optimum stress intensity for size reduction, at which fibrillation parameters are close to maximum at that

specific energy input. Fibrillation was found to decline rapidly at excessive stress intensities due to a deficiency of low intensity stress events to exploit breakages.

However, there were deviations from theory, with finer media being markedly more efficient at fibre breakage and fibrillation at a given stress intensity. This is expected from the Hertzian contact mechanics model, where the sharper media curvature for fine media enhances cell wall penetration depth. Accommodating this largely solves this discrepancy, but the author does not consider this explanation sufficient and further work is needed to address this.

Data from many grinds using various media sizes, densities, roughnesses and impeller speeds were analysed, showing that a higher surface roughness lowers the optimum stress intensity. Multiplying stress intensity and surface roughness produces a *roughness-adjusted stress intensity*, which below the optimum energy input was found to predict size reduction fairly well. However, this relationship breaks down above the optimum stress intensity, with the curves for different media roughnesses diverging. These results did demonstrate, however, that surface roughness and stress intensity have somewhat interchangeable effects.

There are several promising areas for future work on this subject:

- Further work is needed to better understand why fine media performs better than expected from stress intensity theory. This could involve PEPT work to measure collision forces and frequencies, in a manner similar to the work of Skuse[81].

- In Chapter 6, the effect of energy input was not sufficiently explored; the conditions which maximised fibrillation parameters at the applied energy input may not give the best *peak* fibrillation and strength, as Chapter 4 hints. To characterise this, energy

sweeps should be carried out with several permutations of impeller speed, media size, media density, and roughness.

- Since the optimum roughness-adjusted stress intensity is expected to decrease with increasing grinding progress, cascade grinding should be investigated, applying a lower roughness-adjusted stress intensity after partially processing the MFC under intense conditions, improving the efficiency of further breakage and increasing the opportunities for fibrillation. This could be done by various combinations of input parameters, with the best choice dependent on effectiveness, throughput, media wear rate, and screening issues.
- Media volume concentration should be investigated as it is known to affect MFC properties, probably by affecting media mobility and degree of intimate media-media contact.

9.4. Fibre Properties versus MFC Quality

Under standard grinding conditions, peak tensile strength varies greatly with fibre feedstock. Chapter 7 compared many fibre feedstocks to relate MFC strength to feed fibre properties. Fibre hemicellulose content was found to correlate positively with MFC strength, since it decreases forces between microfibrils, thereby promoting fine fibril liberation. Feed fibre geometry showed no obvious effect, but by considering product MFC length alongside hemicellulose, an excellent correlation with MFC tensile strength was obtained.

However, the objective was to predict MFC strength from feed properties alone, so a parameter which predicted MFC length was needed. Fibre zero-span tensile strength was found to do this, being inversely related to the presence of flaws within fibril and fibre cross-sections. A low zero-span strength fibre contains fibrils that are more vulnerable to damage,

thereby producing short liberated fibrils and low strength MFC. Combining feed zero-span strength with hemicellulose content gives a fairly good prediction of MFC quality based upon feed properties, which would aid shortlisting feedstocks to trial only those expected to yield good MFC, given the standard operating conditions were maintained.

The best avenues for future work on this subject involve investigating how various fibre species perform under different operating conditions, which is partially addressed in Chapter 8. However, one new experiment is recommended here; much of the hemicellulose present in the tree is removed during pulping, so obtaining samples of a fibre species at different stages of the pulping process and producing MFC with them would likely demonstrate a neater correlation between hemicellulose and MFC strength, and since lignin content would also change would permit an investigation into how much lignin can be present before fibrillation is inhibited.

9.5. Effect of Fibre Properties on Optimum Operating Conditions

Chapter 8 tested numerous fibre species under different operating conditions, including reducing the stress intensity by decreasing media size, reducing the pressure-concentrating factors by using smoother media with no mineral addition, and changing the number of fibres stressed per collision by varying the grinding fibre solids content.

Weak fibres (i.e. low zero-span strength) were found to benefit from reducing pressure-concentrating factors, since they still readily break down, but the liberated fibrils are better preserved. The same pattern was seen with the fine media grinds, often giving large strength improvements. Weak fibres still readily disintegrate under low stress intensities, but liberated fibrils are damaged less, whilst the high stress number promotes extensive fibril generation. However, long fibres perform very poorly with fine media due to extreme viscous dampening.

Lowering the grinding solids concentrates the collision pressure into fewer fibres, and lowers viscous dampening, enhancing breakage probability, whilst decreasing capturing probability. For fibres that readily produce long, thin fibrils upon breaking, this increase in collision effectiveness produces extensive external fibrillation that is protected from damage by short grind times, dramatically improving MFC strength. This benefit is greatly decreased or even reversed when fibres are used that typically produce short, coarse fibrils under standard conditions, since preserving these fibrils is not worth the decrease in capturing efficiency.

Critically, depending on the fibre properties, one should employ different operating conditions to maximise MFC quality. The conclusion from Chapter 7 that low zero-span strength fibres produce poor MFC is only true under the relatively intense standard conditions that were used; instead, these weak fibres need not be avoided as a feedstock, so long as pressure-concentrating factors or stress intensity are reduced to preserve the relatively delicate fibrils.

The following additional work is suggested:

- The low stress intensity grinds gave just one data point per fibre species; despite this, large improvements in MFC quality were often seen. Consequently, investigating several intermediate stress intensities would allow interpolation to predict where the optimum operating conditions for each species reside (by constructing a cruder version of the $SI \cdot R_a$ versus MFC properties curve in Chapter 6).

- This study should be repeated at a much lower energy input (e.g. 1500 kWh/t), to determine whether some combination of fibres and operating conditions can produce good quality MFC at a greatly reduced energy cost.

- Combinations of lowering roughness-adjusted stress intensity with lowering the grinding fibre solids content should be attempted for weak fibres as a possible route for maximising fibril generation whilst minimising fibril damage.

9.6. Overall Thesis Conclusions

The objectives stated in Chapter 1 have largely been met; the evolution of a fibre into MFC during grinding was characterised in detail, and demonstrated the presence of two mechanisms; fibril cross-sectional breakage, and fibrillation, which are somewhat independent. The role of media surface roughness is in concentrating collision pressure at localised points, enhancing fibre breakage and advancing subsequent fibrillation processes. The mineral content appears to have a similar role in concentrating collision pressure, though it is disproportionately effective at liberated fibril breakage, probably due to its finer size.

The concept of stress intensity can mostly be applied to cellulose grinding, although finer media appears to perform better than expected from this theory. So long as the stress intensity is below the optimum, stress intensity and roughness can be combined into a factor that predicts fibre breakage rate, which consequently influences subsequent fibrillation processes. Lower stress intensities are, however, more effective at fibrillation for a given breakage rate due to the higher stress number and lower energy requirement of this process.

A high fibre hemicellulose content promotes generation of fine fibrils and microfibrils upon fibre disintegration, producing high strength MFC. Under standard operating conditions, a high fibre zero-span tensile strength produces long, strong fibrils that are more resistant to damage once liberated, so combining this factor with hemicellulose content yields a parameter which predicts MFC tensile strength well. It was then identified that depending on feed fibre zero-span strength, length, and propensity for fibrillation, different strategies for

changing operating conditions should be attempted to maximise MFC quality, including changing the stress intensity, the pressure-concentrating factors, or the grinding solids content, with the goal of balancing the effective stress intensity, the number of stress events, and the cross-sectional area stressed per collision to maximise fibril generation and minimise fibril degradation.

With this knowledge, *FiberLean* is better able to make an informed judgement on appropriate operating conditions based upon feed fibre property measurements. Fibre solids content, mineral content, impeller speed, and media size, density, and surface roughness are all tools that are available for doing this, and the findings for each, presented in this work, provide guidance on how these are best used to reduce cost, increase throughput, and improve product quality during stirred media mill production of microfibrillated cellulose.

10. REFERENCES

[1] Turbak, A. F., Snyder, F. W., Sandberg, K. R., 1983. ***Microfibrillated cellulose, a new cellulose product: properties, uses, and commercial potential.*** Journal of Applied Polymer Science Applied Polymer Symposia, 37, pp.815-827. Syracuse, NY, USA, 24 May 1982.

[2] Herrick, F. W., Casebier, R. L., Hamilton, J. K., Sandberg, K. R., 1983. ***Microfibrillated Cellulose: Morphology and Accessibility.*** Journal of Applied Polymer Science Applied Polymer Symposia, 37, pp.797-813. Syracuse, NY, USA, 24 May 1982.

[3] Klemm, D., Kramer, F., Moritz, S., Lindström, T., Ankerfors, M., Gray, D., Dorris, A., 2011. ***Nanocelluloses: A New Family of Nature-Based Materials.*** Angewandte Chemie International Edition, 50, pp.5438-5466.

[4] Shatkin, J. A., Wegner, T. H., Bilek, E. M., Cowie, J., 2014. ***Market projections of cellulose nanomaterial-enabled products – Part 1: Applications.*** Tappi Journal, 13(5), pp.9-16.

[5] Cowie, J., Bilek, E. M., Wegner, T. H., Shatkin, J. A., 2014. ***Market projections of cellulose nanomaterial-enabled products – Part 2: Volume estimates.*** Tappi Journal, 13(6), pp.57-69.

[6] Husband, J. C., Svending, P., Skuse, D. R., Motsi, T., Likitalo, M., Coles, A., FiberLean Technologies Ltd., 2015. ***Paper filler composition.*** U.S. Pat. US9127405B2.

[7] FiberLean Technologies, 2018. ***Paper Solutions PDF*** [brochure]. Available at: https://www.fiberlean.com/wp-content/uploads/2018/04/FiberLean.pdf (accessed 10th August 2020).

[8] IndexMundi, 2020. ***Wood Pulp Monthly Price - Euro per Metric Ton*** [online]. Available at: https://www.indexmundi.com/commodities/?commodity=wood-pulp&months=120&currency=eur (accessed 10th August 2020).

[9] Statista, 2020. ***Average price of kaolin in the U.S. from 2007 to 2019*** [online]. Available at: https://www.statista.com/statistics/248194/average-price-of-kaolin (accessed 10th August 2020).

[10] Chinga-Carrasco, G., 2011. ***Cellulose fires, nanofibrils, and microfibrils: The morphological sequence of MFC components from a plant physiology and fibre technology point of view.*** Carbohydrate Polymers, 84, pp.1033-1038.

[11] Fengel, D., Wegener, G., 1989. ***Wood: chemistry, ultrastructure, reactions.*** Walther de Gruyter.

[12] Plomion, C., Leprovost, G., Stokes, A., 2001. ***Wood Formation in Trees.*** Plant Physiology, 127, pp.1514-1523.

[13] Neagu, R. C., Gamstedt, E. K., Bardage, S. L., Lindström, M., 2006. ***Ultrastructural features affecting mechanical properties of wood fibres.*** Wood Material Science and Engineering, 2006, 1, pp.146-170.

[14] Gharehkhani, S., Sadeghinezhad, E., Kazi, S. N., Yarmand, H., Badarudin, A., Safaei, M. R., Zubir, M. N. M., 2015. ***Basic effects of pulp refining on fiber properties - A review.*** Carbohydrate Polymers, 115, pp.785-803.

[15] Hubbe, M., Venditti, R., Rojas, O. J., 2007. ***What Happens to Cellulosic Fibers During Papermaking and Recycling? A Review.*** BioResources, 2(4), pp.739-788.

[16] Kang, T., Paulapuro, H., 2006***. Recycle Potential of Externally Fibrillated Chemical Pulp.*** Progress in Paper Recycling, 15(2), pp.11-17.

[17] Siró, I., Plackett, D., 2010. ***Microfibrillated cellulose and new nanocomposite materials: a review.*** Cellulose, 17, pp.459-494.

[18] Poletto, M., Orgaghi, H. L. Jr., 2015. ***Cellulose: Fundamental Aspects and Current Trends.*** InTech Open.

[19] Taniguchi, T., Okamura, K., 1998. ***New films produced from microfibrillated natural fibres.*** Polymer International, 47, pp.291-294.

[20] Zimmermann, T., Pöhler, E., Geiger, T., 2004. ***Cellulose Fibrils for Polymer Reinforcement.*** Advanced Engineering Materials, 6(9), pp.754-761.

[21] Jonoobi, M., Oladi, R., Davoudpour, Y., Oksman, K., Dufresne, A., Hamzeh, Y., Davoodi, R., 2015. ***Different preparation methods and properties of nanostructures cellulose from various natural resources and residues: a review.*** Cellulose, 22(2), pp.935-969.

[22] Henriksson, M., Henriksson, G., Berglund, L. A., Lindström, T., 2007. ***An environmentally friendly method for enzyme-assisted preparation of microfibrillated cellulose (MFC) nanofibers.*** European Polymer Journal, 43, pp.3434-3441.

[23] Yoo, S., Hsieh, J. S., 2010. ***Enzyme-assisted preparation of fibrillated cellulose fibers and its effect on physical and mechanical properties of paper sheet composites.*** Industrial and Engineering Chemical Research, 49(5), pp.2161-2168.

[24] Pääkkö, M., Ankerfors, M. Kosonen, H., Nykänen, A., Ahola, S., Österberg, M., Ruokolainen, J., Laine, J., Larsson, P. T., Ikkala, O., Lindström, T., 2007. ***Enzymatic hydrolysis combined with mechanical shearing and high-pressure homogenization for nanoscale cellulose fibrils and strong gels.*** Biomacromolecules, 8(6), pp.1934-1941.

[25] Saito, T., Isogai, A., 2006. ***Introduction of aldehyde groups on surfaces of native cellulose fibers by TEMPO-mediated oxidation.*** Colloids and Surfaces A: Physicochemical and Engineering Aspects, 289, pp.219-225.

[26] Saito, T., Kimura, S., Nishiyama, Y., Isogai, A., 2007. ***Cellulose Nanofibers Prepared by TEMPO-Mediated Oxidation of Native Cellulose.*** Biomacromolecules, 8, pp.2485-2491.

[27] Wågberg, L, Decher, G., Norgren, M., Lindström T., Ankerfors, M., Axnäs, K., 2008. ***The build-up of polyelectrolyte multilayers of microfibrillated cellulose and cationic polyelectrolytes.*** Langmuir, 24(3), pp.784-795.

[28] Alila. S., Besbes, I., Vilar, M. R., Mutjé, P., Boufi, S., 2013. ***Non-woody plants as raw materials for production of microfibrillated cellulose (MFC): a comparative study.*** Industrial Crops and Products, 41, pp.250-259.

[29] Chaker, A., Alila, S., Mutje, P., Vilar, M. R., Boufi, S., 2013. ***Key role of the hemicellulose content and the cell morphology on the nanofibrillation effectiveness of cellulose pulps.*** Cellulose, 2013, 20, pp.2863-2875.

[30] Desmaisons, J., Boutonnet, E., Rueff, M., Dufresne, A., Bras, J., 2017. ***A new quality index for benchmarking of different cellulose nanofibrils.*** Carbohydrate Polymers, 174, pp.318-329.

[31] Page, D. H., 1969. ***A theory for the tensile strength of paper.*** Tappi Journal., 52(4), pp.674-681.

[32] Lindström T., Fellers, C., Ankerfors, M., Nordmark, G. G., 2016. ***On the nature of joint strength of paper – effect of dry strength agents – Revisiting the Page equation.*** Nordic Pulp & Paper Research Journal, 31(3), pp.459-468.

[33] Courchene, C. E., Peter, G. F., Litvay, J., 2006. ***Cellulose microfibril angle as a determinant of paper strength and hygroexpansivity in Pinus Taeda L.*** Wood and Fiber Science, 38(1), pp.112-120.

[34] El-Hosseiny, F., Page, D. H., 1975. ***The mechanical properties of single wood pulp fibres: Theories of strength.*** Fibre Science and Technology, 8(1), pp.21-31.

[35] Zeng, X., Retulainen, E., Heinemann, S., Fu, S., 2012. ***Fibre deformations induced by different mechanical treatments and their effect on zero-span strength.*** Nordic Pulp and Paper Research Journal, 27(2), pp.335-342.

[36] Joutsimo, O., Wathén, R., Tamminenm T., 2005. ***Effects of fiber deformations on pulp sheet properties and fiber strength.*** Paperi Ja Puu/Paper and Timber, 87(6).

[37] Nevell, T. P., Nugawela, D., 1987. ***Effect of Treatment with Very Dilute Acids on the Wet Tensile Srength and Chemical Properties of Paper.*** Carbohydrate Polymers, 7, pp.169-181.

[38] Wathén, R., 2006. ***Studies on fiber strength and its effect on paper properties.*** PhD Thesis, Department of Forest Products Technology, Helsinki University of Technology, Finland.

[39] Ebringerová, A., 2006. ***Structural Diversity and Application Potential of Hemicelluloses.*** Macromolecular Symposia, 232, pp.1-12.

[40] Liitiä, T., Maunu, S. L., Hortling, B., Tamminen, T., Pekkala, O., Varhimo, A., 2003. ***Cellulose crystallinity and ordering of hemicelluloses in pine and birch pulps as revealed by solid-state NMR spectroscopic methods.*** Cellulose, 10, pp.307-316.

[41] Uetani, K., Yano, H., 2012. ***Zeta Potential Time Dependence Reveals the Swelling Dynamics of Wood Cellulose Nanofibrils.*** Langmuir, 28, pp.818-827.

[42] Hult, E. -L., Larsson, P. T., Iversen T., 2001. ***Cellulose fibril aggregation – an inherent property of kraft pulps.*** Polymer, 42, pp.3309-3314.

[43] Virtanen, T., Maunu, S. L., Tamminen, T., Hortling, B., Liitiä, T., 2008. ***Changes in fiber ultrastructure during various kraft pulping conditions evaluated by 13C CPMAS NMR spectroscopy.*** Carbohydrate Polymers, 73, pp.156-163.

[44] Duchesne, I., Hult, E. L., Molin, U., Daniel, G., Iversen, T., Lennholm, H., 2001. ***The influence of hemicellulose on fibril aggregation of kraft pulp fibres as revealed by FE-SEM and CP/MAS 13C-NMR.*** Cellulose, 8, pp.103-111.

[45] Bolam, F. M., 1965. ***Stuff Preparation for Paper and Paperboard Making: Monographs on paperboard and papermaking.*** Pergamon.

[46] Iwamoto, S., Abe, K., Yano, H., 2008. ***The Effect of Hemicelluloses on Wood Pulp Nanofibrillation and Nanofiber Network Characteristics.*** Biomacromolecules, 9, pp.1022-1026.

[47] Rahman, S., Petroudy, D., Ghasemian, A., Resalati, H., Syverud, K., Chinga-Carrasco, G., 2015. ***The effect of xylan on the fibrillation efficiency of DED bleached soda bagasse pulp and on nanopaper characteristics.*** Cellulose, 22, pp.385-395.

[48] Spence, K. L., Venditti, R. A., Habibi, Y., Rojas, O. J., Pawlak, J. J., 2010. ***The effect of chemical composition on microfibrillar cellulose films from wood pulps: Mechanical processing and physical properties.*** Bioresource Technology, 101, pp.5961-5968.

[49] Arola, S., Malha, J. M., Laaksonen, P., Lille, M., Linder, M. B., 2013. ***The role of hemicellulose in nanofibrillated cellulose networks.*** Soft Matter, 9, pp.1319-1326.

[50] Meyer, V., Lecourt, M., Tapin-Lingua, S., Petit-Conil, M., 2018. ***Production of Microfibrillated Cellulose (MFC) from Chemical and Mechanical Pulps to Enhance TMP and DIP Paper Properties.*** Cellulose, 72(3), pp.6-16.

[51] Lahtinen, P., Liukkonen, S., Pere, J., Sneck, A., Kangas, H., 2014. ***A Comparative Study of Fibrillated Fibers from Different Mechanical and Chemical Pulps.*** BioResources, 9(2), pp.2115-2127.

[52] Taylor, L., Skuse, D., Blackburn, S., Greenwood, R., 2020. ***Stirred media mills in the mining industry: Material grindability, energy-size relationships, and operating conditions.*** Powder Technology, 369, pp.1-16.

[53] Yokoyama, T., Inoue, Y., 2007. ***Chapter 10 Selection of Fine Grinding Mills.*** In: A. D. Salman, M. Ghadiri, M. J. Hounslow, (eds.), ***Handbook of Powder Technology*** (Volume 12). Elsevier Science B.V.

[54] Theuerkauf, J., Schwedes, J., 1999. ***Theoretical and experimental investigation on particle and fluid motion in stirred media mills.*** Powder Technology, 105, pp.406-412.

[55] Theuerkauf, J., Schwedes, J., 2000. ***Review - Investigation of Motion in Stirred Media Mills.*** Chemical Engineering & Technology, 23(3), pp. 203-209.

[56] Blecher, L., Kwade, A., Schwedes, J., 1996. ***Motion and stress intensity of grinding beads in a stirred media mill. Part 1: Energy distribution and motion of single grinding beads.*** Powder Technology, 86, pp.59-68.

[57] Hogg, R., 1999. ***Breakage Mechanisms and Mill Performance in Ultrafine Grinding.*** Powder Technology, 105, pp.135-140.

[58] Strobel, A., Romeis, S., Wittpahl, J., Herre, P., Schmidt, J., Peukert, W., 2017. ***Characterization of stressing conditions in mills – A comprehensive research strategy based on well-characterized model particles.*** Particle Technology, 305, pp.652-661.

[59] Kwade, A., 1999. ***Determination of the most important grinding mechanism in stirred media mills by calculating stress intensity and stress number.*** Powder Technology, 105, pp.382-388.

[60] Beinert, S., Fragnière, G., Schilde, C., Kwade, A., 2015. ***Analysis and modelling of bead contacts in wet-operated stirred media mills and planetary ball mills with CFD-DEM simulations.*** Chemical Engineering Science, 134, pp.648-662.

[61] Weit, H., Schwedes, J., 1987. ***Scale up and power consumption in agitated ball mills.*** Chemical Engineering & Technology, 10(1), pp.398-404.

[62] Kwade, A., Blecher, L., Schwedes, J., 1996. ***Motion and stress intensity of grinding beads in a stirred media mill. Part 2: Stress intensity and its effect on comminution.*** Powder Technology, 86, pp.69-76.

[63] Kwade, A., Schwedes, J., 2002. ***Breaking characteristics of different materials and their effect on stress intensity and stress number in stirred media mills.*** Powder Technology, 122, pp.109-121.

[64] Kwade, A., 2003. ***A Stressing Model for the Description and Optimization of Grinding Processes.*** Chemical Engineering & Technology, 26(2), pp.199-205.

[65] Becker, M., Kwade, A., Schwedes, J., 2001. ***Stress intensity in stirred media mills and its effect on specific energy requirement.*** International Journal of Mineral Processing, 61, pp.189-208.

[66] Breitung-Faes, S., Kwade, A., 2009. ***Produktgestaltung bei der Nanozerkleinerung durch Einsatz kleinster Mahlkörper.*** Chemie Ingenieur Technik, 81(6), pp.767-774.

[67] Knieke, C., Steinborn, C., Romeis, S., Peukert, W., Breitung-Faes, S., Kwade, A., 2010. ***Nanoparticle Production with Stirred Media Mills: Opportunities and Limits.*** Chemical Engineering & Technology, 33(9), pp.1401-1411.

[68] Strobel, A., Schwenger, J., Wittpahl, J., Schmidt, J., Romeis, S., Peukert, W., 2018. ***Assessing the influence of viscosity and milling bead size on the stressing conditions in a stirred media mill by single particle probes.*** Chemical Engineering Research and Design, 136, pp.859-869.

[69] Stender, H. H., Kwade, A., Schwedes, J., 2004. ***Stress energy distribution in different stirred media mill geometries.*** International Journal of Mineral Processing, 74S, pp.S103-S117.

[70] Walker, W. H., Lewis, W. K., McAdams, W. H., Gilliland, E. R., 1937. ***Principles of Chemical Engineering.*** McGraw-Hill, New York, United States.

[71] von Rittinger, P. R., 1867. ***Lehrbuch der Aufbereitung-Kunde in ihrer neuesten Entwickelung und Ausbildung systematisch dargestellt.*** Ernst and Korn, Berlin, Germany.

[72] Bond, F. C., 1952. ***The Third Theory of Comminution.*** Transactions on AIME Mining Engineering, 193, pp.484-494.

[73] Riley, M., 2015. ***FiberLean: Production, applications and impacts.*** EngD Thesis, Department of Chemical Engineering, University of Birmingham, United Kingdom.

[74] Rowland, C. A., 1978. ***Determination and use of operating work indices in controlled grinding circuits – a proposed concept.*** Mill Operator's Conference and Exhibit, Australasian Institution of Mining and Metallurgy.

[75] Mucsi, G., 2013. ***Grindability of Quartz in Stirred Media Mill.*** Particulate Science and Technology, 31, pp.399-406.

[76] Motsi, T., Skuse, D. R., Alary, J. A., Borger, A., Rowson, N., Skuse, T. R., 2017. ***Grinding Method and Grinding Medium.*** United States Patent Application Publication, Pub. No. US 2017/0145635 A1.

[77] Durant, B., Farber, B., Rule, C., Mainza, A., 2012. ***Ceramic Media Selection for Optimization of Energy Efficiency in IsaMills.*** Chemical Engineering & Technology, 35(11), pp.1949-1953.

[78] Farber, B. Y., Knopjes, L., Bedesi, N., 2009. ***Advances in ceramic media for high energy milling applications.*** Minerals Engineering, 22, pp.704-709.

[79] Becker, M., Schwedes, J., 1999. ***Comminution of ceramics in stirred media mills and wear of grinding beads.*** Powder Technology, 105, pp.374-381.

[80] Tamblyn, R. J., 2009. ***Analysis of Energy Requirements in Stirred Media Mills.*** EngD Thesis, Department of Chemical Engineering, University of Birmingham, United Kingdom.

[81] Skuse, T., 2015. ***The use of Positron Emission Particle Tracking (PEPT) to Determine the Grinding Mechanisms within a Vertically Stirred Media Mill.*** PhD Thesis, Department of Chemical Engineering, University of Birmingham, United Kingdom.

[82] Bjoerkqvist, T., Gustafsson, H., Gustafsson, S., Koskinen, T., Nuopponen, M., Vehniaeinen, A., Upm-Kymmene Corporation, 2015. ***Method and an Apparatus for Producing Nanocellulose.*** United States Patent, Patent No. US 8945346 B2.

[83] Bjoerkqvist, T., Gustafsson, H., Koskinen, T., Nuopponen, M., Vehniaeinen, A., Fredrikson, A., Gustafsson, S., Upm-Kymmene Corporation, 2015. ***Method and an Apparatus for Fibrillation of Cellulose Containing Materials.*** United States Patent Application Publication, Pub. No. US 2015/0057442 A1.

[84] Pinkney, S. Z. R., 2015. ***Formulation of Microfibrillated Cellulose in Vertically Stirred Media Mills.*** EngD Thesis, Department of Chemical Engineering, University of Birmingham, United Kingdom.

[85] Johnson, K. L., 1985. **Contact Mechanics**. Cambridge University Press.

[86] Jones, D. R. H., Ashby, M. F., 2019. ***Chapter 3 - Elastic Moduli.*** In: Jones, D. R. H., Ashby, M. F., 2019. ***Engineering Materials 1 - An Introduction to Properties, Applications, and Design*** (5th Edition). Butterworth-Heinemann.

[87] Advanced Optics Inc., 2020. ***Soda Lime Glass Technical Data Sheet*** [online]. Available at: https://advancedoptics.com/SodaLimeGlassTechnicalDataSheet.pdf (accessed 30/06/2020).

[88] Superior Technical Ceramics, 2015. ***Zirconia Ceramic Materials.*** [online] Available at: https://www.ceramics.net/sites/default/files/stc-zirconia_brochure_final.pdf (accessed 16/01/2020).

[89] Ferro Ceramic Grinding Inc., 2012. ***Ceramic Property Tables – Mullite.*** [online] Available at: http://www.ferroceramic.com/mullite_table.htm (accessed 16/01/2020).

[90] Imerys Carbonates, 2009. ***Intracarb^{TM} 60L*** [Technical Data Sheet].

[91] Technical Association of the Pulp and Paper Industry, 2006. ***Tensile properties of paper and paperboard (using constant rate of elongation apparatus).*** Test Method T 494 om-01.

[92] Technical Association of the Pulp and Paper Industry, 2007. ***Zero-span breaking strength of pulp (dry zero-span tensile)***. Test Method T 231 cm-07.

[93] Technical Association of the Pulp and Paper Industry, 2012. ***Forming Handsheets for Physical Tests of Pulp***. Test Method T 205 cm-12.

[94] Scandinavian Pulp, Paper and Board Testing Committee, 2009. ***Carbohydrate Composition.*** Test Method SCAN CM-71:09.

[95] K. S. Prado, M. A. S. Spinacé, 2015. ***Characterization of Fibers from Pineapple's Crown, Rice Husks and Cotton Textile Residues.*** Materials Research, 18(3), pp.530-537.

[96] Technical Association of the Pulp and Paper Industry, 1988. ***Acid-Insoluble Lignin in Wood and Pulp.*** Test Method T 222 om-88.

[97] Alén, R., Hartus, T., 1988. ***UV Spectrophotometric Determination of Lignin from Alkaline Pulping Liquors.*** Cellulose Chemistry and Technology, 22, pp.613-618.

[98] Padberg, J., Bauer, W., Gliese, T., 2016. ***The influence of fibrillation on the oxygen barrier properties of films from microfibrillated cellulose.*** Biorefinery, Nordic Pulp & Paper Research Journal, 31(4), 548-560.

[99] Sajaniemi, V., 2018. ***Proof of Concept for Manufacturing Microfibrillated Cellulose.*** Master's Thesis, School of Chemical Engineering, Aalto University, Finland.

[100] Whitehouse, D. J., 2004. **Surfaces and their Measurement.** Elsevier.

[101] Czibula, C., Ganser, C., Seidlhofer, T., Teichert, C., Hirn, U., 2019. ***Transverse viscoelastic properties of pulp fibers investigated with an atomic force microscopy method.*** Journal of Materials Science, 54, pp.11448-11461.

[102] Cabrera, R. Q., Meersman, F., McMillan, P. F., Dmitriev, V., 2011. ***Nanomechanical and Structural Properties of Native Cellulose under Compressive Stress.*** Biomacromolecules, 12(6), pp.2178-2183.

[103] Nakamura, K., Wada, M., Kuga, S., Okano, T., 2003. ***Poisson's Ratio of Cellulose Iβ and Cellulose II.*** Journal of Polymer Science Part B: Polymer Physics, 42, pp.1206-1211.

[104] Fontana, A. J., 2008. ***Appendix B: Water Activity of Unsaturated Salt Solutions at 20°C.*** In: Fontana, A. J., 2009. ***Water Activity in Foods.*** Blackwell Publishing Ltd.

[105] Baudet, G., Perrotel, V., Seron, A., Stellatelli, M., 1999. ***Two dimensions comminution of kaolinite clay particles.*** Powder Technology, 105, pp.125-134.

[106] Knieke, C., Berger, A., Voigt, M., Taylor, R. N. K., Röhrl, J., Peukert, W., 2010. ***Scalable production of graphene sheets by mechanical delamination.*** Carbon, 48, pp.3196-3204.

[107] Damm, C., Körner, J., Peukert, W., 2013. ***Delamination of hexagonal boron nitride in a stirred media mill.*** Journal of Nanoparticle Research, 15, 1561.

[108] Taylor, L., Phipps, J., Blackburn, S., Greenwood, R., Skuse, D., 2020. ***Using fibre property measurements to predict the tensile index of microfibrillated cellulose nanopaper.*** Cellulose, 27, pp.6149-6162.

[109] Horn, R. A., 1974. ***Morphology of pulp fiber from softwoods and influence on paper strength.*** Research Paper FPL 242, Forest Product Laboratory, Forest Service, United States Department of Agriculture.

[110] Horn, R. A., 1978. ***Morphology of pulp fiber from hardwoods and influence on paper strength.*** Research Paper FPL 312, Forest Product Laboratory, Forest Service, United States Department of Agriculture.

[111] Derakhshandeh, B., Hatzikiriakos, S. G., Bennington, C. P. J., 2010. ***Rheology of pulp suspensions using ultrasonic Doppler velocimetry.*** Rheologica Acta, 49, pp.1127-1140.

[112] Kerekes, R. J., Schell, C. J., 1992. ***Characterization of Fibre Flocculation Regimes by a Crowding Factor.*** Journal of Pulp and Paper Science, 18(1) J32-38.

[113] Thygesen, A., Oddershede, J., Lilholt, H., Thomsen, A. B., Ståhl, K., 2005. ***On the determination of crystallinity and cellulose content in plant fibres.*** Cellulose, 12, pp.563-576.

[114] Beazley, K. M., Petereit, H., 1975. ***Die Einflüsse von China Clay und Calciumcarbonate auf die Papiereigenschaften.*** Wochenblatt für Papierfabrikation, 4, pp.143-147.

APPENDIX A1 – MATLAB SCRIPT FOR ANALYSING MEDIA SURFACE ROUGHNESS

```
% Script for calculating surface roughness of LaserScape
(laser profilometer) input data for the
% purposes of measuring grinding media surface roughness
% Lewis Taylor 29th March 2019
clear, clc, close all

% Replace this example file with the input file
A = importdata('SampleData.txt');
SampleName = 'Sample 1'
DataTitle = 'Sample_1_RoughnessB2_512micronT';
B = A.data(:,:);
lengthB = length(B);

% Limit data to 512 µm by 512 µm square in centre to avoid
noise at edges
Bselect = B(129:384,129:384);
lengthBselect = length(Bselect);
Xax = B(1,2:lengthBselect+1);
Yax = B(1,2:lengthBselect+1);
Z = Bselect;
lengthZ = length(Z);

% Plot raw surface map
figure; surf(Xax,Yax,Z), axis equal, shading interp, xlabel('x
(µm)'),ylabel('y (µm)'),zlabel('z (µm)'), title(['Raw surface
map of ',num2str(SampleName)]), savefig([num2str(DataTitle),'
Figure 1']), saveas(1,[num2str(DataTitle),' Figure 1'],'png');

%This is an equation to find the location of zero points
zci = @(v) find(v(:).*circshift(v(:), [-1 0]) <= 0);

 % pre-assign matrices used in the 'for' loop
FitZ = zeros(lengthZ,lengthZ);
 PFZ = zeros(lengthZ,7);
 PFZ_1 = zeros(1,lengthZ);
 PFZ_2 = zeros(1,lengthZ);
 PFZ_3 = zeros(1,lengthZ);
 PFZ_4 = zeros(1,lengthZ);
 PFZ_5 = zeros(1,lengthZ);
 PFZ_6 = zeros(1,lengthZ);
 PFZ_7 = zeros(1,lengthZ);
 Diff_Z = zeros(lengthZ,lengthZ);
 Abs_Diff_Z = zeros(lengthZ,lengthZ);
 R_a = zeros(1,lengthZ);
 R_q = zeros(1,lengthZ);
```

```
 Rv = zeros(1,lengthZ);
 Rp = zeros(1,lengthZ);
 Sorted_Diff_Z = zeros(lengthZ,lengthZ);
 Diff_Z_d1 = zeros(lengthZ,lengthZ-1);
 Rda = zeros(1,lengthZ-1);
 Rdq = zeros(1,lengthZ-1);
 ws = warning('off','all');
%'For' loop which, for each y-directional cross-section, fits
a polynomial curve to the roughness profile, and then
subtracts this from the roughness profile, in order to account
for the surface curvature.

% Set Tolerance for determining outliers (in stdevs)
 Tol = 1;

for n = 1:lengthZ
% make the 6th order polynomial fit for each profile
currentZ = Z(n,:);
f = fittype('poly6');
fit1 = fit(Xax',Z(n,:)',f);
fdata1(n,:) = feval(fit1,Xax);
Diff_Z_1(n,:) = Z(n,:) - fdata1(n,:);
I(n,:) = abs(fdata1(n,:) - Z(n,:)) > Tol*std(Diff_Z_1(n,:));
outliers1(n,:) = excludedata(Xax,Z(n,:),'indices',I(n,:));
fit2 = fit(Xax',Z(n,:)',f,...
           'Exclude',outliers1(n,:));
fdata2(n,:) = feval(fit2,Xax);
fdata_diff(n,:) = fdata1(n,:)-fdata2(n,:);

% subtract fit from data
Diff_Z(n,:) = Z(n,:)-fdata2(n,:);
% calculate absolute difference
Abs_Diff_Z(n,:) = abs(Diff_Z(n,:));
% calculate R_a roughness parameter, by determining the mean
of the
% absolute difference
R_a(n) = mean(Abs_Diff_Z(n,:));

% Calculate R_q,
R_q(n) = (mean((Diff_Z(n,:)).^2)).^0.5;

% Rda is the absolute average slope of the profile. Rdq is the
RMS average
% slope of the profile
% calculate first derivative of Diff_Z
Diff_Z_d1(n,:) = diff(Diff_Z(n,:));
Rda(n) = mean(abs(Diff_Z_d1(n,:)));
Rdq(n) = (mean((Diff_Z_d1(n,:)).^2)).^0.5;

% Calculate skewness Rsk and kurtosis Rku
Rsk(n) = (1/(R_q(n).^3)).*(mean((Diff_Z(n,:)).^3));
```

```
Rku(n) = (1/(R_q(n).^4)).*(mean((Diff_Z(n,:)).^4));

end
% separated the 'for' loops into two because the second one
requires
% different sized cells for each iteration of n.
for n = 1:length(Z)
ZCDZ{n,:} = zci(Diff_Z(n,:));
LengthZC(n) = length(ZCDZ{n,:});

%temporary variable b to extract data from cell array
b = ZCDZ{n,:};
% Define temporary Diff_Z(n)to use in for loop
Diff_Z_T = Diff_Z(n,:);
% Set initial values for 'for' loop
Diff_Z_T_1 = Diff_Z_T(1);
Grad_Z_T(1) = Diff_Z_T(b(1));
int{1} = 1:b(1);
[MaxDiff_Z_T_1 maxinZC_T_1] = max(Diff_Z_T(int{1}));
[MinDiff_Z_T_1 mininZC_T_1] = min(Diff_Z_T(int{1}));
PseudoXaxmax_T_1 = maxinZC_T_1;
PseudoXaxmin_T_1 = mininZC_T_1;

% Storing initial conditions for error checking
Grad_Z_1(n) = Grad_Z_T(1);
Diff_Z_1(n) = Diff_Z_T_1;
int_1{n} = int{1};
MaxDiff_Z_T(1) = MaxDiff_Z_T_1;
maxinZC_T(1)=maxinZC_T_1;
mininZC_T(1) = mininZC_T_1;
PseudoXaxmax_T(1) = PseudoXaxmax_T_1;
PseudoXaxmin_T(1) = PseudoXaxmin_T_1;

for i = 2:1:LengthZC(n)-1
    int{i} = (b(i-1)+1:b(i));
    [MaxDiff_Z_T(i) maxinZC_T(i)] = max(Diff_Z_T(int{i}));
    PseudoXaxmax_T(i) = maxinZC_T(i)+b(i-1);
    [MinDiff_Z_T(i) mininZC_T(i)] = min(Diff_Z_T(int{i}));
    PseudoXaxmin_T(i) = mininZC_T(i)+b(i-1);
end
% Storing the results of the 'i' loop for each iteration of
the 'n' loop
intn{n} = int;
MaxDiff_Z{n} = MaxDiff_Z_T;
maxinZC{n} = maxinZC_T;
PseudoXaxmax{n} = PseudoXaxmax_T;
MinDiff_Z{n}=MinDiff_Z_T;
mininZC{n}=mininZC_T;
PseudoXaxmin{n}= PseudoXaxmin_T;

% Now identifying the true peaks from the 'i' loop for each n
```

```
% Required temporary variable c to unpack the data
cmax = MaxDiff_Z{n};
cmin = MinDiff_Z{n};
cXmax = PseudoXaxmax{n};
cXmin = PseudoXaxmin{n};
Positive_Max_Diff_Z_T = cmax(cmax>=0);
PositivePseudoXaxmax_T = cXmax(cmax>=0);
Negative_Min_Diff_Z_T = cmin(cmin<=0);
NegativePseudoXaxmin_T = cXmin(cmin<=0);

% Calculating Rp and Rv
Max_Positive_Max_Diff_Z_T = max(Positive_Max_Diff_Z_T);
Min_Negative_Min_Diff_Z_T = min(Negative_Min_Diff_Z_T);
Rp(n) = Max_Positive_Max_Diff_Z_T;
Rv(n) = Min_Negative_Min_Diff_Z_T;

% Storing temporary data
Positive_Max_Diff_Z{n} = Positive_Max_Diff_Z_T;
PositivePseudoXaxmax{n} = PositivePseudoXaxmax_T;
Negative_Min_Diff_Z{n} = Negative_Min_Diff_Z_T;
NegativePseudoXaxmin{n} = NegativePseudoXaxmin_T;

% Calculating Rz_JIS requires max and min 5 peaks and valleys
from each y-directional profile.
% For particularly smooth media with large defects, there
sometimes are not even five peaks on a single profile. To
accommodate for these cases, the matrices are pre-filled with
zeros.
SortedpeaksT = zeros(1,5);
SortedvalleysT = zeros(1,5);
SortedpeaksA = sort(Positive_Max_Diff_Z{n},'descend');
SortedvalleysA = sort(Negative_Min_Diff_Z{n},'ascend');
SortedpeaksTA = [SortedpeaksA SortedpeaksT];
SortedvalleysTA = [SortedvalleysA SortedvalleysT];
Sortedpeaks{n} = SortedpeaksTA;
Sortedvalleys{n} = SortedvalleysTA;
max5{n} = Sortedpeaks{n}(1:5);
min5{n} = Sortedvalleys{n}(1:5);

%Convert from placement number to actual size (x2 to get µm)
Xax_max_T = 2*PositivePseudoXaxmax{n};
Xax_min_T = 2*NegativePseudoXaxmin{n};
Xax_max{n} = Xax_max_T;
Xax_min{n} = Xax_min_T;
% Determine spacing by combining matrix x values and sorting
Xax_tot_unsort_T = [Xax_min_T Xax_max_T];
Xax_tot_prel_T = sort(Xax_tot_unsort_T,'ascend');
Xax_tot_prel{n} = Xax_tot_prel_T;

% Spacing between profile peaks
Xax_max_forsubtprel_T = Xax_max_T(1:(length(Xax_max_T)-1));
```

```
Xax_max_forsubtprel{n} = Xax_max_forsubtprel_T;
Xax_max_forsubt_T = [0 Xax_max_forsubtprel_T];
Xax_spac_T = Xax_max_T - Xax_max_forsubt_T;
Xax_spac{n} = Xax_spac_T;
Spac_Average(n) = mean(Xax_spac_T);
Spac_Median(n) = median(Xax_spac_T);
Spac_Stddev(n) = std(Xax_spac_T);

% The temporary variables are recycled, but if the length of
the previous
% iteration of n is bigger, then those larger values are not
overwritten.
% Therefore, it is necessary to clear all temporary variables
here:
clear b Diff_Z_T int{1} MaxDiff_Z_T maxinZC_T PseudoXaxmax_T
MinDiff_Z_T mininZC_T PseudoXaxmin_T;
clear cmax cmin cXmax cXmin Positive_Max_Diff_Z_T
PositivePseudoXaxmax_T Negative_Min_Diff_Z_T
NegativePseudoXaxmin_T
clear Max_Positive_Max_Diff_Z_T Min_Negative_Min_Diff_Z_T
Xax_max_T Xax_min_T Xax_tot_unsort_T Xax_tot_prel_T
clear Xax_max_forsubtprel_T Xax_max_forsubt_T Xax_spac_T
end

% Total difference from outliers:
SumOutliersprel = sum(abs(fdata_diff));
SumOutliers = sum(SumOutliersprel);
%PLOTTING SURFACE
% Plots a map of the surface with the curvature extracted.
This is to
% scale, with the whole map, so the roughness appears small,
figure;surf(Xax,Yax,Diff_Z), axis equal, shading interp,
xlabel('x (µm)'),ylabel('y (µm)'),zlabel('z
(µm'),title(['Surface map of ' num2str(SampleName),' with
subtracted curvature']), savefig([num2str(DataTitle),' Figure
2']), saveas(2,[num2str(DataTitle),' Figure 2'],'png');

% To zoom in for a real-scale image of five different 100 x
100 areas, to
% check that they are consistent
figure;surf(Xax,Yax,Diff_Z),xlim([0 100]), ylim([0 100]),
zlim([-50 50]), shading interp, xlabel('x (µm)'),ylabel('y
(µm)'),zlabel('z (µm)'),title(['Surface map of
',num2str(SampleName),' zoomed in at [0 100; 0 100]']),
savefig([num2str(DataTitle),' Figure 3']),
saveas(3,[num2str(DataTitle),' Figure 3'],'png');
figure;surf(Xax,Yax,Diff_Z),xlim([100 200]), ylim([100 200]),
zlim([-50 50]), shading interp, xlabel('x (µm)'),ylabel('y
(µm)'),zlabel('z (µm)'),title(['Surface map of
',num2str(SampleName),' zoomed in at [100 200; 100 200]']),
```

```
savefig([num2str(DataTitle),' Figure 4']),
saveas(4,[num2str(DataTitle),' Figure 4'],'png');
figure;surf(Xax,Yax,Diff_Z),xlim([200 300]), ylim([200 300]),
zlim([-50 50]), shading interp, xlabel('x (µm)'),ylabel('y
(µm)'),zlabel('z (µm)'),title(['Surface map of
',num2str(SampleName),' zoomed in at [200 300; 200 300]']),
savefig([num2str(DataTitle),' Figure 5']),
saveas(5,[num2str(DataTitle),' Figure 5'],'png');
figure;surf(Xax,Yax,Diff_Z),xlim([300 400]), ylim([300 400]),
zlim([-50 50]), shading interp, xlabel('x (µm)'),ylabel('y
(µm)'),zlabel('z (µm)'),title(['Surface map of
',num2str(SampleName),' zoomed in at [300 400; 300 400]']),
savefig([num2str(DataTitle),' Figure 6']),
saveas(6,[num2str(DataTitle),' Figure 6'],'png');
figure;surf(Xax,Yax,Diff_Z),xlim([400 500]), ylim([400 500]),
zlim([-50 50]), shading interp, xlabel('x (µm)'),ylabel('y
(µm)'),zlabel('z (µm)'),title(['Surface map of
',num2str(SampleName),' zoomed in at [400 500; 400 500]']),
savefig([num2str(DataTitle),' Figure 7']),
saveas(7,[num2str(DataTitle),' Figure 7'],'png');

% R_a and R_q
%%%%%%%%%%%%%%%%%%%%%%%%%%%%%%%%%%%%%%%%%%%%%%%%%%%%%%%%%%%%%%%%%%%%
%%%%
% Determining the R_a average across all roughness profiles
R_a_ave = mean(R_a);
R_a_std = std(R_a);
R_a_med = median(R_a);
disp(['The mean R_a value over the whole surface is
',num2str(round(R_a_ave,3)),' µm ','with a standard deviation
of ',num2str(round(R_a_std,3)),' µm'])
disp(['The median R_a value over the whole surface is
',num2str(round(R_a_med,3)),' µm '])

% Plotting the variation of R_a in the x direction, in order
to determine
% if any optical effects due to the sphericity of the media or
angle of
% sputter coating etc. have influenced anything.
PFITR_a = polyfit(Xax,R_a,4);
PFITR_a_1 = PFITR_a(1);
PFITR_a_2 = PFITR_a(2);
PFITR_a_3 = PFITR_a(3);
PFITR_a_4 = PFITR_a(4);
PFITR_a_5 = PFITR_a(5);
FitR_a =
PFITR_a_1*Xax.^4+PFITR_a_2*Xax.^3+PFITR_a_3*Xax.^2+PFITR_a_4*X
ax+PFITR_a_5;

% Finding a minimum in the fit curve, which should preclude
any strange
```

```
% edge effects from interfering with the average. Hopefully
the 4th order
% polynomial fit is sufficiently coarse to not mask any real
deviations
% in R_a across the x axis. If there are no strange effects
due to the
% edges, then R_a_min will roughly = R_a_ave. In any case,
having both
% numbers in order to make a sensible judgement about whether
there are any
% artefacts is a good idea.
R_a_min = min(FitR_a);
Xax_at_R_a_min = Xax(FitR_a==R_a_min);
NormalisedXax_at_R_a_min= Xax_at_R_a_min/max(Xax);
disp(['The fit of R_a values in the x direction reaches a
minimum of ',num2str(round(R_a_min,3)),' µm ','at
',num2str(round(100*NormalisedXax_at_R_a_min,2)),'% of the way
along the x axis'])
disp('_')

% Determining the R_q average across all roughness profiles
R_q_ave = mean(R_q);
R_q_std = std(R_q);
R_q_med = median(R_q);
disp(['The mean R_q value over the whole surface is
',num2str(round(R_q_ave,3)),' µm ','with a standard deviation
of ',num2str(round(R_q_std,3)),' µm'])
disp(['The median R_q value over the whole surface is
',num2str(round(R_q_med,3)),' µm '])

% Plotting the variation of R_q in the x direction
PFITR_q = polyfit(Xax,R_q,4);
PFITR_q_1 = PFITR_q(1);
PFITR_q_2 = PFITR_q(2);
PFITR_q_3 = PFITR_q(3);
PFITR_q_4 = PFITR_q(4);
PFITR_q_5 = PFITR_q(5);
FitR_q =
PFITR_q_1*Xax.^4+PFITR_q_2*Xax.^3+PFITR_q_3*Xax.^2+PFITR_q_4*X
ax+PFITR_q_5;
R_q_min = min(FitR_q);
Xax_at_R_q_min = Xax(FitR_q==R_q_min);
NormalisedXax_at_R_q_min= Xax_at_R_q_min/max(Xax);
disp(['The fit of R_q values in the x direction reaches a
minimum of ',num2str(round(R_q_min,3)),' µm ','at
',num2str(round(100*NormalisedXax_at_R_q_min,2)),'% of the way
along the x axis'])
disp('_')

figure;plot(Xax,R_a,Xax,R_q,Xax,FitR_a,Xax,FitR_q), xlabel('x
(µm)'),ylabel('R_a and R_q value of y-direction profile
```

```
(µm)'),legend('R_a','R_q','R_a 4th order poly fit','R_q 4th
order poly fit'),title(['Variation of R_a and R_q value in the
x direction for ',num2str(SampleName)]),
savefig([num2str(DataTitle),' Figure 8']),
saveas(8,[num2str(DataTitle),' Figure 8'],'png');

% Skew Rsk and Kurtosis
Rku%%%%%%%%%%%%%%%%%%%%%%%%%%%%%%%%%%%%%%%%%%%%%%%%%%%%%%%%

% Determining skew Rsk average across all roughness profiles
Rsk_ave = mean(Rsk);
Rsk_std = std(Rsk);
Rsk_med = median(Rsk);
disp(['The mean Rsk value over the whole surface is
',num2str(round(Rsk_ave,3)),' µm ','with a standard deviation
of ',num2str(round(Rsk_std,3)),' µm'])
disp(['The median Rsk value over the whole surface is
',num2str(round(Rsk_med,3)),' µm '])

% Plotting the variation of skew Rsk in the x direction
PFITRsk = polyfit(Xax,Rsk,4);
PFITRsk_1 = PFITRsk(1);
PFITRsk_2 = PFITRsk(2);
PFITRsk_3 = PFITRsk(3);
PFITRsk_4 = PFITRsk(4);
PFITRsk_5 = PFITRsk(5);
FitRsk =
PFITRsk_1*Xax.^4+PFITRsk_2*Xax.^3+PFITRsk_3*Xax.^2+PFITRsk_4*X
ax+PFITRsk_5;
Rsk_max = max(FitRsk);
Xax_at_Rsk_max = Xax(FitRsk==Rsk_max);
NormalisedXax_at_Rsk_max= Xax_at_Rsk_max/max(Xax);
disp(['The fit of Rsk values in the x direction reaches a
maximum of ',num2str(round(Rsk_max,3)),' µm ','at
',num2str(round(100*NormalisedXax_at_Rsk_max,2)),'% of the way
along the x axis'])
disp('_')

% Determining kurtosis Rku average across all roughness
profiles
Rku_ave = mean(Rku);
Rku_std = std(Rku);
Rku_med = median(Rku);
disp(['The mean Rku value over the whole surface is
',num2str(round(Rku_ave,3)),' µm ','with a standard deviation
of ',num2str(round(Rku_std,3)),' µm'])
disp(['The median Rku value over the whole surface is
',num2str(round(Rku_med,3)),' µm '])

% Plotting the variation of kurtosis Rku in the x direction
PFITRku = polyfit(Xax,Rku,4);
```

```
PFITRku_1 = PFITRku(1);
PFITRku_2 = PFITRku(2);
PFITRku_3 = PFITRku(3);
PFITRku_4 = PFITRku(4);
PFITRku_5 = PFITRku(5);
FitRku =
PFITRku_1*Xax.^4+PFITRku_2*Xax.^3+PFITRku_3*Xax.^2+PFITRku_4*X
ax+PFITRku_5;
Rku_min = min(FitRku);
Xax_at_Rku_min = Xax(FitRku==Rku_min);
NormalisedXax_at_Rku_min= Xax_at_Rku_min/max(Xax);
disp(['The fit of Rku values in the x direction reaches a
minimum of ',num2str(round(Rku_min,3)),' µm ','at
',num2str(round(100*NormalisedXax_at_Rku_min,2)),'% of the way
along the x axis'])
disp('_')

figure;plot(Xax,Rsk,Xax,Rku,Xax,FitRsk,Xax,FitRku), xlabel('x
(µm)'),ylabel('Skew R_s_k and Kurtosis R_k_u values of y-
direction profile (µm)'),legend('R_s_k','R_ku','R_s_k 4th
order poly fit','R_k_u 4th order poly fit'),title(['Variation
of R_s_k and R_k_u values in the x direction for
',num2str(SampleName)]),  savefig([num2str(DataTitle),' Figure
9']), saveas(9,[num2str(DataTitle),' Figure 9'],'png');

%Rv and
Rp%%%%%%%%%%%%%%%%%%%%%%%%%%%%%%%%%%%%%%%%%%%%%%%%%%%%%%%%%%%%
%%%%%%%%%%%%%%%%%%%%%%%%%%%%%%%%%%%%%%%%%%%%%%%%%%%%%%%%%%%%%%
%%%%%%%%%%%%%%%%%
%Plotting max peak Rp and min valley Rv
% Plotting the variation of Rv in the x direction
PFITR_v = polyfit(Xax,Rv,4);
PFITR_v_1 = PFITR_v(1);
PFITR_v_2 = PFITR_v(2);
PFITR_v_3 = PFITR_v(3);
PFITR_v_4 = PFITR_v(4);
PFITR_v_5 = PFITR_v(5);
FitR_v =
PFITR_v_1*Xax.^4+PFITR_v_2*Xax.^3+PFITR_v_3*Xax.^2+PFITR_v_4*X
ax+PFITR_v_5;
R_v_max = max(FitR_v);
Xax_at_R_v_max = Xax(FitR_v==R_v_max);
NormalisedXax_at_R_v_max= Xax_at_R_v_max/max(Xax);

% Plotting the variation of Rp in the x direction
PFITR_p = polyfit(Xax,Rp,4);
PFITR_p_1 = PFITR_p(1);
PFITR_p_2 = PFITR_p(2);
PFITR_p_3 = PFITR_p(3);
PFITR_p_4 = PFITR_p(4);
PFITR_p_5 = PFITR_p(5);
```

```
FitR_p =
PFITR_p_1*Xax.^4+PFITR_p_2*Xax.^3+PFITR_p_3*Xax.^2+PFITR_p_4*X
ax+PFITR_p_5;
R_p_min = min(FitR_p);
Xax_at_R_p_min = Xax(FitR_p==R_p_min);
NormalisedXax_at_R_p_min= Xax_at_R_p_min/max(Xax);

figure;plot(Xax,Rp,Xax,Rv,Xax,FitR_p,Xax,FitR_v), xlabel('x
(μm)'),ylabel('Max peak height R_p and max valley depth R_v of
y-direction profile (μm)'),legend('R_p','R_v','R_p 4th order
poly fit','R_v 4th order poly fit'),title(['Variation of max
peak height R_p and max valley depth R_v in the x direction
for ',num2str(SampleName)]),  savefig([num2str(DataTitle),'
Figure 10']), saveas(10,[num2str(DataTitle),' Figure
10'],'png')

% Calculating and displaying average results
Rv_ave = mean(Rv); Rv_med = median(Rv); Rv_std = std(Rv);
Rp_ave = mean(Rp); Rp_med = median(Rp); Rp_std = std(Rp);

disp(['The mean Rv value over the whole surface is
',num2str(round(Rv_ave,3)),' μm ','with a standard deviation
of ',num2str(round(Rv_std,3)),' μm'])
disp(['The median Rv value over the whole surface is
',num2str(round(Rv_med,3)),' μm '])
disp(['The fit of R_v values in the x direction reaches a
maximum of ',num2str(round(R_v_max,3)),' μm ','at
',num2str(round(100*NormalisedXax_at_R_v_max,2)),'% of the way
along the x axis'])
disp('_')
disp(['The mean Rp value over the whole surface is
',num2str(round(Rp_ave,3)),' μm ','with a standard deviation
of ',num2str(round(Rp_std,3)),' μm'])
disp(['The median Rp value over the whole surface is
',num2str(round(Rp_med,3)),' μm '])
disp(['The fit of Rp values in the x direction reaches a
minimum of ',num2str(round(R_p_min,3)),' μm ','at
',num2str(round(100*NormalisedXax_at_R_p_min,2)),'% of the way
along the x axis'])
disp('_')

%RzJIS%%%%%%%%%%%%%%%%%%%%%%%%%%%%%%%%%%%%%%%%%%%%%%%%%%%%%%%
%%%%%%%%%%%%%%%%%%%%%%
% Because by definition, max5 and min5 values all have the
same lengths,
% they can be recombined into a single matrix whereas the full
data cannot.
max5mat=cell2mat(max5');
min5mat=cell2mat(min5');
Sum_max5 = sum(max5mat,2);
Sum_min5 = sum(min5mat,2);
```

```
Rz_JIS = (Sum_max5 - Sum_min5)./5;
Rz_JIS_ave = mean(Rz_JIS); Rz_JIS_med = median(Rz_JIS);
Rz_JIS_std = std(Rz_JIS);

%Plotting the variation of Rz_JIS in the x direction
PFITRz_JIS = polyfit(Xax,Rz_JIS',4);
PFITRz_JIS_1 = PFITRz_JIS(1);
PFITRz_JIS_2 = PFITRz_JIS(2);
PFITRz_JIS_3 = PFITRz_JIS(3);
PFITRz_JIS_4 = PFITRz_JIS(4);
PFITRz_JIS_5 = PFITRz_JIS(5);
FitRz_JIS =
PFITRz_JIS_1*Xax.^4+PFITRz_JIS_2*Xax.^3+PFITRz_JIS_3*Xax.^2+PF
ITRz_JIS_4*Xax+PFITRz_JIS_5;
figure;plot(Xax,Rz_JIS,Xax,FitRz_JIS), xlabel('x
(µm)'),ylabel('R_z_J_I_S roughness of y-direction profile
(µm)'),legend('R_z_J_I_S','4th order poly
fit'),title(['Variation of R_z_J_I_S in the x direction for
',num2str(SampleName)]),  savefig([num2str(DataTitle),' Figure
11']), saveas(11,[num2str(DataTitle),' Figure 11'],'png')
Rz_JIS_min = min(FitRz_JIS);
Xax_at_Rz_JIS_min = Xax(FitRz_JIS==Rz_JIS_min);
NormalisedXax_at_Rz_JIS_min= Xax_at_Rz_JIS_min/max(Xax);

%Displaying results
disp(['The mean Rz_JIS value over the whole surface is
',num2str(round(Rz_JIS_ave,3)),' µm ','with a standard
deviation of ',num2str(round(Rz_JIS_std,3)),' µm'])
disp(['The median Rz_JIS value over the whole surface is
',num2str(round(Rz_JIS_med,3)),' µm '])
disp(['The fit of Rz_JIS values in the x direction reaches a
minimum of ',num2str(round(Rz_JIS_min,3)),' µm ','at
',num2str(round(100*NormalisedXax_at_Rz_JIS_min,2)),'% of the
way along the x axis'])
disp('_')

% Mean Slope Parameters Rda
Rdq%%%%%%%%%%%%%%%%%%%%%%%%%%%%%%%%%%%%%%%%%%%%%%%%%%%%

PFITRda = polyfit(Xax,Rda,4);
PFITRda_1 = PFITRda(1);
PFITRda_2 = PFITRda(2);
PFITRda_3 = PFITRda(3);
PFITRda_4 = PFITRda(4);
PFITRda_5 = PFITRda(5);
FitRda =
PFITRda_1*Xax.^4+PFITRda_2*Xax.^3+PFITRda_3*Xax.^2+PFITRda_4*X
ax+PFITRda_5;
Rda_min = min(FitRda);
Xax_at_Rda_min = Xax(FitRda==Rda_min);
NormalisedXax_at_Rda_min= Xax_at_Rda_min/max(Xax);
```

```
PFITRdq = polyfit(Xax,Rdq,4);
PFITRdq_1 = PFITRdq(1);
PFITRdq_2 = PFITRdq(2);
PFITRdq_3 = PFITRdq(3);
PFITRdq_4 = PFITRdq(4);
PFITRdq_5 = PFITRdq(5);
FitRdq =
PFITRdq_1*Xax.^4+PFITRdq_2*Xax.^3+PFITRdq_3*Xax.^2+PFITRdq_4*X
ax+PFITRdq_5;
Rdq_min = min(FitRdq);
Xax_at_Rdq_min = Xax(FitRdq==Rdq_min);
NormalisedXax_at_Rdq_min= Xax_at_Rdq_min/max(Xax);

figure;plot(Xax,Rda,Xax,Rdq,Xax,FitRda,Xax,FitRdq), xlabel('x
(µm)'), ylabel('Absolute average slope R_d_a, RMS average
slope R_d_q'), legend('R_d_a','R_d_q','R_d_a 4th order poly
fit','R_d_q 4th order poly fit'), title(['Variation in average
slope in the x direction for ',num2str(SampleName)]),
savefig([num2str(DataTitle),' Figure 12']),
saveas(12,[num2str(DataTitle),' Figure 12'],'png')
Rda_ave = mean(Rda); Rda_med = median(Rda); Rda_std =
std(Rda);
Rdq_ave = mean(Rdq); Rdq_med = median(Rdq); Rdq_std =
std(Rdq);
disp(['The mean Rda value over the whole surface is
',num2str(round(Rda_ave,3)),' µm ','with a standard deviation
of ',num2str(round(Rda_std,3)),' µm'])
disp(['The median Rda value over the whole surface is
',num2str(round(Rda_med,3)),' µm '])
disp(['The fit of Rda values in the x direction reaches a
minimum of ',num2str(round(Rda_min,3)),' µm ','at
',num2str(round(100*NormalisedXax_at_Rda_min,2)),'% of the way
along the x axis'])
disp('_')
disp(['The mean Rdq value over the whole surface is
',num2str(round(Rdq_ave,3)),' µm ','with a standard deviation
of ',num2str(round(Rdq_std,3)),' µm'])
disp(['The median Rdq value over the whole surface is
',num2str(round(Rdq_med,3)),' µm '])
disp(['The fit of Rdq values in the x direction reaches a
minimum of ',num2str(round(Rdq_min,3)),' µm ','at
',num2str(round(100*NormalisedXax_at_Rdq_min,2)),'% of the way
along the x axis'])
disp('_')


%
Spacing%%%%%%%%%%%%%%%%%%%%%%%%%%%%%%%%%%%%%%%%%%%%%%%%%%%%%%%%
%%%%%%%%%
% Spacing between profile peaks over the whole area
```

```
Surf_Spac_Average = mean(Spac_Average);
Surf_Spac_Stddev = mean(Spac_Stddev);
Surf_Spac_Median_Median = median(Spac_Median);
Surf_Spac_Average_Median = mean(Spac_Median);
% Combine entire cell array into matrix
All_spac = cell2mat(Xax_spac);
figure; histogram(All_spac,512), xlabel('spacing between peaks
(µm)'), ylabel('frequency (-)'), xlim([0 100]),
title(['Distribution of peak spacing across the surface for
',num2str(SampleName)]),  savefig([num2str(DataTitle),' Figure
13']), saveas(13,[num2str(DataTitle),' Figure 13'],'png')
[counts centres] = hist(All_spac,512);
weighted_counts = counts.*centres;
figure;bar(centres,weighted_counts,'k','BarWidth',1),
xlabel('spacing between peaks (µm)'), ylabel('length-weighted
frequency (µm)'), xlim([0 100]), title(['length-weighted
distribution of peak spacing across the surface for
',num2str(SampleName)]),  savefig([num2str(DataTitle),' Figure
14']), saveas(14,[num2str(DataTitle),' Figure 14'],'png')

% Plot histogram of all the Diff_Z data
figure; histogram(Diff_Z, 200), xlabel('Deviation from Z datum
(µm)'), xlim([-25 25]), ylabel('frequency (-)'),
title(['Distribution of heights across the surface  for
',num2str(SampleName)]),  savefig([num2str(DataTitle),' Figure
15']), saveas(15,[num2str(DataTitle),' Figure 15'],'png')
disp(['The mean spacing between peaks of the entire surface is
',num2str(round(Surf_Spac_Average,3)),' µm ','with a standard
deviation of ',num2str(round(Surf_Spac_Stddev,3)),' µm'])
disp(['The median median spacing between peaks of the entire
surface is ',num2str(round(Surf_Spac_Median_Median,3)),' µm
'])
disp(['The average median spacing between peaks of the entire
surface is ',num2str(round(Surf_Spac_Average_Median,3)),' µm
'])

%For checking to see whether the polynomials are fitted
properly;
figure;plot(Xax,Z(1,:),Xax,fdata1(1,:),'-r',Xax,fdata2(1,:),'-
g'), xlabel('x (µm)'),ylabel('height (µm)'),
legend('data','6th order poly fit',['6th order poly fit with
',num2str(Tol), ' std.dev tolerance outlier removal']),
title('Profile at y = 2 µm for central 512 µm'),
savefig([num2str(DataTitle),' Figure 16']),
saveas(16,[num2str(DataTitle),' Figure 16'],'png')
figure;plot(Xax,Z(25,:),Xax, fdata1(25,:),'-
r',Xax,fdata2(25,:),'-g'), xlabel('x (µm)'),ylabel('height
(µm)'), legend('data','6th order poly fit',['6th order poly
fit with ',num2str(Tol), ' std.dev tolerance outlier
removal']),  title('Profile at y = 50 µm for central 512 µm'),
```

```
savefig([num2str(DataTitle),' Figure 17']),
saveas(17,[num2str(DataTitle),' Figure 17'],'png')
figure;plot(Xax,Z(50,:),Xax,fdata1(50,:),'-
r',Xax,fdata2(50,:),'-g'), xlabel('x (µm)'),ylabel('height
(µm)'), legend('data','6th order poly fit',['6th order poly
fit with ',num2str(Tol), ' std.dev tolerance outlier
removal']),  title('Profile at y = 100 µm for central 512
µm'), savefig([num2str(DataTitle),' Figure 18']),
saveas(18,[num2str(DataTitle),' Figure 18'],'png')
figure;plot(Xax,Z(75,:),Xax,fdata1(75,:),'-
r',Xax,fdata2(75,:),'-g'), xlabel('x (µm)'),ylabel('height
(µm)'), legend('data','6th order poly fit',['6th order poly
fit with ',num2str(Tol), ' std.dev tolerance outlier
removal']),  title('Profile at y = 150 µm for central 512
µm'), savefig([num2str(DataTitle),' Figure 19']),
saveas(19,[num2str(DataTitle),' Figure 19'],'png')
figure;plot(Xax,Z(100,:),Xax,fdata1(100,:),'-
r',Xax,fdata2(100,:),'-g'), xlabel('x (µm)'),ylabel('height
(µm)'), legend('data','6th order poly fit',['6th order poly
fit with ',num2str(Tol), ' std.dev tolerance outlier
removal']),  title('Profile at y = 200 µm for central 512
µm'), savefig([num2str(DataTitle),' Figure 20']),
saveas(20,[num2str(DataTitle),' Figure 20'],'png')
figure;plot(Xax,Z(125,:),Xax,fdata1(125,:),'-
r',Xax,fdata2(125,:),'-g'), xlabel('x (µm)'),ylabel('height
(µm)'), legend('data','6th order poly fit',['6th order poly
fit with ',num2str(Tol), ' std.dev tolerance outlier
removal']),  title('Profile at y = 250 µm for central 512
µm'), savefig([num2str(DataTitle),' Figure 21']),
saveas(21,[num2str(DataTitle),' Figure 21'],'png')
figure;plot(Xax,Z(150,:),Xax,fdata1(150,:),'-
r',Xax,fdata2(150,:),'-g'), xlabel('x (µm)'),ylabel('height
(µm)'), legend('data','6th order poly fit',['6th order poly
fit with ',num2str(Tol), ' std.dev tolerance outlier
removal']),  title('Profile at y = 300 µm for central 512
µm'), savefig([num2str(DataTitle),' Figure 22']),
saveas(22,[num2str(DataTitle),' Figure 22'],'png')
figure;plot(Xax,Z(175,:),Xax,fdata1(175,:),'-
r',Xax,fdata2(175,:),'-g'), xlabel('x (µm)'),ylabel('height
(µm)'), legend('data','6th order poly fit',['6th order poly
fit with ',num2str(Tol), ' std.dev tolerance outlier
removal']),  title('Profile at y = 350 µm for central 512
µm'), savefig([num2str(DataTitle),' Figure 23']),
saveas(23,[num2str(DataTitle),' Figure 23'],'png')
figure;plot(Xax,Z(200,:),Xax,fdata1(200,:),'-
r',Xax,fdata2(200,:),'-g'), xlabel('x (µm)'),ylabel('height
(µm)'), legend('data','6th order poly fit',['6th order poly
fit with ',num2str(Tol), ' std.dev tolerance outlier
removal']),  title('Profile at y = 400 µm for central 512
µm'), savefig([num2str(DataTitle),' Figure 24']),
saveas(24,[num2str(DataTitle),' Figure 24'],'png')
```

```
figure;plot(Xax,Z(225,:),Xax,fdata1(225,:),'-
r',Xax,fdata2(225,:),'-g'), xlabel('x (µm)'),ylabel('height
(µm)'), legend('data','6th order poly fit',['6th order poly
fit with ',num2str(Tol), ' std.dev tolerance outlier
removal']),  title('Profile at y = 450 µm for central 512
µm'), savefig([num2str(DataTitle),' Figure 25']),
saveas(25,[num2str(DataTitle),' Figure 25'],'png')
figure;plot(Xax,Z(256,:),Xax,fdata1(256,:),'-
r',Xax,fdata2(256,:),'-g'), xlabel('x (µm)'),ylabel('height
(µm)'), legend('data','6th order poly fit',['6th order poly
fit with ',num2str(Tol), ' std.dev tolerance outlier
removal']),  title('Profile at y = 512 µm for central 512
µm'), savefig([num2str(DataTitle),' Figure 26']),
saveas(26,[num2str(DataTitle),' Figure 26'],'png')

Titles = {'Arithmetic Mean Deviation R_a';'RMS Mean Deviation
R_q';'Skewness R_sk';'Kurtosis R_ku';'Max Peak Height
R_p';'Max Valley Depth R_v';'Japanese Industrial Standard
Roughness R_zJIS';'Mean Absolute Slope R_da';'RMS Mean
Absolute Slope R_qa';'Peak Spacing'};
Mean = [R_a_ave;
R_q_ave;Rsk_ave;Rku_ave;Rp_ave;Rv_ave;Rz_JIS_ave;Rda_ave;Rdq_a
ve;Surf_Spac_Average];
Stdev = [R_a_std;
R_q_std;Rsk_std;Rku_std;Rp_std;Rv_std;Rz_JIS_std;Rda_std;Rdq_s
td;Surf_Spac_Stddev];
Median = [R_a_med;
R_q_med;Rsk_med;Rku_med;Rp_med;Rv_med;Rz_JIS_med;Rda_med;Rdq_m
ed;Surf_Spac_Average_Median];
Lowest_deviation_from_zero_of_poly = [R_a_min;
R_q_min;Rsk_max;Rku_min;R_p_min;R_v_max;Rz_JIS_min;Rda_min;Rdq
_min;NaN];
Location_of_zero_point = [NormalisedXax_at_R_a_min;
NormalisedXax_at_R_q_min;NormalisedXax_at_Rsk_max;NormalisedXa
x_at_Rku_min;NormalisedXax_at_R_p_min;NormalisedXax_at_R_v_max
;NormalisedXax_at_Rz_JIS_min;NormalisedXax_at_Rda_min;Normalis
edXax_at_Rdq_min;NaN];
 T =
table(Titles,Mean,Stdev,Median,Lowest_deviation_from_zero_of_p
oly,Location_of_zero_point)

writetable(T,'Sample_1_Roughness_B2_512micronT.xlsx','Sheet',1
);
 figure; spy
```

APPENDIX A2 – ESTIMATION OF GRINDER SHEAR RATE

For the purposes of attributing an apparent viscosity from any rheology measurements to the charge within the grinder, it is necessary to have an estimate of the shear rate experienced, since fibre suspensions and MFC are shear-thinning over certain shear rate ranges. Here, the shear rate within the charge between the impeller and the wall is estimated assuming an impeller speed of 800 rpm, with 3 mm media.

One can first estimate the shear rate in a Newtonian fluid in the absence of media, using the following assumptions: no slip at the wall, and the charge at the impeller tip has a velocity of around 40% of the impeller tip speed (as some studies imply[54-55]). The fluid velocity at the impeller tip, at an impeller speed of 800 rpm (where v_t = 5.45 m/s) is therefore estimated as 2.18 m/s. Assuming the fluid velocity is zero at the wall, a Newtonian fluid will have a constant velocity gradient across the gap between the impeller and the wall, *r*. The shear rate is calculated by dividing the velocity difference between the charge at the impeller and the wall, by the separation distance *r*. The gap between the impeller tip and the wall is around 7 mm, therefore the shear rate considering just the fluid is evaluated as 311 s^{-1}.

However, when media is added, this entire gap is not available for the fluid to be shearing, since most of it is taken up by media beads, the shear rate across which is zero. Consequently, the entire shear gradient is concentrated between the media streamlines, and between the media and the wall, and the media and the impeller (see Figure A2.1), giving a much higher shear rate than with the fluid alone.

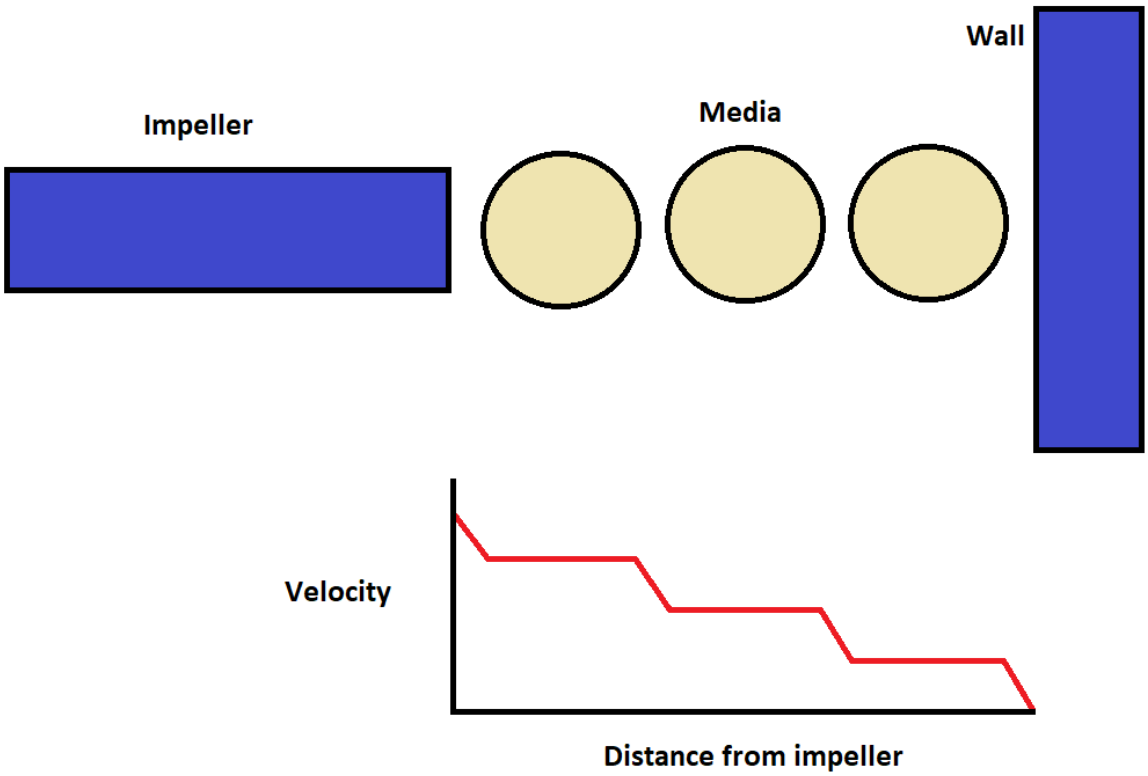

Figure A2.1 *– A diagram showing the expected velocity gradient between the impeller tip and the wall; the media occupies a large part of the shear length, thereby concentrating the shear gradient into narrow gaps between objects.*

When using 3 mm media, with a 7 mm gap, there are on average 2.3 media beads between the impeller and the wall (realistically, in most places there will be 2 media beads in the gap, whereas in some there will be 3. The average number of gaps over which shear can take place is equal to the number of media minus one, plus the media-impeller gap, and the media-wall gap, so therefore the average number of gaps to transfer this shear is 3.3.

Now one must estimate the size of these gaps, which requires an estimation of the average separation distance between media. This can be done by calculating the volume of a single bead, the total volume of media added, and from there the number of media present. Then the average charge volume per media bead can be calculated, and by cube rooting this, the average separation distance between bead centre-points is determined. Finally, by subtracting this distance from the media diameter, one can estimate the average gap between

the media. These calculations are shown in Table A2.1, with this gap estimated to be 0.1 mm. By multiplying this by the average number of gaps over which to transfer this shear, this leads to a total shear length of just 0.33 mm. By using this to divide the total velocity change between the charge at the impeller and the wall (2.18 m/s), one obtains a shear rate estimation in the gaps between media of around 6600 s^{-1}.

Table A2.1 *– Estimation of the shear rate between media beads within the grinder with a media diameter of 3 mm and an impeller speed of 800 rpm*

Impeller tip speed (m/s)	5.45
Charge velocity at impeller (m/s)	2.18
Media diameter (mm)	3
Volume of single media bead (mm^3)	14.14
Volume of media added (mm^3)	5.2×10^5
Number of media present	36966
Total volume of charge (including media) (mm^3)	1.1×10^6
Charge volume per media bead (mm^3)	29.76
Average separation distance between media centre points (mm)	3.10
Gap between media (mm)	0.10
Average total shear length in gap (mm)	0.33
Estimated shear rate between media (s^{-1})	**6607**

APPENDIX A3 – SUPPLEMENTARY DATA FOR CHAPTER 5

A3.1. Supplementary Figures and Tables

Table A3.1 *– Roughness parameters of each batch of media.*

Name	R_a (µm)	R_q (µm)	R_{sk} (-)	R_{ku} (-)	R_p (µm)	R_v (µm)	$R_{z,JIS}$ (µm)	$R_{\Delta q}$ (-)	Peak Spacing RS_m (µm)	Asperity Curvature k_s (µm^{-1})
Mullite A	0.97	1.47	-1.60	6.91	2.74	-5.96	5.09	0.57	25.50	0.192
Mullite B	0.38	0.51	-0.45	4.11	1.37	-1.70	2.27	0.30	19.13	0.198
Mullite C	0.76	1.08	-0.99	4.99	2.36	-3.61	3.64	0.36	28.44	0.200
Glass A	0.12	0.17	-0.17	5.15	0.50	-0.52	0.70	0.09	18.10	0.118
Glass B†	1.69	2.58	-1.36	6.64	5.49	-10.11	8.65	0.90	33.37	0.279
Glass B‡	1.90	2.83	-1.40	6.44	6.03	-11.42	10.11	1.06	32.94	0.315
Glass C†	2.07	2.94	-1.00	5.33	6.30	-10.51	10.41	1.06	33.98	0.332
Glass C‡	2.00	2.92	-1.28	6.04	6.16	-11.47	10.71	1.11	31.76	0.335
Glass D†	2.34	3.25	-0.90	4.67	7.19	-11.39	11.65	1.19	32.83	0.343
Glass D‡	1.75	2.48	-1.14	5.24	5.25	-9.22	8.97	0.93	30.27	0.272
Glass E†	0.87	1.39	-1.87	8.58	2.61	-6.22	5.07	0.59	24.86	0.210
Glass E‡	0.88	1.44	-1.95	8.82	2.75	-6.76	5.24	0.60	25.76	0.255
Glass F†	0.99	1.41	-1.26	6.71	2.98	-5.71	5.91	0.70	23.66	0.267
Glass F‡	0.92	1.37	-1.63	7.88	2.72	-5.93	5.65	0.67	24.07	0.275
Glass G†	0.65	0.97	-1.65	8.02	2.12	-4.47	4.12	0.50	21.34	0.214
Glass G‡	0.63	0.98	-1.96	9.16	1.95	-4.71	4.02	0.48	22.72	0.222
Glass H†	1.97	2.71	-0.95	4.80	5.80	-9.86	10.26	1.08	30.58	0.325
Glass H‡	1.57	2.26	-1.35	5.86	4.53	-8.67	8.31	0.88	29.51	0.271
Glass I†	1.69	2.42	-1.32	5.82	4.73	-9.80	9.40	1.03	28.78	0.321
Glass I‡	1.48	2.19	-1.71	7.12	4.15	-9.50	8.60	0.96	27.61	0.315
Glass J†	0.40	0.64	-1.57	9.34	1.46	-2.87	2.56	0.32	20.16	0.175
Glass J‡	0.35	0.54	-1.51	9.31	1.30	-2.47	2.26	0.28	21.45	0.196
Glass K†	0.37	0.60	-1.76	9.50	1.31	-2.81	2.43	0.30	20.72	0.186
Glass K‡	0.45	0.77	-2.11	10.53	1.53	-3.69	3.00	0.36	22.58	0.219
Glass L	0.67	1.05	-2.03	9.63	1.90	-5.39	4.33	0.52	21.92	0.222
Zirconia A	0.13	0.19	0.02	6.73	0.63	-0.67	0.84	0.13	19.24	0.158
Zirconia B‡	0.38	0.52	-0.42	4.30	1.29	-1.80	2.25	0.28	19.87	0.231
Zirconia C‡	0.32	0.45	0.00	4.56	1.11	-1.62	1.94	0.24	20.98	0.286
Zirconia D	0.20	0.31	-1.03	7.02	0.76	-1.29	1.25	0.16	19.68	0.164
Zirconia E	0.34	0.46	-0.79	4.95	1.14	-1.71	1.97	0.25	20.36	0.215
Alumina	0.55	0.82	-1.10	5.28	1.65	-3.04	2.78	0.30	26.64	0.174
Zir. Sil. A	0.38	0.52	-0.28	4.37	1.52	-1.71	2.13	0.26	21.92	0.161
Zir. Sil. B	0.37	0.50	-0.13	4.38	1.51	-1.54	1.97	0.24	22.14	0.164
Zir. Sil. C	0.18	0.24	-0.03	4.06	0.79	-0.79	1.13	0.15	19.83	0.210

† Average of before and after the 1000 kWh/t grind.

‡ Average of before and after the 3000 kWh/t grind.

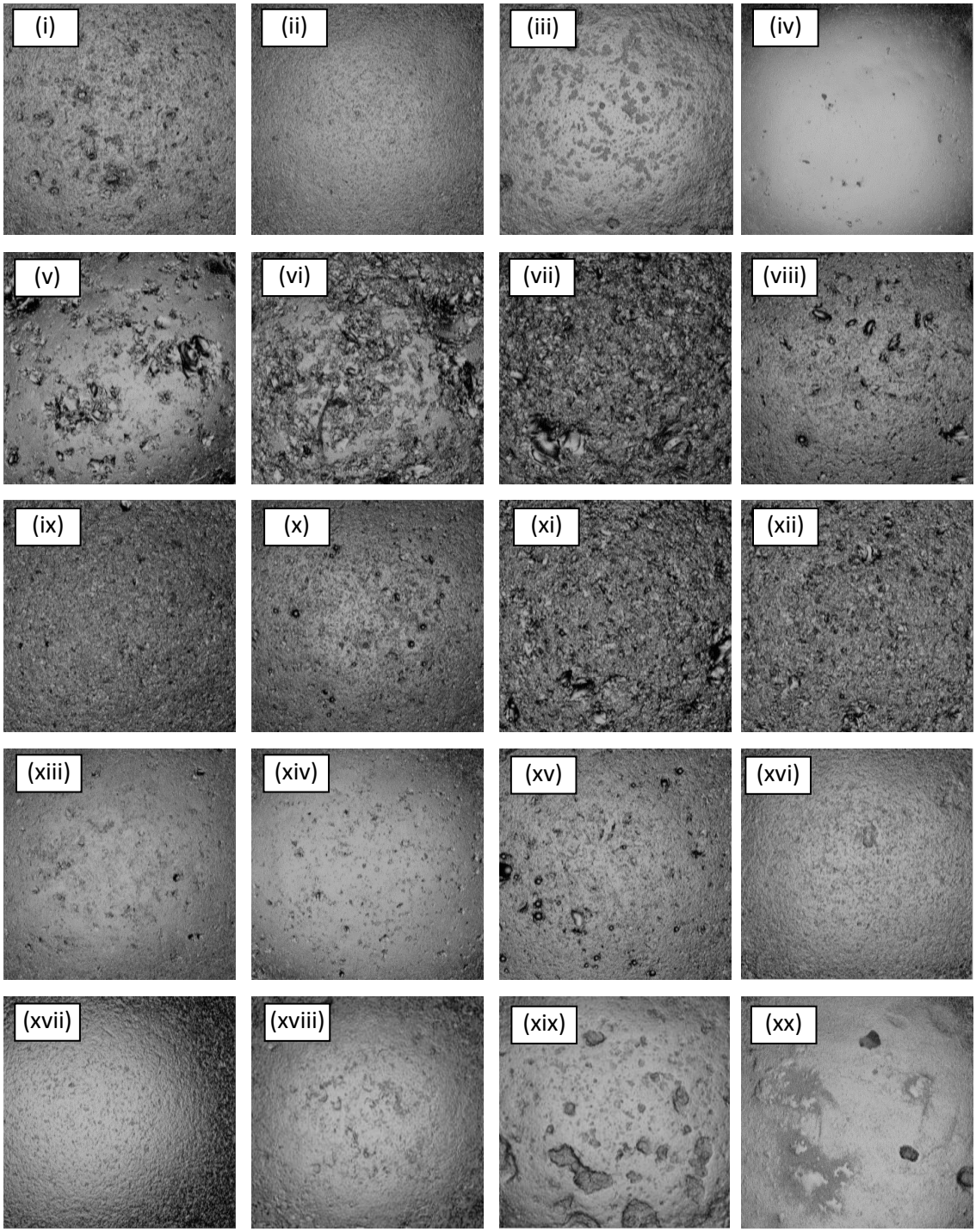

Figure A3.1 *– Intensity surface maps of (i) Mullite A, (ii) Mullite B, (iii) Mullite C, (iv) Glass A, (v) Glass B, (vi) Glass C, (vii) Glass D, (viii) Glass E, (ix) Glass F, (x) Glass G, (xi) Glass H, (xii) Glass I, (xiii) Glass J, (xiv) Glass K, (xv) Glass L, (xvi) Zirconia B, (xvii) Zirconia C, (xviii) Zirconia E, (xix) Alumina, and (xx) Zirconium Silicate B. Each image is 1024 µm wide.*

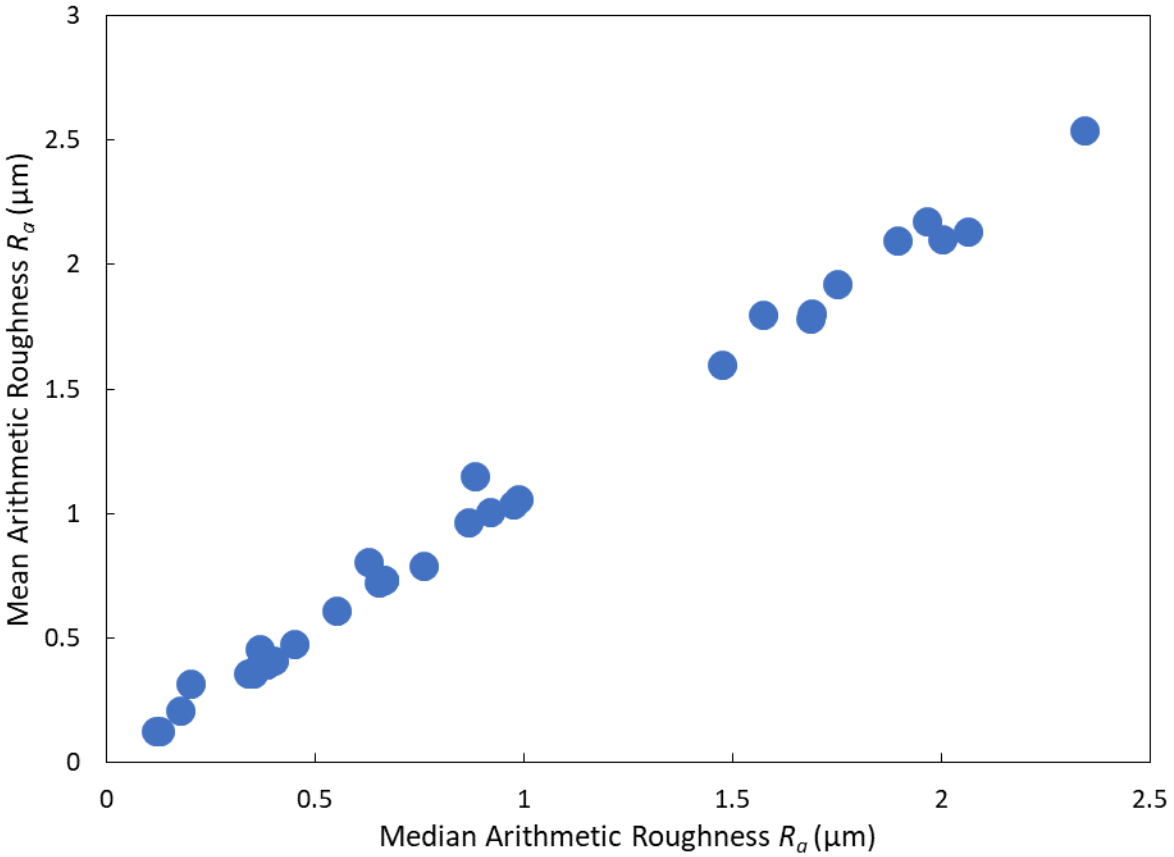

Figure A3.2 *– Mean arithmetic roughness R_a versus median arithmetic roughness R_a.*

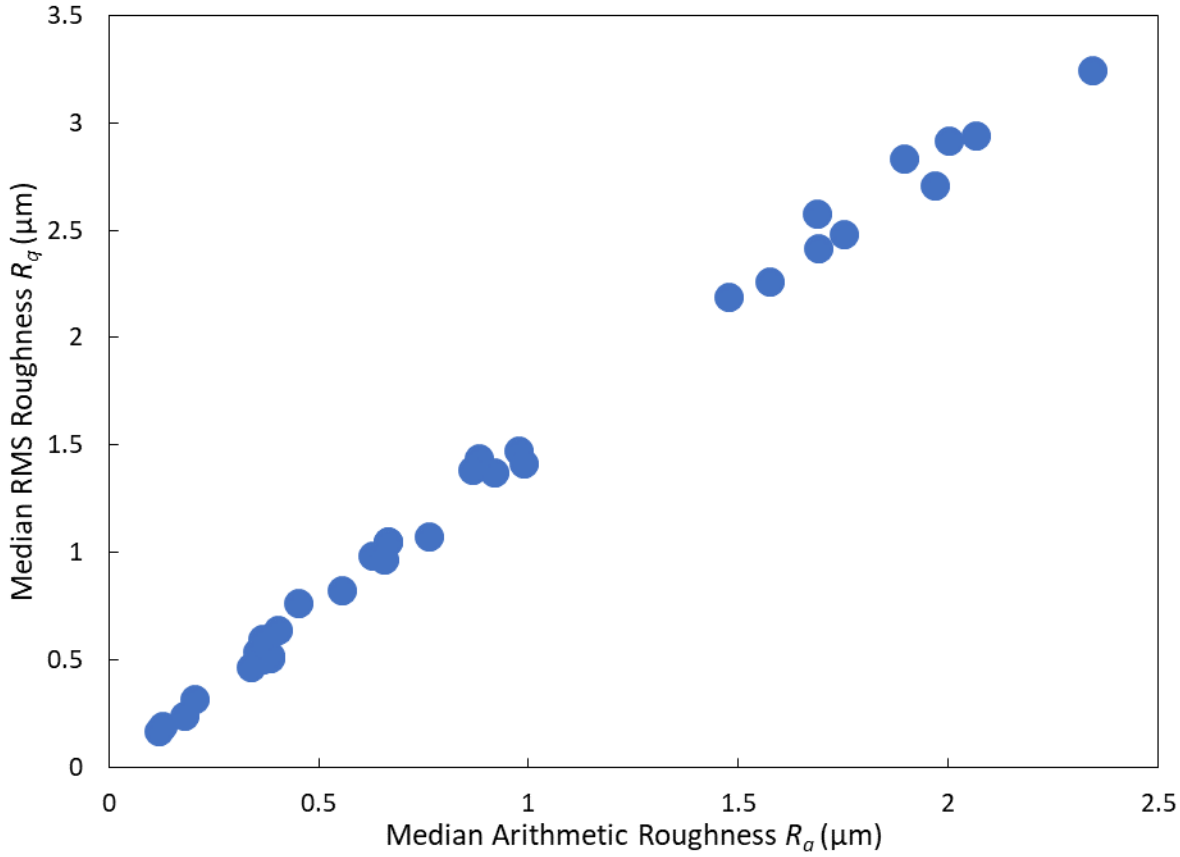

Figure A3.3 *– Median RMS roughness R_q versus median arithmetic roughness R_a.*

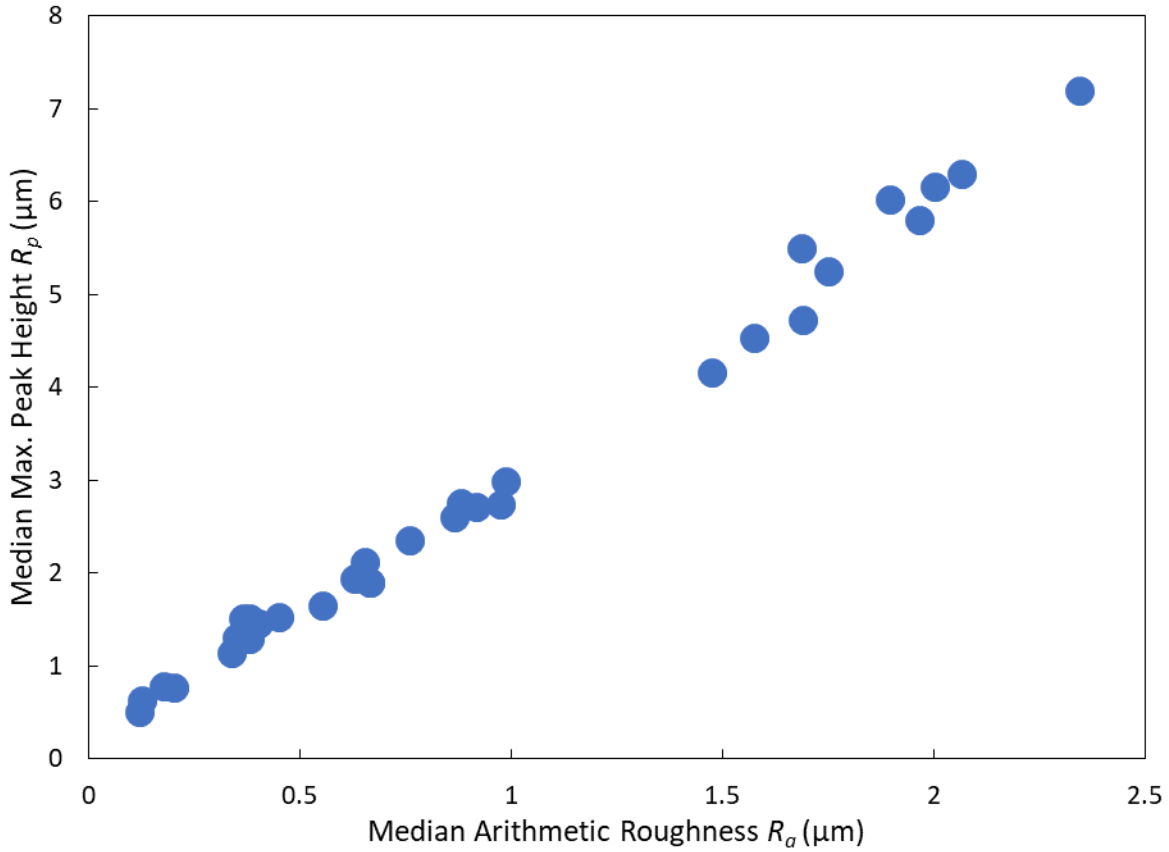

Figure A3.4 *– Median max. peak height R_p versus median arithmetic roughness R_a.*

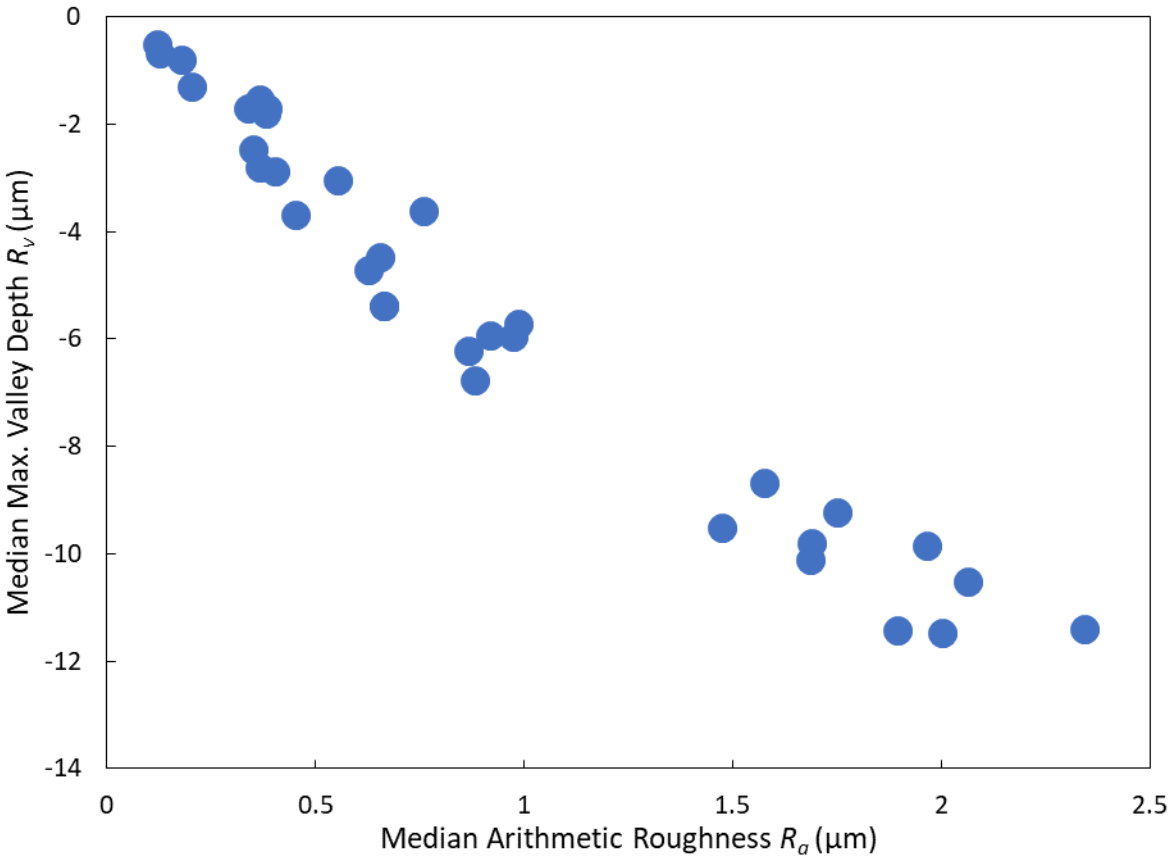

Figure A3.5 *– Median max. valley depth R_v versus median arithmetic roughness R_a.*

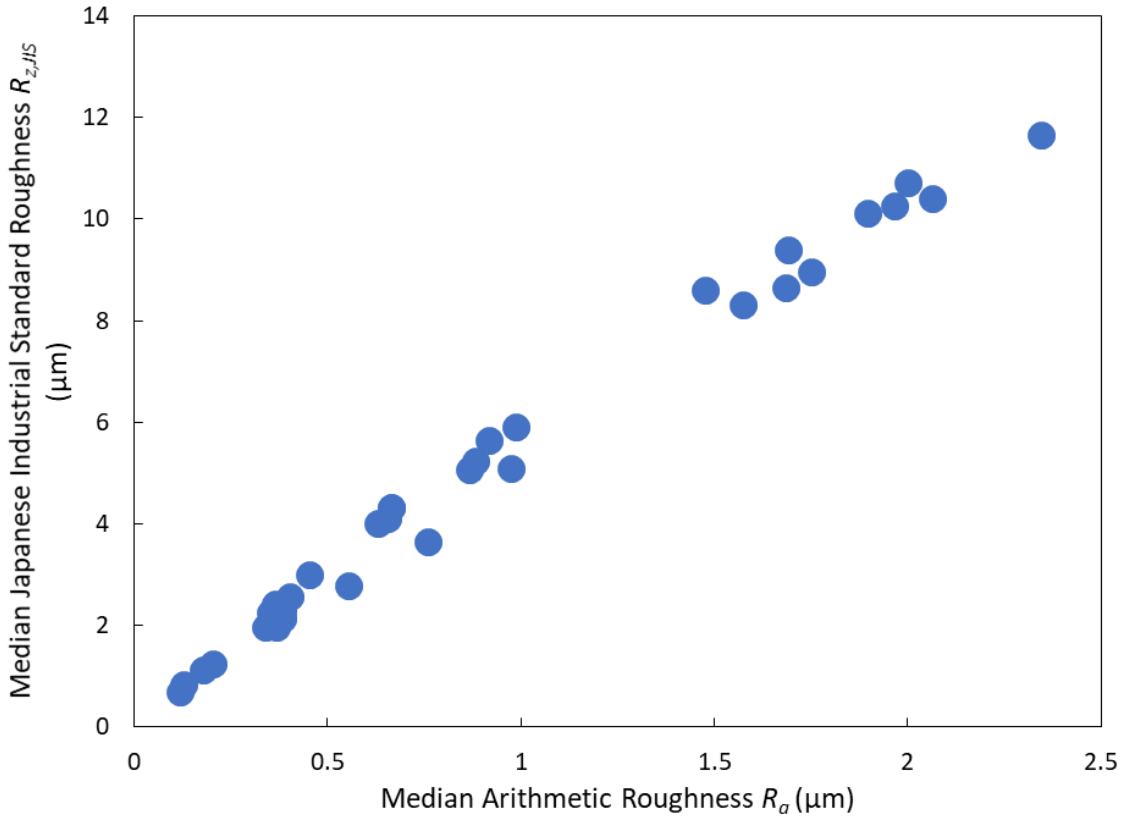

Figure A3.6 – *Median Japanese Industrial Standard roughness $R_{z,JIS}$ versus median arithmetic roughness R_a.*

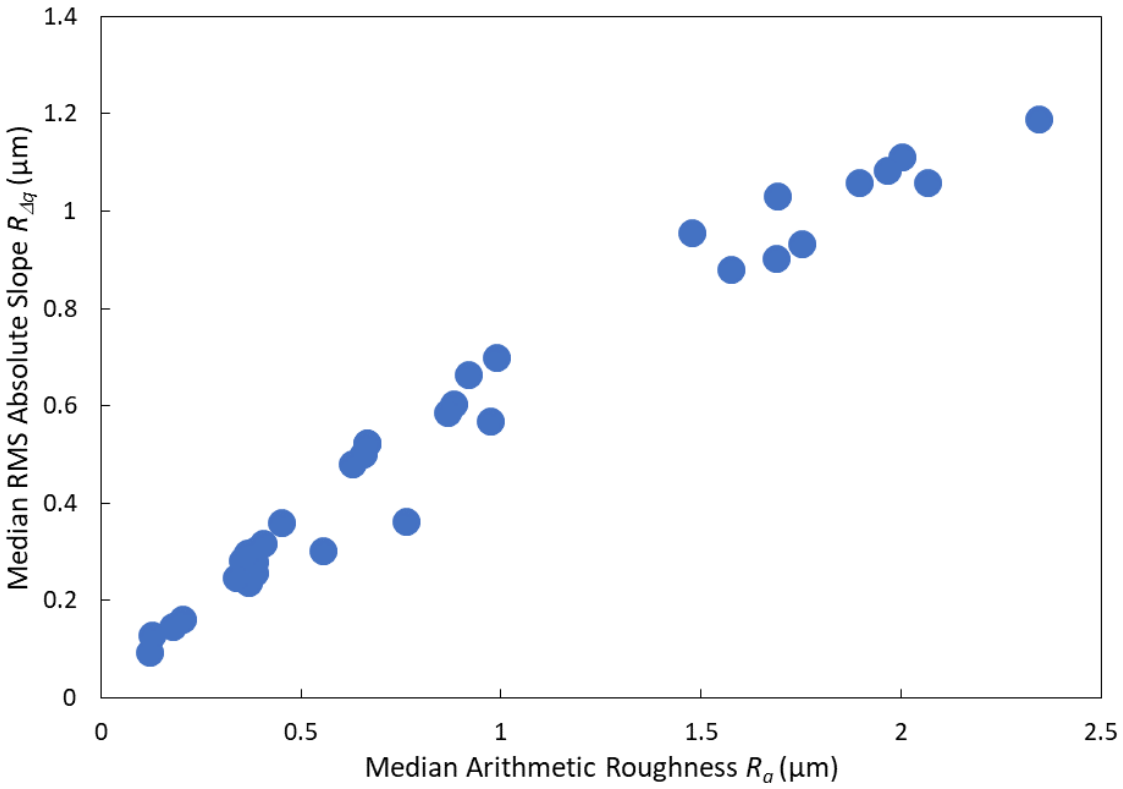

Figure A3.7 *– Median RMS mean absolute slope $R_{\Delta q}$ versus median arithmetic roughness R_a. (note that this is the mean slope within each individual profile, but the median value of these means is taken across all 512 profiles).*

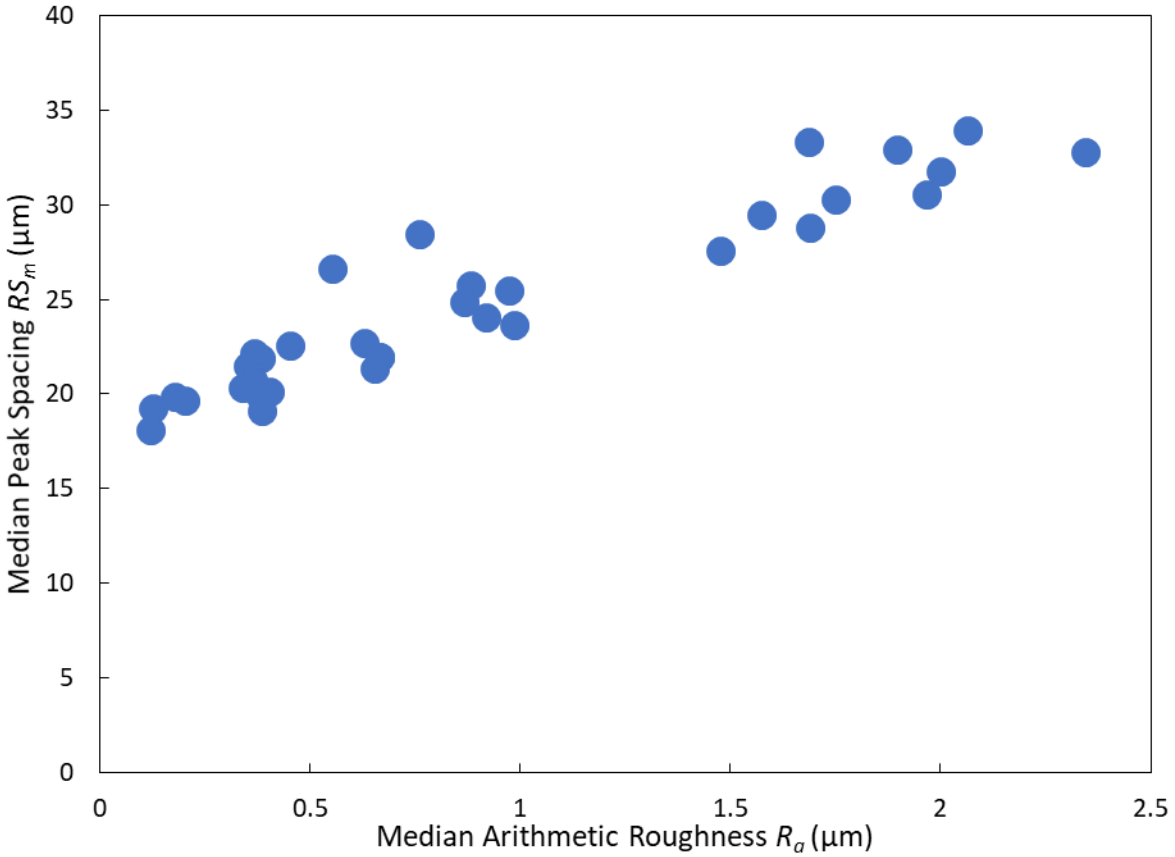

Figure A3.8 *– Median peak spacing RS_m versus median arithmetic roughness R_a.*

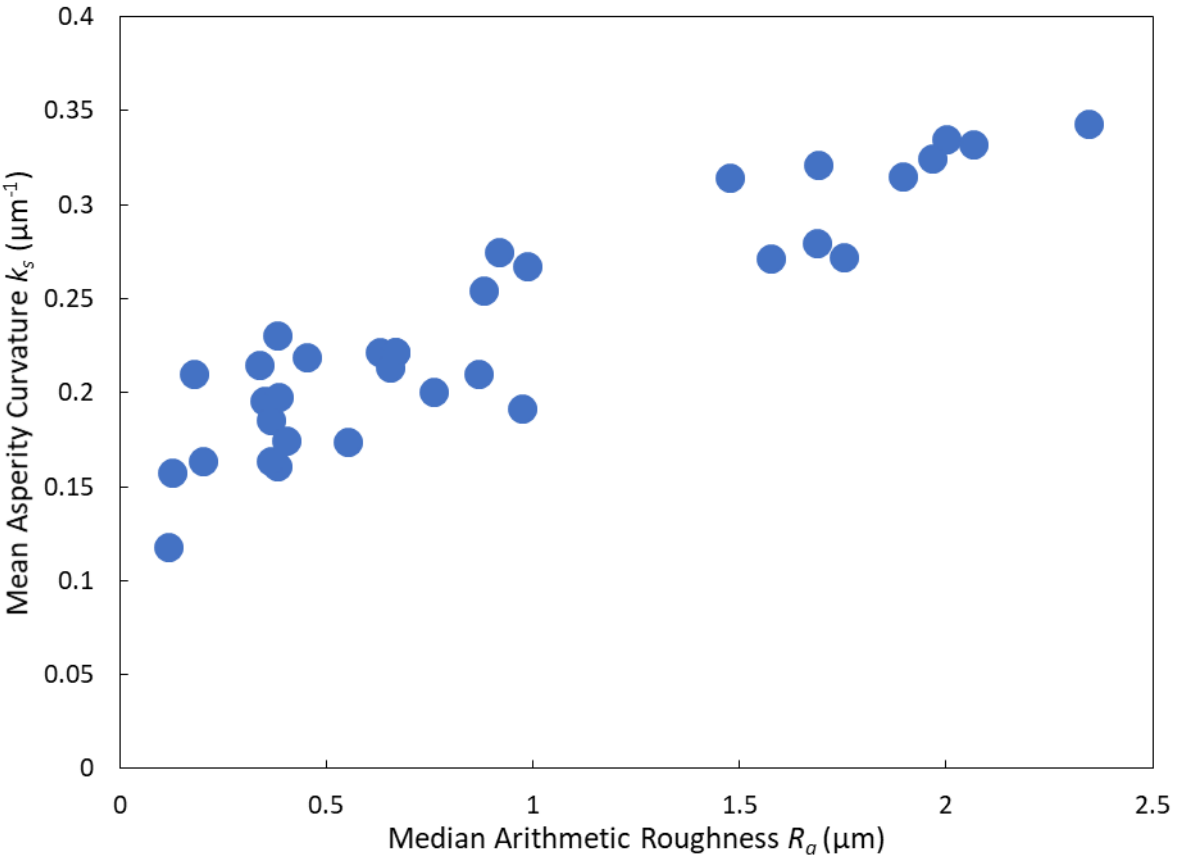

Figure A3.9 *– Mean asperity curvature k_s versus median arithmetic roughness R_a.*

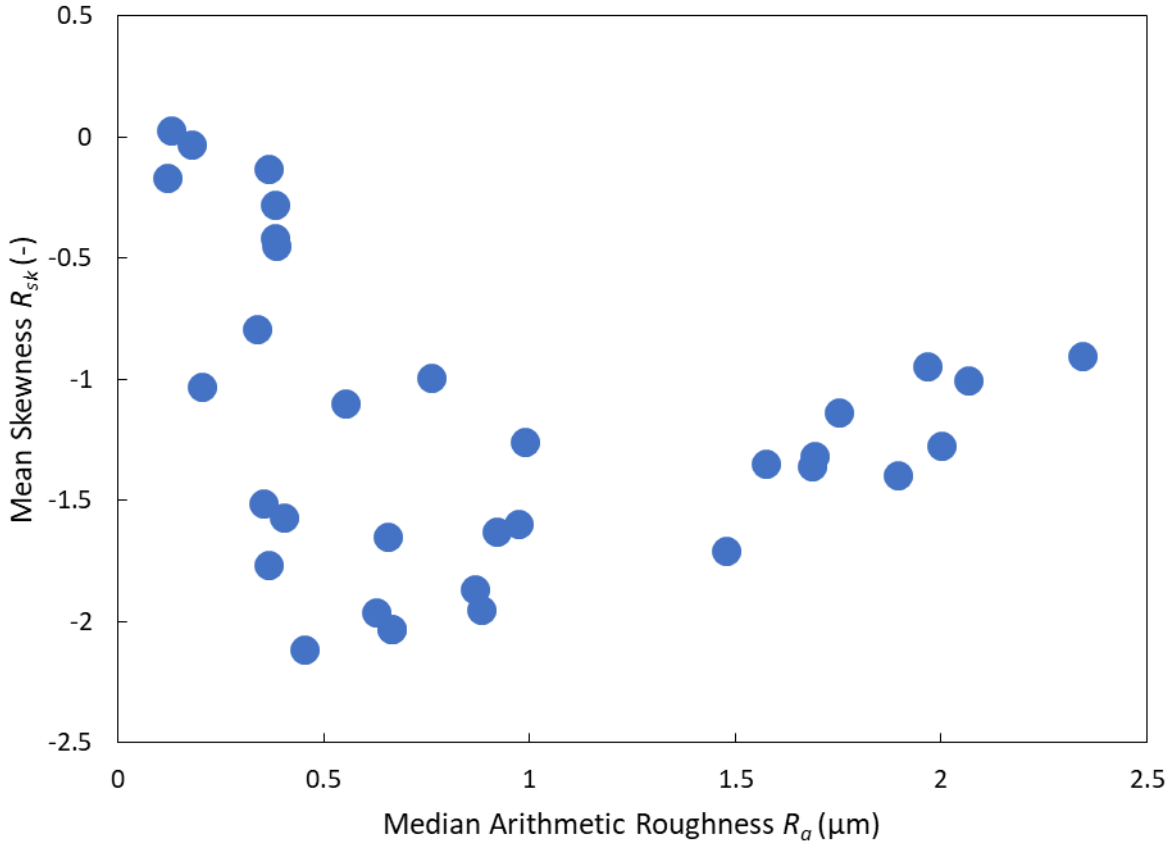

Figure A3.10 *– Median skewness R_{sk} versus median arithmetic roughness R_a.*

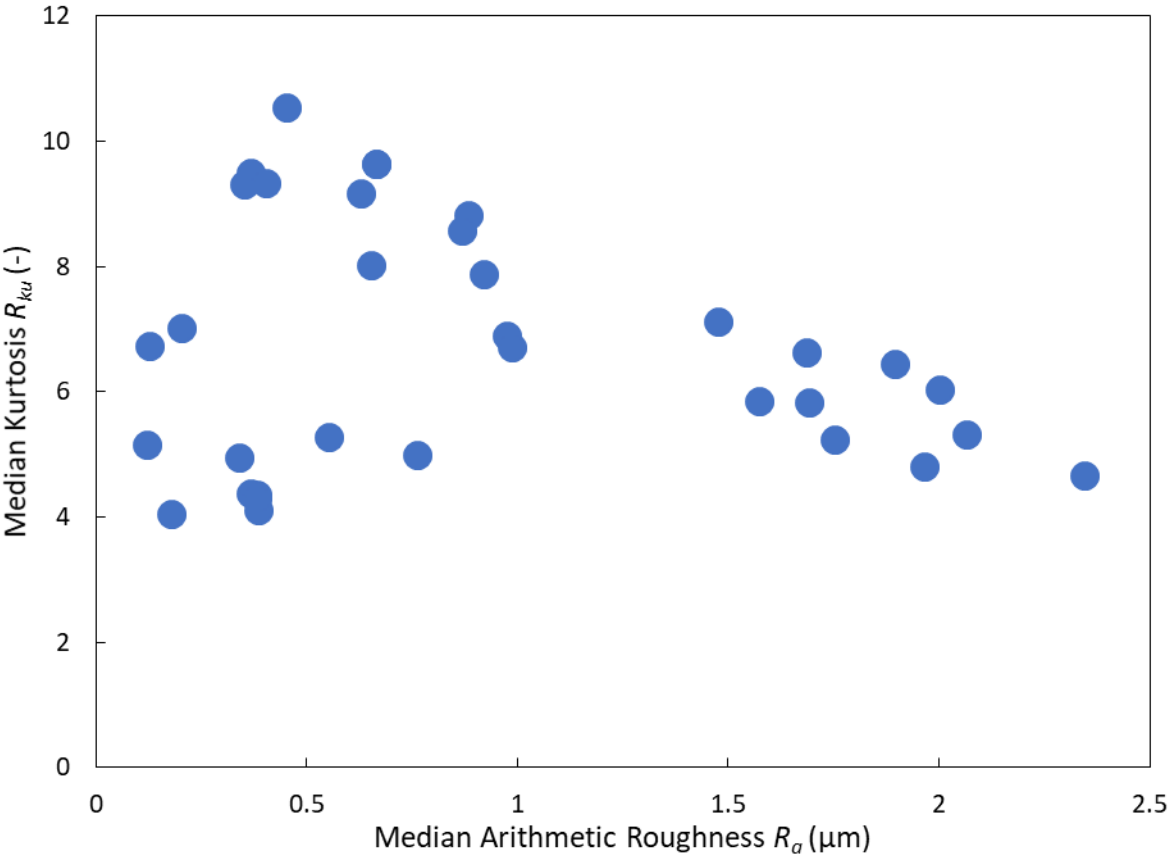

Figure A3.11 *– Median kurtosis R_{ku} versus median arithmetic roughness R_a.*

Table A3.2 *– A comparison of the tensile index and fibre analyser results of MFC produced from Glass H and Glass I, before and after washing out most of the worn media with a 25 µm screen. The %MOP value decreased greatly after screening, and fibre analyser parameters did not change significantly, showing that the screening was effective at removing the worn glass, whilst minimising MFC losses. The tensile index barely changes after screening, showing that the worn glass media in the MFC is not a concern.*

Sample		Media Wear (%MOP)	Tensile Index (Nm/g)	*Lc(n)* (mm)	*Fines B* (%)	*Fibrillation %*
Glass H	Pre-screen	32.8	9.95 ± 0.29	0.144	37.75	5.81
	Post-screen	7.7	9.58 ± 0.32	0.147	38.58	5.81
Glass I	Pre-screen	34.4	9.89 ± 0.43	0.142	37.96	5.7
	Post-screen	9.0	9.97 ± 0.32	0.145	38.97	5.85

Table A3.3 *– The tensile index and fibre analyser results of MFC produced at 3000 kWh/t using smooth glass (Glass A) and rough glass media (Glass F), and smooth glass again, but with the impeller speed increased to match the power draw of the rough glass. The tensile index increases by around 1 Nm/g, between the normal and high power draw smooth glass, and the fibre analyser results develop somewhat. However, even when power draw is increased, the smooth glass results are still much closer to the original values than they are to rough glass, showing that the apparent effect of roughness is mostly not an artefact of a rough media's ability to pull a higher power draw.*

Sample	Average Power Draw (W)	Tensile index (Nm/g)	*Lc(n)* (mm)	*Lc(l)* (mm)	*Fines B* (%)	*Fibrillation %*
Glass A	72	5.91 ± 0.54	0.361	1.25	9.4	2.6
Glass A high power draw	131	7.16 ± 0.29	0.268	0.67	14.9	3.4
Glass F	129	10.10 ± 0.16	0.158	0.257	35.8	5.9

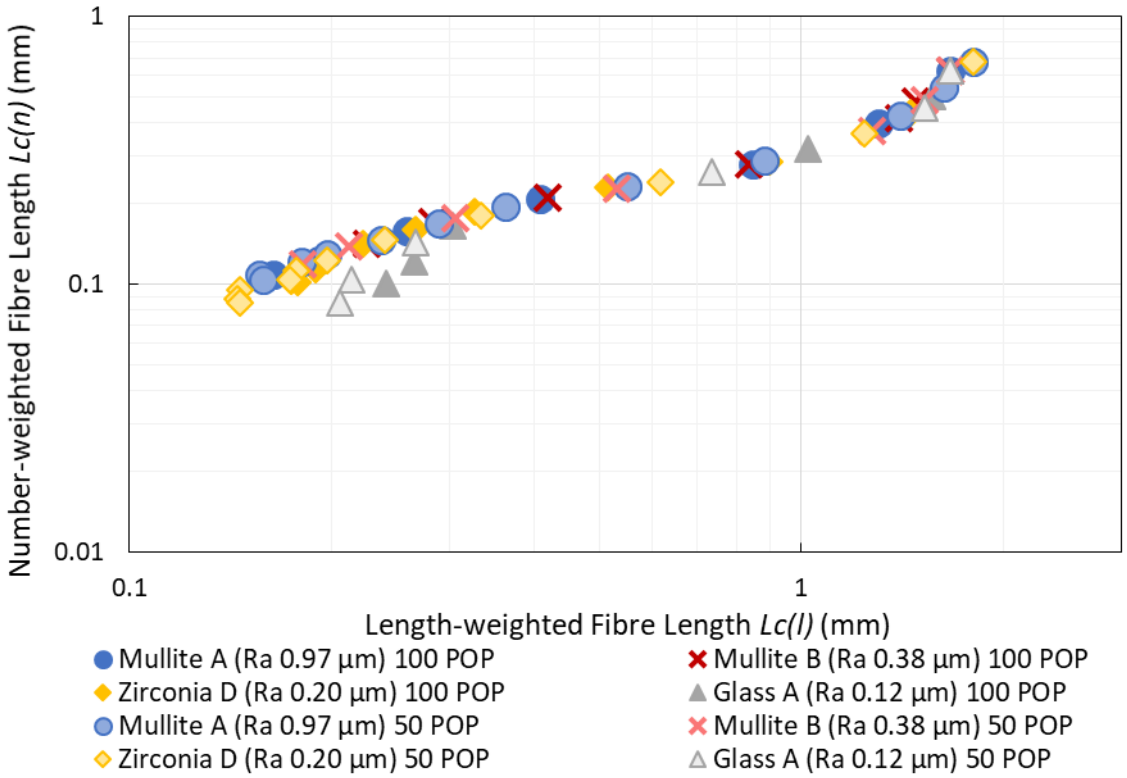

Figure A3.12 *– Number-weighted fibre length versus length-weighted fibre length for all series.*

Figure A3.13 *– DIC Microscopy Image of 100 POP MFC produced with Glass A media (R_a = 0.12 µm) at 12000 kWh/t, showing that some fibres resist breakage, skewing Lc(l) values to higher than they would otherwise be. It is not clear if this is due to the existence of dead zones in the grinder, or if the toughest fibres are able to completely resist grinding from such smooth media.*

A3.2. Estimation of Asperity Numbers and Mineral Particle Numbers

Table A3.4 shows the calculations for the total number of asperities present and the total number of mineral particles present in a 50% POP lab grind. There are several assumptions made in these calculations. Firstly, it is assumed that every media bead is 3 mm in diameter. Secondly, it is assumed that only the *peak asperities* are important, since asperities between peaks are less likely to contact other media. Most media species had a mean peak separation of between 20 µm and 30 µm; in Table A3.4, the calculations assume 20 µm spacing to give an upper bound for asperity number, though the results for the 30 µm spacing are also stated, and were calculated to approximately halve the number of asperities present.

Simple calculations were performed to estimate the number of media beads present in the grind, given a known weight of media, media size, and density, and since media size is known, the surface area of a single bead can easily be calculated. From there, the entire surface area of the media can be found. If the asperities are assumed to be in a square arrangement, with separation distances of their peak spacing, by dividing the total area by the area of a single asperity, the number of asperities can be estimated. This comes to a value of 2.6×10^9 for a peak spacing of 20 µm or 1.2×10^9 for 30 µm spacing.

The mineral specification of IC60 is 60 wt% below 2 µm. The number-average particle size is the value required, but this is not available, and was assumed to be 2 µm. This is expected to give a considerable underestimate of the number of mineral particles present, but for the purposes of the arguments made with these calculations, it is sufficient. From the POP value and mineral density, the dry mineral volume in the grinder was calculated. Then, assuming that all mineral particles were 2 µm diameter spheres, the volume of a single particle was

calculated. Then, dividing total volume by mineral volume yields an estimation of the number of mineral particles present, which came to a value of 1.3×10^{12}.

There are therefore around 500 – 1000 times more mineral particles present as there are roughness asperities in a 50 POP grind. Considering these mineral particles are of the order of a micron in size, it is not a surprise that they have such a strong effect compared to the roughness asperities of degrading liberated fibrils when they are caught alongside the fibrils between two colliding media.

Table A3.4 *– Calculations for the estimation of the total number of asperities present and the total number of mineral particles present in a 50% POP lab grind with a media asperity spacing of 20 µm. For media with an asperity spacing of 30 µm, the asperity concentration is approximately halved, so the ratio of mineral particles to media asperities in that case is 1000.*

Media Asperity Number		**Mineral Particle Number**	
Media size (cm)	0.3	Mineral content (POP)	50%
Single bead volume (cm^3)	0.0141	Mineral content (g/g fibre)	1
Total media mass in grinder (g)	1411	Fibre present (g)	14.8
Media density (g/cm^3)	2.7	Total dry mineral content (g)	14.8
Total media volume (cm^3)	523	Mineral density (g/cm^3)	2.7
Number of media present	36966	Total mineral volume (cm^3)	5.48
Surface area of single bead (cm^2)	0.2827	Average mineral size (µm)	2
Total surface area (cm^2)	10450	Average mineral size (cm)	0.0002
Average width of asperity (cm)	0.002	Mineral particle volume (cm^3)	4.19×10^{-12}
Average asperity area (cm^2)	0.000004		
Number of asperities present	**2.61×10^9**	**Total mineral particles present**	**1.31×10^{12}**
Ratio of mineral particles to media asperities		**500**	

APPENDIX A4 – SUPPLEMENTARY DATA FOR CHAPTER 6

A4.1. Additional Graphs for Section 6.2

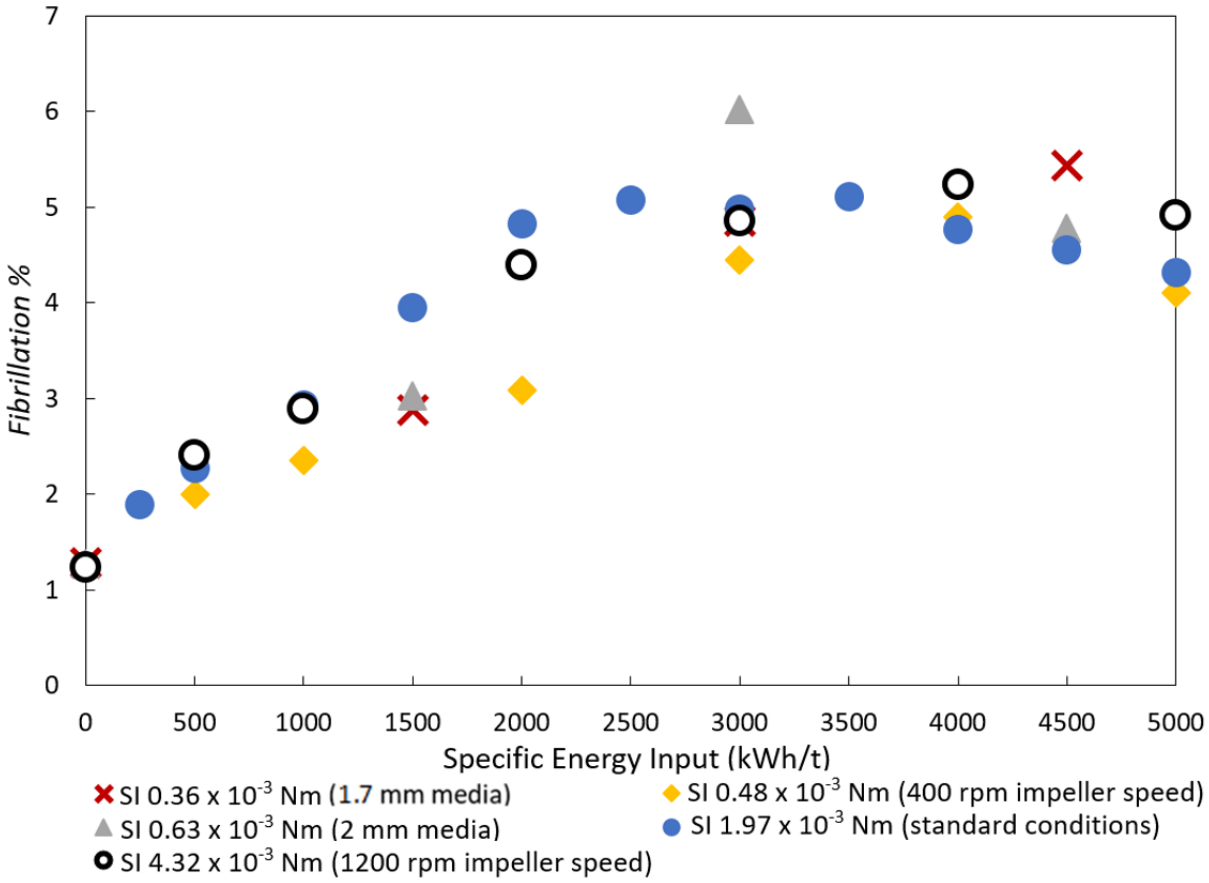

Figure A4.1 *– Fibrillation % versus energy input for the five Mullite A energy sweep series investigated in Chapter 4.*

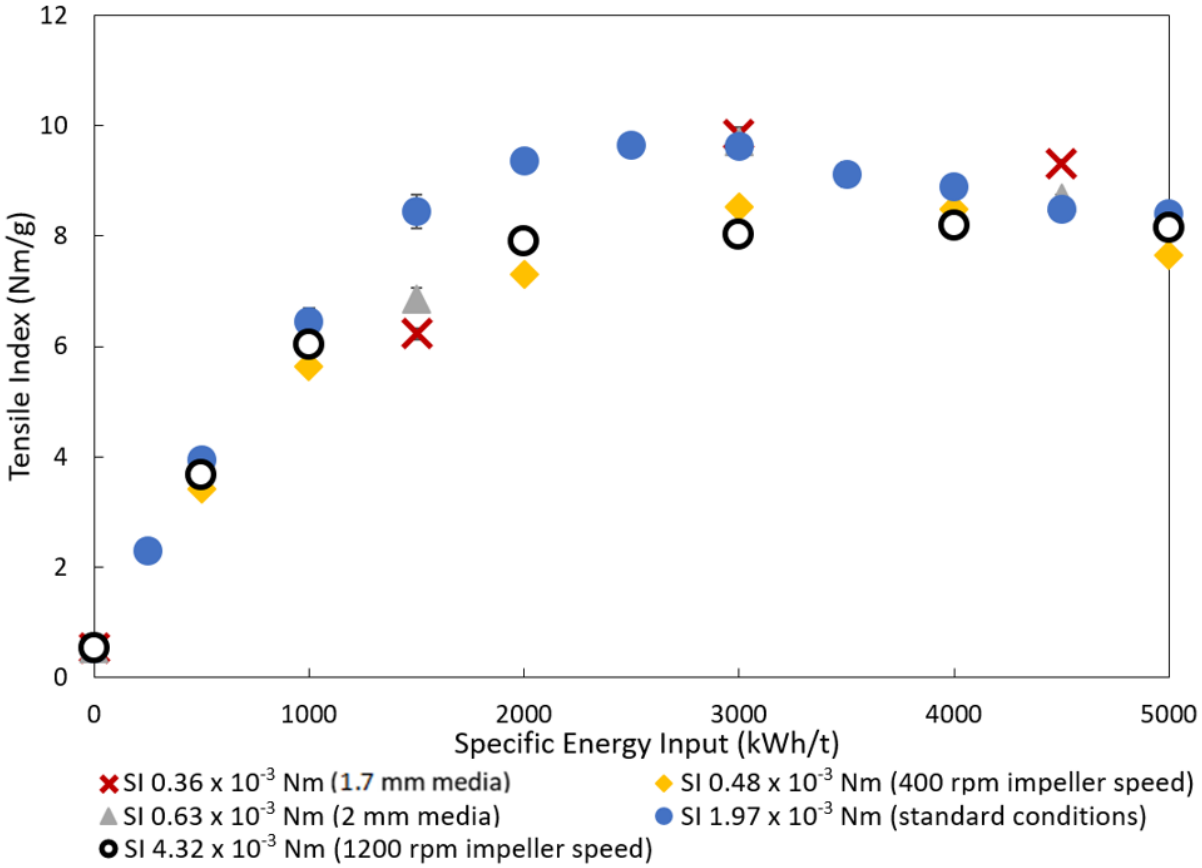

Figure A4.2 *– Tensile index versus energy input for the five Mullite A energy sweep series investigated in Chapter 4.*

A4.2. Alternative Explanations for the Advantages of Finer Media

A4.2.1. Stress Number

Stress number is defined using Equation 2.2, and is theoretically expected to be proportional to the impeller speed and grinding time, and inversely proportional to the square of the media diameter. Since Equation 2.2 is a proportionality, evaluating the right hand side does not give a *real* stress number value, and instead gives a *relative* stress number, which was calculated for all grinds and plotted against stress intensity in Figure A4.3. One can see that for a given stress intensity, finer media has a much higher stress number. However, this is contradicted by stress intensity theory itself, where it is expected that energy input is proportional to the product of stress intensity and stress number. If true, one can manipulate Equations 2.2 and 2.3 to obtain a proportionality for power draw:

$$SI \propto SE \propto SE_{GM} = d_{GM}^3 v_t^2 \rho_{GM}$$

$$SN \propto \frac{\varphi_{GM}(1-\varepsilon)}{\big(1-\varphi_{GM}(1-\varepsilon)\big)c_V} \frac{nt}{{d_{GM}}^2}$$

As φ_{GM}, ε, and c_V are constant:

$$SN \propto \frac{nt}{{d_{GM}}^2} \ldots [A4.1]$$

The impeller revolution speed n is proportional to tip speed v_t:

$$SN \propto \frac{v_t t}{{d_{GM}}^2} \ldots [A4.2]$$

Therefore:

$$SI \cdot SN \propto d_{GM}^3 v_t^2 \rho_{GM} \frac{v_t t}{{d_{GM}}^2} \ldots [A4.3]$$

As, theoretically, $SI \cdot SN \propto E$, where E is energy input:

$$E \propto d_{GM} v_t^3 \rho_{GM} t \ldots [A4.4]$$

Power, P, is the energy input divided by the grind time, t. Therefore:

$$P \propto \rho_{GM} d_{GM} v_t^3 \ldots [A4.5]$$

Although the notion that power draw is much more sensitive to tip speed than media size is supported by Figure 6.5, the proportionalities stated, i.e. that power is proportional to the *cube* of tip speed, is not matched by the linear proportionality observed. It appears that in this system, some of the assumptions used in the stress intensity or stress number calculations are inaccurate. Consequently, the author is not confident in this mechanism as the cause for the disparities. It is unrealistic to expect 'transfer coefficients' to vary by a factor of up to 8, under

reasonable conditions where the theory is supposed to hold. Due to these doubts, whenever differences in 'stress number' are claimed, the actual values as defined by Equation 2.2 should not be considered reliable, but one can still say, for example, that stress number is higher when media size is lower due to the proportionalities in this equation.

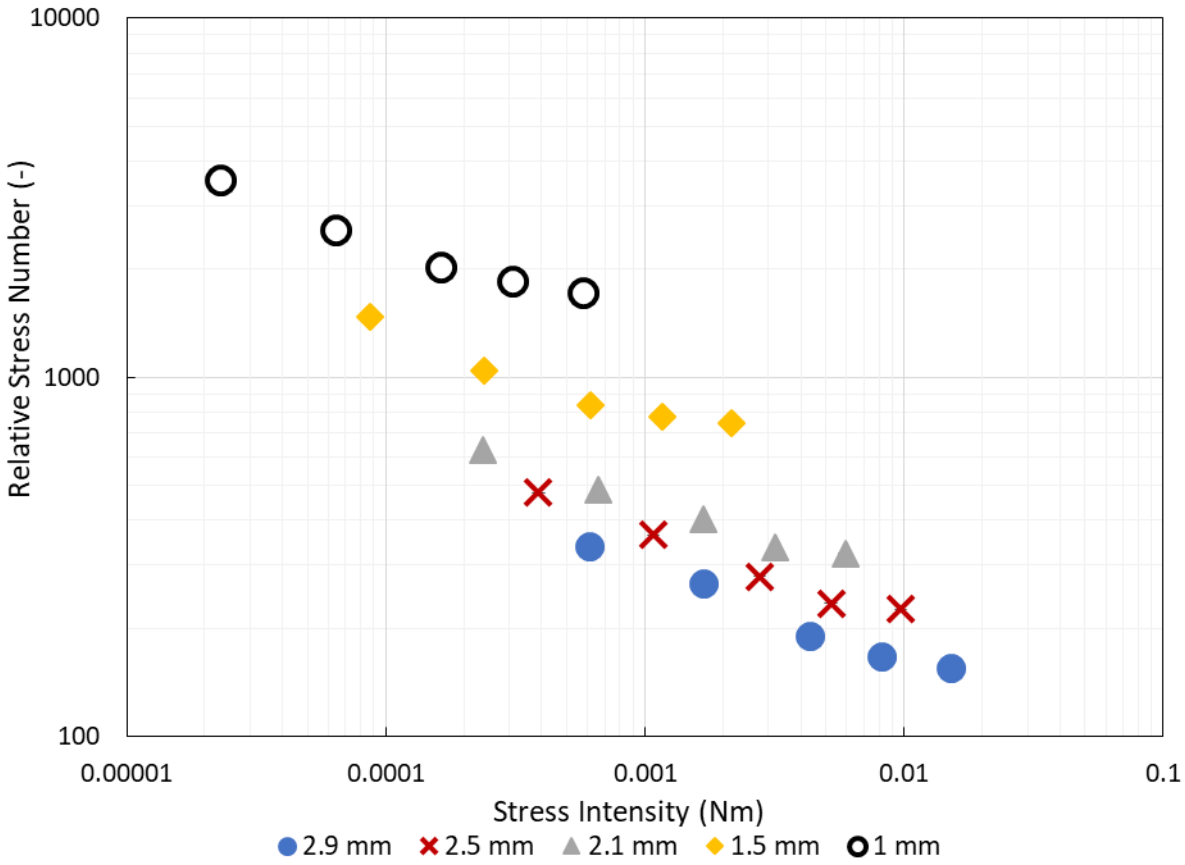

Figure A4.3 *– Relative stress number versus stress intensity for each grind.*

A4.2.2. Viscous Dampening

A higher viscosity dampens media motion, reducing effective stress intensity. This can be calculated using Equation 2.6, but requires two unknowns; the maximum separation distance required for comminution, x, and the charge viscosity, η. As is discussed in Section 8.1, a reasonable estimate for x is 4 µm, and a liberal estimation for charge viscosity of 0.2 Pas is used. In reality, this is likely to be somewhat lower, since shear rates are likely much higher in the high intensity grinding zone than those for which this viscosity was measured, and with

increasing grinding progress, high shear viscosity is expected to decrease (supported by PEPT observations by Riley that media velocity increases with grinding progress[73], demonstrating a reduction in dampening).

Using these assumptions, Equation 2.6 is evaluated for each grind, and plotted against stress intensity as Figure A4.4. This at first looks encouraging, as at given stress intensities, coarser media (at lower impeller speed) suffer from more viscous dampening than finer media (at higher impeller speed), which is in the order needed to explain these observations. However, when multiplying this factor by the stress intensity and replotting against fibre length (Figure A4.5), only minor differences are seen on log-log scale, except a stretched tail at very low stress intensities. This is despite the belief that the effect of viscous dampening is *overestimated* here. This role of viscosity appears insufficient as an explanation, though likely has some contribution to the discrepancies.

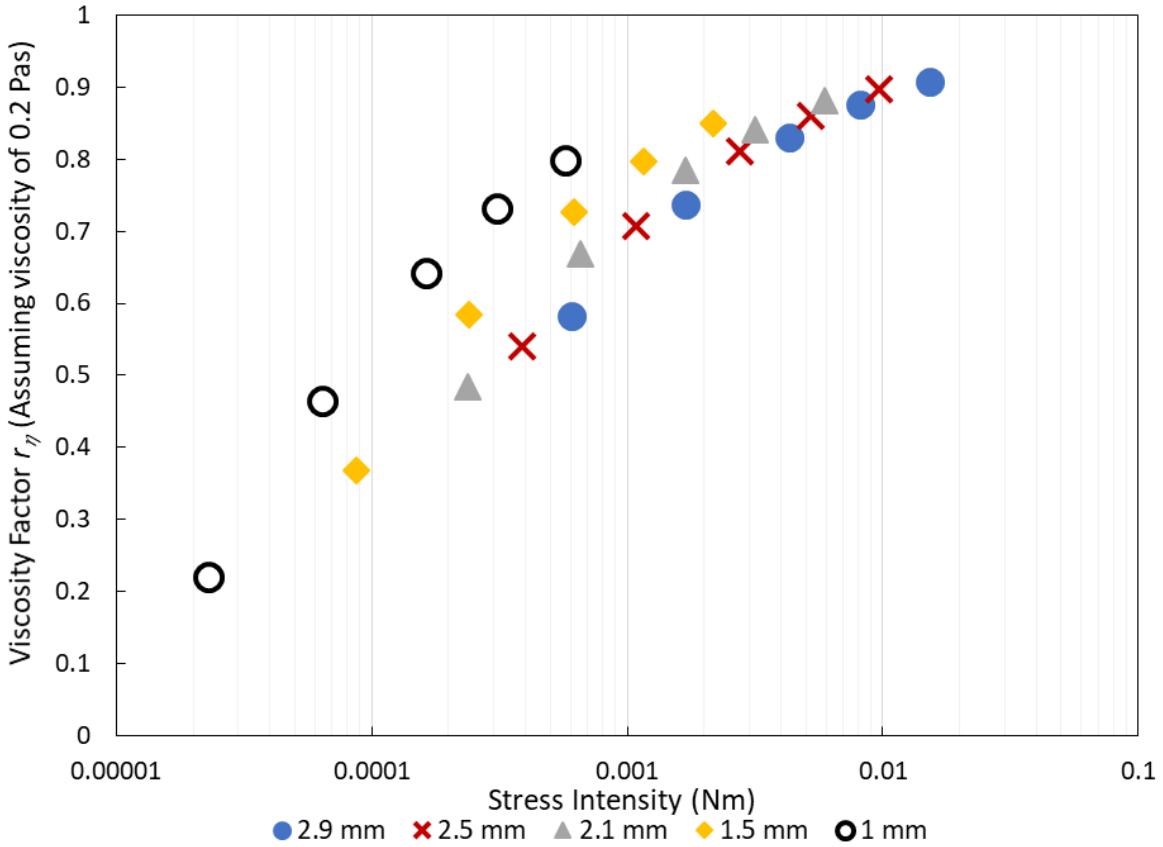

Figure A4.4 *– Viscosity factor versus stress intensity for the five media sizes.*

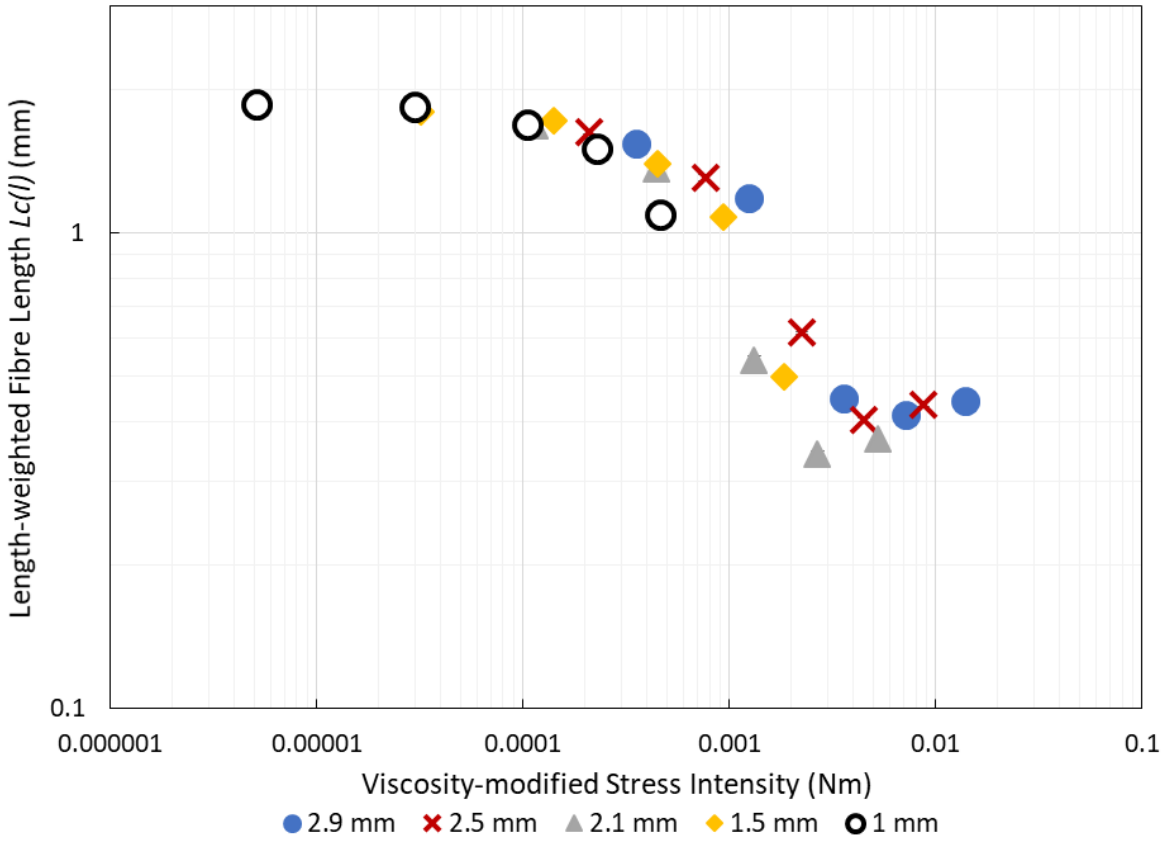

Figure A4.5 *– Lc(l) versus viscosity-modified stress intensity for the five media sizes.*

A4.2.3. Media Suspension

The other viscosity-related mechanism which may differ between media sizes is a difference in media suspension. Poor media suspension could be expected to lower grinding efficiency by locally increasing MVC and wasting more energy with increased continuous media-media contact, and perhaps this increased intimate media-media contact increases the damage to liberated fibrils caused by the mineral particles. Fine media at higher impeller speeds are expected to be much easier to suspend than coarse media at low impeller speeds. A form of Stokes' Law can be used to calculate settling velocity, u_s:

$$u_s = \frac{d_{GM} g(\rho_{GM} - \rho_s)}{18\eta} \dots [A4.6]$$

where g is acceleration due to gravity, and ρ_s is suspension density. The ratio of tip speed to the settling velocity is expected to be indicative of the tendency of the media to be fluidised. This ratio is plotted against stress intensity as Figure A4.6; all grinds give values much greater than 1, indicating suspension, but this should not be considered at face-value; firstly, the typical media velocity is substantially lower than the tip speed, and only a minor component of this is translated in the vertical direction, and secondly, the high-shear viscosity of MFC is probably lower than the value assumed. Failures in these assumptions should not affect the relative order of each media species, however, and the results are striking, with finer media having a much lower tendency to settle than coarser media at a given stress intensity. This is therefore a *plausible* mechanism to explain some inaccuracies of the stress intensity model in this case, and may especially explain the poor performance at high energy inputs of the 400 rpm series in Section 4.4.

However, once a media is suspended, increasing this ratio to make it *more* suspended is not expected to further help with efficiency, as the alleged detrimental effect of poor suspension has already been removed. Consider Figure 6.6 at stress intensities of 6 x 10^{-4} Nm, where all sizes except 1 mm media seem to coincide; if this suspension argument is assumed to be the complete explanation, one has to believe that *only* the 1 mm media at 1500 rpm is adequately suspended, and even the 1.5 mm media at 800 rpm is not. Even with larger media, visual observations show that the charge is clearly fluidised at 800 rpm, so the author does not accept this explanation.

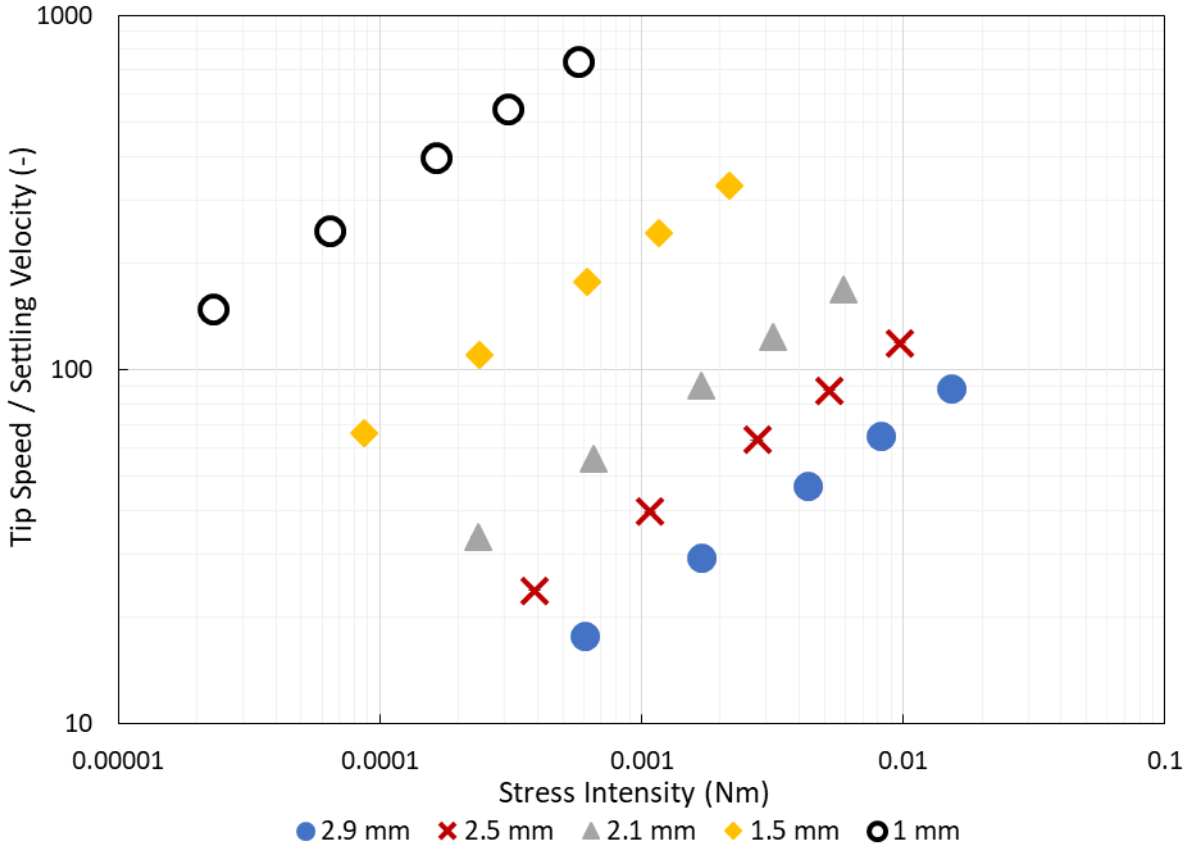

Figure A4.6 *– Ratio of the tip speed to the settling velocity (assuming a viscosity of 0.2 Pas) versus stress intensity for the five media sizes.*

A4.3. Grind Operating Conditions used in Section 6.4

Table A4.1 *– Parameters of grinds investigating the effect of media roughness carried out in Section 5.2, also used as data for Section 6.4.*

Media Species	Energy Input (kWh/t)	Media Density (g/cm^3)	Media Size (mm)	Impeller Speed (rpm)	Stress Intensity (x10^{-3}) (Nm)	Surface Roughness R_a (µm)
Glass A	3000	2.48	3.11	800	2.21	0.12
Glass A	3000	2.48	3.11	1050	3.81	0.12
Zirconia A	3000	6.05	2.77	800	3.83	0.13
Zirconium Silicate C	3000	4.06	2.87	800	2.83	0.18
Zirconia D	3000	6.04	2.89	800	4.32	0.20
Zirconia C	3000	6.05	2.77	800	3.83	0.32
Zirconia E	3000	6.05	2.79	800	3.91	0.34
Glass J	3000	2.48	3.11	800	2.21	0.35
Zirconium Silicate B	3000	4.17	3.23	800	4.17	0.37
Zirconia B	3000	6.05	2.77	800	3.83	0.38
Zirconium Silicate A	3000	4.05	2.89	800	2.88	0.38
Mullite B	3000	2.80	2.96	800	2.15	0.38
Glass K	3000	2.48	3.11	800	2.21	0.45
Alumina	3000	3.63	3.31	800	3.89	0.55
Glass G	3000	2.48	3.11	800	2.21	0.63
Glass L	3000	2.48	3.11	800	2.21	0.67
Mullite C	3000	2.71	3.03	800	2.23	0.76
Glass E	3000	2.48	3.11	800	2.21	0.88
Glass F	3000	2.48	3.11	800	2.21	0.92
Mullite A	3000	2.69	2.91	800	1.97	0.97
Glass I	3000	2.48	3.11	800	2.21	1.48
Glass H	3000	2.48	3.11	800	2.21	1.57
Glass D	3000	2.48	3.11	800	2.21	1.75
Glass B	3000	2.48	3.11	800	2.21	1.90
Glass C	3000	2.48	3.11	800	2.21	2.00
Glass A	1000	2.48	3.11	800	2.21	0.12
Zirconia A	1000	6.05	2.77	800	3.83	0.13
Zirconium Silicate C	1000	4.06	2.87	800	2.83	0.18
Zirconia D	1000	6.04	2.89	800	4.32	0.20
Zirconia C	1000	6.05	2.77	800	3.83	0.32
Zirconia E	1000	6.05	2.79	800	3.91	0.34
Glass K	1000	2.48	3.11	800	2.21	0.37
Zirconium Silicate B	1000	4.17	3.23	800	4.17	0.37
Zirconium Silicate A	1000	4.05	2.89	800	2.88	0.38
Mullite B	1000	2.80	2.96	800	2.15	0.38
Glass J	1000	2.48	3.11	800	2.21	0.40
Alumina	1000	3.63	3.31	800	3.89	0.55
Glass G	1000	2.48	3.11	800	2.21	0.65
Glass L	1000	2.48	3.11	800	2.21	0.67
Mullite C	1000	2.71	3.03	800	2.23	0.76
Glass E	1000	2.48	3.11	800	2.21	0.87
Mullite A	1000	2.69	2.91	800	1.97	0.97
Glass F	1000	2.48	3.11	800	2.21	0.99
Glass B	1000	2.48	3.11	800	2.21	1.69
Glass I	1000	2.48	3.11	800	2.21	1.69
Glass H	1000	2.48	3.11	800	2.21	1.97
Glass C	1000	2.48	3.11	800	2.21	2.07
Glass D	1000	2.48	3.11	800	2.21	2.34

Table A4.2 *– Parameters of grinds investigating stress intensity, carried out in Section 6.3, also used as data for Section 6.4.*

Media Species	Energy Input (kWh/t)	Media Density (g/cm^3)	Media Size (mm)	Impeller Speed (rpm)	Stress Intensity (x 10^{-3}) (Nm)	Surface Roughness R_a (µm)
Zirconia D	3000	5.99	0.97	300	0.02	0.20
Zirconia D	3000	5.99	0.97	500	0.06	0.20
Zirconia D	3000	6.04	1.51	300	0.09	0.20
Zirconia D	3000	5.99	0.97	800	0.16	0.20
Zirconia D	3000	6.04	2.11	300	0.24	0.20
Zirconia D	3000	6.04	1.51	500	0.24	0.20
Zirconia D	3000	5.99	0.97	1100	0.31	0.20
Zirconia D	3000	6.02	2.49	300	0.39	0.20
Zirconia D	3000	5.99	0.97	1500	0.57	0.20
Zirconia D	3000	6.04	2.89	300	0.61	0.20
Zirconia D	3000	6.04	1.51	800	0.61	0.20
Zirconia D	3000	6.04	2.11	500	0.66	0.20
Zirconia D	3000	6.02	2.49	500	1.08	0.20
Zirconia D	3000	6.04	1.51	1100	1.16	0.20
Zirconia D	3000	6.04	2.89	500	1.69	0.20
Zirconia D	3000	6.04	2.11	800	1.69	0.20
Zirconia D	3000	6.04	1.51	1500	2.16	0.20
Zirconia D	3000	6.02	2.49	800	2.76	0.20
Zirconia D	3000	6.04	2.11	1100	3.20	0.20
Zirconia D	3000	6.04	2.89	800	4.32	0.20
Zirconia D	3000	6.04	2.89	800	4.32	0.20
Zirconia D	3000	6.02	2.49	1100	5.22	0.20
Zirconia D	3000	6.04	2.11	1500	5.96	0.20
Zirconia D	3000	6.04	2.89	1100	8.17	0.20
Zirconia D	3000	6.02	2.49	1500	9.70	0.20
Zirconia D	3000	6.04	2.89	1500	15.19	0.20

Table A4.3 *– Additional grinds carried out for Section 6.4, to supplement the data from Table A4.1 and A4.2.*

Media Species	Energy Input (kWh/t)	Density (g/cm^3)	Media Size (mm)	Impeller Speed (rpm)	Stress Intensity ($x\ 10^{-3}$) (Nm)	Surface Roughness R_a (µm)
Glass A	3000	2.48	0.91	800	0.06	0.12
Mullite A	3000	2.69	1.66	400	0.09	0.97
Glass A	3000	2.48	0.91	1200	0.12	0.12
Mullite A	3000	2.69	1.66	800	0.36	0.97
Glass A	3000	2.48	1.81	800	0.43	0.12
Glass A	3000	2.48	3.11	400	0.55	0.12
Zirconium Silicate A	3000	4.05	2.89	400	0.72	0.38
Alumina	3000	3.63	3.31	400	0.97	0.55
Zirconia A	3000	6.05	2.23	800	2.04	0.13
Mullite D	3000	2.74	3.45	800	3.34	0.61
Zirconia F	3000	6.2	2.93	800	4.63	0.27
Mullite A	3000	2.69	2.91	1500	6.93	0.97
Glass A	3000	2.48	3.11	1500	7.77	0.12
Zirconium Silicate A	3000	4.05	2.89	1500	10.13	0.38
Alumina	3000	3.63	3.31	1500	13.69	0.55
Zirconia D	1000	5.99	0.97	300	0.02	0.20
Zirconia D	1000	6.04	2.11	300	0.24	0.20
Zirconia D	1000	5.99	0.97	1500	0.57	0.20
Zirconia D	1000	6.04	2.89	300	0.61	0.20
Zirconia D	1000	6.04	1.51	1100	1.16	0.20
Mullite D	1000	2.74	3.45	800	3.34	0.61
Zirconia D	1000	6.04	2.89	1500	15.19	0.20

A4.4. Additional Graphs for Section 6.4

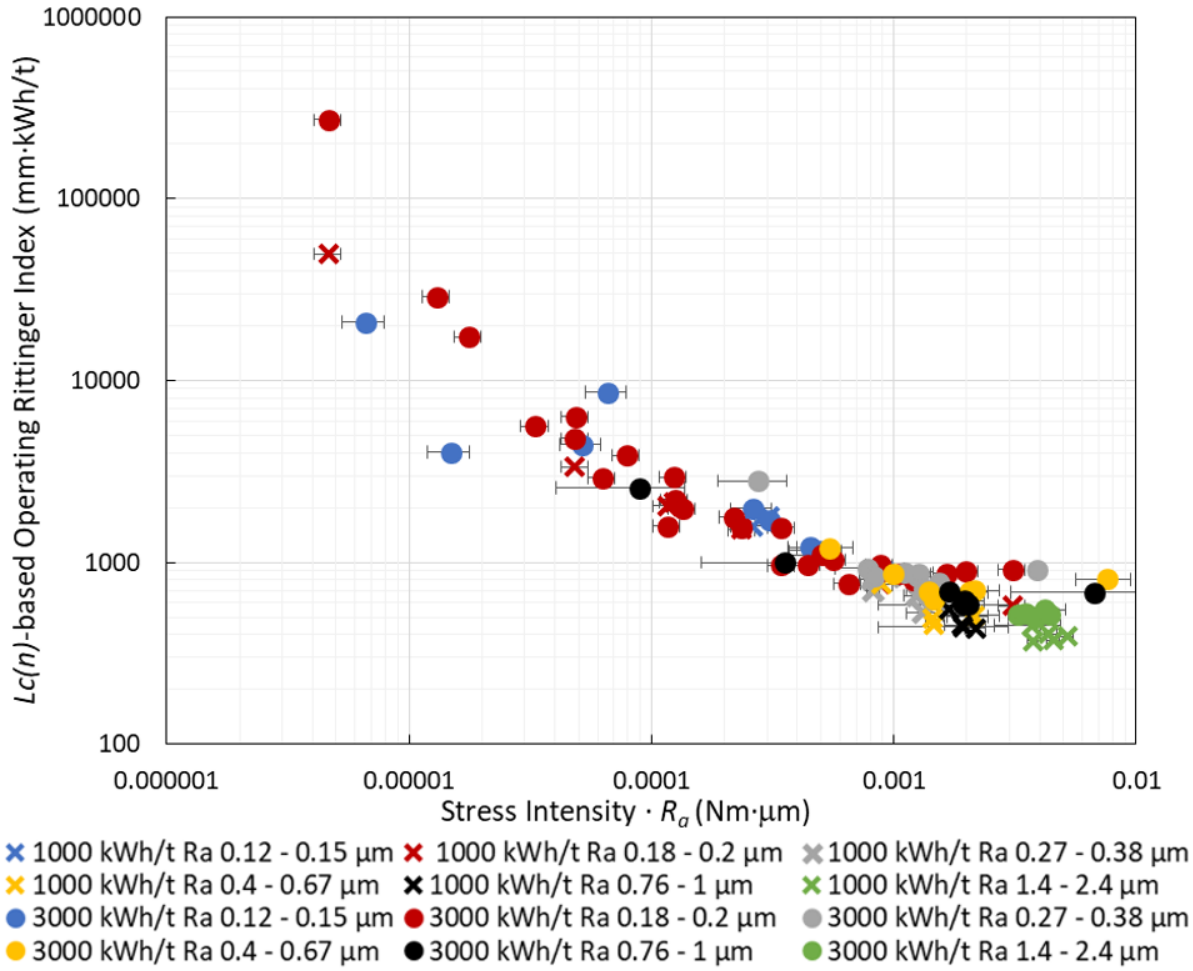

Figure A4.7 *– Lc(n)-based $K_{R,Op}$ versus the product of stress intensity and surface roughness at 1000 kWh/t and 3000 kWh/t for media of various surface roughness values.*

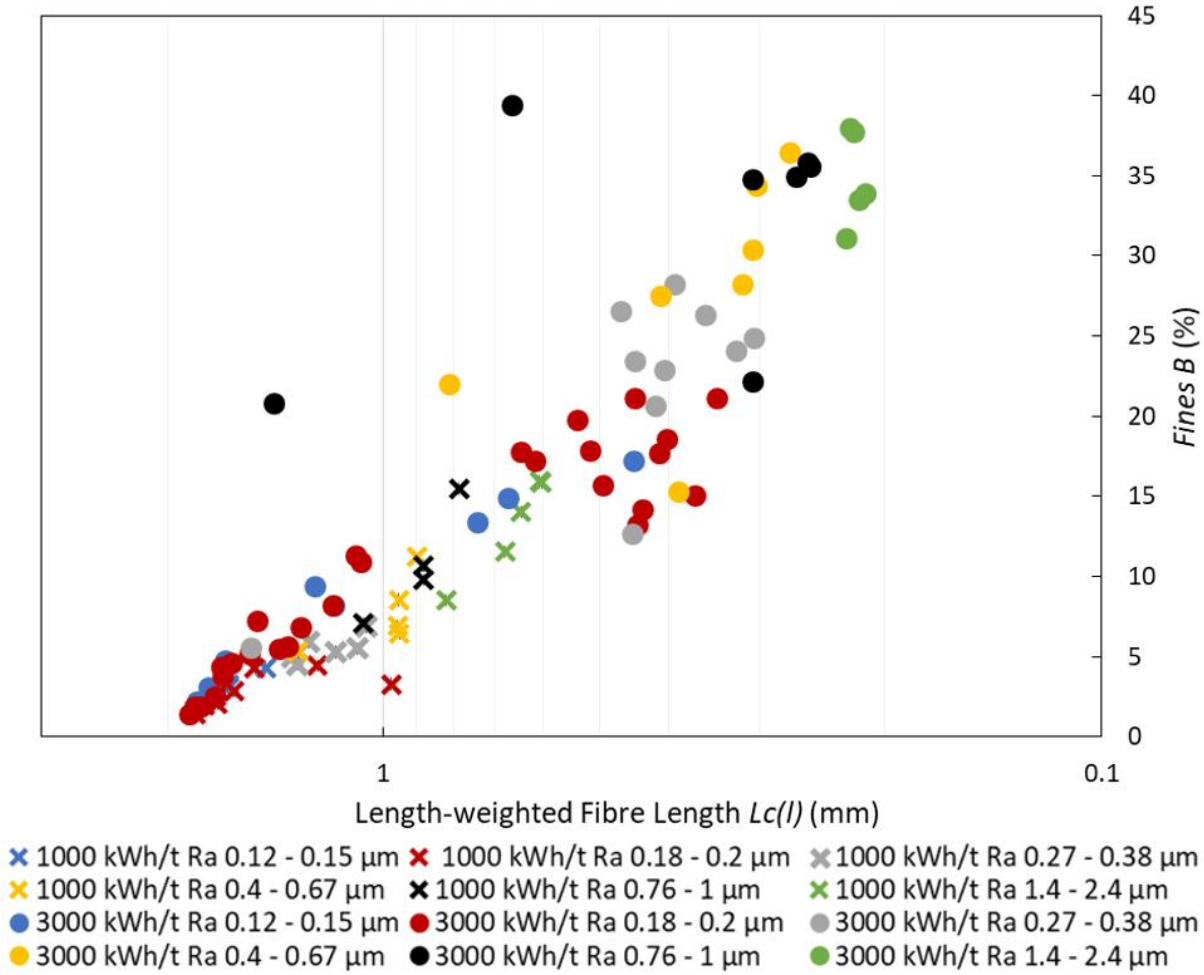

Figure A4.8 *– Fines B content versus Lc(l) for 1000 kWh/t and 3000 kWh/t grinds of various stress intensities and media roughnesses.*

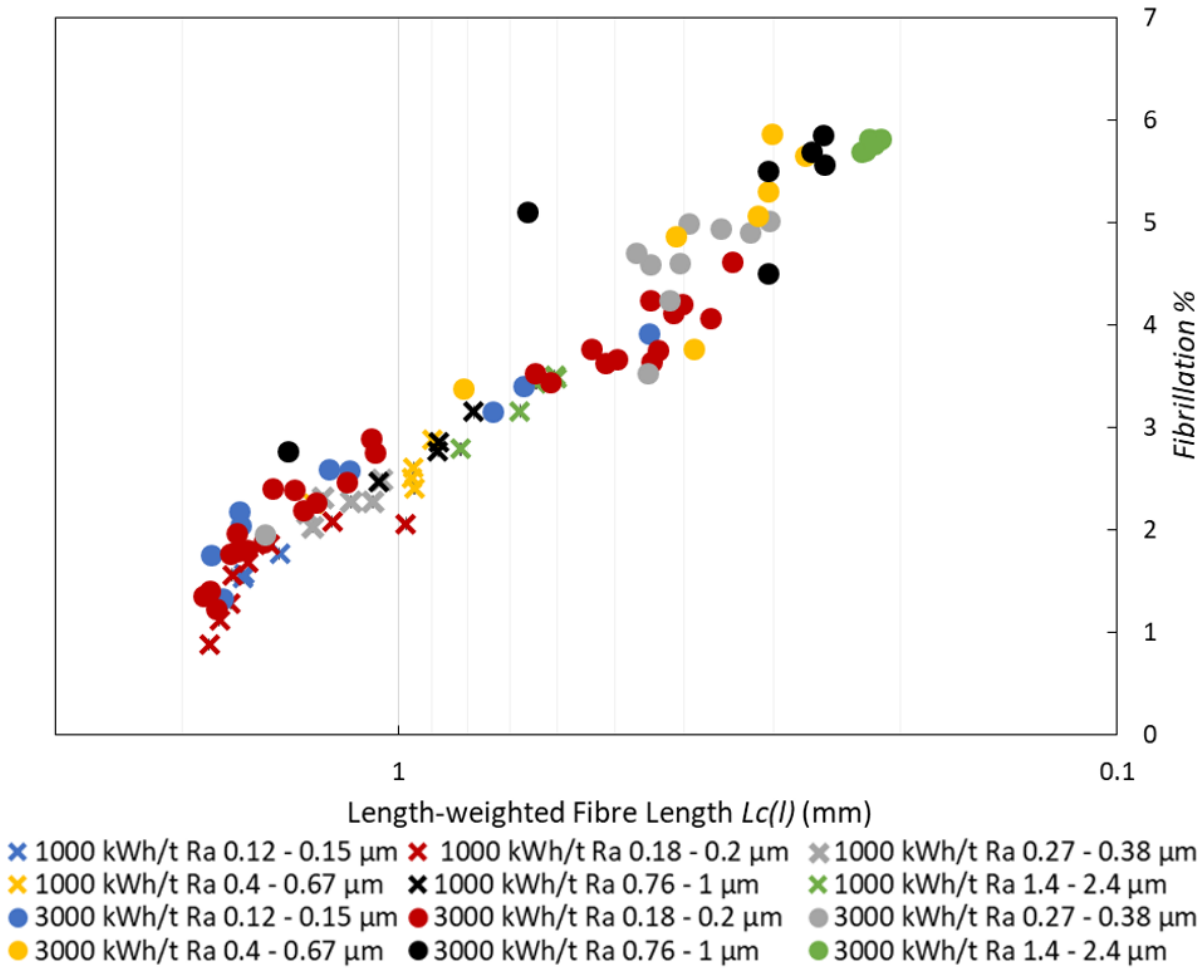

Figure A4.9 *– Fibrillation % versus Lc(l) for 1000 kWh/t and 3000 kWh/t grinds of various stress intensities and media roughnesses.*

APPENDIX A5 – SUPPLEMENTARY DATA CHAPTER 7

A5.1. Supplementary Graphs and Tables for Chapter 7

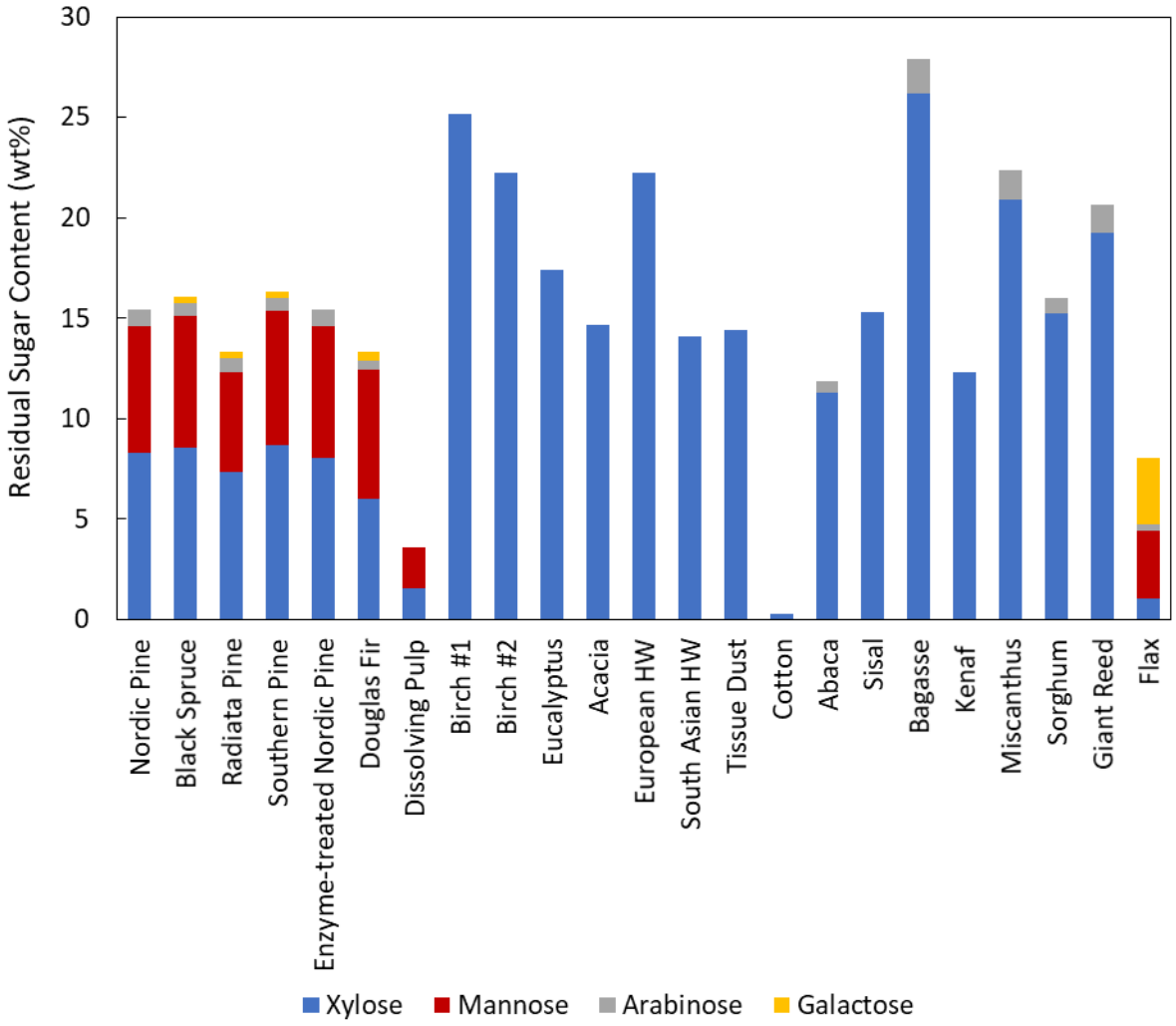

Figure A5.1 *– Constituent monomer sugars of each fibre species investigated.*

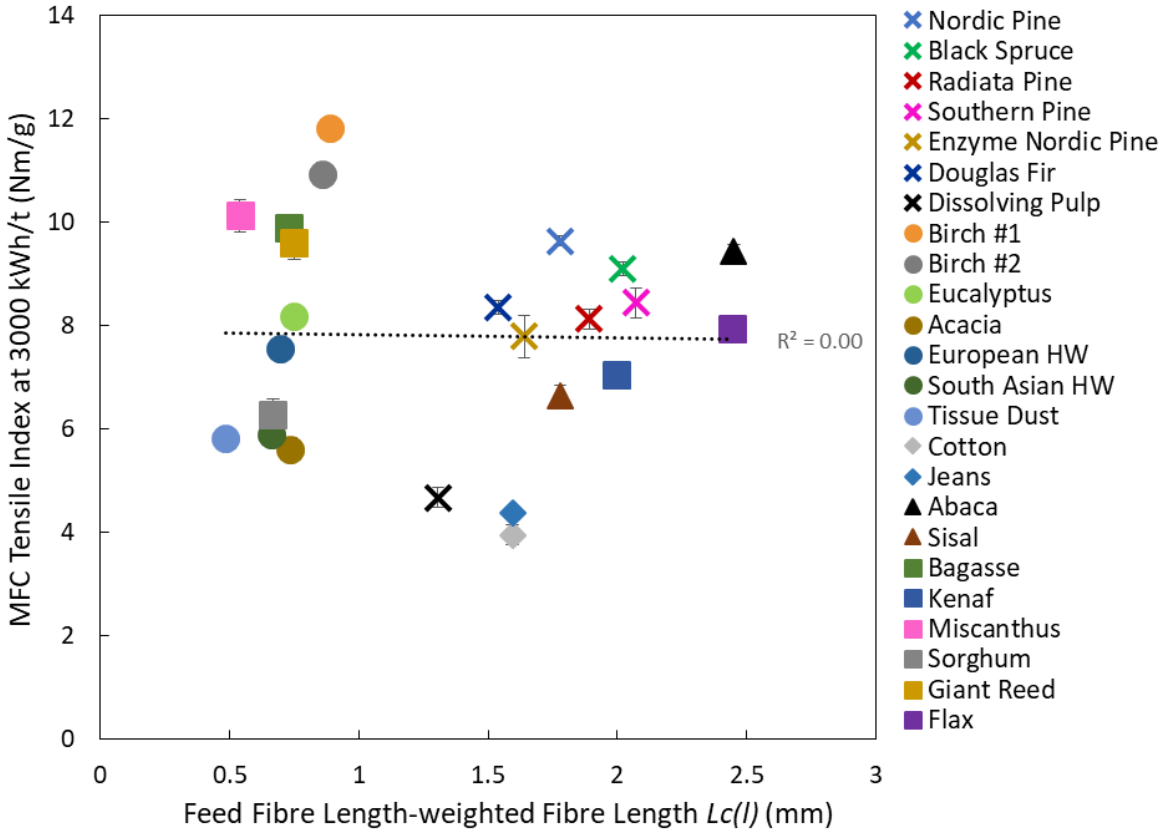

Figure A5.2 *– MFC tensile index versus feed fibre length-weighted fibre length for various fibre species.*

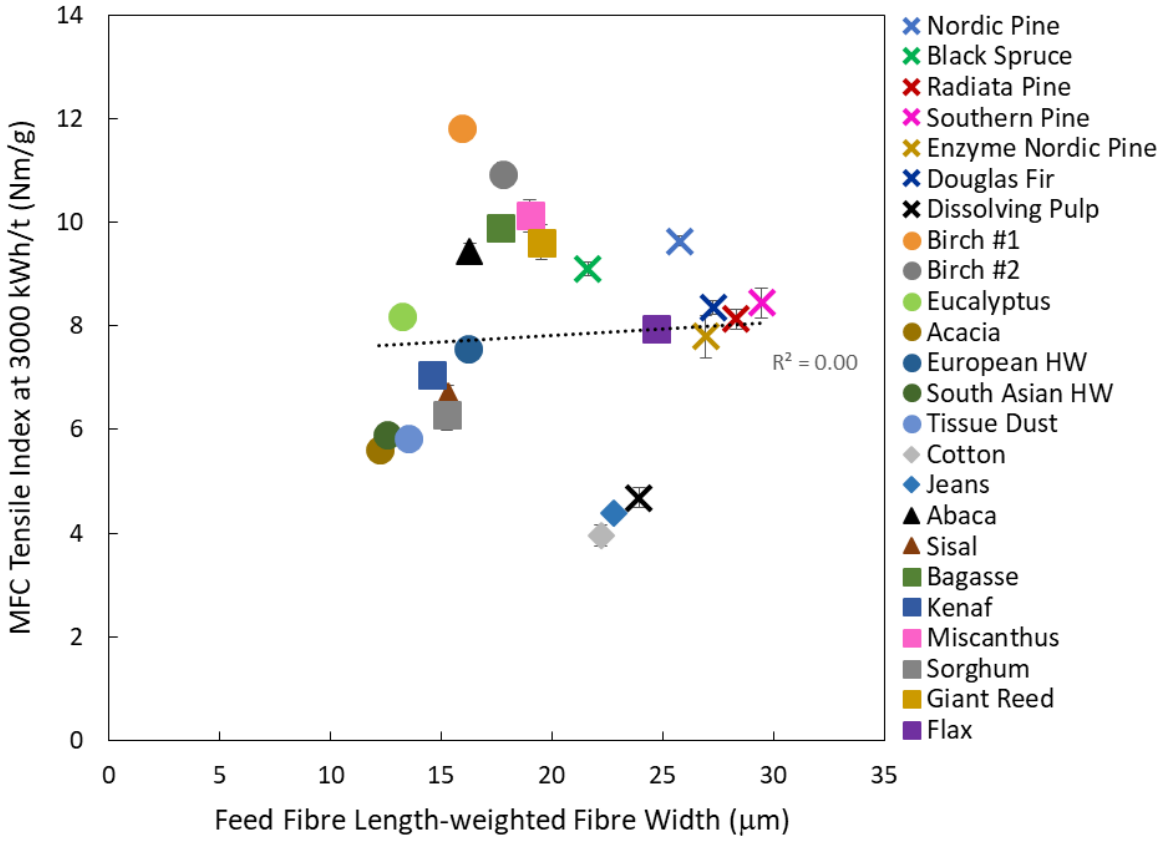

Figure A5.3 *– MFC tensile index versus feed fibre length-weighted fibre width for various fibre species.*

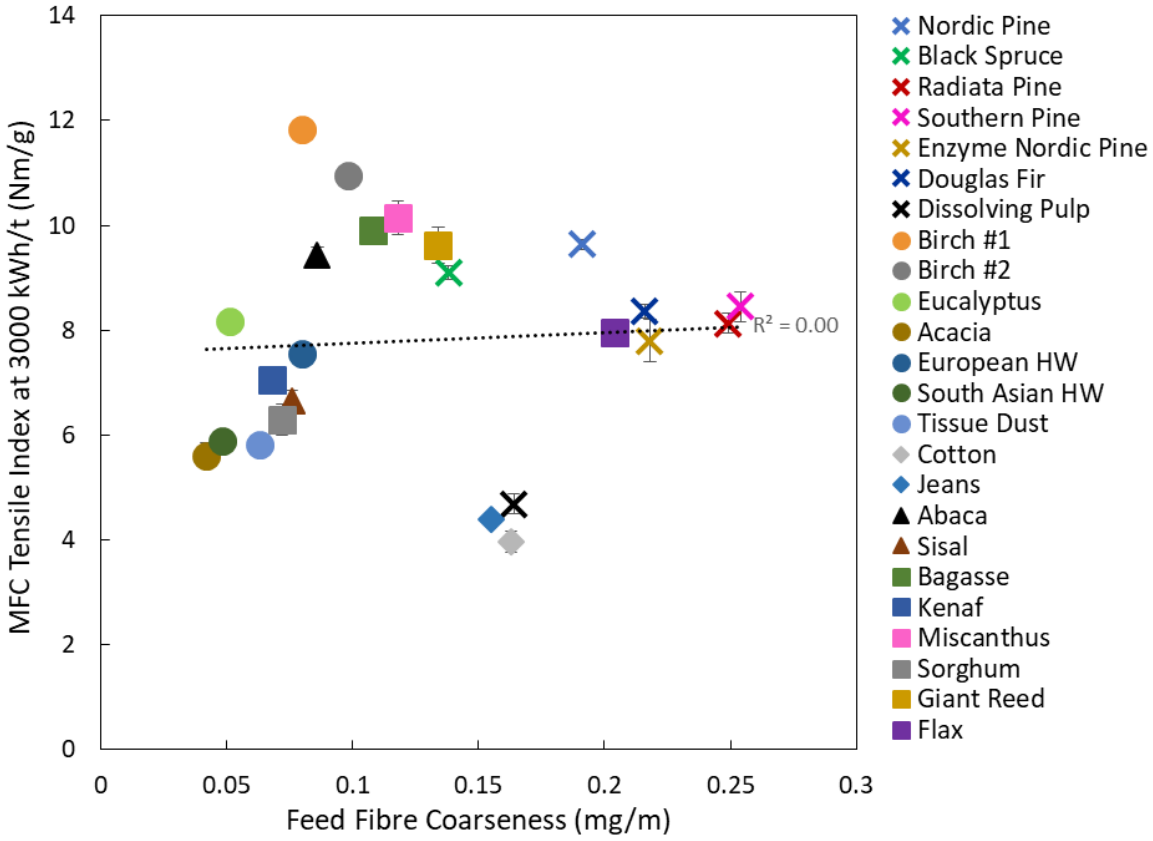

Figure A5.4 *– MFC tensile index versus feed fibre coarseness for various fibre species.*

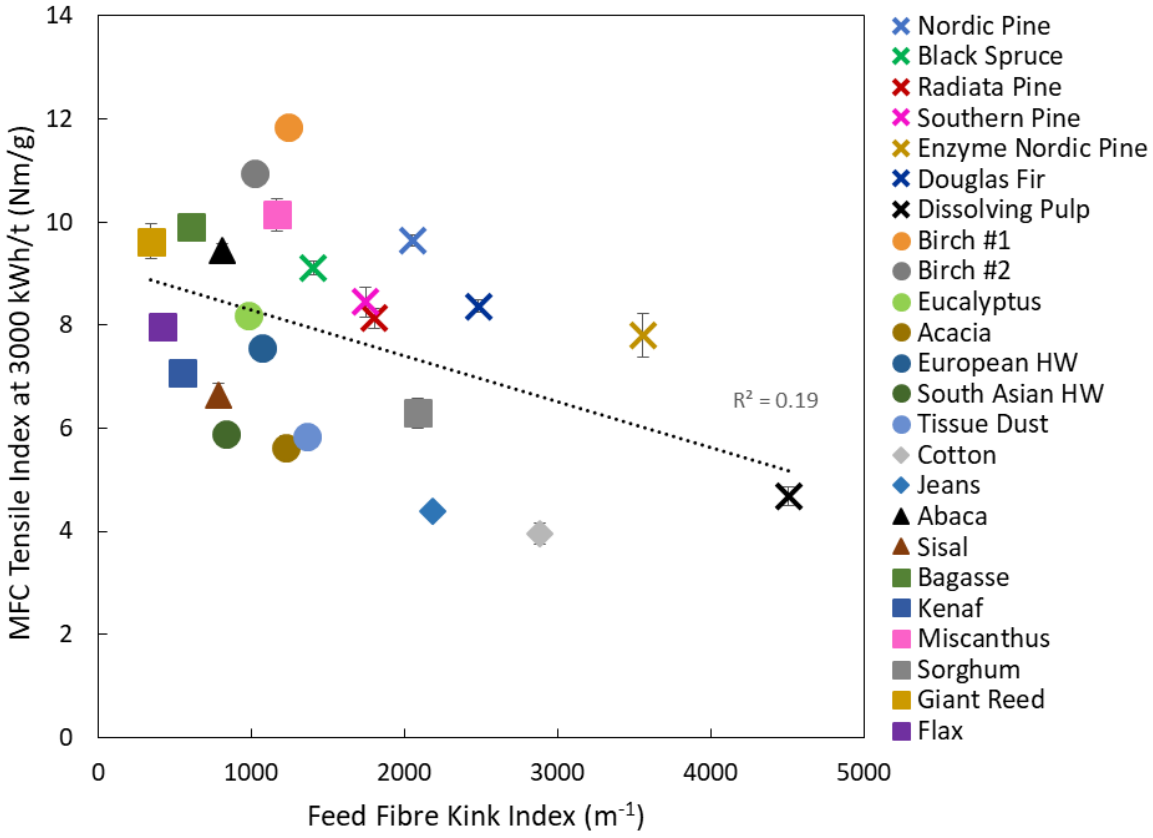

Figure A5.5 *– MFC tensile index versus feed fibre kink index for various fibre species.*

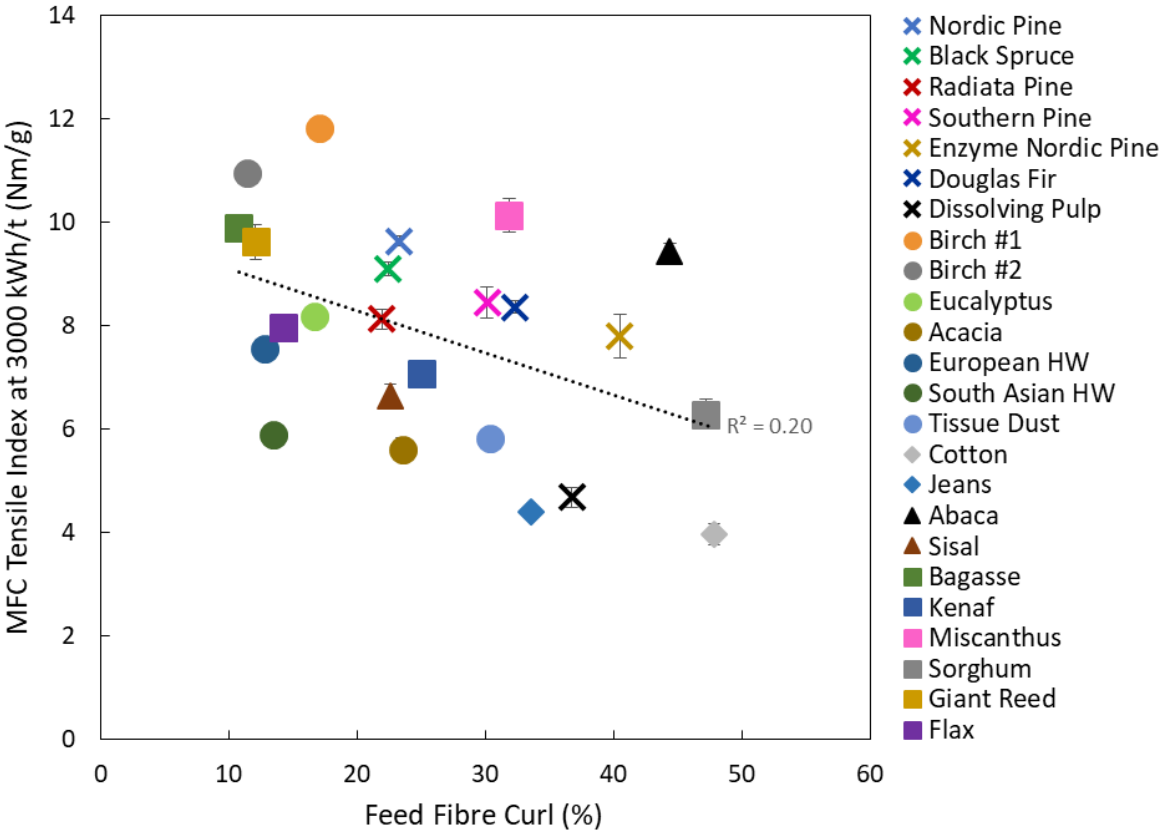

Figure A5.6 *– MFC tensile index versus feed fibre curl for various fibre species.*

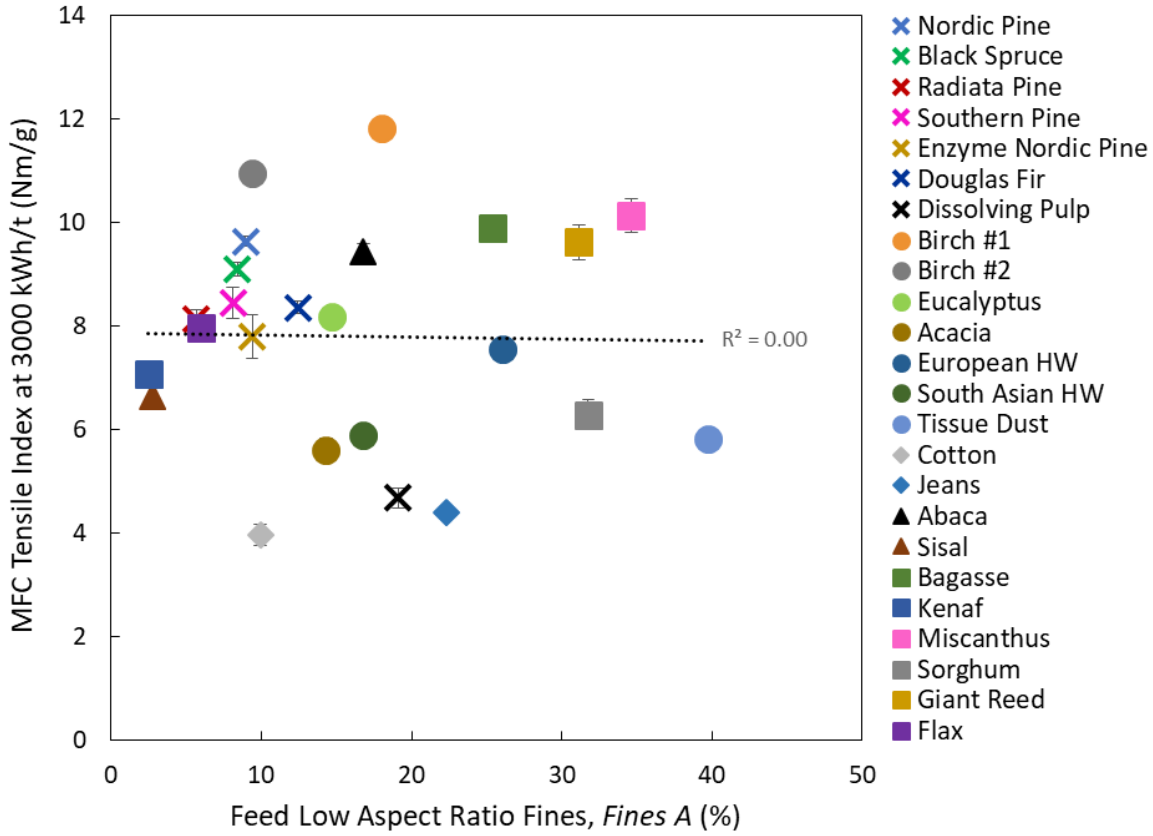

Figure A5.7 *– MFC tensile index versus feed fibre Fines A content for various fibre species.*

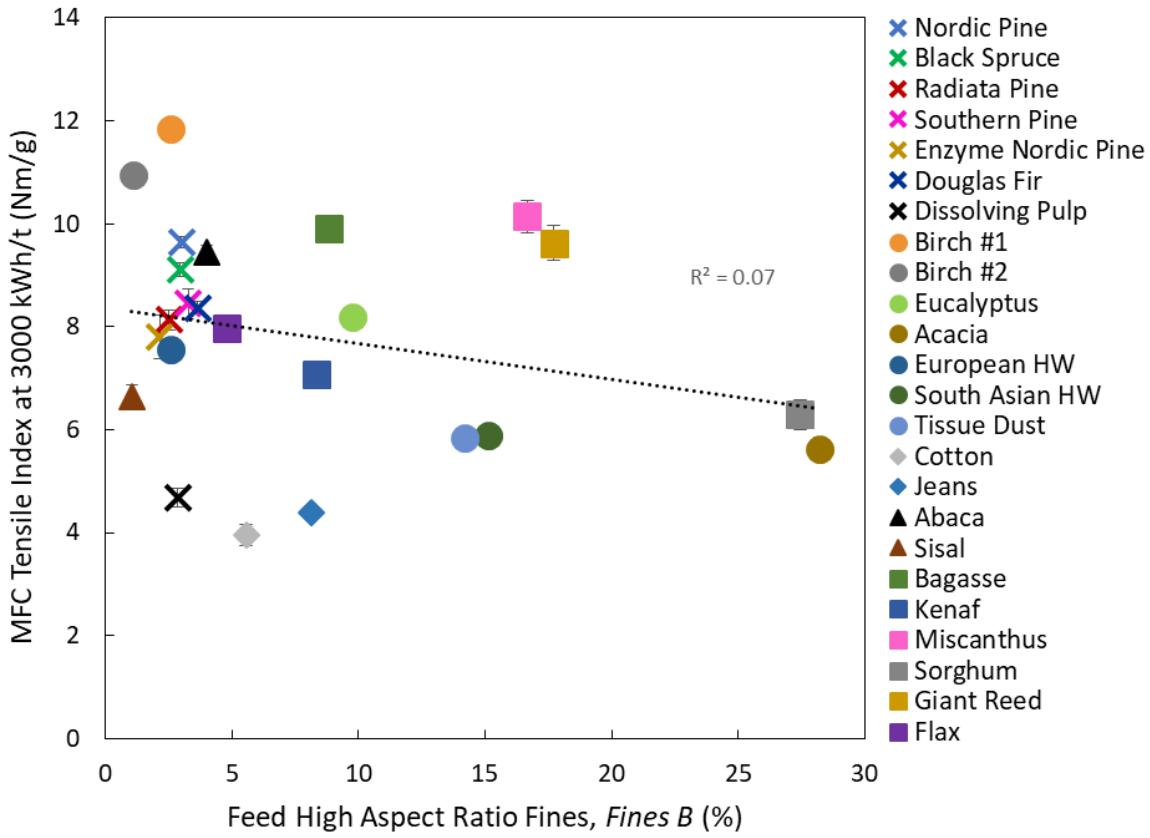

Figure A5.8 *– MFC tensile index versus feed fibre Fines B content for various fibre species.*

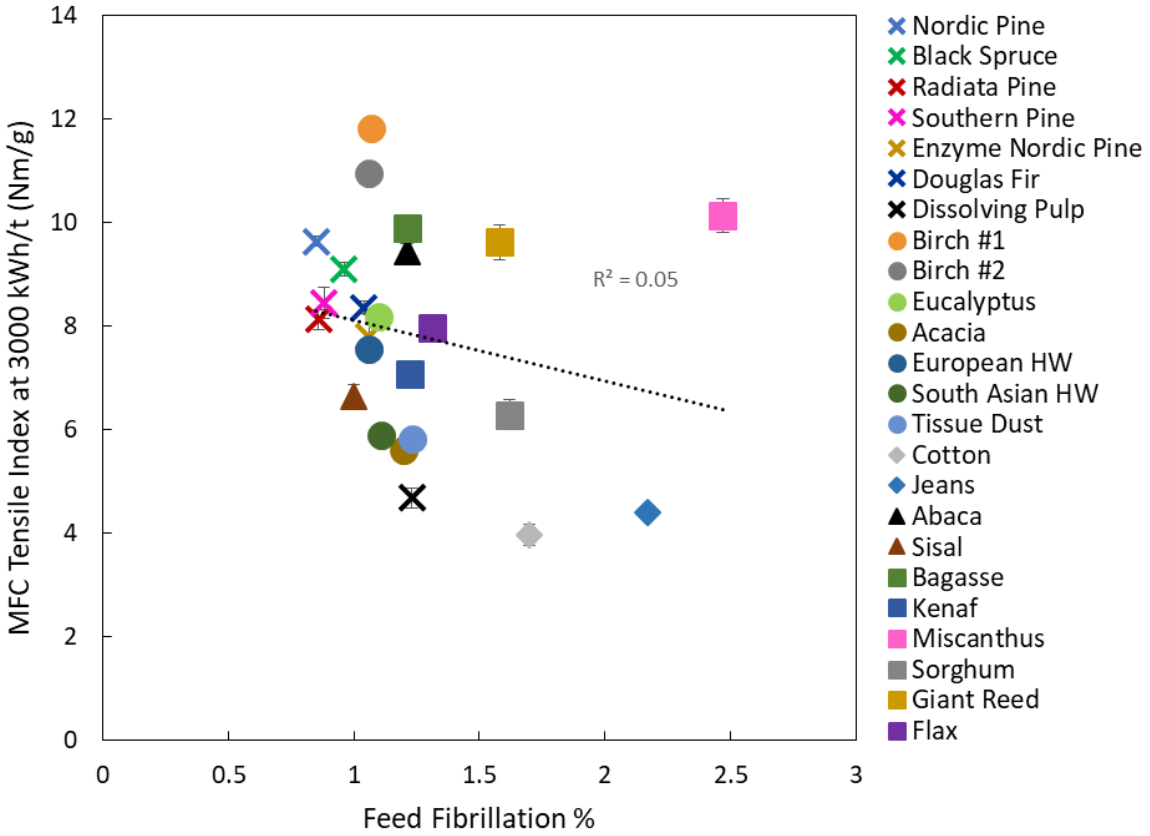

Figure A5.9 *– MFC tensile index versus feed fibre Fibrillation %, for various fibre species.*

Table A5.1 *– Feed fibre geometric properties as measured by the fibre analyser for all fibre species used.*

Fibre Species	Feed Fibre Analyser Data								
	Lc(n) **(mm)**	***Lc(l)*** **(mm)**	**Fibre Width (μm)**	**Coarseness (mg/m)**	**Kink (m^{-1})**	**Curl (%)**	***Fines A* (%)**	***Fines B* (%)**	***Fibrillation %***
Nordic Pine	0.672	1.778	25.75	0.191	2053	23.29	8.95	2.99	0.85
Black Spruce	0.918	2.021	21.62	0.138	1406	22.39	8.39	2.95	0.96
Radiata Pine	0.810	1.891	28.32	0.249	1803	21.92	5.67	2.51	0.86
Southern Pine	0.667	2.071	29.45	0.254	1745	30.11	8.1	3.27	0.88
Enzyme Nordic Pine	0.646	1.640	26.94	0.218	3556	40.49	9.38	2.15	1.06
Douglas Fir	0.453	1.540	27.28	0.216	2482	32.32	12.44	3.63	1.04
Dissolving Pulp	0.432	1.306	23.93	0.164	4506	36.73	19.11	2.85	1.23
Birch #1	0.662	0.887	15.95	0.08	1238	17.09	17.99	2.59	1.07
Birch #2	0.637	0.860	17.77	0.098	1017	11.38	9.34	1.07	1.06
Eucalyptus	0.504	0.746	13.2	0.051	982	16.62	14.72	9.75	1.10
Acacia	0.482	0.735	12.2	0.042	1225	23.52	14.3	28.21	1.20
European HW	0.301	0.693	16.21	0.08	1072	12.74	26.04	2.56	1.06
South Asian HW	0.444	0.660	12.53	0.048	835	13.45	16.75	15.14	1.11
Tissue Dust	0.258	0.485	13.53	0.063	1361	30.31	39.73	14.2	1.23
Cotton	0.764	1.594	22.2	0.163	2884	47.81	9.92	5.55	1.7
Jeans	0.531	1.594	22.78	0.155	2183	33.59	22.35	8.11	2.17
Abaca	0.683	2.450	16.29	0.086	811	44.38	16.79	3.99	1.21
Sisal	1.343	1.778	15.28	0.076	783	22.58	2.76	1.04	1.00
Bagasse	0.323	0.728	17.68	0.108	607	10.75	25.4	8.83	1.21
Kenaf	1.431	1.995	14.58	0.068	547	25.03	2.46	8.31	1.22
Miscanthus	0.247	0.540	19.00	0.118	1165	31.84	34.62	16.67	2.47
Sorghum	0.282	0.668	15.24	0.072	2085	47.2	31.75	27.45	1.62
Giant Reed	0.304	0.750	19.52	0.134	344	12.09	31.14	17.71	1.58
Flax	1.104	2.443	24.71	0.204	422	14.25	5.95	4.78	1.31

Table A5.2 *– Feed fibre chemical composition, showing the measured monomer sugar compositions, the derived hemicellulose species, total hemicellulose content, and acid insoluble and acid soluble lignin.*

Fibre Species	Hemicelluloses									Lignin		
	Monomer Sugar Content (mg / 100 mg sample)					Polysaccharide Content (mg / 100 mg sample)						
	Arabinose	Galactose	Glucose	Xylose	Mannose	Xylan	Glucomannan	Cellulose	Total Hemicellulose (wt% sample)	Acid Insoluble (wt%)	Acid Soluble (wt%)	Max. Total Lignin
Nordic Pine	0.8	0	88.8	8.3	6.3	9.2	7.8	87.2	**17.0**	< 0.4%	0.3%	**0.7%**
Black Spruce	0.6	0.3	87.5	8.6	6.5	9.2	8.5	85.8	**17.7**	< 0.4%	0.2%	**0.6%**
Radiata Pine	0.7	0.3	87.9	7.4	5.0	8.1	6.5	86.6	**14.6**	< 0.4%	0.2%	**0.6%**
Southern Pine	0.6	0.3	88.3	8.7	6.7	9.3	8.7	86.6	**18.0**	< 0.4%	0.2%	**0.6%**
Enzyme Nordic Pine	0.8	0	88.2	8.1	6.5	8.9	8.2	86.5	**17.1**	< 0.4%	0.3%	**0.7%**
Douglas Fir	0.5	0.5	78.8	6.0	6.4	6.4	8.5	77.2	**15.0**	< 0.4%	0.2%	**0.6%**
Dissolving Pulp	0	0	89.1	1.6	2.0	1.6	2.5	88.6	**4.1**	< 0.4%	0.2%	**0.6%**
Birch #1	0	0	76.3	25.2	0	25.2	0	76.3	**25.2**	< 0.4%	0.6%	**1.0%**
Birch #2	0	0	74.1	22.3	0	22.3	0	74.1	**22.3**	< 0.4%	0.6%	**1.0%**
Eucalyptus	0	0	86.8	17.4	0	17.4	0	86.8	**17.4**	< 0.4%	0.3%	**0.7%**
Acacia	0	0	89.4	14.7	0	14.7	0	89.4	**14.7**	< 0.4%	0.3%	**0.7%**
European HW	0	0	71.3	22.3	0	22.3	0	71.3	**22.3**	< 0.4%	0.5%	**0.9%**
South Asian HW	0	0	77.4	14.1	0	14.1	0	77.4	**14.1**	< 0.4%	0.4%	**0.8%**
Tissue Dust	0	0	85.8	14.4	0	14.4	0	85.8	**14.4**	1.1%	0.5%	**1.6%**
Cotton	0	0	106.1	0.3	0	0.3	0	106.1	**0.3**	< 0.4%	0.1%	**0.5%**
Jeans†	-	-	-	-	-	-	-	-	**0.3**†	3.2%	0.5%	**3.7%‡**
Abaca	0.6	0	83.9	11.3	0	11.9	0	83.9	**11.9**	0.7%	0.7%	**1.4%**
Sisal	0	0	84.7	15.3	0	15.3	0	84.7	**15.3**	< 0.4%	0.7%	**1.1%**
Bagasse	1.7	0	73.1	26.2	0	27.9	0	73.1	**27.9**	< 0.4%	0.4%	**0.8%**
Kenaf	0	0	88.8	12.3	0	12.3	0	88.8	**12.3**	< 0.4%	0.6%	**1.0%**
Miscanthus	1.5	0	76.1	20.9	0	22.4	0	76.1	**22.4**	< 0.4%	0.6%	**1.0%**
Sorghum	0.8	0	78.6	15.2	0	16.0	0	78.6	**16.9**	0.6%	0.4%	**1.0%**
Giant Reed	1.4	0	60.6	19.3	0	20.7	0	60.6	**20.7**	11.2%	1.5%	**12.7%**
Flax	0.4	3.3	81.6	1.1	3.3	1.4	7.5	80.8	**8.9**	2.0%	0.3%	**2.3%**

† Due to concern regarding the presence of the indigo dye and other additives interfering with the hemicellulose determination test, this was not measured for this sample, and instead it was assumed that the hemicellulose content of jeans cotton is essentially the same as that of the undyed cotton linters (i.e. essentially zero).
‡ This unexpected high lignin content for fibres that are textile-grade cotton is believed to be an artefact of the dye and other additives to the jeans. The acid-insoluble lignin test residue was a deep indigo blue.

Table A5.3 *– Dry and wet zero-span tensile indices of the feed fibres for all fibre species investigated.*

Fibre Species	Dry Zero-Span Tensile Index (Nm/g)	Wet Zero-Span Tensile Index (Nm/g)
Nordic Pine	128	108
Black Spruce	146	116
Radiata Pine	127	98
Southern Pine	105	83
Enzyme-treated Nordic Pine	80	33
Douglas Fir	119	72
Dissolving Pulp	50	38
Birch #1	139	109
Birch #2	161	125
Eucalyptus	123	100
Acacia	93	61
Mixed European HW	84	56
Mixed South Asian HW	119	89
Tissue Dust	60	52
Cotton	87	83
Jeans	133	110
Abaca	159	142
Sisal	136	104
Bagasse	112	61
Kenaf	127	96
Miscanthus	89	39
Sorghum	76	26
Giant Reed	85	55
Flax	155	137

Table A5.4 *– MFC fibre analyser parameters and tensile index for all fibre species investigated, at 3000 kWh/t.*

Fibre Species	Fibre Length *Lc(l)* (mm)	Fibre Width (µm)	Coarseness (mg/m)	Kink (m^{-1})	*Fines B* (%)	*Fibrillation %*	Tensile Index (Nm/g)
Nordic Pine	0.237	23.50	0.107	1319	29.39	4.98	9.64
Black Spruce	0.221	23.33	0.107	1234	23.38	5.03	9.10
Radiata Pine	0.198	23.30	0.103	1310	22.17	4.65	8.13
Southern Pine	0.203	20.75	0.079	1028	34.41	5.5	8.45
Enzyme Nordic Pine	0.129	21.16	0.072	1120	31.06	4.76	7.80
Douglas Fir	0.196	21.35	0.087	1048	30.79	5.01	8.36
Dissolving Pulp	0.128	22.18	0.085	1715	21.49	4.56	4.68
Birch #1	0.227	20.17	0.08	1091	37.31	5.64	11.83
Birch #2	0.261	21.07	0.092	759	33.15	6.1	10.95
Eucalyptus	0.185	17.96	0.068	1204	30.94	4.22	8.18
Acacia	0.158	17.95	0.072	1407	17.19	4.64	5.61
European HW	0.152	20.30	0.071	1221	33.19	4.87	7.56
South Asian HW	0.143	19.24	0.08	1537	16.81	4.69	5.90
Tissue Dust	0.144	21.49	0.09	1607	15.93	4.71	5.83
Cotton	0.147	27.07	0.119	2580	9.58	4.00	3.96
Jeans	0.202	32.70	0.19	2861	7.01	3.67	4.39
Abaca	0.262	20.09	0.078	1207	39.67	6.07	9.44
Sisal	0.128	18.32	0.055	994	42.40	4.97	6.64
Bagasse	0.18	19.78	0.076	917	38.99	4.90	9.90
Kenaf	0.142	18.17	0.061	1111	36.06	4.72	7.06
Miscanthus	0.154	18.92	0.066	757	51.23	5.61	10.14
Sorghum	0.117	19.57	0.067	1267	40.15	5.53	6.29
Giant Reed	0.164	21.27	0.08	953	36.06	4.17	9.62
Flax	0.362	21.93	0.101	801	38.64	5.62	7.96

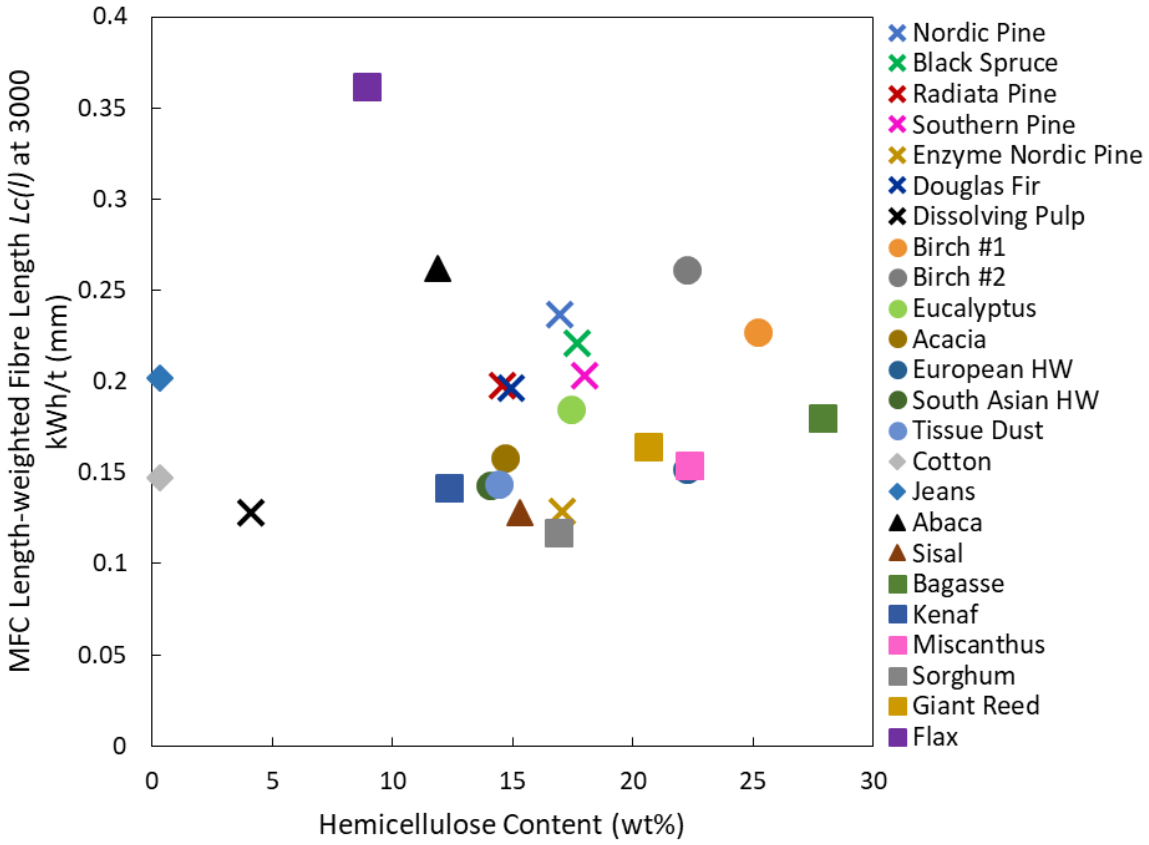

Figure A5.10 *– MFC length-weighted length Lc(l) versus hemicellulose content for all fibre species investigated.*

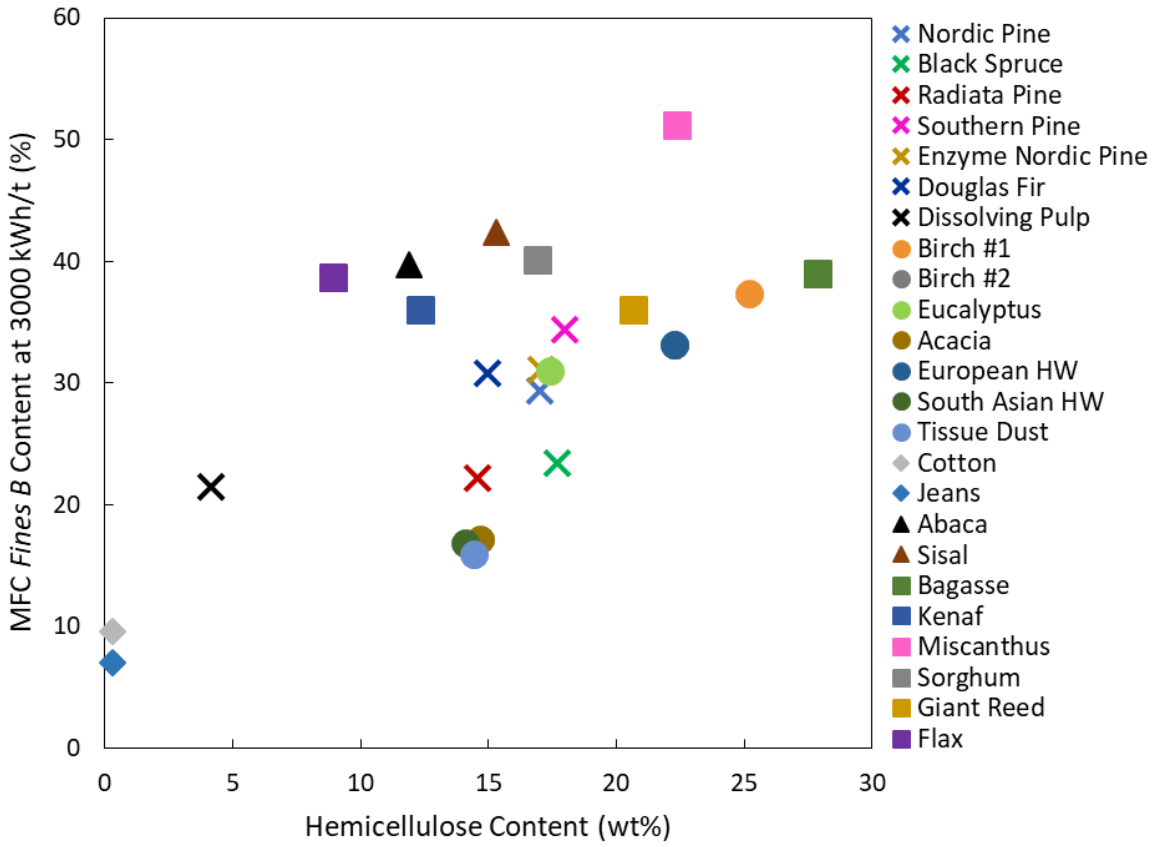

Figure A5.11 *– MFC Fines B content versus hemicellulose content for all fibre species investigated.*

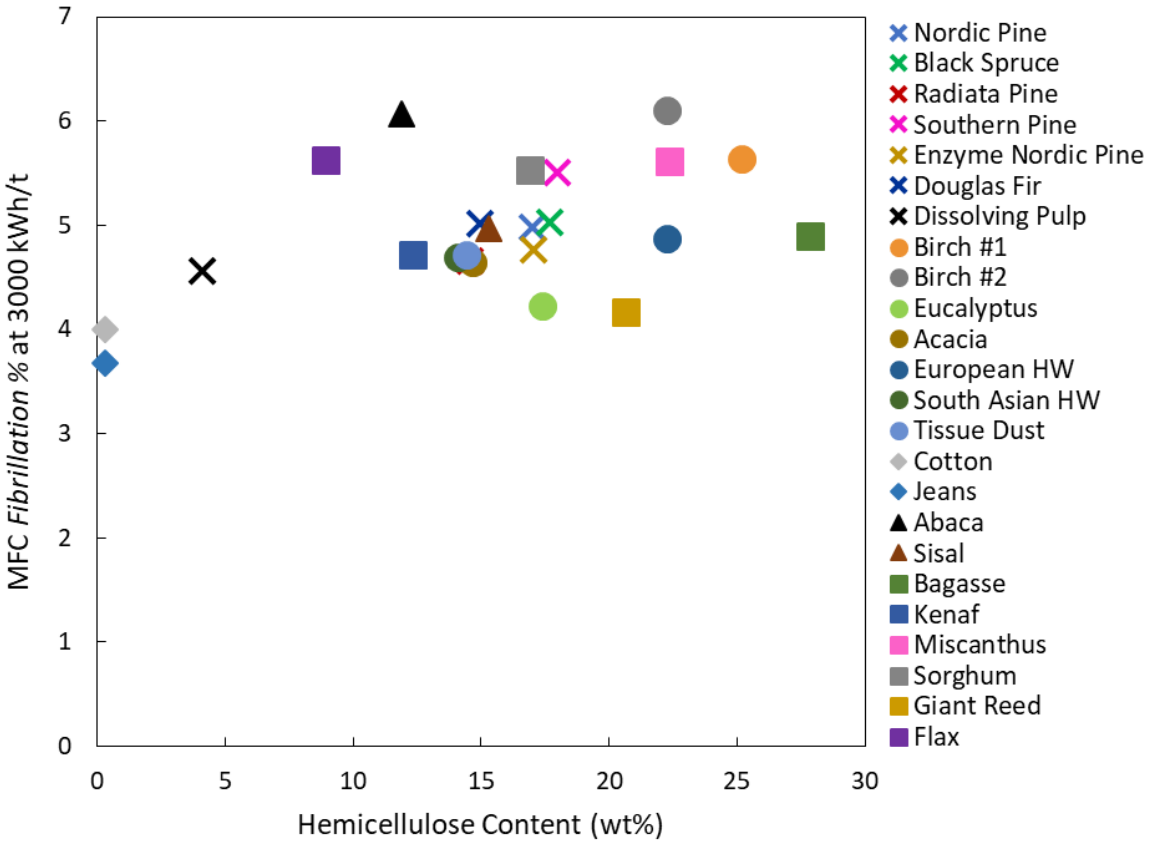

Figure A5.12 *– MFC Fibrillation % versus hemicellulose content for all fibre species investigated.*

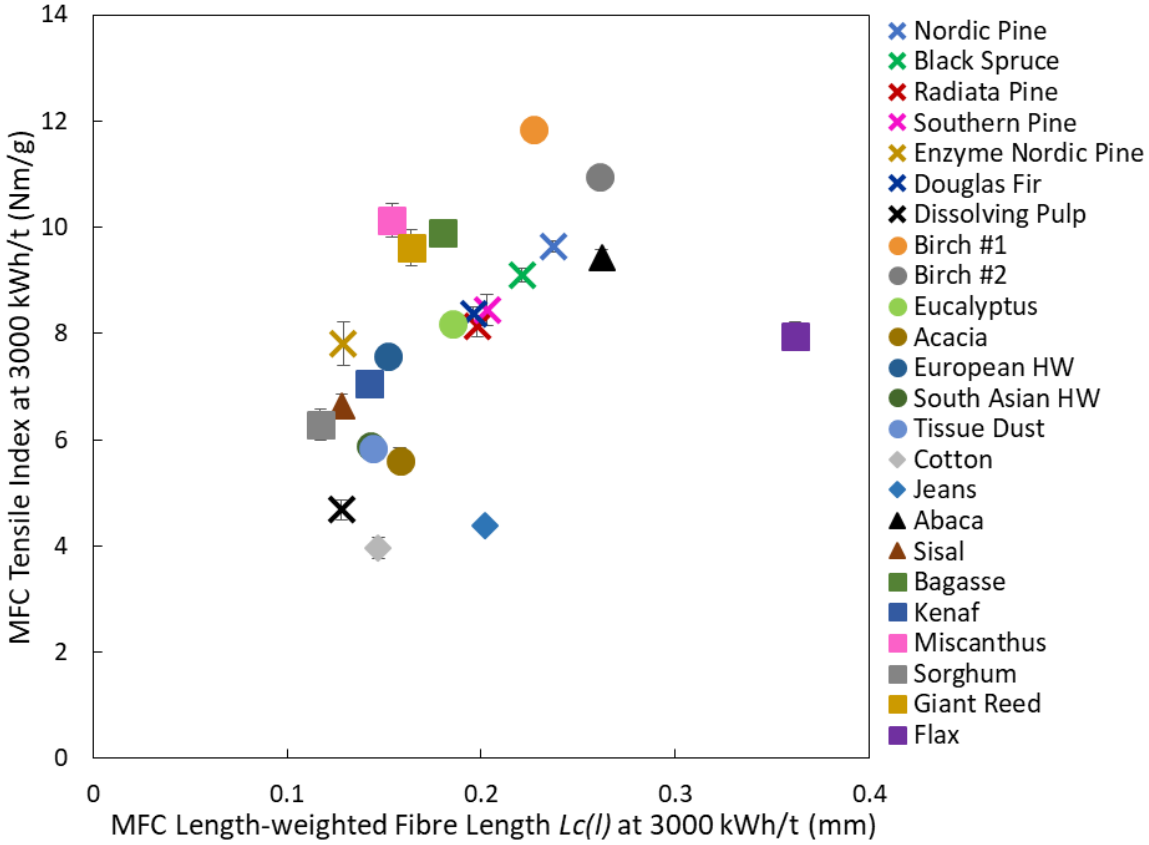

Figure A5.13 *– MFC tensile index versus length-weighted fibre length Lc(l) at 3000 kWh/t.*

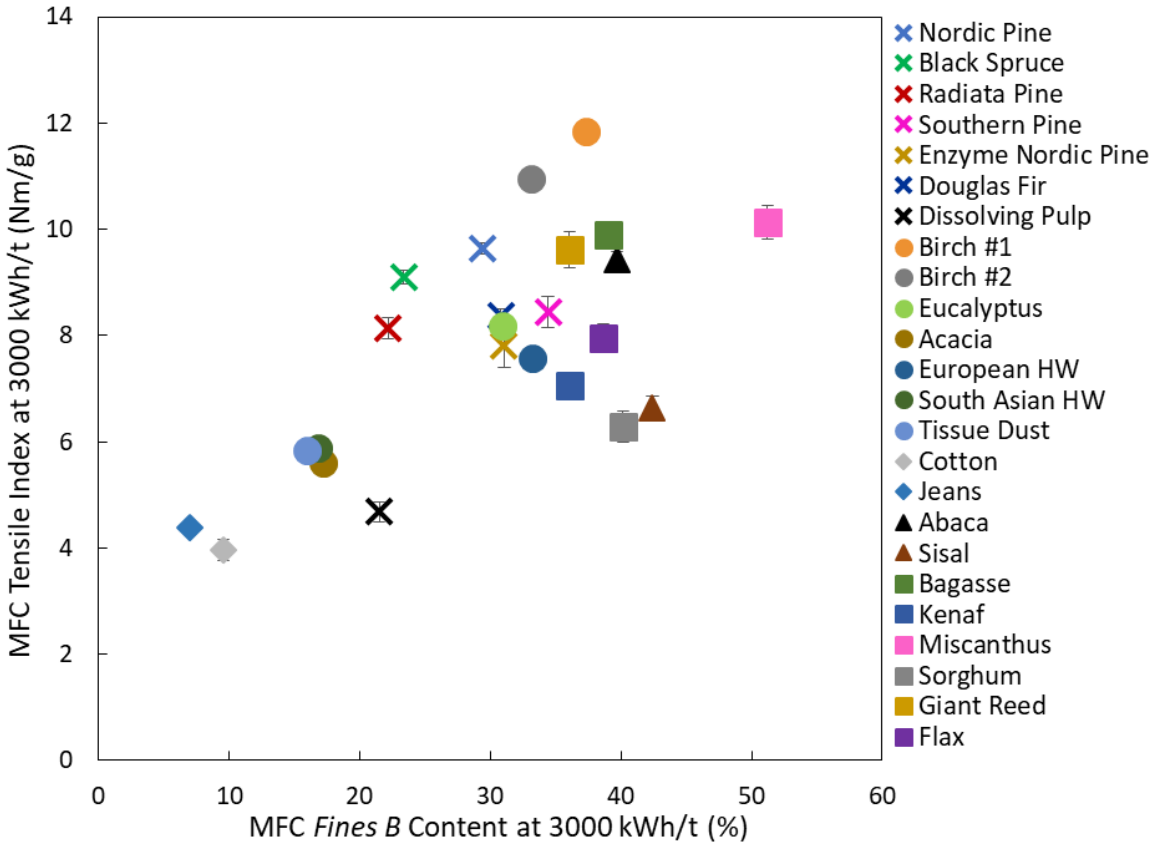

Figure A5.14 *– MFC tensile index versus Fines B content at 3000 kWh/t.*

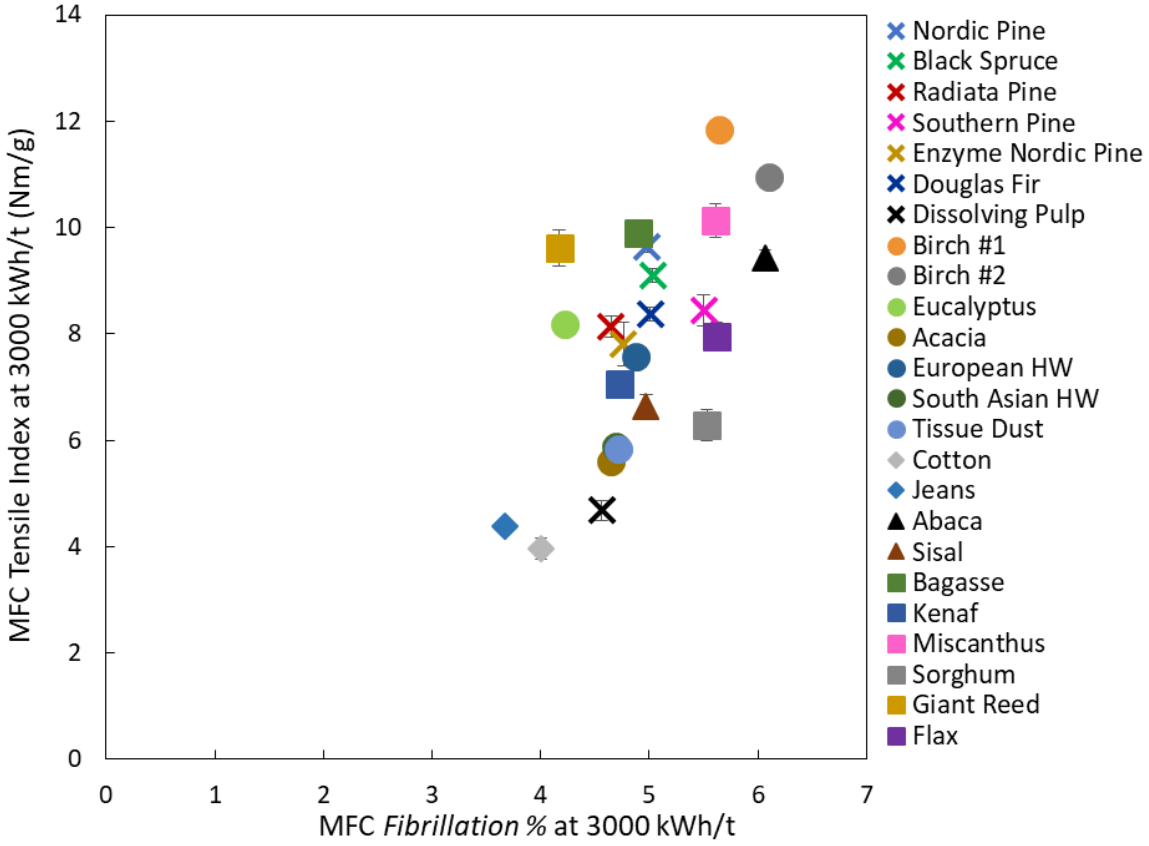

Figure A5.15 *– MFC tensile index versus Fibrillation % at 3000 kWh/t.*

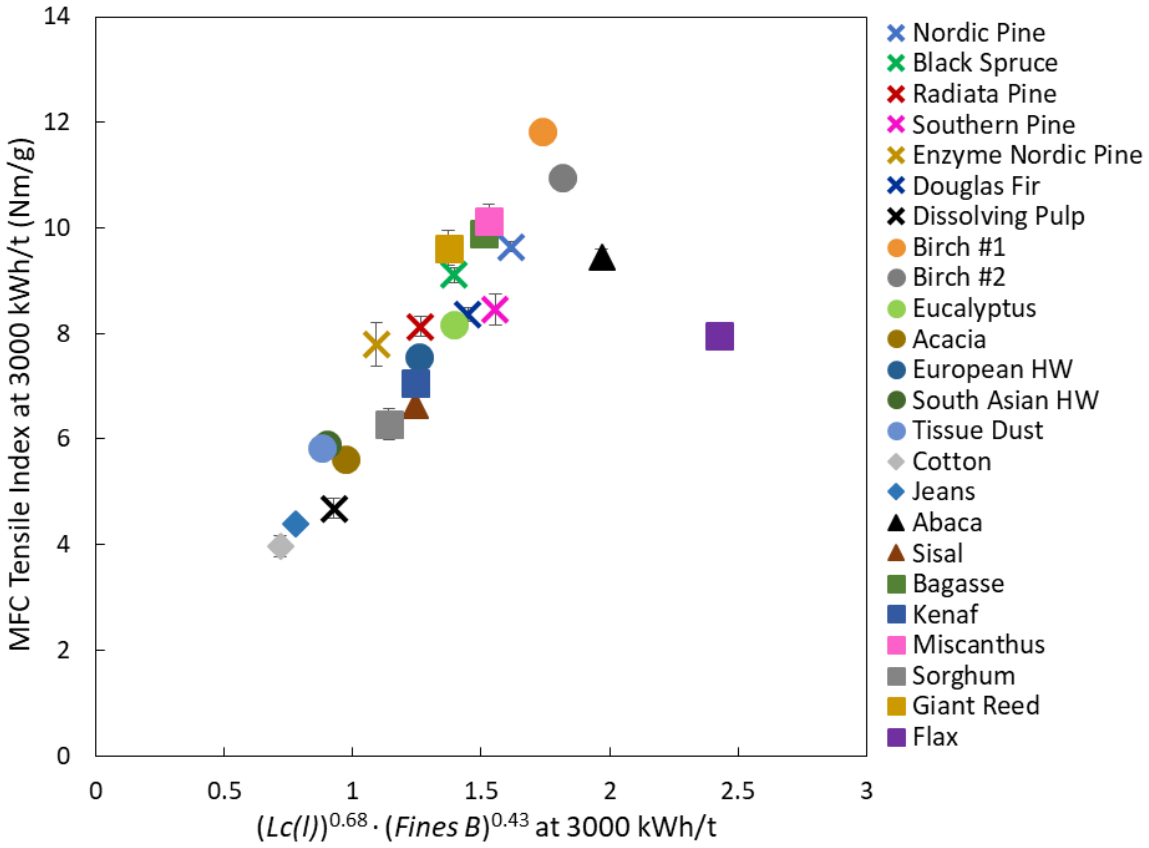

Figure A5.16 *– MFC tensile index versus a function of Lc(l) and Fines B content at 3000 kWh/t. The two outliers are abaca and flax; from microscopy images, flax is substantially under-ground, and abaca may be slightly under-ground, therefore the Lc(l) in that case partly represents unbroken fibre cross-sections rather than long, fibrillated MFC particles, but for the others, where at 3000 kWh/t the MFC is fully disintegrated, there is a good correlation.*

A5.2. Influence of Fibre Crystallinity

The crystallinity of the fibres was initially considered likely to influence the quality of the MFC; Alila et al.[28] found that lower crystallinity fibres tended to give higher quality MFC, though since the lower crystallinity coincided with a higher hemicellulose content, these two effects could not be decoupled. It is not inconceivable, however, that low crystallinity would have a similar effect to hemicellulose, with a larger amorphous cellulose layer facilitating radial separation of microfibrils. Conversely, crystallinity could have the opposite effect; a higher crystallinity could be expected to strengthen microfibrils, and therefore lead to longer MFC particles and higher quality MFC. Therefore, the fibre crystallinity was investigated.

Crystallinity is a notoriously unreliable measurement for cellulose however, especially when comparing different fibre species together. There are numerous techniques for measuring cellulose crystallinity with X-ray diffraction; the two most widely used, and the easiest to apply, are the *Segal method* and the *Ruland-Vonk method*.

An example of a cellulose diffractogram is given as Figure A5.17 to aid in explaining these two methods. The Segal method compares the difference in intensity between the *200* peak at 2θ = 22.7°, I_{200}, and the minimum between the 100 and 200 peaks at 2θ = 18°, I_{AM} (which is assumed to be tangent to the amorphous background):

$$Crystallinity = \frac{I_{200} - I_{AM}}{I_{200}} \dots [A5.1]$$

The peak and corresponding minimum are highlighted in Figure A5.17 (a). This method assumes that at both points, the amorphous background has the same intensity, and that crystalline cellulose gives no contribution at the I_{AM} peak; this assumption is sensitive to the intrinsic crystallite dimensions, which differ between fibre species so should not be considered reliable for comparing crystallinities between fibre species, despite it being by far the most widely used method to do so[113].

The Ruland-Vonk method compares the area under the cellulose diffractogram, A_C, with the area under the amorphous standard, A_{AM}[113] (see Figure A5.17 (b)):

$$Crystallinity = \frac{A_C - A_{AM}}{A_C} \dots [A5.2]$$

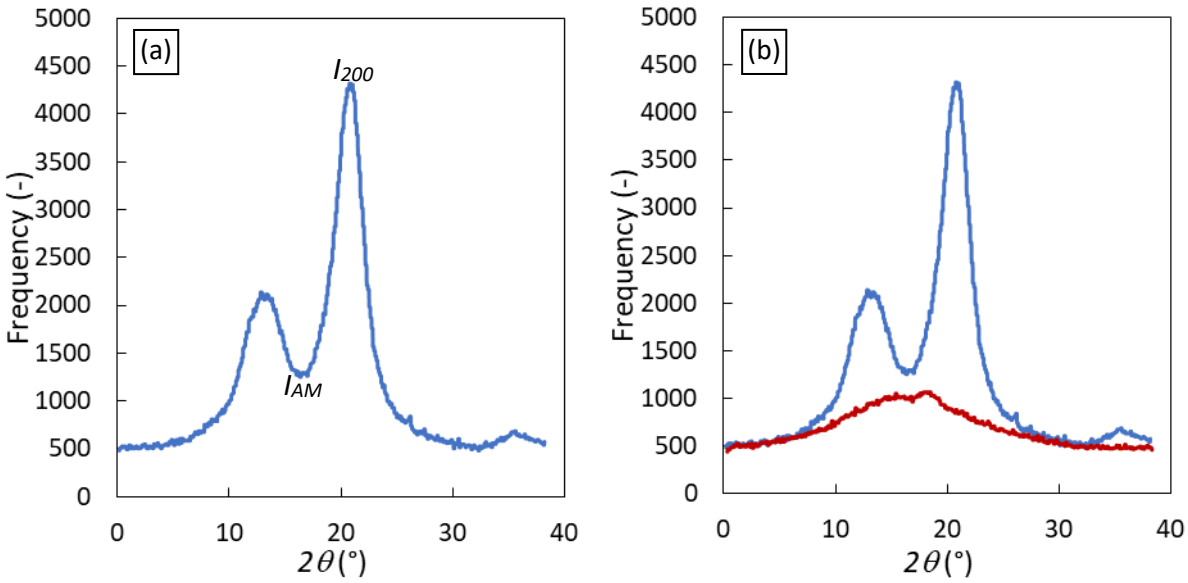

Figure A5.17 – An example of a cellulose X-ray diffractogram, (a) with the 200 peak and the amorphous minimum used in the Segal method calculation highlighted, and (b) the guar gum amorphous standard plotted in red, which is used in the Ruland-Vonk method.

An X-Ray diffractometer was used by *Imerys* to measure the crystallinity of the twenty-four fibre species used in Chapter 7. Measurements were undertaken on a handsheet made from each fibre species, produced using the same method as for the zero-span tensile test. Both lignin powder (from *Sigma-Aldrich*, *product number 370959*) and commercially available guar gum powder were trialled as the amorphous standard, but were found to give essentially the same results. The guar gum powder is the amorphous curve shown in Figure A5.17 (b).

Table A5.5 shows the calculated cellulose crystallinities using both methods for each fibre species. Note that this is *cellulose* crystallinity, where the raw crystallinity result is divided by the cellulose content determined from the carbohydrate measurements. Consequently the Segal method sometimes gives cellulose crystallinities above 100%, with no pulp giving below 83% crystallinity. As expected, the Ruland-Vonk method gave more sensible values.

However, the cellulose crystallinity correlates very weakly with MFC quality, with Figure A5.18 showing the fit with MFC tensile index having an R^2 value of only 0.43. This limited correlation

is likely to be at least in part because the fibres with higher cellulose crystallinity tend to have higher hemicellulose contents, and hemicellulose correlates much better with MFC tensile strength. Surprisingly, no correlation was observed between cellulose crystallinity and fibre zero-span tensile index (see Figure A5.19), implying that the defects that lower the zero-span tensile index are more macroscopic and are not due to weaknesses from amorphous regions in cellulose chains. No other significant correlations between MFC fibre analyser properties and cellulose crystallinity were found, nor did its inclusion in the relationships developed in Chapter 7 significantly improve the model fit. Consequently, it is concluded that the effect of cellulose crystallinity on MFC properties is inconsequential.

Table A5.5 *– Cellulose crystallinities, determined by both the Segal method and Ruland-Vonk method (with a guar gum amorphous background), for each fibre species.*

Pulp	Cellulose Crystallinity (Ruland-Vonk Method (Guar))	Cellulose Crystallinity (Segal Method)
Miscanthus	78%	93%
Bagasse	77%	103%
Birch #2	70%	98%
Black Spruce	68%	98%
Mixed South Asian HW	68%	96%
Kenaf	68%	94%
Flax	68%	97%
Birch #1	66%	101%
Mixed European HW	64%	103%
Sisal	63%	96%
Eucalyptus	62%	95%
Douglas Fir	61%	95%
Nordic Pine	60%	96%
Giant Reed	60%	96%
Abaca	59%	89%
Acacia	58%	94%
Radiata Pine	58%	94%
Enzyme-treated Nordic Pine	58%	95%
Southern Pine	57%	96%
Tissue Dust	55%	91%
Jeans	52%	89%
Dissolving Pulp	50%	83%
Sorghum	49%	86%
Cotton	48%	89%

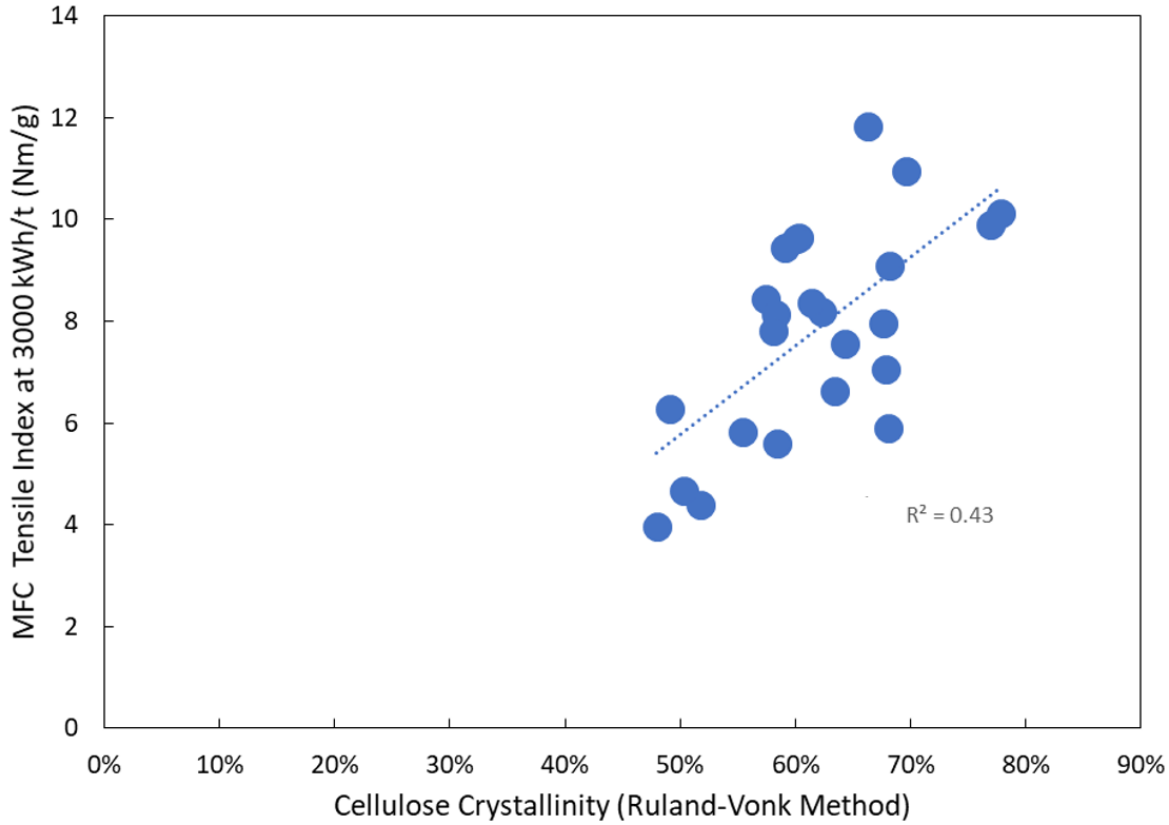

Figure A5.18 *– MFC tensile index at 3000 kWh/t versus cellulose crystallinity (using the Ruland-Vonk method), for all fibre species.*

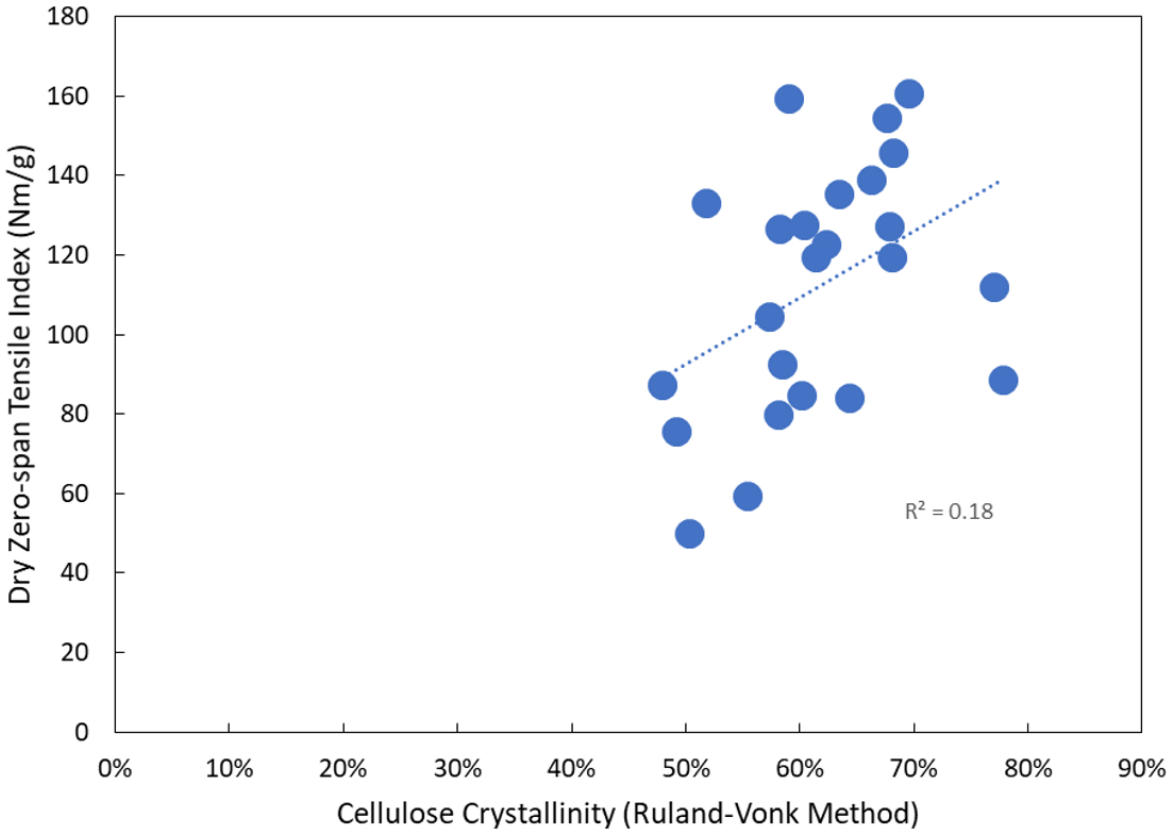

Figure A5.19 *– Fibre zero-span tensile index versus cellulose crystallinity (using the Ruland-Vonk method), for all fibre species.*

A5.3. Zero-Span Tensile Strength of MFC

It is stated in Section 7.3 that the zero-span tensile strength of MFC is much greater than the bonding strength of MFC, so fibril cross-sectional breakage can be assumed to give a very minor contribution to the tensile strip failure and can be ignored. This is investigated in this section.

A 100 % POP *Nordic pine* MFC sample was produced at 3000 kWh/t with *Mullite A* media, and diluted to 85%, 67%, 50%, 33%, 20%, 14.3% and 10% POP with IC60, before being formed into a nanopaper sheet, with the same MFC content as is standard at 20% POP (i.e. total sheet weight increases at lower POP values solely due to mineral addition). These sheets were tested both with the standard ('long span') and zero-span tensile testers.

Unfortunately, it was found that the true zero-span strength of MFC was impossible to measure, because the measured value varied with mineral content, when it should not have done since mineral content only affects inter-fibril bonding. However, by testing the zero-span tensile strength of MFC at different mineral loadings, and transforming the Page Equation, the true MFC zero-span tensile strength can be estimated, to see whether the assumption made in Section 7.3 is valid.

The Page Equation, introduced in Section 2.3, is restated below:

$$\frac{1}{T} = \frac{9}{8Z} + \frac{12A\rho}{\tau_B PL(RBA)} \dots [A5.3]$$

It is not entirely obvious how this relates to the tensile strength of MFC, and how having a mineral loading affects this, but the concept that an MFC sheet can break either due to network failure or breakage of fibril cross-sections is realistic, and could be expected to follow the sum of the resistances in parallel form shown above. Because of this, and because most

of the terms on the right hand side are not directly measurable, the Page Equation is simplified to an empirical form:

$$\frac{1}{T} = \frac{1}{aZ} + \frac{1}{bB} \dots [A5.4]$$

where *a* represents the 8/9 coefficient term of the zero-span tensile index in Equation A5.3, *B* is the total strength of inter-particle bonding, and *b* is an empirical coefficient. Rather than determining the values of *Z* and *B* individually, the products *aZ* and *bB* will be determined and used to assess the relative importance of bonding and zero-span tensile strength on the overall MFC sheet strength. When discussing the long-span tensile strength test, the subscript *F* is added to distinguish it from the zero-span tests.

$$\left(\frac{1}{T}\right)_F = \frac{1}{aZ} + \frac{1}{bB} \dots [A5.5]$$

The bonding term in the long-span tensile test is influenced by the mineral content, since mineral particles cover fibril surface area and acts as spacer particles, preventing fibril contact, so a higher mineral loading decreases the bonding term, which decreases the tensile index, especially if bonding is limiting. Figure A5.20 shows that for both the MFC long-span test and the MFC zero-span test, at low mineral content (corresponding to POP values of 85 – 50 %) there is a steady decay in tensile strength with mineral content. This implies that for *both* the long-span and zero-span tensile test, bonding is at least partially limiting in the case of MFC, even at very high POP. If bonding was so strong that the sheet almost entirely failed by fibril cross-sections breaking (i.e. zero-span failure), then there would be a plateau in the tensile index versus mineral loading curve, before eventually the disruptive effect of the additional mineral content is sufficient to make bonding partially limiting again. As Figure A5.20 shows for both the long-span and zero-span tests, no such plateau is apparent, and therefore

bonding is partially limiting in both cases. Note that unlike in the other tensile tests reported in this work, the tensile index is normalised by *MFC mass alone* rather than total mass.

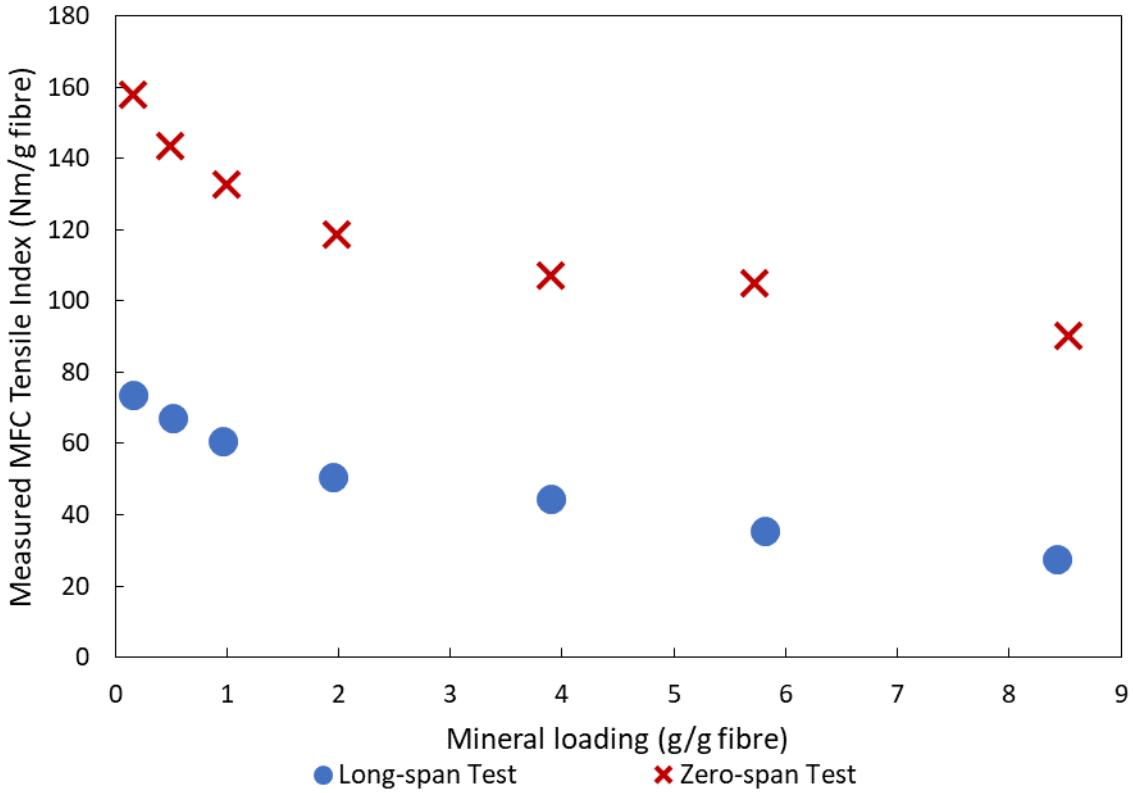

Figure A5.20 *– Mineral loading versus measured MFC tensile index for both the long-span tensile test and the zero-span tensile test.*

The zero-span test therefore cannot truly measure the zero-span tensile strength of MFC, which is likely to be in part because the finer MFC particles are less likely to span the gap between the clamps (and shorter particles are harder to hold in the clamps as there is less area over which friction can act), and it is also expected that the disintegration of the fibre cell wall (so removing the lumen and much of the internal porosity) results in a less compressible sheet (evidenced by the much thinner sheet caliper), thereby making slip from the clamps more likely.

However, as Figure A5.20 shows, even though true zero-span tensile strength of MFC cannot be measured, the zero-span strength values that *are* measured are much higher than for the

long-span test, so there must be some success with clamping both ends of MFC particles and forcing cross-sectional failure. Therefore, in the case of the MFC zero-span tensile test (designated with the *Z* subscript), a coefficient *x* is added before the bonding term, to represent the success of the zero-span test in clamping both ends of the particles and thereby the success of the suppression of bond failure. For a perfect zero-span test, *x* = 0, so the tensile strength measured is entirely the zero-span strength, whereas for a completely ineffective zero-span test, *x* = 1 and so the tensile strength measured is the same as the long-span tensile strength.

$$\left(\frac{1}{T}\right)_Z = \frac{1}{aZ} + x\frac{1}{bB} \dots [A5.6]$$

The value of the zero-span failure term, *1/aZ*, will be invariant of the level of mineral added (which only affects the bonding), and also invariant to whether the tensile test is performed with long-span or zero-span methods (the *x* parameter accommodates for the zero-span test bias). *B* cannot practically be measured in this case, but a relationship can be found between mineral content and tensile index, from which the relationship between mineral content and *B* can be inferred. Plotting *1/T* versus mineral content *M* for the long-span test gives a straight line (see Figure A5.21), implying that bonding is inversely proportional to the mineral content. The zero-span curve is less linear, with the gradient decreasing at higher mineral loadings; this may be an artefact of the test; the different sheet thicknesses and porosities at different mineral loadings likely influence the compressibility of the sheet, and therefore could be expected to change the tendency to slip; additionally, at higher mineral loadings, the sheet is thicker, giving MFC the tendency to form 3-dimensional networks, rather than the more 2-dimensional networks found with no mineral content.

Consequently, the results from the long-span tensile test are considered to be more representative of the 'true' influence of the mineral, but the changing gradient of the zero-span curve is problematic. The gradient is used in subsequent calculations, where the results are compared using the best fit gradient, the gradient of the first four points, and the gradient of the last four points, in order to show the range where the 'true' MFC zero-span strength is likely to reside. It may not give a definitive value, but by using the lowest zero-span value from amongst them, a limit of the effect of fibril breakage on MFC tensile strength can be given.

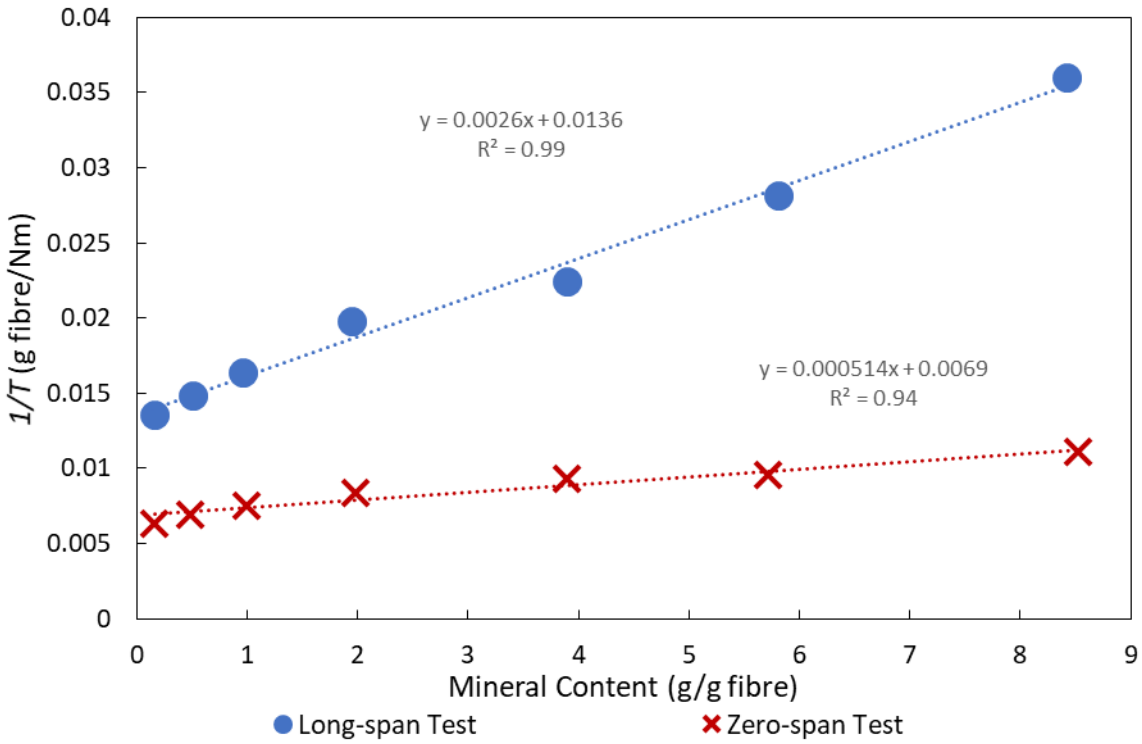

Figure A5.21 *– The reciprocal tensile index versus mineral content for the long-span and zero-span tensile tests.*

Considering the long-span test data in Figure A5.21, since the zero-span tensile index in Equation A5.5 is invariant of mineral loading, the fact that the reciprocal tensile index is proportional to mineral content means that the bonding term in Equation A5.5 is inversely proportional to mineral content. The bonding term is not infinite at zero mineral content, and with decreasing mineral content will tend towards a value of B_0, the bonding with no mineral

loading. A formulation for B that satisfies both the initial B_0 value and the inverse proportionality to mineral content is shown as Equation A5.7:

$$B = \frac{B_0}{1 + qM} \quad \ldots [A5.7]$$

where q is a constant, and M is the mineral content of the sheet (g/g fibre). When mineral content is zero, $B = B_0$, and when mineral content is infinite, $B = 0$. In investigations of the effect of mineral loading on bonding strength, Beazley[114] showed that a similar relationship is followed, which can be algebraically manipulated into an equivalent of Equation A5.7.

By rewriting Equation A5.5 and A5.6 in a form where $1/T$ can be plotted against M, the gradients and intercepts of such curves can be used to determine the various constants, and so the true MFC zero-span tensile index can be estimated, enabling an assessment of whether a MFC sheet fails more by bonding failure or by fibril breakage. Substituting Equation A5.7 into Equation A5.5:

$$\left(\frac{1}{T}\right)_F = \frac{1}{aZ} + \frac{1 + qM}{bB_0}$$

$$\left(\frac{1}{T}\right)_F = \frac{1}{aZ} + \frac{1}{bB_0} + \frac{qM}{bB_0} \ldots [A5.8]$$

Similarly, substituting Equation A5.7 into Equation A5.6:

$$\left(\frac{1}{T}\right)_Z = \frac{1}{aZ} + x\frac{1 + qM}{bB_0}$$

$$\left(\frac{1}{T}\right)_Z = \frac{1}{aZ} + \frac{x}{bB_0} + \frac{xqM}{bB_0} \ldots [A5.9]$$

In a plot of $1/T$ versus M for the long-span tensile strength data, the y-intercept is designated as I_F and the gradient is designated G_F. Similarly, in the same plot for the zero-span tensile

strength data, the *y*-intercept is designated as I_Z and the gradient is designated G_Z. These can be related to model parameters by considering Equations A5.8 and A5.9.

$$G_F = \frac{q}{bB_0} \ldots [A5.10]$$

$$I_F = \frac{1}{aZ} + \frac{1}{bB_0} \ldots [A5.11]$$

$$G_Z = \frac{xq}{bB_0} \ldots [A5.12]$$

$$I_Z = \frac{1}{aZ} + \frac{x}{bB_0} \ldots [A5.13]$$

The parameter representing the effectiveness of the zero-span test, *x*, can be found by dividing Equation A5.12 by Equation A5.10:

$$x = \frac{G_Z}{G_F} \ldots [A5.14]$$

Note that in these calculations, it is assumed that *x* is constant with mineral loading. As discussed earlier, it is likely that the mineral loading influences the effectiveness of the zero-span test for MFC, since the gradient of the *1/T* versus *M* curve varies. Therefore, the results from this calculation give a range within which the true zero-span tensile index is likely to be, and should not be considered a definitive calculation.

The value of bB_0 can be found by subtracting Equation A5.11 from Equation A5.13:

$$I_Z - I_F = \left(\frac{1}{aZ} + \frac{x}{bB_0}\right) - \left(\frac{1}{aZ} + \frac{1}{bB_0}\right)$$

$$I_Z - I_F = (x-1)\left(\frac{1}{bB_0}\right)$$

$$bB_0 = \left(\frac{x-1}{I_Z - I_F}\right) = \left(\frac{\frac{G_Z}{G_F} - 1}{I_Z - I_F}\right) \ldots [A5.15]$$

With bB_0 known, the value of the mineral coefficient q can be found by rearranging Equation A5.10:

$$q = bB_0 G_F = \left(\frac{G_Z - G_F}{I_Z - I_F}\right) \ldots [A5.16]$$

Finally, the term representing the zero-span tensile strength, aZ, can be found by rearranging Equation A5.11 and substituting in Equation A5.15:

$$aZ = \frac{1}{I_F - \frac{1}{bB_0}} = \frac{1}{I_F - \left(\frac{I_Z - I_F}{\frac{G_Z}{G_F} - 1}\right)} \ldots [A5.17]$$

With bB_0 and q calculated, the value of the bonding term bB can be determined at a given mineral content using Equation A5.7.

The gradients and intercepts of both the long-span and zero-span curves on Figure A5.21 are shown in Table A5.6, and were taken as input parameters to solve this model. Note that the zero-span curve gradient changes significantly with mineral content, so the best fit values of I_Z and G_Z were determined alongside values determined with linear best fit lines at both low and high mineral contents.

Table A5.6 *– Gradients and intercept values used as model inputs. The gradient of the curve in Figure A5.21 is constant for the long-span test, but for the zero-span test it changes with mineral content, so the best fit over the whole curve is given, along with the best fit values for the low mineral content and high mineral content regions of the curve.*

I_F	G_F	I_Z			G_Z		
		Best fit	**Low *M***	**High *M***	**Best fit**	**Low *M***	**High *M***
0.013584	0.002593	0.006862	0.006325	0.007635	0.000514	0.001094	0.000389

The calculated values of I_Z and G_Z for each best fit line were used in this model, with the results shown in Table A5.7. According to the Page Equation, the value of a is 8/9, and so to estimate the true value of the zero-span tensile index, the aZ value is multiplied by 9/8.

Table A5.7 *– Calculated model parameters.*

Parameter	Best Fit	Low Mineral Content Fit	High Mineral Content Fit
q (-)	0.309	0.207	0.370
x (-)	0.198	0.422	0.150
bB_0 (Nm/g)	119	80	143
aZ (Nm/g)	192	973	152
Z (Nm/g)	216	1095	171

Table A5.7 shows that for the best fit value of G_Z and I_Z, the value of x is 0.2; this means that the effectiveness of the zero-span tester in measuring the true zero-span strength for this MFC is around 80%. This effectiveness is much lower, at around 58% if the low mineral fit is used, or is higher at around 85% if the high mineral fit is used. Although in no case does bonding dominate in the zero-span test, even in the most optimistic case, bond failure still contributes to around 15% of the breakage energy in this case. Note that for MFC of smaller particle lengths, it is expected that the contribution of the bonds to failure would be higher since a smaller MFC particle is less likely to be successfully held by both clamps.

The value of the calculated zero-span tensile index varies from 170.8 Nm/g for the high mineral content fit, 216.3 Nm/g for the general best fit, and is excessively high at 1095 Nm/g for the low mineral content fit. Even the lowest value of these is much higher than the *Nordic pine* feed fibre zero-span strength of 127 Nm/g; this may be because in a fibre there are localised cross-sectional flaws or dislocations which cause a non-uniform load distribution, facilitating failure. When the fibre is disintegrated into MFC, these flaws become liberated fibril endpoints, and so become much more homogenously distributed; this more uniform

load distribution enhances sheet strength. A similar hypothesis, regarding the improvement in zero-span strength seen with refining, was made by Joutsimo et al.[36].

To assess the extent to which the fibril breakage dominates the total breakage in a long-span tensile test, for each choice of G_Z and I_Z values, the ratio of the measured long-span tensile strength T to the derived zero-span term in the Page Equation aZ was determined, and plotted against mineral content. This is shown as Figure A5.22. For the low mineral content fit, the T/aZ value is close to zero since the zero-span strength is more than an order of magnitude higher than the bonding strength. If the best fit and the high mineral content fit values are to be believed, at 100% POP, around 40 – 50% of the breakage is due to fibril breakage, with the rest due to bond breakage; the influence of zero-span strength and bonding strength are comparable. At 20% POP (corresponding to a mineral content of 4 g/g fibre), the conventional value for the tensile test, the T/aZ value is 23% using the best fit values and 30% using the high mineral content fit values.

Therefore, with this particular MFC sample, at 20% POP, fibril breakage can be considered to contribute to a maximum of a third of the total breakage; bonding failure therefore dominates. Unfortunately, variations in MFC tensile index under different circumstances could be to such an extent that the T/aZ value varies significantly, with the relative importance of fibril breakage varying. This can be expected to differ between fibre species (some having intrinsically weaker cross sections, or have more of the initial flaws remaining in the MFC) and processing conditions.

This minor contribution of fibril breakage, and the fact that its importance will differ somewhat between cases, is likely a contribution to some of the noise seen in the relationship between the product of hemicellulose and fibre zero-span tensile index and the long-span

tensile index shown in Section 7.3. It stands to reason that high hemicellulose content and high fibre zero-span strength will aid both bonding and MFC zero-span strength, with a high initial zero-span strength meaning fewer flaws remaining in the MFC fibrils, and a high hemicellulose content facilitates finer microfibril liberation, creating a more homogenous load distribution across the strip cross-section. The relative importance of these two factors, however, may be different between bonding failure and fibril breakage, and so cause spread in the relationship.

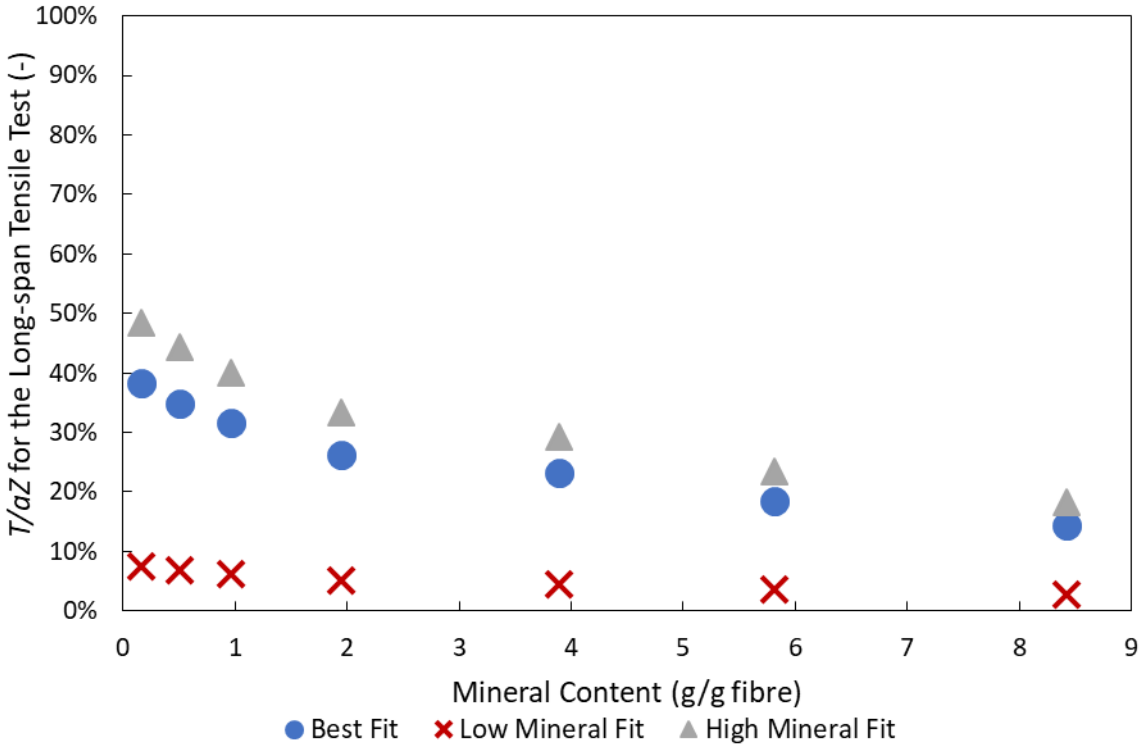

Figure A5.22 *– Ratio of long-span tensile index to the calculated zero-span term of the Page Equation using the measured MFC zero-span tensile index data.*

APPENDIX B1 – PUBLICATION: STIRRED MEDIA MILLS IN THE MINING INDUSTRY: MATERIAL GRINDABILITY, ENERGY-SIZE RELATIONSHIPS, AND OPERATING CONDITIONS

Reference:

Taylor, L., Skuse, D., Blackburn, S., Greenwood, R., 2020. ***Stirred media mills in the mining industry: Material grindability, energy-size relationships, and operating conditions.*** Powder Technology, 369, pp.1-16. https://doi.org/10.1016/j.powtec.2020.04.057.

Post-print article shown on the following page:

Stirred Media Mills in the Mining Industry: Material Grindability, Energy-Size Relationships, and Operating Conditions

Lewis Taylor[a, b,*], David Skuse[a, b], Stuart Blackburn[a], Richard Greenwood[a]

[a] School of Chemical Engineering, University of Birmingham, Birmingham, B15 2TT, UK

[b] FiberLean Technologies, Par Moor Centre, Par Moor Road, Par, PL24 2SQ, UK

*Corresponding author. Email: lxt189@bham.ac.uk; lewis.taylor@fiberlean.com; Phone: +441726 818000

Abstract

Stirred media mills are used by the mining industry for ultrafine grinding to enhance liberation, and to decrease particle sizes of industrial minerals to tailor functional properties. This review describes stirred media mill technologies and operating principles, and summarises stress intensity theory which can be used for selecting efficient operating conditions. For fine and ultrafine grinding, the Bond work index is an inappropriate measure of grindability, so alternatives are discussed. Using literature data, the variation in the appropriate energy-size models between examples is assessed, and rationalised with stress intensity theory. A Rittinger operating index was found to be the best choice for assessing operation efficiency. Finally, a modification of stress intensity theory that tunes operating conditions based upon material properties, and the f_{mat} mastercurve theory are discussed, with the conclusions that, although promising, laboratory-scale milling tests remain the most practical method of assessing material grindability and predicting industrial energy requirements.

Keywords: comminution; stirred media mill; stress intensity; Bond work index; metalliferous ore grinding

1. Introduction

1.1. Fine Grinding in the Mining Industry

It has been estimated that approximately 2% of the world's energy usage is applied to mineral comminution, and around a quarter of this is used specifically in metalliferous ore grinding [1] where it is typically the most energy intensive set of operations [2]. The purpose of comminution in ore processing is to reduce particle size in order to improve liberation of valuable minerals and so enable separation from the undesirable gangue to improve grade and recovery. This involves several crushing stages, followed by grinding stages. These crushing stages usually involve several unit operations in series, such as jaw crushers, cone crushers, hammer mills, and

autogenous or semi autogenous grinding mills to reduce particle size from the scale of boulders down to several millimetres. The final stage of crushing is increasingly carried out using high pressure grinding rolls (HPGRs), which involve the relatively efficient process of the slow compression of a particle bed, and can produce a fine feed for the grinding circuit [3], in some cases even making the coarser grinding stages redundant [4-5].

Conventional grinding is typically carried out by tumbling mills. These can be rod mills which are suitable for relatively coarse grinding, and ball mills which are practically capable of grinding down to finer sizes. Both types use a rotating shell containing either rod or ball shaped grinding media, which are lifted and dropped as the mill rotates, grinding the charge down with impact and attrition forces. Conventional grinding with ball mills can comminute particles down to around 100 μm [6].

If economical, subsequent fine and ultrafine grinding takes place, using either ball mills or stirred media mills. The definition of fine and ultrafine grinding varies, but fine grinding is often considered to take place below P_{80} values (the size that 80 wt% of particles pass below) of 100 μm [7] and ultrafine grinding below P_{80} values of 20 μm [8] with lower size limits of several μm [9].

In the mining industry, the ideal target particle size for comminution is the *liberation size*, the size around which the valuable mineral can be effectively separated from the gangue by physical or chemical methods [10] (usually froth flotation), thereby minimising gangue particles in the concentrate and minimising valuable mineral particles lost to the tailings. The liberation size is related to the mineral grain size, although not necessarily equal to it; since it is rare that a mineral preferentially fractures at the grain boundaries, the liberation size is often significantly below the mineral grain size [11].

The optimum grade in the final concentrate depends primarily on a balance between the cost of further comminution and beneficiation versus the cost of extracting the metal from the concentrate. Metal extraction is carried out either by pyrometallurgical processes (i.e. smelting or roasting) or through hydrometallurgy (i.e., leaching, followed by a purification step such as precipitation or electrowinning to deposit the metal from the solution). In the case of hydrometallurgy, finer particle sizes increase leaching rate [12] as well as valuable metal recovery. Flotation tailings often undergo ‘regrinding’ in order to liberate middling and locked valuable mineral grains from larger gangue particles, with the optimum grinding duty balancing the required energy input of liberation with the value of the material that would otherwise be lost.

The most economical ores available, with the highest grades and largest liberation sizes, tend to be exploited first. Consequently, the average ore quality of many metals has decreased over the decades. For example, in the

case of copper, the mean ore grade in the United States declined greatly from 1.8% in 1932 [13] to 0.34% in 2010 [14], and additionally the remaining ores in the case of many metals are becoming increasingly fine-grained [8]. These trends result in a finer liberation size requirement, and more ore comminution per unit mass of metal, and so fine and ultrafine grinding are becoming increasingly important.

Ball mills have traditionally been used for fine grinding of minerals, and in these cases smaller ball sizes than in conventional grinding are used to increase contact area and decrease collision intensity [15], and lower mill speeds are used to cause the media to cascade rather than cataract, shifting the typical forces experienced from impact and towards attrition [16]. Despite such modifications, inefficiency rapidly increases when grinding below 75 μm and ball mills are rarely economical below around 30 μm [6]. Stirred media mills are increasingly replacing ball mills for fine and ultrafine grinding, typically having around 30 – 40% less power consumption than ball mills when grinding to the same product size [8].

1.2. Stirred Media Mills

Efficient grinding of fine and ultrafine particles requires small media to increase the surface area and the consequent collision frequency, but ball mills are fundamentally limited in the momentum that can be applied to such small beads by the force of gravity, which sets a practical lower limit in media size. Stirred media mills overcome this limitation by applying momentum to the media with an impeller, which enables the utilisation of small media on the scale of millimetres, whilst still being able to apply arbitrarily high collision intensities based upon the impeller speed. Accelerations experienced can be remarkably high, up to several thousand m/s^2 [17], and stirred mills can have high power densities of between 40 – 300 kW/m^3 (compared to around 20 kW/m^3 for a ball mill) [18] which can substantially reduce plant space requirements at a given throughput.

The first example of using an agitated vessel and grinding media for comminution was in 1922 when Szegvari stirred a gallon can full of pebbles to rapidly disperse a sulphur suspension [19]. This was developed into the first ‘stirred ball mill’ by Klein and Szegvari in 1928 [20]. This prototype was refined into the *Attritor* mill, a low tip speed (3 – 5 m/s [21]) vertical pin mill which has been produced in various forms by *Union Process* since 1946 [19]. Several other stirred media mill designs have been developed over the subsequent decades, with the most common types used in the mining industry introduced below.

- *Gravity-induced Stirred Mill* – In these mills, media motion is driven by the rotation of a helical impeller; the speed is not sufficient to fully suspend the media, and so at the top of the helix, the media cascades downwards under gravity; this settling ensures that the media remains in intimate contact for efficient

grinding, and leads to a settled zone of charge above the media which can be extracted as the product without the need for screens [8]. To ensure settling, the media is relatively large, with diameters typically at least 12 mm, up to several cm [16]. The first gravity-induced stirred mill was the Tower Mill, invented in the 1950s by the *Japan Tower Mill Company*, and in the 1980s *Metso* developed the Vertimill, which is an adaptation of this technology [22]. Early uses included wet grinding of limestone used for neutralisation purposes [23], and by the 1980s and 1990s, gravity-induced stirred mills had been adopted in the mining industry.

- *Stirred Media Detritor* – The Stirred Media Detritor (SMD) consists of a vertical octagonal tank, and a high-speed multi-layer pin impeller which fluidises the media (with media diameters typically on the order of several millimetres) [16]. This is similar in concept to the Attritor mill, but in fact originated from the high speed *sand grinder*, invented in 1948 by *Du Pont* for pigment grinding, which utilised Ottawa sand as grinding media [24]. In the 1960s *English China Clay* (now *Imerys*) developed the SMD which originally used sand as media, although in recent decades sand was replaced with small ceramic grinding media beads. For the last 45 years, SMDs have been used in kaolin and calcium carbonate grinding applications, producing particle sizes down to a scale of 1 – 2 μm [25] and *Metso* now manufacture them for use in ultrafine grinding of metalliferous ores [22].
- *IsaMill* – The IsaMill is a horizontal disc mill, developed by *Mount Isa Mines Ltd*. and *Netzsch* and commercialised for ultrafine grinding of ore in 1999 [26]. It consists of a horizontal cylindrical chamber, with the agitator being a series of perforated discs attached to a central shaft. As with the SMD, it is considered a high speed 'fluidised' mill, and very fine product sizes are possible, with P_{80} values as low as 7 μm being practical [8], enabled by the relatively fine grinding media, at around 1 – 8 mm in diameter [23]. IsaMills have similar ultrafine grinding efficiencies to SMDs given similar operating conditions (tip speeds and media diameters), but IsaMills have a narrower particle size distribution due to a lower tendency for coarse particle bypassing, which is beneficial for efficient leaching of precious metals [27].

The gravity-induced mills, Tower Mills and Vertimills, are more efficient in the particle size range typical of regrind circuits, down to P_{80} values of around 20 – 40 μm, and below this limit fluidised mills are more efficient [22]. This is primarily due to the differences in grinding media size [28], since gravity-induced mills require media large enough to settle under gravity in order to function. Stirred media mills have been used for many decades in the industrial minerals, pharmaceutical, and pigments industries (wherein they target a particular size distribution for product functionality reasons rather than liberation). Since the 1990s they have also penetrated

the mining industry, increasingly replacing ball mills for regrinding, fine grinding and ultrafine grinding applications [8].

The high intensity environment in stirred media mills can also induce mechanochemical processes, such as modifying the surface chemistry or crystal structure of the minerals (they are sometimes used expressly for this purpose, see a review by Mucsi [29]). This mechanical activation can enhance recovery in downstream separation processes [29], with some examples showing striking benefits in leaching recovery even when surface area increase is considered [30, 31]. However, these benefits are rarely accounted for when assessing grinding efficiency [29].

Stirred media mills typically operate as a wet process, since the water promotes mixing, and disperses product particles to suppress reagglomeration [17]. In dry grinding, reagglomeration can be somewhat mitigated by the addition of grinding aids to lower surface energy [32], but even with this, the residual effect leads to a much higher practical grinding limit compared to wet grinding, resulting in substantial efficiency drops at finer sizes [33]. However, in some cases dry grinding is prudent, or even necessary. Dry grinding eliminates the cost of downstream drying or wastewater treatment, which may sometimes offset the degradation in grinding efficiency, and in fact may be essential in arid regions with poor water availability [34]. Dry grinding may also be preferred for chemical reasons; for example, stirred media mills show promise in efficiently milling cement clinker, particularly for specialised fine cements [29, 35], but this must be a dry process to prevent premature cement hydration [36]. In other cases, dry grinding can promote a specific mechanochemical effect, such as zeolite amorphisation [33]. For some minerals, this induced mechanochemistry can enhance recovery in flotation [37]. However, in fine and ultrafine grinding for ore liberation, wet grinding dominates due to the greater efficiency, and because subsequent separation processes tend to require wet operation, making the advantages of dry milling in terms of water usage redundant.

Regardless of which type of media mill is used, the breakage processes that take place are fundamentally similar. The impeller (helix, disc, or pin) imparts momentum to the grinding media closest to it, accelerating the media to a significant fraction of the impeller tip speed (from particle tracking velocimetry studies in a horizontal fluidised mill, this is around 20 - 40% of the impeller tip speed, with the lower values at higher impeller speeds [38-39]). This grinding media circulates about the impeller, and by collision transfers kinetic energy to other grinding media radially outwards, and so on until the chamber wall is reached, creating a shear rate distribution across the chamber radius. Colliding media beads with different velocities transfer momentum to particles

trapped in between, with the intensity that the particle experiences dependent on the relative momenta of the media. The velocity gradient has been found from particle tracking velocimetry to be very high close to the impeller, decaying rapidly in an exponential-like manner to negligible values near the wall [39]. Because of this velocity distribution, approximately 90% of the energy applied is dissipated in 10% of the grinder volume, close to the impeller tip [40].

There is some debate regarding the dominant grinding mechanism that takes place in stirred media milling. Hogg [41] produced a population balance model, with breakage functions considering massive fracture of a particle into smaller units, and attrition of very small particles from larger particles, and found that experimental results matched better with the model when breakage was mostly due to attrition, implying the domination of shear forces over compressive normal forces. Modelling by Kwade [42] indicates that the dominant stressing mechanism in a fluidised mill is media moving in a tangential direction, colliding with media in other streamlines radially outwards that are travelling at lower velocity, which would involve both compression and attrition forces. Strobel et al. [43] used plastically deformable microscopic copper and silica spheres as probe particles in a stirred media mill. Microscopy of the product particles showed deformations consistent with compressive normal forces, but no evidence of the uneven flattening expected from shear forces. DEM and CFD simulations by Beinert et al. [44] for a disc mill show that shear dominates the interaction events at lower collision energies (below 10^{-9} J), whereas normal forces from translational impact dominate above this.

From the above studies, it is apparent that both attrition and compression forces are utilised in a stirred media mill. The relative importance of each mechanism can be expected to depend on operating conditions such as media size, density, and surface roughness, the impeller speed, mill geometry, and material properties such as particle compressive strengths and particle size. The mill type will also influence this, since gravity-induced mills have additional compressive stresses applied due to gravitational pressure [45]. A well-developed theory on how stirred media mills comminute particles via compressive forces was developed by Kwade et al. since 1996, and is summarised below.

2. Stress Intensity Theory

It has long been known that the specific energy input, the energy applied divided by the total mass or volume of particles, is the most influential parameter for affecting product particle size [46]. Therefore, within certain limits, changing the particle solids concentration at a given specific energy input (i.e. *absolute* energy input scales proportionally to solids content) does not significantly influence product size, and this has been found in

numerous examples [47-50]. This may not seem intuitive, since it stands to reason that the more particles present in the grinder, the greater the fraction of energy that is transferred to the particles rather than wasted in other interactions such as media-media contact. This can be rationalised by the concept of the *active volume*, which is the region of space between two colliding media beads where particles are stressed, and the *capturing efficiency*, with represents the number of particles stressed per collision, and both concepts were developed by Kwade et al. when introducing stress intensity theory [51].

The particles that first bridge the gap between two colliding media, either by being larger particles or by being close to the point of minimum separation between the media, absorb most of the energy available for comminution. At low solids contents, capturing efficiency is less than 1, so in some collisions there are no particles to stress, wasting energy. In the optimum solids content region, particles being present in an active volume is almost guaranteed, but there are unlikely to be several particles that bridge the gap between the media at the same time, so almost all the energy is transferred into a single particle; capturing efficiency is approximately 1, and energy efficiency is maximised. At excessively high solids contents, several particles are likely to be stressed simultaneously (capturing efficiency is greater than 1), distributing the energy over a greater area and so reducing the likelihood of particle comminution; additionally, dampening of media motion by viscous dissipation can become considerable [42]. There is a wide range of solids contents between avoiding collisions with no particles and avoiding collisions where multiple particles are stressed at once, which explains the range of solids contents in which product size appears to follow *specific* energy input and not *absolute* energy input.

Specific energy input is proportional to the product of two components; the *stress number* (*SN*), and the *stress energy* (*SE*). Stress number is the average number of collisions per particle within a certain grinding time, and stress energy is a measure of the average energy of these collisions. For mineral comminution, given a capturing efficiency of 1, the stress number is proportional to [52]:

$$SN \propto \frac{\varphi_{GM}(1-\varepsilon)}{\left(1-\varphi_{GM}(1-\varepsilon)\right)c_V}\frac{nt}{{d_{GM}}^2} \quad \dots (1)$$

where ϕ_{GM} is the mill fill fraction, ε is the media porosity (volume of slurry divided by the total filled volume), n is the impeller revolution speed, t is the grind time, c_V is the solids content (vol%) and d_{GM} is the grinding media diameter. The stress energy of a collision is assumed to be proportional to the maximum possible collision

energy, defined as the energy of a grinding media bead changing its velocity from the impeller tip speed to zero, SE_{GM} [53]:

$$SE \propto SE_{GM} = d_{GM}^3 v_t^2 \rho_{GM} \quad \ldots (2)$$

where ρ_{GM} is the grinding media density and v_t is the impeller tip speed. Stress energy is the energy applied to the media by the mill; *stress intensity*, on the other hand, was introduced by Kwade to represent the stresses that the media imparts upon the product [53]. They are technically not the same, since there are various factors that affect this energy transfer (for example, media elasticity, as discussed below), but they are at least considered proportional when these transfer factors are constant, and so can be used interchangeably in Equation (2).

For a given material and a given energy input, there is an optimum stress intensity, SI_{opt}, at which a minimum particle size is obtained, and the stress intensity vs. particle size curve at a constant energy input follows a characteristic shape about this minimum [47] (see Fig. 1a). This is rationalised by particles of a certain size and composition having a critical stress at which they break apart; at too low stress intensities, the particles deform elastically, and no grinding takes place. With increasing stress intensity, an increasing fraction of collisions have sufficient energy for effective comminution, causing the rapid drop in particle size. At higher stress intensities, there is excess energy per collision, which is wasted, resulting in a lower rate of particle size reduction (since with higher collision energies, there are fewer stress events at a given energy input). At the confluence of these two effects is the optimum stress intensity, with the minimum particle size for a given energy input [47].

Smaller particles have less cross-sectional area to break in a collision, and so the minimum required stress intensity is lower, hence the optimum stress intensity decreases with decreasing particle size [47] (see Fig. 1b). By the same principle, a coarser feed requires a larger media size. This has been understood since before stress intensity theory was developed; for example, Mankosa et al. in 1986 [54] found that dry stirred media milling of coal with different feed sizes and ball sizes found that a ratio of ball size to feed size of around 20 gave the highest breakage rate, with a very sharp decline in rate at lower ratios and a more moderate decline at higher ratios (mirroring the shape of the stress intensity vs. particle size curve in Fig. 1a).

Although such a ratio in many cases will not be consistent at different sizes, a rule of thumb is followed that the most efficient media size is the smallest that is capable of effectively breaking the largest feed particles. Due to the decrease in optimum stress intensity at finer media sizes, when a large particle size reduction is required, it is often economical to employ *cascade grinding*, which employs several grinder stages in series, each with a progressively finer media size, to maximise energy efficiency. Stress intensity is very sensitive to grinding media

size (see Equation (2)), which can explain why Vertimills, which typically have larger media, are better suited for fine grinding, whereas SMDs and IsaMills with fine media are more suitable for ultrafine grinding.

Becker et al. [47] noticed that hard minerals such as alumina are comminuted less effectively when media of relatively low hardness is used, due to collision energy being wasted in elastic deformation of the grinding media. They rewrote Equation (2) in terms of the stress intensity applied to the product, SI_P, and found that including the ratio of the Youngs' moduli of the particles to the grinding media resulted in a common stress intensity – particle size curve between all series:

$$SI_P = d_{GM}^3 \rho_{GM} v_t^2 \left(1 + \frac{Y_P}{Y_{GM}}\right)^{-1} \quad \ldots (3)$$

where Y_P and Y_{GM} are the Youngs' moduli of the particles and the grinding media respectively. Additionally, towards higher solids loadings, the influence of viscosity becomes considerable so Breitung-Faes and Kwade included a viscosity factor r_η into the above equation [55]:

$$SI_P = r_\eta d_{GM}^3 \rho_{GM} v_t^2 \left(1 + \frac{Y_P}{Y_{GM}}\right)^{-1} \quad \ldots (4)$$

This viscosity factor can be calculated from a consideration of Stokes Law, with Equation (5) defined by Knieke et al. [56]:

$$r_\eta = \left[1 + \frac{1}{St_{GM}} ln\left(\frac{x}{d_{GM}}\right)\right]^2 \qquad where\ St_{GM} = \frac{v_{GM} d_{GM} \rho_{GM}}{9\eta} \quad \ldots (5)$$

where x is the product particle size, St_{GM} is the grinding media Stokes' number, and η is the suspension viscosity. There is a critical viscosity η_C at which the media momentum cannot exclude enough fluid from between them to reach the target particle, making r_η zero, resulting in zero stress intensity and a cessation of grinding (a viscous grinding limit) [56]:

$$\eta_c = \frac{v_{GM,max} d_{GM} \rho_{GM}}{9\big(ln(d_{GM}) - ln(x)\big)} \quad \ldots (6)$$

where $v_{GM,max}$ is the maximum velocity of the grinding media (which is some fraction of the tip speed).

At a given solids concentration, finer particle sizes give a higher charge viscosity by increasing colloidal particle-particle interactions. If grinding efficiency falls faster than expected at finer particle sizes, it should be considered whether the effective viscosity is approaching η_C. Consequently, an appropriate feed solids content

must be chosen to prevent significant amounts of viscous dissipation, but also to ensure optimum capturing efficiency as discussed previously. At high reduction ratios, these two priorities may conflict due to the wide particle size change. This is not so much a problem in typical ultrafine grinding in the mining industry due to minimum P_{80} values being several μm (a single solids content is often appropriate for the whole size range), but in industrial minerals such as kaolin or calcium carbonate, this viscosity increase is considerable, and in nanogrinding it is often critical and limiting without stabilising additives [56]. If it is not possible for a single solids content to be optimal for a whole size range, then cascade grinding can be applied, using several grinders in series, with decreasing solids concentration (and finer media sizes) in later grinders as particles become finer.

Stress intensity theory assumes that the grinder system geometry is invariant [53]. Stress energies, however, have a frequency distribution that varies over many orders of magnitude, with this distribution dependent on grinder geometry. Stender et al. noticed differences in the stress energy vs. particle size curves for three different mill sizes [57]. They calculated velocity distributions and stress energy distributions in each mill and found that for a given *maximum* stress energy SE_{GM}, the *median* stress energy was higher for smaller mills. When using median stress energy rather than maximum stress energy, all mill sizes followed the same curve, indicating that the median stress energy or intensity is a more representative characteristic number. This should be considered when scaling up laboratory scale experiments.

Recently, measurements of stress intensity and stress number were carried out using microscopic spherical probe particles [43, 58]. The stress number was determined by observing the number of impact sites on the particles using electron microscopy, and the stress intensity was inferred from the size of these deformations, using a model created with finite element analysis and uniaxial compression test data. This supports many of the claims made by stress intensity theory, such as stress number being directly proportional to impeller tip speed [43] and stress intensity increasing greatly with media diameter. They also give a measurement of the broadness of the stress intensity distributions, and find that they vary over around two or three orders of magnitude [43, 58], supporting Stender et al. [57]. Particularly for very fine probe particles, grinding rate is determined by capturing efficiency since exclusion of particles from between the media beads due to fluid drag becomes increasingly dominant [43, 58].

Stress intensity theory was developed for wet grinding, but there have been some limited attempts to apply it to dry grinding. Rácz, and Csőke found that it was necessary to define an effective stress intensity to account for the increased level of caking of the powder on the grinder wall and grinding media at finer particle sizes; energy

is consumed in compressing these powder layers, which must be subtracted from the stress intensity [59]. In later work, Prziwara et al. found that dry grinding performed as one would expect from stress intensity theory, but powder flowability was of critical importance; poor powder flowability appeared to lower effective stress intensity, and has an analogous dampening effect of a high charge viscosity in wet milling [60].

From this consideration of stress intensity theory, several key points can be taken away to aid in appropriate grinding condition selection (and to rationalise different energy-size curves):

1. The optimum stress intensity (and therefore the optimum grinding media size and impeller speed) decreases with decreasing particle size.
2. Increasing the number density of particles at low concentrations will increase the number of particles per active volume, reducing the likelihood of no stressing happening in a collision.
3. Increasing the number density of particles at high concentrations will increase the chances that several particles are stressed at once, reducing grinding efficiency. Whether this will dominate over the previous factor will in part be determined by the solids concentration.
4. Viscosity increases at finer sizes as particle-particle interactions increase; this can cause viscous dampening of the media, and eventually result in a viscous apparent grinding limit.
5. If the grinding media is not considerably harder than the particles, grinding efficiency can drastically decrease.

In summary, the optimum processing conditions including media size, impeller speed, and solids concentration can change drastically between different materials and at different particle sizes. Although this complicates the application of a standard set of operating conditions with which to test all materials for grindability parameters (as with the Bond work index test), there is sufficient theoretical understanding to be able to perform lab scale trials to identify the optimum conditions and scale up successfully.

3. Energy-Size Relationships

Numerous grinding laws for describing the reduction in particle size with energy input during comminution have been developed. The first was by von Rittinger in 1867, who postulated that the energy input to comminute to a certain particle size is directly proportional to the specific surface area generated [61]:

$$E = K_R \left(\frac{1}{x_P} - \frac{1}{x_f} \right) \quad \ldots (7)$$

E is the specific energy input, K_R is Rittinger's constant, x_p is the product size, and x_f is the feed size. Rittinger's Law is more appropriate for finer particle sizes, around 50 – 100 μm, where particle breakup is primarily due to overcoming surface energy rather than exploiting pre-existing cracks.

For coarse particle sizes, such as in crushing, Kick's Law is more appropriate, which postulates that energy input is proportional to the reduction ratio [62]:

$$E = K_K log\left(\frac{x_f}{x_p}\right) \dots (8)$$

where K_K is Kick's constant. For ball mills, which are usually used at particle sizes intermediate of those found in fine grinding processes and crushing processes, Bond's Law is usually used [63]:

$$E = 10W_i\left[\frac{1}{\sqrt{x_p}} - \frac{1}{\sqrt{x_f}}\right] \dots (9)$$

where W_i is the Bond Work Index. The particle sizes in Bond's Law are almost always defined as 80% passing F_{80} (feed) and P_{80} (product) values. Each grinding law has a domain over which they match the data well, though none are appropriate over a wide range of particle sizes. These laws can all be considered forms of the general grinding law, the Walker model [64]:

$$dE = -K_n\frac{dx}{x^n} \dots (10)$$

where x is a particle size representative of the distribution, and K_n is a constant. When n does not equal 1, this can be integrated between the limits of feed size x_p and product size x_f [51]:

$$E = \frac{K_n}{n-1}\left(\frac{1}{x_p^{n-1}} - \frac{1}{x_f^{n-1}}\right) \dots (11)$$

When n = 2, this becomes Rittinger's Law, when n = 1.5, this becomes Bond's Law. For large reduction ratios typically seen in fine and ultrafine grinding, the influence of the product particle size greatly dominates the feed particle size, and so can be ignored [7]; consequently, empirical energy-size relationships for stirred media mill grinding typically take the form of:

$$E = Cx_p^{-\alpha} \dots (12)$$

$$where\ C = \frac{K_n}{n-1}\ and\ \alpha = n-1$$

It is common knowledge that as particles are comminuted from coarse rocks to micrometre-sized powders, the most appropriate grinding law changes from Kick to Bond and then to Rittinger, and so the best fit value of *n* increases with decreasing particle size (since there are fewer pre-existing cracks to be exploited by the mechanisms behind Bond and Kick laws). Considering this fact, Hukki redefined the Walker model to account for variations in *n*, which in the form of Equation (10) replaces the exponent with a generic variable *f(x)* [65]:

$$dE = -K_H \frac{dx}{x^{f(x)}} \dots (13)$$

where K_H is a constant. Some attempts have been made to find appropriate expressions for *f(x)*. Voller created an expression that allows for a combination of both Kick's and Rittinger's laws, which change with particle size [66]; this gave a better fit to data than using a constant *n*, as in Walker's Law, but is only able to function between $n = 1$ and $n = 2$. Morrell found that $f(x) = a + b(x)$ where *a* and *b* are constants allowed for accurate prediction of ball mill and AG/SAG mill energy input between product sizes of 100 μm and 100 mm [67]. However, to the author's best knowledge, a robust expression for *f(x)* within the fine and ultrafine grinding sizes has not yet been developed.

Technically, Walker's equation and its variants are only valid for a representative *mean* particle size [68]. However, in ore processing applications, it is conventional to use the 80 wt% passing size, P_{80}, to represent the particle sizes at different stages in comminution. This is easy to measure (i.e. weighing the separated fractions after sieving), although two P_{80} values can have vastly different size distributions and therefore differ greatly in mean particle sizes. However, % passing values such as P_{80} can still be used in these energy-size relationships so long as the size distribution shape is scale invariant [69]. Although it may be sensible to use a mean particle size, or even include a measurement of polydispersity, as indications of how a product will perform in the separation stage, one must be consistent with the particle size definition between different comminution stages and between different processes being compared if energy efficiencies are to be effectively assessed.

Another important consideration is that these models were derived based upon energy *applied to the particles*; this is impractical to measure so in practice energy *supplied to the machine* is used. Therefore, differences in energy transfer functions between the mill and the particles (e.g. losses from media-media contact) could be wrongly interpreted as differences in particle breakage mechanisms.

In terms of benchmarking the comminution efficiency of an industrial process, and for estimating ore grindability, using several fitting parameters per material ground or per process, such as would be required to

solve Equation (11), makes comparison between materials or processes awkward. If it still fits the data well, it is preferable to have a single fitting parameter which can readily be compared; in conventional grinding, the *Bond Work Index* has long been such a parameter.

4. Bond Work Index

The Bond standard grindability test produces a work index that is a measure of grindability for a given ore. There are three variants of this test; crushing work index, rod mill work index, and ball mill work index [2]. In this review, only the ball mill work index will be discussed, since ball mills are the only equipment of the three that are capable of significant degrees of fine grinding.

The ball mill standard grindability test utilises a particular lab-scale ball mill, with dimensions of 305 mm internal diameter and 305 mm length, and 20.125 kg of steel media with a specified distribution of different sizes. Closed circuit operation, used in most ball mill operations, is emulated by the Bond ball mill test by carrying out numerous consecutive batch grinds, screening the product, reapplying the coarse fraction, and adding new feed material for the next batch grind until steady state is reached. A condensed description of the procedure is shown below (see the appropriate publication by the Global Mining Guidelines Group for the full procedure [70]).

1. Crush the ore material of interest until all particles pass through a 3.36 mm screen.
2. Measure the packed bulk density, and add the weight required for 700 cm^3 of feed material as the charge to the ball mill. The *Ideal Potential Product* (*IPP*) required to emulate 250% circulating load is this weight divided by 3.5.
3. Add the dry charge to the mill and run at 70 rpm for 150 revolutions.
4. Remove charge from the mill, screen it with the closing screen (typically 106 μm [71], though any appropriate size can be used) and determine weight of screen oversize and undersize.
5. Calculate net product weight (g) by subtracting the undersize of the feed from the undersize of the product; divide this by the number of revolutions (150 revolutions in the first grind) to obtain the 'grams per revolution' (G_{Pr}).
6. Add the screen oversize back to the mill and add fresh feed material until the initial weight is reobtained.
7. Run the mill again for a number of revolutions determined by: [(IPP – weight of undersize in fresh feed) / previous G_{Pr}], in an attempt to achieve a circulating load of 250%.
8. Carry out steps 4 – 8 at least five times, or until G_{Pr} reaches an equilibrium, or reverses its rate of change.

9. Carry out screen analysis on the undersize of the last three cycles combined, and the oversize of the last cycle, in order to determine P_{80}. Use the mean G_{Pr} of the last three cycles as the ball mill G_{Pr}, and use this mean G_{Pr} in the following calculation to determine the Bond Ball Mill Index Wi_{BM}, in kWh/t:

$$Wi_{BM} = \frac{49.05}{{P_{100}}^{0.23} G_{pr}^{0.82} \left(\frac{10}{\sqrt{P_{80}}} - \frac{10}{\sqrt{F_{80}}} \right)} \quad \ldots (14)$$

where P_{100} is the closing screen aperture size (which separates net product from recycled coarse oversize material). Wi_{BM} is the energy required to reduce the feed size from infinity to 80% passing 100 μm [72] and is a value dependent only on the feed material.

In order to gauge the efficiency of an industrial grinding circuit, Rowland proposed the *Operating Bond Work Index* [73]. This requires taking a grinding circuit feed and product, conducting screen analysis to determine F_{80} and P_{80}, measuring the mass of material processed in a given time, and measuring the energy used by the mill in a given time. This calculation is a rearrangement of Equation (9) [72]:

$$Wi_O = \frac{E}{\frac{10}{\sqrt{P_{80}}} - \frac{10}{\sqrt{F_{80}}}} \ldots (15)$$

where E is the specific energy input (kWh/t), and Wi_O is the operating work index. By dividing Wi_O by Wi_{BM}, a measure of the efficiency of a ball mill comminution circuit compared to the lab scale Bond ball mill test for a given material can be established. However, Bond derived the correlation used in Equation (14) based upon industrial results from a 2.44 m internal diameter ball mill, operating under wet closed circuit grinding with a circulating load of 250%. If an industrial ball mill circuit deviates from the type used by Bond in some way, the ratio of the operating to lab work index is not a fair measure of efficiency. Therefore, Bond introduced various efficiency factors [74] which are used to accommodate for differences in mill diameter, differences in feed and product size distributions, low reduction ratios, whether mill operation is wet or dry, and whether closed or open circuit operation takes place [72]. Of particular relevance is the fine grinding efficiency factor (EF_5), for which an empirical relation exists to estimate the loss in efficiency when grinding to P_{80} values below 75 μm:

$$EF_5 = \frac{P_{80} + 10.3}{1.145 P_{80}} \ldots (16)$$

These efficiency factors multiply Wi_{BM} to allow a fairer comparison to Wi_O.

However, there are many problems with the Bond work index. The need to use a batch process to emulate closed circuit grinding is very time-consuming. Some have tried to instead use open circuit batch grinds to obtain a measure of ore grindability (e.g. Levin [75]); however, for ores containing several phases of significantly different grindabilities (which is common), this is not appropriate because in closed circuit grinding there will be the accumulation of the harder phase within the mill, which an open circuit grind would not emulate [2]. In addition, open and closed circuit grinding give different product particle size distributions, even at the same P_{80} value [76]. Another issue is the fact that the Bond ball mill index test is carried out dry, whereas many industrial ball mill processes are wet; agglomeration in dry ball milling often becomes limiting at P_{80} values of around 87 μm [76] which is a factor that limits its applicability to fine grinding.

The Bond work index cannot sensibly be applied to stirred media mills. Firstly, almost all stirred media mill processes are wet, and grind to below the limit where agglomeration would be limiting for dry ball milling. Secondly, many efficiency factors are already required to correlate the work indices of the lab Bond ball mill with industrial ball mills; changing to a different type of mill with different geometries, different operating principles and different types of stressing conditions present makes the application of a stirred media mill efficiency factor unlikely to work generally. Additionally, the feed size and product size in typical stirred media mill operating ranges are much finer than the standard work index test can account for, even with the efficiency factors; for example, the feed to a Bond grindability test must be coarse enough to allow crushing to below 3.35 mm [76], which is a top size about an order of magnitude higher than for typical stirred media mill feed. Finally, the Bond grinding model tends to be a poor fit in the stirred media mill operating range [7] and so will give misleading results if used to estimate energy input at different P_{80} or F_{80} values.

Levin modified the standard Bond ball mill test to apply to finer grinding. In the Levin test, several open circuit batch grinds are carried out, each with a different grinding time [77]. The % passing 75 μm was measured and plotted as a function of time. By knowing the energy input per revolution of the mill (which is similar for most materials), the energy input required to obtain a certain % passing 75 μm could be estimated. This appears to give much better accuracy in predicting the energy input for the coarser end of fine grinding, compared to the Bond work index [77]. Using the change in <75 μm fraction is better as an assessment of a change in specific surface area (more appropriate for fine grinding, by Rittinger's Law) than the P_{80} because the latter is skewed by the change in the particle size distribution shape between ball mill product and stirred media mill product [78].

Although 75 μm is the screen size which Levin chose to use, which is still very coarse for stirred media mill product, screen analysis could be carried out on the products of these tests at different screen sizes (e.g. 45 μm) to obtain a relationship more appropriate for finer grinding. From screen analysis, a P_{80} vs. energy input curve can therefore be created, and an appropriate coefficient and exponent for the Walker equation applied.

The Levin test is commonly used for fine grinding with ball mills, though because it is an open circuit test and most ball mills are closed circuit, it typically overestimates energy requirements due to the test wasting energy grinding fines that would otherwise have been removed [79]. It is more appropriate for stirred media milling than the Bond ball mill test, because it does not rely on Bond's Law holding, and product sizes can be in a similar range (for Vertimill / Tower Mill products at least). However, it suffers from the same problem as the Bond ball mill test in that the ball mill is not representative of stirred media mills and will tend to greatly overestimate the energy input required towards finer product sizes. Methods other than the Bond or Levin tests are therefore used to estimate energy input required for a specific performance in a stirred media mill, which are discussed below.

5. Grindability Tests for Stirred Media Mills

By far the most common approach for estimating the energy requirements of industrial scale stirred media mills involve series of batch grinds using a laboratory-scale equivalent mill. These batch grinds apply a range of specific energy inputs and measure the P_{80} results, to form a 'signature plot'. Typically, a power law model (Equation (12)) fits the results, which is a straight line on a log-log plot of energy input vs. P_{80}, with the gradient giving the exponent α and the y intercept giving the coefficient C.

In a ball mill, scale-up from laboratory tests is complicated by the fact that at smaller scales the total acceleration due to gravity of the falling balls is lower due to a shorter falling time, and so the impact energy applied is lower. This is partly true for gravity-induced stirred media mills such as the Vertimill, where there is a considerable gravitational contribution to the total stress intensity that scales with height [45]. For fluidised stirred media mills (i.e. SMDs and IsaMills), using scaled-down mills to emulate industrial operations is more practical, since all forces are driven by the impeller, and can be scaled up by controlling impeller tip speed.

For gravity-induced stirred media mills, the most common grindability test is the Jar Mill test, developed by *Metso* for sizing Vertimills. Rather than using a lab scale Vertimill, which suffers from scaling problems, this test utilises a lab scale ball mill that is smaller than in the Bond and Levin tests, and uses 19 mm media (typical of industrial Vertimills) [8], to carry out a series of batch grinds on the feed material at different energy inputs. This allows for better representation of the types of stressing that takes place in a gravity-induced vertical mill

(lower stress intensity, higher stress frequency, less impact, more attrition) than with the Bond test. In addition, the Jar Mill test is not limited to dry grinding, and so the influence of feed solids content can be assessed. With the energy vs. size relationship producing power law parameters, the energy required for the Jar Mill to obtain a given P_{80} can be found. By multiplying this by a factor of 0.65, the energy requirements of an industrial Vertimill can be predicted [16].

The use of a single scale-up coefficient does not take into consideration the fact that taller Vertimills have higher stress intensity contribution from gravitational pressure. Despite this, examples show that the correlation between Jar Mill and industrial Vertimill data is good. Mazzinghy et al. found that Jar Mill tests over-predicted the energy input of moderately sized industrial Vertimills by only 12% [80], and for data from Villalobos et al. using a pilot Vertimill on four different ores, the Jar Mill prediction was within 10% once the correction factor was included [81]. Accurate predictions of the operating work index of industrial Vertimills was also found for a copper concentrator circuit by Bergerman et al. [82], though this was jeopardised when the feed material was changed to be finer than what was used in the Jar Mill test. These examples indicate that the Jar Mill produces a grinding environment that is sufficiently analogous to a gravity-induced mill to allow for practical scale-up. Unfortunately, the same problem with grinding heterogeneous ores with components of different grindability arises as with the Bond grindability test, since most Vertimill operations are closed circuit [28], and so the open circuit Jar Mill test would not emulate the accumulation of hard material in the grinder. This is usually not an issue for SMDs and IsaMills, where almost all operations are open circuit [26, 28].

In the case of IsaMills, a 4-litre lab scale IsaMill is commonly used to produce a *signature plot* for the prediction of full-scale energy requirements. A description of this test, and examples where it has been applied successfully is provided by Larson et al. [83]. In these cases, the same size and composition grinding media as for the full-scale mill is used, as is the feed particle size distribution and solids content. The tip speed of the lab mill is run at around a third of the industrial IsaMill, meaning that maximum stress intensity SI_{GM} is six times higher for the latter [9]; at least some of this is because smaller mills have narrower stress intensity distributions, leading to a lower median stress intensity for a given value of SI_{GM} [57], as discussed in the stress intensity theory section.

The slurry is passed through the IsaMill, and collected in a product tank, and a sample is taken for P_{80} measurement. The slurry is once again passed through the mill and collected in another tank, and the particle size is once again measured. This is repeated around five times, which allows the production of a P_{80} vs. energy input curve. It is essential to ensure that steady state is reached within the mill, and for a 4-litre mill, it was found that

15 kg of 4.2 g/cm^3 specific gravity feed was sufficient to comfortably achieve this [83]. The signature plot method aims to ensure that the physics, geometry, velocity distributions, and the mechanisms of grinding in the lab scale mill are very similar to those found in the industrial mill. Because of this, it was found that the 4 litre IsaMill emulated the energy-size relationship of larger mills (3,000 and 10,000 litres) very well in terms of P_{80} values, although the fine end of the distribution extended to smaller sizes in the case of the lab mill [83]. In order to assess the steepness of the particle size distribution, both P_{80} and P_{98} (98% passing) values are often measured. In the example of the GPM gold operation in Armenia, the signature plot method predicted the energy required for the industrial mill to grind to a P_{80} of 10 μm to a very high accuracy (within 2%) [84]. The IsaMill signature plot method is now widely used in fluidised stirred media mill scale-up; as of 2012, over 100 such trials have been carried out worldwide [85].

It was also found that this 4-litre lab IsaMill was able to match the energy-size relationship of industrial SMD grinders, given that media size is matched, and appropriate tip speed used, despite the former mill being horizontal and the latter vertical [83]. The Jar Mill test can also be used for SMD scale-up, with an energy input prediction found by multiplying jar mill energy by a factor of 1.1 [16], though at finer media sizes the stress intensities in the jar mill would become increasingly unrepresentative. As with IsaMills, lab-scale SMD units can typically be used to accurately predict energy inputs for industrial units, as has long been done in areas of industrial minerals grinding such as kaolin and calcium carbonate (for an example, see work by Tamblyn [86]).

A serious disadvantage of the signature plot method is that the model cannot be extrapolated to the feed size at 0 kWh/t; more experiments must therefore be undertaken to create a new signature plot every time the feed particle size distribution changes. Rather than the power law, Larson et al. [87] fitted data using a relationship of energy input vs. the square of the % passing value enabling extrapolation to the feed size, and accommodating changes in feed size just by changing the y intercept; although this has potential, there has been a paucity of data since then that validates this alternative model [9]. Alternatively, Equation (11) could be used rather than a power law model, but because the optimum value of the exponent is expected to change with particle size, making the model broader to include the feed and low energy product sizes may jeopardize the fit of the model in the region of the target product particle size.

6. Investigating a New Operating Work Index for Stirred Media Mills

In terms of an equivalent of a Bond ball mill work index for a given feed material, the power law models used to fit signature plots from lab scale grindability tests give two parameters; a coefficient and an exponent. For easy

comparison between different materials, it is better to have just one number, and so often a Bond work index is calculated for the material from signature plot data, which is effectively an operating Bond work index of the lab scale mill. This work index will show which materials are harder to grind at a given P_{80} under the operating conditions used, and can be used to benchmark the operating work index of the industrial plant in order to track efficiency and compare systems.

However, Bond's grinding law tends to be a poor fit below around 100 μm [7]. The further away Bond's Law is extrapolated away from its applicability range, the more misleading the results. If Bond's Law is applied to the fine and ultrafine grinding range, a rapid increase in work index at finer sizes will usually be noticed. This means that accurate extrapolation of the energy input required at significantly different P_{80} values to the one used in the test is less likely, and the relative grindability of different materials cannot be accurately assessed from their work indices if they differ considerably in particle sizes. In these cases, more Bond ball mill tests would have to be carried out at different P_{80} values in order to determine variation in work index with particle size, which multiplies the time and resources required for an already time-consuming test. A more appropriate choice of energy-size law for a redefinition of the work index in this range would reduce the variability of the work index with size and be much more useful as a material parameter. In this section, the most appropriate alternative for the operating Bond work index is discussed.

Stamboliadis et al. [88] recognised that the apparent changes in Bond work index with size are due to n deviating from 1.5, and so generalised the Bond work index as follows:

$$W_i = \frac{E}{100^{n-1}\left(\frac{1}{x_p^{n-1}} - \frac{1}{x_f^{n-1}}\right)} \quad \dots (17)$$

where n is the exponent of Walker's equation (Equation (10)). They then found the value of n at which the variation in work index with size is at a minimum, and used that to calculate a modified work index. They found that cryptocrystalline materials like limestone and magnetite, and materials with cleavage, follow Bond's Law well, but materials with larger crystals that must be broken for comminution to occur have larger n values, approaching Rittinger's Law; clearly the value of n within a certain size range differs between materials.

Mucsi ground quartz in a stirred media mill to very fine sizes, and defined an operating Rittinger index $C_{R,Op}$ with an equation in the same form as Equation (17), with $n = 2$ (though the 100^{n-1} factor was not included) [89]. He tracked whether $C_{R,Op}$ changes with particle size, to determine the regions in which Rittinger's Law was

being followed; in general it held reasonably well down to P_{80} values of around 0.5 μm, after which $C_{R,Op}$ rapidly increases, almost asymptotically, indicating that a grinding limit was reached (which he believes is due to reaching the primary grain size of the material).

An investigation of the literature was carried out in order to determine variation in n exponent values in various fine and ultrafine grinding examples. The literature was searched for energy-size relationship data for stirred media mill grinding, and Equation (11) was applied to model the energy input vs. P_{80} particle size. Using the Excel solver tool, the optimum values of n and K_n were found in order to minimise the average error between the model and experimental data points. Additionally, the average error when $n = 1.5$ (Bond's Law) and $n = 2$ (Rittinger's Law) was investigated, as was the power law model. These results are displayed in Table 1.

The mean error from the four fitted models were as follows:

- Bond model ($n = 1.5$) = 16%
- Rittinger model ($n = 2$) = 12.5%
- Walker model (variable n) = 5.1%
- Power law model (variable α) = 5.9%

The Bond model is a poor fit in most cases, due to most of the relevant particle sizes below its range of applicability. The Rittinger model is a better fit, but still relatively poor. The Walker model has a much better fit and is slightly better than the power law model. The power law model is slightly worse than the Walker model because at some of the coarser product sizes, the influence of the feed size is significant.

It was found that the mean best fit value of n was 2.05, which is very close to what is expected from Rittinger's Law. The range of optimum n values, however, varied from 1.12 to 2.97, with a standard deviation around the mean of 0.50. It is expected that as particle size becomes finer, the value of the exponent n would increase towards 2, since particle breakage transitions from exploiting pre-existing cracks to breaking pristine surface area. To investigate this, the optimum n exponent value of the Walker model was plotted against the mean P_{80} of the data points for which the optimum is calculated (see Fig. 2). In general, finer particle sizes result in higher n exponent values as was expected, but the correlation is very poor; obviously other factors are complicating this relation.

The n exponent values between 1 and 2 can be rationalised using the idea that the relative influence of the Kick, Bond, and Rittinger grinding mechanisms differ between cases. However, over half of the series investigated

have best fit exponent values greater than 2, which are beyond the Rittinger model; exponents higher than 2 mean that finer particles are harder to grind than could be expected from the energy required to produce new surface area.

Higher exponents can be explained with stress intensity theory. As particles are ground finer, their number concentration increases, influencing capturing efficiency; whether this is advantageous or detrimental to finer grinding depends on the initial solids content. For typical solids contents (on the order of 50 wt%) and media diameters, at very fine sizes it can be expected that the probability of multiple particles being stressed in a single stress event increases with decreasing size, and so grinding efficiency can be expected to decrease [42]. In addition to this effect, viscosity increases at finer sizes, which can result in a dampening of grinding media motion. If Rittinger's Law was otherwise followed at a capturing efficiency of exactly 1, then capturing efficiencies increasing to greater than 1 at finer sizes (which reduce efficiency of grinding per impact) would increase the best fit value of *n* to greater than 2 if product particle size is fine enough, as would the higher charge viscosities at finer sizes.

Additionally, for finer particle sizes, the optimum stress intensity decreases; if the grinding conditions are optimised for the coarser part of the energy-size curve, this would result in an increase in the exponent n, whereas *n* would decrease if the grinding conditions are optimised for the finer part of the energy-size curve. Table 1 shows that grinder operating conditions clearly influence the exponent of the energy-size relationship; in Tower Mill trials by Yan et al. [90], pyrite and quartz were ground with three different media sizes. The smaller media tested had lower *n* values than the larger media (which have higher stress intensities) and so the relative efficiency of smaller media versus larger media increases at finer particle sizes.

In addition to differences in operating conditions, the feed material influences the *n* exponent value; Shi et al. [91] used a lab scale IsaMill to grind four sources of ore from different areas of a comminution circuit, including a pyritic gold ore flotation concentrate, iron ore from the undersize stream of an autogenous grinder trommel, and lead-zinc ore from both cyclone underflow and the undersize stream of an autogenous grinder trommel. These gave a wide range of exponent values, though it is not clear how much of this is from the material composition and how much is due to the differences in feed and product size.

From the limited data set available, it is difficult to distinguish between the influences of operating conditions, feed composition, feed and product size, and grinder type. It is obvious, however, that there are many factors other than the current particle size that influences the exponent of the energy-size relationship. Within the size

ranges of interest, a single value of *n* cannot be expected to apply for all materials and operating conditions. This wide variation in exponent values was found in similar analyses by Doll [7] and de Bakker [9]. However, it is also problematic to define a general work index based upon Equation (17) with varying n; though not shown here, such a general work index was calculated for all series considered, and varied greatly between 0.007 (at *n* = 3.5) and 214 (*n* = 1.1). Since no two ores are going to differ in grindability by five orders of magnitude, collapsing the Walker model parameters into a single work index number is not useful, since the value of *n* must be similar for a meaningful comparison.

The competing priorities of using an accurate energy-size model and producing a single grindability number can be reconciled by the fact that for a comparison of different feed materials or milling operations it is often not necessary to model the entire energy-size relationship from the feed size to beyond the desired product size; it is typically only the region surrounding the desired product size, wherein the actual particle size achieved is likely to be, that is of interest in terms of assessing efficiency. When fitted to just this region, the error from the model not having an accurate value of *n* is lower than for the complete energy-size curve. The closer the value of *n* that is chosen for this operating index is to the 'true' value of n, the larger the range of particle sizes about the target size for which an accurate estimation of the energy requirement can be determined. Since the average best fit of *n* found in this analysis approximates Rittinger's Law, and because it fits an intuitive grinding model, for efficiency benchmarking of stirred media mills, it is suggested to use the Rittinger operating index as defined by Mucsi [89] (see Equation (18)); although in many cases it will still be inaccurate, it will usually be significantly more accurate than the Bond operating work index.

$$C_R^{Op} = \frac{E}{\frac{1}{P_{80}} - \frac{1}{F_{80}}} \dots (18)$$

This can be used both as an operating work index to track and compare industrial efficiencies, and to encapsulate the results of the lab scale signature plot test in an equivalent of Wi_{BM} for a material. For a single number to compare different milling operations to each other, the Rittinger operating index is the most appropriate that has been found, though if the P_{80} values differ greatly between compared situations, both the exponent and coefficients from the power law or Walker models should be used instead to accommodate deviations from the Rittinger model.

Laboratory scale batch grinding equivalents can accurately predict industrial stirred media mill energy requirements, can provide material grindability parameters, and can determine how these grindability parameters

and energy requirements vary at different operating conditions. This is facile if such lab scale equipment is available, but if not, this can be expensive to do at external laboratories (e.g. the IsaMill signature plot method costs around $50,000 per test series [85]). Consequently, any ore measurements that can accurately predict grindability, and so allow for energy requirement estimations without the need for batch grinding, would be welcome. For fine and ultrafine grinding, this is not yet possible, but there are two parallel streams of research that are approaching this; one is based upon stress intensity theory, and the other is an adaption of a breakage model developed for impact mills. These are discussed in the following two sections.

7. Using Stress Intensity Theory to Predict Material Grindability

Breitung-Faes and Kwade proposed that the optimum stress energy to apply would be a function of the compressive strength of the macroscopic material, σ_{CS}, and the ratio of the current particle size, x, to the particle size of the absolute grinding limit, x_{min} [95]. They found an inverse relation with various mineral species between the ratio of the optimum median stress energy to the compressive strength, and the ratio of the current particle size to the minimum particle size (see Fig. 3). This concept was used in another paper by Breitung-Faes and Kwade [96] where they derived an expression for the optimum median stress energy:

$$\overline{SE}_{P,Opt} = K\sigma_{CS}x_{50}^{3}\frac{x_{min}}{x_{50}} \quad \ldots (19)$$

where x_{50} is the current median particle size, and K is a constant which sums up various factors including inaccuracies in the median stress intensity calculation, and energy losses. Given that K, σ_{CS}, and x_{min} are known, and a target value of x_{50} is chosen, optimum grinding conditions can then be calculated [96]:

$$d_{GM}^{3}v_{t}^{2}\rho_{GM} = \frac{\overline{SE_P}}{f_{Mill}}\left(1+\frac{Y_P}{Y_{GM}}\right) \quad \ldots (20)$$

where f_{mill} is a factor to convert the median stress energy to the maximum stress energy of the grinding media as defined by Equation (2); this value characterises the broadness of the frequency distribution of the stress energy. As discussed previously, this depends at least on grinder volume [57], and probably other factors such as grinder geometry and charge viscosity.

The value of x_{min} is considered the shortest distance between edge dislocations of an average crystal grain, and was estimated in the work by Breitung-Faes and Kwade [95-96] using an equation developed by Nieh and Wadsworth [97]:

$$x_{min} = \frac{3Gb}{\pi(1-v)H} \quad \ldots (21)$$

where G is the shear modulus, b is the burgers vector length, v is Poisson's ratio, and H is the hardness (Breitung-Faes and Kwade used Vickers Hardness *HV10*).

Breitung-Faes and Kwade supported their model by calculating optimum parameters, and experimentally determining the energy input required to achieve a target particle size for silicon carbide [96]. They then experimentally determined the energy input required for two sets of non-optimum conditions, and so showed that the optimum conditions gave the lowest energy input.

The specific energy input under given conditions can be predicted from the following equation [98]:

$$E = \frac{\overline{SE}_P SN_{GM}}{v_{mill} v_\eta v_P} \ldots (22)$$

where SN_{GM} is the grinding media-related stress number (not the *product-related* stress number shown by Equation (1)), v_{mill} is the mill-related transfer coefficient, v_η is the viscosity-related transfer coefficient, and v_P is the product-related transfer coefficient. SN_{GM} is determined by [98]:

$$SN_{GM} = n \frac{m_{GM}}{\frac{\pi}{6} d_{GM}^3 \rho_{GM}} t \ldots (23)$$

where m_{GM} is the mass of grinding media. SN_{GM} is a measure of the number of media collisions (not the number of product stress events). The value of v_P depends on the elastic moduli of the product and grinding media [99]:

$$v_P = \left(1 + \frac{Y_P}{Y_{GM}}\right)^{-1} \ldots (24)$$

The value of v_η can be found by dividing the power draw when the mill is operated with a water charge, by the power draw with the product charge. The value of v_{mill} is found by operating the mill with a water charge (so v_P and $v_\eta = 1$) for a given energy input E_L, and comparing with the median stress energy and calculated SN_{GM} [99]:

$$v_{mill} = \frac{\overline{SE}_P SN_{GM}}{E_L} \ldots (25)$$

These transfer coefficients are relatively easy to determine, and enable the conversion of calculated stress energies and stress numbers into a specific energy input. By obtaining the median stress energy from Equation (19), the minimum possible energy input for a given duty can be determined, and so long as the mill scale-up

factor f_{mill} has been determined (in a similar 'benchmarking' way as v_{mill}), the optimum operating conditions can be determined from Equation (20). The energy input prediction was over 90% accurate in the example of Breitung-Faes and Kwade [98].

Material characterisation techniques including compression tests and indentation tests produce the input data for this model (except for v_η determination, though this is likely to be similar across most materials and so may be approximated with historical data). In principle it is not necessary for the material to even be processed in a grinder for the prediction. However, there are serious problems with the practical applicability of this model for the grinding of ore. For example, ore materials are often highly heterogeneous, and so different regions will have different crystal sizes, and strengths. This is particularly a problem for the x_{min} calculation; for each ore sample, tests to determine the parameters used in Equation (21) must be carried out on enough areas to be representative of the whole, which is an unreasonable requirement, particularly when ore properties can vary on a daily basis. This problem is compounded if it cannot be taken for granted that the Young's modulus of the product is much lower than the grinding media, since these tests must also be undertaken to determine v_P and optimum operating conditions. This effort is likely to be more costly and time consuming than equivalent laboratory grinds.

Another problem is that the sensitivity of v_{mill}, f_{mill}, and K to various operating conditions and mill geometries is not yet understood. Operation of the industrial mill under various conditions is required to determine these values and understand any variation, and so until a database of these values for different mills at different conditions exists, this cannot be used for sizing new mills for a given application. However, this method does enable an existing mill to change operating conditions and specific energy input in response to a feed with different mechanical properties in order to maximise energy efficiency given that these mechanical properties can practically be measured.

Although the model of Breitung-Faes and Kwade appears to match with experimental data for the pure mineral species that they used in their experiments, to practically implement this industrially in the mining industry would require some way of determining an equivalent of x_{min} empirically, without requiring extensive single particle mechanical testing; for example, as Knieke et al. [100] did this by grinding for an extremely long time, with the addition of appropriate dispersants to prevent reagglomeration. This would still have the problem of a heterogeneity of grinding limit sizes, so an average would have to be used in the calculations. This could use any grinding equipment suitable for nanoscale grinding (e.g. several consecutive IsaMill / SMD batch grinds, each with progressively smaller media) since the rate of size decrease does not matter; only the value of x_{min}.

The accuracy of this model is likely to be much worse than lab scale grinding tests such as the IsaMill signature plot method; although the fit in Fig. 3 looks good, it is a log-log plot, and so disguises the relatively wide spread of data points. However, practically it can be used to select appropriate operating conditions to trial in these lab scale grinding tests, which could save time and resources if ore is used that is markedly different to what has been tested previously.

Although currently not practical for the mining industry, a form of this model may one day replace the empirical tests in predicting specific energy input (or at least in identifying suitable operating conditions). In addition to the requirements for determining x_{min}, the influence of various parameters on v_{mill}, f_{mill}, and K must also be understood first, along with other factors that have not been included that are responsible for the wide spread of data in the correlation. For now, material characterisation of a typical ore and estimation of the model parameters could at least give a ballpark figure of an optimum stress intensity for which signature plot lab scale grinding tests could be carried out at, and can be used to determine specific energy input once benchmarking tests are completed.

8. $W_{m,min}$ and f_{mat} Mastercurve, and the JK Size-Dependent Breakage Model

A separate phenomenological approach for modelling the breakage of materials in comminution was developed by Vogel and Peukert [101]. They used dimensional analysis and fracture mechanics considerations to derive characteristic material parameters which together can predict the probability of particle breakage under certain impact conditions. The first parameter, f_{mat}, is the resistance of the material against impact fracture, and consists of various properties such as the Young's modulus and Poisson's ratio [102]. The second parameter, $W_{m,min}$, is the 'threshold energy' that the particle can absorb before breakage [101]. Vogel and Peukert used Weibull statistics to obtain an equation for the breakage probability S:

$$S = 1 - e^{-f_{mat} x k (W_{m,kin} - W_{m,min})} \quad \ldots (26)$$

where $W_{m,kin}$ is the mass-specific impact energy (the kinetic energy of the collision), x is the initial particle size, and k is the number of impacts that occur per particle. For seven different materials, in size bands between 8 – 0.095 mm, Vogel and Peukert carried out single-particle impact tests, and were able to obtain f_{mat} and $W_{m,min}$ for each material by observing the variation on breakage probability with impact velocity. A plot of the breakage probability S vs. the dimensionless stressing parameter $f_{mat} x k (W_{m,kin} - W_{m,min})$ shows that the results for all of these materials collapse onto one mastercurve (see Fig. 4). $W_{m,min}$ varied strongly with particle size, so Vogel and Peukert used the product $xW_{m,min}$ as a material parameter as it remains roughly constant with size [101]. In

further work, they used an impact mill with the outlet screen removed in order to stress many particles at once whilst still ensuring single impacts per particle, and found similar results [103].

Meier et al. [104] found that for organic pharmaceutical powders, f_{mat} and $W_{m,min}$ can be predicted from a correlation with the brittleness index (the ratio of hardness to fracture toughness), and can therefore be derived from Vickers indentation tests rather than empirically from milling. However, to the author's best knowledge, this has not been demonstrated for metalliferous ore particles. In the case of ore, the heterogeneity of grain sizes and composition means that an excessive number of indentation tests are likely to be required for representative f_{mat} and $W_{m,min}$ values, and so empirical lab scale milling tests are probably more appropriate.

The f_{mat} and $W_{m,min}$ method can predict breakage probability, but it alone does not give an indication of the breakage distribution function, i.e. the size distribution of the resulting fragments. To remedy this, Shi and Kojovic modified this theory, allowing for a calculation of a breakage index t_{10} [105]:

$$t_{10} = M\left(1 - e^{-f_{mat} x k(E_{cs} - E_{min})}\right) \quad \ldots (27)$$

where t_{10} is the percentage of product material that passes below $1/10^{th}$ of its feed size, E_{CS} is the mass specific impact energy (equivalent of $W_{m,kin}$), E_{min} is the threshold energy (equivalent of $W_{m,min}$), and M is a material specific parameter which describes the t_{10} value that results given that the particle breaks. The t_{10} value can be readily converted into other t_n values (t_n being the percent product passing $1/n^{th}$ of the feed size) (see work by Narayanan [106]). Shi and Kojovic validated Equation (27) with various ore types and sizes (from 5 – 82 mm). Equation (27) is called the *JK size-dependent breakage model* and has been used to characterise breakage of ore and coal particles [107].

Bonfils and Powell [108] and Davaanyam [109] reformulated Equation (27) to include a size-dependency exponent α, which in many cases greatly improves the fit with the data:

$$t_{10} = M\left(1 - e^{-f_{mat} x^{\alpha} k(E_{cs} - E_{min})}\right) \quad \ldots (28)$$

The JK size-dependent breakage model was formulated for impact breakage, as experienced in SAG mills for example. One of the first to apply it to compression breakage was Nadolski et al. [110], who derived f_{mat}, E_{min} and α (0.5 in their case) using slow loading compression tests with a piston press. Further work with compression was done by Shi and Xie, who modelled ball mill comminution with the JK size-dependent breakage model using data from a JK fine-particle breakage characteriser (JKFBC) test [111]. The JKFBC employs a ball-and-race mill, which is a modification of the Hardgrove Mill commonly used for coal grindability

measurements [112] and uses compression and attrition forces to break down the charge. Material parameters such as f_{mat} are determined by varying the energy applied and observing the change in product particle size distribution. When such parameters were used in a population balance, they predicted ball mill particle size distributions at a given energy input [111].

Palaniandy applied this to gravity-induced stirred media mills, again using data from a JKFBC test [113]. Due to the JKFBC mill and the stirred mill both relying on compression and attrition forces, and because stress intensities are thought to be similar between both cases, the JKFBC mill appears to be appropriate equipment for particle breakage characterisation in this case [113]. In stirred media milling, the energies experienced are typically much higher than the minimum threshold energy E_{min}, and so Palaniandy assumed that $E_{min} = 0$ (this is generally true for comminution of brittle particles, so long as stresses are high enough that low energy incremental breakage does not dominate [107]). Palaniandy found that Equation (28) holds for four different ore types, at various size bands between 1180 and 53 μm, even when E_{min} was ignored. They also defined an ore hardness parameter SM_i based upon the values used in Equation (28):

$$SM_i = Mf_{mat}x^{\alpha} \quad \ldots (29)$$

Huang found breakage parameter values M, f_{mat}, and α of an industrial Vertimill feed using the JKFBC test, and used them as inputs in a modified form of Equation (28) in order to produce a transfer matrix for a mass-size population balance [114]. This population balance predicted the performance of the industrial Vertimill with high accuracy.

To summarize, the f_{mat} breakage model was originally formulated by Vogel and Peukert [101] to model impact breakage, though numerous studies have shown that it is also applicable to compression breakage [109-111,113-114], and adapted to include a particle size exponent and to predict a breakage index t_{10}. The parameters needed to model breakage in a comminution-attrition device such as a Vertimill can be derived from various size fractions of ore samples in a lab scale ball-and-race mill according to the JKFBC test. These enable the prediction of a t_{10} value, which for typical minerals can be extrapolated to describe a particle size distribution according to Narayanan [106].

This information can be used to describe the breakage function in a population balance model in order to predict the energy input required for a given particle size distribution. This method has a distinct advantage over conventional population balance models, as the breakage and selection functions can be recalculated whenever the ore changes, by carrying out more lab grinding tests to obtain f_{mat}, M, and α, and permits changing the mill

energy input in advance in order to achieve the target particle size distribution. In addition, an ore SM_i value can be calculated from these parameters, which can be used to compare ore types, similar to how the Bond work index is used.

However, there are serious issues regarding the use of the t_{10} value; the t_{10} vs. t_n relationships have been found to not apply for certain ore types, including soft ores or ores that are highly heterogeneous with components of different competencies. In such cases, t_{10} cannot accurately characterise the particle size distribution, and likely gives misleading energy requirement predictions [115]. Additionally, Equations (26-28) were developed generally for relatively coarse feed particles, and are more applicable to crushing than for grinding (where Rittinger's Law increasingly applies) [115]; the x^{α} term allows for accurate extension down to sizes of several hundred μm, but in this review no data was found validating the correlation at sizes near typical fluidised stirred mill feed sizes (less than 100 μm). For the stirred media mill size range, correlations between f_{mat}, M, α, and a more appropriate particle size such as P_{80} or % passing a certain value (as with the Levin test) should be sought before applying this model.

Another disadvantage is that milling tests must still be carried out for each material to obtain f_{mat}, M, and α, just with a different type of mill (JKFBC); it is not obvious whether this test saves time and resources compared to carrying out batch grinds with a lab-scale IsaMill, for example, and if a choice had to be made, the equipment more directly applicable to the industrial mill should be used. It would be much more useful if equivalent parameters could be found from lab scale stirred media mill tests, but no examples have been found in the literature of attempts to do so.

This approach can be considered on the basis of stress intensity theory. When using the original Vogel and Peukert mastercurve (Fig. 4), with given values of f_{mat} ($W_{m,min}$ being negligible for stirred milling of brittle materials), the lowest collision energy that gives near-100% breakage probability can be identified. This is the optimum stress intensity [116], and so energy efficiency can be maximised by choosing appropriate media sizes, densities and velocities to obtain this. Additionally, calculating stress intensities and stress frequencies, and including them in a population balance model along with the f_{mat} theory parameters, may allow the model to suggest optimum operating conditions to minimise energy input given feed material of certain properties, and predict the optimum energy input value.

9. Conclusions

As typical ore quality declines over the years, fine and ultrafine grinding become increasingly necessary in many operations to improve recovery and grade. Stirred media mills tend to be much more efficient than ball mills at finer sizes, and so are now widely used for this purpose. One of the reasons for their greater efficiency is the ability to use smaller media than ball mills, whilst applying an arbitrarily high energy input with an impeller, enabling a balance between stress intensity and stress frequency that is optimal for finer sizes.

Stress intensity theory provides some key insights that are useful for choosing stirred mill operating conditions. There is an optimum stress intensity where media beads have marginally enough energy to break particles, which varies with material, and decreases with decreasing particle size. Additionally, the solids content must be maintained within a certain range in order to optimise the particle capturing efficiency and minimise viscous effects; this solids content range also decreases with particle size.

The Bond ball mill work index is inappropriate for use with stirred media mills, since it is a dry test, and involves stress intensities and forces that are dissimilar to what a stirred mill experiences. Additionally, the Bond grinding law usually does not hold for finer sizes typical in these applications. Industry therefore uses several open circuit batch grinding tests on laboratory scale analogues, including the *Metso* Jar Mill for Vertimills, and scaled down grinder units for SMDs and IsaMills that typically predicts industrial mill performance well. Unlike the Bond ball mill test, various operating conditions, including media size, impeller speed, and solids content, can be tested to optimise processing conditions, with stress intensity theory being able to rationalise these results. However, any measure of material grindability is dependent on the operating conditions, and from stress intensity considerations it can be considered that different materials and particle sizes have different optimum conditions; this complicates the application of a standard set of conditions for comparing material grindability.

These batch grind tests produce a ‘signature plot’ that fits a power law model of P_{80} vs. energy input, with the exponent and coefficient of this model being characteristic parameters of both the material and the test operating conditions. These different values of the exponent complicate the application of an equivalent of the operating Bond work index that is used to compare operation efficiencies. Literature was reviewed to consider how the best fit value of the exponent varies with material, operating conditions, and mill type, and it was concluded that there is a very broad range of exponent values, likely dependent on all these conditions. Again, these differences in exponents can be explained with stress intensity theory, due to differences in stress intensities and particle capture efficiencies between conditions; if these conditions make it harder to grind particles than expected according to new surface area generation, the exponent is greater than 2, and vice versa. However, a Rittinger

operating work index with a Walker equation exponent of 2 allows for a good comparison between systems, so long as particle sizes of the feeds and products between samples are similar, and can be used to accurately track efficiency given that feed and product sizes do not vary excessively.

There are some attempts to be able to characterise material grindability based upon mechanical characterisation tests, to avoid the necessity of laboratory grind tests. One of these uses stress intensity theory, the macroscopic compression strength of the material, and the absolute grinding limit of a material in order to predict the optimum operating conditions at a given particle size, from which energy input can be predicted from stress intensity theory and a consideration of energy transfer coefficients. The other method is the JK size-dependent breakage model, which uses three material parameters derived from JKFBC ball-and-race grinder tests that together can predict a material breakage index and therefore a particle size distribution. Unfortunately, the effort required to carry out the characterisation necessary on representative samples of metalliferous ores is unlikely to be less than carrying out batch grinds with appropriate laboratory-scale grinders and determining signature plots. It is, however, reasonable to expect that once variations of these model parameters under different conditions and with different materials are understood, that a modified form of these models could lead to a facile and accurate way of determining ore grindability in stirred media mills, and an alternative to the Bond work index for fine and ultrafine grinding.

References

[1] T. Napier-Munn, Is progress in energy-efficient comminution doomed?, Minerals Engineering 73 (2015) 1-6. https://doi.org/10.1016/j.mineng.2014.06.009.

[2] B. A. Wills, J. A. Finch, 2016, Chapter 5 – Comminution, in: B. A. Wills, J. A. Finch, (eds.), Wills' Mineral Processing Technology (Eighth Edition) - An Introduction to the Practical Aspects of Ore Treatment and Mineral Recovery, Butterworth-Heinemann, 2016. ISBN 9780080970530.

[3] S. Rashidi, R. K. Rajamani, D. W. Fuerstenau, A Review of the Modeling of High Pressure Grinding Rolls, KONA Powder Part. J. 34 (2017) 125-140. https://doi.org/10.14356/kona.2017017.

[4] A. Gupta, D. S. Yan, Roll Crushers, in: A. Gupta, D. S. Yan, (eds.), Mineral Processing Design and Operations: An Introduction (Second Edition), Elsevier, 2016. ISBN: 9780444635921.

[5] C. Wang, S. Nadolski, O. Mejia, J. Drozdiak, B. Klein, Energy and Cost Comparisons of HPGR-based Circuits, Eng. Min. J., December 2013, 104-108.

[6] A. Jankovic, Variables affecting the fine grinding of minerals using stirred mills, Miner. Eng. 16 (2003) 337-345. https://doi.org/10.1016/S0892-6875(03)00007-4.

[7] A. G. Doll, Fine grinding, a refresher, 49th Annual Canadian Mineral Processors Operators Conference, Ottawa, Canada, 2017.

[8] A. Gupta, D. S. Yan, Stirred Mills – Ultrafine Grinding, in: A. Gupta, D. S. Yan, (eds.), Mineral Processing Design and Operations: An Introduction (Second Edition), Elsevier, 2016. ISBN: 9780444635921.

[9] H. de Bakker, Energy Use of Fine Grinding in Mineral Processing, Metall. Mater. Trans. E 1E (2014) 8-19. https://doi.org/10.1007/s40553-013-0001-6.

[10] R. P. King, Modeling & Simulation of Mineral Processing Systems, Elsevier, 2001. ISBN 0080511848.

[11] R. P. King, C. L. Schneider, Mineral Liberation and the Batch Comminution Equation, Miner. Eng. 11(12) (1998) 1143-1160. https://doi.org/10.1016/S0892-6875(98)00102-2.

[12] O. Celep, A. D. Bas, E. Y. Yazici, I. Alp, H. Deveci, Improvement of Silver Extraction by Ultrafine Grinding Prior to Cyanide Leaching of the Plant Tailings of a Refractory Silver Ore, Miner. Process. Extr. M. Rev. 36 (2015) 227-236. https://doi.org/10.1080/08827508.2014.928621.

[13] G. M. Mudd, Z. Weng, S. M. Jowitt, A Detailed Assessment of Global Cu Resource Trends and Endowments, Econ. Geol. 108 (2013) 1163-1183. https://doi.org/10.2113/econgeo.108.5.1163.

[14] W. G. B. Phillips, D. P. Edwards, Metal prices as a function of ore grade, Resour. Policy 2(3) (1976) 167-178. https://doi.org/10.1016/0301-4207(76)90016-7.

[15] H. Cho, J. Kwon, K. Kim, M. Mun, Optimum choice of the make-up ball sizes for maximum throughput in tumbling ball mills, Powder Technol. 246 (2013) 625-634. https://doi.org/10.1016/j.powtec.2013.06.026.

[16] B. A. Wills, J. A. Finch, Chapter 7 – Grinding Mills, in: B. A. Wills, J. A. Finch, (eds.), Wills' Mineral Processing Technology (Eighth Edition) - An Introduction to the Practical Aspects of Ore Treatment and Mineral Recovery, Butterworth-Heinemann, 2016. ISBN 9780080970530.

[17] T. Yokoyama, Y. Inoue, Chapter 10 Selection of Fine Grinding Mills, A. D. Salman, M. Ghadiri, M. J. Hounslow, (eds.), Handbook of Powder Technology (Volume 12), Elsevier Science B.V., 2007. ISSN 0167-3785.

[18] B. D. Burford, E. Niva, Comparing energy efficiency in grinding mills, Metallurgical Plant Design and Operating Strategies (MetPlant 2008), Perth, Australia, 18 - 19 August 2008.

[19] Union Process, The Evolution of Milling Technology [brochure] (2012). Available online at: https://unionprocess.com/pdfs/up-corporate-brochure.pdf

[20] A. Kwade, J. Schwedes, Chapter 6 – Wet Grinding in Stirred Media Mills, in A. D. Salman, M. Ghadiri, M. J. Hounslow, (eds.), Handbook of Powder Technology: Volume 12 – Particle Breakage, Elsevier BV, 2007. ISSN 0167-3785.

[21] A. Szegvari, M. Yang, Union Process Inc., Attritor Grinding and Dispersing Equipment, (2019). Available online at: https://unionprocess.com/tech_papers/Attritor_-Grinding-and-Dispersing-Equipment.pdf

[22] Metso, VERTIMILL® Grinding Mills & Stirred Media Detritor [brochure] (2015). Available online at: https://www.metso.com/globalassets/saleshub/documents---episerver/stirred_mills_brochure_en_lr.pdf

[23] A. J. Lynch, C. A. Rowland, The History of Grinding, Society for Mining, Metallurgy, and Exploration, 2005. ISBN: 9780873352383.

[24] S. Hochberg, E. I. du Pont de Nemours & Company, Process for Dispersing Pigments in Film-Forming Materials, United States Patent, US2581414A (1948).

[25] C. H. Lofthouse, F. E. Johns, The Svedala (ECC International) Detritor and the Metals Industry, Miner. Eng. 12(2) (1999) 205-217. https://doi.org/10.1016/S0892-6875(98)00132-0.

[26] Glencore Technology, IsaMill™: Breaking the Boundaries [brochure] (2015). Available online at: http://www.isamill.com/EN/Downloads/Brochures/IsaMillBrochure.pdf (accessed 6th January 2020).

[27] J. D. Pease, M. F. Young, D. C. Curry, Fine grinding as enabling technology—the IsaMill, Proceedings of the 6th Annual Crushing and Grinding Conference, Perth, Australia, 29–30 March 2004.

[28] C. Ntsele, J. Allen, Technology Selection of Stirred Media Mills for Energy Efficiency in Primary and Regrinding Applications for the Platinum Industry, The Southern African Institute of Mining and Metallurgy – Platinum 2012, 781-808, South Africa, 2012.

[29] G. Mucsi, A review on mechanical activation and mechanical alloying in stirred media mill, Chem. Eng. Res. Des. 148 (2019) 460-474. https://doi.org/10.1016/j.cherd.2019.06.029.

[30] R. K. Asamoah, W. Skinner, J. Addai-Mensah, Leaching behaviour of mechano-chemically activated bio-oxidised refractory flotation gold concentrates, Powder Technol. 331 (2018) 258-269. https://doi.org/10.1016/j.powtec.2018.03.040.

[31] S. Palaniandy, Impact of mechanochemical effect on chalcopyrite leaching, Int. J. Miner. Process. 136 (2015) 56-65. https://doi.org/10.1016/j.minpro.2014.10.005.

[32] O. Altun, H. Benzer, A. Toprak, U. Enderle, Utilization of grinding aids in dry horizontal stirred milling, Powder Technol. 286 (2015) 610-615. https://doi.org/10.1016/j.powtec.2015.09.001.

[33] Á. Rácz, K. Bohács, F. Kristály, É. Gregus, G. Mucsi, Comparison of Wet and Dry Stirred Media Milling from Energetic and Mechanochemical Point of View. XXIX International Mineral Processing Congress, Moscow, Russia, 15-21st September 2018.

[34] M. R. Pryor, Chapter 7: Dry Grinding, in: M. R. Pryor (ed.), Mineral Processing (Third Edition), Springer Science & Business Media, 2012. ISBN 9789401029414.

[35] A. Jankovic, W. Valery, E. Davis, Cement grinding optimisation, Miner. Eng. 17 (2004) 1075-1081. https://doi.org/10.1016/j.mineng.2004.06.031.

[36] A. K. Chatterjee, Cement Production Technology: Principles and Practice (1st Edition), CRC Press, 2018. ISBN 9780203703335.

[37] S. C. Chelgani, M. Parian, P. S. Parapari, Y. Ghorbani, J. Rosenkranz, A comparative study on the effects of dry and wet grinding on mineral flotation separation - a review, J. Mater. Res. Technol. 8(5) (2019) 5004-5011. https://doi.org/10.1016/j.jmrt.2019.07.053.

[38] J. Theuerkauf, J. Schwedes, Theoretical and experimental investigation on particle and fluid motion in stirred media mills, Powder Technol. 105 (1999) 406-412. https://doi.org/10.1016/S0032-5910(99)00165-5.

[39] J. Theuerkauf, J. Schwedes, Review - Investigation of Motion in Stirred Media Mills, Chem. Eng. Technol. 23(3) (2000) 203-209. https://doi.org/10.1002/(SICI)1521-4125(200003)23:3<203::AID-CEAT203>3.0.CO;2-3.

[40] L. Blecher, A. Kwade, J. Schwedes, Motion and stress intensity of grinding beads in a stirred media mill. Part 1: Energy distribution and motion of single grinding beads, Powder Technol. 86 (1996) 59-68. https://doi.org/10.1016/0032-5910(95)03038-7.

[41] R. Hogg, Breakage Mechanisms and Mill Performance in Ultrafine Grinding, Powder Technol. 105 (1999) 135-140. https://doi.org/10.1016/S0032-5910(99)00128-X.

[42] A. Kwade, Determination of the most important grinding mechanism in stirred media mills by calculating stress intensity and stress number, Powder Technol. 105 (1999) 382-388. https://doi.org/10.1016/S0032-5910(99)00162-X.

[43] A. Strobel, S. Romeis, J. Wittpahl, P. Herre, J. Schmidt, W. Peukert, Characterization of stressing conditions in mills – A comprehensive research strategy based on well-characterized model particles, Particle Technol. 305 (2017) 652-661. https://doi.org/10.1016/j.powtec.2016.10.048.

[44] S. Beinert, G. Fragnière, C. Schilde, A. Kwade, Analysis and modelling of bead contacts in wet-operated stirred media mills and planetary ball mills with CFD-DEM simulations, Chem. Eng. Sci. 134 (2015) 648-662. https://doi.org/10.1016/j.ces.2015.05.063.

[45] A. Jankovic, Media Stress Intensity Analysis for Vertical Stirred Mills, Miner. Eng. 14(10) (2001) 1177-1186. https://doi.org/10.1016/S0892-6875(01)00135-2.

[46] H. Weit, J. Schwedes, Scale up and power consumption in agitated ball mills, Chem. Eng. Technol. 10(1) (1987) 398-404. https://doi.org/10.1002/ceat.270100149.

[47] M. Becker, A. Kwade, J. Schwedes, Stress intensity in stirred media mills and its effect on specific energy requirement, Int. J. Miner. Process. 61 (2001) 189-208. https://doi.org/10.1016/S0301-7516(00)00037-5.

[48] S. Ouattara, C. Frances, Grinding of calcite suspensions in a stirred media mill: Effect of operational parameters on the product quality and the specific energy, Powder Technol. 255 (2014) 89-97. https://doi.org/10.1016/j.powtec.2013.11.025.

[49] A. B. G. Simpson, J. A. Byrne, J. A. D. McLaughlin, M. Strawhorne, Effect of solids concentration on particle size distribution of deagglomerated barium titanate in stirred media mills, Chem. Eng. Res. Des. 93 (2015) 287-292. https://doi.org/10.1016/j.cherd.2014.04.006.

[50] D. Katircioglu-Bayel, S. G. Ozkan, O. Y. Toraman, Effect of Operating Parameters on the Breakage Process of Calcite in a Stirred Media Mill, Mining, Metallurgy & Exploration 36 (2019) 399-408. https://doi.org/10.1007/s42461-018-0008-8.

[51] A. Kwade, L. Blecher, J. Schwedes, Motion and stress intensity of grinding beads in a stirred media mill. Part 2: Stress intensity and its effect on comminution, Powder Technol. 86 (1996) 69-76. https://doi.org/10.1016/0032-5910(95)03039-5.

[52] A. Kwade, J. Schwedes, Breaking characteristics of different materials and their effect on stress intensity and stress number in stirred media mills, Powder Technol. 122 (2002) 109-121. https://doi.org/10.1016/S0032-5910(01)00406-5.

[53] A. Kwade, A Stressing Model for the Description and Optimization of Grinding Processes, Chem. Eng. Technol. 26(2) (2003) 199-205. https://doi.org/10.1002/ceat.200390029.

[54] M. J. Mankosa, G. T. Adel, R. H. Yoon, Effect of Media Size in Stirred Ball Mill Grinding of Coal, Powder Technol. 49 (1986) 75-82. https://doi.org/10.1016/0032-5910(86)85008-2.

[55] S. Breitung-Faes, A. Kwade, Produktgestaltung bei der Nanozerkleinerung durch Einsatz kleinster Mahlkörper, Chem. Ing. Tech. 81(6) (2009) 767-774. https://doi.org/10.1002/cite.200800166.

[56] C. Knieke, C. Steinborn, S. Romeis, W. Peukert, S. Breitung-Faes, A. Kwade, Nanoparticle Production with Stirred Media Mills: Opportunities and Limits, Chem. Eng. Technol. 33(9) (2010) 1401-1411. https://doi.org/10.1002/ceat.201000105.

[57] H. H. Stender, A. Kwade, J. Schwedes, Stress energy distribution in different stirred media mill geometries, Int. J. Miner. Process. 74S (2004) S103-S117. https://doi.org/10.1016/j.minpro.2004.07.003.

[58] A. Strobel, J. Schwenger, J. Wittpahl, J. Schmidt, S. Romeis, W. Peukert, Assessing the influence of viscosity and milling bead size on the stressing conditions in a stirred media mill by single particle probes, Chem. Eng. Res. Des. 136 (2018) 859-869. https://doi.org/10.1016/j.cherd.2018.06.040.

[59] Á. Rácz, B. Csőke, Application of the product related stress model for product dispersity control in dry stirred media milling, Int. J. Miner. Process. 157 (2016) 28-35. https://doi.org/10.1016/j.minpro.2016.09.005.

[60] P. Prziwara, L. D. Hamilton, S. Breitung-Faes, A. Kwade, Impact of grinding aids and process parameters on dry stirred media milling, Powder Technol. 335 (2018) 114-123. https://doi.org/10.1016/j.powtec.2018.05.021.

[61] P. R. von Rittinger, Lehrbuch der Aufbereitung-Kunde in ihrer neuesten Entwickelung und Ausbildung systematisch dargestellt, Ernst and Korn, Berlin, Germany, 1867.

[62] F. Kick, Das Gesetz der proportionalen Widerstände und Seine Anwendungen: Nebst Versuchen über das Verhalten verschiedener Materialien bei gleichen Formänderungen sowohl unter der Presse als dem Schlagwerk, Felix, Leipzig, Germany, 1885.

[63] F. C. Bond, The Third Theory of Comminution, Transactions on AIME Mining Engineering 193 (1952) 484-494.

[64] W. H. Walker, W. K. Lewis, W. H. McAdams, E. R. Gilliland, 1937, Principles of Chemical Engineering, McGraw-Hill, New York, United States, 1937.

[65] R. T. Hukki, Proposal for a Solomonic settlement between the theories of von Rittinger, Kick, and Bond, Transactions on AIME Mining Engineering 223 (1962) 403-408.

[66] V. R. Voller, A Note on Energy-Size Reduction Relationships in Comminution, Powder Technol. 36 (1983) 281-286. https://doi.org/10.1016/0032-5910(83)85014-1.

[67] S. Morrell, An alternative energy-size relationship to that proposed by Bond for the design and optimisation of grinding circuits, Int. J. Miner. Process. 74 (2004) 133-141. https://doi.org/10.1016/j.minpro.2003.10.002.

[68] L. G. Austin, A Commentary on the Kick, Bond, and Rittinger Laws of Grinding, Powder Technol. 7 (1973) 315-317. https://doi.org/10.1016/0032-5910(73)80042-7.

[69] P. C. Kapur, D. W. Fuerstenau, Energy-Size Reduction 'Laws' Revisited, Int. J. Miner. Process. (1987) 20 45-57. https://doi.org/10.1016/0301-7516(87)90016-0.

[70] J. M. Burke, Determining the Bond Efficiency of industrial grinding circuits, Global Mining Guidelines Group, 20150505_Bond_Efficiency-GMG-ICE-v1-r04, 2016.

[71] A. Gupta, D. S. Yan, Size Reduction and Energy Requirement, in: A. Gupta, D. S. Yan (eds.), Mineral Processing Design and Operations: An Introduction (Second Edition), Elsevier, 2016. ISBN 9780444635891.

[72] C. A. Rowland, Using the Bond work index to measure operating comminution efficiency, Miner. Metall. Proc. 15(4) (1998) 32-36. https://doi.org/10.1007/BF03403155.

[73] C. A. Rowland, Determination and use of operating work indices in controlled grinding circuits – a proposed concept, Mill Operator's Conference and Exhibit, Australasian Institution of Mining and Metallurgy, 1978.

[74] F. C. Bond, Crushing and grinding calculations, British Chemical Engineering, 6 (1960) 378-385 and 8 (1960) 543-548.

[75] J. Levin, Indicators of grindability and grinding efficiency, J. South. Afr. Inst. Min. Metall. 92(10) (1992) 283-290. ISSN: 0038-223X.

[76] J. Levin, 1989, Observations on the Bond standard grindability test, and a proposal for the standard grindability test for fine materials, J. South. Afr. Inst. Min. Metall. 89(1) (1989) 13-21. ISSN: 0038/223X/3.00.

[77] J. Levin, A Proposed Test for the Determination of the Grindability of Fine Materials, Report No. M177, Council for Mineral Technology, Randburg, South Africa (1984). ISBN: 0869996789.

[78] F. Musa, R. Morrison, A more sustainable approach to assessing comminution efficiency, Miner. Eng. 22 (2009) 593-601. https://doi.org/10.1016/j.mineng.2009.04.004.

[79] D. David, M. Larson, M. Li, Optimising Western Australia Magnetite Circuit Design, Metallurgical Plant Design and Operating Strategies (MetPlant) Perth, Australia, 8-9 August 2011.

[80] D. B. Mazzinghy, J. F. C. Russo, J. Lichter, C. L. Schneider, J. Sepulveda, A. Videla, The Grinding Efficiency of the Currently Largest Vertimill Installation in the World, SAG Conference, Vancouver, Canada, 20-24 September 2015.

[81] S. Villalobos, D. Suarez, J. Opazo, R. Noriega, F. Gallardo, S. Dikmen, Vertimill as the definitive step before concentration. 14th International Mineral Processing Conference, 5th International Seminar on Geometallurgy, Santiago, Chile, 28-30 November 2018.

[82] M. G. Bergerman, L. C. de RennoMachado, V. K. Alves, H. Delboni, Copper Concentrate Regrind at Sossego Plant Using Vertical Mill - An Evaluation on the First Years of Operation, XXVI International Mineral Processing Congress, New Delhi, India, 24-28 September 2012.

[83] M. Larson, G. Anderson, R. Morrison, M. Young, Regrind Mills: Challenges of Scaleup, SME Annual Meeting, Denver, Colorado, USA, Feb 27 - Mar 2, 2011.

[84] P. Voigt, D. Walker, O. Kloiber-Deane, A. Tsvetkov, Ramp-up and long-term performance of the Albion Process plant at GeoProMining Gold Armenia, Proceedings 14th AusIMM Mill Operators' Conference (2018) 339–350.

[85] M. Larson, G. Anderson, K. Barns, V. Villadolid, IsaMill – 1:1 Direct Scaleup from Ultrafine to Coarse Grinding, Proceedings of Comminution 2012, Cape Town, South Africa, 17-20 April 2012.

[86] Tamblyn, R. J., Analysis of energy requirements in stirred media mills, EngD Thesis, University of Birmingham, United Kingdom, 2009. https://etheses.bham.ac.uk/id/eprint/1225/.

[87] M. Larson, R. D. Morrison, F. Shi, M. F. Young, Improving grinding efficiency with the IsaMill, Centre for Sustainable Resource Processing 2nd Annual Conference, Brisbane, Australia, 18-19 November 2008.

[88] E. Stamboliadis, S. Emmanouilidis, E. Petrakis, A New Approach to the Calculation of Work index and the Potential Energy of a Particulate Material, Geomaterials 1 (2011) 28-32. https://doi.org/10.4236/gm.2011.12005.

[89] G. Mucsi, Grindability of Quartz in Stirred Media Mill, Particul. Sci. Technol. 31 (2013) 399-406. https://doi.org/10.1080/02726351.2013.767294.

[90] D. S. Yan, R. C. Dunne, M. E. Freeman, Efficiency of Stirred Ball Mills, XIX International Mineral Processing Congress, San Francisco, 22-27 October 1995.

[91] F. Shi, R. Morrison, A. Cervellin, F. Burns, F. Musa, Comparison of energy efficiency between ball mills and stirred mills in coarse grinding, Miner. Eng. 22(7) (2008) 673-680. https://doi.org/10.1016/j.mineng.2008.12.002.

[92] S. Ellis, M. Gao, 2003, Development of ultrafine grinding at Kalgoorlie Consolidated Gold Mines, Mining, Metallurgy & Exploration 20(4) (2003) 171-177. https://doi.org/10.1007/BF03403172.

[93] M. Gao, M. Young, P. Allum, IsaMill Fine Grinding Technology and its Industrial Applications at Mount Isa Mines, CIM-ICM Vancouver 2002, Canadian Institute of Mining, Metallurgy and Petroleum, Vancouver, 28th April - 1st May 2002.

[94] Y. Yang, N. A. Rowson, R. Tamblyn, A. Ingram, Effect of operating parameters on fine particle grinding in a vertically stirred media mill. Sep. Sci. Technol. 52(6) (2017) 1143-1152. https://doi.org/10.1080/01496395.2016.1276931.

[95] S. Breitung-Faes, A. Kwade, Prediction of energy effective grinding conditions, Miner. Eng. 43-44 (2013) 36-43. https://doi.org/10.1016/j.mineng.2012.07.015.

[96] S. Breitung-Faes, A. Kwade, Use of an enhanced stress model for the optimization of wet stirred media milling processes, Chem. Eng. Technol. 37(5) (2014) 819-826. https://doi.org/10.1002/ceat.201300686.

[97] T. G. Nieh, J. Wadsworth, Hall-Petch Relation in Nanocrystalline Solids, Scr. Metall. Mater. 25 (1991) 955-958. https://doi.org/10.1016/0956-716X(91)90256-Z.

[98] S. Breitung-Faes, A. Kwade, Mill, material, and process parameters – A mechanistic model for the set-up of wet-stirred media milling processes, Adv. Powder Technol. 30(8) (2019) 1425-1433. https://doi.org/10.1016/j.apt.2019.04.013.

[99] S. Breitung-Faes, Estimation of product relating energy of wet operated stirred media mills in terms of process transfer to other mill geometries and sizes, Miner. Eng. 103-104 (2017) 33-42. https://doi.org/10.1016/j.mineng.2016.08.008.

[100] C. Knieke, M. Sommer, W. Peukert, Identifying the apparent and true grinding limit, Powder Technol. 195 (2009) 25-30. https://doi.org/10.1016/j.powtec.2009.05.007.

[101] L. Vogel, W. Peukert, Breakage behaviour of different materials – construction of a mastercurve for breakage probability, Powder Technol. 129 (2003) 101-110. https://doi.org/10.1016/S0032-5910(02)00217-6.

[102] W. Peukert, Material properties in fine grinding, Int. J. Miner. Process. 74S (2004) S3-S17. https://doi.org/10.1016/j.minpro.2004.08.006.

[103] L. Vogel, W. Peukert, Determination of material properties relevant to grinding by practicable labscale milling tests, Int. J. Miner. Process. 74S (2004) 329-338. https://doi.org/10.1016/j.minpro.2004.07.018.

[104] M. Meier, E. John, D. Wieckhusen, W. Wirth, W. Peukert, Influence of mechanical properties on impact fracture: Prediction of the milling behaviour of pharmaceutical powders by nanoindentation, Powder Technol. 188 (2009) 301-313. https://doi.org/10.1016/j.powtec.2008.05.009.

[105] F. Shi, T. Kojovic, Validation of a model for impact breakage incorporating particle size effect**,** Int. J. Miner. Process. 82 (2007) 156-163. https://doi.org/10.1016/j.minpro.2006.09.006.

[106] S. S. Narayanan, Development of a laboratory single particle breakage technique and its application to ball mill scale-up, PhD Thesis, University of Queensland (JKMRC), Australia, 1985. https://espace.library.uq.edu.au/view/UQ:287172.

[107] F. Shi, A review of the applications of the JK size-dependent breakage model. Part 1: Ore and coal breakage characterisation, Int. J. Miner. Process. 155 (2016) 118-129. https://doi.org/10.1016/j.minpro.2016.08.012.

[108] B. Bonfils, G. R. Ballantyne, M. S. Powell, Developments in incremental rock breakage testing methodologies and modelling, Int. J. Miner. Process. 152 (2016) 16-25. https://doi.org/10.1016/j.minpro.2016.04.010.

[109] Z. Davaanyam, Piston Press Test Procedures for Predicting Energy-Size Reduction of High Pressure Grinding Rolls, PhD Thesis, University of British Columbia, Vancouver, Canada, 2015. https://open.library.ubc.ca/cIRcle/collections/ubctheses/24/items/1.0166420.

[110] S. Nadolski, B. Klein, Z. Davaanyam, An energy benchmarking model for mineral comminution, Miner. Eng. 65 (2014) 178-186. https://doi.org/10.1016/j.mineng.2014.05.026.

[111] F. Shi, W. Xie, A specific energy-based size reduction model for batch grinding ball mill**,** Miner. Eng. 70 (2015) 130-140. https://doi.org/10.1016/j.mineng.2014.09.006.

[112] F. Shi, W. Zuo, Coal breakage characterisation - Part 1: Breakage testing with the JKFBC, Fuel 117 (2014) 1148-1155. https://doi.org/10.1016/j.fuel.2013.07.042.

[113] S. Palaniandy, Extending the application of JKFBC for gravity induced stirred mills feed ore characterisation, Miner. Eng. 101 (2017) 1-9. https://doi.org/10.1016/j.mineng.2016.08.012.

[114] M. Huang, Development of a Tower Mill Model Using Hardgrove Mill Tests, PhD Thesis, University of British Columbia, Vancouver, Canada, 2018. https://open.library.ubc.ca/cIRcle/collections/ubctheses/24/items/1.0364582.

[115] M. S. Powell, M. Hilden, G. Ballantyne, L. Liu, L. M. Tavares, The appropriate, and inappropriate, application of the JKMRC t10 relationship, XXVII International Mineral Processing Congress, Santiago, Chile, 20-24 October 2014.

[116] G. Fragnière, S. Beinert, A. Overbeck, I. Kampen, C. Schilde, A. Kwade, Predicting effects of operating condition variations on breakage rates in stirred media mills, Chem. Eng. Res. Des. 138 (2018) 433-443. https://doi.org/10.1016/j.cherd.2018.09.009.

Lewis Taylor graduated with an M.Eng in Chemical Engineering (University of Birmingham, UK). He is currently undertaking a PhD with the University of Birmingham and FiberLean Technologies on producing nanocellulose with a stirred media mill.

David Skuse is VP Technology for FiberLean Technologies. He has a BSc in Chemistry (University of Wales, UK) and a PhD in Colloid and Polymer Chemistry (University of Bristol, UK). Previously, David worked as a Research Fellow at the University of British Columbia where his projects were funded by MRC Canada, Domtar and NASA. He then worked for 26 years for Imerys. He joined FiberLean Technologies on its formation in 2016. He is an Honorary Professor in the Department of Chemical Engineering at the University of Birmingham, UK and is a Fellow of the Royal Society of Chemistry.

Stuart Blackburn has worked in the field of materials processing for 35 years. He started his career working for Foseco developing of fine zirconia powders by a fusion and comminution route. The process was eventually awarded the Queen's award for Innovation in 2001. In 1990 he joined the University of Birmingham, working on the processing of highly loaded suspensions. He was awarded the British Foundry Medal in 2007 (ICME) and the Ivor Jenkins Medal for contributions in the field of particulate processing in 2008 (IOM^3). Today his work remains focused on particulate processing in the casting and chemical industries.

Richard Greenwood graduated with a BSc in Chemistry from Bristol University and studied for a PhD at Imperial College, London. He is currently the programme manager for the CDT in Formulation Engineering at the School of Chemical Engineering, University of Birmingham. He is currently a Fellow of the Royal Society of Chemistry and sits on the RSC / SCI joint colloids committee where is organiser of the UK Colloids conference.

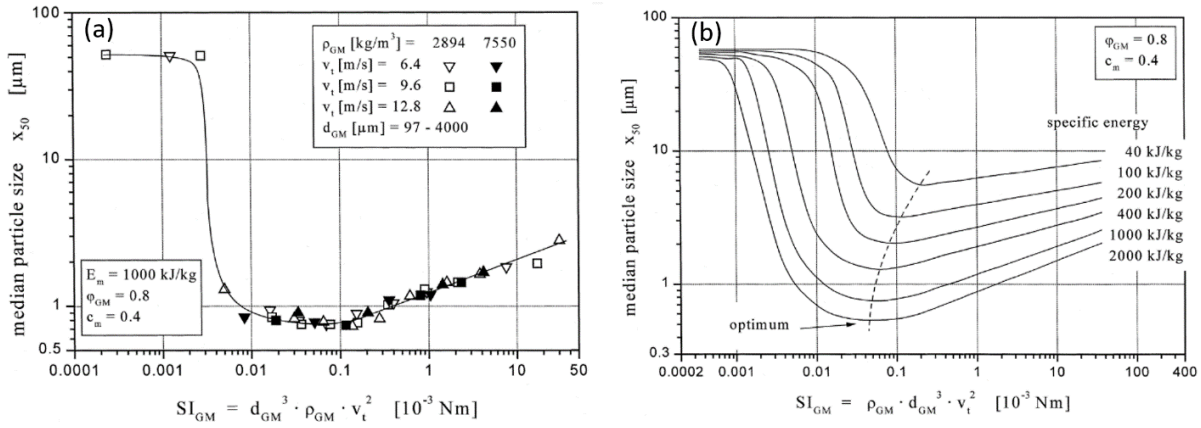

Fig. 1. **(a) Median particle size vs. maximum stress intensity for the comminution of limestone under different impeller speeds, media densities, and media sizes; (b) how the characteristic curve in (a) varies with energy input (figures taken from Becker et al. [47]).**

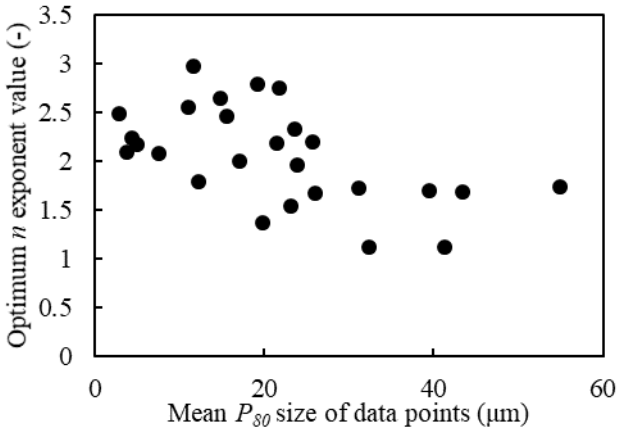

Fig. 2. **Calculated optimum *n* exponent value of the Walker model vs. the mean P_{80} value of the energy-size relationship data points from numerous sources (see Table 1).**

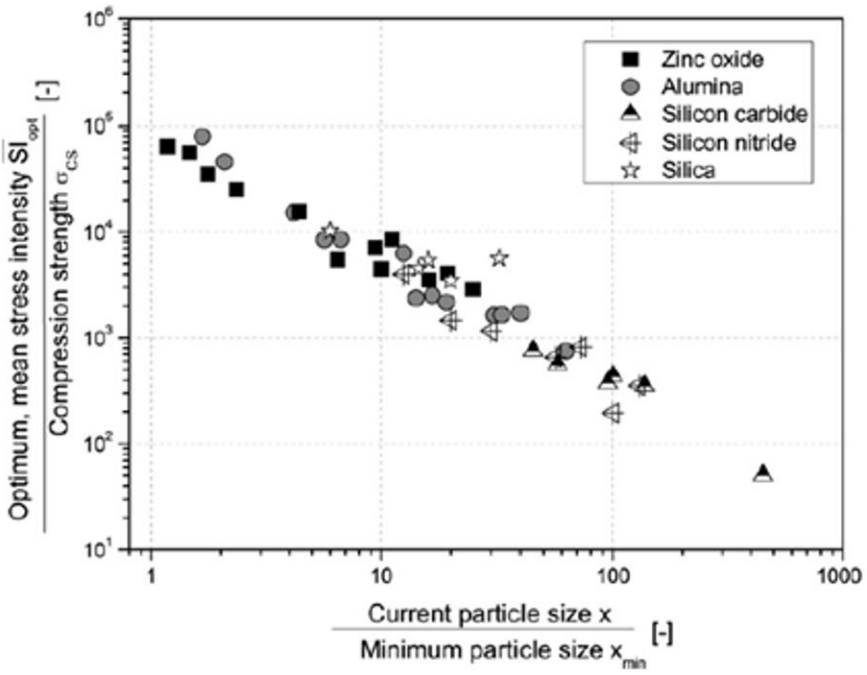

Fig. 3. **Correlation of the ratio of the optimum stress intensity and compressive strength vs the ratio of the current particle size to the absolute grinding limit (figure taken from Breitung-Faes and Kwade [95]).**

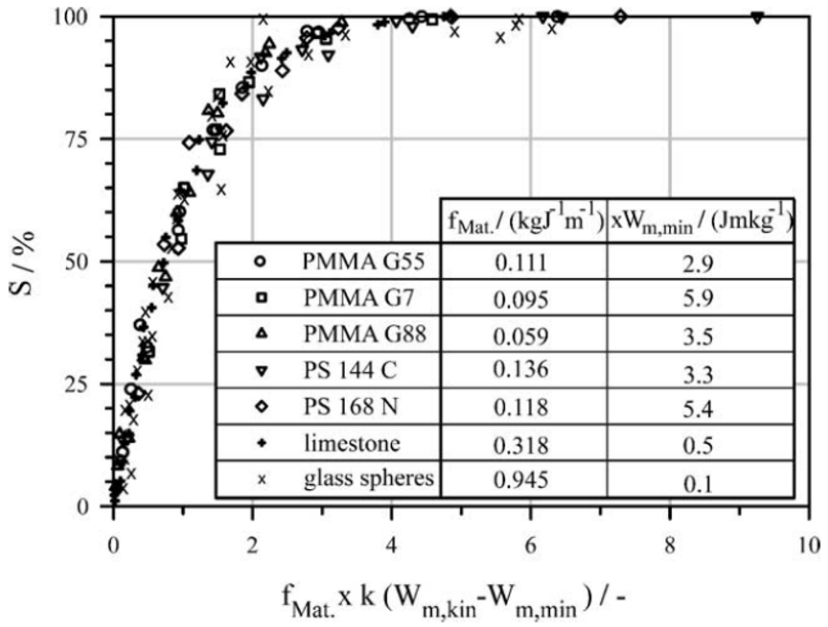

Fig. 4. **Breakage probability vs. dimensionless stressing parameter for various materials (figure taken from Vogel and Peukert [101]).**

Source	Mill Type	Material	Series	Specific Energy Input (kWh/t)	P_{80} Size Range (µm)	Mean P_{80} (µm)	Walker Model			Rittinger Model	Bond Model	Power Law Model		
							K_w	n	Error	Error	Error	C	α	Error
[90]	Tower Mill	Gold ore	6 mm media	39	109-15.9	55.0	223	1.74	8.78%	10.09%	15.54%	24702	2.25	59.89%
		Quartz	3 mm media	83	249-8.5	32.3	33	1.12	8.96%	23.82%	11.33%	301	0.62	4.79%
		Quartz	6 mm media	59	249-13.5	39.5	292	1.70	0.07%	13.21%	7.58%	693	0.94	3.34%
		Quartz	9 mm media	79	249-12.8	25.8	2085	2.20	0.91%	8.27%	23.44%	2206	1.30	1.09%
		Pyrite	3 mm media	96	210-7.1	41.3	41	1.12	7.76%	39.79%	21.09%	322	0.59	5.31%
		Pyrite	6 mm media	82	210-9.3	31.2	302	1.72	4.98%	12.39%	8.86%	656	0.95	2.65%
		Pyrite	9 mm media	88	210-10.0	43.5	326	1.68	14.03%	25.58%	15.42%	448	0.73	5.84%
[91]	IsaMill	Pyritic gold ore	flotation concentrate	133	163-8.3	17.1	1130	2.01	3.89%	3.94%	16.77%	1378	1.13	2.41%
		Lead - zinc ore	cyclone underflow	194	354-4.6	7.6	1097	2.08	3.61%	4.08%	14.05%	864	1.00	4.11%
		Iron ore	AG trommel undersize	73	135-14.4	19.1	15537	2.79	1.96%	12.64%	19.56%	10074	1.85	2.19%
		Lead - zinc ore	AG trommel undersize	83	360-8.0	12.3	356	1.79	0.15%	5.20%	6.36%	483	0.85	0.22%
[92]	SMD	Pyritic gold ore	6.5 mm steel media	243	110-4.9	11.6	12177	2.97	10.54%	35.67%	43.86%	6849	2.01	10.99%
[93]	IsaMill	Zinc concentrate	Lead slag media	61	30-9.1	11.0	3264	2.55	2.26%	6.78%	10.40%	7134	2.16	0.03%
[94]	SMD	Marble	*Zirpro* 75% solids	300	62.8-3.25	4.9	1412	2.18	1.49%	4.04%	14.59%	1290	1.25	1.62%
		Marble	*Zirpro* 65% solids	300	62.8-2.70	4.4	1415	2.24	3.09%	4.89%	15.75%	1079	1.23	3.58%
		Marble	*Carbolite* 75% solids	300	62.8-2.35	3.7	848	2.09	2.06%	3.07%	14.39%	792	1.16	2.09%
		Marble	*Carbolite* 65% solids	300	62.8-2.00	2.9	1262	2.49	2.79%	11.93%	20.94%	918	1.56	3.07%
[3]	SMD	Zinc concentrate	2.8 - 1.4 mm media	173	47-14.8	14.8	3849	2.65	8.44%	22.56%	36.39%	4909	2.03	11.20%
		Zinc concentrate	4 - 3.35 mm media	199	47-15.6	15.6	2263	2.46	6.95%	17.83%	32.05%	3961	1.91	9.72%
[3]	Sala peg mill	Zinc concentrate	2 mm media	27	47-19.8	19.8	57	1.37	10.32%	16.10%	10.42%	641	1.30	1.72%
		Zinc concentrate	4.8 mm media	43	47-23.9	23.9	787	1.96	7.96%	7.99%	9.47%	10665	2.02	2.52%
		Zinc concentrate	6.8 mm media	46	47-23.15	23.2	265	1.54	5.09%	5.59%	5.16%	11936	1.94	2.78%
		Zinc concentrate	8 mm media	45	47-26-1	26.1	550	1.67	3.71%	5.41%	4.09%	31122	2.16	1.44%
		Zinc concentrate	40.2% solids	98	47-21.8	21.8	28451	2.74	2.95%	10.13%	14.66%	112112	2.49	2.68%
		Zinc concentrate	55% solids	74	47-21.5	21.5	3088	2.19	4.06%	5.78%	11.84%	28467	2.16	3.60%
		Zinc concentrate	64.2% solids	47	47-23.6	23.6	4137	2.33	4.58%	7.55%	11.13%	52647	2.41	4.23%

Table 1. Modelling energy-size relationships of stirred media mill grinds from various sources, using the Walker, Rittinger, Bond, and Power Law models. Mean P_{80} is the mean of all data points used in the model optimization, and the error is defined as the mean absolute error between the data points and the model.

APPENDIX B2 – PUBLICATION: USING FIBRE PROPERTY MEASUREMENTS TO PREDUCT THE TENSILE INDEX OF MICROFIBRILLATED CELLULOSE NANOPAPER

Reference:

Taylor, L., Phipps, J., Blackburn, S., Greenwood, R., Skuse, D., 2020. ***Using fibre property measurements to predict the tensile index of microfibrillated cellulose nanopaper.*** Cellulose, 27, pp.6149-6162.

Post-print article shown on the following page:

Using Fibre Property Measurements to Predict the Tensile Index of Microfibrillated Cellulose Nanopaper

Lewis Taylor[a, b,*], Jonathan Phipps[b], Stuart Blackburn[a], Richard Greenwood[a], David Skuse[a, b]

[a] School of Chemical Engineering, University of Birmingham, Birmingham, B15 2TT, UK

[b] FiberLean Technologies, Par Moor Centre, Par Moor Road, Par, PL24 2SQ, UK

*Corresponding author. Email: lxt189@bham.ac.uk; lewis.taylor@fiberlean.com

Abstract

A wide variety of wood and non-wood cellulosic fibre sources were used as a feed to produce microfibrillated cellulose (MFC) using a grinding process. Nanopaper was formed using this product, and the tensile index was measured. The hemicellulose content of the feed fibres was measured, and was found to correlate with the production of finer microfibrils and a higher MFC tensile strength. The correlation with tensile strength was improved by the inclusion of a measurement of the MFC particle lengths as measured by a fibre image analyser, with the resulting relation fitting a modified Page Equation. It was hypothesised that the frequency of flaws in the feed fibre cross-section influences the length of the MFC particles produced, and so the zero-span tensile index of the fibres was measured as a proxy for this since it forces cross-sectional fibre breakage. The fibre zero-span tensile index was found to correlate with MFC particle length and so was used in its place in the equation. The resultant equation can predict MFC tensile strength from zero-span tensile index and hemicellulose content measurements of cellulosic fibres and can aid in optimising feedstock selection for mechanical MFC production processes.

Keywords: microfibrillated cellulose, hemicellulose, zero span tensile strength, tensile strength

Introduction

Microfibrillated Cellulose

Cellulose is an essential structural component in higher plants and is the most abundant polymer on Earth, with an almost inexhaustible supply of around 1.5 x 10^{12} tonnes per year produced by biomass (Klemm et al. 2005). Cellulose fibres can be separated from other biomass components by pulping and bleaching processes, producing a cellulose fibre pulp that is used primarily in the production of paper and cellulose-based packaging to impart mechanical strength properties.

These mechanical properties are a consequence of the fibre microstructure. Cellulose fibres have a fractal-like structure with several hierarchies of fibre-like sub-units that extend down to the nanoscopic scale. A cellulose fibre consists of parallel chains of long fibrils with micron-scale diameters, which are similarly made up of microfibrils around 30 nm in diameter. These microfibrils in turn consist of elementary fibrils around 3.5 nm in diameter. (Chinga-Carrasco 2011)**.**

In 1982, Turbak et al. (1983) and Herrick et al. (1983) reported that cellulose fibres could be disintegrated to liberate these finer structural components, greatly increasing the specific surface area and hydrogen bonding capability. This product was termed *microfibrillated cellulose* (MFC), and has been found to have many applications that exploit its hydrophilicity, renewability, biodegradability, and high specific strength and surface area (for reviews regarding applications, see Klemm et al. 2011 and Shatkin et al. 2014).

The original production process involved disintegrating cellulose pulp fibres into MFC using a homogenizer (Turbak et al. 1983). In the decades since, other equipment has been used as an alternative, such as microfluidizers and friction grinders, and chemical pre-treatment methods including enzymatic degradation and 2,2,6,6-

tetramethylpiperidine-1-oxl radical (TEMPO) oxidation have been applied to reduce the energy input (for a review on production methods, see Siró and Plackett 2010).

FiberLean Technologies has adapted minerals grinding technology to mechanically disintegrate cellulose fibres into MFC cost-effectively at large scales, without requiring cellulose pre-treatment. This method uses stirred media detritor technology (Husband et al. 2015), which disintegrates fibres into MFC by agitating grinding media beads. In this process, a paper filler mineral such as calcium carbonate is added as a grinding aid, greatly reducing the energy required. A laboratory scale equivalent of this process is used to produce the MFC that is the subject of this research.

MFC has been made from numerous sources including hardwoods (e.g. birch, eucalyptus, and acacia), softwoods (various species of coniferous trees) and non-wood sources (e.g. cotton, abaca, flax, bamboo, and sugar beet (Jonoobi et al. 2015). The fibre source can have a strong influence on MFC quality. For example Alila et al. (2013) found that abaca and sisal fibres produced finer MFC than flax and hemp. Others have investigated the influence of fibre species on MFC quality (e.g. Chaker et al. 2013; Desmaisons et al. 2017) but these are limited to comparisons of a small number of species at a time, making the drawing of conclusions applicable to most fibre sources problematic.

Fibres can differ from each other in many ways, so it cannot be taken for granted that differences in MFC quality between two fibre sources are due to a difference in one parameter rather than another. This work therefore analyses twenty-four different fibre species in order to have a large enough data set that such comparisons are more valid, and so the relative importance of a fibre property can be assessed with a greater degree of confidence.

Paper Tensile Strength Theory

The MFC produced by the FiberLean process is in the form of a MFC-mineral composite that was originally created to service the paper filler additive market. In this application, the addition of MFC to a paper formulation increases the specific strength, allowing for a disproportionate amount of native fibres to be removed and replaced with paper filler mineral; this reduces the cost of the paper considerably and improves optical properties. The MFC quality is assessed by forming nanopaper sheets and testing their tensile strength; this strength appears proportional to the specific strength increase that this MFC would impart on paper when added to a fibre furnish.

Page (1969) introduced what is today the most commonly used theory for predicting the tensile strength of paper. This postulates that the failure of a sheet occurs partly by bonds between fibres being broken, and partly by the fibres themselves breaking across their cross-sections, and that the tensile index of the sheet is more dependent on the weakest of these two mechanisms. The Page Equation describing this is stated below:

$$\frac{1}{T} = \frac{9}{8Z} + \frac{12A\rho}{\tau_B PL(RBA)} \dots [1]$$

where T is the sheet tensile index (Nm/g), Z is the zero-span tensile index (Nm/g), A is the fibre cross-sectional area (m^2), P is the fibre cross-section perimeter (m), ρ is the fibre density (kg/m^3), L is the fibre length (m), τ_B is the shear bond strength per unit area (Pa), and RBA is the relative bonded area.

Zero-span tensile index is a measure of individual fibre strength and is discussed later in this work. RBA is a measure of the fraction of the fibre surface area that is used for inter-fibre bonding. The first term on the right-hand side represents the weakness of the individual fibres, whereas the second term represents the weakness of the bonds between fibres. Usually, a sheet of paper fails due to bonds between fibres breaking rather than the fibres themselves breaking, so the second term is limiting. Adding MFC to a fibre furnish greatly increases relative bonded area (Lindström et al. 2016), and so tensile index tends to improve considerably.

Hemicellulose

Fibre chemical composition is known to be important in papermaking. Most raw plant material from which cellulose fibres are extracted are rich in hemicellulose. Though pulping and bleaching removes much of the

hemicellulose, there is still typically a large residual fraction within the fibre cell wall, with the amount dependent on fibre species and pulping conditions.

Hemicellulose is a broad term for a wide variety of polysaccharides with differing monomer sugars, functional groups, and degrees of branching, but for woods and many non-woods, there are only two important families; xylans and glucomannans. Xylans are found in the vast majority of plants, and account for almost all the hemicellulose in hardwoods, whereas glucomannans are found in large quantities in softwoods (in comparable amounts to xylans) (Ebringerová 2005). Compared to cellulose, hemicellulose is always amorphous, whereas cellulose is partly crystalline, and hemicellulose molecules have relatively short chain lengths of 70 – 200 units (Fengel and Wegener 1983), compared to 300 – 1700 units typical for cellulose (Klemm et al. 2005).

Within a fibre cell wall, hemicellulose closely associates with the cellulose microfibril surface, forming a layer separating neighbouring microfibrils. NMR spectroscopy work by Liitiä et al. (2003) indicates that both xylan and glucomannan do this, and are comparable in function. Hemicellulose has a branched, amorphous structure, and readily swells in water, as shown by work investigating the change in zeta potential during this process (Uetani et al. 2012). This hydrophilicity also aids in the plasticity of the fibre to deformation (Bolam 1965), which would be expected to facilitate disintegration into MFC.

NMR studies by several authors using fibres that have undergone different pulping conditions have shown that reducing the hemicellulose content appears to increase the fibril aggregate dimension size appreciably (Hult 2001; Virtanen et al. 2008; Duchesne et al. 2001). This supports the notion that hemicellulose inhibits the spontaneous coalescence of neighbouring microfibrils.

Hemicellulose has long been understood to aid in conventional fibre refining for papermaking; chemically removing the hemicellulose content prior to refining reduces the tensile strength of the refined fibres (Bolam 1965). Sorbing hemicellulose onto fibres prior to refining has been found to improve sheet tensile strength, primarily by reducing the ‘kink’ deformations induced in the fibres (Mäkelä et al. 2010).

It is therefore plausible that a higher hemicellulose content would lead to high quality MFC. Existing work in the literature has supported this idea. Iwamoto et al. (2008) showed that drying a pulp after removing hemicellulose by alkali treating results in irreversible microfibril aggregation, inhibiting fibrillation compared to an untreated pulp. Numerous authors have found that a high hemicellulose content coincides with a high microfibril yield and better individualisation. This appears true whether comparing fibres from different plant species (Alila et al. 2013; Desmaisons et al. 2017; Chaker et al. 2013) or from the same plant species but with different pulping conditions (Chaker et al. 2013; Petroudy et al. 2015; Spence et al. 2010).

There are two major mechanisms thought to explain this. The presence of surface hemicellulose itself improves inter-fibre bonding (or inter-fibril bonding in the case of MFC), since amorphous hemicellulose chains extend out from the microfibrils when immersed in water, and form bridges between neighbouring microfibrils when dried (Bolam 1965). Therefore, when disintegrating a high hemicellulose pulp into MFC, the liberated surface area has a higher surface concentration of hemicellulose, and so this strengthening effect is enhanced compared to a low hemicellulose pulp. Arola et al. (2013) removed hemicellulose from nanocellulose with xylanase enzymes, which resulted in poorer tensile properties, even with similar nanocellulose geometry, clearly demonstrating this effect.

The second mechanism is that a high hemicellulose pulp produces finer microfibrils with better individualisation, as microscopy images in various studies has demonstrated (e.g. Alila et al. (2013); Iwamoto et al. (2008); Chaker et al. (2013)). Given similar microfibril lengths, this increases particle aspect ratio, improving tensile strength. Hemicellulose forms an amorphous layer between microfibrils that readily swells in water, and so this would be expected to provide a preferred plane of breakage parallel to the microfibril lengths, thereby facilitating the production of finer microfibrils. Additionally, xylan develops a surface charge due to carboxyl group dissociation under typical processing conditions, causing mutual microfibril repulsion, enhancing this effect to some degree.

Due to the importance of hemicellulose indicated so far in the literature, and its expected influence on MFC geometry and bonding, the hemicellulose content was investigated for all fibre species tested in this study.

Zero-span tensile strength

It is later suggested that the fibril lengths of the MFC correlate with a high MFC tensile strength. It is desirable to be able to predict the resultant MFC fibril length from intrinsic fibre properties. It is reasonable to believe that having long fibrils within the fibre structure will, all other things being equal, lead to long liberated fibrils. Also, having fibrils with few pre-existing defects should reduce the degree of fibril length degradation during processing. Both of these factors are expected to affect the individual fibre strength; intrinsically long fibrils results in fewer discontinuities at fibril endpoints, and having undamaged fibrils means fewer microscopic weak points in the fibre. Both can be seen to influence the 'quality' of the fibre cross-sectional area, i.e. having long, undamaged fibrils should result in the cross-sectional area having few flaws.

A measurement that could assess the specific strength of the fibre cross-sectional area could therefore be useful for indicating the frequency of fibril flaws and intrinsic fibril length; and is therefore expected to correlate with long fibril lengths of the MFC product. The zero-span tensile index of a fibre sheet prior to MFC production is believed to be such a measurement. In the zero-span tensile test, the two clamps are essentially touching (within microns of each other), forcing the vast majority of the fibres between the clamps to be held by both clamps at once, since the separation distance between clamps is a small fraction of typical fibre lengths. When the sample is broken under tensile stress, these clamped fibres will fail by cross-sectional breakage, rather than the bonds between fibres as with conventional tensile testing. Since the zero-span tensile test is normalised by weight, the thickness of the fibre cell wall and fibre diameter are accounted for.

The notion that zero-span tensile strength is a measure of fibre damage is well-supported. Zeng et al. (2012) damaged fibres by refining, finding that the zero-span tensile strength was inversely proportional to the frequency of fibre kinks induced (i.e. sharp bends in the fibre). Joutsimo et al. (2005) induced cell wall damage (dislocations) by homogenization, which decreased fibre strength; they attributed this to inducing non-uniform load distributions across the cross-section.

Research has shown that fibril and microfibril-scale damage is also important. Nevell and Nugawela (1987) treated fibres with acids, causing localised damage to microfibrils that substantially reduced zero-span tensile strength. Wathén (2006) damaged fibrils homogeneously throughout the fibre by thermal ageing degradation, and found that the zero-span strength decreased.

Definition of Research Objectives

MFC is produced by a mechanical process with a large and diverse range of fibre species, and attempts are made to correlate the tensile index of this MFC with the feed fibre properties, including the fibre hemicellulose content, and the fibre zero-span tensile index.

Materials and Methods

Fibre sources

In total, twenty-four separate fibre species were investigated, from a variety of wood and non-wood sources. These are listed in Table 1 below.

Softwoods	**Hardwoods**	**Non-woods**
Nordic Pine	Birch #1	Cotton (linters)
Black Spruce	Birch #2	Jeans‡
Radiata Pine	Eucalyptus	Abaca

Southern Pine	Acacia	Sisal
Douglas Fir	Mixed South Asian Hardwood	Kenaf
Enzyme-treated Nordic Pine	Mixed European Hardwood	Giant Reed (*Arundo Donax*)
Dissolving Pulp*	Tissue Dust†	Bagasse (sugar cane)
		Miscanthus
		Sorghum
		Flax

Table 1 Fibre species used in this study
* Dissolving Pulp is a Nordic pine/spruce blend (Domsjö Fabriker AB – Domsjö Cellulose Plus) that was subjected to the sulphite bleaching process, rather than the kraft (sulphate) process which all other softwoods and hardwoods listed underwent.
† Waste short fibres collected from the dust extraction system of a tissue mill.
‡ Cotton fibres from recycled jeans, following disintegration into individual fibres and formation into a pulp board.

Pulp Preparation

Fibres were added to the grinding process as a 30% solids cake. Miscanthus, sorghum, bagasse, enzyme-treated Nordic pine, and Giant Reed were supplied in this form, whereas most other fibre sources were supplied as dry pulp boards. These dry pulps were soaked in water and broken down into individual fibres using a pulp disintegrator for 10 minutes. Excess water was removed by a vacuum filter, forming a cake. To avoid choking of the grinder due to entanglement of very long fibres, the flax fibres were cut with a guillotine into fragments around 3 mm in length.

MFC Production by Stirred Media Detritor Grinding

MFC was produced from these fibres using a lab-scale version of the FiberLean production process. This involves a grinder that uses the motion of media beads to disintegrate the fibres. The presence of micron-scale mineral particles greatly improves the efficiency of this process, so the fibre charge was complemented with an equal amount (on a dry mass basis) of *IC60* (60 wt% < 2 μm) ground calcium carbonate mineral (*Imerys*). Sufficient water was also added to form a slurry with the target fibre solids content. The precise operating conditions, including the energy input, are proprietary. When a grind was completed, the slurry was separated from the media with a vibrating screen, or by a washing method when particles were too coarse for the screen.

Previous experience with this process has shown that almost all fibre sources reach a peak tensile strength at around the same energy, and an unpublished investigation with seven of the fibre species in listed in Table 1 has confirmed this. The relationships between energy input and MFC tensile strength for these seven fibre species are displayed in the *Energy Sweeps* tab in the *Supplementary Material*. Consequently, a single energy input was chosen which was applied to all fibre species listed in Table 1 to produce MFC.

Nanopaper Sheet Preparation

The MFC-mineral composite product was collected as an aqueous slurry. The solids content was measured by weighing a sample before and after oven drying. The mineral content was determined from the change in weight of an oven-dried sample after burning off the cellulose in a 450°C furnace for 2 hours. Using this information, sufficient IC60 calcium carbonate mineral was added to the sample to dilute the MFC content to 20 wt% on a dry mass basis. These samples were used to form a nanopaper sheet in a vacuum sheet former and dried using a *Rapid-Köthen* dryer, targeting a weight of 220 gsm. These sheets were conditioned in a controlled environment at 23°C and 50% relative humidity overnight prior to tensile testing.

Nanopaper Tensile Testing

The nanopaper samples were weighed and cut into strips 15 mm wide. These strips were clamped in a *Testometric M350* tensile tester and strained at a constant rate until failure. The force applied at break was divided by the strip width and gsm to obtain the tensile index in Nm/g. The tensile index of this MFC-mineral composite nanopaper is much weaker than pure MFC due to the mineral disrupting inter-fibril bonding. However, work with MFC made from this process by Phipps et al. (2017) has shown that the tensile indices of FiberLean MFC with or without a given fraction of mineral added are roughly proportional (i.e. breakage is mainly bonding-limited in both cases), so the conclusions are still believed to be applicable to pure MFC. Three nanopaper sheets were produced for each sample, each cut into five strips. The mean tensile index of these fifteen strips is reported as the sample tensile index here. Fibre content was verified to be on target by measuring the ash content after burning off the cellulose in a 450°C furnace for 2 hours (these results are displayed in the *Tensile Sheet Mineral Content* tab in the *Supplementary Material*).

Fibre Image Analysis

A *Valmet FS5* fibre image analyser was used to measure geometric parameters of the original fibres before grinding, and the MFC particles after grinding. This equipment operates by pumping a sample suspension past a camera that takes thousands of images, and parameters such as length and width distributions are determined by a computer algorithm. Though designed for fibre measurement, this is sensitive enough to measure MFC particles with lengths around a hundred microns and above.

Hemicellulose Content

Hemicellulose measurements were subcontracted to *Labtium Oy*, who used the *SCAN-CM 71:09* method (Scandinavian Pulp, Paper and Board Testing Committee 2009). Fibre samples underwent sulphuric acid hydrolysis, and the resultant concentration of various monomer sugar residues were detected by chromatography. This included glucose, xylose, mannose, arabinose, and galactose. To convert these sugar contents into xylan and glucomannan hemicellulose contents, it was assumed that the xylan content was the sum of all the xylose and arabinose, and the glucomannan content consisted of all the galactose, mannose, and 1 unit of glucose for every 4 units of mannose, since a ratio of 1:4 glucose to mannose is typical in softwood glucomannan (Ebringerová 2005). Total hemicellulose content was determined by adding together the xylan and glucomannan fractions. The hemicellulose content of cotton linters (which is negligible) was also used as the hemicellulose content of the jeans cotton, since it was expected that the presence of dye and other additives in the jeans cotton would give misleading results. This is a reasonable assumption as textile-grade cotton contains negligible hemicellulose (Prado and Spinacé (2015)).

Lignin Content

Acid-soluble and acid-insoluble lignin content of the pulps were measured by *Labtium Oy* according to a modified TAPPI standard *T 222 om-88* test.

Fibre Zero-Span Tensile Testing

Zero-span tensile tests were carried out on the initial fibre samples rather than the MFC. The TAPPI standard *T 231 cm-07* (Technical Association of the Pulp and Paper Industry 2007) was followed, using 60 gsm mineral-free handsheets for each fibre species produced according to TAPPI standard *T 205 sp-12* (Technical Association of the Pulp and Paper Industry 2012). Each handsheet was cut into five strips, which were clamped in a *Pulmac* zero-span tensile tester and strained until broken. As with conventional tensile testing, the force measured was converted to a zero-span tensile index. Four dry sheets were tested for each fibre species, and a mean average result is reported here.

Scanning Electron Microscopy

A *Jeol 6700* Scanning Electron Microscope was used to image several MFC samples at x10000 magnification. Preparation involved filtering a dilute MFC sample through a 0.2 μm nucleopore membrane. The samples were

sputter coated with platinum to form a conductive monolayer. Secondary electrons emitted from the sample during measurement were used to form the images.

Results and Discussion

Influence of Hemicellulose Content

Hemicellulose within bleached chemical pulp resides within the fibre cell wall, where it forms a layer around the microfibrils, separating them from their neighbours. It was expected both from mechanistic considerations and from results previously reported in the literature that it would positively correlate with MFC quality. The hemicellulose content for each fibre species was measured, and is plotted against the MFC tensile index as Fig. 1.

Fig. 1 shows that a high hemicellulose content of the fibre correlates with a high MFC tensile index. Fitting the data to a general straight line equation gave an R^2 value of around 0.63, which is moderately good for a single parameter, considering that cellulose is a natural product with a complex hierarchy of structures with different scales and chemistries between plant species.

As discussed in the introduction, there are two mechanisms by which hemicellulose is thought to improve MFC tensile index. One mechanism is that a high hemicellulose fibre when disintegrated to form MFC has more of this liberated surface area coated in hemicellulose, which is thought to form bridges between particles upon drying and thereby improve relative bonded area and specific bonding strength. The other mechanism is that the presence of hemicellulose, being a relatively mechanically weak amorphous layer, provides a preferred plane of breakage along the microfibril lengths, thereby facilitating disintegration into finer microfibrils, increasing the aspect ratio. To assess whether the latter mechanism is taking place, SEM images were taken of samples with a range of hemicellulose contents to assess fibril and microfibril diameters. Four of such images are displayed as Fig. 2.

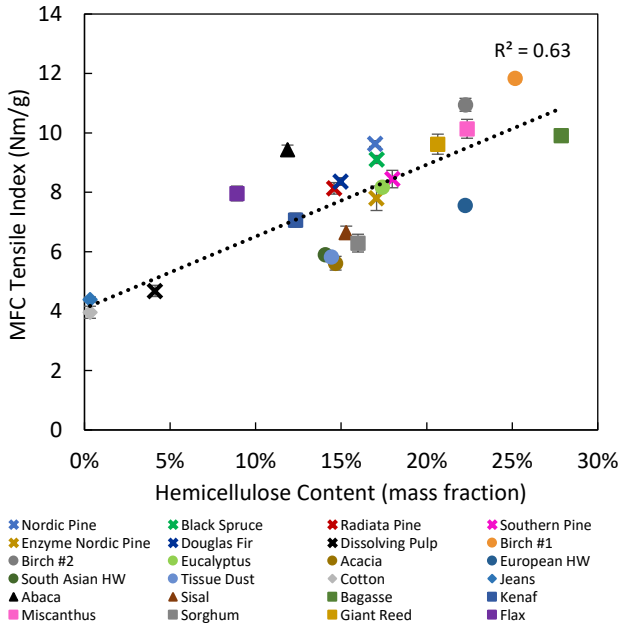

Fig. 1 **Fibre hemicellulose content (wt%) vs. tensile index at the selected energy input. For this figure and all subsequent plots, crosses represent softwoods, circles represent hardwoods, diamonds represent cotton fibres, triangles represent leaf fibres, and squares represent other miscellaneous non-wood sources**

Fig. 2(a) shows bagasse MFC, which had the highest hemicellulose content of any fibre tested, at 28%. There appears to be a much higher frequency of finer microfibrils in this case than dissolving pulp and cotton MFC, shown as Fig. 2(c) and Fig. 2(d), which have 4% and 0% hemicellulose respectively. Nordic pine MFC with a hemicellulose content of 17% is displayed as Fig. 2(b), and also shows a high abundance of fine microfibrils, though to a lesser extent than bagasse MFC.

A comparison of Fig. 2(b) and Fig. 2(c) is important; the dissolving pulp used in the latter is a Scandinavian pine/spruce blend, similar to the Nordic pine used in the former; the major difference is in their processing. The Nordic pine pulp underwent a kraft pulping process, which cannot penetrate well into the fibres to remove hemicellulose, whereas the dissolving pulp was pulped with the sulphite process, which is capable of this, removing the vast majority of the hemicellulose. Consequently, the fact that the liberated microfibrils in Nordic pine MFC tend to be much finer than with dissolving pulp MFC implies that the correlation of hemicellulose content with finer microfibrils is causal.

There is also the question of whether the two dominant types of hemicellulose found in these fibres, xylan and glucomannan, are equivalent in terms of enhancing microfibrillation. Correlations between MFC tensile strength and xylan or glucomannan alone, or a weighted sum of the two were investigated, but the best fit was found by treating the two as identical and correlating tensile strength with the sum of the two species. These data are displayed in the *Pulp Chemical Composition* tab in the *Supplementary Material*.

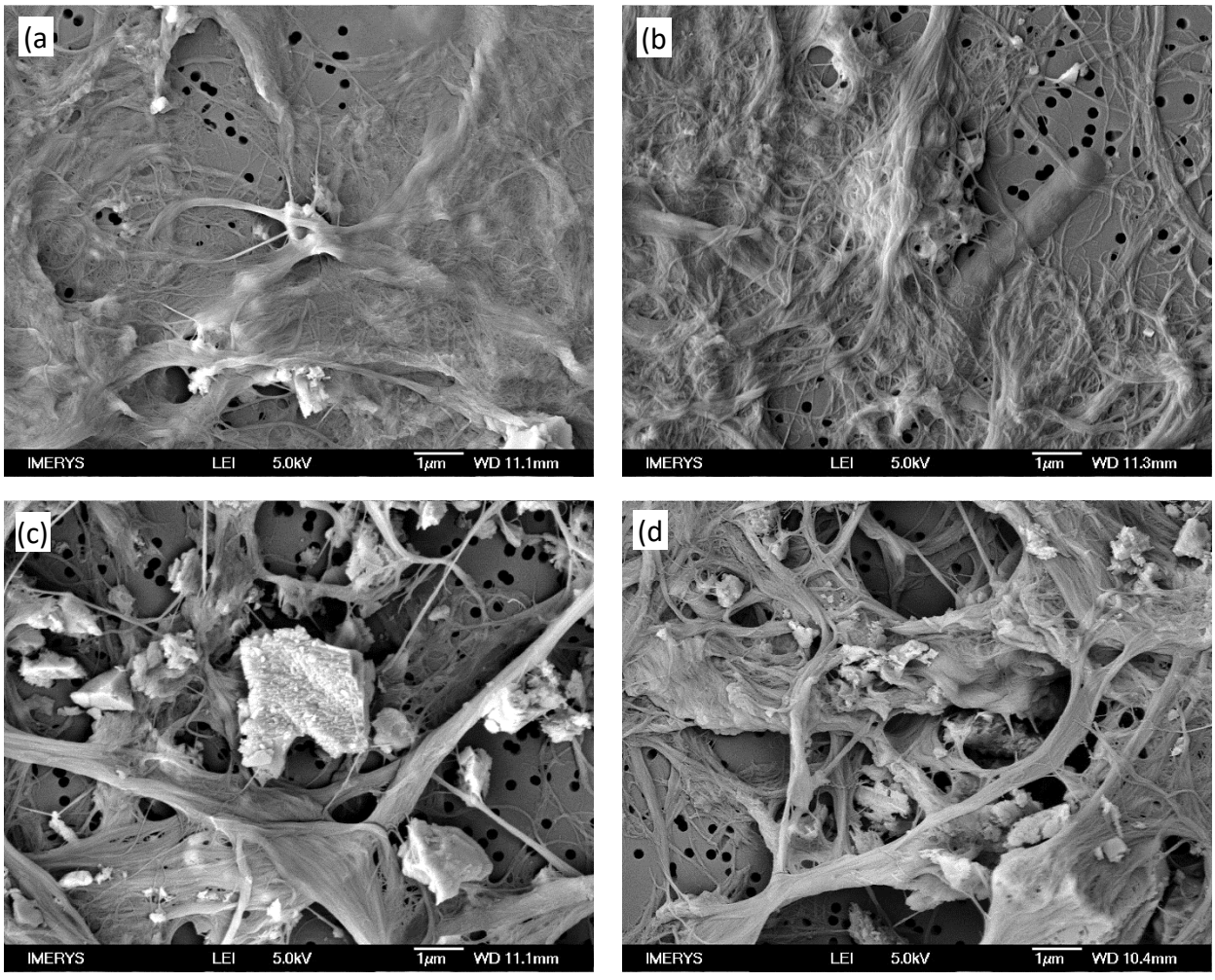

Fig. 2 **Secondary electron SEM images of MFC-mineral composite made from (a) bagasse (28% hemicellulose), (b) Nordic pine (17% hemicellulose), (c) dissolving pulp (4% hemicellulose) and (d) cotton (0% hemicellulose). The low hemicellulose fibres give coarser and more strongly defined fibrils and**

Influence of Lignin Content

Given that the influence of hemicellulose is established, it was an open question as to what the influence of the lignin content would be. For thermomechanical or chemithermomechanical pulp, there is an extensive lignin coating on the fibre surface, which seriously inhibits the ability of the fibre to fibrillate and form high quality MFC, at least for entirely mechanical processes (e.g. Meyer et al. 2018, Lahtinen et al. 2014). However the role of lignin

within the fibre cell wall is less clear, since good quality MFC can still be made at high lignin contents with unbleached chemical pulp (e.g. Spence et al. 2010).

Especially considering the numerous relatively novel non-wood pulps of unknown chemistry used in the present study, it was initially conceivable that differences in lignin content could be contributing to the noise seen in Fig. 1. The lignin contents of the fibre species used in this study were measured, and the results are shown in the *Pulp Chemical Composition* tab in the *Supplementary Material*. Lignin was found to be present only at very low concentrations in all samples, except Giant Reed, which contained 12.7% lignin and does not seem to perform unusually compared to other fibre species. Therefore, for this study, the influence of lignin on these results can be neglected.

Influence of Feed Fibre Geometry

Fibre geometry has a strong influence in tensile strength in paper made from cellulose fibres; all other things being equal, longer and thinner fibres result in higher tensile strengths because they maximise aspect ratio. Longer fibres increase the number of connections that each individual fibre can make, and thereby distribute stress over a larger area. Finer fibres (with a thinner cell wall) result in more fibres per unit mass. The fact that a high fibre aspect ratio leads to high sheet tensile strength has been found experimentally for both softwoods (Horn 1974) and hardwoods (Horn 1978). The Page Equation, shown as Equation [1] earlier in this paper, makes use of such fibre dimensions to model paper tensile strength.

Though established as true for fibres, the influence of feed fibre dimensions on MFC properties was an open question. It stands to reason that in the case of partially processed MFC where the initial fibre structure is partly intact that this would be somewhat accurate, but it is intuitive that as the fibre structure degrades into fully processed MFC, that such a correlation would disappear. It was not ruled out, however, that the dimensions of the fibre such as length or cell wall thickness affect how the fibre disintegrates into MFC.

Geometric parameters of the fibres were measured using a fibre image analyser, including length and length distributions, widths, and coarseness (a measure of fibre wall cross sectional area). Attempts were made to plot such geometric parameters against tensile index, and no clear correlation was apparent. The geometry of the feed fibres is therefore not thought to have any obvious influence on the quality of fully processed MFC. The geometric parameters measured by the fibre analyser and their near-zero correlations with MFC tensile strength are displayed in the *Pulp Geometry* tab in the *Supplementary Material*.

Influence of MFC Length

Stirred media detritor grinding produces MFC mostly in the form of fibril 'aggregate' particles rather than fully individualised fibrils, i.e. the fibrils are liberated from the fibre, but are imperfectly separated from their neighbours and so are physically rooted to other fibrils to form a network (The *Microscopy* tab in the *Supplementary Material* gives several examples of what this looks like for different fibre species). These particles are large enough to have some geometric properties inferred from measurement in the fibre analyser. In this study, the length-weighted fibre length of these MFC particles, called from here onwards *MFC length* was found to be useful. The fibre analyser interprets the 'fibre length' in this case as the longest dimension of an MFC particle. When plotting MFC length against MFC tensile index for all fibre species, there is no general correlation, but for fibres of a similar hemicellulose content, there appears to be a clear positive trend (see Figure D1 in the *MFC Correlation Investigation* tab in the *Supplementary Material*). Therefore, using the product of hemicellulose and MFC length to predict tensile index appeared promising.

In order to have some theoretical grounding for this correlation, the Page Equation was used as a starting point. The Page Equation, shown as Equation [1] in the introduction, was formulated to predict tensile strength for straight, individualised fibres with lengths on the scale of millimetres, when formed into a mineral-free sheet. It is not obvious whether this would be directly applicable to MFC nanopaper, which is in the form of highly entangled and conformable, physically connected networks of fibrils, and in this study forms a composite that is 80% paper filler mineral. However, the Page Equation is conceptually useful since parameters such as fibre length and relative bonded area are expected to be applicable in a similar way to this MFC-mineral composite nanopaper. This

equation will be used to justify a semi-empirical model to predict MFC tensile strength using hemicellulose and MFC length.

It stands to reason that as relative bonded area increases greatly with MFC production, the bonding term of the Page Equation becomes less limiting, and strength would eventually be dominated by the zero-span term representing fibre or fibril breakage if fibrillation is extensive enough. For chemical-treated nanocellulose (i.e. TEMPO MFC) with very fine microfibrils and very extensive bonding, this may be the case, but at least for the relatively coarse mechanically processed FiberLean MFC under consideration, further work not published here shows that this limit is not reached. It was found that the tensile strength of MFC produced using this method varies strongly with mineral content, demonstrating that bonding failure is still important.

Additionally, the zero-span tensile strength of the MFC at 50 dry wt.% mineral was measured, and for most fibre species was over 2.5 times the long span tensile strength of the MFC, when normalised by fibre content. This MFC zero-span tensile strength was also found to vary strongly with mineral content, implying that bonding failure was not completely suppressed (likely because smaller MFC particles are more prone of slipping out of the gap between the clamps). The notion that MFC fails mainly by network failure even in a zero-span tensile test is supported by electron microscopy of breakage sites by Varanasi et al. (2012). This makes the measured MFC zero-span strength a gross underestimate of the true value, and so fibril failure is responsible for much less than 40% of the breakage.

Therefore, the fibre weakness term will be assumed to be zero as the MFC zero-span tensile strength is believed to be much higher than the bonding strength. The Page Equation is therefore reduced to:

$$\frac{1}{T} = \frac{12A\rho}{\tau_B PL(RBA)} \dots [2]$$

Hemicellulose on microfibril surfaces would be expected to increase relative bonded area since extended hemicellulose chains allows for more extensive and intimate contact between microfibrils. Additionally, hemicellulose appears to result in finer microfibrils when MFC is produced. Finer diameter microfibrils could be expected to be more flexible, and so be more capable of deforming for a more intimate contact with other particles. It is also expected that finer microfibrils would be more susceptible to capillary forces drawing them in contact with other surfaces during drying. These effects would imply that a high hemicellulose content would lead to a high relative bonded area. It is conceivable that these same factors could lead to a higher specific bond strength τ_B within a given region of bonded area (i.e. more hemicellulose chains likely means a higher fraction of the bonded area in *molecular* contact).

The perimeter to cross-sectional area ratio, *P/A*, would also correlate with increased bonding; since this increases as fibril diameter decreases, this would also correlate with hemicellulose content. Though *P/A*, *RBA*, and τ_B are all believed to be influenced by hemicellulose content, their relative influences cannot be distinguished. If hemicellulose correlated linearly with all three, then it would be expected that, all other things being equal, tensile index would be proportional to the cube of the hemicellulose content; however, Fig. 1 shows that this correlation is linear, and the maximum R^2 value of the fit between hemicellulose and MFC tensile strength was obtained with a hemicellulose exponent value close to unity. Therefore, rather than distinguishing between the three, the *RBA* term, the *P/A* term, and the τ_B term in the denominator of the Page Equation are replaced with the hemicellulose content *H* in Equation [3] below. Since the larger MFC particles are the primary load-bearing particles, the corresponding MFC length term L_{MFC} is expected to be analogous to the fibre length term *L* in the Page Equation, and so this substitution is also made:

$$\frac{1}{T} = k\frac{12\rho}{L_{MFC}H} \dots [3]$$

where *k* is a proportionality constant. Density ρ is constant for all MFC, so can be combined with *k* under a single coefficient B_1:

$$\frac{1}{T} = \frac{1}{B_1 L_{MFC} H} \ldots [4]$$

which can be inverted to obtain the MFC tensile index:

$$T = B_1 L_{MFC} H \ldots [5]$$

The product of L_{MFC} and H was calculated for all fibre sources and plotted against MFC tensile index in Fig. 3. As can be seen, the fit to a general straight line is much better when MFC length is included in this analysis compared to just hemicellulose content alone, with the R^2 improving from 0.63 to 0.87. However, this fit requires an intercept that is not accounted for in Equation [5]. This intercept is at least in part because fibrillation can take place in the absence of hemicellulose, as the cotton linter and jeans MFC demonstrate. Other contributions to this intercept may be due to some of the assumptions being inaccurate, for example if the contribution of fibre weakness to the strength was significant, or if the tensile strength at 80% mineral loading was not directly proportional to mineral-free tensile strength for all samples. Despite this, the fit is good, and so an empirical residual strength term, σ_0, is added to Equation [5], representing at least in part the MFC tensile strength when hemicellulose is absent.

$$T = B_1 L_{MFC} H + \sigma_0 \ldots [6]$$

Fig. 3 gives σ_0 a value of 4.1 Nm/g on a basis of the fit with the twenty-four fibre sources tested.

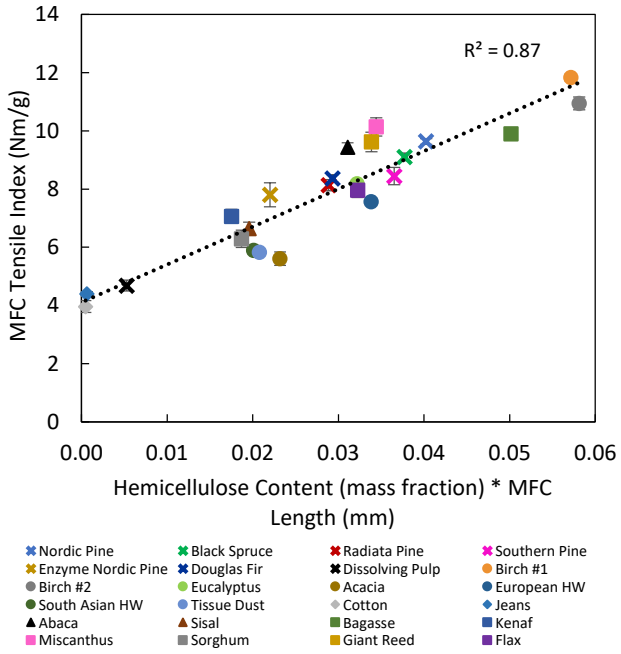

Fig. 3 **Tensile index vs. the product of the hemicellulose content and the MFC length**

Despite the good fit, using the MFC length in order to shortlist which fibre sources are worth using as a feed source is impractical; the MFC must first be created to obtain this length value, and so this only reduces the need of the tensile test, saving little effort overall. Instead, it is more useful to identify the reasons behind why different fibres give MFC of different MFC particle lengths, and relate this to a parameter that can be measured in the unprocessed fibres.

Influence of Fibre Zero-Span Tensile Index

It stands to reason that if the fibrils that form the cell wall are long, that once the fibre is disintegrated the liberated fibrils will also be long. Additionally, a greater number of flaws in the fibril structure would make breaking the fibril (and the larger scale fibre) across the cross-section easier. Therefore, a fibre that has intrinsically long fibrils

with few discontinuities and cross-sectional flaws would be expected to produce long fibrils when ground down into MFC, and would therefore give a relatively high MFC particle lengths as measured by the fibre analyser. As discussed in the introduction, the zero-span tensile test gives an indication of the frequency of these flaws by forcing fibres to break across their cross section, with a high value indicating a lack of flaws and discontinuities.

Fig. 4 shows the correlation between the fibre zero-span tensile index and the fibre length of the resultant MFC. There appears to be a linear relation between these two parameters when considering most fibre species, although there are several exceptions that deviate significantly, including flax, sisal, and kenaf.

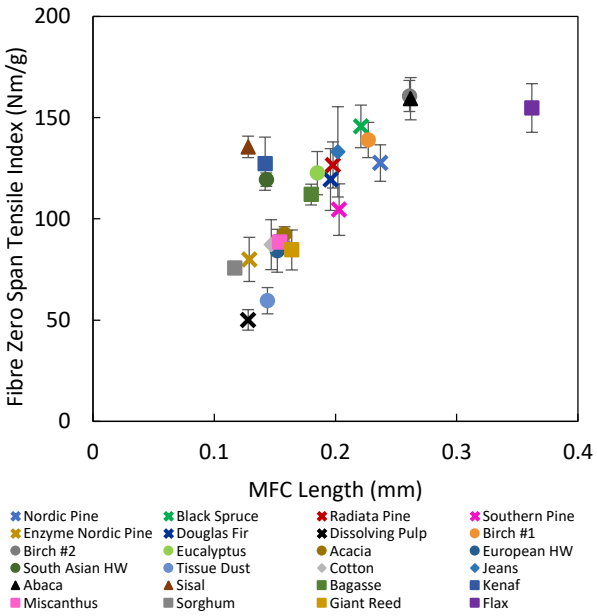

Fig. 4 **The relationship between the zero-span tensile index of unground fibres and the resultant MFC**

The zero-span tensile test is not solely a measure of fibre and fibril damage. A good correlation has been found between the microfibril angle and the zero-span tensile strength, at least with fibres that are relatively undamaged by processing (Courchene et al. 2005). This agrees with data and theoretical modelling from El-Hosseiny et al. (1975). However, the microfibril angle is not expected to directly influence intrinsic fibril lengths or frequency of fibril damage, and it would therefore be surprising if it influences fibril length in MFC. Although easy to measure in wood, the microfibril angle is difficult to measure accurately in pulped fibres, and so was not attempted in this study, particularly because it is impractical in an industrial setting. This is likely a significant cause of some of the data spread seen in Fig. 4.

Despite this complication, the fit between MFC length and zero-span tensile index for most fibre species appears sufficient for most of the other fibre species to use zero-span tensile index as a replacement for MFC length in Equation [6]. This equation is therefore modified below:

$$T = B_2 Z H + \sigma_0 \ldots [7]$$

where Z represents the zero-span tensile index of the fibre and B_2 is a proportionality coefficient. Fig. 5 shows the correlation between the product of the fibre zero-span tensile index and hemicellulose content, with the MFC tensile index.

As Fig. 4 shows, the assumption that fibre zero-span tensile index correlates with MFC length is not completely accurate, so it is not surprising that the fit shown in Fig. 5 for Equation [7] ($R^2 = 0.78$) is poorer than when MFC length was used ($R^2 = 0.87$). Although this relationship fits well considering the extremes, towards the centre of the graph certain fibre species such as miscanthus, abaca, and sisal deviate considerably from the best fit curve.

A particularly notable comparison can be made between Nordic pine and enzyme-treated Nordic pine fibres, which are essentially identical in all ways measured *except* the zero-span tensile index, which has been greatly degraded

in the case of the latter. The enzyme-treated variant consequently has much lower MFC particle length and lower MFC tensile strength. This is evidence that the correlation seen with zero-span tensile index is causal.

Despite the increase in data spread compared to when MFC length is used directly, Fig. 5 shows a good fit for most fibre species, and this relationship comes with the important advantage that both predictive parameters are fibre properties that can be measured relatively easily without having to produce the MFC first. This relationship would be a practical tool for shortlisting a large number of fibre species, in order to determine which are worth pursuing to use as a feed for MFC production.

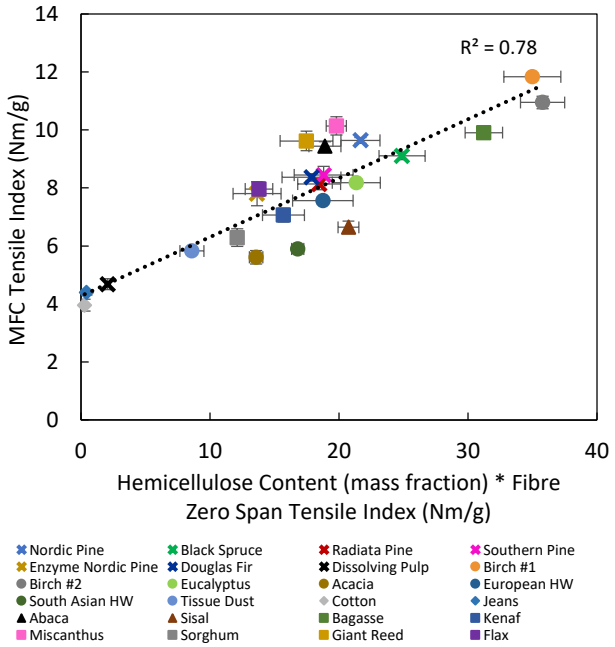

Fig. 5 **The correlation between the product of the hemicellulose content and zero-span tensile index of the unground fibres, with the resultant MFC tensile index when ground to the standard energy input**

Conclusions

In this work, microfibrillated cellulose was produced from twenty-four fibre species using a stirred media detritor. The product was used in a composite with calcium carbonate mineral to form nanopaper sheets, which were tested to assess the tensile index. The hemicellulose content of the fibres prior to MFC production was measured and was found to correlate moderately with the tensile index of the respective MFC produced. Additionally, SEM images show that higher hemicellulose fibres result in the liberation of microfibrils with finer widths, which is consistent with what others have reported using alternative MFC production methods.

Various geometric parameters of the fibres such as length and width were measured with a fibre analyser and did not correlate with the MFC tensile index. However, measurements of the apparent length of the MFC product particles were taken with this equipment, and multiplying this length by the hemicellulose content resulted in a parameter that correlated strongly with MFC tensile index. The Page Equation was applied and modified to give this correlation some theoretical basis, with some of the parameters in the bonding term being substituted with hemicellulose content and MFC length. It was found that the addition of a constant σ_0 to represent the residual strength in the absence of hemicellulose was required for the model to fit the data.

In order to make this model useful, the zero-span tensile strength of the initial fibres was used as a proxy for the MFC length, since it appears that the frequency of flaws in the fibril structures that is represented by the zero-span tensile strength affects the particle lengths when MFC is produced. This replacement resulted in a weaker fit, but still a substantial improvement over hemicellulose content alone. From this work, it is shown that measurements of the hemicellulose content and zero-span tensile strength of pulp fibres can be used for a reasonably accurate

prediction of the resultant MFC tensile strength, providing a facile method to aid in the selection of cellulose sources for use as a feedstock for microfibrillated cellulose production.

Conflict of Interest: The authors declare that they have no conflict of interest.

References

Alila S, Besbes I, Vilar M R, Mutjé P, Boufi S (2013) Non-woody plants as raw materials for production of microfibrillated cellulose (MFC): a comparative study. Ind Crop Prod 41:250-259

Arola S, Malha J M, Laaksonen P, Lille M, Linder M B (2013) The role of hemicellulose in nanofibrillated cellulose networks. Soft Matter 9:1319-1326

Bolam F M (1965) Stuff Preparation for Paper and Paperboard Making: Monographs on paperboard and papermaking. Pergamon

Chaker A, Alila S, Mutjé P, Vilar M R, Boufi S (2013) Key role of the hemicellulose content and the cell morphology on the nanofibrillation effectiveness of cellulose pulps. Cellulose 20(6):2863-2875

Chinga-Carrasco G (2011) Cellulose fibres, nanofibrils, and microfibrils: The morphological sequence of MFC components from a plant physiology and fibre technology point of view. Nanoscale Res. Lett. 6:417

Courchene C E, Peter G F, Litvay J (2006) Cellulose microfibril angle as a determinant of paper strength and hygroexpansivity in Pinus Taeda L. Wood Fiber Sci 38(1):112-120

Desmaisons J, Boutonnet E, Rueff M, Dufresne A, Bras J (2017) A new quality index for benchmarking of different cellulose nanofibrils. Carbohydr Polym 174:318-329

Duchesne I, Hult E, Molin U, Daniel G, Iversen T, Lennholm H (2001) The influence of hemicellulose on fibril aggregation of kraft pulp fibres as revealed by FE-SEM and CP/MAS 13C-NMR. Cellulose 8(2):103-111

Ebringerová A (2005) Structural Diversity and Application Potential of Hemicelluloses. Macromol Symp 232(1):1-12

El-Hosseiny F, Page D H (1975) The mechanical properties of single wood pulp fibres: Theories of strength. J Fiber Sci Technol 8(1):21-31

Fengel D, Wegener G (1983). Wood – chemistry, ultrastructure, reactions. De Gruyter

Herrick F W, Casebier R L, Hamilton J K, Sandberg K R (1983) Microfibrillated Cellulose: Morphology and accessibility. J Appl Polym Sci: Appl Polym Symp 37:797-813

Horn R A (1974) Morphology of pulp fiber from softwoods and influence on paper strength. Research Paper FPL 242, Forest Product Laboratory, Forest Service, United States Department of Agriculture

Horn R A (1978) Morphology of pulp fiber from hardwoods and influence on paper strength. Research Paper FPL 312, Forest Product Laboratory, Forest Service, United States Department of Agriculture

Hult E -L, Larsson P T, Iversen T (2001) Cellulose fibril aggregation – an inherent property of kraft pulps. Polymer 42(8):3309-3314

Husband J C, Svending P, Skuse D R, Motsi T, Likitalo M, Coles A, Fiberlean Technologies Ltd. (2015) Paper filler composition. U.S. Pat. US9127405B2

Iwamoto S, Abe K, Yano H (2008) The Effect of Hemicelluloses on Wood Pulp Nanofibrillation and Nanofiber Network Characteristics. Biomacromolecules 9(3):1022-1026

Jonoobi M, Oladi R, Davoudpour Y, Oksman K, Dufresne A, Hamzeh Y, Davoodi R (2015) Different preparation methods and properties of nanostructures cellulose from various natural resources and residues: a review. Cellulose 22(2):935-969

Joutsimo O, Wathén R, Tamminen T (2005) Effects of fiber deformations on pulp sheet properties and fiber strength. Paperi Ja Puu/Paper and Timber 87(6)

Klemm D, Heublein B, Fink H P, Bohn A (2005) Cellulose: Fascinating Biopolymer and Sustainable Raw Material. Angew Chem Int Ed 44(22):3358-3393

Klemm D, Kramer F, Moritz S, Lindström T, Ankerfors M, Gray D, Dorris A (2011) Nanocelluloses: A New Family of Nature-Based Materials. Angew Chem Int Ed 50(24):5438-5466

Lahtinen P, Liukkonen S, Pere J, Sneck A, Kangas H (2014) A Comparative Study of Fibrillated Fibers from Different Mechanical and Chemical Pulps. BioResources 9(2):2115-2127

Liitiä T, Maunu S L, Hortling B, Tamminen T, Pekkala O, Varhimo A (2003) Cellulose crystallinity and ordering of hemicelluloses in pine and birch pulps as revealed by solid-state NMR spectroscopic methods. Cellulose 10(4):307-316

Lindström T, Fellers C, Ankerfors M, Nordmark G G (2016) On the nature of joint strength of paper – effect of dry strength agents – Revisiting the Page equation. Nord Pulp Pap Res J 31(3):459-468

Mäkelä P, Bergnor E, Wallbäcks L, Öhman F (2010) Sorption of birch xylan to softwood kraft pulps and its influence on the tensile properties of previously-dried papers under different papermaking conditions. Innventia Report No. 121 2nd Version

Meyer V, Lecourt M, Tapin-Lingua S, Petit-Conil M (2018) Production of Microfibrillated Cellulose (MFC) from Chemical and Mechanical Pulps to Enhance TMP and DIP Paper Properties. Cellulose 72(3):6-16

Nevell T P, Nugawela D (1987) Effect of treatment with very dilute acids on the wet tensile strength and chemical properties of paper. Carbohydr Polym 7(3):169-181

Page D H (1969) A theory for the tensile strength of paper. Tappi J, 52(4):674-681

Petroudy S R D, Ghasemian A, Resalati H, Syverud K, Chinga-Carrasco G (2015) The effect of xylan on the fibrillation efficiency of DED bleached soda bagasse pulp and on nanopaper characteristics. Cellulose 22(1):385-395

Phipps J, Larson T, Ingle D, Eaton H (2017) The Effect of Microfibrillated Cellulose on the Strength and Light Scattering of Highly Filled Papers. In: Batchelor W, Söderberg D (eds) Advances in Pulp and Paper Research: Transactions of the 16th Fundamental Research Symposium 231-254

Prado K S, Spinacé M A S (2015) Characterization of Fibers from Pineapple's Crown, Rice Husks and Cotton Textile Residues. Mat. Res. 18(3):530-537

Scandinavian Pulp, Paper and Board Testing Committee (2009) Carbohydrate Composition. Test Method SCAN CM-71:09

Shatkin J A, Wegner T H, Bilek E M, Cowie J (2014) Market projections of cellulose nanomaterial-enabled products – Part 1: Applications. TAPPI J 13(5):9-16

Siró I, Plackett D (2010) Microfibrillated cellulose and new nanocomposite materials: a review. Cellulose 17(3):459-494

Spence K L, Venditti R A, Habibi Y, Rojas O J, Pawlak J J (2010). The effect of chemical composition on microfibrillar cellulose films from wood pulps: Mechanical processing and physical properties. Bioresour Technol 101(15):5961-5968

Technical Association of the Pulp and Paper Industry (1988) Acid-Insoluble Lignin in Wood and Pulp. Test Method T 222 om-88

Technical Association of the Pulp and Paper Industry (2007) Zero-span breaking strength of pulp (dry zero-span tensile). Test Method T 231 cm-07

Technical Association of the Pulp and Paper Industry (2012) Forming Handsheets for Physical Tests of Pulp. Test Method T 205 cm-12

Turbak A F, Snyder F W, Sandberg K R (1983) Microfibrillated cellulose, a new cellulose product: properties, uses, and commercial potential. J Appl Polym Sci: Appl Polym Symp 37:815-827

Uetani K, Yano H (2012) Zeta Potential Time Dependence Reveals the Swelling Dynamics of Wood Cellulose Nanofibrils. Langmuir 28(1):818-827

Varanasi S, Chiam H H, Batchelor W (2012) Application and interpretation of zero and short-span testing on nanofibre sheet materials. Nord Pulp Pap Res J 27(2):343-506

Virtanen T, Maunu S L, Tamminen T, Hortling B, Liitiä T (2008) Changes in fiber ultrastructure during various kraft pulping conditions evaluated by 13C CPMAS NMR spectroscopy. Carbohydr Polym 73(1):156-163

Wathén R (2006) Studies on fiber strength and its effect on paper properties. PhD Thesis, King's College London. ISSN 1457-6252

Zeng X, Retulainen E, Heinemann S, Fu S (2012) Fibre deformations induced by different mechanical treatments and their effect on zero-span strength. Nord Pulp Pap Res J 27(2):335-342